TU Clausthal
Clausthal University of Technology

Habilitationsschrift

Modeling of solid fuel conversion processes for CFD applications

zur Erlangung der Lehrbefugnis für das Fachgebiet
Hochtemperaturverfahrenstechnik

vorgelegt von
Marco Mancini
Dr.-Ing. habil.
aus Lucca (Italien)

Institut für Energieverfahrenstechnik und Brennstofftechnik
der Technischen Universität Clausthal

Fakultät für Energie- und Wirtschaftswissenschaften

Tag der Probevorlesung
02 Juli 2019

Version: 20th December 2019

Modeling of solid fuel conversion processes for CFD applications

Dr.-Ing. habil. Marco Mancini

Clausthal University of Technology

Institute for Energy Process Engineering and Fuel Technology

Agricolastrasse 4, 38678 Clausthal-Zellerfeld, Germany

20th December 2019

Contents

Abstract

The utilization of fossil fuels in industrial processes is not only reduced to the field of combustion but is extended to other various technologies in which biomass or wastes are converted into more easily usable gases.

The massive use of computers in today's engineering requires flexible but accurate tools for calculating important quantities (for example the conversion level or the thermal efficiency of specific reactors. Numerical simulations based on Computational Fluid Dynamic (CFD) software are the fundamental step towards such a tool since improvements in energy efficiency, fuel flexibility and capital effectiveness of modern solid fuel boilers as well as gasifiers, increasingly rely on CFD modeling. The accuracy of CFD calculations is often limited by the lack of knowledge of fundamental conversion rate parameters since the need for efficiency improvements is pushing the technologies towards higher temperatures and higher pressures, where measurements and modeling reach their limit of validity and accuracy.

The primary objective of this work is then to explain and demonstrate how the CFD tool can be helpful in predicting solid fuel conversion for industrial applications with emphasis on high temperatures and high pressures processes. Attention will be given to the theory and the modeling needed for the description of the conversion of the solid. Since solid fuels are complex and heterogeneous, there is no single theory able to explain and predict all aspects of the complex thermo-chemical changes involved.

In many situations, we must, therefore, rely on measurements to generate the parameters needed to feed the model. The correct mathematical analysis of those experiments is of fundamental importance for the further CFD calculation. It will be shown that CFD can help the analysis also of this preparatory step.

Finally, it will be demonstrated that a high level of knowledge (and accuracy) is still nowadays a challenge for modeling. Detailed chemistry and high-performance computing are required, but also turbulence modeling must be improved. More sophisticated models and more advanced approaches can now be used since computer technology is so developed that memory, speed and parallelization are easily obtainable. Following the advance in computing power, models can be refined in such details that they can be of use also in the interpretation of measured data.

A well-established procedure in fuel characterization and solid fuels modeling at the Institute for Energy Process Engineering and Fuel Technology of The Clausthal University of Technology is based on the synergy between experiments and theory, in which both methods provide a substantial contribution to achieving the highest level of the description. The chapters of this book show examples and contain detailed information concerning the above-introduced methodology.

Zusammenfassung

Die Nutzung fossiler Brennstoffe in industriellen Prozessen beschränkt sich nicht nur auf den Bereich der Verbrennung, sondern erstreckt sich auch auf andere verschiedene Technologien, bei denen Biomasse oder Abfälle in leichter verwertbare Gase umgewandelt werden.

Der massive Einsatz von Computern in der heutigen Technik erfordert flexible, aber genaue Werkzeuge zur Berechnung wichtiger Größen (z. B. die Umwandlung eines Einsatzstoffes oder den thermischen Wirkungsgrad bestimmter Reaktoren). Numerische Simulationen mit Hilfe von CFD-Software (Computational Fluid Dynamic) sind der grundlegende Schritt in Richtung eines solchen Werkzeugs, da Verbesserungen der Energieeffizienz, der Brenn- stoffflexibilität und der Kapitaleffizienz moderner Anlagen (sowohl Kessel als auch Vergaser) sich zunehmend aus der CFD-Modellierung ergeben. Die Genauigkeit von CFD-Berechnungen wird oft durch die mangelnde Kenntnis grundlegender Umwandlungsgeschwindigkeitsparameter beschränkt. Der Bedarf an Effizienzverbesserungen treibt die Technologien in Richtung höherer Temperaturen und höherer Drücke, bei denen Messungen und Modellierungen an ihre Gültigkeits- und Genauigkeitsgrenzen stoßen.

Das Hauptziel dieser Arbeit ist es dann zu erklären und zu demonstrieren, wie das CFD-Tool funktioniert und bei der Vorhersage der Umwandlung fester Brennstoffe für industrielle Anwendungen hilfreich sein kann, wobei der Schwerpunkt auf Prozesse mit hohen Temperaturen und hohen Drücken liegt. Es wird auf die Theorie und die Modellierung geachtet, die für die Beschreibung der Umwandlung des Feststoffes erforderlich ist. Da feste Brennstoffe komplex und heterogen sind, gibt es nicht nur eine einzige Theorie, die alle Aspekte der komplexen thermochemischen Veränderungen erklären und vorhersagen kann.

In vielen Situationen müssen zur Versorgung des Modells daher Parameter aus Messungen benutzt werden. Die korrekte mathematische Analyse dieser Experimente ist für die weitere CFD-Berechnung von grundlegender Bedeutung. Es wird gezeigt, dass CFD auch die Analyse dieses Schritts unterstützen kann.

Abschließend soll gezeigt werden, dass ein hohes Maß an Wissen (und Genauigkeit) auch heute noch eine Herausforderung für die Modellierung darstellt. Detaillierte Chemie und Hochleistungsrechner sind erforderlich, aber auch Turbulenzmodellierung muss verbessert werden. Weiterentwickelte Modelle und fortgeschrittenere Ansätze können jetzt verwendet werden, da die Computertechnologie so entwickelt ist, dass Speicher, Geschwindigkeit und Parallelisierung leicht erhältlich sind. Durch den Fortschritt in der Rechenleistung, können Modelle soweit verfeinert werden, dass sie auch bei der Interpretation von Messdaten von Nutzen sein können.

Ein etabliertes Verfahren zur Brennstoffcharakterisierung und Modellierung fester Brennstoffe am Institut für Energieverfahrenstechnik und Brennstofftechnik der Technischen Universität Clausthal, basiert auf der Synergie zwischen Experimenten und Theorie, bei denen beide Methoden einen wesentlichen Beitrag zur Erreichung der höchsten Genauigkeit leisten. Die Kapitel dieses Buches zeigen Beispiele und enthalten detaillierte Informationen zur oben eingeführten Methodik.

1. Introduction

1.1. Energy demand

Human activity needs energy, and this energy must be provided in various forms to be converted into heat, electricity, and work. The estimated amount of energy consumed in the World in 2013 is $E = 510\ \frac{\mathrm{EJ}}{\mathrm{a}}$ (see for more details [313]) while for Germany the consumption amounts to $E = 14.3\ \frac{\mathrm{EJ}}{\mathrm{a}}$. Estimating a World population of about 6974 million and a German population of 81.73 million, the energy demand pro capita amounts to 1.74 TOE (Tonne of Oil Equivalent) [1] for the World and 4.17 TOE for Germany. Referring to Table 1 in the cited reference [313], without any attempt for interpretation, it is possible to see that the primary energy demand depends strongly on the country, being equal to 7.87 TOE per person for the USA with a total amount $E = 103\ \frac{\mathrm{EJ}}{\mathrm{a}}$) and 0.1 TOE per person for Kenya with a total amount $E = 0.2\ \frac{\mathrm{EJ}}{\mathrm{a}}$.

In Germany, the distribution of the primary energy demand among various energy sources is as follows: renewable 11.7%, nuclear 7.5%, crude oil 32% and coal 24%. Still for Germany, it is interesting to note that 32% of the primary energy is from own resources, the rest being imported.

Energy is not used directly in its primary (as received) form but must be converted into secondary energy forms, like Coke, Oil, Benzine, Briquets, Electricity. Only around 65% of the primary energy is available, as secondary energy, to the end user. This loss is due partly to the efficiency of the conversion process from primary to secondary energy (mainly electrical energy production in conventional power stations), and partly it is due to losses during transportation.

Primary energy consumption can be divided into four sectors:

1. Electricity production;
2. High temperature industrial processes for production of materials (steel, glass, cement, ceramics);
3. Transport;
4. Heating in households.

The resulting available energy used in Germany in the 2014 it for the aforementioned sectors is shown in Table 1.1.

From the above table, it is possible to observe that the direct use of coal is almost exclusively in the industry (direct firing of coal), while most of the oil is used in the transportation sector as petrol, diesel, gasoline). Among those sectors a particularity important place is taken by electricity production. In Germany electricity production is based (2014 date) on fossil fuels 51%, nuclear plants 18% and renewable energy (wind, biomass, solar and a smaller portion of hydropower) 31%.

The process of *Energiewende* (energy transition from fossil to renewable) is defined in the key policy document published by the German Government in September 2010 and legislative support was passed in 2011. Important aspects include:

[1] TOE = tonne of oil equivalent $= 10^{18}$ J

	Industry	Transportation	Residential	Commerce	Total
EJ	2.599	1.397	2.571	2.431	8.998
TWh	722	714	675	388	2499
%	28.9	28.6	27.0	15.5	100
Coal	4.1	0.0	0.6	0.2	4.8
Oil	0.9	26.2	5.6	3.3	36.0
Gas	10.4	0.4	10.1	4.9	25.8
Electricity	9.0	0.7	5.5	5.6	20.8
Renewable	1.9	0.0	1.9	1.1	4.9
Other	1.4	1.3	3.4	0.5	6.5

Table 1.1.: End-user energy demand in Germany in 2014 [313]

- 80% greenhouse gas reduction by 2050;
- 100% share of renewable energy by 2050 in electricity production;
- Electricity production efficiency up to 50% by 2050;
- An associated research and development drive.

The following technological changes should achieve those goals:

- Shut down nuclear power stations;
- Reduction of number of conventional power stations (first of all coal power stations);
- Increase the development of electric cars (electromobility);
- Improvement of efficiencies (power plants, energy savings in buildings);
- Development of new technologies for energy conversion.

1.2. Energy consumption reduction

Energy consumption reduction is one of the big challenges that all nations have to aim at in the near future. Reducing the amount of energy needed by a country increases the possibility of that nation to have a more florid future, with fewer concerns about the energy availability and more opportunities to enjoy life in a less polluted environment.

If the challenge is extended to the entire World, less energy consumption (mainly in the industrialized countries) will open the possibility for a fairer development in the young economies providing, as a direct effect, more sustainability and social equality.

On the other side, energy reduction cannot be achieved by just closing down industrial sectors or just by decreasing the standard of living, because such changes will turn up against the society itself, creating even more social differences and creating more friction among nations. Therefore, a balanced and sustainable way to create a nicer place to live for everybody is the development of more advanced technologies or even entirely new technologies, that will combine a clean environment with a still acceptable style of living. Together with new processes and new energy sources, the increase of efficiency for existing processes must be put in place. This option

also creates advantages that can be immediately implemented on already existing technologies, building up an instant comfort and saving energy for the future generations.

As already seen before, in Germany, the primary energy consumption sectors absorb each around 25% of the primary energy demand therefore, to reduce the global amount of resources used, all four sectors must be considered as potential sources of savings. For a better understanding of the restructuring of the energy demand, it must be taken into consideration that each sector has a specific characteristics and some methods may work well to reduce energy for one application but they could not work well, or even have adverse effects, in other areas. The thermodynamic approach, increasing the thermal efficiency, is a valid method applicable to all of the four sectors.

Specifically, energy savings in high-temperature processes for the production of materials (steel, cement, glass) has high potential to be a driving force in reducing energy consumption, since the thermal efficiencies in those processes are relatively low due to a high temperature at the furnace outlet and high energy losses.

This situation opens options for large improvements. Moreover, those processes require a high amount of energy, and even a small relative reduction in energy consumption (or increase in efficiency) provides considerable absolute savings.

Specifically in Germany, the *Energiewende* gives an extra impulse to the development of different technologies but the will to drastically reduce CO_2 emissions increases the challenges for many industrial sectors, reducing the available technical and economical options.

1.3. Modeling and simulation

Two methods are generally considered while examining when technological changes can lead to a positive outcome in the processes: experimentation and modeling.

Experiments must satisfy several requirements to obtain valid information about a certain process but the fundamental assumption is that observed variables are solely affected by the controlled variables. Controlled variables (like the temperature in a TGA test) are variables that, inside a specific range, can be freely imposed by the experimenter and observed variables are those that can be measured, directly or indirectly. The validity of the imposed conditions on controlled variables must be continuously checked during the tests, and in many circumstances, it becomes difficult to enforce that the measurements are not affected by unwanted external influences. Even if all those influences are kept under control, measurements are always affected by uncertainties and statistical errors. Therefore to minimize them and reduce possible biases, a sufficient number of tests must be performed, all under the same controlled conditions. When correctly performed, experiments allow direct observations that can be employed in understanding a particular process, or in extracting parameters to be used in the model. Ideally, within a given (and often known) range of conditions, the observations are believed to be independent on a particular experimental setup. The observations can be generalized and used in mathematical models that combine them with other phenomena.

On the other side, modeling and simulations are nowadays a primary tool for achieving improvements in industrial technologies where theoretical calculations must be performed:

1. before the implementation of changes aiming at thermal efficiency improvements;
2. before the utilization of new fuels;
3. before the development of new technologies.

The two most typical questions about modeling and experiments can be summarized as follow [87]:

1. If the device is working, why to take the effort to simulate its performance?
2. Is it not possible to find an optimum performance just by experimentation?

The answers to both questions are somehow linked, and they are based on the fundamental difference between experiment and theory. In conjunction with the second question, it has to be considered that experimental methods, as previously stated, have limitations in the number of possible quantities that can be measured and on many occasions, experiments are more expansive than modeling. In conjunction with the first question, it is worth noticing that mathematical modeling can help a deep understanding of a process. Mathematical modeling gives access to much more data than experiments, and after analyzing the amount of data, insight about critical or problematic features can be obtained. We will apply this way of thinking to the analysis of the experimental facilities used to measure properties of solid fuels. In fact, it is essential to be able to answer the fundamental question concerning the relationship between theory and experiments: *When measurements have been performed, what exactly has been measured?* Or posed in a way less biased towards theoreticians: *How modelers can use what has been measured?*

The answer to the question of what has been measured is of high importance for a suitable mathematical model. Sometimes it is difficult to know precisely what has been measured (for example wictih temperature is measured using difficult measurements techniques) or under witch conditions, the test has been performed (for instance which local temperature prevails in Thermogravimetric Analysis (TGA) experiments). One may get the impression that by raising the above question the importance of experiments is being lowered. The contrary is correct since there is no useful mathematical model without validation and without parameters and properties derived from experiments. Since experiments are vital for a modeler, then he or she wants to gain the most out of them.

The experimental method used in process optimization has a few stringent limitations:

Limited amount of accessible variables. In many cases of industrial interest, the number of variables is much larger than the experimenter can access. As a consequence, imposing variations on a single input parameter can induce variations in several observable quantities affecting the process in several unknown ways. What is observed as a final result is then the combination of several changes, that sometimes drive the system in different and unwanted directions.

Limited knowledge of details. Details are essential when industrial processes must be improved. Many technologies are well known for many years, with performances already well established and efficiencies already at high levels. Improving such a situation requires fine tuning on parameters and this cannot be achieved without detailed knowledge.

Scale effects. Direct optimization on working plants is too costly (massive changes must be made, production must be stopped, time must be invested) therefore a good procedure is to start with a small laboratory testing, followed by semi-industrial scale testing. Then implementation at industrial scale takes place. This method, much safer than the direct testing on *ab initio*, requires to scale up from a small scales to big ones. The scaling up is not an easy procedure [398, 352] and many failures have been reported.

The use of mathematical modeling in industrial design helps to reduce the impact of the aforementioned three limitations and nowadays there is no large industrial plant that has not been at least checked with the help of some kind of simulation software. Summarizing, the advantages of the theoretical method are the following [87]:

- Mathematical modeling requires much fewer resources than experimental investigations;
- Mathematical modeling provides knowledge concerning quantities in devices which cannot be measured;
- Mathematical modeling can be used to infer the behavior of the plant at conditions far from the ones experimentally tested;
- Mathematical modeling allows a much better understanding of experimental data since it can easily show dependencies that are hidden into the black-box way of thinking of experiments;
- Mathematical modeling can help in experiment design, identifying conditions of no use or even dangerous for the plant itself;
- Mathematical modeling can be easily employed in the scale-up process of big industrial plants;
- Mathematical models can be improved or changed at any time, following the need of the moment and the availability of better data.

Caution must be advised in interpreting the results obtained by mathematical calculations because they are affected by the following facts:

Uncertainties due to numerical errors and approximations. Uncertainties arise in numerical calculations, and commonly they can be divided into truncation errors and approximation errors [152]. The first kind of errors is related to the finite representation that computers use in storing numbers. That errors propagate and increase as the calculation advances, and if many operations must be performed, that kind of inaccuracy can become relevant. If the algorithm is mathematically ill-posed, this kind of errors are dominant and the results may not have physical meaning. The second kind of uncertainties is due to the approximation introduced at any level by the algorithm itself (truncation errors). Most of the algorithms used in the numerical analysis are based on the truncation of infinite series. That truncation is required to be able to perform computer operations, but naturally, they are coupled with inaccuracies.

Limitation in the available knowledge of the process. Since the theory is an abstraction of our understanding of processes, it is evident that a lack of understanding or failure in this step has a direct impact on the quality of the predictions. This kind of error is difficult to be quantified mainly because the exact model is not a priori known. The uncertainty due to inaccurate models is still present in any research activity and only by cross-checking every step in the mathematical procedure its potential damage can be minimized.

Level of modeling adopted. Many theoretical approaches and many tools are available in modeling. Some of the methods are easy and cheap to implement, quick in computing but limited in its capability of predictions. As an example, a 1-D model approach can be adequate for a fixed-bed reactor or a plug-flow reactor but become unsuitable if 3-D effects play an important role. If more accurate theoretical descriptions are available, it should be easy to control the impact of this kind of uncertainties, by just repeating the calculation with a better model or a better approximation. In reality, this is not an easy task since usually better models, if available, are not (yet) in the position to be used directly in industrial calculations (for example Direct Numerical Simulations (DNS) and in several

aspects also Large-Eddy Simulations (LES) in simulating turbulent effects). Parameters variations are in many cases a possible way to establish a range of validity for the solutions. The parameters must be chosen in an accurate way and sensitivities can be inferred from the results.

Errors in the implementation of the model into a software. The software is the translation of a mathematical model into a computer algorithm, and it is always affected by mistakes that modelers and programmers may make. This kind of errors is difficult to identify since an a priori knowledge of the correct behavior of the software is not available.

The utilization of mathematical modeling to high-temperature processes can be split into the following steps:

1. Understanding of high-temperature processes;
2. Design of high-temperature devices;
3. Prediction of unknown behavior.

In addition to the above steps, mathematical modeling can be applied in interpretation of experiments; they may identify and reduce uncertainties present in the measurement device.

1.4. The mathematical modeling

Mathematical modeling is a term indicating the use of mathematics with the scope of simulating a process or a device starting from basic assumptions, resorting to experiments as less as possible. Ideally, experiments should enter the analysis only as external data so that the model should be a stand-alone procedure. Nowadays the large majority of calculations are performed using computers, and instead of analytical models, numerical modeling is used. Both kinds of modeling are interconnected, and in this work, the terms *mathematical modeling* and *numerical modeling* will be used indifferently.

Such definition is general so that the features and the characteristics of the resulting mathematical model is dependent on the process considered. In simulations of solid fuel conversion systems, the analysis is based on conservation equations for mass, energy, and momentum. The resulting model, from the mathematical point of view, is in general a system of non-linear partial differential equations that sometimes can be reduced to a system of ordinary differential equations. Auxiliary data for the thermodynamic properties are needed, together with the equation of state, chemical reaction rates, and various correlations defining the behavior of the components present in the system. For more complex applications, extra differential equations are necessary (like the equation for the turbulent kinetic energy k, the dissipation ϵ and the intensity of the radiation field).

Boundary conditions are an integral part of the model as well as, initial conditions, if applicable. The boundary conditions behavior describe several properties at the boundary, and their formulations depend on what is happening and what is known. The importance of a correct and detailed description of the boundary conditions cannot be underestimated since they can change the structure of the mathematical problem affecting the solution. In the case of a solid wall, as an example, if the temperature in the internal face is known, then Dirichlet boundary conditions can be used. If instead the heat flux is known then Neumann boundary conditions can be applied. If nothing can be directly measured, a simplified model of the heat extraction must be used ending up with Robin boundary conditions.

1.4.1. The thermodynamic model

The formulation of a set of conservation equations follows some preliminary steps:

1. Choice of the *thermodynamic system* for which the equations must be formulated;
2. Identification of the *boundaries* of the system and consequently identification of the *Volume* containing the thermodynamic system;
3. Identification of the *thermodynamic quantities* necessary for the simulation;
4. Identification of the *fluxes* crossing the boundaries;
5. Formulation of the mathematical conservation equations.

The first step requires the choice of a thermodynamic system. A thermodynamic system is a general macroscopic physical system that can be quantitatively identified using measurable thermodynamic quantities. In thermodynamic equilibrium, the system is described by a unique thermodynamic state but for systems for which global equilibrium is not achieved, more thermodynamic states are required. For what concerns this work, the system can be as complex as a whole reactor, containing several heterogeneous interacting components in complex geometry, or a simpler system comprising a small (but still macroscopic) amount of homogeneous material. The choice of the system is somewhat arbitrary. For a chemical reactor, the walls can be included in the system (defined, for example, by a mixture of gas and reacting particles), but a valid thermodynamic formulation of the problem can be done without the walls. It is worth noticing here that the two formulations of the chemical reactor problem differ since the interaction of the wall with the rest of the system must be anyway taken into account in different ways.

The second step requires the choice of a volume, dividing what is inside the system and what is outside the system. For such a volume, called *control volume*, balance equations are written, therefore (see later) the boundaries of the control volume must be clearly defined and what flows through them must also be precisely determined. The control volume can be a finite volume, as in the case of an entire furnace, or it can be a small infinitesimal volume. The geometry of the device under investigation and the choice of what is considered inside the system put limitations on this choice but some freedom is left. A portion of the inlets pipes, as well as a portion of the exhausts pipes, can be part of the system but those pipes can be removed, if desired, from the description of the system. A small infinitesimal volume can have Cartesian geometry but the formulation in cylindrical or spherical coordinates is also possible. In all those cases the choice is free, but it must be helpful in simplifying the description of the process and the solution of the mathematical equations. If the control volume is divided into smaller volumes, then we speak about *sub-volumes*.

In a complex thermodynamic system, several smaller parts can be identified. These parts are called *sub-systems*. The need to split a system into sub-systems is determined by the availability of required information:

- In a mixture of reacting gases, the chemical rates are usually expressed in terms of components (mass fraction, mole fraction or concentration) therefore the components must be separated in writing the mass balance. Each component has the same temperature and the same velocity, therefore, there is no need to separate them in the energy and the mass balances.
- In a mixture of gas and solid components (reacting or inert) usually the components have different temperatures. Therefore, they must be separated not only in formulating the mass balance but also in formulating the energy balance. In this case, the system is divided into sub-systems, the gas-phase, and the solid-phase.

- If the different components have different velocities they must also be separated in the momentum balance. This is often the case if solid or liquid components are present. Also in this cases, the gas-phase and the second phase are considered as two different sub-systems.

Balance equations can be written for extensive quantities only and, as previously stated, they are formulated for a given control volume. The following balance equations must be formulated:

1. balance equation for the *total mass*;
2. balance equation for the *momentum*;
3. balance equation for the *energy*;
4. balance equation for the *mass of each component*.

Balance equations can be formally written using a general formulation (shown below) in which a generic scalar variable is denoted Φ. For extensive quantities capital letters are used. Extensive quantities can be expressed using specific quantities ϕ (small letters) and the relation with the corresponding extensive quantity is given by:

$$\Phi = \rho \cdot \phi$$

where ρ is the density of the system. Other variables must be used in the formulation of the equations, and their definitions are listed below. The flux $\vec{j}^{\phi}$ is the flow-rate per unit of surface while the flow-rate $\dot{\Phi}$ is related to it by:

$$\dot{\Phi} = \int \vec{j}^{\phi} \cdot \widehat{n} \, dS$$

Rate of change for the quantity Φ is its change per unit of time:

$$\frac{\partial \Phi}{\partial t}$$

In the case of energy, the rate of change should not be confused with the power of a certain device even if both quantities have the same unit, namely $\frac{\mathrm{J}}{\mathrm{s}}$. and W.

For an arbitrary control volume, any of the previously listed quantity (Φ) increases due to amount entering the control volume (crossing the boundaries), decreases due to amount leaving the control volume (crossing the boundaries) and can increase or decrease if sources or sinks are present. If inside the control volume several sub-systems are present, the exchange of Φ among the sub-systems usually appears as a source term.

In mathematical language, the general balance equation is written in the following way:

$$\frac{\partial}{\partial t}\Phi = \dot{\Phi} + \dot{\Phi}_s \tag{1.1}$$

where: $\dot{\Phi}$ - Net in-flow through the boundary

$\dot{\Phi}_s$ - Source/sink inside the control volume

Depending on the specific quantity Φ, the terms in the above balance equation must be differently formulated.

The flux of a quantity Φ through a surface S is due to the following two processes:

1. **advection**, in which the flow-rate is proportional to the gas velocity U: $\dot{\Phi} \sim U\Phi$
2. **diffusion**, in which the flow-rate is proportional to the gradient: $\dot{\Phi} \sim \nabla\Phi$

Total Mass balance If the quantity Φ is the mass m (and ρ is the density) the identification of the aforementioned terms is straightforward since no diffusion takes place (in the case of the total mass, $\phi = 1$ and its gradient is identically zero). The mass flow $\dot{m}$ is defined by the following integral over the external surface of the control volume S:

$$\dot{m} = \int \vec{j}^m \cdot \widehat{n}\, dS = \int \rho \vec{U} \cdot \widehat{n}\, dS \tag{1.2}$$

where $\widehat{n}$ is the unitary vector orthogonal to the surface S at the integration point.

The convention used here is that a positive value indicates a flow entering the volume, therefore, $\widehat{n}$ is pointing inside the system. Using this definition the total flow $\dot{m}$ can be positive or negative if more mass is added or is removed from the system respectively.

The general equation for the mass balance reads:

$$\frac{\partial m_{sys}}{\partial t} = \dot{m} + \dot{S}_m \tag{1.3}$$

where:

m_{sys}	-	Mass of the system inside the control volume	kg
$\dot{m}$	-	Mass flow through the boundaries	$\frac{\text{kg}}{\text{s}}$
$\dot{S}_m$	-	Mass generation or sink inside the control volume	$\frac{\text{kg}}{\text{s}}$

The source term $\dot{S}_m$ is responsible for the mass exchange between sub-systems inside the same volume.

Species balance The balance equation for each species is a mass balance for a specific component a. If the mass of each single component inside the control volume is denoted as m^a the balance reads:

$$\frac{\partial m^a}{\partial t} = \int \vec{j}^a \cdot \widehat{n}\; dS + \dot{S}^a_m \tag{1.4}$$

The flow rate $\vec{j}^a$ is formed by an advection term and by a diffusion term:

$$\vec{j}^a = \rho\vec{U} + D^a \nabla Y^a \tag{1.5}$$

where D^a is the diffusivity of the species a inside the mixture and $Y^a = \frac{m^a}{m}$ is its the mass fraction.

Since:

$$m_{sys} = \sum_a m^a \tag{1.6}$$

$$\dot{m}_i = \sum_a \dot{m}^a_i \tag{1.7}$$

$$\dot{S}_m = \sum_a \dot{S}^a_m \tag{1.8}$$

summing up Equations 1.4 for each component a, Equation 1.3 for the total mass is obtained. The species balance can be written also using explicitely the mass fraction Y^a:

$$\frac{\partial(m \cdot Y^a)}{\partial t} = \int \vec{j}^m Y^a + \dot{S}_m^a \tag{1.9}$$

where $\vec{j}^m$ is the flux of the mass at the boundary.

The energy balance The starting point of the thermal analysis of a system is the first law of thermodynamics written for an open system as:

$$\dot{Q} + \dot{W}_t + \int \vec{j}^e \cdot \widehat{n}\, dS = \frac{\partial E_{sys}}{\partial t} \tag{1.10}$$

The energy flux $\vec{j}^e$ is composed, as in the general case, by an advection term and by a diffusion term:

$$\vec{j}^e = \rho \vec{U} e + k \nabla T \tag{1.11}$$

	$\dot{Q}$	-	Heat flux	kJ
with:	$\dot{W}_t$	-	Rate of technical work	$\frac{\text{kJ}}{\text{s}}$
	k	-	heat conduction coefficient	$\frac{\text{kW}^2}{\text{m K}}$

The term:$e = h + \frac{U^2}{2} + gz$ is the total energy per unit of mass,

	h	-	Specific Enthalpy	$\frac{\text{kJ}}{\text{kg}}$
and:	$\frac{U^2}{2}$	-	Kinetic energy using the velocity of the gas U	$\frac{\text{kJ}}{\text{kg}}$
	gz	-	Potential energy	$\frac{\text{kJ}}{\text{kg}}$

The total energy of the system E_{sys} is defined using the following integral over the volume:

$$E_{sys} = \int \rho \left(u + \frac{U^2}{2} + gz \right)_{sys} dV$$

	ρ	-	Density	$\frac{\text{kg}}{\text{m}^3}$
where:	u	-	Internal energy per unit of mass	$\frac{\text{kJ}}{\text{kg}}$
	U	-	Macroscopic velocity of the system	$\frac{\text{m}}{\text{s}}$
	gz	-	Specific potential energy of the system	$\frac{\text{kJ}}{\text{kg}}$

The technical work per unit of mass can be written in the following way:

$$\dot{W}_t = \Psi + \int \left(\frac{U^2}{2} \right) \vec{j}^m \cdot \widehat{n}\, dS + \int V dp \tag{1.12}$$

where Ψ is the dissipation due to irreversibility.

When the above considerations are applied to a furnace, the following simplifications can be made:

1. The furnace is not moving and the kinetic energy $\frac{U^2}{2}$ in the total energy e is not present;
2. Potential energy difference between streams can be neglected and the therm dgz can be omitted;
3. No technical work is done, therefore $w_t = 0$;
4. The kinetic energy can be neglected [2]

Implementing the above-listed assumptions, the balance equations can be simplified as follows. The mass balance and the species balance equations remain unchanged while the energy balance can be written:

$$\dot{Q} = \sum \dot{m}_i h_i + \frac{dE_{sys}}{dt} \tag{1.13}$$

If it can be assumed that the process is stationary, each time derivative $\frac{d}{dt}$ must vanish. The equations take their final form. For the mass balance:

$$\sum \dot{m}_i + \dot{S}_m = 0 \tag{1.14}$$

the species balance:

$$\sum \dot{m}_i^a + \dot{S}_m^a = 0 \tag{1.15}$$

and the energy balance:

$$\dot{Q} = \sum \dot{m}_i h_i \tag{1.16}$$

The link between the energy conservation equation in differential form and those written in integral form can be found in [112].

1.4.2. Differential formulation

The balance equations presented in the previous section must be accompanied with an equation of state for each sub-system and with other several thermodynamic quantities. This is an easy task if the system is in full thermodynamic equilibrium, but most of the processes used in industry are far from equilibrium. If Local Thermodynamic Equilibrium (LTE) is invoked, the balance equations can be formulated only for an infinitesimally small control volume. The previous balance equations for the small control volume are still valid, but the mathematical problem in its final form is formulated with a set of partial differential equations. The differential equations

[2] To substantiate this point, let us consider the following calculation. Gas at normal conditions is injected into a furnace with velocities up to $U = 200\ \frac{\mathrm{m}}{\mathrm{s}}$, corresponding to a kinetic energy per unit of mass of $k = 20.0\ \frac{\mathrm{kJ}}{\mathrm{kg}}$. This energy must be compared with the energy released in combustion that for a typical fuel is around $l = 20.0\ \frac{\mathrm{MJ}}{\mathrm{kg}}$. The amount of air injected in a combustion chamber is substantially higher than the amount of gas by a factor of around 20, also increasing the kinetic energy of the incoming stream, but also, in this case, the energy released by combustion is substantially higher than the kinetic energy.

are listed below, postponing the discussion of further details to Chapter 4:

$$\frac{\partial \rho}{\partial t} + \nabla \rho \vec{U} = \dot{m} \tag{1.17}$$

$$\rho \frac{\partial \vec{U}}{\partial t} + \rho \vec{U} : \nabla \vec{U} = \nabla \mathbf{T} + \dot{p} \tag{1.18}$$

$$\rho \frac{\partial h}{\partial t} + \rho \vec{U} \cdot \nabla h = \nabla \rho \Gamma \nabla h + \dot{q} \tag{1.19}$$

$$\rho \frac{\partial Y^a}{\partial t} + \rho \vec{U} \cdot \nabla Y^a = \nabla \rho D_a \nabla Y^a + \dot{m}^a \tag{1.20}$$

1.4.3. Dimensionality of the equations

Four types of mathematical modeling can be used, and they are related to the number of spatial dimensions taken into consideration. Zero-dimensional (0-D) modeling requires no partial differential equations and consequently is mathematically simple. If the process is unsteady, time differentiation is needed. The description using 0-D modeling neglects the internal structures that must be then revealed with further modeling only. This approach can be used if the system inside the volume is in thermodynamic equilibrium and with minor effort if the assumption of a well-mixed reactor is a valid one. Most industrial reactors cannot be described by any of those two assumptions. In industrial practice, this approximation is usually too crude but 0-D modeling is anyway important since more advanced approaches base their mathematical description on it. For example, the Control Volume method for solving multi-dimensional problems is based on the 0-D level description.

One dimensional (1-D) modeling applies to plug flow reactors, and this assumption can be a valid simplification also in some industrial reactors. The mathematical problem is then formulated by a system of parabolic partial differential equations with one coordinate and the time as variables. When stationary solutions are of interest, then the system reduces to a system of ordinary differential equations.

Two dimensional (2-D) modeling can be used if the geometry has translational or rotational symmetry. The geometry is not the only requirement for the applicability of 2-D symmetry since also the boundary conditions and the expected solution must follow the same symmetry. The solution itself must follow the same symmetry, requiring in practice that no instabilities (that break of the symmetry) must occur. The mathematical problem is always formulated by a system of partial differential equations, even for a stationary solution.

Full three dimensional (3-D) modeling is required most of the time. All the details can be implemented, and no peculiar assumption or restrictions are necessary. The mathematical description is always formulated by partial differential equations also if the steady-state assumption is invoked.

1.4.4. The solid phase sub-system

A similar structure, as the one presented before, can be applied to the modeling of solid particles present in a complex solid fuel conversion reactor. It will be explained in Chapter 10 that the most commonly used technique is to simulate the solid fuels (particles) as a different sub-system. Regardless of which particular description of the solid phase are used, the simulation of a single fuel particle is required. Consequently, in accordance with what has been described in the previous sections, also for a single particle, all of the aforementioned approaches (0D, 1D, 2D, and 3D) are available, and it could be concluded that the best simulations are 3D unsteady simulations. But, contrary to the case of an entire reactor, in the case of single particles, assumption

reducing the complexities of the calculations are more appropriate. It will be shown in further chapters that the pseudo-steady state approximation can be employed here. Moreover, it is well known from heat transfer theory that the lumped capacitance method, reducing a thermal system to a number of discrete lumps and assuming that the temperature difference inside each lump is negligible (i.e., 0D assumption), is a reasonable assumption if the Biot number $Bi \ll 1$. It will be shown that this is the case for small particles of industrial pulverized fuel boilers or entrained flow gasifiers.

1.5. Solid fuel conversion

Pulverized coal combustion in boilers for electrical energy production is a typical example of solid fuel conversion. Nowadays the interest is not any more only on coal as fuel and combustion is not anymore the only application in which solid fuels are involved.

Following the path of the *Energiewende* in Germany and recent developments in other countries in the World, the perception that solid fuels are "dirty" and must be abandoned, is reinforced by political decisions. But contrary to the common perception, the interest in coal and biomass, and more generally in solid fuel conversion is increasing. Coal remains one of the cheapest fuel available and biomasses utilization gain interest due to renewable and zero carbon dioxide emission aspects.

The fact that solid fuels conversion is used in combustion for energy production only is partially true. Combustion is used not only for electrical energy production but in many industrial branches coal, and other various solid fuels are oxidized to produce heat for the processes. In the cement industry for example, due to the high temperatures combined with the oxidizing atmosphere and long residence times, various types of wastes are used in the kilns. Refuse Derived Fuels (RDF) combusted in the cement industry contain the following: [249]:

- Car and truck tires;
- Paint sludge from automobile industries;
- Waste solvents and lubricants;
- Meat, bone meal and slaughterhouse waste;
- Waste plastics;
- Sewage sludge;
- Rice hulls;
- Sugarcane waste;
- Used wooden railroad ties (railway sleepers);
- Spent cell liner from the aluminum smelting industry.

In the steel industry, coke or anthracite is used as fuel in blast furnaces. The CO produced reacts with Fe_2O_3 to Fe and CO_2. Also other materials like Manganese, Silicon and Phosphor have similar reactions with carbon. In limestone conversion, coke or anthracite are used for both, heat generation and CO_2 generation to be used in for the carbonization of CaO.

Wastes from industry, communal wastes and also wastes from households are mostly in the form of solids. This waste must be *converted* and several technologies are available. Thermal treatment is one of them.

As already mentioned, combustion is not the only technology where solid fuel *conversion* takes place. Gasification is also a technology where solid fuels of low quality (here *low* quality is to be understood as low calorific value) are converted into gaseous fuels of higher quality (high calorific value).

1.6. Objectives

Improvements in energy efficiency, fuel flexibility and capital effectiveness of modern solid fuel boilers as well as gasifiers, increasingly rely on CFD modeling. The accuracy of CFD calculations is often limited by the lack of knowledge of fundamental conversion rate parameters, since the need for efficiency improvements is pushing the technologies towards higher temperatures and higher pressures, where measurements and modeling reach their limit of validity and accuracy. The primary objective of this work is then to explain and demonstrate how the CFD tool can be helpful in predicting solid fuel conversion for industrial applications with emphasis on high temperatures and high pressures processes. Since the general theory of CFD can be found elsewhere [388], only a short description will be provided. Instead, more attention will be given to the modeling needed for the description of the solids conversion. Since solid fuels are complex and heterogeneous, there is no a single theory able to explain and predict all aspects of the complex thermo-chemical changes involved. In many situations, we must therefore relay on measurements to generate the parameters needed to feed the model.

According to Weber et al. [408], three different levels of information can be achieved by CFD-based modeling of combustion systems:

Level 1: Knowledge of flame shape and length with a temperature prediction with an accuracy of around $200\,^{\circ}\mathrm{C}$. Estimation of the heat fluxes with an accuracy of around 30-40 %. Location of regions of high and low mixing intensity.

Level 2: Knowledge of temperature distribution with accuracy within $100\,^{\circ}\mathrm{C}$. Oxygen concentration with uncertainties around 0.3 % and fuel unburned with an accuracy of 0.3 %. Identification of furnace and burner regions of high slagging potential.

Level 3: Knowledge of flame emissions, NO_x, CO, PAH, sulfur oxides and char burnout. The prediction of the temperature distribution with an accuracy of $50\,^{\circ}\mathrm{C}$, detailed chemistry with the identification of the region of high pollutants formation.

The first level of knowledge can be achieved by using the proximate and ultimate fuel analysis, a rough estimation of high-temperature volatile yield, devolatilization and char reaction rates. Often literature data on the fuel conversion rates are sufficient. An adequate turbulence model, like the k-ϵ (if applicable) can be combined with a simplified global chemistry model. Numerics remains essential and coarse grids with first order approximation should be avoided.

The second level of knowledge can be achieved only if the boundary conditions are precisely known (mean values, fluctuations, distributions), and the solid fuel must be comprehensively characterized. High-temperature volatile yield and rates of devolatilization and char combustion must be measured at the conditions found in the flame (the same temperature and the high heating rate). For many flames the model used for the turbulent closure of the equations plays a lesser role, providing that the numerical solution is accurate enough. Therefore finer grids and possibly second order schemes are required.

Achievement of the third level of description is still nowadays a challenge for the modeling. Detailed chemistry and high-performance computing are required, but also turbulence modeling must be improved. More sophisticated models and more advanced approaches can now be used

since the computer technology is so developed that memory, speed and parallelization are easily obtainable. Following the advance in computing power, models can be refined in such details that they can be of use also in the interpretation of measured data.

A well-established procedure in fuel characterization and solid fuels modeling at the Institute for Energy Process Engineering and Fuel Technology of the The Clausthal University of Technology (IEVB is an acronym originating from the German name *Institute für Energieverfahrenstechnik und Brennstofftechnik*) is based on the synergy between experiments and theory, in which both methods provide a substantial contribution to achieving the third level of the description mentioned by Weber et al. in [408]. The steps to follow can be roughly listed below:

1. An analysis of the industrial process to determine the conditions of the fuel conversion process. This first step is critical because, as already mentioned, most of the models developed have a restricted range of validity, and the behavior of the fuel changes drastically with the process conditions.
2. Fuel analysis and characterization using appropriate techniques.
3. Development of sub-models for describing the mechanisms of fuel conversion and implementation of the resulted sub-models into an existing CFD software.
4. Deduction of parameters that cannot be measured directly.
5. Validation of the resulting CFD model against in-flame data obtained in small scale and semi-industrial scale reactors.
6. Application to industrial plants.

The chapters of this book show examples and contain detailed information concerning the above-introduced methodology.

Part I.

Basics

2. Solid Fuels

Fuels are materials able to produce heat after reacting. If the fuel reacts with oxygen, the reaction is called combustion or oxidation, but other processes can be considered as well. Nuclear reactions, for example, involve nuclear decomposition (fission) or fusion of some elements (in technical applications the fuels are Uranium and Hydrogen respectively). Combustion is not the only chemical conversion process which involves solid fuels. Gasification and pyrolysis are two endothermic processes that become more important in industry and research in the last 15 years. In those processes, fuels do not oxidize completely. Only just amount needed to sustain thermally the process, providing the required heat, undergoes oxidation while the rest is converted.

Hydrocarbons are by far the most commonly used fuels. They are mainly composed of carbon C, hydrogen H, oxygen O, with a small amount of nitrogen N and sulfur S. They react with oxygen to form carbon dioxide and water as a final product. They can be classified as:

gaseous fuels as methane CH_4, carbon monoxide CO, hydrogen H_2;

liquid fuels as benzine, oil, glycol;

solid fuels as coal, wood, bio-fuels as derivatives from agriculture products.

Independently of its aggregation state, fuels can be divided into two mains categories, *biofuels* and *fossil fuels*. In the last years also *plastic* wastes and polymers are considered as fuels for several processes. Fossil fuels are fuels formed by natural processes such as anaerobic decomposition of buried dead organisms. The age of the organisms and their resulting fossil fuels is typically millions of years. Fossil fuels include coal, petroleum, and natural gas.

A bio-fuels are those fuels whose energy is derived from biological carbon fixation. Biofuels include fuels derived from biomass conversion, as well as solid biomass, liquid fuels and various biogases.

The primary processes in which solid fuels are involved are combustion, gasification, and pyrolysis. The objective of combustion is to decompose the feed material thermally and to generate heat. The objective of pyrolysis and gasification is to decompose the solid macromolecular structure into smaller gaseous products. In pyrolysis, this is achieved using only thermal decomposition while in gasification the solid structure reacts with other molecules, namely CO_2, steam, and hydrogen.

To understand solid fuel conversion, is essential first to understand the properties of fuels, which determine the behavior of the whole process. Therefore, to facilitate the discussion, a brief review of fuels properties and their conversion fundamentals is presented, with emphasis on those characteristics relevant to coal and biomass conversion. The interrelated processes through which a single solid fuel particle undergoes during thermal conversion are: heating, drying, devolatilization (pyrolysis), combustion of Volatile Matter (VM), char burnout, and char gasification. During over stoichiometric combustion, gasification is not relevant, and the entire process is shown schematically in Figure 2.1. In that figure the particle temperature-history is qualitatively sketched, identifying various reaction steps.

The particles enter the reactor at a low temperature and start almost immediately to be heated up. When the particle temperature reaches nearly the boiling temperature of the water, moisture

is given off from the particle. Particles enter the flame region, and their temperature rapidly increases. The weakly linked molecules thermally decompose, and gases in the form of light gases and tars [1] are released. When the temperature of the particles reaches a maximum, and all the volatiles are removed, the remained part of the solid structure starts to react heterogeneously. The particles leave the high-temperature flame region, and due to heat transfer with colder parts of the reactor, their temperature decreases. During the heating process and the devolatilization, the diameter of the particles may increase (swelling). During the burnout phase, the mean diameter can decrease and during the last stages of the process, the structure of remaining ash may become weak, and the particle undergoes fragmentation.

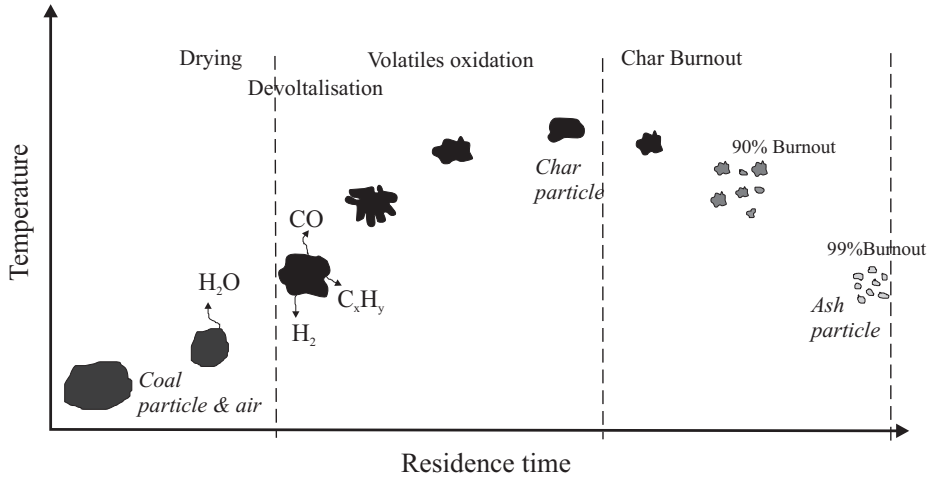

Figure 2.1.: Combustion steps of solid fuel particle

Both coal and biomass conversion can be split into these four fundamental steps, but the time needed for each step depends on the composition and size of the fuel, on the gas temperature, and on the concentration of the reactants.

Solid fuel analysis are often reported as

1. a proximate analysis,
2. an ultimate analysis.

Proximate analysis is a broad analysis that determines the amounts of moisture, volatile matter, fixed carbon and mineral matter (ash). The moisture consists of surface moisture and chemically bound moisture, the fixed carbon is the amount of reacting organic matter and the mineral matter is the amount of inorganic material, which when the fuel is thermally converted, produces ash. Decomposition of some inorganic minerals in a high-temperature environment cause that ash and mineral matter composition differs.

The ultimate analysis is the determination of the chemical elements in the fuel, that is carbon, hydrogen, oxygen, nitrogen, and sulfur. Besides, the calculation of the amounts of elements that have a direct impact on the utilization of the fuel may be necessary. These may include the forms of sulfur, chlorine, and phosphorus, and an analysis of elements present in the mineral matter. The analysis may be reported using the following basis [374] (see Figure 2.2):

[1] Tars are the heaviest components in the volatilized gases. In the scientific literature they are defined in many ways, but here we will consider tars as all those components that are liquid at room temperatures. Water is excluded from the tars category. In some applications, tars are defined as all those components heavier than benzene, C_6H_6 , which liquified at 80 °C.

As received (ar) (sometimes called *as fired*) The data are expressed as percentages of the fuel including both the surface and the air-dried moisture content

Air dried The data are expressed as percentages of the air-dried fuel. The surface moisture is removed from the particle but the inherent moister remains.

Dry The data are expressed as percentages of the fuel after all the moisture has been removed.

Dry ash-free (daf) The fuel is considered to consist of volatile matter and fixed carbon by recalculation with moisture and ash removed.

Dry mineral-matter-free (dmmf) For this analysis the total amount of mineral matter rather than ash is determined so that the volatile matter content in the mineral matter can be removed.

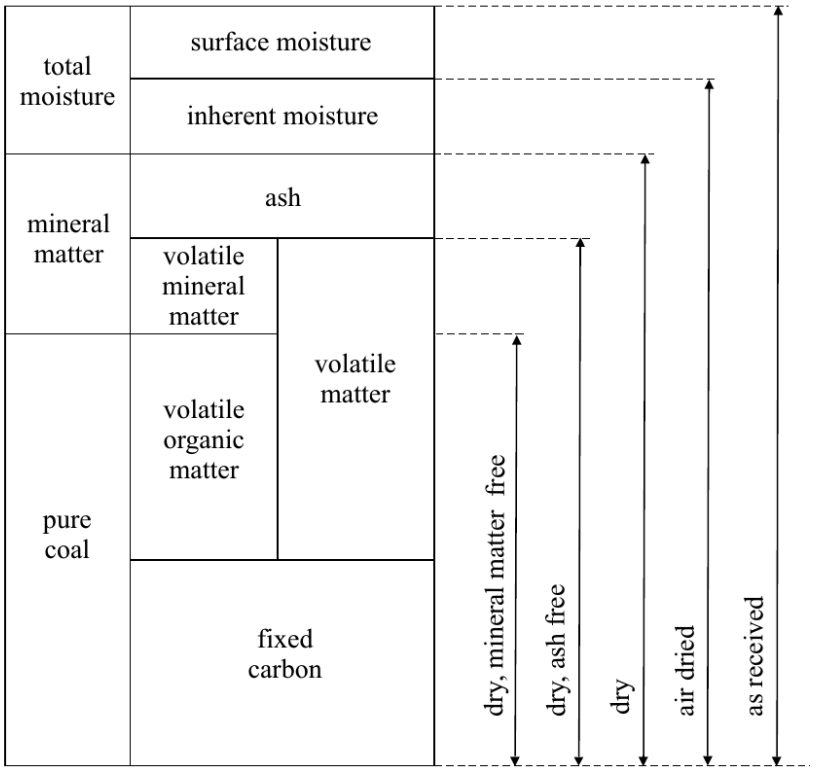

Figure 2.2.: Different analytical bases

2.1. Formation

Biomass and coal are complex polymers consisting primarily of carbon with variable quantities of other elements. Coal is a compact, aged form of biomass containing combustibles, moisture, intrinsic mineral matter (originating from dissolved salts in water) and extrinsic ash (due to mixing with soil). It is formed following the chain:

vegetation $\longrightarrow$ peat $\longrightarrow$ lignite (low rank coal)
$\longrightarrow$ bituminous coals $\longrightarrow$ anthracite (high rank coal)

In the past, the Earth was broadly cover by vegetation that due to natural processes, have been buried under the soil and heavily compressed. The buried material experienced an increase in temperate under high pressure, and it was protected from bio-degradation and oxidation, usually by mud or acidic water. This process trapped the former vegetation into reservoirs that were subsequently covered by sediments. Under high pressure and high temperature, dead vegetation was slowly converted to coal. As coal contains mainly carbon, the conversion of dead vegetation into coal is called carbonation. The process of coal formation is slow and complex, but it can be divided into four main stages.

- During the first stage, dead biomasses accumulate into peat reservoir. At relatively low temperature and atmospheric pressure, they are converted by a biochemical process (diagenesis) partially in the presence of water.
- In the second stage, lignite is formed as soon as pressure increases. It contains already a small amount of plant matter. During these stages the material can undergo the following processes [372]:

  Disintegration The organic matter after exposure to atmospheric oxygen is decomposed. The main products of this stage are carbon dioxide, methane, and water.

  Mouldering or rotting Oxygen is not anymore available due to the high presence of water. The final product of this step is hummus.

  Peatification If the content of water is high, the material is preserved in a reducing environment. The end products are humic coals, low hydrogen content coals.

  Putrefaction This process takes place in stagnant water, where dead material accumulates. A final product of sapropelic coal is formed. Sapropelic coals are hydrogen-rich coal, derived from sapropels (loose deposits of sedimentary rock rich in hydrocarbons). Sapropelic coals are rich in liptinites (microscopic organic matter derived from waxy or resinous plant parts) and have high yields of volatile matter. Examples of sapropelic coals are cannel coal and boghead coal. Cannel coals are rich in spores, whereas boghead coals are rich in algae.

  Increasing the pressure, the moisture content of the already formed peat decreases and the carbon content increases (as shown by the decrease O/C ratio in Figure 2.3. This process proceeds in parallel with the humification and the gelification of the bio-material. The primary coal precursor, lignin, is slowly oxidized to form humic acid and humines [2]. The lipid-rich fraction and the woody part of the material are relatively resistant to degradation and do not undergo humification. These components have already a high degree of aromatization and suffer very little alteration during the entire process. Chemically, the material undergoes hydration, compaction, loss of O-bearing groups and expulsion of $-$COOH groups.

[2] Soil consists of both mineral (inorganic) and organic components. The organic components can be subdivided into fractions that are soluble, largely humic acids, and insoluble, the humins. Humic acids are a complex mixture of many different acids containing carboxyl 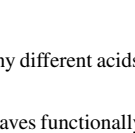 and phenyl groups 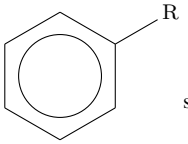 so that the mixture behaves functionally as a dibasic acid or, occasionally, as a tribasic acid, an acid that has two or three hydrogen cations to donate to a base in an acid-base reaction. The formation of humic substances is one of the least understood aspects of humus chemistry [164].

- The last two stages are driven by geochemical processes (metamorphism). Bituminous coal formation is the third stage of coal production. The lignite continues experiencing high pressure until it turns dark brown and becomes soft coal. The material experience generation and entrapment of hydrocarbons, depolymerization of the matrix, increased hydrogen bonding. Soft coal becomes hard coal under intense pressure and high temperatures. The structure begins to crack and low molecular weight hydrocarbons, mainly methane, leave the structure.

- The final stage of coal production is the formation of anthracite. During this stages, material continues to increase the amount of carbon, losing the weak bonds that link together aromatic rings. Coal now undergoes coalescence and ordering of pre-graphitic aromatic lamellae, loss of hydrogen, loss of nitrogen. The structure becomes more compact, and at the end of the process the matter is formed only by strong bonds and aromatic rings [374] (anthracite).

2.2. Classification and properties

Solid fuels are broadly classified according to the extent of their coalification, the process underwent by burial and tectonic, and that determines their rank. Coal rank is also related to the relative proportions of Volatile Matter (VM) and Fixed Carbon (FC) present in the coal and it increases with decreasing VM [302]. With time and higher temperatures, higher ranks of coal are developed.

Figure 2.3 representing the position of several coals and biomass according to the ration of hydrogen to oxygen versus the ratio of carbon to oxygen. The diagram reporting the ratio H/C versus O/C is also called the Van Krewelen diagram. The O/C and H/C ratios decrease through the formation process as shown in the figure. In the left upper part of the diagram, biomasses are positioned, where still H and O are present in the material. The position of peat and lignite shows that already half of the oxygen left the material together with hydrogen. Coals have a certain stable ration of H/C and a more significant variation in oxygen content (reaching almost zero while the ration of hydrogen to carbon is still approximately equal to 0,8). In the lower right corner of the diagram is graphite (pure carbon) anthracite, with almost no oxygen left and a small residue of hydrogen in the range of 0 to 0.4. The lower the respective ratios, the greater the energy content of the material. Fuels with high O/C ratio have a smaller heating value than those with low O/C ratio.

Many properties depend on carbon content, that determines the calorific value and flame temperature. The Volatile matter content determines the flame stability and the parameter FC/VM (flame ratio) plays a role in correlating flame properties. It is widely used in industry as an indicator of fuel reactivity and carbon in ash [424].

2.2.1. Coal

Coal is extremely heterogeneous in nature as shown in Table 2.1. Its moisture can be as high as 60% for young lignite and decreases almost to 0% for anthracite. The volatile fraction lays in a range of around 50% for brown coals to almost few percents for anthracite. The carbon fraction follows an opposite trend, from 60% for brawn coals up to 95% for anthracites. Due to the trend of the fraction of carbon concerning oxygen, the low calorific value (LCV) of lignites is the lowest, around $15\ \frac{\mathrm{MJ}}{\mathrm{kg}}$, and the low calorific value of anthracites is the highest, around $33\ \frac{\mathrm{MJ}}{\mathrm{kg}}$.

It is of importance for modeling to be able to adequately characterize a solid fuel. One strategy is to measure the ultimate or the proximate composition of the fuel and then derive

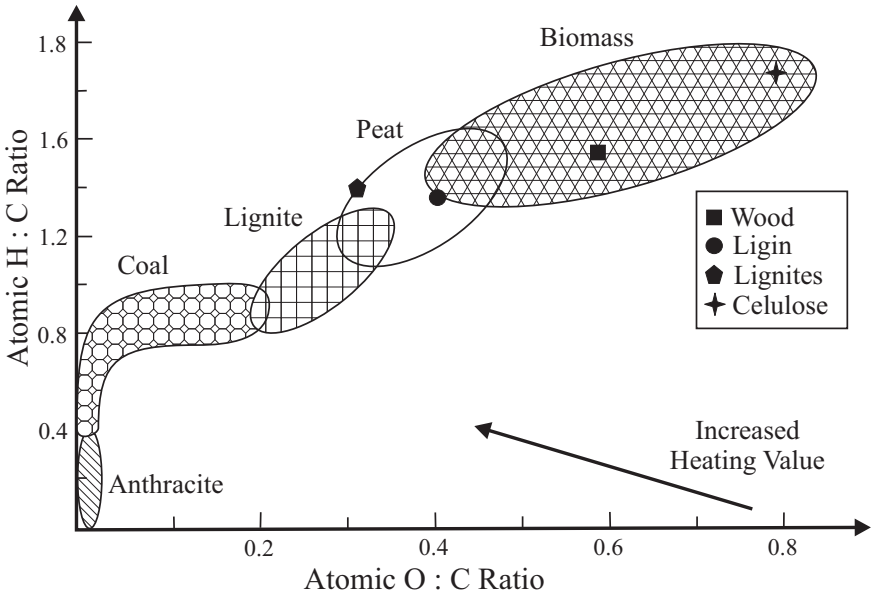

Figure 2.3.: Coalification diagram showing compositional differences among coals and biomass

the remaining (needed) quantities by using appropriate correlations. In [437] several of such correlations are presented. The main components, C and O correlate with the volatile fraction V_{daf} relatively well but more difficulties arise in the interpretation of the correlations for nitrogen and sulfur. The formulas are reported below (the correlation of the hydrogen has been given in term of the carbon fraction because of the better statistics):

$$C_{daf}(\%) = 93.010 - 0.1864 \cdot V_{daf} - 0.004971 \cdot V_{daf}^2 \quad (2.1)$$

$$O_{daf}(\%) = 2.178 + 0.008 \cdot V_{daf}^{1.9} \quad (2.2)$$

$$H_{daf}(\%) = -57.68 + 1.637 \cdot C_{daf} - 0.01054 \cdot C_{daf}^2 \quad (2.3)$$

Correlations have been developed also for the calorific value of the coal. The Dulong correlation [136] is based on the calorific content of every single pure element irrespective of any associated functional group. The correlation provides topically higher values than the measured ones and it should be used only as a vague indicator. The equation of Boie [51] slightly underpredicts the real values:

$$LCV_{daf} = 33.91 \cdot C_{daf} + 93.87 \cdot H_{daf} + 10.47 \cdot S_{daf} - 15.18 \cdot O_{daf} - 2.44 \cdot W_{daf} \quad (2.4)$$

Other fitting formulas can be found in [235]. In the author's opinion, a better fitting of the measured data is given by the equation:

$$LCV_{daf} = 0.46 \cdot C_{daf} + 1.44 \cdot H_{daf} + 0.19 \cdot S_{daf} + 0.10 \cdot A_{daf} - 11.99 \quad (2.5)$$

where V_{daf} is the fraction of Volatile in % and LCV_{daf} is in $\frac{\mathrm{kJ}}{\mathrm{kg}}$. More Recently [227] better correlations are obtained considering only the ash and the water content. It is worth noticing here that the calorific value of many chars are statistically near the graphite value of 33.9 $\frac{\mathrm{MJ}}{\mathrm{kg}}$.

Chemically coal and biomass are complex macromolecules formed principally by aromatic and aliphatic groups. In Figure 2.4 examples of a chemical coal structure for different coal

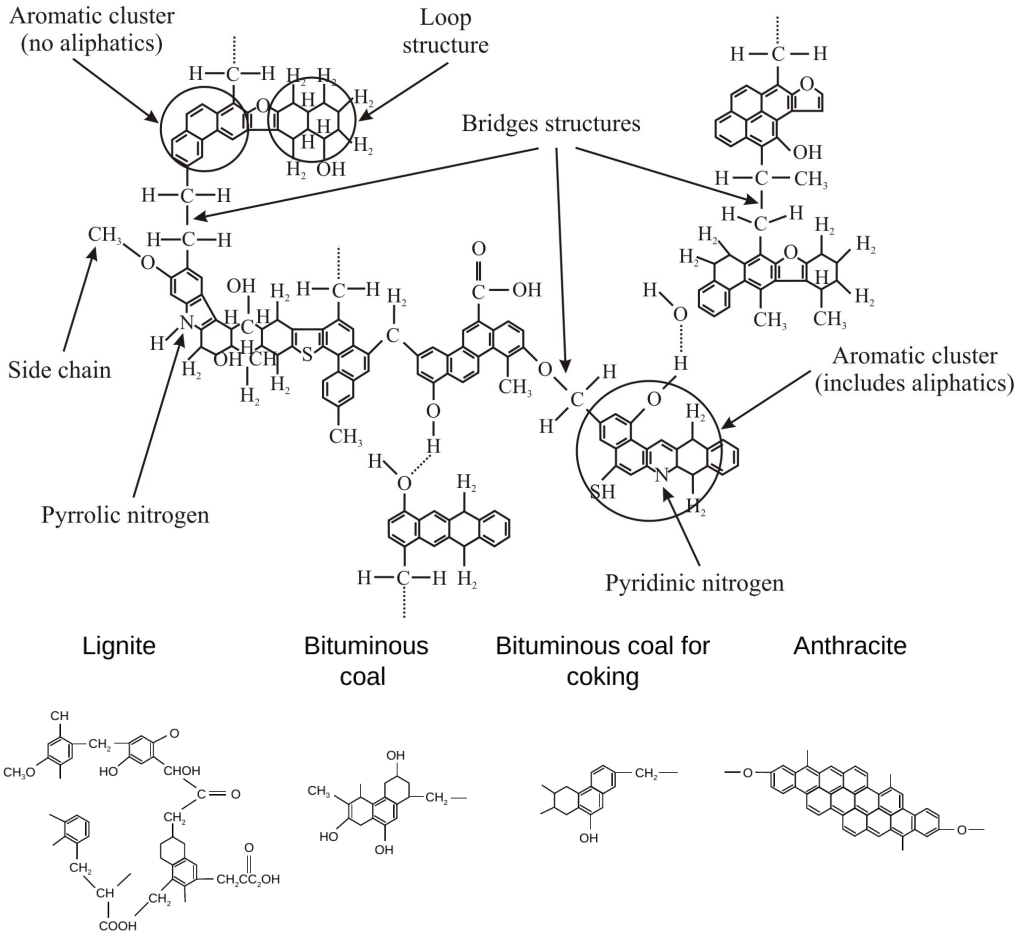

Figure 2.4.: Examples of chemical coal structure for different coal ranks [172]

ranks are given. The fundamental hydrogen containing structures are the polynuclear aromatic (multiple benzene rings), the hydroaromatic (benzene rings with the addition of hydrogen atoms as a link) and aliphatic structures (linear chains). The hydroxyl ($-OH$), carboxyl ($-OOOH$) and carbonyl ($=CO$) groups are the major oxygen functional groups. Lower rank coals can have more complex groups like ether (R_1-O-R_2), quinone (compounds in which a odd number of $C-H$ bounds in a ring structure are converted into $C=O$ bound with rearrangements of the double

bonds [3]), methoxyl ($-OCH_3$) and hetherocyclic oxygen structures [4]. Nitrogen and Sulfur appear as a substitute in the aromatic or as heterocyclic.

Typical bituminous coal consists of a series of aromatic groups, containing an average of 2-5 rings per cluster. The clusters are joined by methylene linkages ($-CH_2-$) with 1-3 carbon atoms in length. Clusters are 3-dimensionally disposed of with crosslinking among planes, a structure that promotes porosity.

Chars are characterized by a carbon-rich polynuclear aromatic structure. High-rank coals are associated with a lamellar disposition of the clusters. Therefore, the structure is less porous.

Aromatic carbon is mainly responsible for char formation while tar comes from hydroaromatic carbon. Light gases (CH_4, CO and CO_2) are produced by aliphatic carbon.

Coal classification by rank The coal classification commonly used is the ASTM (American Standard of Technology and Materials) a ranking system that is based on the fixed carbon, and calorific value on the dry mineral matter free basis (dmmf). This system was adopted in 1938 and is a general guideline to classify different coals. Table 2.1 lists coal rank classification under ASTM standard. The bituminous class is the only coal group used for the metallurgical coal purpose. It is primarily classified into three types by the varied volatile matter, including Low Volatile Bituminous, Medium Volatile Bituminous, and High Volatile Bituminous coal. The High Volatile Bituminous coal is further classified into A, B, and C levels, with a descending heating value on a moisture mineral matter free basis (mmf). The German classification is similar to the international standard and it is reported in Table 2.2 [214].

Coal classification by petrography Maceral is a component, organic in origin, of coal or oil shale. The term maceral in reference to coal is analogous to the use of the term mineral in reference to igneous or metamorphic rocks. Examples of maceral groups are inertinite, huminite, vitrinite, and liptinite. As expected the aromaticity increases in the order: exinite, inertinite, vitrinite.

Inertinite is considered to be the equivalent of charcoal and degraded plant material. It is highly oxidized in nature and may be said to be burnt.

Liptinite macerals are considered to be produced from decayed leaf matter, spores, pollen and algal matter. Resins and plant waxes can also be part of liptinite macerals. Liptinite macerals tend to retain their original plant form, i.e., they resemble plant fossils. These are hydrogen rich and have the highest calorific values of all coal macerals. Macerals of liptinite are sporinite, cutinite, resinite, alginite (telalginite and lamalginite), liptodetrinite, fluorinite, and bituminite [367]. For low-rank coals, liptinite is also called exinite.

[3]The benzoquinone is an example of quinone 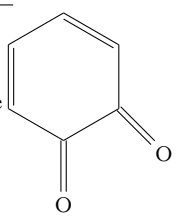

[4]pyridines 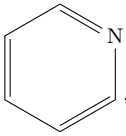

, pyrol 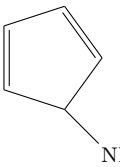

and thiophenes 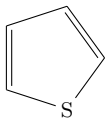

Coal Rank	Volatile Content %	GCV $\frac{\text{kJ}}{\text{kg}}$ mmf	Agglomeration
I. Anthracites Class			Not
Meta-Anthracit	< 2%		
Anthracite	2 to 8%		
Semi-Anthracite (Lean Coal)	8 to 14%		
II Bituminous			Commonly yes
Low Volatile Bituminous	14 to 22%		
Medium Volatile Bituminous	22 to 31%		
High Volatile A Bituminous	> 31%	32.6	
High Volatile B Bituminous	> 31%	30.2 to 32.6	
High Volatile C Bituminous	> 31%	24.4 to 30.2	
III Subbituminous	> 31%		Not
Subbituminous A Coal		24.4 to 26.7	
Subbituminous B Coal		19.3 to 22.1	
Subbituminous C Coal		22.1 to 24.4	
IV Lignite			Not
Lignite A		14.7 to 19.3	
Lignite B		< 14.7	

Table 2.1.: Classification of coal by rank (ASTM D-388)

Classification		VM %	C %	H %	O %	S %	LCV $\frac{kJ}{kg}$
Braunkohle	Lignite (brown coal)	45–65	60–75	6.0–5.8	34-17	0.5-3	<28,470
Flammkohle	Flame coal	40-45	75-82	6.0-5.8	>9.8	1	<32,870
Gasflammkohle	Gas flame coal	35-40	87.5-89.5	5.8-5.6	9.8-7.3	1	<33,910
Gaskohle	Gas coal	28-35	85-87.5	5.6-5.0	7.3-4.5	1	<34,960
Fettkohle	Fat coal	19-28	82-85		4.5-3.2	1	<35,380
Esskohle	Forge coal	14-19	89.5-90.5 5.0-4.5	4.5-4.0	3.2-2.8	1	<35,380
Magerkohle	Nonbaking coal	10-14	90.5-91.5	4.0-3.75	2.8-3.5	1	35,380
Anthrazit	Anthracite	7-12	>91.5	<3.75	<2.5	1	<35,300

Table 2.2.: Classification of coal following the German system

Vitrinite Vitrinite is shiny, glass-like material that is considered to be composed of cellular plant material such as roots, bark, plant stems and tree trunks. Vitrinite macerals when observed under the microscope show a boxlike, cellular structure, often with oblong voids and cavities which are likely the remains of plant stems. This has a high calorific value (24 - 28 MJ/kg) and a large proportion of volatile matter (24 - 30%). It often occurs interbanded or interlaminated with inertinite and can be recognized as bright bands. In low-rank coals, the term this maceral group is called huminite.

Coal classification by industrial application As an example, the classification of coals used in the steel industry and power plants is also reported. The division is based on coking coal, required for the production of coke which is used in steel industries, and non-coking coal required for thermal power plants for steam production. Coals that are to be used for conventional coke production must have three essential properties:

1. They must be within a specific range in rank for the coking process to occur, that is bitu-

minous coal.

2. They must possess a high proportion of fusible macerals (>40% vitrinite) to form a strong well-fused coke.

3. They must have low levels of certain elements, notably sulfur and phosphorus, and be generally low in mineral matter.

A non-caking coal is a coal which, when heated in the absence of air, leaves a powdery residue. A caking coal when similarly heated, leaves a solid, coherent residue. The caking coal might produce a coke unsuitable for steel making plants as it does not possess the requisite physical and chemical properties.

A coking coal is a coal which, when heated in the absence of air, leaves a solid, coherent residue possessing metallic grayish luster and which owns all the physical and chemical properties in the coke when manufactured commercially. A non-coking coal also leaves a solid, coherent residue which may not possess the physical and chemical properties of the coke.

Char classification by morphology Char morphology is generally a function of parent coal rank, parent coal petrography and process conditions [18] and [33]. According to [428] and [33], chars can be classified by morphology into three groups:

1. Group I particles have a very porous structure, with large voids inside the particle and a thin wall,

2. Group II particles have a medium porosity and wall thickness;

3. Group III char particles have low porosity.

The morphology of the chars shows then a strong response to pressure and that response is stronger for char of increasing vitrinite content. The fraction of Groups I, II and III chars from bituminous coals arranged in order of increasing parent coal vitrinite content and generated at several furnace pressures (at 5, 10 and 15 atm), has been analyzed in [33]. Increasing the pressure, the fraction of Group I chars increases, while chars belonging to the group III decreases.

2.2.2. Biomass

Biomass is the name given to all of the Earths living matter. In general, it can be categorized into:

wastes such as sewage sludge, refuse derived fuel (RDF), animal manure;

herbaceous biomasses like grass, stakes, straw, crops;

aquatic for example kelp;

wood hardwood and softwood;

derivatives such as paper.

The components forming biomass include cellulose, hemicelluloses, lignin, extractives, lipids, proteins, simple sugars, starches, water, ash, and other compounds. Two larger carbohydrate categories that have significant value are cellulose and hemicellulose. The lignin fraction consists of non-sugar-type molecules. Biomass can also be generally defined as any hydrocarbon material which mainly consists of carbon, hydrogen, oxygen, and nitrogen. Sulfur is also present

in smaller proportions. The concentration of the ash arising from these inorganics changes from less than 1% in softwoods to 15% in herbaceous biomass and agricultural residues [433].

Cellulose is an organic compound with the formula $(C_6H_{10}O_5)_n$, a polysaccharide consisting of a linear chain of several hundred to over ten thousand $\beta(1 \rightarrow 4)$ linked D-glucose units. Cellulose is the main component of plant cell walls.

Hemicellulose is any of several heteropolymers (matrix polysaccharides), such as arabinoxylans, present along with cellulose in almost all plant cell walls. While cellulose is crystalline, strong, and resistant to hydrolysis, hemicellulose has a random, amorphous structure with little strength. It is easily hydrolyzed by dilute acid or base as well as myriad hemicellulase enzymes. Unlike cellulose, hemicellulose (also a polysaccharide) consists of shorter chains 500 to 3000 sugar units as opposed to 7000 to 15000 glucose molecules per polymer seen in cellulose. Besides, hemicellulose is a branched polymer, while cellulose is unbranched. Hemicellulose binds the cellulose microfibrils of the cell walls.

Lignin is a complex chemical compound which is an integral part of the secondary cell walls of plants and some algae. It is one of the most abundant organic polymers on Earth, exceeded only by cellulose, employing 30% of non-fossil organic carbon, and constituting from a quarter to a third of the dry mass of wood. As a biopolymer, lignin is unusual because of its heterogeneity and lack of a defined primary structure. Lignin is a cross-linked racemic macromolecule with molecular masses more than 10,000 amu. Lignin is the strengthening component of the cell wall and is mainly present in woody biomass.

The wide variety of biomass sources result in a wide range of biomass physical and chemical properties. The properties of biomass as a fuel can be measured by standard methods, some biomass materials and their properties are summarized in Table 2.3.

Material	Moisture	FC	VM	Ash	Alkali metal (as Na and K oxides)	HHV MJ/kg
Fir	6.5	17.2	82	0.8	-	21
Danish pine	8	19	71.6	1.6	4.8	21.2
Willow	60	-	-	1.6	15.8	20
Poplar	45	-	-	2.1	16	18.5
Cereal straw	6	10.7	79	4.3	11.8	17.3
Miscanthus	11.5	15.9	66.8	2.8	-	18.5
Bagasse	45–50	-	-	3.5	4.4	19.4
Switchgrass	13–15	-	-	4.5	14	17.4
Bituminous coal	8–12	57	35	8	-	22-26

Table 2.3.: Properties of selected biomass materials (wt. %) [238]

Moisture, for instance, can only be a few percents with pre-dried biomass or as high as 50% with freshly harvested crops. Volatile matter in biomass is much higher than in coals, ranging from 65 to 85%, while fixed carbon is much lower, ranging from 7 to 20 %. Ash is generally under 5%, but can be as high as 20% with some specific biomass, for example, rice hulls. For elemental analysis, a noticeable feature is the high oxygen content (32 to 45 %). The LCV ranges from 10 to 22 $\frac{\text{MJ}}{\text{kg}}$ while their size can range from pulverized particles ($\sim$ 1 mm) to that of whole wood logs ($\sim$ 100 mm). Biomass particles are rather non-spherical, generally with high

dimension ratios. Bulk densities of biomass are low compared to coal. For very light dry straw the bulk density of (20 $\frac{kg}{m^3}$) is typical, while for coals figures of 600 to 900 $\frac{kg}{m^3}$ are applicable. The low densities of the biomass complicate their processing, transportation, storage, and firing. This wide variation in biomass properties can significantly affect the burning characteristics of the biomass fuels. When comparing biomasses with coals, see Figure 2.3, it can be seen, that the higher proportion of oxygen and hydrogen, compared with carbon, reduces the energy value of a fuel, due to the lower energy contained in carbon–oxygen and carbon-hydrogen bonds, than in carbon-carbon bonds.

The alkali metal content of biomass, namely Na, K, Mg, P and Ca, is especially important for any thermochemical conversion processes. These components influence the physical properties of the ash: ash fusibility behavior, sintering, and hardness of the formed ash deposit. During mineral mater transformation occurring in combustion a sticky, mobile liquid phase can be formed, which can lead to blockages of furnace and boiler ducting [238].

2.3. Morphology

Morphology plays a fundamental role in solid fuel conversion (see for more details Chapter 8). It has been already pointed out that chars are highly porous, increasing enormously the surface available for the reactions, but also introducing an additional resistance to diffusion of reactants towards the active sites where reactions take place. The structure and the development of the pores is then a fundamental aspect that must be investigated. The internal surface is deeply linked with the porosity and the pore structure since both coals and biomasses are highly porous solids; this partially explains the variations in conversion behavior among different fuels and at different conversion stages.

Pores diameters δ range from tenths of nanometers to several microns and are divided into three groups: micropores (δ <1 nm), mesopores (δ = 1–20 nm) and macropores (δ >20 nm). This denomination suggests cylindrical pores, but detailed analysis shows that together with the cylindrical shape, pores can have conical structures as well as flat geometries. In special biomasses and chars after fast pyrolysis, spherical cavities can also be found. Micropores can be interpreted as weak cross-linked clusters in the chemical structure while mesopores and macropores can be seen as physical cracks in the solid particle.

Porosity also affects the following important properties:

1. Effective density of the solid;
2. Specific internal pore volume;
3. Specific internal surface area;
4. Distribution of specific area or volume over the pore diameter δ.

Micropores and mesopores have a high specific area but contribute less to the averaged porosity. Macropores and mesopores are transition pores driving the reactants to the reactive site (mostly in the micropores). Macropores dominate in low-rank coals while micropores dominate in high-rank coals. Therefore both, low-rank coal and high-rank coals, are less reactive (absence of micropores and lack of transitional pores, respectively).

Under thermal treatment, morphology does not undergo significant changes until devolatilization. After that, an increase of porosity and an increase of macropores size is expected. To the contrary, micropores, and mesopores can decrease their size due to polymerization particularly for coals that undergo a plastification phase. At high heating rates those effects are stronger and also meso- and micropores can increase their dimensions and consequently available surface.

Generally the internal surface area increases with temperature until about $\theta = 1000\,^{\circ}\mathrm{C}$ and it is reduced at higher temperatures. The increase is magnified (even by a factor 5) for non-caking coals while the growth is reduced for caking coals. The loss in surface development can be associated with the closures of pores by polymerization and graphitization. The surface changes in the micropores structure, together with the increase in devolatilization yield at higher temperatures and heating rates is the reason why intrinsic char reactivity is a function of the fuel history and devolatilization conditions. Since high temperature treatment (higher than 1000 °C) causes a decrease in active sites [5] and a decrease in internal surface, it results in a reduction in reactivity.

During carbonization, the development of the pore structure and the internal surface is more complex and it is also influenced by the conversion rate. Slow conversion rates allow a better diffusion of reactants into the most active available area therefore developing micro-pores while a rapid conversion favors the development of meso- and macro-pores. In general, the internal surface area increases with burnout (due to development of the pores and the opening of new ones) until a maximum surface is reached and then it decreases due to the breakdown of the structure or coalescence of the pores. The conversion fraction where the pore structure starts to break up is a function of the previous treatment temperature. As that temperature increases, the breakup begins at lower conversion fraction.

2.4. Drying

Drying is a mass transfer process consisting of the removal of water by evaporation from a solid particle. The mass transfer between a particle and the surrounding gas is driven by the difference between the partial pressure of water vapor in the gas and the saturation pressure at the particle surface temperature. At the separation surface, thermodynamic equilibrium is rapidly established between liquid water and vapor. The amount of liquid water removed from the particle is controlled by the rate the evaporated vapor is removed from the liquid surface by diffusion or advection.

If the temperature of the solid is high enough, eventually the saturation pressure equalizes the pressure of the gas. In such conditions, liquid water is not thermodynamically stable, and equilibrium between liquid water and water vapor cannot be achieved anymore. All the water present inside the solid particle will tend to evaporate completely. In this regime, the rate of boiling is controlled by the amount of energy added to the particle.

Pressure influences the molecular diffusion coefficient of the water vapor, the partial pressure, and the boiling temperature. As a combination of those effects, at high pressures, the process is shifted towards higher temperatures with a slower rate.

2.5. Devolatilization

2.5.1. Coal devolatilization

When coal is heated up in an inert atmosphere, combustible gases are released due to thermal decomposition of the solid. This process is called devolatilization or pyrolysis, depending on the availability of oxygen in the atmosphere. If O_2 is present, as in boilers or furnaces, then usually the process is called *devolatilization*. If oxygen is not available, as in gasifiers, then the process is called *pyrolysis*. This stage has a significant influence on the conversion process, mainly in combustion since it controls the particle ignition and it is responsible for stabilizing

[5] Active sites, see Chapter 3 are lost due to thermal annealing. At temperatures higher than 700 °C a reorganization of the structure occurs, and usually, impurities and carbon edges are lost.

the flame. The temperature at which pyrolysis occurs depends on the coal type and the heating rate. For bituminous coals, devolatilization starts at 350–400 °C and a constant weight loss is observed at temperatures higher than 650 °C [414]. The products of devolatilization are gases ranging from light components (CH_4, C_2H_4, C_2H_6, CO, CO_2, H_2, H_2O, etc.) to heavier tars that represent an extremely complex mixture of various organic compounds. Nitrogen is also released from the fuel during pyrolysis in the form of NH_3, HCN, and other N_2–containing species which are generally represented as XN. The release of Nitrogen occurs typically towards the end of the pyrolysis process. Nitrogen leaving the fuel undergoes oxidation to NO_x. Once the volatiles is released, they mix with oxygen and promptly oxidized. During this stage, the gas phase temperature is much higher than the particle temperature [315]. After the VM is oxidized, a solid material called char remains.

Reactions involved in devolatilization are very complex, but in general, this process can be described in three following sequences, as shown at Figure 2.5. In the first step, coal undergoes a reduction of hydrogen bonding, and the non-covalently bounded (weak links) molecules are released from the particle. The structure starts to melt, the weakest bound disrupt, and a metaplast or liquid components are formed. Tars evaporate from the generated metaplast, and they are released from the solid structure. Low-rank coals also produce at this stage a small amounts of metaplast.

In the second step (primary pyrolysis) bond breaking leads to the evolution of tars and gases, and repolymerization of coal fragments provides char. In this phase functional groups [6] are decomposed to form light molecule mainly CO_2, methane, and H_2O. Methane is formed by substitution reactions in which a bigger molecule releases the methyl group; CO_2 is formed by condensation, after a radical is formed on the ring when a carboxyl is removed and water is formed by the condensation of two OH groups (or one OH group and a $-CHHO$ group) to establish an ether link. When those molecules reattach from the solid structure, they leave open active sites favoring the reattachment of several clusters (cross-linking [345]).

In the last step (secondary pyrolysis) products of the polymerization process react with tars forming soot and char. Char produces carbon monoxide and hydrogen while continuing to crosslink and condense [341].

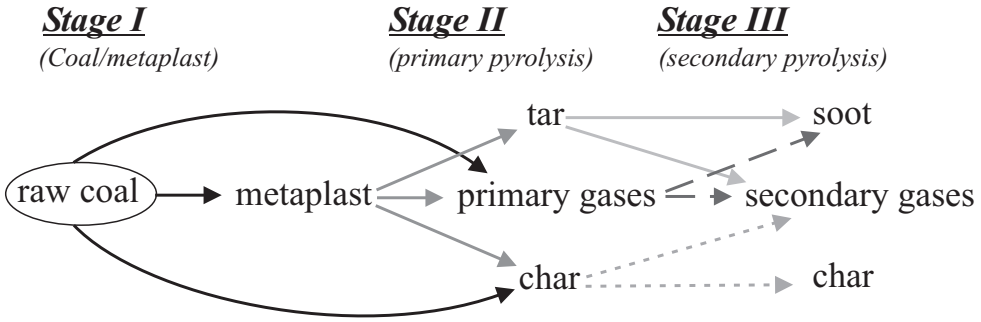

Figure 2.5.: Pyrolysis steps of coal

Composition of the gas Volatiles composition can be roughly divided into three main categories as already discussed, i.e. pyrolysis water, light gases, and tars. The fraction of water is

[6] In organic chemistry, functional groups are lexicon-specific groups of atoms or bonds within molecules that are responsible for the characteristic chemical reactions of those molecules. The same functional group will undergo the same or similar chemical reaction (s) regardless of the size of the molecule it is a part of. However, its relative reactivity can be modified by nearby functional groups.

always around 20-25% of the entire volatiles for lignite and sub-bituminous coal while slightly less for bituminous coal and anthracite [437]. The amount of tars is around 25% for low-rank coals, increasing up to 40% for bituminous coals and then decreasing until approximately 10% for anthracite. The rest of the volatiles is in light gases, around 50% for lignite, 20-30% for bituminous coals and 70% for anthracite. It is important noticing that these values are applicable for standardized labor measurements and they can be significantly different in industrial applications. The second observation is that usually during measurements, independently of the coal rank, around 5% of the mass remains undetected [345].

The composition of the light gases can also be correlated to the fraction of carbon present in the parent coal and consequently even to the rank. For low-rank coals, the main component is oxidized carbon, mainly CO_2 and CO, with a smaller amount of CH_4 and eventually traces of H_2. As the fraction of carbon in the parent coal increases, also the amounts of methane and hydrogen increase, while both CO and CO_2 decreases. With an increase in C content the calorific value of the volatiles increases, from roughly $15\,\frac{\mathrm{MJ}}{\mathrm{kg}}$ in the case of lignite to approximately $40\,\frac{\mathrm{MJ}}{\mathrm{kg}}$ in the case of anthracite. In Figure 2.6 some measurements are presented together with their correlations (from [437]).

Standard proximate analysis of coal allows determining the VM content. However, under high-temperature combustion conditions, such as those found in real utility boilers, part of the carbon in the coal matrix is also volatilized, yielding a higher volatile content than the one obtained from the proximate analysis. The yield released at higher temperatures may increase from 20 to 70 % (dry ash free, d.a.f.) to the proximate analysis. This has a significant influence on the next stage of combustion [285].

Dependency on the Temperature Both, mass loss and tars yield, differs strongly even among coals of the same nominal rank and both are sensitive to pyrolysis conditions, One of the major influencing parameters is the temperature. As the temperature of the particle increases the amount of volatile given off increases. The devolatilization process starts around $\theta = 400\,^{\circ}\mathrm{C}$ with the yield increasing roughly linearly until $\theta = 1000\,^{\circ}\mathrm{C}$. At higher temperature the yield reaches an asymptotic value at $\theta = 1200\,^{\circ}\mathrm{C}$. An important factor is the holding time at the maximum temperature [309]. The time required for a given degree of devolatilization is less at high temperatures than at lower temperatures therefore, as the time increases, the importance of the temperature history become less significant. Since the temperature influences directly the primary decomposition rates as well as the second decomposition reactions, the composition of the volatiles is different at different temperatures. As observed in [366], at low temperatures oxygen is used to form pyrolysis water, while at higher temperatures O_2 is used to form oxides of carbon. Temperature also increases the rate of secondary reactions resulting in a higher rate of cracking and polymerization. This leads to a decrease in tars yield and an increase in char and gases. Also, the composition of the final char and gases are strongly influenced by temperature. At higher temperature char contains less oxygen and less hydrogen as both species evolve as volatile. Tars, in comparison with the parent coal, have less hydrogen and oxygen strongly depleted. Increasing the temperature, the hydrogen content is reduced while the temperature effects on nitrogen and oxygen are barely observable.

Dependency on the heating rate The effect of heating rate is more difficult to asses. According to [12], [362] and [366] the degree of devolatilization depends only on peak temperature and holding time. It is difficult to separate both effects since during experiments high temperatures are always linked with high heating rates. In Figure 2.7 some published results are presented.

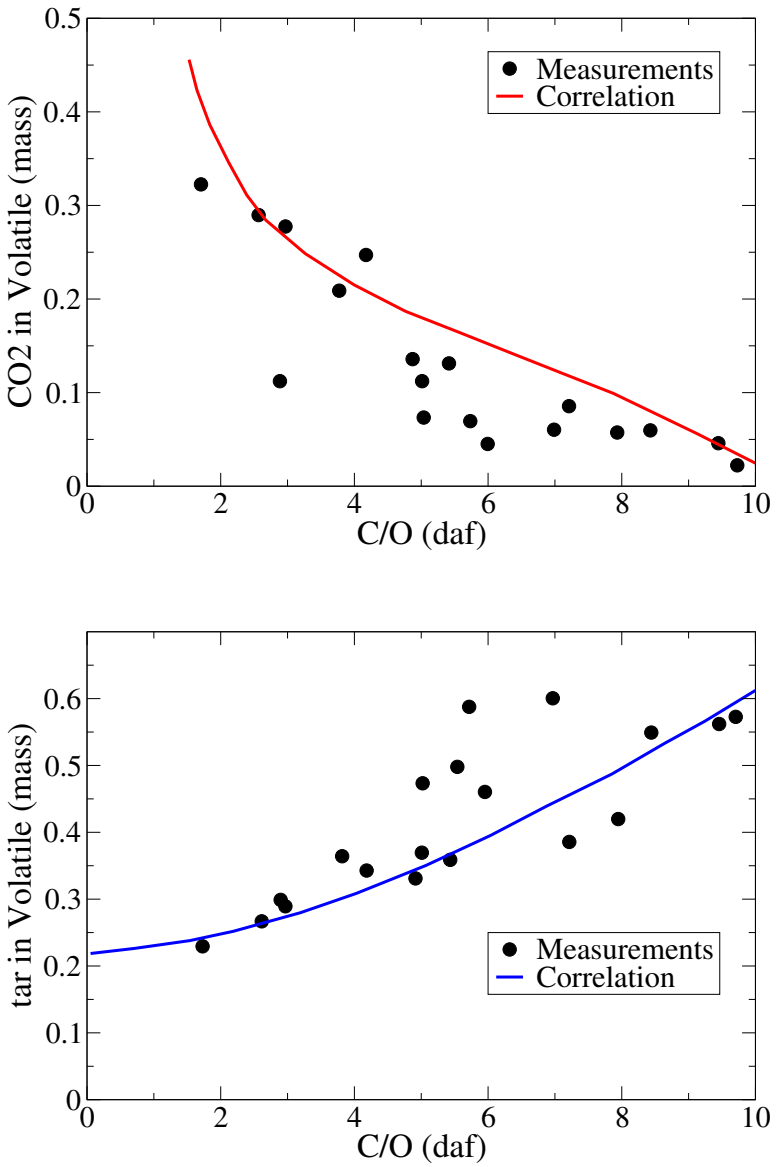

Figure 2.6.: Fraction of CO_2 and tar in volatiles. The continuous lines is the correlations from [437]

Dependency on the pressure The pressure at which the parent coal is devolatilized changes the rates of the pyrolysis, the yields and the composition of the released products. The pressure (together with the temperature as previously explained) also plays an important role in the reactivity of the resulting char [393]. The experiments suggest that the pyrolysis pressure significantly influences the physical structure of coal chars, but it has little effect on the chemical structure of char which determines the intrinsic reactivity to a larger extent, therefore, in other words, chars produced at different pyrolysis pressures have different apparent reaction rates, but have similar intrinsic rates, suggesting that morphology rather than chemistry is responsible for the measured differences.

The yield of gas and tars together decreases with the increase of pressure while the gas yield

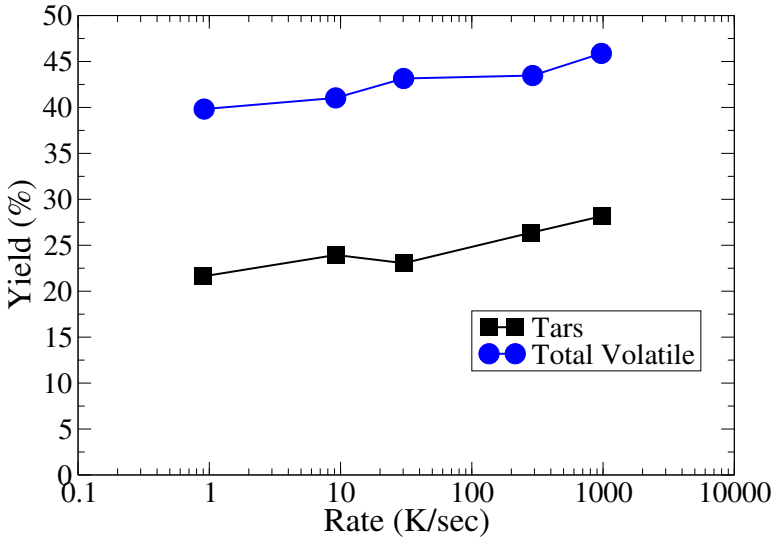

Figure 2.7.: Total volatile yields as a function of heating rate [393].

alone increases with the pressure. The effect is particularly important at high temperatures. With an increase of the pressure, the influence of the temperature is limited. The reduction is more pronounced for bituminous coals than for lignite.

Pressure also influences the gas composition. When increasing the pressure, more CO and aliphatic hydrocarbons, especially CH_4, are produced while CO_2 and H_2O do not change. Tars shift toward lower molecular weights. It appears that tars generated under elevated pressures show more significant enhancements in hydrogen than those generated at atmospheric pressure [261]. Estimated oxygen contents of the tars varied from 8 to 20%, which are only half to two-thirds of the values reported for atmospheric pyrolysis with the same coals. This difference probably reflects the elimination of oxygen functional groups from intermediate fragments of coal molecules at elevated pressure before they were released as tars compounds [261]. In Figure 2.8 some results are shown (see [393]) where the tars yield and the total amount of volatiles are plotted as a function of the pressure.

To explain the above observations, several mechanisms have been proposed. It is generally agreed that the secondary reactions and mass transport limitations are the processes that influence pyrolysis at ambient pressure, and the influence of pressure on the tars yields is found to be on the evaporation of tars precursors. Following the explanation in [364] while the vapor pressure of tar precursors is inversely proportional to their molecular weight, higher pressure inhibits the escape of larger tar molecules that may evaporate at low pressures. This is a reason that explains the tar yield decreases and tars shift toward lower molecular weights with increasing pressure. On the other hand, the experimental observation that the effect of pressure on the total volatiles and tars yields is significant at high temperatures imply that also secondary reactions contribute to the pressure influence on product yields. Moreover, increases in gas yields (particularly for methane) have been attributed to the secondary polymerization of the tars and the auto-hydrogenation phenomenon at elevated pressure, where hydrogen evolved from coal and reacts back to form CH_4.

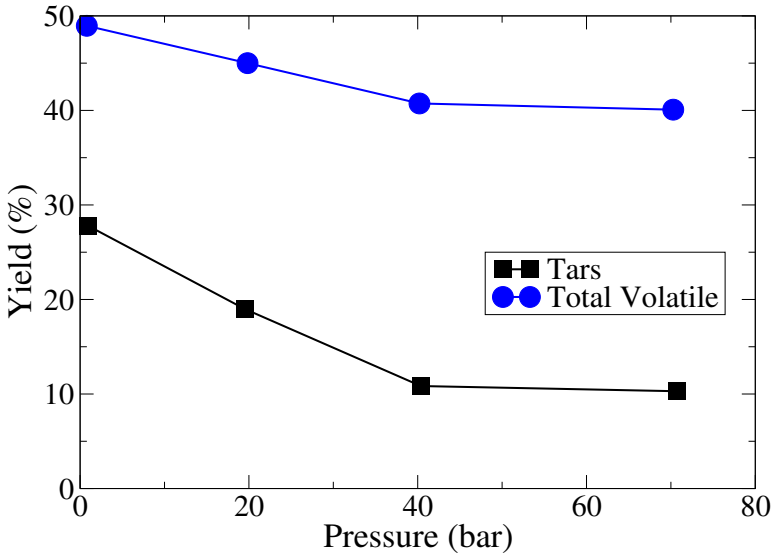

Figure 2.8.: Total volatile yields as a function of pressure [393]

Swelling Swelling is the most significant feature of softening coals during heating, which determines the particle size, porosity, density and reactivity of the residual char. As observed in [346] the swelling ratio increases when pressure increases and reaches a maximum value, then drops again. The pressure at which this maximum occurs is independent of coal rank and occurs typically between 10 and 20 atm. In Figure 2.9 the swelling ratio of chars generated from devolatilisation of different coals at a gas temperature of 1573K [393] is plotted as a function of the pressure.

Morphology Pyrolysis pressure has a significant effect on char morphology, and it has been observed that more porous chars are formed at elevated pressures. The apparent density decreases while in many samples the true density increases. The increase of porosity together with the increase of swelling ratio is consistent with the development of bubble structure separated by thin walls [439] (thinner at higher pressures). The higher reactivities of chars produced at higher pressure are consistent with a higher measured internal surface [106, 296, 107], an effect due to mainly higher micropores development. In fact, the intrinsic reactivity (per unit of the internal surface) increases only slightly with the pressure and this increase is less pronounced at higher pyrolysis temperatures [106, 73].

It is worth noticing that the trend of increase of reactivity and internal surface is in some cases reversed at higher pressures as in [439] where a decrease in the internal surface has been measured in the case of oxidation.

The effects of the pressure have been related to the vitrinite content of the parental coal therefore pyrolysis of bituminous coals forms chars whose structure is particularly affected by the pressure. For those chars, the intra-particle walls are thinner, and fragmentation can occur more frequently.

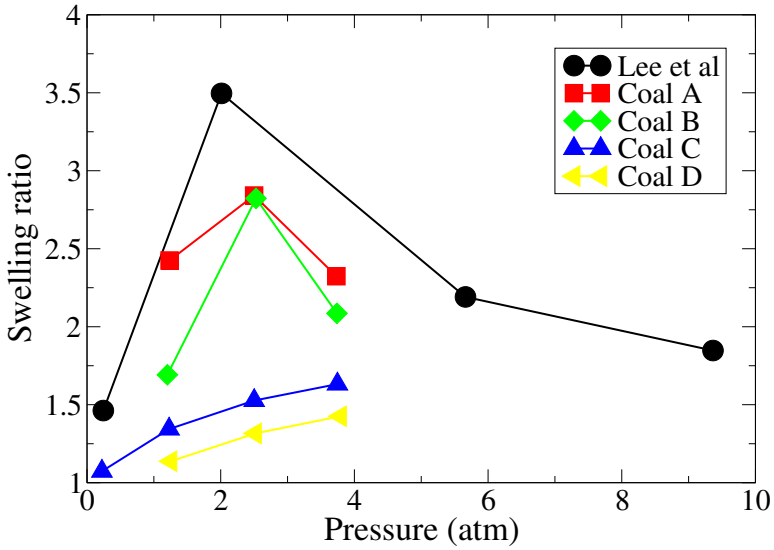

Figure 2.9.: Swelling ratio of chars generated from devolatilization of different coals at a gas temperature of 1573 K [393]

2.5.2. Biomass devolatilization

Devolatilization is an important part of the entire combustion process of biomass, because of their high VM content, which causes easier ignition and rapid burning. For the design of combustion burners, the high content of VM (up to 90%) needs to be taken into consideration. As for coal, tars are formed during devolatilization of biomass. Compared with coal, devolatilization of biomass and ignition occur at much lower temperatures. In [414] it is shown that the devolatilization of the coffee husks and the wood chips starts (upon completion of drying) at temperatures in range 160 to 200 °C. At around 200 °C, the devolatilization is rapid and significant weight loss is noticeable, while above 500 °C, the mass stays more or less constant. Also it can be observed, that devolatilization products from different biomasses are mainly CO, H_2, CO_2 and CH_4. As the devolatilization temperature increases, CO_2 decreases, while CO and H_2 increase rapidly. At higher temperatures, the combustibles (CO, H_2, CH_4) accounted for more than 70–80 vol% of the gas components. Despite the high VM content of biomass fuels, the heating values of their volatiles are lower than that of coal.

Pyrolysis of biomasses can be considered as a superposition of the pyrolysis of the single components, cellulose, hemicellulose, and lignin [88, 46]. Cellulose conversion proceeds in two stages: a gradual degradation, decomposition and charring on heating at lower temperatures, and a rapid devolatilization with the formation of levoglucosan at higher temperatures. The glucose chains are decomposed into glucose and, in a second stage, glucosan is formed by the splitting off of one molecule of water. Since cellulose and levoglucosan have the same elementary formula, a yield of 100% of the latter might be expected. The initial degradation reactions include depolymerization, hydrolysis, oxidation, dehydration, and decarboxylation [88]. High pressure blocks the depolymerization of the cellulose, reducing the amount of gas, while at the same time, allowing competing reactions such as dehydration and crosslinking to become dominant. The net effect is a decrease in the volatile production and an increased yield of char cellulose. Hemicellulose is decomposed in a way similar to cellulose: by dehydration at low temperatures (< 280 °C)

and depolymerization at higher temperatures. Hemicelluloses contain more combined moisture than lignin and the hemicelluloses softening point is low compared to lignin. Also, exothermic peaks of hemicelluloses appear at lower temperatures than that of lignin, and their thermal decomposition occurs at a lower temperature. The aromatic structure of lignin is reflected in the higher stability of the molecule, and consequently, the conversion temperature is higher than the one for cellulose or hemicellulose. Lignin produces higher amount of char and tars and products are characterized by guaiacol and pyrogallol dimethyl ether [7]. Phenolics are obtained by cracking of the phenyl-propane units [8] of the macromolecule lattice.

It has been found that pyrolysis of hemicellulose and lignin are exothermic processes while pyrolysis of cellulose is endothermic at lower temperatures and becomes exothermic at higher temperatures. The variations seen for cellulose are believed to be the effect of combined primary and secondary reactions. Primary reactions (active at low temperatures) are endothermic while secondary reactions, dominant at higher temperature are exothermic.

As pointed out in [47] and references therein, the total yield and the relative proportion among bio-char volatiles and bio-char tars depend, as for coal, on the heating rate and temperature of the devolatilization process. Tars yield in fast pyrolysis experiments tend to increase as the temperature increases until 750 °C where they reach a maximum of about $70 - 80\%$ (dry solid basis). For higher temperatures, the yield decrees sharply. In slow pyrolysis experiments, the trend of the tars yield shows a much slower increase until a constant value of around $50 - 60\%$ is reached. This behavior is explained by the presence of secondary reactions active only at higher temperatures producing tars cracking into secondary tars and light gases. In fact, light gases whose yield at a lower temperature is only around 10%, increase quickly with temperature for both fast pyrolysis and slow pyrolysis. For fast pyrolysis, the increase in the light gas component is more evident. Char yield shows in both condition a quicker decrease in lower temperature and remains constant for all the range at higher temperatures. For slow pyrolysis, biochar yield remains in all the conditions twice as high as for fast pyrolysis, indicating a competition between tars transport and reattachment.

2.6. Definition of the reaction rates

The following definitions are here provided since they are important for the understanding of the following sections. A complete description of the reaction rates equations is postponed to Chapter 8.

The mass loss of a fuel particle $\frac{dm}{dt}$ (in $\frac{\text{kg}}{\text{s}}$) is measured by the reactivity $\dot{R}$ (in $\frac{1}{\text{s}}$) defined as:

$$\dot{R} = -\frac{1}{m}\frac{dm}{dt} \tag{2.6}$$

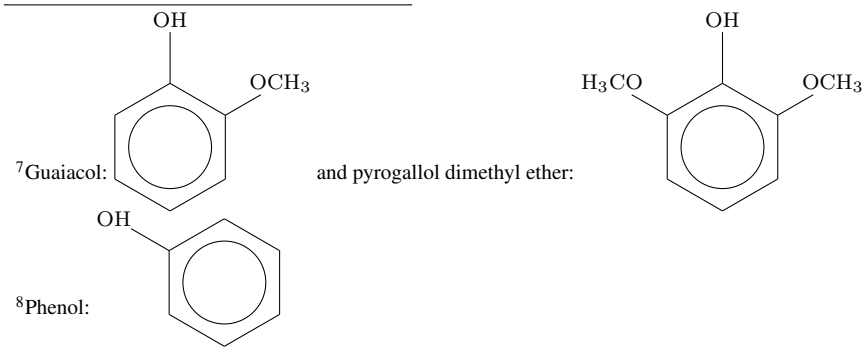

[7] Guaiacol: and pyrogallol dimethyl ether:

[8] Phenol:

It is proved that the reactivity $\dot{R}$ is proportional to a surface as every heterogeneous processes. The *apparent* reaction rate is defined as the mass loss per unit of the external particle surface while the *intrinsic* reaction rate is defined as the mass loss per actual (or internal) available surface.

The partial pressure of the reactant p_r plays also a role and in the simplest case the reaction rate can be expressed by the following formula:

$$\frac{dm}{dt} = -S \cdot k(T) \cdot p_r \tag{2.7}$$

The function $k(T)$ is called *rate constant*.

2.7. Char combustion

During the release of volatiles, char is formed. The char is richer in carbon than the original fuel and it consists of porous networks into which oxygen can diffuse and react. Two basic overall reactions for char oxidation can be written:

$$\mathrm{C} + \frac{1}{2}\,\mathrm{O_2} \longrightarrow \mathrm{CO} \tag{R 2.1}$$

$$\mathrm{C} + \mathrm{O_2} \longrightarrow \mathrm{CO_2} \tag{R 2.2}$$

but for thermodynamical reasons the first one is predominant (see Section 3.2.1).

Compared to rapid VM oxidation, heterogeneous char oxidation requires much longer time. Typical total combustion time for a 100 µm char particle is on the order of 1 s. Thus it can be regarded as the rate-limiting step of the overall combustion process. During char oxidation, the reactant, usually oxygen, diffuses from the gas phase through the boundary layer to the surface of the particle and into the particle's pore system.

The oxygen reacts with carbon in the pore walls producing CO and CO_2. The CO can react in the gas-phase to form CO_2, which further reacts with the carbon in the char. Characterization of a universal intrinsic kinetic reactivity per active site, applicable for all chars, and the connection between concentration of active site and structural coal or char properties are still fields of research. Carbon in the solid phase is consumed, altering spatially and temporally the pore structure. This phenomenon influences the available surface area, active site concentrations, and pore diffusional characteristics.

The rate of char oxidation is controlled by the sequential or parallel processes of boundary layer diffusion and pore diffusion. Several works, such [392] and [133] have postulated the existence of three different temperature zones, where one or more different processes limit the overall char oxidation rate.

- At low temperatures, the intrinsic reaction is slow, reactant gases diffuse into the particle center, and the particle burns internally at a constant diameter with a decreasing particle density (Zone I).

- At moderate temperatures, the intrinsic reaction rate increases and the consumption of the reactant gas is higher than the rate of internal diffusion. The reactant gas is consumed before diffusing completely into the particle. Particle burns both internally and externally with a decreasing diameter and particle density (Zone II).

- When high temperatures are reached, the reaction occurs only on the particle surface, while

reaction rate is controlled by the diffusion rate of the boundary layer film. The particle burns with decreasing particle diameter, while density remains constant (Zone III).

Since intrinsic kinetic mechanisms are dependent on surface area, changes in porosity and surface area with burnout affect the char reaction rates in Zones I and II. With changing the pore structure and the surface area, the oxidation process may occur through all three zones before the carbon is completely consumed. The conditions under which a char is produced, such as heating rate, peak temperature, gas environment and residence time, affect a char's chemical and physical structure, and consequently the resulting char reactivity [341, 82].

Many investigations have been published on the effect of oxidant pressure on the combustion reaction rate of coal, in which both oxygen partial pressure and total pressure have been studied (see [393] and cited references). The combustion rates were observed to increase with increasing pressure. At low pressures, the chemical reaction rate controlled the overall reaction rate. With an increase in pressure, the reaction approached pore diffusion controlled conditions. The pressure dependence appears to invert for very small particles, as seen in some oxidation rate experiments [260] and [207]. For particles with a dimension of the order of few microns burning rates would probably be limited by a combination of pore diffusion and chemical reaction. Consequently, a major portion of the internal surface area would participate in the oxidation. The reported oxidation rates decreased for higher total pressures, especially at the higher gas temperatures.

Since lignite chars have the highest intrinsic char oxidation reactivities, film diffusion might be expected to approach the theoretical Zone III limit, but the situation is more complicated. The burnout of some lignite char is independent of total pressure, consistent with a strictly diffusion-limited burning rate but burnout of the other lignite char exhibits a strong pressure dependence [393]. Similarly, the burnout of some of the hv bituminous chars is independent of pressure up to 0.5 MPa, becoming higher for progressively higher pressures. But the burnout of the other hv bituminous char is especially sensitive to pressures below 0.5 MPa, then it becomes insensitive to further increases in the pressure. Compared to the lignite char, the bituminous and anthracite chars are converted at slower burning rates for pressures above 0.25 MPa. The particles always burn hotter for progressively higher pressures, except for the lignite whose burning rate is film-diffusion-limited.

Biomass chars contain high levels of oxygen and low levels of hydrogen compared to coals. Hence, graphitic structures do not develop in biomass chars as they do in bituminous coal chars, which contain lower oxygen levels. The structural disorder may also lead to higher reactivities of biomass in the late stages of combustion since more edge carbon (which is more reactive) is available. Nevertheless, biomass chars are quite reactive in the early stages of char conversion and burn almost under diffusion control. Biomass char burning rates are comparable to burning rates of high–volatile matter bituminous coal chars [427].

2.8. Char gasification

After drying and devolatilization, the remaining solid structure does not react only with oxygen as described in Section 2.7. The fixed carbon in the char can react also with water vapor, carbon dioxide and hydrogen:

$$\mathrm{C} + \mathrm{CO_2} \longrightarrow 2\,\mathrm{CO} \tag{R 2.3}$$

$$\mathrm{C} + \mathrm{H_2O} \longrightarrow \mathrm{CO} + \mathrm{H_2} \tag{R 2.4}$$

$$\mathrm{C} + 2\,\mathrm{H_2} \longrightarrow \mathrm{CH_4} \tag{R 2.5}$$

The steam gasification is the fastest among all, and the methanation reaction is by far the slowest. All the gasification reactions are endothermic, and their rates are lower than for the oxidation reactions. The relative rates of the four reactions (oxidation plus gasification), at $\theta = 800\,^{\circ}\mathrm{C}$ and $p = 1\,\mathrm{atm}$ are estimated to be 10^5 for oxygen, 10^3 for steam, 10 for carbon dioxide, and 10^{-3} for hydrogen with variations among different fuels.

The basic features of gasification reactions do not differ much from those of the oxidation reaction. At low temperatures, all the reactions increase their rate exponentially, and for high temperatures, the increase follows a power law trend. While for oxidation reactions the change in slope happens at around $500\,^{\circ}\mathrm{C}$, for gasification reactions that change is more towards higher temperatures, around $1100\,^{\circ}\mathrm{C}$. That change in temperature dependency is due to the reaction shift from zone I to zone II, where pore diffusion is the rate controlling mechanism. A very similar temperature dependence appears for steam gasification but at significantly hotter temperatures and for much shorter reaction times.

The apparent gasification rates are significantly accelerated at higher pressures. For both gasification reactions, R 2.3 and R 2.4, the incremental conversion becomes smaller at progressively higher pressures, indicating that this effect saturates. The gasification reactions are controlled by pore diffusion, and normally a pore diffusion rate is independent of pressure because the pressure dependence in the reactant concentration cancels the inverse proportionality to pressure in the diffusivity. But since the partial pressure of the gasification agent is uniform during experiments, the diffusivity determines the pressure dependence in the transport rate, which would tend to diminish the overall gasification rate at progressively higher pressures.

The pressure dependence is most substantial in the lower pressure range, as expected. But the asymptotic saturation at high pressures becomes less pronounced with chars of progressively lower rank. Indeed, no asymptotes are apparent with subbituminous chars. In general, gasification rates diminish for coals of progressively higher rank, but only for ranks of high volatiles bituminous. Mineral catalysis becomes more significant than the generic rank dependence for low-rank chars, so the carbon content of the parent coal no longer correlates this portion of the rank dependence.

A feature of gasification kinetic, hardly observed in oxidation experiments, is the influence of external molecules like the CO for the reaction R 2.3 and H_2 for the steam gasification. It seems to be experimentally verified that those molecules (and some others too) decrease the gasification reaction rates and it is proved that this effect is pressure dependent.

2.9. Fragmentation of porous char during conversion

Char fragmentation has been found to play a significant role in ash formation (see [33]). Frequent fragmentation reveals a reduced coalescence of included minerals during combustion. Various char fragmentation studies have also shown that fragmentation is strongly associated with the porous char structure and highly porous chars tend to fragment frequently. Fragmentation of char begins below a burnout level of 54%, and becomes intensive at burnout levels between 54 and 70%, due to a significant number of cenospherical char particles in the bulk samples. Percolation theory has been applied to the fragmentation study, and it has been shown that the fragmentation of char particles (at least of the char of Group I) appears to be associated with the macropores in the external particle shell, which provide weak points from which a fragment can detach. Macropores in the shell are formed during both devolatilization and char combustion.

Char particles of various structures have significantly different behavior, regarding char fragmentation, reaction mode, and burnout. Char particles of Group I type (see Section 2.2.1 for the classification by morphology) are highly porous with a thin wall, and have been found to burn quickly during the early combustion stage, which leads to a significant decrease in the amount

of the Group I type char particles observed during the combustion. This type of char particles also fragments significantly during combustion, reducing the extent of coalescence of included mineral matter. Coalescence of the included mineral particles is possible only for the small fragments, which are produced by the fragmentation of Group I particles, containing more than one mineral particle inclusion. Complete combustion of these small fragments results in the fine ash particles being liberated in early stages. Fragmentation of Groups II and III particles occur at the late stages of combustion, and the burnout of these particles and ash liberation occur at much longer times than those of Group I particles. Group I type char particles fragment extensively during the early and middle combustion stages and burn out early. The extent of coalescence for the included mineral particles is very low. One Group I type char particle may produce some small ash particles, resulting in small size distribution. Group II type char particles fragment less compared to the Group I type char particles. Char fragmentation is still the dominant mechanism for ash formation, but the included mineral particles undergo some coalescence. One Group II type char particle may produce several ash particles with a relatively larger size compared to the Group I type char particle, resulting in an increase in the size distribution of the ash during the middle burnout stage. Group III type char particles exhibit low or no fragmentation. The included mineral particles undergo a considerable degree of coalescence. One Group III type particle may form only one or two ash particles of a larger size compared to Groups I and II type char particles, resulting in a significant shift to a larger size of ash size distribution during the late combustion stage.

Char structure has been found to have a significant role in explaining pressure effects in ash formation. At 15 atm, the charred sample contains mainly highly porous Group I particles. However, at 1 atm, it is dominated by the Groups II and III type particles. As a consequence, at high pressures, char fragmentation is more pronounced, as more cenospherical char particles are formed by high-pressure pyrolysis. It indicates that ash formed at high pressure has a much finer size.

2.10. Reactivity reduction

At higher temperatures and higher burnouts, many solid fuels show a reduction in their conversion rates, ([441, 219] and reference herein). Experimental evidence is based on TGA experiments using different chars either generated in laboratory scaled experiments or extracted from industrial plants. Generally, the chars collected from industrial plants are more reactive than the chars generated in laboratory conditions. Morphologies analyzed using quantitative X-ray diffraction analysis, high-resolution transmission electron microscopy, high-resolution scanning electron microscope and multi-point gas adsorption [219] have confirmed that chars from utility boilers are indeed more ordered than chars produced in entrained flow, TGA or even fluidized bed reactors.

The deactivation are usually explained in term of the following phenomena ([219, 365]):

- Number of active sites available;
- Annealing of the solid structure;
- Ash inhibition;
- Pores closure;
- Changes in the amount, nature and distribution of catalytic materials;

Since the chars are extremely heterogeneous the hypothesis of the active site with different reactivity is reasonable (and probably valid) but the knowledge available on different active sites chemistry suggest that this cannot be the only reason for the deactivation.

Annealing is the process of changing chemical structure under heat treatment. Transformations in the carbonaceous matrix include the loss of hydrogen and oxygen, elimination of edge carbon sites due to coalescence of aromatic rings, and defect elimination [317, 161]. The order of the structure in the char increases approaching, in the limit, the structure of graphite. In practical applications, due to cross-linking and relatively lower peak particle temperatures, the final stage is never perfectly ordered graphite. For biomass fuels, the cross-linking is more pronounced and hence their annealing propensity due to changes in the carbonaceous phase is less than for coals. The above transformations are usually taken into account using a parameter that combines the effect of reduction in intrinsic char reactivity as well as internal surface area [161, 160], as introduced in Section 8.7.4.

3. Heterogeneous Chemistry

Char oxidation and gasification reactions are heterogeneous reactions. Heterogeneous reactions are defined as those reactions taking place between reactants in different phases. For the processes taken here into consideration, the oxygen, the carbon dioxide or the water vapor are in gas phase while the carbon is in the solid phase. The correct mathematical description of both process, i.e., oxidation and gasification respectively, is the first step for modeling of solid fuel conversion applications.

3.1. Mechanisms of chemical reaction rates

Heterogeneous reactions are described as a result of several sub-processes:

1. Firstly the reactants diffuse from the bulk through the particles boundary layer until they reach the surface;

2. The reactant is in gaseous form and it will react with the solid structure;

3. The products will diffuse finally back into the bulk phase.

Each of the aforementioned steps must be described mathematically and the influence of the thermodynamic quantities must be determined.

The porosity of the char is also a fundamental ingredient for the total reaction rate. Char from coals or biomasses are both highly porous, increasing enormously the surface available for the reactions. On the other side, after bulk diffusion, the reactant is not yet in contact with the most available surface, and molecules must continue to diffuse inside the porous structure of the solid particle. Pores diffusion, is in most cases the limiting rate of the process and it is strongly coupled with kinetic rates. While reactions progress, the solid structure is altered, creating a two-way coupling between diffusion and kinetics. More information are given in Section 2.3.

The chemical reactions with the carbon atoms of the surface are described by the active site theory. Reactions occur only in favorite sites of the solid structure (called *active sites*) where the gaseous reactant will be bounded (adsorbed), and bonds will be broken. The newly formed molecules will be then released from the active site (desorption) into the gas phase. At each active site, it may occur that, after the reactant is adsorbed, an eventual intermediate can migrate to nearby sites.

The theory is based on the following assumptions:

1. Localized adsorption via collision with empty active sites;

2. One adsorbed molecule or atom per site;

3. A constant surface mechanism (chemisorption/migration/desorption);

4. Surface coverage less than a complete mononuclear layer.

Adsorption Two types of interactions between solid structure and gas species usually occur, namely physical adsorption and chemisorption. Physical adsorption is non-specific and somewhat similar to the process of condensation. The forces attracting gas molecules to the solid surface are rather weak. Because of the small amount of energy requirement, the adsorbed gas molecules are quickly removed from coal surfaces. Chemisorption is surface specific and involves forces much stronger than those operating in physical adsorption. It is argued that only particular sites at internal surfaces of the fuel can attract the reactant molecules, and hold them by valence forces of the same type as those occurring between atoms in molecules. Those particular sites are the one where irregularities induce electron transfer causing gas-solid bounding. For coal and biomass, the irregularities can be formed by [205]:

1. carbon edges or dislocations;
2. inorganic impurities;
3. oxygen and hydrogen functional groups [1].

Physically adsorbed or chemically adsorbed reactants can be easily distinguished experimentally, as the gas chemically absorbed by the structure cannot be recovered since chemisorption is irreversible while physically adsorption is a reversible process. It has been found that physical adsorption plays a major role below $273\,\mathrm{K}$, while at higher temperatures, the irreversible chemisorption is the dominant process during adsorption. The different mechanisms of adsorption cause differences in mass balance at the surface since physical adsorption results in single or multiple layers of adsorbed molecules, while chemisorption is limited to a monolayer of molecules at the surfaces. Adsorption mechanisms also play distinct roles in the total heat balance during the conversion process. Physical adsorption is characterized by the heat of adsorption, which is in the same order of magnitude as the heat of vaporization. Figures of between 6.7 and 20.9 $\frac{\mathrm{kJ}}{\mathrm{mol}}$ are quoted as reasonable limits for the heat of physical adsorption of O_2 on solids. In contrast, the heat of chemisorption of gases by coal and biomass is much higher, in the range from 83.6 to 418.0 $\frac{\mathrm{kJ}}{\mathrm{mol}}$ depending on the coal type and the amount of O_2 consumed. Mineral matter and trace elements can provide direct catalytic activity.

Both adsorption and desorption can occur via a single or dual site mechanism. Migration allows for changes in the mobility or stability of surface intermediate. Examples of single site chemisorption requires one free carbon site:

$$\mathrm{C}_f + \mathrm{CO}_2 \longleftrightarrow \mathrm{CO} + \mathrm{C(O)} \tag{R 3.1}$$

$$\mathrm{C}_f + \mathrm{O} \longleftrightarrow \mathrm{C(O)} \tag{R 3.2}$$

where C_f is a free carbon site and $C(O)$ denotes a carbon site filled with atomic oxygen. Dual site adsorption requires two free carbon sites. An example is given below:

$$\mathrm{C_{f_1}} + \mathrm{C_{f_2}} + \mathrm{O}_2 \longleftrightarrow 2\,\mathrm{C(O)} \tag{R 3.3}$$

Surface migration involves movement of adsorbed atom from a site to a more mobile site as in the following reaction:

$$\mathrm{C'(O)} \longrightarrow \mathrm{C(O)} \tag{R 3.4}$$

[1] In organic chemistry, functional groups are lexicon-specific groups of atoms or bonds within molecules that are responsible for the characteristic chemical reactions of those molecules. The same functional group will undergo the same or similar chemical reaction(s) regardless of the size of the molecule it is a part of. However, its nearby functional groups can modify relative reactivity. The atoms of functional groups are linked to each other and to the rest of the molecule by covalent bonds. When the group of covalently bound atoms bears a net charge, the group is referred to more properly as a polyatomic ion or a complex ion. Any subgroup of atoms of a compound also may be called a radical, and if a covalent bond is broken homolytically, the resulting fragment radicals are referred to as free radicals.

where $C(O)$ is a stable site and $C'(O)$ is a mobile site.

Examples of desorption reactions are given below:

$$\mathrm{C(O)} \longrightarrow \mathrm{CO} + \mathrm{C}_f \tag{R 3.5}$$

$$\mathrm{C(O)} + \mathrm{C(O)} \longrightarrow \mathrm{CO_2} + \mathrm{C_{f_1}} + \mathrm{C_{f_2}} \tag{R 3.6}$$

In the first reaction, the rapture of the bond of a carbon site filled with atomic oxygen produce the emission of a molecule and the exposure of a new free carbon site. In the second reaction, the interaction of two near carbon site produces the emission of e CO_2 molecule and the disclosure of two different free sites.

3.1.1. Heterogeneous reaction rates

The mass loss of a fuel ($\frac{dm}{dt}$), to be determined in Chapter 8, requires an expression of the intrinsic reaction rate $\dot{R}$. The intrinsic rate (called also surface reaction rate in some works) is defined as the amount of carbon removed per unit of real (internal) surface and its unit is $\frac{\mathrm{kg}}{\mathrm{m^2\,s}}$. The intrinsic reaction rate is a complex function of temperature, gas composition and surface properties, but it can be usually simplified using the following equation, in which the parameters are effective parameters:

$$\dot{R} = k \cdot [C]^m \tag{3.1}$$

where $[C]$ (in $\frac{kg}{m^3}$) is the local gas concentration, m is the reaction order and k the reaction rate constant. The reaction rate constant is usually expressed using an Arrhenius form:

$$k = AT^b e^{-\frac{E}{RT}} \tag{3.2}$$

where A is the pre-exponential factor and E is the activation energy.

Intrinsic heterogeneous reaction rates can be quantitatively described by the active site theory. The model describing a single site or a double site mechanism is denoted as the Langmuir-Hinshelwood kinetics [154]. The following assumptions are usually made:

1. The surface is homogeneous and, consequently, also the active site are distributed homogeneously;
2. The adsorbed species are non-interacting with the consequence that the amount of adsorbed species does not affect the rate of adsorption;
3. Surface migration is non-existent or so quick that adsorption or desorption is the controlling rate.

In the characterization of the conversion velocity, the following rates are involved (the rates are expressed in $\frac{\mathrm{kg}}{\mathrm{m^2\,s}}$):

- The adsorption rate $\dot{R}_a$;
- The desorption rate $\dot{R}_d$;
- The migration rate $\dot{R}_m$;
- The kinetic rate $\dot{R}_c$;
- The intrinsic rate $\dot{R}$;

Each of the aforementioned rates has a different dependency on temperature and reactant pressure and therefore their combination gives rise to complex laws for different regimes.

As a first example of the application of the methods of the active site theory, let us consider the case in which the kinetic of formation of intermediate products $\dot{R}_c$ is not the limiting rate because it is much quicker than absorption. Even if this assumption is not usually acceptable in coal or biomass conversion rate, it has pedagogical importance.

Chemisorption is due to molecules that strike a non-covered active site. If θ is the fraction of free site it follows that the intrinsic rate of adsorption $\dot{R}_a$ (in $\frac{kg}{m^2 sec}$) can be written in the following way:

$$\dot{R}_a = k_a \cdot [C] \cdot (1-\theta)^n \tag{3.3}$$

where $[C]$ is the concentration of gas and $n = 1$ for a single site mechanism or $n = 2$ for a double site mechanism. The kinetic rate k_a (in $\frac{m}{sec}$) is calculated using the kinetic theory of gas:

$$k_a = A_a \cdot e^{-\frac{E_a}{RT}} = \frac{\epsilon\Lambda}{\sqrt{2\pi MRT}} \cdot e^{-\frac{E_a}{RT}} \tag{3.4}$$

where ϵ is the efficiency of collision and Λ is a stoichiometric coefficient.

The rate of desorption can be assumed to be proportional to the fraction of covered surface:

$$\dot{R}_d = k_d \cdot \theta^{n'} \tag{3.5}$$

where n' refers indifferently to the single or doubles site desorption mechanism. For single site mechanism, Equation 3.3 and Equation 3.5 are exact, independent from site mobility. For dual site mechanisms, both equations imply either mobility or non-mobility with low site coverage. In the last case, desorption mobility is required to allow site interactions.

If adsorption and desorption have the same reaction order $n = n'$, and after imposing steady state ($\dot{R}_a = \dot{R}_d$):

$$\left(\frac{\theta}{1-\theta}\right)^n = K_{ad,eq} \cdot [C] \tag{3.6}$$

where the equilibrium constant $K_{ad,eq}$ is defined by:

$$K_{ad,eq} \equiv \frac{k_a}{k_d} = \frac{A_a}{A_d} \cdot e^{-\frac{E_a - E_d}{RT}} \tag{3.7}$$

It is worth noticing that $K_{ad,eq}$ is a function of the temperature only. Rearranging Equation 3.6, the fraction of available sites can be written in the following way:

$$\theta = \frac{\left(K_{ad,eq} \cdot [C]\right)^{1/n}}{1 + \left(K_{ad,eq} \cdot [C]\right)^{1/n}} \tag{3.8}$$

This equation describes the classical Langmuir-Hinshelwood isotherm for adsorption and it is the basis for the Langmuir-Hinshelwood kinetic rate.

Several characteristics can be derived from the model.

- Assuming $n = 1$ and introducing Equation 3.8 into Equation 3.3:

$$\dot{R} = \dot{R}_a = \dot{R}_d = k_a \cdot \frac{[C]}{1 + K_{ad,eq} \cdot [C]} \tag{3.9}$$

Comparing the results of Equation 3.9 with the definition of $\dot{R}$ given in equation 3.1

$$\dot{R} = k \cdot [C]^m$$

it becomes evident that the global reaction order m changes according to the temperature and the pressure. If $K \cdot [C] \ll 1$ the reaction rate simplifies to $\dot{R} = k \cdot [C]$ and then $m = 1$ while if $K \cdot [C] \gg 1$ the reaction rate simplifies to $\dot{R} = k$ and then $m = 0$.

- If $n = 2$ neither $m = 0$ nor $m = 1$ are obtained.

- If $n = 2$ and $n' = 1$ the combination of Equation 3.3 and Equation 3.5 gives:

$$K_{ad,eq}[C] \cdot \theta^2 - (2K_{ad,eq}[C] - 1) \cdot \theta K_{ad,eq}[C] = 0 \tag{3.10}$$

and it offer the possibility to have half order kinetic.

3.1.2. Multicomponent systems

If more than one species adsorbs and reacts on a single site material, assuming steady state, it is possible to derive the following relation:

$$k_{a,i} \left(1 - \sum_1 a_1 \right) = k_{d,i}\theta_i \tag{3.11}$$

where the index i refers to each single species and θ_i is the fraction of active sites covered by the i_{th} specie. For a binary mixture the previous equation can be solved and the following relation for the reaction rate $\dot{R}_1$ is obtained:

$$\dot{R}_1 = k_{a_1} \frac{K_1 \cdot [C]_1}{1 + K_1 \cdot [C]_1 + K_2 \cdot [C]_2} \tag{3.12}$$

where, as before, the equilibrium constant $K_1 = \frac{k_{a,1}}{k_{d,i}}$ have been introduced. It follows from Equation 3.12 that the presence of a second adsorbed species (it can also be an inert) reduces the reactivity closing part of the actives sites.

3.1.3. Influence of surface migration

The rate of migration among sites can me modeled as:

$$\dot{R}_m = k_m \cdot \theta \tag{3.13}$$

where as before θ is the fraction of active sites and the factor k_m is written in an Arrhenius form with an activation energy E_m. The surface migration process can be significant at a lower temperature since $E_m < E_d$. In fact, migration requires weak bond while desorption involves bond breaking.

If the intrinsic rate is controlled by surface migration then the steady state relation

$$\dot{R} = \dot{R}_m \tag{3.14}$$

predicts the following reaction rate in the case of single site adsorption:

$$\dot{R} = k_m \frac{K \cdot [C]}{1 + K \cdot [C]} \tag{3.15}$$

and in the case of double side adsorption:

$$\dot{R} = k_m \frac{(K \cdot [C])^{1/2}}{1 + (K \cdot [C])^{1/2}} \tag{3.16}$$

It is worth noticing that the expression 3.15 is identical to the expression previously derived in equation 3.9. Therefore, different assumption for chemisorption, adsorption, desorption and surface migration, often lead to similar results.

3.1.4. Non-homogeneous surface

In non-homogeneous surface model [149] the sites most reactive are filled first. If the sites are also interacting, then the presence of adsorbed molecule favors the desorption of neighboring molecules and disfavor further adsorption. This effect is increased with the temperature. Therefore, following this model, it can be assumed

$$E_d = E_d^0 - \omega_d \cdot \theta \tag{3.17}$$
$$E_a = E_a^0 + \omega_a \cdot \theta \tag{3.18}$$

As a function of temperature the chemisorption rate can be written in the following form:

$$\dot{R}_a = \dot{R}_a^0 \cdot e^{-\omega_a / RT} \tag{3.19}$$

For char reactions, there is no evidence of such a mechanism.

3.2. Detailed Kinetics

In the present section, the ideas developed in the previous one, will be applied in the more realistic case when the chemical reactions become a limiting step for the intrinsic rate $\dot{R}$. It is worth noticing that the reaction rate is not proportional to the total surface area (TSA) but the active surface area (ASA), where:

$$ASA = A_g \cdot [C_t]$$

where $[C_t]$ is the concentration of total active sites expressed per kg of solid fuel. The ratio $r = \frac{ASA}{TAS}$ decrease at the beginning of the reactions and then increase somewhat at higher burnout [240]. The total internal surface has an inverse behavior therefore for many chars it is found that the reactivity is proportional to the internal specific surface area A_g without the effect of the concentration of total active sites $[C_t]$. The active site concentration $[C_t]$ is promoted by carbon edges, metallic impurities and heterocyclic sites (mainly oxygen). If metallic impurities predominate, the reaction rate remains constant with the burnout. If oxygen sites are predominant the reaction rate decrease with the burnout due to oxygen depletion. If carbon edges are predominant, then the reactivity can increase with the burnout. However, at higher temperature thermal annealing occurs reducing $[C_t]$ and therefore the reactivity.

As in the case of homogeneous reactions (see Chapter 5) two levels are available for the description of heterogeneous reaction rates:

Global mechanisms in which the mechanism is simplified to include only the main components. The rates derived from this approach are expressed by simple mathematical expressions, quickly implemented into a CFD software, but the accuracy is limited to narrow temperature, pressure and composition ranges.

Detailed mechanisms in which more fundamental steps are taken into consideration. The final mechanism is more physically and chemically accurate, and the rate is accurate also for a wider range of temperature and pressure,

In the following sections, more attention is given to the detailed description of the heterogeneous reaction of solid fuels. The simplifications needed for the implementation in a CFD software are described in Chapter 8.

3.2.1. The $C + O_2$ reaction

The reaction of Carbon with oxygen, probably one of the most important reactions, is also one of the most difficult to investigate because:

- it has an high reaction rate;
- it is exothermic, producing temperature uncertainties;
- thermal annealing produces a change in $[C_t]$

Each proposed mechanism should be able to reproduce the correct magnitudes of the temperature dependence (global intrinsic activation energy) and concentration dependence (global intrinsic reaction order) during steady-state combustion across the various temperature and pressure ranges of technological interest. The experimental data available for the comparison with the predictions is extensive and there is no universal consensus even on the magnitude of the global orders or activation energies involved ([162]) [2]. The following observation can be taken for established:

1. Global intrinsic activation energies fall between 105 and 180 $\frac{\text{kJ}}{\text{mol}}$ with many values in the range 130 to 150 $\frac{\text{kJ}}{\text{mol}}$
2. The reaction order change from $n = 1$ for lower temperatures (typically $T < 1000 - 1300$K) to $n = 0$ for higher temperatures ($T > 1400 - 2000$ K). For even higher temperatures, experiments indicate an increase of the reaction order.
3. Many studies didn't find any saturation region of the reaction rate as a function of the partial pressure. (Only in the case of gasification with CO_2 and H_2O an asymptotic behavior has been found around 20-30 bars).
4. A mixture of CO and CO_2 has been measured in many experiments, and it is now assumed that both are primary products. It has been experimentally observed that at higher temperatures, typical of combustion applications, the sole product is CO but at lower temperatures, the amount of carbon dioxide increases. There is evidence that catalytic effects at lower temperature can increase the formation of CO_2. The ratio of carbon dioxide to

[2] Part of the scatter is because of problems with experimental techniques and data analysis methods, both of which have been in a continuous state of development, part is because of real fuel-to-fuel differences, and part is because of the limited size of individual datasets, which makes many kinetic analyses formally correct, but statistically not significant [162].

carbon monoxide in the product, is mathematically described by an exponential relation of the form:

$$\frac{[\mathrm{CO}]}{[\mathrm{CO2}]} = Ae^{-E/RT} \tag{3.20}$$

with the following values for the rate parameters:

$A \simeq 10^{2.5}$	$E \simeq 24 - 50\ \frac{\mathrm{kJ}}{\mathrm{mol}}$	at low pressures
$A \simeq 10^{3.5}$	$E \simeq 50 - 70\ \frac{\mathrm{kJ}}{\mathrm{mol}}$	at higher pressures

Mechanism Oxi-A: The following 2-steps mechanism is the easiest mechanism based on elementary reactions:

$$\mathrm{C}_f + \mathrm{O}_2 \longrightarrow \mathrm{C(O)} + \mathrm{O} \tag{R 3.7}$$

$$\mathrm{C(O)} \longrightarrow \mathrm{CO} + \mathrm{C}_f \tag{R 3.8}$$

The oxygen is adsorbed on a free site, forming the complex C(O) and releasing the radical O. The C(O) group will detach from the carbon structure and desorbed as carbon monoxide only.

If the second reaction is non-dissociative then, as explained in Section 3.1, a Langmuir-Hinshelwood type reaction is obtained:

$$\dot{R} = \frac{k_1 k_2}{k_1 \cdot [C]_{\mathrm{O}_2} + k_2} \cdot [C]_{\mathrm{O}_2}$$

The Langmuir-Hinshelwood kinetic predicts an effective reaction order that varies with temperature. Activation energies for desorption have been measured in the range 160 to 400 $\frac{\mathrm{kJ}}{\mathrm{mol}}$ and those for adsorption in the range 10 to 125 $\frac{\mathrm{kJ}}{\mathrm{mol}}$, therefore, for most surface sites, $E_{des} \gg E_{ads}$. Under this circumstances, for a given pressure, $r_g = k_2$ in the low temperature regime, predicting a zeroth reaction order (desorption controlled) behavior, and $r_g = k_1 p_{O2}$ in the high temperature regime, predicting a reaction order $n = 1$ (adsorption controlled). The experiments show the opposite trend. The Langmuir-Hinshelwood kinetic expression can be fitted to experimental data, providing mostly good results (see [438]), but then it looses his theoretical soundness and it must be considered as an empirical expression that contains an additional parameter to allow a variable reaction order within a given data set. Another problem with this form of the reaction rate is its impossibility of predicting fractional reaction order, holding for several orders of the oxygen partial pressure [363]. Finally, the inverted ($E_{des} < E_{ads}$) Langmuir-Hinshelwood is an useful form for the reaction rates but fails to predict the transition region from adsorption controlled to a desorption controlled region.

Mechanism Oxi-B: An enhancement to the 2-steps mechanism has been proposed in [356]:

$$\mathrm{C}_f + \mathrm{O}_2 \longrightarrow \mathrm{C(O)} + \mathrm{O} \tag{R 3.9}$$

$$\mathrm{C}_f + \mathrm{O} \longrightarrow \mathrm{C(O)} \tag{R 3.10}$$

$$\mathrm{C(O)} \longrightarrow \mathrm{CO} + \mathrm{C}_f \tag{R 3.11}$$

$$\mathrm{C}_f \longrightarrow \mathrm{C}_i \tag{R 3.12}$$

As in the previous mechanism, an O radical from the adsorbed oxygen is linked with a free carbon site and the complex is released as CO only. In the present mechanism the free radical O can itself react with a free site forming an equal complex C(O). The last reaction takes into account the transformation of an active site into an inactive one due to thermal annealing. If this reaction

is neglected and the steady state assumption for $C(O)$ is invoked, the Langmuir-Hinshelwood kinetic is also obtained for this mechanism. The obtained expression allows reaction rates order between $n = 0$ and $n = 1$ but does not explain the high reactivity compared to the reactions with CO_2 and with H_2O (unless the total number of active sites $[C_t]$ drastically changes).

Mechanism Oxi-C: An alternative mechanism to the Oxi-A mechanism [333] is the following:

$$\mathrm{C}_f + \mathrm{O}_2 \longleftrightarrow \mathrm{C(O_2)} \tag{R 3.13}$$

$$\mathrm{C}_f + \mathrm{C(O_2)} \longrightarrow 2\,\mathrm{CO} \tag{R 3.14}$$

In this mechanism the adsorbed oxygen forms the complex $C(O2)$ without previously splitting into O radicals. This mechanism explains the high reactivity of oxygen with carbon (due to the high desorption rate) but the first reaction is probably not elementary because of the observations that $C(O)$ is favored in place of $C(O2)$.

Mechanism Oxi-D: Experimental evidence has been found that in the middle range of temperature a lower order reaction rate is present. Suggested by this observation, the following mechanisms has been proposed [50], based on a two side dissociative chemisorption and site migration:

$$2\,\mathrm{C}_f + \mathrm{O}_2 \longleftrightarrow 2\,\mathrm{C}_a\mathrm{(O)} \tag{R 3.15}$$

$$\mathrm{C}_a\mathrm{(O)} \longrightarrow \mathrm{C}_b\mathrm{(O)} \tag{R 3.16}$$

$$\mathrm{C}_b\mathrm{(O)} \longrightarrow \mathrm{CO} + \mathrm{C}_f \tag{R 3.17}$$

The oxygen is adsorbed on two different carbon sites and after site migration carbon monoxide is released.

The disadvantages of this mechanism are the following:

1. The production of CO_2 at low temperature as a primary product is not explained;
2. The reaction R 3.15 cannot be reversible according to experimental data;
3. The rapidity of the combustion is not explained.

Mechanism Oxi-E: A possible alternative is the following mechanism:

$$2\,\mathrm{C}_f + \mathrm{O}_2 \longrightarrow 2\,\mathrm{C}_a\mathrm{(O)} \tag{R 3.18}$$

$$\mathrm{C}_a\mathrm{(O)} \longrightarrow \mathrm{C}_b\mathrm{(O)} \tag{R 3.19}$$

$$\mathrm{C}_b\mathrm{(O)} \longrightarrow \mathrm{CO} + \mathrm{C}_f \tag{R 3.20}$$

$$\mathrm{C}_a\mathrm{(O)} \longrightarrow \mathrm{CO} + \mathrm{C}_f \tag{R 3.21}$$

$$\mathrm{C}_a\mathrm{(O)} + \mathrm{C}_b\mathrm{(O)} \longrightarrow \mathrm{CO_2} + \mathrm{C}_f \tag{R 3.22}$$

As in the mechanism before, oxygen is adsorbed on two different sites.After adsorption the following can happen:

1. Oxygen migration and desorption of CO as in the mechanism Oxy-D;
2. Direct desorption of CO;
3. Exchange interaction of the C(O) complex to form CO_2.

Comparing Reaction R 3.21 and Reaction R 3.22 the rate of desorption of CO_2 to the desorption of CO is given by:

$$\frac{d[C]_{\mathrm{CO_2}}}{d[C]_{\mathrm{CO}}} = [C_t]\frac{k_{10}}{k_9}\theta'_O \tag{3.21}$$

where k_9 and k_{10} are the reaction constants for reactions R 3.21 and R 3.22 respectively. After application of steady state assumption for $C_a(O)$ and $C_b(O)$ the following relation can be derived:

$$\Delta_1\theta_O^2 - \Delta_2\theta_O + \Delta_3 = 0 \tag{3.22}$$

where the terms Δ_1, Δ_2 and Δ_3 are expressed by:

$$\begin{aligned}
\Delta_1 &= 2k_7\left(1+\frac{k_3}{k_8}\right)^2[C_t]C_{O2} - 2k_{10}\left(\frac{k_3}{k_8}\right)^2[C_t] \\
\Delta_2 &= 4k_7\left(1+\frac{k_3}{k_8}\right)[C_t]C_{O2} + k_3\left(1+\frac{k_9}{k_8}\right) \\
\Delta_3 &= 2k_7[C_t]C_{O2}
\end{aligned}$$

and k_7 and k_8 are the reaction constants for reactions R 3.19 and reaction R 3.18 respectively.

If the production of CO_2 is negligible the reaction rate can be approximated in the following way:

$$\dot{R} = m_c[C_t]k_3\left(1+\frac{k_9}{k_8}\right)\theta_O \tag{3.23}$$

with θ_O solution of the equation 3.22.

With further simplifications it is possible to show [205] that:

- At high temperatures:
$$\dot{R} = m_c[C_t]\frac{k_9}{2} \tag{3.24}$$
predicting a reaction order $n = 0$ and a rate controlled by mobile site desorption;
- At low temperatures:
$$\dot{R} = 2m_c[C_t]^2k_7[C]_{\mathrm{O_2}} \tag{3.25}$$
predicting a reaction order $n = 1$ and a rate controlled by dissociative chemisorption;
- At intermediate temperatures:
$$\dot{R} = m_c[C_t]k_8\left(\frac{k_7}{k_{10}}\right)^{1/2}[C]_{\mathrm{O_2}}^{1/2} \tag{3.26}$$
predicting a reaction order $n = \frac{1}{2}$ and a rate controlled by migration.

Mechanism Oxi-F A simple improvement for the 2-steps mechanism Oxi-C suggested in [162] is the inclusion of the following reaction:

$$\mathrm{C(O) + O_2 \longrightarrow CO_2 + C(O)} \tag{R 3.23}$$

where oxygen react with a complex C(O) to form CO_2. The reaction rate is given by:

$$\dot{R} = \frac{k_1k_2[C]_{\mathrm{O_2}}^2 + k_1k_3[C]_{\mathrm{O_2}}}{k_1\,[C]_{\mathrm{O_2}} + k_3/2} \tag{3.27}$$

The destabilization of surface complex C(O) can be formed by more elementary steps and there are some experimental evidences for this kind of reactions (see the references in [162] for more details). This reaction is also the most accepted path of CO_2 formation in most recent literature, instead of the previously suggested reaction R 3.22 (C_a(O) + C_b(O) $\longrightarrow$ CO_2 + C_f.

It is expected that for Reaction R 3.23 the activation energies follow the relation $E_3 > E_2 > E_1$, where the index 1, 2 and 3 refer to the reactions R 3.7, R 3.8, and R 3.23 respectively. The aforementioned activation energy chain differs than the one obtained from the mechanism Oxi-E. The tree step mechanism with this chain of activation energies reproduces the following asymptotic behavior:

- At low temperatures:
$$dotR = k_2 \cdot p_{\mathrm{O}_2} \tag{3.28}$$
explaining a first order reaction;

- At extremely high temperatures:
$$\dot{R} = 2k_1 \cdot p_{\mathrm{O}_2} \tag{3.29}$$
a first order reaction;

- At low-moderate temperatures ($k_1 \cdot p_{\mathrm{O}_2} \gg k_3$) the rate is given by
$$\dot{R} = k_2 \cdot p_{\mathrm{O}_2} + k_3 \tag{3.30}$$

- At moderate temperatures ($k_1 \cdot p_{\mathrm{O}_2} \gg k_3 \gg k_2 \cdot p_{\mathrm{O}_2}$) the rate is given by
$$\dot{R} = k_3 \tag{3.31}$$

- At moderate-high temperatures ($k_1 \cdot p_{\mathrm{O}_2} \gg k_3 \gg k_2 \cdot p_{\mathrm{O}_2}$) the rate is given by
$$\dot{R} = \frac{k_1 k_2}{k_1 p_{\mathrm{O}_2} + k_3/2} \cdot p_{\mathrm{O}_2} \tag{3.32}$$

This model is able to correctly predict the aforementioned measured observations with the following constant (see [162] for more information). $A_2 = 5.7 \cdot 10^{-4}$ 1/bar, $E_2 = 130\,\frac{\mathrm{kJ}}{\mathrm{mol}}$ $E_3 = 180\,\frac{\mathrm{kJ}}{\mathrm{mol}}$ (normalized by $A_3 = 1.0$). All this activation energies are in the correct ranges reported by the litterature. It is finally interesting to mention that this model is able to predict also the CO/CO_2-ratio by:
$$\frac{[\mathrm{CO}]}{[\mathrm{CO}_2]} = \frac{k_3}{k_2} \cdot \frac{1}{p_{\mathrm{O}_2}} \tag{3.33}$$
with the correct activation energy reported by [13] $E_{\mathrm{CO/CO_2}} = E_3 - E_2 = 52\,\mathrm{kJ\,mol}$.

This model is still not able to reproduced some expected features of the carbon-oxygen system, but more sophisticated models as the one presented in Section 3.3 or the simplified one presented in the paper [162] are too complex to be expressed into simple analytical expressions.

3.2.2. The $C + CO_2$ reaction

The reaction of solid carbon with CO_2 produces mainly carbon monoxide. The main task for a detailed mechanism is the handling of its low reactivity when compared with oxidation and its inhibition if CO is present.

Mechanism CO2-A: The simplest gasification reaction with CO_2 proceeds following the oxygen exchange mechanism:

$$\mathrm{C}_f + \mathrm{CO}_2 \longleftrightarrow \mathrm{CO} + \mathrm{C(O)} \tag{R 3.24}$$

$$\mathrm{C(O)} \longrightarrow \mathrm{CO} + \mathrm{C}_f \tag{R 3.25}$$

In this simple mechanism the CO_2 molecule reacts with a free carbon site to form the complex C(O) with release of carbon monoxide. Also the complex will evolve into a desorbed molecule of CO. Assuming steady state for the free carbon sites $\theta_o \equiv \frac{[C(O])}{[C_t]}$, i.e. $\frac{d\theta_o}{dt} = 0$, the following relation can be derived:

$$\theta_o = \frac{k_{1,f} \cdot [C]_{\mathrm{CO}_2}}{k_{1,f} \cdot [C]_{\mathrm{CO}_2} + k_{1,b} \cdot [C]_{\mathrm{CO}} + k_2} \tag{3.34}$$

where k_1 and k_2 are reaction rates for reactions R 3.24 and R 3.25 respectively. The intrinsic reaction rate is given by the release of products from the surface and it is written in the following way:

$$\dot{R} = m_c[C_t]k_3\theta_o$$

and after inserting in the previous equation, the relation obtained for θ_o, the final rate follows:

$$\dot{R} = \frac{k \cdot [C]_{\mathrm{CO}_2}}{1 + a \cdot [C]_{\mathrm{CO}} + b \cdot [C]_{\mathrm{CO}_2}} \tag{3.35}$$

where $[C_t]$ is, as before, the total number of active sites per unit of surface and $m_c = 2.3243 \cdot 10^{-23}\mathrm{gram}$ is the mass of a carbon atom. Equation 3.35 is written as a function of the quantities:

$$\begin{aligned} k &= m_c[C_t]k_{1,f} \\ a &= \frac{k_{1,b}}{k_2} \\ b &= \frac{k_{1,f}}{k_2} \end{aligned}$$

From the previous equation is important to notice that the presence of CO inhibits the reaction rate. The described mechanism suggests that the inhibition occurs not by adsorption but because carbon monoxide reacts with the chemisorbed oxygen.

Mechanism CO2-B: The following proposed mechanism [114] predicts a deactivation for the reaction rate due to CO adsorption:

$$\mathrm{C}_f + \mathrm{CO}_2 \longrightarrow \mathrm{CO} + \mathrm{C(O)} \tag{R 3.26}$$

$$\mathrm{C(O)} \longrightarrow \mathrm{CO} + \mathrm{C}_f \tag{R 3.27}$$

$$\mathrm{CO} + \mathrm{C}_f \longleftrightarrow \mathrm{C(CO)} \tag{R 3.28}$$

in which the CO can reacts with a free carbon site. The mechanism leads to an equation rate equal to the 3.35. The oxygen exchange mechanism is probably more accurate in predicting the deactivation from CO presence.

The equation 3.35 shows that $\dot{R} \sim [C_t]k_{1,f}$. The total amount of free active sites $[C_t]k_{1,f}$ changes drastically for each type of solid fuels, explaining (as in [240]) the great variation of reactivities found, while activation rate and pre-exponential factors for the single steps are inde-

pendent of the type of fuel. The partial equilibrium for the oxygen exchange reaction leads to the relation:

$$K_{eq,1} = \frac{[C]_{\mathrm{CO}}\theta_o}{[C]_{\mathrm{CO_2}}\theta_f}$$

and if the following assumptions are valid (law temperature regime):

$$\begin{aligned} a \cdot [C]_{\mathrm{CO}} &\gg 1 \\ c \cdot [C]_{\mathrm{CO_2}} &\gg 1 \end{aligned}$$

the global reaction rate 3.35 can be written as

$$\dot{R} = \frac{k_2[C_t]}{1 + \frac{[C]_{\mathrm{CO}}}{[C]_{\mathrm{CO_2}} \cdot K_{eq,1}}} \tag{3.36}$$

The previous equation allows the determination of the unknown quantities $K_{eq,1}$:

$$K_{eq,1} = 4.15 \cdot 10^3 e^{-11.43/T} \tag{3.37}$$

Moreover $k_2[C_t] = A_2[C_t]e^{-E_2/RT}$ while the Arrehnius form has been validated by experiments.

Mechanism CO2-C: The simple exchange oxygen mechanism described by reaction R 3.24 has been assumed to be single site but the chmisorption reaction could be composed by even more fundamental steps as, for example:

$$\mathrm{CO_2} + 2\,\mathrm{C}_f \longleftrightarrow \mathrm{C(CO)} + \mathrm{C(O)} \tag{R 3.29}$$

$$\mathrm{C(CO)} \longleftrightarrow \mathrm{CO} + \mathrm{C}_f \tag{R 3.30}$$

but if $C(CO)$ is in steady state, the previous mechanism generates the reaction R 3.24, therefore it remains formally a single site mechanism.

Mechanism CO2-D: The first results of high pressure gasification of carbon has been published in [45] suggesting a global reactivity of the form:

$$\dot{R} = \frac{k \cdot [C]_{\mathrm{CO_2}} + c \cdot [C]^2_{\mathrm{CO_2}}}{1 + a \cdot [C]_{\mathrm{CO}} + b \cdot [C]_{\mathrm{CO_2}}} \tag{3.38}$$

showing a higher reactivity at high pressure. The CO adsorption predominates, therefore the high reactivity is due to an higher $C(O)$ (or a lower $C(CO)$) concentration. The following simple mechanism is able to reproduce a quadratic reaction rate as shown by the measurements:

$$\mathrm{CO_2} + \mathrm{C}_f \longrightarrow \mathrm{CO} + \mathrm{C(O)} \tag{R 3.31}$$

$$\mathrm{C(O)} \longrightarrow \mathrm{CO} + \mathrm{C}_f \tag{R 3.32}$$

$$\mathrm{CO} + \mathrm{C}_f \longleftrightarrow \mathrm{C(CO)} \tag{R 3.33}$$

$$\mathrm{C(CO)} + \mathrm{CO_2} \longrightarrow 2\,\mathrm{CO} + \mathrm{C(O)} \tag{R 3.34}$$

$$\mathrm{C(CO)} + \mathrm{CO} \longrightarrow \mathrm{CO_2} + 2\,\mathrm{C}_f \tag{R 3.35}$$

The firs three reactions are equal to the reactions proposed in mechanism CO2-C and the last two reactions describe the fate of the C(CO) complex. When the complex reacts wuith $\mathrm{CO_2}$, two

carbon monoxide atoms are formed and after an oxygen exchange a complex C(O) is left. If CO reacts with C(O) a carbon dioxide molecule is desorbed and two free carbon sites are left.

Mechanism CO2-E: A valid mechanism consistent with the available experimental data is to add to the reactions R 3.24 and R 3.25 the following:

$$\mathrm{C(O)} + \mathrm{CO_2} \longrightarrow \mathrm{CO} + ... \tag{R 3.36}$$

suggesting the formation of other stable products. In this case, the coefficients in equation 3.38 become:

$$k = m_c[C_t]k_{1,f} \tag{3.39}$$

$$a = \frac{k_{1,b}}{k_2} \tag{3.40}$$

$$b = \frac{k_{1,f} + k_3}{k_2} \tag{3.41}$$

$$c = m_c[C_t]k_{1,f}\frac{k_3}{k_2} \tag{3.42}$$

where k_3 is the rate coefficient for the reaction R 3.36.

3.2.3. The $C + H_2O$ reaction

The study of the wet gasification reaction is more complex than the gasification with CO_2 because of the presence of extra reactions among the products H_2, CO_2, CO and H_2O itself, with the water gas shift reaction playing an important role at middle and higher temperatures. An observed feature of the steam gasification is that the presence of H_2 inhibits steam gasification reactions from taking place [44]. In-depth understanding of the inhibition mechanism gives the possibility to extend the calculated reaction rates further in pressure and temperature.

Mechanism H2O-A: Two primary mechanisms have been proposed for the wet gasification reaction [205]. The first mechanism proposes a reversible adsorption of water followed by inhibition by oxygen exchange [240]:

$$\mathrm{C}_f + \mathrm{H_2O} \longleftrightarrow \mathrm{H_2} + \mathrm{C(O)} \tag{R 3.37}$$

$$\mathrm{C(O)} \longrightarrow \mathrm{CO} + \mathrm{C}_f \tag{R 3.38}$$

The adsorption of the water vapor molecule produces a C(O) complex with release of hydrogen while the oxygen exchange produces carbon monoxide.

The surface reaction rate can be written as:

$$\dot{R} = \frac{k \cdot [C]_{\mathrm{H_2O}}}{1 + a \cdot [C]_{\mathrm{H_2}} + b \cdot [C]_{\mathrm{H_2O}}} \tag{3.43}$$

with the following definitions:

$$\begin{aligned} k &= m_c[C_t]k_{1,f} \\ a &= \frac{k_{1,b}}{k_2} \\ b &= \frac{k_{1,f}}{k_2} \end{aligned}$$

Mechanism H2O-B: In the second mechanism the adsorption is irreversible and the inhibition is due to reversible hydrogen adsorption [168]:

$$\mathrm{C}_f + \mathrm{H_2O} \longrightarrow \mathrm{C(O)} + \mathrm{H_2} \tag{R 3.39}$$

$$\mathrm{C(O)} \longrightarrow \mathrm{CO} + \mathrm{C}_f \tag{R 3.40}$$

$$\mathrm{C}_f + \mathrm{H_2} \longleftrightarrow \mathrm{C(H_2)} \tag{R 3.41}$$

Both mechanisms are equivalent and both give a surface reaction rate of the Langmuir form:

$$\dot{R} = \frac{k_a \cdot [C]_{H2O}}{1 + k_b \cdot [C]_{H2O} + k_c \cdot [C]_{H2}} \tag{3.44}$$

Mechanism H2O-C: A variant of the reversible adsorption of water in H2O-A mechanism is given by the more complex chain:

$$2\,\mathrm{C}_f + \mathrm{H_2O} \longleftrightarrow \mathrm{C(H)} + \mathrm{C(OH)} \tag{R 3.42}$$

$$\mathrm{C}_f + \mathrm{C(OH)} \longleftrightarrow \mathrm{C(O)} + \mathrm{C(H)} \tag{R 3.43}$$

$$2\,\mathrm{C(H)} \longleftrightarrow \mathrm{H_2} + 2\,\mathrm{C}_f \tag{R 3.44}$$

The adsorption of water molecule is a double site adsorption with formation of the two complexes C(H) and C(OH). After migration, the C(OH) complex creates the two simpler complex C(O) and C(H) with desorption of hydrogen and carbon monoxide. This mechanism reduces to the R 3.37 if C(H) and C(OH) are short living intermediates.

The mechanism H2O-A is better accepted even if it is not possible to exclude the presence of the hydrogen adsorption inhibition mechanism. The arguments for that acceptance are based on the following reasons:

1. The analogy with the $\mathrm{C} + \mathrm{CO_2}$ system;
2. The agreement between the experimental values for the equilibrium constant K_2 for the reaction R 3.37 and the equilibrium constant calculated based on the C + CO_2 equilibrium and the water gas shift reaction constant;
3. The agreement of the activation energy E for steam gasification;
4. The evidence that $\mathrm{H_2}$ undergoes dissociative chemisorption;
5. The simplified explanation for the water-gas equilibrium (see later).

Mechanism H2O-D A more complex mechanism that take into consideration also the production of methane has been proposed in [125]:

$$\mathrm{C}_f + \mathrm{H_2O} \longleftrightarrow \mathrm{C(O)} + \mathrm{H_2} \tag{R 3.45}$$

$$\mathrm{C}_f + \mathrm{H_2} \longleftrightarrow \mathrm{C(H_2)} \tag{R 3.46}$$

$$\mathrm{C}_f + \frac{1}{2}\,\mathrm{H_2} \longleftrightarrow \mathrm{C(H)} \tag{R 3.47}$$

$$\mathrm{C(O)} \longrightarrow \mathrm{CO} + \mathrm{C}_f \tag{R 3.48}$$

$$\mathrm{C(O)} + \mathrm{H_2O} \longrightarrow \mathrm{CO_2} + \mathrm{H_2} + \mathrm{C}_f \tag{R 3.49}$$

$$\mathrm{C(H_2)} + \mathrm{H_2} \longrightarrow \mathrm{CH_4} + \mathrm{C}_f \tag{R 3.50}$$

In this mechanism the hydrogen inhibition is achieved in different ways and to different extents but the most important inhibition effect is the dissociative chemisorption of hydrogen described by the reaction R 3.47. Considering the reactions R 3.45 to R 3.48 state approximation for $C(O)$ and $C(H_2)$ leads to the expression for the rate:

$$\dot{R} = \frac{k_a \cdot [C]_{H_2O}}{1 + k_b \cdot [C]_{H_2O} + k_c \cdot [C]_{H_2} + (1 + k_c \cdot [C]_{H_2})(k_d \cdot [C]_{H_2} + k_e \cdot \sqrt{[C]_{H_2}})} \tag{3.45}$$

that for low H_2 partial pressures can be reduced to the following:

$$\dot{R} = \frac{k_a \cdot [C]_{H_2O}}{1 + k_b \cdot [C]_{H_2O} + k_c \cdot \sqrt{[C]_{H_2}}} \tag{3.46}$$

The previous surface reaction rate can also be obtained considering the Mechanism H2O-A with dissociative chemisorption of hydrogen given in reaction R 3.47.

More complex surface reaction rates with dependencies from hydrogen and water vapor partial pressures can be obtained if reaction R 3.49 and reaction R 3.50 are taken into consideration.

Mechanism H2O-E: Usually, carbon dioxide arises always as a secondary product during gasification, also considering that the water gas shift reaction is almost in equilibrium for high temperature. The observation is in agreement with the following mechanism:

$$\mathrm{CO_2} + \mathrm{C}_f \longleftrightarrow \mathrm{CO} + \mathrm{C(O)} \tag{R 3.51}$$

$$\mathrm{H_2O} + \mathrm{C}_f \longleftrightarrow \mathrm{H_2} + \mathrm{C(O)} \tag{R 3.52}$$

$$\mathrm{C(O)} \longrightarrow \mathrm{CO} + \mathrm{C}_f \tag{R 3.53}$$

The previous mechanism obviously explain the water gas shift equilibrium (controlled by the absorption of water). The reaction rates are denoted k_1, k_2 and k_3 respectively.

The global reaction rate for the mechanism previously suggested can be written as follows (assuming steady state for $C(O)$):

$$\dot{R} = m_c[C_t]\frac{k_{1,f} \cdot [C]_{\mathrm{CO_2}} + k_{2,f} \cdot [C]_{\mathrm{H_2O}}}{1 + {}^1\!/_{k_3}(k_{1,f} \cdot [C]_{\mathrm{CO_2}} + k_{2,f} \cdot [C]_{\mathrm{H_2O}} + k_{1,b} \cdot [C]_{\mathrm{CO}} + k_{2,b} \cdot [C]_{\mathrm{H_2}})} \tag{3.47}$$

The reaction rate given above suggests that inhibition can be caused by both, CO and H_2. Some experiments suggest however that CO does not participate in the inhibition process while H_2 it does. If water and carbon dioxide prefer different active site, then equation 3.47 is an oversim-

plification.

Mechanism H2O-F At higher pressures (as in [44]) larger rates are found. Moreover, methane becomes to play a role in the mechanism, its formation having a first-order dependence on steam concentration. At relatively low temperature the global rate is given by:

$$\dot{R} = \frac{k \cdot [C]_{\mathrm{H_2O}} + c \cdot [C]^2_{\mathrm{H_2O}} + d \cdot [C]_{\mathrm{H_2}} \cdot [C]_{\mathrm{H_2O}}}{1 + a \cdot [C]_{\mathrm{H_2}} + b \cdot [C]_{\mathrm{H_2O}}} \tag{3.48}$$

High pressure promote the conversion of H_2 to methane, increasing the $C(O)$ concentration and consequently the rate.

Another mechanism for high pressure has been proposed [321], where dissociative chemisorption predominates:

$$\mathrm{C(H) + H_2 \longrightarrow CH_3 + C}_f \tag{R 3.54}$$

$$\mathrm{C(H) + H_2O \longrightarrow CH_3 + C(O)} \tag{R 3.55}$$

$$\mathrm{CH_3 + H_2 \longrightarrow CH_4 + H} \tag{R 3.56}$$

$$\mathrm{CH_3 + H_2O \longrightarrow CH_4 + OH} \tag{R 3.57}$$

$$\mathrm{C}_f + \mathrm{H \longrightarrow C(H)} \tag{R 3.58}$$

$$\mathrm{C}_f + \mathrm{OH \longrightarrow C(OH)} \tag{R 3.59}$$

where the C(H) + H_2O is much faster than the step C(H) + H_2.

3.2.4. The $C + H_2$ reaction

Mechanism H2-A: The reaction with hydrogen under consideration is the following:

$$\mathrm{C + 2\,H_2 \longrightarrow CH_4} \tag{R 3.60}$$

Its rate is slow even at higher pressures where it plays a more significant role than at lower pressure. At low char temperatures, the global rate is increased by the interaction of hydrogen with pyrolysis products. At higher temperatures measurements have shown that the global reaction rate has a first order dependance on hydrogen concentration:

$$\dot{R} = k \cdot [C]_{H_2} \tag{3.49}$$

At higher pressures several more complex expressions have been suggested. For example in [104]:

$$\dot{R} = \frac{k \cdot [C]^2_{H_2}}{1 + a \cdot [C]_{H_2}} \tag{3.50}$$

while at higher methane concentrations [43]:

$$\dot{R} = \frac{k \cdot [C]^2_{H_2} - d \cdot [C]_{CH_4}}{1 + a \cdot [C]_{H_2} + b \cdot [C]^2_{H_2} + c \cdot [C]_{CH_4}} \tag{3.51}$$

Mechanism H2-B: Both expressions 3.50 and 3.51 are provided by the following mechanism:

$$\mathrm{H_2 + C}_f \longleftrightarrow \mathrm{C(H_2)} \tag{R 3.61}$$

$$\mathrm{C(H_2)} + \mathrm{C}_f \longleftrightarrow 2\,\mathrm{C(H)} \tag{R 3.62}$$

$$2\,\mathrm{C(H)} + \mathrm{H_2} \longleftrightarrow 2\,\mathrm{C(H_2)} \tag{R 3.63}$$

$$\mathrm{C(H_2)} + \mathrm{H_2} \longleftrightarrow \mathrm{CH_4} + \mathrm{C}_f \tag{R 3.64}$$

It can been shown that the final rate is proportional to the amount of oxygen in the char and that addition of steam increase the reactivity.

Compared to the n-th rate equation, the Langmuir-Hinshelwood type equation has the following advantages.

- does not involve the pressure order which is uncertain for the nth order equation;
- is derived from reaction mechanism, whereas the nth order equation is empirical;
- accounts for the inhibiting effect of H_2 and CO, which are considerably present at high pressures.

3.3. A unified mechanism

Regarding the gasification and oxidation with a mixture of steam, O_2, CO_2, CO, and H_2, there are two possible scenarios that have been proposed. The first scenario assumes that reactions occur at common active sites, while the other believes that reactions occur at separate active sites.

As an example, gasification reactions are described by the simple CO2-A mechanism:

$$\mathrm{C}_f + \mathrm{CO_2} \longleftrightarrow \mathrm{CO} + \mathrm{C(O)}$$

$$\mathrm{C(O)} \longrightarrow \mathrm{CO} + \mathrm{C}_f$$

and the simple H2O-A mechanism:

$$\mathrm{C}_f + \mathrm{H_2O} \longleftrightarrow \mathrm{H_2} + \mathrm{C(O)}$$

$$\mathrm{C(O)} \longrightarrow \mathrm{CO} + \mathrm{C}_f$$

where both C_f and C(O) can be the same site or different sites.

When CO and CO_2 only are present, the intrinsic rate is (see equation 3.35):

$$\dot{R}_1 = \frac{k_1 \cdot [C]_{\mathrm{CO_2}}}{1 + a_1 \cdot [C]_{\mathrm{CO}} + b_1 \cdot [C]_{\mathrm{CO_2}}}$$

When H_2O and H_2 only are present, the the intrinsic rate is (see equation 3.43):

$$\dot{R}_2 = \frac{k_2 \cdot [C]_{\mathrm{H_2O}}}{1 + a_2 \cdot [C]_{\mathrm{H_2}} + b_2 \cdot [C]_{\mathrm{H_2O}}}$$

If the sites C_f are different ($C_{f,1} \neq C_{f,2}$) then molecules do not compete for free active sites and the total intrinsic reaction rate is given by the sum of both reactions:

$$\dot{r} = \dot{R}_1 + \dot{R}_2 = \frac{k_1 \cdot [C]_{\mathrm{CO_2}}}{1 + a_1 \cdot [C]_{\mathrm{CO}} + b_1 \cdot [C]_{\mathrm{CO_2}}} + \frac{k_2 \cdot [C]_{\mathrm{H_2O}}}{1 + a_2 \cdot [C]_{\mathrm{H_2}} + b_2 \cdot [C]_{\mathrm{H_2O}}} \tag{3.52}$$

If the mechanism allows to share the same active sites, an analysis based on steady state

conditions for the C(O) complex, leads to the following total intrinsic reaction rate:

$$\frac{k_1 \cdot [C]_{\mathrm{CO_2}} + k_2 \cdot [C]_{\mathrm{H_2O}}}{1 + a_1 \cdot [C]_{\mathrm{CO}} + b_1 \cdot [C]_{\mathrm{CO_2}} + a_2 \cdot [C]_{\mathrm{H_2}} + b_2 \cdot [C]_{\mathrm{H_2O}}} \tag{3.53}$$

Some results (for example in [159, 135]) indicate that, at atmospheric pressure, both gasification reactions proceed on separate active sites while others (see for example [384]) indicate that sites are partially shared, more precisely steam gasification is independent on CO_2, while CO_2 reaction is inhibited by steam (see [76]).

At higher pressures, there are indications that the situation could be different since the partial pressure of the molecules affects the degree of surface saturation [296, 295].

Among the many mechanisms proposed only two of them are reported below with some details.

Mechanism Global-A: The model presented in [260, 217] is based on a three-steps mechanism for char oxidation:

$$2\,\mathrm{C}_{f,1} + \mathrm{O_2} \xrightarrow{\mathrm{k_1}} \mathrm{C(O)} + \mathrm{CO} \tag{R 3.65}$$

$$\mathrm{C}_{f,1} + \mathrm{C(O)} + \mathrm{O_2} \xrightarrow{\mathrm{k_2}} \mathrm{CO_2} + \mathrm{C(O)} \tag{R 3.66}$$

$$\mathrm{C(O)} \xrightarrow{\mathrm{k_3}} \mathrm{CO} \tag{R 3.67}$$

and a 5 steps-mechanism for CO_2 gasification and steam gasification:

$$\mathrm{C}_{f,2} + \mathrm{CO_2} \xleftrightarrow{\mathrm{k_4}} \mathrm{C(O)} + \mathrm{CO} \tag{R 3.68}$$

$$\mathrm{C(O)} \xrightarrow{\mathrm{k_5}} \mathrm{CO} \tag{R 3.69}$$

$$\mathrm{C}_{f,3} + \mathrm{H_20} \xleftrightarrow{\mathrm{k_6}} \mathrm{C(O)} + \mathrm{H_2} \tag{R 3.70}$$

$$\mathrm{C(O)} \xrightarrow{\mathrm{k_7}} \mathrm{CO} \tag{R 3.71}$$

$$\mathrm{C}_{f,3} + 2\,\mathrm{O_2} \xrightarrow{\mathrm{k_8}} \mathrm{CH_4} \tag{R 3.72}$$

The adsorption reactions are reversible while the other are irreversible. The model is based on several assumptions:

- Oxidation and gasification do not share the same active sites while gasification reactions shares them. The desorption rates for the C(O) complex from carbon dioxide and steam are different, depending on temperature but not on pressure;
- The mechanism neither include CO chemisorption nor the reactions of C(CO) complex, which give rise to quadratic higher order terms (see [253] and equation 3.48 in the mechanism H2O-F), while the kinetic rate constants associated with the quadratic terms are small for temperature higher than 900°C.
- Gasification with hydrogen does not share the same active site with oxygen. The kinetics for hydrogasification are resolved separately

The reaction rate $\dot{R}_{tot}$ is then the sum of the oxidation reaction ($\dot{R}_{Comb}$)) and the gasification reactions ($\dot{R}_{Gas}$):

$$\dot{R}_{tot} = \dot{R}_{Comb} + \dot{R}_{Gas} \tag{3.54}$$

where $\dot{R}_{Comb}$ and $\dot{R}_{Gas}$ are given by the following expressions:

$$\dot{R}_{Comb} = \frac{k_1 \cdot k_2 \cdot [C]^2_{\mathrm{O_2}} + k_1 \cdot k_3 \cdot [C]_{\mathrm{O_2}}}{k_1 \cdot [C]_{\mathrm{O_2}} + k_3/2} \tag{3.55}$$

$$\dot{R}_{Gas} = \frac{(k_7 + k_5) \cdot (k_{4,f} \cdot [C]_{\mathrm{CO_2}} + k_{6,f} \cdot [C]_{\mathrm{H_2O}})}{k_7 + \gamma k_4 \cdot [C]_{\mathrm{CO_2}} + \gamma k_{4,b} \cdot [C]_{\mathrm{CO}} + k_{6,f} \cdot [C]_{\mathrm{H_2O}} + k_{6,b} \cdot [C]_{\mathrm{H_2}}} + k_8 \cdot [C]_{\mathrm{H_2}} \tag{3.56}$$

where $\gamma = \frac{k_7}{k_5}$ is the ratio of the desorption rates in reactions R 3.69 and reaction R 3.71. It is worth noticing that also this mechanism predicts the combustion product ratio between CO and CO_2 to be given by:

$$\frac{[\mathrm{CO}]}{[\mathrm{CO2}]} = \frac{k_3}{k_2} \cdot \frac{1}{[C]_{\mathrm{O_2}}} \tag{3.57}$$

The parameters for the Arrhenius rate constant k_i can be find in [260] and in [217].

Mechanism Global-B: An attempt to combine all three conversion mechanisms has been presented in [368]. The elementary scheme is reported below.

$$2\,\mathrm{C}_f + \mathrm{H_2O} \longleftrightarrow \mathrm{C(OH)} + \mathrm{C(H)} \tag{R 3.73}$$

$$\mathrm{C(OH)} + \mathrm{C}_f \longleftrightarrow \mathrm{C(O)} + \mathrm{C(H)} \tag{R 3.74}$$

$$\mathrm{C(H)} + \mathrm{C(H)} \longleftrightarrow \mathrm{H_2} + 2\,\mathrm{C}_f \tag{R 3.75}$$

$$\mathrm{C(O)} + \mathrm{C}_b \longrightarrow \mathrm{CO} + \mathrm{C}_f \tag{R 3.76}$$

$$\mathrm{C(OH)} + \mathrm{C}_b = \mathrm{HCO} + \mathrm{C}_f \tag{R 3.77}$$

$$\mathrm{C}_b + \mathrm{C}_f + \mathrm{C(H)} + \mathrm{H_2O} \longleftrightarrow \mathrm{CH_3} + \mathrm{C(O)} + \mathrm{C}_f \tag{R 3.78}$$

$$\mathrm{C}_b + \mathrm{C}_f + \mathrm{C(H)} + \mathrm{H_2} \longleftrightarrow \mathrm{CH_3} + 2\,\mathrm{C}_f \tag{R 3.79}$$

$$\mathrm{C}_f + \mathrm{C(H)} + \mathrm{CO} \longrightarrow \mathrm{HCO} + 2\,\mathrm{C}_f \tag{R 3.80}$$

$$\mathrm{C(H)} + \mathrm{C(H)} \longrightarrow \mathrm{CH_2} + \mathrm{C}_f \tag{R 3.81}$$

$$\mathrm{CO_2} + \mathrm{C}_f \longleftrightarrow \mathrm{C(O)} + \mathrm{CO} \tag{R 3.82}$$

$$\mathrm{C}_b + \mathrm{CO_2} + \mathrm{C(O)} \longrightarrow 2\,\mathrm{CO} + \mathrm{C(O)} \tag{R 3.83}$$

$$\mathrm{CO} + \mathrm{C}_f \longleftrightarrow \mathrm{C(CO)} \tag{R 3.84}$$

$$\mathrm{CO} + \mathrm{C(CO)} \longrightarrow \mathrm{CO_2} + \mathrm{C}_f + \mathrm{C}_b \tag{R 3.85}$$

$$2\,\mathrm{C}_f + \mathrm{O_2} \longrightarrow \mathrm{C(O)} + \mathrm{CO} \tag{R 3.86}$$

$$2\,\mathrm{C}_f + \mathrm{O_2} \longrightarrow \mathrm{C_2(O_2)} \tag{R 3.87}$$

$$\mathrm{C}_f + \mathrm{C}_b + \mathrm{C(O)} + \mathrm{O_2} \longrightarrow \mathrm{CO_2} + \mathrm{C(O)} + \mathrm{C}_f \tag{R 3.88}$$

$$\mathrm{C}_f + \mathrm{C}_b + \mathrm{C(O)} + \mathrm{O_2} \longrightarrow \mathrm{CO} + 2\,\mathrm{C(O)} \tag{R 3.89}$$

$$\mathrm{C}_b + \mathrm{C_2(O_2)} \longrightarrow \mathrm{CO_2} + 2\,\mathrm{C}_f \tag{R 3.90}$$

where $C(X)$ denotes an adsorbed species (a carbon site filled with an adsorbed species X), C_f denotes a free carbon site (a carbon site available for adsorption), and C_b denotes a bulk carbon site (an underlying site that will be exposed upon desorption of a carbon atom).

The first nine reactions represent the reactivity of carbon to H_2O where as previously dis-

cussed dual site chemisorption of steam is assumed (reaction R 3.73). As a result, H and OH species are adsorbed on the surfaces. The adsorbed OH further dissociates yielding adsorbed O and H. Hydrogen is produced via reactions R 3.75 and CO is produced via reaction R 3.76. The next reactions do not play a major role in the conversion of carbon but are important for the formation of methane. The released radicals CH_2, CH_3, and HCO form CH_4 via gas phase reactions (see [368] for further details about the choices of the mechanism).

The next 4 reactions, together with reaction R 3.76 describe the conversion of carbon by reactions with CO_2. Single-site chemisorption of oxygen atoms is assumed, leading to CO formation and an adsorbed oxygen atom. The inhibition of the carbon gasification rate by CO is due, to the reverse of reaction R 3.82, which removes an adsorbed oxygen atom from the surface.

The last reactions, together with reaction R 3.76 describe the oxidation mechanism. Dual site chemisorption of oxygen is assumed, yielding adsorbed oxygen species on the surfaces. Part of this adsorbed oxygen is on adjacent carbon sites denoted by $C_2(O_2)$. Complex enhanced adsorption is also taken into account, leading to both CO_2 and CO formation. CO is produced after desorption by reaction R 3.76 and CO_2 by reaction R 3.90.

It is possible that ash impurities within the carbon matrix play a role in influencing the reactivity of the char. The presence of Mg and Ca tends to increase char reactivity to both O_2 and CO_2 [155] while Si and Al reduce the reactivity of H_2O [316]. The derived parameters for the model are presented in Table 5 in the previously cited reference [368].

Part II.

Modeling

4. The CFD method

The balance equation 1.10, when applied to the volume of a whole reactor, gives useful but most of the time limited information. Reactors are not in thermodynamic equilibrium and techniques of irreversible thermodynamic must be used. In devices of practical interest for solid fuel conversion, the assumption of Local Thermodynamic Equilibrium (LTE) can be applied and the balance relations can be written for infinitesimal volumes, resulting in a system of partial differential equations. In practice, the description of the system based on differential equations enlarge the possibility for the calculations of wanted quantities, linking them to more fundamental mechanisms.

The method of CFD (Computational Fluid Dynamic) form the basis for many simulations of heat transfer and fuel conversion prediction. In fact, heat transfer rates are usually one of the required quantities for high temperature processes. To have reliable predictions, the temperature distribution inside the reactor must be known with good accuracy. To this end a differential equation for the temperature field is the basis for the calculations. That equation alone does not solve the problem because conversion rates greatly influence the temperature field. The rates depend on the concentrations of reactant and these must be calculated solving extra differential equations, namely, the mass conservation equations for each component. Mixing (both macro-mixing and micro-mixing) plays in that equations an important role and mixing is driven by flow field (velocity) and turbulence.

For more details of the advantage of using a CFD method in predictions of solid fuel conversion and heat transfer see Section 4.9.

4.1. The balance equation

The general form of the balance equation has been already written in equation 1.1:

$$\frac{d}{dt}\Phi = \dot{\Phi}_{input} + \dot{\Phi}_{source}$$

with an infinitesimal volume as control volume. As already underlined in Section 1.4, two mechanisms are responsible for the flow rate of the quantity Φ across the boundaries:

- Convection;
- Diffusion.

The *convection* is the mechanism for which a flow across the boundary of the control volume is due to the presence of a flow with velocity $\vec{u}$. Its expression is given by an equation similar to 1.2:

$$\dot{\Phi} = \int \rho\phi\, \vec{u} \cdot \widehat{n}\, dS \tag{4.1}$$

where the specific quantity for unit of mass is used $\Phi = m\phi$.

The *diffusion* is the mechanism for which a flow across the boundary of the control volume is due to the presence of a gradient of Φ. This mechanism is irrelevant in the case of global

balances approach because usually the boundary of the global volume are taken in region of no gradient of Φ. The diffusive flux will now be indicated with $\vec{J}_\phi$.

The balance equation 1.1 is then explicitly written in the following integral form:

$$\frac{\partial \Phi}{\partial t} = \oint_S (\rho\phi\, \vec{U} \cdot \hat{n}\, dS) + \oint_S \vec{J}_\phi \cdot \hat{n}\, dS + \dot{S}_\phi \tag{4.2}$$

Each term can be now expressed as a volume integral using the divergence theorem [1]:

$$\Phi = \int \rho\phi\, dV \tag{4.3}$$

$$\oint_S (\rho\phi\, \vec{u} \cdot \hat{n}\, dS) = -\int \nabla \cdot (\rho\phi\, \vec{u})\, dV \tag{4.4}$$

$$\oint_S \vec{J}_\phi \cdot \hat{n}\, dS = -\int \nabla \cdot \vec{J}_\phi\, dV \tag{4.5}$$

$$\dot{S}_\phi = \int \dot{s}_\phi\, dV \tag{4.6}$$

After elimination of the volume integral, the final balance equation can be written in differential form as:

$$\frac{\partial}{\partial t}(\rho\phi) + \nabla \cdot (\rho\phi\, \vec{u}) = \nabla \cdot \vec{J}_\phi + \dot{s}_\phi \tag{4.7}$$

If the diffusion flux vector can be expressed by the following relation:

$$\vec{J}_\phi = -\Gamma_\phi \nabla\phi \tag{4.8}$$

(see anyway later in this chapter) the general balance equation can be now rewritten:

$$\frac{\partial}{\partial t}(\rho\phi) + \nabla \cdot (\rho\phi\, \vec{u}) = \nabla \cdot (\Gamma_\phi \nabla\phi) + \dot{s}_\phi \tag{4.9}$$

The relation 4.9 is the final form of the balance equation in *conservative form*. Balance equations for every thermodynamic quantity of interest can be written in this conservative form with a proper choice of the variable ϕ, its transport properties expressed by Γ_ϕ, and its interaction with the other quantities expressed by the source term $\dot{s}_\phi$.

Mass balance The equation for the total mass balance is obtained from the general transport equation with the choice $\phi = 1$ and since diffusion is not present, take the form:

$$\frac{\partial \rho}{\partial t} + \nabla \cdot \left(\rho\vec{u}\right) = \dot{s}_m \tag{4.10}$$

Species balance For the species balance $\phi = Y_i$ equation 4.7 can be written as:

$$\frac{\partial}{\partial t}(\rho Y_i) + \nabla \cdot (\rho Y_i\, \vec{u}) = \nabla \cdot \vec{J}_i + \dot{s}_i \tag{4.11}$$

[1] The divergence theorem require a different direction for $\hat{n}$, therefore the $-$ sign.

In the terms on the left hand side the derivative of the quantity (ρY_i) and $(\rho Y_i\,\vec{u})$ can be explicitly performed and after utilization of the mass balance equation 4.10, the equations of the species are given by the following scalar equations:

$$\rho\frac{\partial Y_i}{\partial t} + \rho\left(\vec{u}\cdot\nabla\right)Y_i = -\nabla\cdot\vec{J_i} + \dot{s}_i \tag{4.12}$$

where:
- Y_i - mass fraction of species i
- $\vec{J_i}$ - mass flux
- S_i - source term due to reactions

It is possible to relate the mass transfer rate to the mass fraction gradient, using *Fick's law of diffusion* and the mass diffusion coefficient $D_{i,m}$[2]:

$$\vec{J_i} = D_{i,m}\nabla Y_i \tag{4.13}$$

Using the above equation, Equation 4.12 can be written:

$$\rho\frac{\partial Y_i}{\partial t} + \rho\vec{u}\cdot\nabla Y_i = -\nabla\cdot\left(D_{i,m}\nabla Y_i\right) + \dot{S}_i \tag{4.14}$$

This equation is the mass balance equation written in *non-conservative form*.

It is worth noticing that the use of the Fick law requires a correction for the diffusion fluxes when the mass diffusion coefficients $D_{i,m}$ are not equal (in which case the Lewis number are different for each component). Equation 4.14 written in conservative form is:

$$\frac{\partial \rho Y_i}{\partial t} + \nabla\rho\vec{u}Y_i = -\nabla\cdot\left(D_{i,m}\nabla Y_i\right) + \dot{S}_i$$

and, since $\sum_i \dot{S}_i = 0$, after summing on the index i, with the meaning of summing up over all

[2] A more rigorous approach to the multicomponent mass transport equation gives the following result, written in terms of the mole fraction X_I:

$$\begin{aligned}\nabla X_i \quad = \quad & \sum_j \frac{X_i X_j}{D_{i,j}}(\vec{u}_i - \vec{u}_j) + (X_i - X_j)\frac{\nabla p}{p} + \\ & + \frac{\rho}{p}\sum_j Y_i Y_j(\vec{f}_i - \vec{f}_j) + \sum_j \frac{X_i X_j}{\rho D_{ij}}\left(\frac{\alpha_j}{Y_j} - \frac{\alpha_i}{Y_i}\right)\end{aligned}$$

The first term on the right hand side is the molecular diffusion, the second term is the gradient pressure diffusion and the third is the diffusion due to different forces for each component ($\vec{f}$ is the force per unit of mass). The last term is the Soret effect, diffusion of species due to a temperature gradient. The exact diffusion equation reduces to the Flick diffusion if:

1. thermal diffusion is negligible;
2. the body forces per unit of mass are the same for each species;
3. the pressure is constant.

The above equation reads then:

$$\nabla X_i = \sum_j \frac{X_i X_j}{D_{i,j}}(\vec{U}_i - \vec{U}_j)$$

Usually, instead of using the binary diffusion coefficient, it is useful to define a diffusion coefficient for the mixture $D_{i,m}$ and then Equation 4.13 is found.

the component in the mixture:

$$\frac{\partial \rho}{\partial t} + \nabla \rho \vec{u} = -\nabla \cdot \sum_i (D_{i,m} \nabla Y_i) \tag{4.15}$$

which should be identical to the total mass balance equation, in which the right hand side is zero. If the Lewis numbers are not equal, the right hand side is not zero and a correction to the flux is needed:

$$\vec{J_i} = D_{i,m} \nabla Y_i + \vec{J_c} \tag{4.16}$$

and total mass balance is ensured if the correction flux is defined in the following way:

$$\vec{J_c} = \sum_i (D_{i,m} \nabla Y_i) \tag{4.17}$$

Momentum balance The second law of dynamics relates the momentum variation of a body with the forces acting on it. Two types of forces may act on a volume of a fluid:

1. The mass force $\vec{f}$ acting on each volume element. For gravity this becomes: $\vec{f} = \rho \vec{g}$.
2. Surface forces $\vec{t}$ acting only at the boundaries. These forces are written as: $\vec{t} = \mathbf{T} \cdot \vec{n}$, where $\mathbf{T}$ is the *s*tress tensor.

The resulting balance equation for the momentum is a vector equation:

$$\frac{\partial}{\partial t}(\rho \vec{u}) + \nabla \cdot \left(\rho \vec{u} : \vec{u}\right) = -\nabla \cdot \mathbf{T} + \rho \vec{g} + \vec{f} \tag{4.18}$$

where the term $(\vec{u} : \vec{u})_{i,j} = u_i u_j$ is a diadic form.

As for the species, combining the previous equation with the continuity equation 4.10, it is possible to obtain:

$$\rho \frac{\partial \vec{u}}{\partial t} + \rho \left(\vec{u} \cdot \nabla\right) \vec{u} = -\nabla \cdot \mathbf{T} + \rho \vec{g} + \vec{f} \tag{4.19}$$

The tensor $\mathbf{T}$ can be split into a part $p \cdot \mathbf{I}$ ($\mathbf{I}$ is the unit tensor) representing the normal stress (p is the pressure in the fluid) and a part $\mathbf{D}$ representing the shear stresses: $\mathbf{T} = \mathbf{D} + p \cdot \mathbf{I}$.

$$\rho \frac{\partial \vec{u}}{\partial t} + \rho \left(\vec{u} \cdot \nabla\right) \vec{u} = -\nabla p + \nabla \cdot \mathbf{D} + \rho \vec{g} + \vec{f} \tag{4.20}$$

where:

p	-	pressure of the fluid
$\mathbf{D}$	-	stress-strain tensor
$\vec{g}$	-	gravitational acceleration
$\vec{f}$	-	other volumetric forces

For a Newtonian fluid, the stress tensor $\mathbf{D}$ can be related, as a first approximation, to the velocity gradients. In Cartesian coordinates it can be written in the following form[3]:

$$\mathbf{D}_{ij} = \mu \left(\frac{\partial u_i}{\partial x_j} + \frac{\partial u_j}{\partial x_i} \right) + \delta_{ij} \left(\beta - \frac{2}{3} \mu \right) \frac{\partial u_l}{\partial u_l} \tag{4.21}$$

[3] When in a product a tensor is written in components the summation over two repeated indices applies.

where:
- μ - molecular dynamical viscosity
- β - bulk viscosity
- δ - Kronecker's delta

With the exception of shock waves studies, or in the absorption or attenuation of acoustic waves, it is *convenient* to ignore the coefficient of bulk viscosity[4]. The pressure p and the density ρ are related to each other through the equation of state. In Cartesian coordinates, the Navier-Stokes equation is written in the following way:

$$\rho\frac{\partial v_i}{\partial t}+\rho u_j\frac{\partial v_i}{\partial x_j}=-\frac{\partial p}{\partial x_i}+\frac{\partial}{\partial x_i}\left(\mu\left(\frac{\partial u_i}{\partial u_j}+\frac{\partial u_j}{\partial x_i}\right)+\delta_{ij}\left(\beta-\frac{2}{3}\mu\right)\frac{\partial u_l}{\partial x_l}\right)+\rho g_i+f_i \quad (4.22)$$

Energy balance The energy balance is written for the total energy $e=h+\frac{u^2}{2}-\frac{p}{\rho}$:

$$\rho\frac{\partial e}{\partial t}+\rho\left(\vec{u}\cdot\nabla\right)e+\nabla\cdot(\vec{u}p)=\Psi+\dot{Q}-\nabla\cdot\vec{q}+\mathcal{L} \quad (4.23)$$

where:
- Ψ - dissipation by viscous stress
- $\dot{Q}$ - heat source or sink
- $\vec{q}$ - heat flux
- $\mathcal{L}$ - rate of work done by external forces

The dissipation by viscous stress Ψ is, for a Newtonian fluid is written using the strain tensor $s_{ij}=\frac{1}{2}\left(\frac{partialu_i}{\partial x_j}+\frac{partialu_j}{\partial x_i}\right)$:

$$\Psi\equiv-\frac{2}{3}(\nabla\cdot\vec{v})^2+2\mu s_{ij}s_{ij} \quad (4.24)$$

and can be written in the following form:

$$\Psi=\mathbf{T}\nabla\cdot\vec{u} \quad (4.25)$$

The viscous term is important only if the Brinkman number:

$$Br=\frac{\mu u^2}{k\Delta T}$$

is greater than unity. In combustion the Brinkman number is of the order of $Br\sim10^{-4}$ and therefore the viscous term is usually neglected.

The rate of work done by external forces can be written in the following way:

$$\mathcal{L}\equiv\rho\sum_k Y_k\vec{F}_k\left(\vec{u}+\vec{u}_k\right) \quad (4.26)$$

[4]This assumption is strictly valid only for a monoatomic gas. For polyatomic gases the non zero values for the bulk viscosity are from relaxation effect for translational motions and the various internal degree of freedom. Up to now there is no satisfactory theories and the experimental data are incomplete.

where:
- Y_k - mass fraction of the k_{th} component
- $\vec{F}_k$ - force acting on the k_{th} element
- $\vec{u}_k$ - relative mass diffusion velocity component

The only external force acting on the components under consideration is the gravity force whose influence is anyway small.

The heat flux vector consists of several contributions:

1. Heat flux due to thermal conduction $\vec{q}_c$;
2. Heat flux due to component diffusion $\vec{q}_m$;
3. Heat flux due to concentration gradients $\vec{q}_D$ (Dofour effect).

The heat flux due to thermal conduction is written using the Fourier law:

$$\vec{q}_c = -k\nabla T \tag{4.27}$$

where k is the thermal conductivity of the gas.

The multicomponent heat transfer rate reads:

$$\vec{q}_m = \nabla \cdot \left(\rho \sum_j h_j Y_j \vec{u}_j \right) \tag{4.28}$$

The relative mass diffusion velocity component $\vec{u}_j$ can be expressed in terms of concentration gradients and the above equation can be written as:

$$\vec{q}_m = \nabla \cdot \left(\sum_j h_j \vec{J}_j \right) \vec{J}_j = D_{j,m} \nabla Y_j \tag{4.29}$$

Onsager's reciprocal relations for the thermodynamics of irreversible process imply that if a temperature gradient gives rise to a diffusion velocity (the Soret effect) then concentration gradients must produce a heat flux. This effect is known as the Dofour effect. In terms of the relative diffusion velocity it can be written in the following way:

$$\vec{q}_D = RT \sum_i \sum_j \left(\frac{X_j \alpha_{T,i}}{\mu_i D_{i,j}} \right) (\vec{u}_i - \vec{u}_j) \tag{4.30}$$

where:
- R - ideal gas constant
- X_j - mole fraction of species j
- $\alpha_{T,i}$ - thermal diffusivity for species i
- μ_i - molar mass for species i

Even if the thermal diffusion is not negligible, the Dofour effect is. After the simplification

described above, Equation 4.23 reads:

$$\rho\frac{\partial e}{\partial t} + \rho\vec{U}\nabla e + \nabla\cdot(\vec{U}p) = \dot{Q} - \nabla\cdot\left(\nabla\cdot\left(\sum_j h_j\vec{J}_j\right) - k\nabla T\right) \tag{4.31}$$

The processes that can add or remove heat from the system are the following two, considered in more detail later:

1. radiative heat transfer;
2. combustion reactions.

A different and more rigorous approach to derive the equations for the reactive CFD can be found in [112].

4.2. Turbulence

The flows described by the previous equations have the characteristic to become unstable if the Reynolds number Re is bigger than a characteristic value. This non-stationary behavior is called turbulence. There is no unique definition of a turbulent flow, but such a flow has a number of characteristic features (see [137]) such as:

Irregularity Turbulent flow is irregular, random and chaotic. The flow consists of a spectrum of different scales (eddy sizes) where largest eddies are of the order of the flow geometry. At the other end of the spectra the smallest eddies are by viscous forces (stresses) dissipated into internal energy. Even though turbulence is chaotic it is deterministic and is described by the Navier-Stokes equations.

Diffusivity In turbulent flow the diffusivity increases. This means that the spreading rate of boundary layers, jets, etc. increases as the flow becomes turbulent. The turbulence increases the exchange of momentum in e.g. boundary layers and reduces or delays thereby separation at bluff bodies such as cylinders, airfoils and cars. The increased diffusivity also increases the resistance (wall friction) in internal flows such as in channels and pipes.

Three-Dimensionality Turbulent flow is always three-dimensional. However, in particular geometries and after time averaging the equations the flow can be treated as two-dimensional.

Dissipation Turbulent flow is dissipative, which means that kinetic energy in the small (dissipative) eddies are transformed into internal energy. The small eddies receive the kinetic energy from slightly larger eddies. These larger eddies receive their energy from even larger eddies and so on. The largest eddies extract their energy from the mean flow. This process of transferred energy from the largest turbulent scales (eddies) to the smallest is called cascade process

According to Kolmogorov [184], the size of the eddies spans a wide range of length scales, from a macroscale (integral length scale L) corresponding to the geometrical dimension of the system, to the smallest size of the eddies (Kolmogorov microscale η). The energy is supplied to the largest scales of motion through the production mechanism. These eddies transfer their energy sequentially to the smaller ones during energy cascade (introduced historically by Richardson [292]). During this energy transfer, the Reynolds number decreases until it becomes equal

to unity corresponding to the dissipation scale, where the molecular viscosity converts the turbulent kinetic energy into heat. Since the information of the large scales is lost during the cascade process, the small-scale motions are characterized by statistically universal characteristics, function of the two parameters controlling the cascade process, i.e. the rate at which the energy is transferred and the viscous dissipation ϵ. This property leads to the definition of the Kolmogorov length η, velocity u_η and time τ_η scales, defined as:

$$\eta \equiv \left(\frac{\nu^3}{\epsilon}\right)^{1/4} \tag{4.32}$$

$$u_\eta \equiv (\nu\epsilon)^{1/4} \tag{4.33}$$

$$\tau_\eta \equiv \left(\frac{\nu}{\epsilon}\right)^{1/2} \tag{4.34}$$

where ν is the kinematic viscosity and ϵ the dissipation rate of turbulent kinetic energy k. Another important property, summarized by Kolmogorov second similarity hypothesis, is that, for high Reynolds number turbulent flows, the statistics of the motion of scales larger than η are only dependent on ϵ. From this characteristic and the previous definition of the Kolmogorov scale, the following identity can be written:

$$\epsilon = \frac{u'^3}{L} = \frac{u_\eta^3}{\eta} \tag{4.35}$$

It can be seen that the Reynolds number calculated at the Kolmogorov scale is equal to 1:

$$Re_\eta = \frac{\eta u_\eta}{\nu} = 1$$

The turbulent scales are distributed over a range of scales which extends from the largest scales L which interact with the mean flow to the smallest scales η where dissipation occurs. Each single scale contain an amount of (turbulent) energy $E(\kappa)d\kappa$, where $\kappa = \frac{1}{\eta}$. The energy spectrum $E(\kappa)$ can be subdivided into three region of different characteristics, according to the previous discussion about Kolmogorov hypotheses:

1. The region where the large eddies carry most of the energy. These eddies interact with the mean flow and extract energy from the mean flow. Their energy is transferred to slightly smaller scales.

2. The dissipation range. The eddies are small and isotropic and it is here that the dissipation occurs. The scales of the eddies are described by the Kolmogorov scales

3. The inertial sub-range. The existence of this region requires that the Reynolds number is high (fully turbulent flow). The eddies in this region represent the mid-region. Energy per time unit is coming from the large eddies at the lower part of this range and is given off to the dissipation range at the higher part. The eddies in this region are independent of both the large, energy containing eddies and the eddies in the dissipation range.

In practical applications, where the flow becomes turbulent, it is imperative to take into account the effects of turbulence on all the thermodynamic variables, since turbulence change dramatically the characteristics of the flow. According to the previous description, turbulence has the following impact on a flow:

- The first important characteristic of turbulence is its ability to transport and mix fluid more effectively than in a laminar flow. Modern applications strongly confirmed this phenomena. The aforementioned feature is of great importance in many industrial applications, where several streams are brought together to mix (and eventually to react, as in a combustion chamber).

- Turbulence also has the ability to transport momentum of the fluid. As a consequence, for example, the penetration of jets inside a combustion chamber (and related to that, the length of a flame) is reduced in comparison to the laminar case.

- Due to the velocity fluctuations, the species concentration and the temperature field also fluctuate. Those fluctuations must be taken into account in calculations of reacting flows. In fact the reaction rates between the species are strongly non-linear in the species concentrations and, mainly, in temperature. Therefore not only an average values but also their fluctuations must be taken into account.

The following list summarizes shortly the most frequently used approaches in turbulent flow calculations:

Direct Numerical Simulation (*DNS*): In this approach the Navier-Stokes equations are solved without any approximation or modeling for the turbulence. All the scales in the eddy cascade are resolved from the macroscopic scale to the Kolmogorov scale. The simulations based on this model are intrinsically time dependent.

Large Eddy Simulation (*LES*): Only the largest scales are spatially resolved and time-dependently simulated. These scales are directly affected by the macroscopic geometry and therefore it is difficult to create a model valid for all the physical situations and for all the geometries. The smallest scales are less dependent on a macroscopic geometry and are not resolved but modeled. Even these models are intrinsically time dependent.

Reynolds Averaged Models (*RAM*): Only the averaged quantities are considered and equations are written only as a function of them. Mathematically, the thermodynamic variables are split into two parts. The average and the fluctuating parts are related by the following equation:

$$\Phi = \overline{\Phi} + \Phi'$$

The operator previously referred as $\overline{f}$ denotes averaging over the fluctuating variable f.

Probability Density Function (*PDF*): In these type of models the variables are considered as stochastic fields and the methods of stochastic analysis must be used. For each variable, its *PDF*, a function of time and space, can be derived from the *NS* equations. The *PDF* describes the probability that the variable has a certain values in a certain range. The numerical algorithm solves directly for the *PDF*.

4.3. Reynolds averaged models

The decomposition of a variable into its mean value and its fluctuation is referred as *Reynolds decomposition* and it was first discussed by Reynolds in 1894. The equations derived from this approach are called Reynolds Averaged Navier-Stokes (RANS) equations. For the velocity this decomposition reads:

$$\vec{u}(\vec{r},t) = \vec{U}(\vec{r},t) + \vec{u}'(\vec{r},t) \tag{4.36}$$

where the variable $\vec{U}(\vec{r},t)$ is the *mean* velocity. The Fevre *ensemble* averaging needs to be used:

$$\overline{\vec{u}(\vec{r},t)} \equiv U(\vec{r},t) = \lim \frac{1}{\overline{\rho}N} \sum^{N} \rho\vec{u}(\vec{r},t) \tag{4.37}$$

where

$$\overline{\rho} = \frac{1}{\Delta t} \int_{t}^{t+\Delta t} \rho(\vec{r},\tau)d\tau \tag{4.38}$$

From the above definition, the following relations are derived:

$$\langle \vec{u}\,'(\vec{r},t)\rangle = 0 \tag{4.39}$$

$$\langle \vec{U}(\vec{r}_1,t)\vec{U}(\vec{r}_2,s)\rangle = |U(\vec{r},t)|^2\delta^3(\vec{r}_1-\vec{r}_2)\delta(t-s) \tag{4.40}$$

The first equation means that the first statistical moment of the turbulent field is zero. The higher order moments do not vanish as will be seen hereafter. The second equation says that the mean velocity field has no fluctuations: it is not a stochastic variable. Higher moments of the mean velocity vanish too. Since $U(x,t)$ is not stochastic, its correlations with any other variables are zero:

$$\langle \vec{U}(\vec{r}_1,t_1)\vec{v}(\vec{r}_2,t_2)\rangle = 0 \tag{4.41}$$

The Favre averaging process makes possible the decoupling between the average of the density and the average of other variables. Considering the velocity as an example, it is possible to write the definition 4.37 in a different form:

$$\overline{\rho}\vec{U}(\vec{r},t) = \frac{1}{\Delta t} \int_{t}^{t+\Delta t} \rho(\vec{r},\tau)\vec{v}(\vec{r},\tau)d\tau \tag{4.42}$$

If now again the averaging of the continuity equation is performed, because of relationships like the one above, the term inside the divergence produces only a term containing the average of the density and the average of the velocity. The term containing the divergence of the correlation of the fluctuations is no longer present.

It is now possible to insert the Favre decomposition into Equations 4.10 and 4.20, and after taking the ensemble averaging, one obtains:

$$\frac{\partial\overline{\rho}}{\partial t} + \nabla\cdot\left(\overline{\rho}\vec{U}\right) = 0 \tag{4.43}$$

$$\overline{\rho}\frac{\partial\vec{U}}{\partial t} + \left(\overline{\rho}\vec{U}\cdot\nabla\right)\vec{U} = \overline{\vec{f_0}} - \nabla\overline{P} + \nabla\cdot\overline{\mathsf{D}} + \nabla\cdot\mathsf{D}' \tag{4.44}$$

The tensor D' is the turbulent stress tensor, known as the *Reynolds stress* tensor . If the fluid is Newtonian, the stress tensor is defined in Equation 4.21 as a function of the averaged values:

$$\mathsf{D}'_{ij} = \overline{\rho}\left(\overline{u_i'u_j'}\right) \tag{4.45}$$

The Reynolds stress tensor is a symmetric second order tensor. Its isotropic part, the turbulent kinetic energy defined by:

$$k \equiv \frac{1}{2}\left(\overline{u_i'u_i'}\right) \tag{4.46}$$

allows the definition of the *deviatoric anisotropic* part of the Reynolds stress:

$$a_{ij} \equiv \overline{u_i' u_j'} - \frac{2}{3} k \delta_{ij} \tag{4.47}$$

It is only the anisotropic part that is effective in transporting momentum. For it is:

$$\rho \frac{\partial \overline{u_i' u_j'}}{\partial x_i} + \frac{\partial P}{\partial x_j} = \rho \frac{\partial a_{ij}}{\partial x_i} + \frac{\partial}{\partial x_j} \left(P + \frac{2}{3} \rho k \right) \tag{4.48}$$

showing that the isotropic part can be absorbed in a modified mean pressure.

The *dissipation of the turbulent energy* ϵ , defined by:

$$\epsilon \equiv \mu \overline{\frac{\partial u_i'}{\partial x_k} \frac{\partial u_i'}{\partial x_k}} \tag{4.49}$$

will be used later.

Equations 4.43 and 4.44 are the equations for the averaged field. They are not in a closed form, due to the presence of the Reynolds stress. This is the well know *closure problem* for the *NS* equations. In fact, if a component of the momentum equation 4.20 is multiplied by a component of the velocity field, an equation containing a term for the triple correlations is obtained (see also Section 4.3.3 and [280]). In Equation 4.76 the terms $D_{T,ij}$, G_{ij}, ϕ_{ij}, and $\mathcal{R}_{ij}$ require a model for the closure. In each equation for an n^{th} correlation a term containing an n^{th+1} correlation appears. All this kind of models require sub-models for closure.

Also a generic passive scalar field ϕ can be divided, as previously done for the velocity, into its mean and its fluctuation part. Applying the same method as previously used for the velocity, it is possible to derive the following equation for a generic specific quantity $\overline{\phi}$:

$$\frac{\partial \rho \overline{\phi}}{\partial t} + \nabla \cdot \rho \left(\vec{U} \overline{\phi} + \overline{\rho \vec{u}' \phi'} \right) = \nabla \cdot \left(\Gamma \nabla \overline{\phi} \right) + \dot{s}_\phi \tag{4.50}$$

The above equation can also be written in the following way:

$$\rho \frac{\partial \overline{\phi}}{\partial t} + \rho \vec{U} \cdot \nabla \overline{\phi} = \nabla \cdot \left(\Gamma \nabla \overline{\phi} - \overline{\vec{u}' \phi'} \right) + \dot{s}_\phi \tag{4.51}$$

The scalar fluxes play a similar role to that of Reynolds stresses in the Reynolds equation. Even in the case of a passive scalar, as discussed before, Equation 4.51 require a closure.

The term $\overline{\rho \vec{u}' \phi'}$ explicitly written for the enthalpy equations and the species equation, arises the following two unclosed correlation, $\overline{\rho \vec{u}' h'}$ and $\overline{\rho \vec{u}' Y_i'}$. The closure of this two terms will be shortly explained in 5.

4.3.1. Turbulent viscosity

The vector $\overline{\vec{u}' \phi'}$ gives the direction and the magnitude of the turbulent transport of the quantity ϕ as the turbulent Reynolds stress $\overline{\vec{u}_i' \vec{u}_j'}$ gives the magnitude and the direction of the turbulent transport for the momentum. Following the *gradient diffusion hypothesis* it is possible to relate the turbulent scalar flux to the gradient of the mean field:

$$\overline{\vec{u}' \phi'} = -\Gamma_T \nabla \overline{\phi} \tag{4.52}$$

The function $\Gamma(\vec{r},t)$ is called the turbulent diffusivity. Using this approximation, Equation 4.51 becomes:

$$\frac{\partial\overline{\phi}}{\partial t}+\left(\vec{U}\cdot\nabla\right)\overline{\phi}=\nabla\cdot\left(\Gamma_{eff}\nabla\overline{\phi}\right)+\dot{s}_{\phi} \tag{4.53}$$

where:

$$\Gamma_{eff}(\vec{r},t)=\Gamma(\vec{r},t)+\Gamma_{T}(\vec{r},t) \tag{4.54}$$

In an analogous way, the *turbulent viscosity hypothesis*, introduced by Boussinesq in 1877, can be used and it is possible to write the correlations for the fluctuating velocity:

$$-\rho\overline{u_i'u_j'}+\frac{2}{3}\rho k\delta_{ij}=-\rho\,\mu_T\left(\frac{\partial U_i}{\partial x_j}+\frac{\partial U_j}{\partial x_i}\right) \tag{4.55}$$

The function $\mu_T(\vec{r},t)$ is called *turbulent viscosity*, in terms of which the *NS* Equation 4.22 becomes:

$$\rho\frac{\partial\vec{U}}{\partial t}+\rho\left(\vec{U}\cdot\nabla\right)\vec{U}=-\nabla\left(P+\frac{2}{3}\rho k\right)+\nabla\sigma+\rho\vec{g}+\vec{f} \tag{4.56}$$

where:

$$\sigma_{ij}=(\mu+\mu_T)S_{ij}$$

and the mean strain rate S_{ij} is defined by:

$$S_{ij}\equiv\frac{1}{2}\left(\frac{\partial U_i}{\partial x_j}+\frac{\partial U_j}{\partial x_i}\right) \tag{4.57}$$

The specification of μ_T and Γ_T, or their measurement, solve the closure problem.

At this point some comments about the introduced hypothesis have to be made (see [280]). The turbulent viscosity hypothesis can be seen as consisting of two parts:

1. the *intrinsic part* assumes that, at each point of the domain, the Reynolds anisotropy is determined by the mean velocity gradient;

2. the *specific assumption* determines the relation between the two tensors to be mediated by the turbulent viscosity.

Regarding the first assumption, even for simple turbulent flows (see for example [371, 280]) it is possible to show that the turbulence behavior is not strictly (and in some cases even not at all) related to the mean strain rate tensor. That stems from the fact that the physics of molecular diffusion is different to the physics of turbulence. Molecular diffusion has a short relaxation time scale and so the molecular motions adjust rapidly to the imposed strain. Turbulent motions, on the other hand, do not have these possibilities because their dynamic time scale is much larger. Using the same arguments the specific assumption can also be questioned.

In simple, almost one dimensional shear flows, the viscosity hypothesis does not bring any constraint to the Reynolds stress and can be interpreted as a definition for the turbulent viscosity. In most general classes of flow, strongly swirling flows [412], flows with strong streamline curvature, some fully developed flows in non-circular ducts, the hypothesis fails. The fact that the simple Newtonian stress-strain relationship applies to the viscous (laminar) stress but not to the turbulent stress is based again on the difference in time scales. Because of the very small relaxation time scales in laminar flows (the molecular transport scales), the ratio between isotropic

stress and homogeneous stress is very small. In turbulent flows, on the contrary, that ratio can be as high as 0.5.

All of the remarks made above regarding the viscosity hypothesis can be made also for the gradient diffusion hypothesis. At high Reynolds numbers both Γ_T and μ_T scale with the velocity and the length scale of the flow, independently from the details of the molecular transfer (i.e μ and Γ). This implies that the ratio between the turbulent diffusion and the molecular diffusion scales with the Reynolds number too. At high Re the diffusion of momentum and scalar is controlled by turbulence only; The *turbulent Prandtl number* is defined by:

$$Pr_T = \frac{\nu_T}{\Gamma_T}$$

and in almost all turbulent flows is found to be around unity.

The sub-models that determine the turbulent viscosity are usually defined in terms of the number of *differential* equations used to resolve them.

4.3.1.1. The zero-equation models

In the zero-equation models the value for μ is given analytically. The turbulent viscosity can be determined in terms of a velocity v_m and a length l_m:

$$\mu_T = C\rho v_m l_m$$

This assumption is called *the mixing length theory* and is based on a similarity between momentum diffusion due to molecular process and the one due to turbulence [422] and [283].

The mixing length still remains unknown: it must be either guessed or measured. This model can be applied with relative success, despite the simplicities of the assumptions, to boundary layer flows or flows in which the main gradients are in one direction only but it fails to reproduce the characteristics of more complex flows.

Some well known zero equation models are the Baldwin-Lomax model [20], and the Cebeci-Smith model [337]. The algebraic Johnson-King model [167] requires the solution of a ODE and sometimes is called a 1/2 equation model.

4.3.1.2. The one-equation models

One of the biggest drawback of each 0-equation models is the difficulties to relate the behavior of the turbulence at one point to the characteristics of the flow at other locations. At a certain point $\vec{r}$ the turbulence is given only as an effect of the local gradient of the mean velocity and does not depend on the history of the turbulence itself. That behavior is obviously not physical. To avoid this deficiency it is possible to express the turbulent viscosity as a function of the turbulent kinetic energy $k = \frac{1}{2}\overline{u_i' u_i'}$:

$$\mu_T = c\rho l_m \sqrt{k} \tag{4.58}$$

It is possible to solve a differential equation for the calculation of the turbulent kinetic energy k. These models are known as *one-equation models* because the only differential equation to be solved is the equation for k. Both sides of Equation 4.20 can be multiplied by the component of the velocity v_i and, after summing up on the i indices and taking the average values (see for

the details [422]), the following equation is derived:

$$\rho\frac{\partial k}{\partial t}+\rho\left(\vec{U}\cdot\nabla\right)\vec{U}=\mathsf{D}'\nabla\cdot\vec{U}-\overline{\mathsf{D}\nabla\cdot\vec{u}'}+$$
$$+\nabla\cdot\left(\overline{\mathsf{D}\vec{u}'}-\frac{1}{2}\overline{\rho\vec{u}'|\vec{u}'|}-\overline{P'\vec{u}'}\right)-\overline{\vec{u}'}\nabla P+\overline{P'\nabla\cdot\vec{u}'} \tag{4.59}$$

In the above equation the following terms are present:

D'	-	the Reynolds stress
$\overline{\mathsf{D}\vec{u}'}$	-	molecular diffusion
$\overline{\rho\vec{u}'\frac{1}{2}\vec{u}'\vec{u}'\vec{u}'}$	-	turbulent transport
$\overline{\mathsf{D}\nabla\cdot\vec{u}'}$	-	dissipation rate
$\overline{\vec{u}'}\nabla P$	-	pressure work
$\overline{P'\nabla\cdot\vec{u}'}$	-	pressure dilatation

Some terms appearing in the above equation need to be closed, but before focusing on a specific closure model, it is worthwhile to citing the most important guidelines that usually are followed in deriving compressible flow closure approximations:

- all closure approximations should approach the proper laminar limit for density fluctuation going to zero;
- all term must be written in tensor form that is coordinate independent;
- all closure approximations must be dimensionally consistent and invariant under Galilean transformation.

The following terms appearing in Equation 4.59 need closures.

The Reynolds stress: In one-equation models and in two-equations models the Boussinesq approximation is used:

$$\mathsf{D}'_{ij}\equiv\overline{\rho\vec{u}'_i\vec{u}'_j}=2\mu_T(S_{ij}-\frac{1}{3}\nabla\cdot\vec{U}\delta_{ij})-\frac{2}{3}\rho k\delta_{ij} \tag{4.60}$$

Sometimes the last term in this equation is omitted. As shown in Equation 4.48 the isotropic part can be absorbed into a modified pressure and for flows up to supersonic the pressure is still several orders of magnitude larger that the correction term due to the turbulence.

Molecular diffusion and turbulent transport: These two terms are often omitted but to ensure exact conservation of the total energy more detailed closure models are required. The most commonly used approximation is the following generalization of the gradient diffusion hypothesis:

$$\overline{\mathsf{D}\vec{u}'}-\frac{1}{2}\overline{\rho\vec{u}'|\vec{u}'|}=\left(\mu+\frac{\mu_T}{\sigma_k}\right)\frac{\partial k}{\partial x_j} \tag{4.61}$$

The factor σ_k is the turbulent Prandtl number and is of the order of unity.

Pressure diffusion and pressure dilatation: Generally these terms are neglected, considering the fact that in incompressible flows they are exactly zero and also because little is really known about them. Several attempts have been made to develop closures for these

two terms but none of them received general acceptance. It is however believed that in compressible flows neglecting them ultimately leads to significant errors. It seems that the most promising approach is to derive the closure from *DNS* simulations, but up to now there are no generally accepted models.

Pressure work: The presence of this term shows that Favre averaging is not able to remove from the *NS* equation all the terms containing correlations between pressure, density and velocity. As with the previous terms, it seems that they are important in sonic flows and the most recent models for closure are obtained in such conditions. The best approach is to derive the correlation from *DNS* calculations.

Dissipation Term: This term gives the Favre averaged expression for the dissipation of the turbulent kinetic energy[5]:

$$\rho\epsilon = \overline{a_{ij}s_{ij}} \tag{4.62}$$

The Cartesian form of the k equation, neglecting the term due to the pressure fluctuation, reads:

$$\frac{\partial \rho k}{\partial t} + \frac{\partial}{\partial x_i}(\rho k U_i) = \frac{\partial}{\partial x_j}\left(\mu_{eff}\frac{\partial k}{\partial x_j}\right) + 2\mu_T S_{ij}S_{ij} - \rho\epsilon \tag{4.63}$$

At high Reynolds numbers the dissipation ϵ scales as u_0^3/l_0 where u_o and l_0 are the velocity and the scale of the energy containing motion, respectively. It is reasonable then to assume:

$$\epsilon = C_D\frac{k^{3/2}}{l_m} \tag{4.64}$$

With the above assumption it is possible to write the molecular viscosity as (from Equations 4.58 and 4.64):

$$\mu_T = \rho C_\mu k^2/\epsilon \tag{4.65}$$

For simple shear flows the quantities μ_T, ϵ and k can be measured and the validity of the assumption can be checked. From [179] it is possible to argue that, excluding the region near the wall $y^+ < 50$, the quantity C_μ is indeed approximately constant, with a value around 0.09. Even for a mixing layer, excluding the edges, the values are practically constant and equal to 0.08, as shown in [297].

In more complex flows, or in other geometries the argument seems to be not so stringent. For example Jovanovic [170] shows that for axisymmetric turbulence the turbulent viscosity is given by:

$$\mu_T = \frac{1}{2}C_{a1}\frac{k}{S} \tag{4.66}$$

where $S = \sqrt{|S_{ij}|}$. One way to produce axisymmetric turbulence is to suddenly expand (or contract) homogeneous turbulence. Pope shows ([280]) that the intrinsic assumption of the turbulent viscosity cannot predict such flows.

Comparison with the measurements (see [422]) shows that this model has modest advantage over the zero-equation models. Moreover the biggest drawback of the zero-equation models is present even in the one-equation models: the mixing length l_m must still be given.

Example of a one equations model is the Spalart-Allmaras model [350], the Baldwin-Barth model [21], the NUT-92 model [325] and the Rahman-Agarwal-Siikonen Model [284].

[5] Only the symmetric part plays a role in the dissipation.

4.3.1.3. The two-equations models

In order to remove the unknown l_m, a second differential equation must be introduced. Using this closure the two equation models are the simplest complete models. The starting point for the two-equations model is the Boussinesq approximation, Equation 4.55, and the equation for the turbulent kinetic energy, Equation 4.59. For the second equation, there is not a unique way to determine a characteristic length l_m or the turbulent dissipation ϵ. The most common assumptions are listed below:

- in terms of the vorticity:

$$\mu_T \sim \rho k\omega \quad \ell \sim k^{1/2}/\omega \quad \epsilon \sim \omega k$$

- in terms of the dissipation rate:

$$\mu_T \sim \rho k^2/\epsilon \quad \ell \sim k^{3/2}/\epsilon$$

- in terms of the mixing scalar length:

$$\mu_T \sim \rho k^{1/2}\ell \quad \epsilon \sim k^{3/2}/\ell$$

- in terms of the turbulent dissipation time:

$$\mu_T \sim \rho k\tau \quad \ell \sim k^{1/2}\tau \quad \epsilon \sim k/\tau$$

It is not clear which of above models is superior. It is also not clear which variable should be used for the most accurate description of turbulence. However it seems to be sure that the highest uncertainty is associated with the formulation of the second equation. By now the most widely method used is the so called $k-\epsilon$ model.

Among the many realizations of the two-equations models the following can be cited:

k-ϵ models: the standard model in [204] and [201], the RNG k-ϵ model in [431], the *realizable* k-ϵ model in [324]

The k-ω models: the Wilcox's k-ω model [421] the modified Wilcox's k-ω model [422] the SST k-ω model [241]

$\overline{v^2} - f$ model in [97]

k-τ model of Speziale in [353]

k-kL model in [3]

One of the most common model used in industrial applications is the standard k-ϵ model therefore more detail will be given. The equation for k is derived directly from the *NS* equations and,as discussed before, is exact [142]. Sub-models are needed anyway for the closure of the various terms. Although equation for ϵ could be derived in the same way, usually a different approach is taken. The flow of energy is seen as a cascade, from the biggest length scales to the dissipation ones, determined by the large scale motion. In the limit of high Reynolds numbers,

the cascade is independent of the viscosity. Consequently the ϵ equation is better viewed as entirely empirical, and can be written as:

$$\frac{\partial \epsilon}{\partial t} + \vec{U}\nabla\epsilon = \nabla\left(\frac{\mu_T}{\sigma_\epsilon}\nabla\epsilon\right) + C_{1\epsilon}\frac{\mathcal{P}\epsilon}{k} - C_{2\epsilon}\frac{\epsilon^2}{k} \tag{4.67}$$

where $\mathcal{P}$ is the production of the turbulent kinetic energy: $\mathcal{P} = \mu_T S_{ij} S_{ij}$. The turbulent viscosity μ_T is computed by combining k and ϵ as follows (see Equation 4.65 and following discussion):

$$\mu_T = \rho C_\mu \frac{k^2}{\epsilon} \tag{4.68}$$

where C_μ is a constant.

The constants of the model are listed below:

$$C_{1\epsilon} = 1.44, \;\; C_{2\epsilon} = 1.92, \;\; C_\mu = 0.09, \;\; \sigma_k = 1.0, \;\; \sigma_\epsilon = 1.3$$

These default values have been determined from experiments on turbulent shear flows including homogeneous shear flows and decaying isotropic grid turbulence. They have been found to work fairly well for a wide range of wall-bounded and free shear flows.

4.3.1.4. More n-equations models

More complex models have been developed with the aim to increase the accuracy. Among the models that need more than 2 partial differential equations the following can be mentioned:

1. the 3-equations k-kl-ω transition model [395];
2. the 4-equations transition SST model [198].

4.3.2. Algebraic stress models

While models based on the Boussinesq approximation provide excellent prediction for many flows of industrial interest (and indeed the two-equation k-ϵ model is the most used in industrial numerical simulations), there are several categories of flows for which the approximation fails completely in the prediction of the main flow:

- flows with sudden changes in mean strain rate;
- flows over curved surfaces;
- flows in duct with secondary motions;
- flows in rotating and stratified flows;
- three dimensional flows;
- flows with boundary layer separations.

One option to overcome the previous problems is to consider the Boussinesq approximation as a first order truncated series. The primary distinction of an algebraic stress model (ASM) is the assumption that the Reynolds stresses are given by a series expansion of functionals, of which the Boussinesq approximation only contains the first terms. Two main approaches can be undertaken. In the first, the transport of the turbulent stresses is assumed proportional to

the turbulent kinetic energy; while in the second, convective and diffusive effects are assumed to be negligible. Following such an idea some other relationships were developed, but even if mathematically correct, they did not succeed in removing all the drawbacks of the models presented here. It is the case of the model presented by Lumley [221] and Saffman [300] that reads:

$$\mathsf{D}'_{ij} = -\frac{2}{3}\rho k\delta_{ij} + 2\mu_T S_{ij} - D\frac{\rho k}{\omega^2}(S_{ik}\Omega_{kj} + S_{jk}\Omega_{ki}) \tag{4.69}$$

or by Speziale [354]:

$$\begin{aligned}\mathsf{D}'_{ij} = -\frac{2}{3}\rho k\delta_{ij} + 2\mu_T S_{ij} + 4C_D C_\mu^2\frac{\rho k^3}{\epsilon^2}(S_{ik}S_{kj} - \frac{1}{3}S_{mn}S_{nm}\delta_{ij}) \\ +4C_E C_\mu^2\frac{\rho k^3}{\epsilon^2}(\overset{o}{S}_{ij} - \frac{1}{3}\overset{o}{S}_{mn}\,\delta_{ij})\end{aligned} \tag{4.70}$$

with the following definition:

$$\overset{o}{S}_{ij} = \frac{\partial S_{ij}}{\partial t} + U_k\frac{\partial S_{ij}}{\partial x_k} - \frac{\partial U_i}{\partial x_k}S_{kj} - \frac{\partial U_j}{\partial x_k}S_{ki} \tag{4.71}$$

The antisymmetric strain of rotation Ω is defined as follows:

$$\Omega_{ij} \equiv \frac{1}{2}\left(\frac{\partial U_i}{\partial x_j} - \frac{\partial U_j}{\partial x_i}\right) \tag{4.72}$$

The closure coefficients C_D and C_E are given by:

$$C_D = C_E = 1.68$$

The Speziales constitutive relationship describes in a good way for example secondary flows (that using the standard Boussinnesq approximation do not develop), but still fails to describe flows with sudden changes in strain rate. In summary the biggest advantage of these non-linear constitutive relations is in the attempt to reproduce the anisotropy of the Reynolds stress tensor.

A more recent example is the explicit algebraic Reynolds stress model, or EARSM, [394]. In this model, the turbulent stress relationship is non linear and it can be given by:

$$\tau_{ij} = 2\mu_t\left(S_{ij} - \frac{1}{3}\frac{\partial U_k}{\partial x_k}\delta_{ij}\right) - \frac{2}{3}\rho k\delta_{ij} - a_{ij}^{(ex)}\rho k \tag{4.73}$$

where:

$$\begin{aligned} a_{ij}^{(ex)} &= \beta_3\left(W_{ik}^*W_{kj}^* - \frac{1}{3}II_\Omega\delta_{ij}\right) \\ &+ \beta_4\left(S_{ik}^*W_{kj}^* - W_{ik}^*S_{kj}^*\right) \\ &+ \beta_6\left(S_{ik}^*W_{kl}^*W_{lj}^* + W_{ik}^*W_{kl}^*S_{lj}^* - II_\Omega S_{ij}^* - \frac{2}{3}IV\delta_{ij}\right) \\ &+ \beta_9\left(W_{ik}^*S_{kl}^*W_{lm}^*W_{mj}^* - W_{ik}^*W_{kl}^*S_{lm}^*W_{mj}^*\right) \end{aligned} \tag{4.74}$$

The turbulent eddy viscosity is computed from:

$$\mu_t = \frac{C_\mu}{\beta^*}\frac{\rho k}{\omega} \tag{4.75}$$

together with a k-ω model.

4.3.3. Reynolds stress models

Even if the second-order closure models are more mathematically complex and require higher computational costs, the advantages of these models are clearly recognizable in complex flows [403]. First of all the models account automatically for anisotropy of the flows without imposing conditions on the tensor components. Secondly, since the equations accounts for convection and diffusion, the formulation includes the effects of the flow history. The presence of diffusion and turbulent transport indicates the presence of time scales that are not related with the mean flow time scales. Moreover the terms in the equations have the potential (with an appropriate closure) to account for stream curvature and sudden change of strain rate.

The exact transport equations for the component of the Reynolds stresses, $\rho\overline{u_i' u_j'}$ may be written as follows [200]:

$$\begin{aligned}
&\underbrace{\frac{\partial}{\partial t}(\rho\,\overline{u_i' u_j'})}_{\text{Local Time Derivative}} + \underbrace{\frac{\partial}{\partial x_k}(\rho u_k \overline{u_i' u_j'})}_{C_{ij}\equiv\text{Convection}} = \\
&\underbrace{-\frac{\partial}{\partial x_k}\left[\rho\,\overline{u_i' u_j' u_k'} + \overline{p\left(\delta_{kj}u_i' + \delta_{ik}u_j'\right)}\right]}_{D_{T,ij}\equiv\text{Turbulent Diffusion}} \\
&\underbrace{-\rho\left(\overline{u_i' u_k'}\,\frac{\partial u_j}{\partial x_k} + \overline{u_j' u_k'}\,\frac{\partial u_i}{\partial x_k}\right)}_{P_{ij}\equiv\text{Stress Production}} \\
&+ \underbrace{\overline{p\left(\frac{\partial u_i'}{\partial x_j} + \frac{\partial u_j'}{\partial x_i}\right)}}_{\phi_{ij}\equiv\text{Pressure Strain}} - \underbrace{2\mu\overline{\frac{\partial u_i'}{\partial x_k}\frac{\partial u_j'}{\partial x_k}}}_{\mathcal{R}_{ij}\equiv\text{Dissipation}} \\
&\underbrace{-2\rho\Omega_k\left(\overline{u_j' u_m'}\epsilon_{ikm} + \overline{u_i' u_m'}\epsilon_{jkm}\right)}_{F_{ij}\equiv\text{Production by System Rotation}}
\end{aligned} \tag{4.76}$$

Of the various terms in these exact equations, C_{ij}, $D_{L,ij}$, P_{ij}, and F_{ij} do not require any modeling. However, $D_{T,ij}$, G_{ij}, ϕ_{ij}, and $\mathcal{R}_{ij}$ need to be modeled to close the equations.

4.3.3.1. Turbulent diffusive transport

As it was discussed before, there are not enough experimental data to asses, without any doubt, the mathematical form of the term $D_{T,ij}$. It can be modeled by the generalized gradient-diffusion

model [84]:

$$D_{T,ij} = C_s \frac{\partial}{\partial x_k}\left(\rho \frac{k\overline{u_k' u_\ell'}}{\epsilon}\frac{\partial \overline{u_i' u_j'}}{\partial x_\ell}\right) \tag{4.77}$$

However, this equation can result in numerical instabilities, so it has been simplified to use a scalar turbulent diffusivity as follows [212]:

$$D_{T,ij} = \frac{\partial}{\partial x_k}\left(\frac{\mu_T}{\sigma_k}\frac{\partial \overline{u_i' u_j'}}{\partial x_k}\right) \tag{4.78}$$

The turbulent viscosity, μ_T, is computed using Equation 4.102.

Lien and Leschziner [212] derived a value of $\sigma_k = 0.82$ by applying the generalized gradient-diffusion model, Equation 4.77, to a planar homogeneous shear flow. Note that this value of σ_k is different from that in the standard and realizable k-ϵ models, in which $\sigma_k = 1.0$.

4.3.3.2. Pressure-strain term

The fluctuating pressure enters Equation 4.76 through the pressure strain tensor $\mathcal{R}_{ij}$ and through the pressure driven turbulent diffusion (second term in $D_{T,ij}$). In flows with constant density the trace of $\mathcal{R}_{ij}$ is zero; this term does not enter in the equation for the turbulent kinetic energy k, but it is important for the redistribution of excess energy between the components of the Reynolds stress. It is possible to show (see for example [280]) that the order of magnitude of this term can be almost equal to the order of magnitude of the production, the dissipation being small (for example in the turbulent boundary layers). Together with the production and the dissipation, the redistribution must be an important process in the balance of the Reynolds stress and that explains the reason for the effort put by researchers in the modeling of that term.

The classical approach to modeling $\mathcal{R}_{ij}$ is through the following decomposition [126, 115, 202, 199]:

$$\mathcal{R}_{ij} = \mathcal{R}_{ij,1} + \mathcal{R}_{ij,2} + \mathcal{R}_{ij,w} \tag{4.79}$$

where:
- $\mathcal{R}_{ij,1}$ - slow pressure-strain term[6]
- $\mathcal{R}_{ij,2}$ - rapid pressure-strain term
- $\mathcal{R}_{ij,w}$ - wall-reflection term.

The decomposition can be understood from an examination of the Poisson equation for the fluctuating pressure:

$$\frac{1}{\rho}\nabla^2 p' = -2\frac{\partial U_i}{\partial x_j}\frac{\partial u_j'}{\partial x_i} - \frac{\partial^2}{\partial x_i \partial x_j}\left(u_i' u_j' - \overline{u_i' u_j'}\right) \tag{4.80}$$

in which it is possible to identify the following terms:

$$\frac{1}{\rho}\nabla^2 p'_{rapid} = -2\frac{\partial U_i}{\partial x_j}\frac{\partial u_j'}{\partial x_i} \tag{4.81}$$

$$\frac{1}{\rho}\nabla^2 p'_{slow} = -\frac{\partial^2}{\partial x_i \partial x_j}\left(u_i' u_j' - \overline{u_i' u_j'}\right) \tag{4.82}$$

[6]The names of the pressure component refer only to the fact that the rapid pressure contains directly the mean pressure gradient, but they have nothing to do with a general response velocity.

The complete solution contains also a third term, a harmonic term solution of the following equation:

$$\frac{1}{\rho}\nabla^2 p'_{arm} = 0 \tag{4.83}$$

Consequently with the previous distinction, also the tensor $\mathcal{R}_{ij}$ can be split into different contributions[7]. In homogeneous turbulence the solution of the above equation leads to the following:

$$\mathcal{R}_{ij} = A_{ij} + M_{ijkl}\frac{\partial U_k}{\partial x_l} \tag{4.84}$$

where:

$$A_{ij} = \frac{1}{4\pi}\iiint_V \left(\overline{\frac{\partial u'_i}{\partial x_j} + \frac{\partial u'_j}{\partial x_i}}\right)\frac{\partial^2(u'_k u'_l)}{\partial y_k \partial y_l}\frac{d^3y}{|x-y|} \tag{4.85}$$

$$M_{ijkl} = \frac{1}{2\pi}\iiint_V \left(\overline{\frac{\partial u'_i}{\partial x_j} + \frac{\partial u'_j}{\partial x_i}}\right)\frac{\partial u'_l}{\partial y_k}\frac{d^3y}{|x-y|} \tag{4.86}$$

The integration domain in Equations 4.85 and 4.86 is the entire volume. If the turbulence is not homogeneous, then the second term in Equation 4.84 becomes an integral with the mean velocity gradient inside the integral. But it is expected that the influence of turbulence at locations two or three eddies away is negligible and so it is possible to assume that turbulence is locally homogeneous and use directly Equation 4.84. The models for the two tensors are based on both the symmetry and kinematic considerations (see [422] for the derivations).

The slow pressure-strain term, $\mathcal{R}_{ij,1}$, is modeled as:

$$\mathcal{R}_{ij,1} \equiv -C_1\rho\,\frac{\epsilon}{k}\left[\overline{u'_i u'_j} - \frac{2}{3}\delta_{ij}k\right] \tag{4.87}$$

with $C_1 = 1.8$.

The rapid pressure-strain term, $\mathcal{R}_{ij,2}$, is modeled as:

$$\mathcal{R}_{ij,2} \equiv -C_2\left[(P_{ij} + F_{ij} + G_{ij} - C_{ij}) - \frac{2}{3}\delta_{ij}(P + G - C)\right] \tag{4.88}$$

where:

C_2	=	0.60
P_{ij}, F_{ij}, G_{ij}, and C_{ij}	=	are defined as in Equation 4.76
P	=	$\frac{1}{2}P_{kk}$
C	=	$\frac{1}{2}C_{kk}$

The wall-reflection term, $\mathcal{R}_{ij,w}$, is responsible for the redistribution of normal stresses near the wall. It tends to dampen the normal stress perpendicular to the wall, while enhancing the

[7] From *DNS* simulation it is possible to see that the harmonic pressure term can be neglected since it is an order of magnitude smaller than the other two terms.

stresses parallel to the wall. This term is modeled as:

$$\begin{aligned}\mathcal{R}_{ij,w} &\equiv C_1'\frac{\epsilon}{k}\left(\overline{u_k'u_m'}n_kn_m\delta_{ij} - \frac{3}{2}\overline{u_i'u_k'}n_jn_k - \frac{3}{2}\overline{u_j'u_k'}n_in_k\right)\frac{k^{3/2}}{C_\ell\epsilon d} \\ &\quad + C_2'\left(\mathcal{R}_{km,2}n_kn_m\delta_{ij} - \frac{3}{2}\mathcal{R}_{ik,2}n_jn_k - \frac{3}{2}\mathcal{R}_{jk,2}n_in_k\right)\frac{k^{3/2}}{C_\ell\epsilon d}\end{aligned} \tag{4.89}$$

where:

C_1' = 0.5
C_2' = 0.3
n_k - is the component of the unit normal to the wall
d - is the normal distance to the wall
C_ℓ = $C_\mu^{3/4}/\kappa$

The constant $C_\mu = 0.09$ and κ is the von Karman constant (= 0.4187).

When the *RSM* model is applied to near-wall flows the pressure-strain model needs to be modified. The modification used, specifies the values of C_1, C_2, C_1', and C_2' as functions of the Reynolds stress invariants and the turbulent Reynolds number, according to the suggestion of Launder and Shima [203]:

$$C_1 = 1 + 2.58A\sqrt{A_2}\left\{1 - \exp\left[-(0.0067Re_t)^2\right]\right\} \tag{4.90}$$

$$C_2 = 0.75\sqrt{A} \tag{4.91}$$

$$C_1' = -\frac{2}{3}C_1 + 1.67 \tag{4.92}$$

$$C_2' = \max\left[\frac{\frac{2}{3}C_2 - \frac{1}{6}}{C_2}, 0\right] \tag{4.93}$$

with the turbulent Reynolds number defined as $Re_t = (\rho k^2/\mu\epsilon)$. The parameter A and the tensor invariants, A_2 and A_3, are defined as

$$A \equiv \left[1 - \frac{9}{8}\left(A_2 - A_3\right)\right] \tag{4.94}$$

$$A_2 \equiv a_{ik}a_{ki} \tag{4.95}$$

$$A_3 \equiv a_{ik}a_{kj}a_{ji} \tag{4.96}$$

a_{ij} is the Reynolds-stress anisotropy tensor, defined as:

$$a_{ij} = -\left(\frac{-\overline{u_i'u_j'} + \frac{2}{3}k\delta_{ij}}{k}\right) \tag{4.97}$$

In [355] a different model for the pressure-strain model have been proposed. This model has been demonstrated to give superior performance in a range of basic shear flows, including plane strain, rotating plane shear, and axisymmetric expansion/contraction. This improved accuracy should be beneficial for a wider class of complex engineering flows, particularly those with

streamline curvature. This model is written as follows:

$$\mathcal{R}_{ij} = -\left(C_1\rho\epsilon + C_1^* P\right) a_{ij} + C_2\rho\epsilon\left(a_{ik}a_{kj} - \frac{1}{3}a_{mn}a_{mn}\delta_{ij}\right) + \left(C_3 - C_3^*\sqrt{a_{ij}a_{ij}}\right)\rho k S_{ij} + +C_4\rho k\left(a_{ik}S_{jk} + a_{jk}S_{ik} - \frac{2}{3}a_{mn}S_{mn}\delta_{ij}\right) + C_5\rho k\left(a_{ik}\Omega_{jk} + a_{jk} + \Omega_{ik}\right) \quad (4.98)$$

The mean strain rate, S_{ij}, and the mean rate-of-rotation tensor, Ω_{ij}, are previously defined.

The constants are:

$$C_1 = 3.4,\ C_1^* = 1.8,\ C_2 = 4.2,\ C_3 = 0.8,\ C_3^* = 1.3,\ C_4 = 1.25,\ C_5 = 0.4$$

This model is know as the *quadratic pressure-strain model*. It does not require a correction to account for the wall-reflection effect in order to obtain a satisfactory solution in the logarithmic region of a turbulent boundary layer.

The *ideal* model for the pressure strain term should satisfy the following criteria (see [280]):

1. In the rapid distortion limit $\mathcal{R}_{ij}$ must be linear in the mean velocity gradient;
2. The rapid pressure part of $\mathcal{R}_{ij}$ must be determined by the tensor M_{ijkl}, which must satisfy the following exact relations:

$$M_{ijkl} = M_{ijlk} \quad M_{ijkl} = M_{jikl} \quad M_{ijjl} = 0 \quad M_{ijkk} = \overline{u_i u_j}$$

3. The rapid pressure tensor must be linear in the Reynolds stresses;
4. The implementation must satisfy realizability conditions;
5. It must be frame independent.

The model previously described does not satisfy the second conditions. An extension of the original model was provided in [355] in order to fill this gap, but the performances of the new models were worst than the original one.

4.3.3.3. The kinetic energy

When the turbulence kinetic energy is needed for modeling a specific term, it is obtained by taking the trace of the Reynolds stress tensor:

$$k = \frac{1}{2}\overline{u_i' u_i'} \quad (4.99)$$

4.3.3.4. The dissipation tensor

The dissipation tensor, ϵ_{ij}, is modeled as:

$$\epsilon_{ij} = \frac{2}{3}\delta_{ij}(\rho\epsilon) \quad (4.100)$$

The scalar dissipation rate, ϵ, is computed with a model transport equation similar to that used in the standard k-ϵ:

$$\frac{\partial}{\partial t}(\rho\epsilon) + \frac{\partial}{\partial x_i}(\rho\epsilon U_i) = \frac{\partial}{\partial x_j}\left[\left(\mu + \frac{\mu_T}{\sigma_\epsilon}\right)\frac{\partial \epsilon}{\partial x_j}\right] C_{\epsilon 1}\frac{1}{2}P_{ii}\frac{\epsilon}{k} - C_{\epsilon 2}\rho\frac{\epsilon^2}{k} \tag{4.101}$$

where the constants have the following values:

$$\begin{array}{lcl} \sigma_\epsilon & = & 1.0 \\ C_{\epsilon 1} & = & 1.44 \\ C_{\epsilon 2} & = & 1.92 \end{array}$$

The turbulent viscosity, μ_T, is computed similarly to the k-ϵ models:

$$\mu_T = \rho C_\mu \frac{k^2}{\epsilon} \tag{4.102}$$

where $C_\mu = 0.09$. Equation 4.100 is based on the Kolmogorov assumption of homogeneity of the small scale eddies where dissipation occurs. In reality also the dissipation can be anisotropic, especially near the walls, and attempts were made to incorporate that effects. For example Hanjalic and Launder [140] postulate that:

$$\epsilon_{ij} = \rho\epsilon(\frac{2}{3}\delta_{ij} + 2f_s a_{ij})$$

where f_s is a low-Reynolds dumping function, postulated as:

$$f_s = (1 + 0.1Re_T)^{-1}$$

4.4. Large-eddy simulations

All the models previously described fail in universality. The reason is that the physical properties of the turbulence are strongly related to the biggest geometrical scales. The approach of the *Large Eddy Simulation* aims to simulate the dynamics of the biggest scale and then to leave the issue of modeling to the smallest scales that are believed to be more universal.

4.4.1. The filtering operators

The filtering operator (see for more mathematical details [301]) is the operator that allows to separate the scales, retaining the variations related to the biggest scales and cutting out the variation of small scales.

The general filtering operator is defined by:

$$\langle\phi\rangle_{LES}(x,t) = \iint_{\mathcal{D}} \phi(x-r, t-\tau)G(x,r,t,\tau)dr\,d\tau \tag{4.103}$$

where $\mathcal{D}$ is the flow domain, and $G(x,r,t,\tau)$ is the filter function that determines the scale of

the resolved eddies. The filter must satisfy the following normalization condition:

$$\int_{\mathcal{D}} G(x,r,t,\tau)dr = 1$$

In the simplest case the filter is homogeneous and it does not depend on x and on t. Using the filtered field, it is possible to decompose the original variable in the following way:

$$\phi(x,t) = \langle\phi\rangle_{LES}(x,t) + \phi'(x,t) \tag{4.104}$$

The analogy with Reynolds or Favre decomposition is evident, but there are several important differences. The filtered variable $\langle\phi\rangle_{LES}(x,t)$ is still a stochastic variable and in general the filtered residuals are not zero:

$$\left\langle\phi'\right\rangle_{LES}(x,t) \neq 0$$

To clarify the effect of the filter function, it is better to work in the spectral space. The spectral field of a variable ϕ is written, using Laplace transform $\mathcal{F}$:

$$\phi(\kappa) \equiv \mathcal{F}(\phi(x)) = \int_{-\inf}^{+\inf} e^{i\kappa r}\phi(r)dr \tag{4.105}$$

Using the properties of the Fourier transform on the convolution operator we can write for the filtered variable:

$$\langle\phi\rangle_{LES}(\kappa) = \mathcal{F}(\left\langle\phi(x)\right\rangle_{LES}) = G(\kappa)\phi(\kappa) \tag{4.106}$$

where $G(\kappa)$ is the *transfer function*, 2π times the Fourier transform for the filter function. The transfer function has always the properties, coming from the normalization relation, that:

$$G(0) = 1$$

and usually for large κ decreasing towards zero. In Table 4.1 the most used one-dimensional filters in *CFD* calculation are reported.

Name	Filter function	Transfer function
General	$G(r)$	$G(\kappa) \equiv \int_{-\inf}^{+\inf} e^{i\kappa r}G(r)dr$
Box	$\frac{1}{\Delta}H(\frac{1}{2}\Delta - \lvert r\rvert)$	$\frac{\frac{1}{2}\kappa\Delta}{\frac{1}{2}\kappa\Delta}$
Gaussian	$\sqrt{\frac{6}{\pi\Delta^2}}\exp\left(-\frac{6r^2}{\Delta^2}\right)$	$\exp\left(-\frac{\kappa^2\Delta^2}{24}\right)$
Sharp spectral	$\frac{\pi r/\Delta}{\pi r}H(\frac{\pi}{\Delta} - \lvert\kappa\rvert)$	
Cauchy	$\frac{a}{\pi\Delta[(r/\Delta)^2+a^2]}\quad a = \frac{\pi}{24}$	$\exp(-a\Delta\lvert\kappa\rvert)$
Pao		$\exp\left(-\frac{\pi^{2/3}}{24}(\Delta\lvert\kappa\rvert)^{4/3}\right)$

Table 4.1.: Filter function and transfer function for one-dimensional filters

From Equation 4.106 it is possible to see that the effect of the filtering process is to cut the frequency of the turbulence above certain values depending on the filter. In such a way the low frequencies (responsible for the slow field variation and related to the biggest eddies) are retained inside the filtered Navier-Stokes equations and the high frequencies must be modeled. The *NS* equations are in this case time dependent. The strategy of the simulations is to place the cut above the energy containing region in such a way that the direct solution of the filtered equations represents the most important features of the flow.

The smallest eddies (the highest frequencies) remain to be modeled. For these eddies even the less sophisticated approaches (homogeneous and isotropic turbulence) are more useful than for the entire turbulence field (that normally is neither homogeneous nor isotropic).

It is possible to show that the time derivative commute with the filtering operator and also the averaging operator does so.

Usually the filtering is done only on the spatial variables and that leads to the following decomposition for the filter operator:

$$G(x, r, t, \tau) = \delta(t - \tau)G_x(x, r)$$

It should be considered that even a pure spatial filter induces a cat on temporal frequencies and similarly, a temporal filter creates a cut on spacial wavelength. Let be Δ the cutoff length and $k_c = \pi/\Delta$ the wave number. Let $E(\kappa)$ be the energy spectrum of the exact solution. The kinetic energy associated to the wave number κ_c is $\kappa_c E(\kappa_c)$ and a velocity can be extracted as $v_c = \sqrt{\kappa_c E(\kappa_c)}$. The characteristic time associated with the length Δ is:

$$t_c = \frac{\Delta}{v_c}$$

The cutoff frequency is then: $\omega_c = 2\pi/t_c$. The spectrum $E(k)$ used in LES simulation is monotonic decreasing function of k. This implies that the imposing a spatial cutoff all the frequencies smaller that ω_c are not taken into consideration.

It is possible to establish a formal link between the LES models and the RANS models. The averaged RANS operator is defined by the time Equation 4.36:

$$\begin{aligned} \vec{v}(\vec{r}, t) &= \vec{U}(\vec{r}, t) + \vec{v}'(\vec{r}, t) \\ \overline{\vec{v}(\vec{r}, t)} \equiv U(\vec{r}, t) &= \frac{1}{\Delta t} \int_{t}^{t+\Delta t} \vec{v}(\vec{r}, \tau) d\tau \end{aligned}$$

In term of filter function it is possible to recognize in the RANS operator the following:

$$G(x, r, t, \tau) = \frac{\mathcal{H}_T}{\Delta t} \cdot \delta(x - r) \tag{4.107}$$

whereH_T is the Heviside function for the time interval. The transfer function associated with the previous operator is:

$$G() = \frac{\sin(0.5\omega\,\Delta t)}{0.5\omega\,\Delta t} \tag{4.108}$$

As pointed out previously, the RANS models were constructed with the intention to have their averaged part, independent of the time. With the filter formalism it is possible to get the same equations, but this time the averaged part is just a *resolved part*, generally dependent on time with frequency less than a certain value $\omega_c = 1/0.5\Delta t$.

4.4.2. The filtered Navier-Stokes equations

Filtering the incompressible Navier-Stokes equations, one obtains:

$$\frac{\partial \rho}{\partial t} + \nabla(\rho \left\langle \vec{v} \right\rangle_{LES}) = 0 \tag{4.109}$$

and:

$$\frac{\partial}{\partial t}(\rho \left\langle \vec{v} \right\rangle_{LES}) + \nabla \cdot (\rho \left\langle \vec{v} \right\rangle_{LES} \left\langle \vec{v} \right\rangle_{LES}) = \nabla \left(\mu \nabla \cdot \left\langle u_i \right\rangle_{LES} \right) - \nabla \left\langle p \right\rangle_{LES} - \nabla \cdot \tau_{ij}^R \tag{4.110}$$

where τ_{ij}^R is the residual stress defined by:

$$\tau_{ij}^R \equiv \rho \big\langle v_i v_j \big\rangle_{LES} - \rho \langle v_i \rangle_{LES} \big\langle v_j \big\rangle_{LES} \tag{4.111}$$

It is possible to define, as in the Reynolds decomposition, the *residual kinetic energy*:

$$k_r \equiv \frac{1}{2} \tau_{ii}^R \tag{4.112}$$

end the *anisotropic residual stress tensor*:

$$\tau_{ij} = \tau_{ij}^R - \frac{2}{3} k_r \delta_{ij} \tag{4.113}$$

The isotropic residual stress tensor can be incorporated in a modified filtered pressure:

$$P \equiv P + \frac{2}{3} k_r$$

With this definition the filtered momentum equation can be written:

$$\frac{\partial}{\partial t}(\rho \left\langle \vec{v} \right\rangle_{LES}) + \nabla(\rho \left\langle \vec{v} \right\rangle_{LES} \left\langle \vec{v} \right\rangle_{LES}) = \nabla \left(\mu \nabla \left\langle u_i \right\rangle_{LES} \right) - \nabla \left\langle p \right\rangle_{LES} - \nabla \tau_{ij} \tag{4.114}$$

4.5. Probability density function method

In turbulent flows the velocity (and more generally each involved field ϕ) can be seen as a fluctuating variable and treated using the methods of stochastic theory in which the solved variables are not anymore averaged quantities as in the models aforementioned, but the distribution functions of that variable $\mathcal{P}(x,t)$. Averaged quantities and correlations must then be calculated as the first and second moments of the function $\mathcal{P}(x,t)$.

The transport equation for the velocity PDF can be derived from the *NS* equation and it is written in the following form [280, 124]:

$$\frac{\partial \mathcal{P}_u}{\partial t} + u_i \frac{\partial \mathcal{P}_u}{\partial x_i} = \left(\frac{1}{\rho} \frac{\partial p}{\partial x_i} - f_i \right) \frac{\partial \mathcal{P}_u}{\partial U_i} - \frac{1}{\rho} \frac{\partial}{\partial U_i} \left[\left\langle \frac{\partial \tau_{ij}}{\partial x_j} - \frac{\partial p'}{\partial x_j} \,\middle|\, U \right\rangle \mathcal{P}_u \right] \tag{4.115}$$

All convective transport are in closed form while models are required for the dissipation terms and for the correlation of the fluctuating pressure. A similar equation can be also written for the PDF of the thermal variables as shown in Chapter 5.

Closures cannot be found using the function $\mathcal{P}$ alone because the PDF does not contain

information on the turbulence scales. One way to overcome this deficiency is to couple the equations for the PDF with equations for the dissipation ϵ. An other way (see [280]) is to solve for the join PDF of velocity and turbulent frequency.

The most common model for the closure of the equation is the generalized Langevin model described in [280] and [279]. The final equation reads:

$$\frac{\partial \mathcal{P}_u}{\partial t} + u_i \frac{\partial \mathcal{P}_u}{\partial x_i} - \left(\frac{1}{\rho} \frac{\partial p}{\partial x_i} \right) \frac{\partial \mathcal{P}_u}{\partial U_i} = \frac{\partial}{\partial U_i} \left[\mathcal{P}_u G_{ij} (U_j - \langle U_j \rangle) \right] + \frac{1}{2} C_0 \epsilon \frac{\partial^2 \mathcal{P}_u}{\partial U_i \partial U_j} \quad (4.116)$$

The RANS equations are obtained from the moment of the equation 4.115. The zeroth-moment describe the equation for the mass balance while the first moment describe the equations for the momentum (the Navier-Stokes equations). Higher moments can be used to obtain equations and closure for the Reynolds stress tensor and consequently detailed RSM equations.

4.6. Direct Numerical Simulations

The idea of the *DNS* models is to resolve all the scales of the turbulence down to the dissipation scale (the Kolmogorov scale). That makes the *DNS* the most complete turbulence model available. The model gives a complete description of the turbulence and it does not need any submodel for the closure. Unfortunately the model is extremely expensive in terms of computing time. For high Reynolds numbers the huge difference between the large scale and Kolmogorov scale needs grids so fine that currently using the most powerful computers only flows on relatively small domains can be simulated.

4.7. Boundary conditions

A mathematical problem based on differential equations is completely defined when the boundary conditions are specified. In the case of CFD applied to an enclosure (most of the cases applications presented in this book are dealing with system bounded by well defined surfaces), the boundary conditions express physical properties of the bounding surface. In this chapter the boundary conditions for

- Momentum;
- Turbulence quantities;
- Energy;
- Components;
- Radiation intensity.

will be considered.

4.7.1. Boundary conditions for Momentum

Inlets Instead of the momentum itself, this boundary condition is expressed in term of the velocity. The velocity at inlets is considered constant over the entire cross-section of the inlet duct and its value is derived from the measured mass flow rate Φ:

$$v = \frac{\Phi}{\rho S} \quad (4.117)$$

where S is the cross-section surface of the inlet duct.

Walls The condition of *no slip velocity* is assumed at the walls therefore the velocity is zero at the surface of the walls. This condition creates a boundary layer composed by three regions. In the innermost layer, called the *viscous sub-layer*, the flow is laminar, and the molecular viscosity plays a dominant role in momentum and heat or mass transfer. In the outer layer, called the *fully-turbulent layer*, turbulence plays a major role. Finally, there is a region between the viscous sub-layer and the fully turbulent layer where the effects of molecular viscosity and turbulence are equally important.

To avoid the exact solution of the near wall effects (the calculation of boundary layers requires fine cells near the wall to be adequately resolved), the wall function approach is used. In the vicinity of the wall the velocity is not resolved, but it is assumed to follow the fully turbulent boundary profile:

$$u^+ = \frac{1}{\kappa}\ln(Eu^+) + C^+ - \Delta B \tag{4.118}$$

where $k = 0.4187$ (von Karman constant), $C^+ = 5,0$ and $E = 9.793$ (wall function constant). The dimensionless velocity velocity $u^+ \equiv \frac{u}{u_\tau}$ is expressed in terms of the dimensionless distance from the wall $y^+ \equiv \frac{y \cdot u_\tau}{\nu}$ and:

$u_\tau \equiv \sqrt{\frac{\tau_w}{\rho}}$	is called the friction velocity or shear velocity
τ_w	is the wall shear stress,
ν	is the kinematic viscosity

ΔB is a roughness function that quantifies the shift of the intercept due to roughness effects. ΔB depends, in general, on the type (uniform sand, rivets, threads, ribs, mesh-wire, etc.) and size of the roughness [8]

The most disadvantage of the presented wall function is its deterioration when the non

[8] There is no universal roughness function valid for all types of roughness. For a sand-grain roughness and similar types of uniform roughness elements, however, ΔB has been found to be well-correlated with the non-dimensional roughness height, $K_s^+ = \rho K_s u^*/\mu$ where K_s^+ is the physical roughness height.

Analysis of experimental data show that the roughness function, ΔB, is not a single function of K_s^+, but takes different forms depending on the K_s^+ value itself. It has been observed that there are three distinct regimes:

1. Hydrodynamically smooth: $K_s^+ < 3 \sim 5$;
2. Transitional: $3 \sim 5 < K_s^+ < 70 \sim 90$;
3. Fully rough: $K_s^+ > 70 \sim 90$.

According to the data, roughness effects are negligible in the hydrodynamically smooth regime, but become increasingly important in the transitional regime, and take full effect in the fully rough regime.

For each regime the software uses different correlation. For the hydrodynamically smooth regime:

$$\Delta B = 0$$

For the transitional regime

$$\Delta B = \frac{1}{\kappa}\ln\left[\frac{K_s^+ - 2.25}{87.75} + C_{K_s}K_s^+\right] \times \sin\left\{0.4258(\ln K_s^+ - 0.811)\right\}$$

where C_{K_S} is a roughness constant, and depends on the type of the roughness.

In the fully rough regime:

$$\Delta B = \frac{1}{\kappa}\ln(1 + C_{K_s}K_s^+)$$

dimensional distance from the wall y^+ is smaller then 30. Many improvements of the 4.118 have been considered. One of the most used is the two layer model where the linear viscous region is resolved together with the logarithmic turbulent region and a blending function is applied [173].

4.7.2. Boundary conditions for turbulence

Inlets: At the inlets the values for he unknown variables must be given. In the case of the 2 equations k-ϵ model both the kinetic energy k and the dissipation ϵ must be assumed. Usually those two values are correlated to more general quantities, like the turbulent intensity and the hydraulic diameter. The correlations valid for a long pipe, function of the turbulent intensity I and a typical length scale l, can be used as conditions at the inlets:

$$k = \frac{3}{2}(UI)^2 \tag{4.119}$$

$$\epsilon = C_\mu^{3/4}\frac{k^{3/2}}{l} \tag{4.120}$$

$$\omega = \frac{k^{1/2}}{C_\mu^{1/4} l} \tag{4.121}$$

where l is the turbulent scale correlated to the diameter of the duct (D) by $l = 0.07D$. The factor 0.07 is based on the maximum value of the mixing length in fully-developed turbulent pipe flow.

In the case of the RMS model the previous relations are completed by the isotropic turbulence assumption such that:

$$\overline{u_i' u_j'} = 0 \tag{4.122}$$

Walls: The presence of the wall is extremely important for the turbulent field for two reasons:

1. the components of the fluctuations orthogonal to the walls are greatly suppressed, leading to non-homogeneous turbulence;
2. the high vorticity of the stream generates turbulence that is transported to the bulk flow.

As a boundary condition for the turbulent energy k the following equation is assumed:

$$\frac{\partial k}{\partial n} = 0 \tag{4.123}$$

where n is the local coordinate normal to the wall. The production of kinetic energy, and its dissipation rate, at the wall-adjacent cells, are computed on the basis of the local equilibrium hypothesis (see [280]). Under this assumption, the production of k and its dissipation rate are assumed to be equal in the wall-adjacent control volume.

$$G_k \approx \tau_w \frac{\partial U}{\partial y} = \tau_w \frac{\tau_w}{\kappa \rho C_\mu^{1/4} k_P^{1/2} y_P} \tag{4.124}$$

The value of ϵ is computed from:

$$\epsilon_P = \frac{C_\mu^{3/4} k_P^{3/2}}{\kappa y_P} \tag{4.125}$$

For the RSM model, using a local coordinate system, where τ is the tangential coordinate, η is the normal coordinate, and λ is the bi-normal coordinate, the Reynolds stresses at the wall-

adjacent cells are computed from:

$$\frac{\overline{u_\tau'^2}}{k} = 1.098, \quad \frac{\overline{u_\eta'^2}}{k} = 0.247, \quad \frac{\overline{u_\lambda'^2}}{k} = 0.655, \quad -\frac{\overline{u_\tau' u_\eta'}}{k} = 0.255 \tag{4.126}$$

The values of k and ϵ are evaluated solving a $k - \epsilon$ two-equations model.

4.7.3. Boundary conditions for energy

Inlets If the diffusion (conduction) can be neglected in comparison with advection (the Pe number calculated at the inlet is approaching infinity), the knowledge of the temperature of the incoming flow is sufficient for the calculation of the incoming energy. A boundary condition of the first art is then assumed.

If, on the contrary, the Peclet number at the inlet is small, the temperature at the inlet differs from the temperature of the free incoming flow and must be calculated from simplified (usually one-dimensional) calculations based on energy transfer in the inlet pipe.

Walls All the three kind of boundary formulation (Neumann, Dirichlet and Robin) can be used as boundary conditions at the furnace walls. If a temperature can be measured or estimated, a boundary of the first kind using the value of the energy calculated from the known temperature can be imposed. If the heat flux is known, a boundary condition of the second kind is applied. The required heat flux knowledge is usually obtained if the walls are cooled, using a cooling medium. An energy balance for the cooling medium gives the required heat extracted from the device. A boundary condition of the third art can be implemented if the mechanism of the heat transfer is known. In the case of convection the relation

$$\dot{q} = h\left(T_w - T_\infty\right)$$

can be applied as boundary condition. In the previous relation the convective coefficient h must be known. The previous relation can be generalized to the situation in which radiation (or a mix of convection and radiation) is responsible for the heat removal and a simplified version of a problem with conjugated heat transfer problem must be solved.

In the case of furnaces, where the walls are made by isolating materials, the temperature gradients along the wall are smaller than the gradients through the wall, since heat transfer along the walls are negligible. In this case, heat transfer from the internal surface can be calculated considering one-dimensional conduction only. If in addition planar geometry and constant wall conductivity k can be assumed, the heat transfer rate is given by:

$$\dot{q} = k\frac{T_w - T_e}{d} \tag{4.127}$$

where the thickness of the wall d, the temperature of the internal surface T_w and the temperature of the external surface T_e are linked together.

The law-of-the-wall for the energy has the following composite form:

$$
\begin{aligned}
T^* &\equiv \frac{(T_w - T_P)\,\rho c_p C_\mu^{1/4} k_P^{1/2}}{\dot{q}} \\
&= \begin{cases} Pr\,y^* + \frac{1}{2}\rho Pr \frac{C_\mu^{1/4} k_P^{1/2}}{\dot{q}} U_P^2 & (y^* < y_T^*) \\ Pr_t \left[\frac{1}{\kappa}\ln(Ey^*) + P\right] + & \\ \frac{1}{2}\rho \frac{C_\mu^{1/4} k_P^{1/2}}{\dot{q}} \left\{ Pr_t U_P^2 + (Pr - Pr_t) U_c^2 \right\} & (y^* > y_T^*) \end{cases}
\end{aligned} \tag{4.128}
$$

where P is computed using the formula:

$$
P = 9.24 \left[\left(\frac{Pr}{Pr_t} \right)^{3/4} - 1 \right] \left[1 + 0.28 e^{-0.007 Pr/Pr_t} \right] \tag{4.129}
$$

and:

k_P	-	turbulent kinetic energy;
ρ	-	density of fluid;
C_p	-	specific heat of fluid;
$\dot{q}$	-	wall heat flux;
T_p	-	temperature at the cell adjacent to wall;
T_w	-	temperature at the wall;
Pr	-	molecular Prandtl number ($\mu c_p / k_f$);
Pr_t	-	turbulent Prandtl number (0.85 at the wall);
A	-	26 (Van Driest constant);
U_c	-	mean velocity magnitude at $y^* = y_T^*$.

4.7.4. Boundary conditions for the components

Inlets The treatment of the component is similar to the treatment sketched in Section 4.7.3. If the diffusion of the component can be neglected at the inlet, then a boundary condition of the first art with a given value for the mass or mole fraction can be used. If the Peclet number is negligible, a similar calculation as the one proposed for the energy can be used.

Walls At the walls several conditions can be applied, considering which chemical or physical process takes place at the surface itself. If the wall is impermeable then a zero-flux conditions is the most appropriate. Other boundaries can be used if mass transfer is present, namely a given mass flux or a constant mass (or mole) fraction. If the wall is in reality a liquid surface and phase change is allowed, then a constant value for the mass fraction can be applied (boundary condition of the first art). The constant value can be calculated from the phase change curve, invoking thermodynamic equilibrium at the surface. Chemical reactions as well as permeable membranes can be simulated assuming a given heat flux of the component.

The law-of-the-wall for species can be expressed for constant property flow with no viscous

dissipation as:

$$
\begin{aligned}
Y^* &\equiv \frac{\left(Y_{i,w} - Y_i\right) \rho C_\mu^{1/4} k_P^{1/2}}{J_{i,w}} \\
&= \begin{cases} Sc\, y^* & (y^* < y_c^*) \\ Sc_t \left[\frac{1}{\kappa} \ln(E y^*) + P_c\right] & (y^* > y_c^*) \end{cases}
\end{aligned} \tag{4.130}
$$

where Y_i is the local species mass fraction, Sc and Sc_t are molecular and turbulent Schmidt numbers, and J_i is the diffusion flux of species at the wall (in this calculation there is no mass transfer through the wall and so $J_i = 0$). P_c and y^* are calculated in a similar way as P and y^*, with the difference being that the Prandlt numbers are always replaced by the corresponding Schmidt numbers.

4.8. Radiative heat transfer

Radiation interacts with both, gas and particles. The theory of radiative heat transfer is complex and is behind the scope of this book. Here only the principles can be given and the interested reader must be referred to specific literature (see for example [247, 158, 385]).

The variation of the spectral intensity I_η along an optical path s due to absorption, emission, and scattering (both, in- and out-scattering) is described by the radiative heat transfer equation (RTE):

$$
\frac{\mathrm{d}\, I_\eta}{\mathrm{d}\, s} = -a_\eta \cdot I_\eta + a_\eta \cdot I_{\eta,\mathrm{b}} - p0^{4\pi} I_\eta \left(\vec{s_i}\right) \cdot \Phi_\eta \left(\vec{s_i}, \vec{s}\right) \cdot \mathrm{d}\, \Omega_i \tag{4.131}
$$

where a_η is the absorption coefficient in cm^{-1}, I_η is the spectral intensity in $\mathrm{W\,cm\,m^{-2}\,sr^{-1}}$, $\sigma_{\eta,s}$ is the scattering coefficient in cm^{-1}, and Φ_η is the so-called scattering phase function (dimensionless). Index η emphasizes that the RTE is valid for one single wavenumber η in cm^{-1} only. However, since gas absorption properties and, therefore, the intensity field strongly depend on wavenumber, simplifications for the treatment of gas properties are essential in conjunction with overall CFD calculations. These simplifications are described in Section C.1. Solution of the intensity field, equation (4.131) is obtained using a form of the discrete ordinates method, e. g. see Ref. [109], which is called finite volume method [79, 256]. In this method, the RTE, see equation (4.131) is solved for a discrete number of solid angles $\Delta\Omega$. Each direction i has a weight given by its finite solid angle $\Delta\Omega_i \,/\, 4\pi$. When the mesh is unstructured, pixelation [256] is used to minimize so-called control-angle overhang which means that solid angle are further subdivided for integration over solid angle. For more details on the radiation solver, the reader is referred to textbooks [247, 158] or the original publications [79, 256].

The modeling of the gas absorptivity a and the modeling of absorption and scattering on droplets have been discussed in Section C.1 and Section C.1.1, respectively.

4.8.1. Boundary conditions

The boundary condition for the intensity can be derived from a formulation of the radiative energy balance at the given surface. The balance at the surface express the condition that the impinging radiation on the surface (the irradiance i) can be reflected, re-emitted or abosrbed by the surface. Mathematically the balance is written in the following way:

$$
\dot{q}_{\lambda,\alpha}(x;\theta) = i_\lambda(x;\theta) + j_\lambda(x;\theta,\alpha) \tag{4.132}
$$

where the radiosity j_λ is the sum of the emitted and the reflected energy. It is important to notice that in the previous equations all the quantities are function of the position on the surface (x), the incoming angle θ and the out coming angle α. Moreover the energy balance previously written is strictly valid for a single wavelength λ. In order to decrease the complexity of the treatment usually in CFD application the assumption of gray body must be taken. For more information see [247, 158].

4.9. Advantages of the CFD method

As already mentioned the CFD method has several advantages that can be exploited in industrial applications. Even if more modeling is required to properly close the previously described equations and they will be introduced in the next chapters, a short list showing few examples of the most advantage aspects of the CFD approach will follows.

Flow field calculation CFD method is the natural tools to solve problems in which the calculation of flow field is required. In many industrial applications complex configurations and geometries are involved. These complexities and the particular geometries involved make it generally difficult to use correlations derived in standard flow configurations.

Turbulent mixing and aerodynamics Mixing and aerodynamics are other two phenomena of industrial interest that are driven directly by velocity distribution and if the flow is turbulent, turbulence effects may play a dominant role. As in the previous case CFD method is successfully employed to overcome the inherent difficulties of turbulence calculations in complex geometries.

Convective heat transfer The standard simplified way of calculating the convective heat transfer rate is using of Nusselt function for the calculation of the Nusselt number Nu [163]. This method requires the knowledge of the Nusselt function for the specific temperatures, velocity and gas composition together with the knowledge for the geometry. In industrial application this details are not all the time easy to be obtained. The CFD method solve the problem calculating the heat transfer process throughout all the boundary layers until the surface. The assumptions behind such an approach are much more general and the CFD method can be applied to more general and complex situation. For the sake of correctness, it must be mentioned that in most of the CFD software a function of wall is employed (see Section 4.7.3) and its limitations must be also taken into account. The applicability of a wall function has anyway less stringent limitations than the ones required by the Nusselt function approach.

Radiative heat transfer Radiation is the most important heat transfer process at high temperature applications, accounting for as high as 90% of the transferred heat. As a typical example, the radiative heat fluxes in the radiative section of a boiler can be considered. The solution of the Radiative Transfer Equation (RTE) in a scattering and absorbing medium, as the gas inside a boiler, is based on the temperature distribution of the gas. Using CFD the calculation of the temperature distribution can be performed with higher accuracy.

Heat transfer by conduction In some calculations of heat transfer by conduction the uncertainties in boundary conditions can deteriorate the accuracy of the entire results. If conjugated heat transfer can be applied at the unknown boundary, a CFD method can then improves the predictability of the heat transfer calculation. The opposite situation can be also of interest, where the calculation of cooling or heating of a body requires the solution

of the heat conduction equation with boundaries given by convective (forced or natural) heat transfer solved using CFD methods.

Flames Flame structure calculations are directly based on CFD because of the knowledge of temperature and specie distribution (mixing) and because of the knowledge of the heat lost by radiation. All those processes, as previously stated, can be easily simulated using CFD.

Particle dispersions Solid particle dispersion is an important issue in most of the industrial application where solid fuel conversion is performed. As for the case of gas mixing, turbulent mixing is the predominant driving effect. Therefore CFD can be successfully employed in this kind of applications.

Burnout of particles or droplets Burnout of particles or droplets can be calculated correctly only if temperature and species distribution are both accurately known. The classical application of CFD software is the calculation of coal paths inside a boiler.

Emissions of CO, NO_x, SO_x, soot, particulate Emissions of flames in general are strongly dependent on the flame structure even if in many case there is no strong effects of the emission back on the flame. The knowledge of the flame structure is, therefore, required and in many cases CFD is the only choice able to provide it with the needed accuracy.

A state of the art of applications of reactive fluid dynamics is presented in [385].

5. Homogeneous Reactions

Homogeneous reactions are present in every solid fuel conversion process and gaseous components interact chemically with each other and with the solid fuel. In order to be able to calculate those interactions, energy and components equations must be added into the CFD tool presented in the previous chapter. The species equation has been already written in equation 4.12:

$$\rho\frac{\partial Y_i}{\partial t} + \rho\left(\vec{v}\cdot\nabla\right)Y_i = -\nabla\vec{J_i} + \dot{S}_i$$

while the energy equation has been written in equation 4.23:

$$\rho\frac{\partial e}{\partial t} + \rho\left(\vec{v}\cdot\nabla\right)e + \nabla\cdot(\vec{v}P) = \Phi + \dot{Q} - \nabla\cdot\vec{q} + \mathcal{L}$$

Homogeneous reactions contribute to both source terms, for the energy and for the components involved in the reactions. If $\dot{\mathcal{R}}_j$ is the molar rate of reaction j expressed in $\frac{\text{kmol}}{\text{s m}^3}$, the source terms in the aforementioned equations are:

$$\dot{S}_i = \sum_j M_j \nu_{j,i} \dot{\mathcal{R}}_j \tag{5.1}$$

$$\dot{Q} = \sum_j M_j \dot{\mathcal{R}}_j \Delta h_j \tag{5.2}$$

where M_j is the molecular weight, $\nu_{j,i}$ is the stoichiometric coefficient for specie i in reaction j and Δh_j is the formation enthalpy per unit mass of reactant.

5.1. The reaction mechanisms

In combustion and gasification hundreds of chemical species are involved in mechanisms of more than 1000 elementary reactions [418, 78, 83]. The number of radicals involved and the number of chemical paths followed by the reactions are dependent on the kind of fuel involved and on the complexity of the used description. Nowadays many mechanisms have been developed with the goal of describing chemical reactions involved in many complex chemical processes. The resulting networks are validated against standard flame configurations like flamelets, spontaneous ignition processes or free flame propagation. References to currently existing mechanisms are given in several review papers [83, 328, 415, 26, 171, 27, 276, 28]. For oxygenated compounds, found in combustion of bio-diesel fuels and in gasification of several biomass and off-specification fuels the mechanisms (see for example [276, 192, 185]) are larger due to a higher number of carbon atoms. As an important example, for natural gas which comprises mainly of alkane compounds (methane, ethane, propane) the GRI 3.0 mechanism [338] was found to give a detailed enough description.

Detailed mechanisms Detailed reaction mechanisms are developed and validated against experimental results from simple laminar flames (e.g. laminar flame velocities, quenching strain

rates, flame structures), from ignition experiments (ignition delay times from shock tube or rapid compression machine experiments) or from flow reactor or perfectly stirred reactor experiments. The goal of the mechanisms is to give a detailed description of all the molecular reactions involved in a chemical process and that allows the application of the mechanisms in many (ideally all) conditions. With the current state of the development the extrapolation to different conditions than the validated ones, must be performed with care [385]. The accuracy of such mechanism is high and the information obtained are quite detailed but the utilization of such large mechanism become prohibitive in many industrial applications due to the requirement in available storage and because of the long calculation times required. To overcome such drawbacks skeleton mechanisms and global mechanisms must be developed.

Skeleton Mechanisms Based on detailed reaction mechanisms so-called skeleton mechanisms can be derived, which describe the system with an appropriate accuracy valid only for a specific domain of interest. Very large reaction mechanisms with thousands of species and reactions can be simplified up to smaller mechanisms with only some hundred or less species and reactions. Due to the loss of information such skeleton mechanisms do no longer cover the range of applicability of the original mechanisms. The reduction can be performed using mathematical tools or just considering some constraints from physics and chemistry of the system. Some of the most common strategies are listed below [385]:

- Removal of peroxyde [1] from the mechanism for hydrocarbon combustion. Above temperatures of about 1100 K the β-decomposition of the primary fuel radicals [2] is so fast that fuel specific peroxides are formed. Mechanisms for the high temperature application are obtained by removing all peroxides of higher hydrocarbons and their reactions from the mechanism.

- Grouping or lumping of chemical species. Many radical reactions of higher hydrocarbons are not very site-specific, and therefore different radicals can be lumped together, thus reducing the number of species.

- Removal of sub-mechanisms. In many cases the mechanism can be simplified by removing sub-mechanisms. that do not couple back to the main mechanism.

Many mathematical tools are available for development of skeleton mechanisms [378]. They help in the identification of unimportant species and unimportant reactions. Reaction paths analysis identifies the major reaction pathways by comparing the contributions of different reactions to the formation and destruction of chemical species while sensitivity analysis identify the rate-limiting elementary reactions.

Skeleton mechanisms have the advantage of being valid in a large range of applications. On the other hand they still involve a relatively large number of chemical species. The idea of *adaptive chemistry* is the adoption of different mechanisms for different regions, depending on their ranges of applicability. Two methods that implement the idea are the method of adaptive chemistry (or dynamic mechanism reduction) [323, 289] and the method of phase optimized reaction mechanisms [48]. The original mechanism is a detailed reaction mechanism valid for a large range. During the simulation the importance of the chemical species and chemical reactions is monitored, and depending on the time or on the location in the reacting flow chemical rate equations are solved only for the so-called active species.

[1] Peroxides are compounds containing an oxygen-oxygen single bond. The O – O group is called the peroxide group.

[2] β-decomposition is an important reaction in the chemistry of thermal cracking of hydrocarbons and it is based on the splitting of the carbon-carbon bond

A skeleton mechanism contain still planty of information and its level of accuracy is still high at least in the region where the mechanism has been validated. The chemical kinetics does not access the whole composition space, but is restricted to smaller subspaces of lower dimension. The space of thermo-chemical states accessed by reacting flows is characterized by two important properties:

- The space of the states accessed in a specific reacting flow is only a small subset of the allowed one;
- After a short relaxation time the thermodynamic state is restricted to a small neighborhood of low-dimensional attractors.

These two observations can be used to simplify further the mechanisms. A further reduction is then based on the application of assumptions about species in steady states or reactions in partial equilibria. The mechanism reduction procedure can then be divided into two tasks, namely the identification of the steady state species or the reactions in partial equilibria, and their subsequent implementation for the mechanism reduction [397, 378, 220]. Many methods have been suggested to do the analysis in a correct way, for example, methods based on CSP (computational singular perturbation) [196, 197], instantaneous QSSA (quasi steady state assumption) [382], or level of importance [218].

The method based on Identification of Low-Dimensional Manifolds reduces the number of thermodynamic states, using the one confined to or at least in the vicinity of a low-dimensional attractors in composition space, and express the chemical variable and the rates as a function of a set of variables belonging to that manifolds (see [385] for more information).

Global mechanisms Global mechanisms express the chemical source terms using a small number of chemical species (see [417] as an example). Many different variations with comparisons of different models can be found (see e.g. [272, 169, 10, 396, 113, 257, 243]). Equivalence ratio or temperature dependent parameters are used to cover a large domain of stoichiometry or the low and high temperature regime, respectively [113, 243, 40]. They have several major advantages [385]:

- They involve only those species which are of interest, and not a large number of intermediates.
- The evaluation of the chemical source terms is computationally inexpensive.
- Storage problems like in tabulation methods are avoided.
- Coupling with any CFD code and transport model is simple.

Despite their simplicity, these global mechanisms can give good results, but only in a small range of applicability. As an example, calculated flame speed for several mixture of methane and air is presented in Figure 5.1. The speed is calculated using the full GRI3.0 mechanism and the 4-step mechanism developed in [169] and both calculations are compared with an optimized 2-step model [40]. The original 4-step mechanism overpredicts the flame speed in the under-stoichiometric region while the agreement is quite satisfactory in the near- and over-stoichiometric conditions. The failure of the original 4-step mechanism in fuel rich conditions is due to an overprediction of the temperature inside the flame front, caused by a non correct prediction of the equilibrium composition for those conditions. This drawback can be corrected after fine tuning of the parameters.

Global mechanisms have also to be used with care because of the following drawbacks [385]:

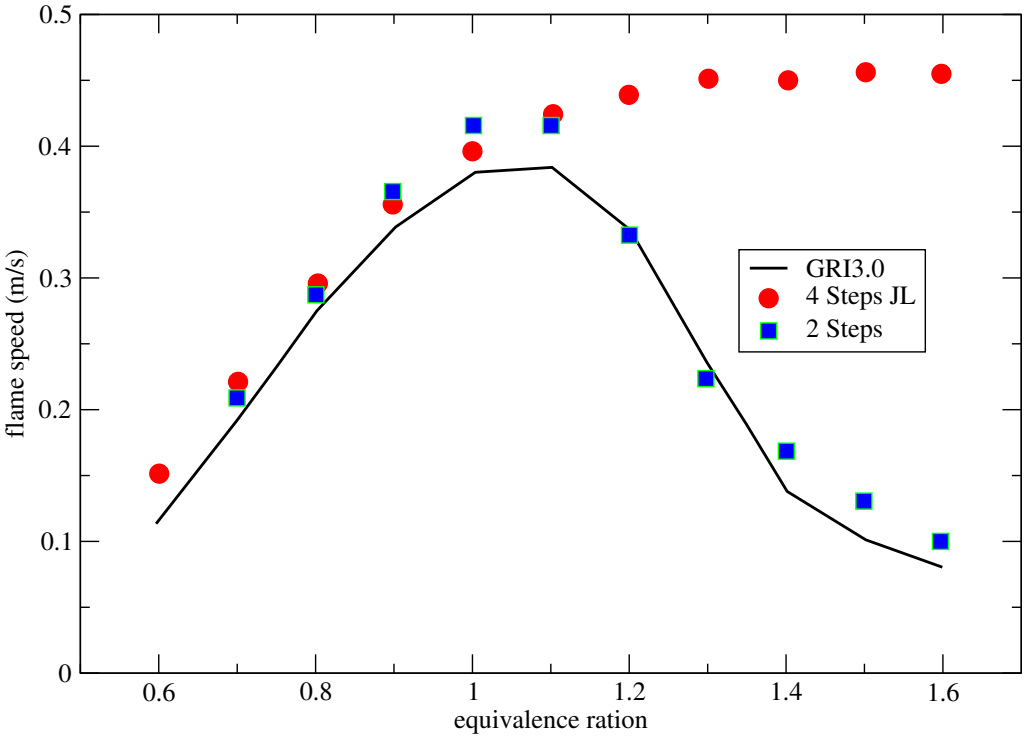

Figure 5.1.: Comparison of laminar flame speed for a mixture of methan air at different stoichiometric conditions

- The range of applicability is usually small, and an extrapolation is not possible;
- Typically the rate parameters have to be "tuned" to each new application;
- The interaction of the chemistry with the transport is a crucial issue and the transport properties have to be tuned to the description by the reduced set of species;
- Some of these mechanisms (due to the fits of the rates) might introduce artificial stiffness into the system.

Few reactions are always present in each global mechanism used for the simulation of conversion of solid fuels:

- Oxidation of light hydrocarbons, as CH_4, CO and H_2;
- The homogeneous water gas shift reaction

$$CO + H_2O = CO_2 + H_2 \tag{R 5.1}$$

- Methanation reaction

$$CO + 3\,H_2 = CH_4 + H_2O \tag{R 5.2}$$

  and its reverse reaction, the steam methane reforming;
- Acetylene formation and oxidation;

- Tar cracking reactions;

Without going into details, it is worth noticing that after reducing a detailed mechanisms the expressions for the reaction rates are not in Arrhenius form, but they are expressed by a more complex algebraic formulas involving the Arrhenius rates of several elementary reactions (see [269]). The reaction rates can then be fitted using $AT^b e^{-\frac{E}{RT}}$ to get the Arrhenius parameters A, b and E with the consequence that their range of validity is only limited to the range fitted. More generally, the parameters for any global reaction are function of the temperature, pressure and air ration for any conditions for which the reduction has been done.

5.2. Reaction rates

Each reaction can be written in the following way:

$$\sum_i \nu_i R_i = \sum_j \nu'_j P_j$$

where R_i are the names of the reactants and P_j are the names of the products; ν_i and ν'_j are the stoichiometric coefficients. The rate of formation or destruction of each species is:

$$\mathcal{R}_i = k_{f,\,i} \prod_j [R_j]^{\nu_{j,i}} - k_{b,\,i} \prod_j [P_j]^{\nu'_{j,i}} \tag{5.3}$$

where:

$k_{f,\,i}$	-	rate constant for the forward reaction
$k_{f,\,i}$	-	rate constant for the backward reaction
$[R]_i$	-	mole concentration of reactant i
$[P]_j$	-	mole concentration of product j

For reversible reactions, the forward and the backward reaction rate constants are linked through the equilibrium constant:

$$\frac{k_f}{k_b} = \left(\frac{P}{RT}\right)^{\Delta\nu} \exp\left(\frac{\Delta S^0}{R} - \frac{\Delta H^0}{RT}\right) \tag{5.4}$$

where $\Delta\nu = \sum_j \nu'_j - \sum_i \nu_i$.

Usually an elementary reaction takes place between two species only. Few reactions, for example recombination or dissociation and few others, need a third body, to provide or remove the reaction energy. The rate of formation or destruction of the species can be written as:

$$\mathcal{R}_i = \left(k_{f,\,i} \prod_j [R_j]^{\nu_{j,i}} - k_{b,\,i} \prod_j [P_j]^{\nu'_{j,i}} \right) [M] \tag{5.5}$$

The third body concentration $[M]$ is written as a function of the other stable species:

$$[M] = \sum_i a_i \, [A_i] \tag{5.6}$$

Not all the species have the same collision efficiency, thus the weighting coefficients a_i take this into account.

The rate coefficients k are a function of the temperature only. These are usually expressed using an Arrhenius form:

$$k_i = A_i T_i^b \exp\left(-\frac{E_i}{RT}\right) \tag{5.7}$$

with R being the ideal gas constant. The coefficient A is the pre-exponential factor, b is the temperature power and E is the activation energy.

It is possible to give a deeper theoretical explanation of the Arrhenius form. A simple theory of chemical reactions (the collision theory of the reaction rates) assumes that reactions occur at a rate proportional to the collision between molecules. According to the kinetic theory of gases the frequency of collision in an ideal gas where n_i and n_j molecules of kind i and j are present respectively, is given by the equation:

$$Z = \pi\sigma^2 n_i n_j \sqrt{\frac{8K_B T}{\pi M}} \tag{5.8}$$

where K_B is the Boltzmann constant, σ represent a typical molecular dimension, and M is the reduced mass of the system. The temperature exponent $\frac{1}{2}$ is not an universal feature. A better calculation of the factor Z, based on the Lennard-Jones potential gives the following result:

$$Z = \pi\sigma^2 n_i n_j \sqrt{\frac{8K_B T}{\pi m}} \Omega^{(2,2)*} \tag{5.9}$$

where the parameter $\Omega^{(2,2)*}$ represent a configuration integral:

$$\Omega^{(2,2)*} = 1.16145 y^{-0.14874} + 0.52487 \cdot e^{-0.7732Ty} + 2.16178 \cdot e{-}2.437887y$$

expressed as a function of a reduced temperature $y = \frac{K_B T}{\sqrt{\epsilon\epsilon_M}}$ and ϵ is the Lennard-Jones parameter. The previous relation shows clearly that the temperature dependency inside the factor Z is a complex analytical function.

Only a fraction of encounters possessing energies higher than a certain amount E^* are capable of reactions. The distribution of such molecules is, according to statistical thermodynamics:

$$\frac{n^*}{n} = \exp\left(-\frac{E^*}{RT}\right) \tag{5.10}$$

If then an activation energy E_a is defined by $E_a \equiv E_i^* + E_j^*$ the reaction rate between the molecules i and j is given by:

$$\frac{d}{dt}[i] = \psi A^v \sigma^2 \sqrt{\frac{8\pi K_B T}{m}} \cdot \exp\left(-\frac{E_a}{RT}\right) \cdot [i] \cdot [j] \tag{5.11}$$

with A^v being the Avogadro's number and ψ is the steric factor, accounting for the effectiveness of each energetically allowed collision.

The transition state theory of reaction rates, allows a even deeper understanding of the Arrhenius form. After any collision with energies in excess of E_a, a non stable molecule called the activated complex is formed. The activated complex can further react following several path, one of which produces back the initial reactants and one (or more) produced new molecules, the products. Assuming that the activated complex is in equilibrium with the products and with the

reactants an Arrhenius form can be formulated:

$$k = Z\psi \cdot \exp\left(-\frac{E^*}{RT}\right) \tag{5.12}$$

with the following identifications (h is the Planck constant):

$$Z = \frac{K_B T}{h}(RT)^{n-1} \tag{5.13}$$

$$\psi = \exp\left(-\frac{\Delta S}{R}\right) \tag{5.14}$$

$$E_a = \Delta H \tag{5.15}$$

Both ΔS and ΔH are differences between the reactant and the activated complex (which thermodynamical properties are usually not known). The equation 5.12 is exactly the expression of the reaction constant in Arrhenius form.

Some reactions are pressure dependent. Typical examples of reactions that show a significant change of the reaction constant k with the pressure are unimolecular reactions, like the isomerazation reactions:

$$\mathrm{A} \longleftrightarrow \mathrm{B} \tag{R 5.3}$$

and the dissociation and association reactions:

$$\mathrm{A} \longleftrightarrow \mathrm{B} + \mathrm{C} \tag{R 5.4}$$

Unimolecular reactions are not elementary reactions since they do not posses the required energy to exceeding the energetic barrier of the reaction. For a unimolecular reaction to proceed, the reactant molecule A must first be excited to the required energy. A molecule that is sufficiently excited is called an activated species and often labeled with an asterisk A^*. The reaction between two excited state is elementary. There are a number of ways that an activated species can be produced:

1. Chemical activation where the exited molecule A^* is the product of a chemical reaction:

$$\mathrm{B} + \mathrm{C} \longrightarrow \mathrm{A}^*$$

2. Thermal activation, where the activated state is produced by bimolecular collision:

$$\mathrm{A} + \mathrm{M} \longrightarrow \mathrm{A}^* + \mathrm{M}$$

3. Photoactivation, ehere A^* is produced as a result of absorption of a photon.

Once an activated molecule has been produced, multiple isomerization and dissociation reactions may become competitive with one another and with collisional stabilization (thermal deactivation). The major pathway will depend on the relative rates of collision and reaction, which in turn is a function of both temperature and pressure. At high pressure the collision rate will be fast, and activated molecules will tend to be collisionally stabilized before reactive events can occur; this is called the high-pressure limit. At low pressures the collision rate will be slow, and activated molecules will tend to isomerize and dissociate, often going thorough multiple reactions before collisional stabilization can occur.

The beginning of the pressure-dependent regime depends on both temperature and molecular size. The Figure 5.2 shows the approximate pressure at which pressure-dependence becomes

important as a function of temperature and molecular size. The parameter $m = N_{vib} + \frac{1}{2}N_{rot}$ represents a count of the internal degrees of freedom (vibrations and rotations, respectively). The ranges of the figure (temperature and pressure) suggest that pressure dependence is in fact important over a wide regime of conditions of practical interest, particularly in high-temperature processes such as pyrolysis and combustion [426].

The theory developed by Lindemann [213] has laid the foundations for understanding unimolecular reactions. As previously described the two elementary reactions:

$$\mathrm{A} + \mathrm{M} \longleftrightarrow \mathrm{A}^* + \mathrm{M} \tag{R 5.5}$$

$$\mathrm{A}^* \longrightarrow \mathrm{P} \tag{R 5.6}$$

lead to the following reaction rates:

$$\frac{d[A]}{dt} = -k_{1,f}[A][M] + k_{1,b}[A^*][M] \tag{5.16}$$

$$\frac{d[A^*]}{dt} = k_{1,f}[A][M] - k_{1,b}[A^*][M] - k_2[A^*] \tag{5.17}$$

and after assuming steady state for the activated molecule, it follows:

$$\frac{d[A]}{dt} = \frac{k_2 \frac{k_{1,f}}{k_{1,b}}}{1 + \frac{k_2}{k_{1,b}[M]}}[A] \tag{5.18}$$

showing that in the high pressure limit ($[M] \to \infty$), the reaction rate is pressure independent.

A rigorous treatment of these processes requires detailed consideration of molecular energy levels. The Lindemann theory consider only translational energy while in real molecules a better energy transfer is through the vibrational energies [154]. A further improvement of the theory considers that molecules posses a distribution of energies $P(E)$ that must be taken into consideration. The RRKM expression (from the name of the Authors) for the microcanonical rate coefficient $k(E)$ was derived in [291, 176, 233] and the reaction constant is calculated after averaging the reaction constants at different energies:

$$k = \int_{E_0}^{\infty} P(E) \frac{k_2(E)}{1 + \frac{k_2(E)}{k_{1,b}(E)[M]}} dE \tag{5.19}$$

In the subsequent refinements of the theory, a master equation models of chemical systems began appearing [326, 23, 250, 188, 116], including an early linear integral-differential equation formulation [420]. Analytical solutions of the master equation for a variety of simple models have been developed in [177, 381, 380], together with the first numerical approaches [370]. Numerical methods are required for complex unimolecular reaction networks and they became much more attractive with the appearance of new algorithms, including methods for solving stiff systems of ordinary differential equations and efficient algorithms for calculating the density of states [34, 357, 14]. Computing power had increased to the point where it is practical to solve the master equation numerically by discretizing the integrals over energy. The results for such predictive calculations are usually expressed using simple functions for the reaction rate, with fitting of parameters helping to achieved the required accuracy (see below).

The other category of reactions with pressure-dependent rate coefficients is bimolecular reactions with formation of a complex. An example of such a pressure-dependent reaction is the reaction of OH with CH_3 radicals, which is important both in combustion and gasification.

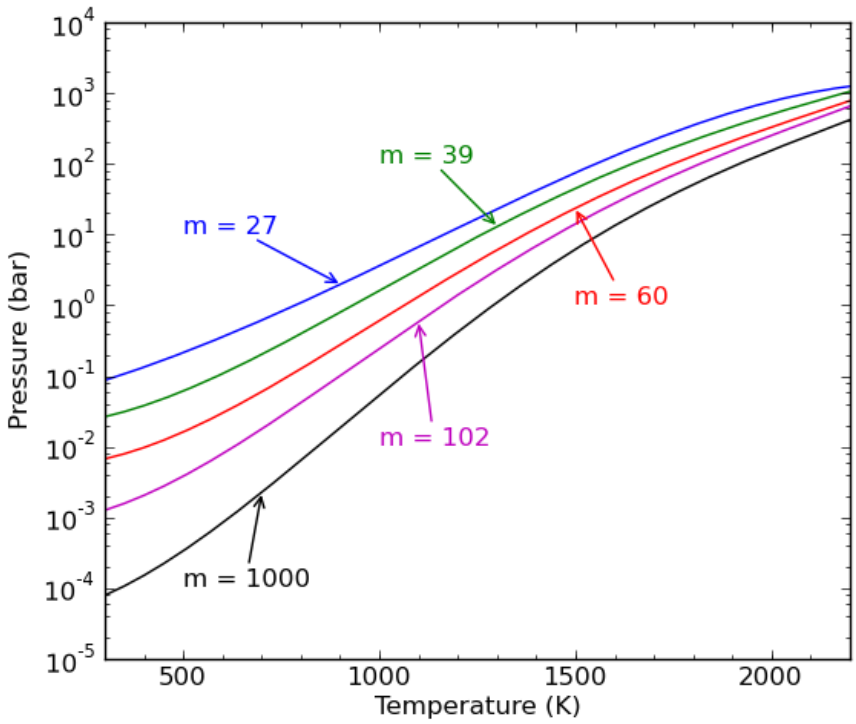

Figure 5.2.: Plot of the switchover pressure - indicating the onset of pressure dependence - as a function of temperature and molecular size. The value $m = N_{vib} + \frac{1}{2}N_{rot}$ represents a count of the internal degrees of freedom. (adapted from [426]

As mentioned before, for pressure dependent reactions the rate constant is often given in the original Lindemann form:

$$k = k_{\text{inf}} \frac{1}{1 + P_r} F \tag{5.20}$$

where P_r is the reduced pressure: $P_r = \frac{k_0[M]}{k_{\text{inf}}}$ and:

$[M]$	-	total concentration of the mixture
k_0	-	low pressure reaction rate in Arrhenius form
k_{inf}	-	high limit pressure reaction rate in Arrhenius form

If $F = 1$ then the above Equation is in the *Lindemann form*. In some rate equations, the *Troe form* is also used:

$$\log F = \left(1 + \left(\frac{\log P_r + c}{n - d\,(\log P_r + c)} \right)^2 \right)^{-1} \log F_{cent} \tag{5.21}$$

where:

$$\begin{aligned} c &= -0.4 - 0.67 \log F_{cent} \\ n &= 0.75 - 1.27 \log F_{cent} \\ d &= 0.14 \\ F_{cent} &= (1-\alpha) e^{-\frac{T}{T_3}} + \alpha e^{-\frac{T}{T_2}} + e^{-\frac{T_1}{T}} \end{aligned}$$

The reaction rate in equation 5.3 has been expressed using the concentration $[X]$. Since the concentration is linked to the partial pressure p_A by:

$$[A] \equiv \frac{N_A}{V} = \frac{p_A}{RT} \tag{5.22}$$

any reaction rates can be expressed also using p_A, rearranging the factors A and b in the Arrhenius form.

5.3. The presence of turbulence

Turbulence, as discussed in Chapter 4, enhances both the mixing of the species and the transport of the energy. The method used for the closure of the balance equations is similar to that used in Chapter 4 for the momentum equations. A Reynolds decomposition applied to the species equation and to the enthalpy equation gives the following relations:

$$\rho \frac{\partial \overline{Y_i}}{\partial t} + \rho \vec{U} \cdot \nabla \overline{Y_i} = -\nabla \cdot (D_{i,m} \nabla \overline{Y_i}) + \nabla \cdot \overline{\vec{v}' Y_i'} + \overline{\dot{S}_i} \tag{5.23}$$

$$\rho \frac{\partial \overline{h}}{\partial t} + \rho \vec{v} \cdot \nabla \overline{h} = +\overline{\dot{Q}} - \nabla \cdot \overline{\vec{q}_c} + \overline{\vec{q}_m} + \nabla \overline{\vec{v}' h'} \tag{5.24}$$

In this equations extra terms require a closure, namely the Reynolds Energy flux $\overline{\rho u_i' h'}$ and the The specie Reynolds-flux $\overline{\rho u_i' Y'}$

The direct approach to calculate the Reynolds Energy flux is to use the gradient transport hypothesis:

$$\begin{aligned} \overline{\rho u_i' h'} &= -\rho D_{e,ij} \tfrac{\partial h}{\partial x_j} \\ D_{e,ij} &= C_e \tfrac{k}{\varepsilon} \overline{u_i' u_J'} \end{aligned} \tag{5.25}$$

Usually the gradient transport hypothesis is written in term of turbulent quantities and dimensionless numbers (here the Pr number). For simplicity of notations $Y_i \equiv \overline{Y}_i$ and $h \equiv \overline{h}$:

$$\overline{\rho u_i' h'} = -\frac{\lambda_t}{c_p} \frac{\partial h}{\partial x_j} = -\frac{\mu_t}{\mathrm{Pr}_t} \frac{\partial h}{\partial x_j} \tag{5.26}$$

Similarly the direct approach for the Reynolds species flux follows from the equation:

$$\begin{aligned} \overline{\rho u_i' Y_a'} &= -\rho D_{t,ij} \tfrac{\partial Y_a}{\partial x_j} \\ D_{t,ij} &= C_a \tfrac{k}{\varepsilon} \overline{u_i' u_J'} \end{aligned} \tag{5.27}$$

and written in terms of turbulent quantities and dimensionless numbers (here the Schmidt number Sc):

$$\overline{\rho u_i' Y_a'} = -\rho D_t \frac{\partial Y_a}{\partial x_j} = -\frac{\mu_t}{Sc_t} \frac{\partial Y_a}{\partial x_j} \tag{5.28}$$

The turbulent diffusivity and the turbulent conductivity are introduced in the previous equa-

tions. Using these two quantities, it is possible to define an *effective* diffusivity and an *effective* conductivity.

For the standard k-ϵ model, for the realizable k-ϵ model as well as for the *RSM* model, the effective thermal conductivity is given by:

$$k_{eff} = k + \frac{c_p \mu_t}{Pr_t} \tag{5.29}$$

where k, in this case, is the thermal conductivity. The default value of the turbulent Prandtl number is 0.85. For the *RNG* k-ϵ model, the effective thermal conductivity is:

$$k_{eff} = \alpha c_p \mu_{eff} \tag{5.30}$$

where α is calculated from a RNG differential equation [431] allowing the variation of the turbulent Prandtl number with turbulence intensity [3].

Turbulent mass transfer is treated similarly:

$$D_{eff} = D + \frac{\mu_t}{\rho Sc} \tag{5.31}$$

where Sc is the Schmidt number.

For the standard k-ϵ, realizable k-ϵ and *RSM* models, the default turbulent Schmidt number is 0.7. For the *RNG* model, the effective turbulent diffusivity for mass transfer is calculated in a way analogous to the method used for heat transport previously explained..

In highly turbulent flows the turbulent diffusion rate is usually much larger than the molecular one, as shown in Table 5.1 taken from [228]. This observation will be used for the simplification of the equations derived in Section 5.9.

Properties	Molecular value	Turbulent Value	Unit
Viscosity	$1.2\,10^{-5}$	$3.0\,10^{-3}$	$\frac{kg}{m\,s}$
Conductivity	~ 7	0.1	$\frac{kJ}{m\,K}$
Diffusivity	$2.8\,10^{-5}$	0.05	$\frac{m^2}{s}$

Table 5.1.: Order of magnitude for the turbulent and for the molecular properties [228]

If the simple gradient diffusion assumption is not accurate enough, a transport equations for the Reynolds averaged term can be computed, in a similar way that has been done for the calculation of the Reynolds stress tensor in Section 4.3.3. Using the equation for the enthalpy h and the Navier-Stokes equations, it is possible to derive an exact equation for the second moment [124]:

$$\frac{\partial}{\partial t}\left(\rho\overline{u_i' h'}\right) + \frac{\partial}{\partial x_k}\left(\rho U_k \overline{u_i' h'}\right) = \rho P_i^h - \frac{\partial T_{ik}^h}{\partial x_k} + \Pi_i^h - \varepsilon_i^h + M_i^h \tag{5.32}$$

where the following terms are present:

1. The production term:

$$P_i^h \equiv -\overline{u_k' h'}\frac{\partial u_i}{\partial x_k} - \overline{u_i' u_k'}\frac{\partial h}{\partial x_k} \tag{5.33}$$

[3] The RNG equation smoothly predicts the variation of effective Prandtl number from the molecular value ($\alpha = 1/Pr$) in the viscosity-dominated region to the fully turbulent value ($\alpha = 1.393$) in the fully turbulent regions of the flow.

takes into account the interaction between moments of the second order and gradients of the averaged quantities. If the turbulent Reynolds stress tensor can be calculated then the production term is closed.

2. The spatial transport:

$$T_{ik}^{h} \equiv \rho\overline{u_i' u_k' h'} - \overline{h'\tau_{ik}'} + \overline{u_i' q} - \overline{u_i' u_j \tau_{jk}} + \overline{p' h'}\delta_{ik} - \overline{p' u_i' u_k} \tag{5.34}$$

can be split into third correlation terms that can be closed using a diffusion gradient assumption of the turbulent kinetic energy k.

3. The pressure scalar gradient:

$$\Pi_i^h \equiv p\overline{\frac{\partial h'}{\partial x_i}} - \overline{p\frac{\partial (u_i' u_k)}{\partial x_i}} + \overline{u_i' \frac{\partial p'}{\partial t}} \tag{5.35}$$

contains a non closed spatial derivative that usually is neglected.

4. The production rate due to viscous forces:

$$M_i^h \equiv \overline{u_j \frac{\partial (u_i' \tau_{jk})}{\partial x_i}} \tag{5.36}$$

5. The dissipation rate:

$$\varepsilon_i^h \equiv -\overline{q_k' \frac{\partial u_i'}{\partial x_k}} + \overline{\tau_{ik}' \frac{\partial h'}{\partial x_k}} \tag{5.37}$$

6. The heat flux:

$$\overline{q_k} \approx -\lambda \frac{\partial T}{\partial x_k} - \rho \sum_{a=1}^{N} D_a h_a \frac{\partial Y_a}{\partial x_k} \tag{5.38}$$

In the case of the components the transport equation reads [124]:

$$\frac{\partial}{\partial t}\left(\rho\overline{u_i' Y_a'}\right) + \frac{\partial}{\partial x_k}\left(\rho u_k \overline{u_i' Y_a'}\right) = \rho P_i^a - \frac{\partial T_{ik}^a}{\partial x_k} + R_i^a - \varepsilon_i^a + \overline{u_i' S_a} \tag{5.39}$$

where the following terms are present:

1. The production term:

$$P_i^a \equiv -\overline{u_k' Y_a'}\frac{\partial u_i}{\partial x_k} - \overline{u_i' u_k'}\frac{\partial Y_a}{\partial x_k} \tag{5.40}$$

correlating the second moment with the averaged quantities gradients. Also this term is closed if the Reynolds turbulent stress tensor is known.

2. The spatial transport term:

$$T_{ik}^a \equiv \overline{u_i' j_{ak}'} - \overline{Y_a' \tau_{ik}'} + \overline{\rho u_i' u_k' Y_a'} + \overline{p Y_a'}\delta_{ik} \tag{5.41}$$

scales as Re^{-1} and can be neglected for high Reynolds flows.

3. The pressure scalar gradient term:

$$R_i^a \equiv \overline{p' \frac{\partial Y_a'}{\partial x_i}} \tag{5.42}$$

4. The dissipation term:

$$\varepsilon_i^a \equiv -\overline{j'_{a,k}\frac{\partial u'_i}{\partial x_k}} + \overline{\tau'_{ik}\frac{\partial Y'_a}{\partial x_k}} \tag{5.43}$$

5. The pressure diffusion

$$\Pi_i^a \equiv -\overline{Y'_a\frac{\partial p'}{\partial x_i}} = R_i^a - \frac{\partial}{\partial x_i}\overline{p'Y'_a} \tag{5.44}$$

The gradient diffusion hypothesis is invoked for the closure of the molecular diffusion:

$$\bar{j}_{a,k} = -\overline{D_a\rho\frac{\partial Y_a}{\partial x_k}} \approx -\rho D_a\frac{\partial Y_a}{\partial x_k} - D_a\rho\overline{\frac{\partial Y'_a}{\partial x_k}} \approx -\rho D_a\frac{\partial Y_a}{\partial x_k} \tag{5.45}$$

and it scales as Re^{-1} and can be neglected for high Reynolds flows.

5.3.1. Generation of turbulence in presence of chemical reactions

If the temperature changes inside the flow, then the presence of the gravitational forces, together with density differences, leads to movements (instability of Kelvin-Helmoltz) that can generate or reduce turbulence. The generation of turbulence due to buoyancy is given by:

$$G_b = \beta g_i\frac{\mu_t}{Pr_t}\frac{\partial T}{\partial x_i} \tag{5.46}$$

where Pr_t is the turbulent Prandtl number for energy and $\vec{g}$ is the gravitational vector For both the standard k-ϵ and the realizable k-ϵ the default value of Pr_t is 0.85. The coefficient of thermal expansion, β, is defined as:

$$\beta = -\frac{1}{\rho}\left(\frac{\partial\rho}{\partial T}\right)_p \tag{5.47}$$

For the ideal gas, Equation 5.46 reduces to

$$G_b = -g_i\frac{\mu_t}{\rho Pr_t}\frac{\partial\rho}{\partial x_i} \tag{5.48}$$

It can be seen from the transport equations for k (equation 4.63), that turbulence kinetic energy tends to be increased ($G_b > 0$) in an unstable stratification. For a stable stratification, buoyancy tends to suppress the turbulence ($G_b < 0$). While the buoyancy effects on the generation of k are relatively well understood, the effect on the turbulent dissipation ϵ is less clear. However, it is possible to include the buoyancy effects in the transport equation for ϵ (Equation 4.67) adding the following source (or sink) terms:

$$S_{buoyancy} = C_{1\epsilon}\frac{\epsilon}{k}(C_{3\epsilon}G_b) \tag{5.49}$$

The degree to which the dissipation is affected by the buoyancy, is determined by the $C_{3\epsilon}$ coefficient calculated according to the following relation [151]:

$$C_{3\epsilon} = \tanh\left|\frac{v}{u}\right| \tag{5.50}$$

where v is the component of the flow velocity parallel to the gravitational vector and u is the component of the flow velocity perpendicular to the gravitational vector. In this way, $C_{3\epsilon}$ will

become 1 for buoyant shear layers for which the main flow direction is aligned with the direction of gravity. For buoyant shear layers that are perpendicular to the gravitational vector, $C_{3\epsilon}$ will become zero.

In the Reynolds stress model the production terms due to buoyancy are:

$$G_{ij} = -\rho\beta(g_i\overline{u_j'T} + g_j\overline{u_i'T}) \tag{5.51}$$

and they are modeled as:

$$G_{ij} = \beta\frac{\mu_t}{Pr_t}\left(g_i\frac{\partial T}{\partial x_j} + g_j\frac{\partial T}{\partial x_i}\right) \tag{5.52}$$

where Pr_t is the usual turbulent Prandtl number for energy. Using the definition of the coefficient of thermal expansion, β, given by Equation 5.47 the following expression is obtained for ideal gases:

$$G_{ij} = -\frac{\mu_t}{\rho Pr_t}\left(g_i\frac{\partial \rho}{\partial x_j} + g_j\frac{\partial \rho}{\partial x_i}\right) \tag{5.53}$$

5.4. Turbulent reacting flows

The interaction between turbulence and chemistry is in two directions. The presence of combustion through heat release affects the formation and dissipation of the turbulence but also the presence of fluctuating fields affects the rate of reactions. The effects of the heat release on the turbulence are believed to be well described by the turbulence models presented in Chapter 4. The increase of temperature, increases the molecular viscosity, leading to an increase of the dissipation rate ϵ. Moreover, in the combustion region, the expansion of the gas causes an increase of the velocity, leading to an increase of the kinetic energy k. Last, the gradients of density and pressure create an extra source for the turbulence [53].

Turbulent reacting flows can be characterized by several non-dimensional numbers. The most important one is the Damköhler number, defined as the ratio between the turbulent time scale τ_t and the chemical time scale τ_c:

$$Da = \frac{\tau_t}{\tau_c} \tag{5.54}$$

In the limit of high Damköhler numbers the chemical time is short in comparison with the turbulent mixing time. The gas in the reacting region has time to complete the combustion before the turbulence destroys the reacting region itself. The opposite scenario occurs when the Damköhler number is less than one. Then, the chemistry is the slowest process and its influence dominates the combustion. If the mixing is too fast, then the gas has no time to ignite and quenching must be taken into consideration.

Another important number is the *Karlovitz* Number Ka, defined as the ratio between the chemical time scale τ_c and the time scale of the structure at the Kolmogorov length scale τ_k:

$$Ka = \frac{\tau_c}{\tau_k} \tag{5.55}$$

In the limit of low Karlovitz numbers the chemical processes are faster than the mixing at the Kolmogorov scale and the spatial structure of the flame front is not affected by the detail of the chemistry.

The Borghi diagram [52], shown in Figure 5.3, incorporates both the Damköhler and the Karlovitz number. The x-axis is the logarithm of the ratio between the integral length l_I and the

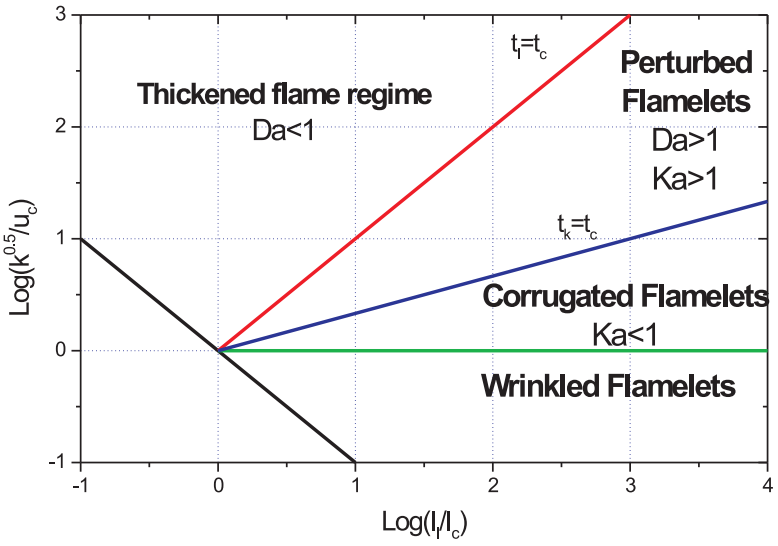

Figure 5.3.: The Borghi diagram [52, 389]

chemical length l_c. On the y-axis is the logarithm of the ratio of the turbulent velocity and the mean flow velocity. In the Borghi diagram the lines where $Da = 1$ and the one with $Ka = 1$ are shown. The diagram is divided into four regions:

Wrinkled Flamelets : In this region, $Ka < 1$ while $Da > 1$, the chemistry time scale is fast if compared with the flow field time scale. The chemistry does not affect the spatial structure of the flame front. This region can be described well by a *flamelet model*.

Corrugated Flamelets : This region is similar to the previous one. The turbulent velocity is anyway bigger than the integral one. The flame front can be still approximated as thin. The turbulence is not able to change the flame front internal structure but corrugates its surface.

Perturbed Flamelets : The chemistry can still be considered as fast with respect to the flow dynamics but now the small Kolmogorov eddies are interacting with the chemistry. In this region both extinction and reignition can take place.

Thickened flame : The turbulence strongly alters the spatial structure of the flame front because $Ka > 1$. Moreover, the non-equilibrium chemistry effects become evident: in the thickened flame regime the assumption of fast chemistry fails.

The difficulties in developing a general turbulence-chemistry interaction model are also mathematical. Let us consider a one-step global reaction of a fuel into a product:

$$A + B \longrightarrow P$$

The source term is given by Equation 5.3 using an Arrhenius form for the kinetic rate constant:

$$\overline{S_A} = -\frac{\rho^2}{M_B}(k+k')(Y_a + Y'_a)(Y_b + Y'_b) \tag{5.56}$$

where the fluctuating and non-fluctuating components are explicitely written. The kinetic rate constant k is non linear in temperature. The two terms containing the temperature are:

$$k_1 = AT^n \tag{5.57}$$

$$k_2 = e^{-E/RT} \tag{5.58}$$

They can be expanded into a series of the fluctuating temperature as follows:

$$k_1 = AT^n \left[1 + \sum_{i=1}^{\infty} Q_n \left(\frac{T'}{T}\right)^i\right] \tag{5.59}$$

$$k_2 = e^{-E/RT} \left[1 + \sum_{i=1}^{\infty} P_n \left(\frac{T'}{T}\right)^i\right] \tag{5.60}$$

The two functions Q_i and P_i are given by:

$$Q_i = \frac{n(n-1)(n-2)\cdots(n-i+1)}{i!} \tag{5.61}$$

$$P_i = \sum_{j=1}^{i} (-1)^{i-j} \frac{(i-1)!}{(j-1)!^2(i-j)!j} \left(\frac{E}{RT}\right)^j \tag{5.62}$$

Putting everything together, the source term can be written in the following complicated form:

$$\begin{aligned}\overline{S}_A = -\frac{\rho^2 AT^n}{M_B} e^{-E/RT} \cdot [1+ \\ + \frac{\overline{Y'_A Y'_B}}{Y_A Y_B} + \frac{Q_1 P_1 + Q_2 + P_2}{T}\overline{T'^2} + \frac{Q_1 + P_1}{Y_A T}\overline{Y'_A T'} + \frac{Q_1 + P_1}{Y_B T}\overline{Y'_B T'} + \\ + \sum_{a=1}^{\infty}\left(C_{1,a}\overline{Y'_A Y'_B T'^a} + C_{2,a}\overline{Y'_A T'^{a+1}} + C_{3,a}\overline{Y'_B T'^{a+1}} + C_{4,a}\overline{T'^{a+2}}\right)\Bigg]\end{aligned}$$

The above equation, even if formally correct, cannot be used for *CFD* calculations for several reasons:

- the series converges only if the fluctuations are small in comparison to the mean temperature;
- even if the ratio $\frac{T'}{T}$ is within the convergence radius of the above series, the convergence is slow. The first two terms do not provide a good enough accuracy;
- in order to evaluate other terms in the above description of the source, closure models for second order correlations (or higher if more terms are considered) are needed, increasing enormously the difficulties.

In order to solve the closure problem for the source term, other approaches are needed.

5.5. The well-mixed reactor limit

The easiest situation in which the reaction rate can be explicitly written, is when the turbulent mixing is quick enough that the turbulent structures have already been dissipated before chemical reactions start to be effective. In such a condition the assumption of well mixed reactor (at the molecular level) can be assumed and the reaction rates can be calculated as a function of the averaged quantities since no fluctuations are present. The reaction rates are then directly expressed by the mathematical relation presented in Section 5.2.

This situation is present in reactors where all the chemical reactions are slower than the turbulent mixing. In reactors for solid fuels conversion this is never the case. Even if slow reactions are present in the system, as for example the NO formation mechanisms, the fluctuations of the temperature, due to the quicker and fluctuating reactions, influence strongly the rates and they cannot be discarded (see Section 9.2).

5.6. Turbulent velocity models

When the flame front is sufficiently thin (low turbulence), it can be seen as a interface between fuel and oxidizer (for non-premixed combustion) and it can be described as a geometrical entity. Two formalisms have been proposed following this assumption, G-field equation (used mainly in premixed flames) and the flame surface density concept (see [389]). The source term due to chemical reactions can be written in term of a turbulent velocity flame S_t and the surface density Σ:

$$\dot{S} = \rho_U S_t \Sigma \tag{5.63}$$

A phenomenological model for the turbulent velocity must be provided. As an example the following relation can be applied [425] :

$$\frac{S_t}{S_L} = 1 + C \cdot \left(\frac{u'}{S_L} \right)^n \tag{5.64}$$

where the exponent n is usually ~ 0.7. A more theoretically derived equation is the one proposed in [271] as a function of the turbulent Damköhler number $Da_t \equiv \frac{\tau_{turb}}{\tau kin} = \frac{\epsilon}{k} \frac{S_L^2}{\nu}$:

$$\frac{S_t - S_L}{u'} = aDa_t + \left(bDa_t + cDa_t^2 \right)^{0.5} \tag{5.65}$$

Instead of 5.63 the flame front can be seen locally as a laminar flame, with the turbulence influencing the surface of the flame:

$$\dot{S} = \rho_U S_L \Sigma_t \tag{5.66}$$

where the laminar flame speed S_L is a characteristic of the flame and can be previously calculated. The turbulent surface density Σ_t may be estimated either from algebraic relations or as a solution of an exact, but unclosed, balance equation. [75, 282].

The Bray-Moss-Libby (BML) model [60, 62] is based on the assumption of infinitely fast chemistry. In this case, the instantaneous flame front are considered as a discontinuity that separates fresh mixture and the flue gases from each other. The flame can then be regarded as an ensemble of quasi-laminar flame structures (flamelets), which are embedded in the turbulent flow

field. It can be derived that in the first approximation, the flame front surface density can be written by an algebraic expression function where the variance c' and an integral length of the flame front curvature $\widehat{L}$ can be linked. In addition, since an infinitely thin flame front is assumed, the distribution of the reaction progress variable is bimodal. The surface density is then:

$$\Sigma_t = g\frac{c(1-c)}{\sigma\widehat{L}} \tag{5.67}$$

where g is a model constant of order unity and σ is an orientation factor, which describes the time-average angle between the normal vector of the flame front and a characteristic isosurface of the reaction progress variable. The constant g is considered to be an universal constant with a value of 0.5. The characteristic flame front curvature must be described by a separate model, being generally assumed that $\widehat{L}$ is proportional to the integral length of the turbulent flow. The final form of the reaction rate for the BML model is:

$$\dot{S} = \rho_u \frac{g}{\sigma C_l}\frac{\epsilon}{k}\frac{(1+\tau_T)c(1-c)}{(1+\tau_T c)^2} \tag{5.68}$$

with C_l an other model constant and the heat release parameter $\tau_T = \frac{T_b}{T_u} - 1$ links the temperatures of the burned and the unburned gas respectively.

5.7. The Probability Density Function method

If the variables in the source term of equation 5.56 are considered as fluctuating variables, the averages present in the equations can be calculated knowing the probability density functions. In CFD methods the control volumes are chosen small enough that the mixture can be considered macroscopically homogeneous. When mixing at the molecular level is also ensured (microscopical mixing) then the probability to find the fluctuating quantity at different values than the averaged one is zero and the PDF become a δ function and the variance of the distribution is zero. Conversely if micromixing is not perfect, i.e. still structures smaller than the cell dimension are present, values different than the averaged one can be found and the functional form of the PDF is different than a δ. In particular, the variance of the fluctuating quantity is different than zero. When the components or the temperature are not perfectly mixed across the entire reactor, the averaged values on a cell basis must be different on each cell. The averaged values calculated from a PDF must reflect that variations, therefore the PDF become explicitly a function of the position inside the reactor.

If the temperature is the only variable considered fluctuating, the average of the source term is given by:

$$\overline{\dot{S}_A} = \int_{T_{min}}^{T_{max}} \mathcal{P}(T)\dot{S}_A(T)\, dT \tag{5.69}$$

where $\mathcal{P}(T)$ is the probability density function of the temperature. The source term $S_A(T)$ is expressed as a function of the fluctuating temperature only while the species concentrations are considered non fluctuating. If other fluctuating variables must be taken into consideration, the average can be easily rewritten:

$$\overline{\dot{S}_A} = \int_{T_{min}}^{T_{max}}\int_{Y_{min}}^{Y_{max}} \mathcal{P}(T)\mathcal{P}(Y\,|T)S_A(T,Y)\, dTdY \tag{5.70}$$

where now a generic mass fraction Y appears explicitly and the conditional probability function $\mathcal{P}(Y\,|T\,)$ must be considered.

5.7.1. Assumed PDF

The easiest way of solving the integral 5.69 is to consider the PDF as a known mathematical function $PDF = \mathcal{F}(T)$. Usually this approach is used with the the RANS approach for the main quantities (see Section 4.3). The function $\mathcal{F}$ must be parametrized in order to have the possibility to satisfy physical constrains. Each n-th moment of the function $\mathcal{F}$ must be equal to each n-th moment calculated using the RANS approach (and the corresponding sub models for the closure of the equations). In practice only the first two moments are used. In the case of probability density function of the temperature, the mean temperature and the variance calculated from $\mathcal{F}(T)$ must be equal to the mean temperature and the variance from the RANS equations [4]. Therefore:

$$\int T\,\mathcal{F}(T)dT = \overline{T} \tag{5.71}$$

$$\int (T-\overline{T})^2\,\mathcal{F}(T)dT = \overline{T'}^2 = \sigma_T^2 \tag{5.72}$$

Similar equations can be written for the PDF of the species.

The variance of the temperature σ_T can be calculated solving a differential equation [112, 124]:

$$\begin{aligned}\frac{\partial}{\partial t}\left(\rho\sigma_T\right) &+ \frac{\partial}{\partial x_k}\left(\rho U_k\sigma_T\right) = \frac{\partial}{\partial x_k}\left[\left(\gamma\frac{\mu}{Pr}+\frac{\mu_t}{Pr_t}\right)\frac{\partial\sigma_T}{\partial x_k}\right] + \\ &+ M^T + P^T + \frac{\partial T_k^T}{\partial x_k} - \gamma\varepsilon^T - \frac{2}{c_V}C^T\end{aligned} \tag{5.73}$$

In the previous equation several terms appear and they are defined in the following.

1. The production term:

$$P^T \equiv -2\rho\overline{u_k'T'}\frac{\partial T}{\partial x_k} = 2\frac{\mu_t}{\mathrm{Pr}_t}\left(\frac{\partial T}{\partial x_k}\right)^2 \tag{5.74}$$

   is a function of the averaged temperature;

2. The transport term:

$$T_k^T \equiv -\rho\overline{u_k'T'^2} - \overline{2T'q_k} \tag{5.75}$$

3. The pressure correlation term:

$$M^T \equiv -\overline{2T'p\frac{\partial u_k}{\partial x_k}} = -2\left(\gamma-1\right)\rho\sigma_T\frac{\partial U_k}{\partial x_k} \tag{5.76}$$

   is modeled in such a way that it vanishes if pressure is a constant.

4. The term:

$$C^T \equiv \overline{2T'\sum_{a=1}^{N}h_{f,a}S_a} \tag{5.77}$$

[4] The conditions $\int\mathcal{F}(T)dT = 1$ must be always satisfied after scaling appropriately the function $\mathcal{F}$.

is responsible for the interaction between chemistry and fluctuations. contain a correlation between chemical reactions and turbulence and it is usually neglected.

5. The dissipation:
$$\varepsilon^T \equiv -2\overline{q_k \frac{\partial T_a'}{\partial x_k}} = C_T \rho \sigma_T \omega \tag{5.78}$$

6. the term
$$\rho\overline{u_k' T'} = -\frac{\mu_t}{\mathrm{Pr}_t}\frac{\partial \sigma_T}{\partial x_k} \tag{5.79}$$

7. and the term
$$q_k \equiv -\lambda\frac{\partial T}{\partial x_k} + \sum_{a=1}^{N} h_a j_{a,k} \approx -\frac{\mu}{\mathrm{Pr}}\frac{\partial \sigma_T}{\partial x_k} \tag{5.80}$$

The equilibrium hypothesis assumes that the production must be equal to the dissipation and it leads to a direct calculation for the variance of the PDF:

$$\sigma_T \equiv \overline{T'^2} = \frac{2\mu_t}{\mathrm{Pr}_t\, C_T \rho \omega}\left(\frac{\partial T}{\partial x_i}\right)^2 \tag{5.81}$$

where $C_T = 2$ and $\omega = \frac{\varepsilon}{k}$

Similar equations can be derived when the variance and covariance of the components are required. The results are similar to the ones presented in this section and they will not be here reported. The details can be found in [112, 124].

Several choices for the function $\mathcal{F}$ are available:

- Constant distribution;
- Delta functions;
- Triangular distributions;
- Gauss distribution;
- Beta function.

Among the aforementioned distribution the β-function can assume non symmetrical profile and it can provide peaks at the highest and lowest boundary. This property can simulate intermittent behavior of turbulent fields or ignition in combustion. The β-function is mathematically defined as:

$$\beta_{a,b}(f) = C(f+1)^{a-1}(1-f)^{b-1} \tag{5.82}$$

where C is the constant that assures the normalization. The previous definition is valid for the the variable f in the interval $-1 \leq f \leq 1$ and it must be appropriately rescaled if the described variable is defined in a different interval. The two parameters a and b are linked to the first and the second moment of the PDF. In the case of the PDF for the Temperature the 2 parameters a and b can be written as:

$$a = \overline{T}\left(\frac{\overline{T}(1-\overline{T})}{\sigma^2} - 1\right) \tag{5.83}$$

$$b = (1-\overline{T})\left(\frac{\overline{T}(1-\overline{T})}{\sigma^2} - 1\right) \tag{5.84}$$

In Figure 5.4 few examples of a β-PDF are given. As before the independent variable f is in the interval $-1 \leq f \leq 1$.

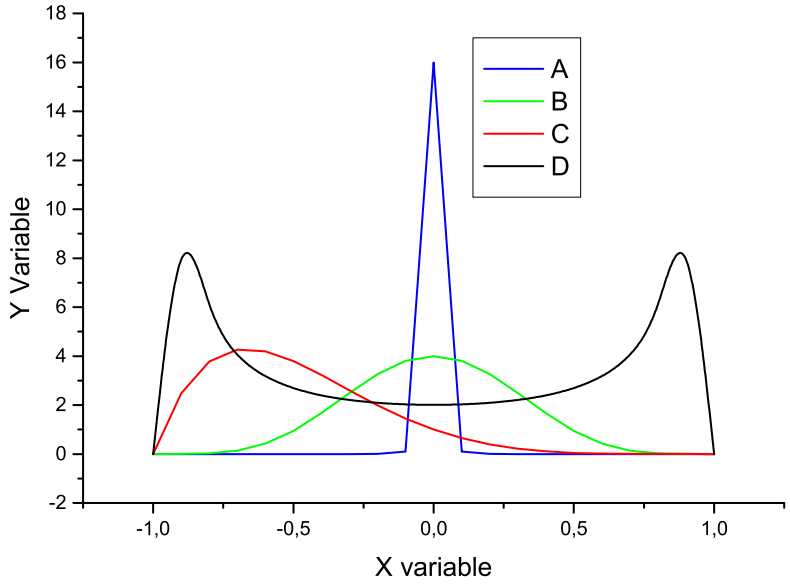

Figure 5.4.: Example of several $beta$-PDF for different parameters a and b

The functions denoted as A,B and D are symmetric while the function C presents an asymmetry towards negative f. The function D shows the possibility to describe fields that present two high probability values, one in the upper and in the lower range of the independent variable.

5.7.2. Transport equation for the PDF

Following the line exposed in Section 4.5, a transport equations for the PDF $\mathcal{P}_T$ can be written (see [124] for the derivation). The PDF is considered to be a function of the temperature T (or the enthalpy h) and of the species Y_i. The differential equation that gives the evolution of $\mathcal{P}_T$ is:

$$\begin{aligned} \frac{\partial\left(\rho\mathcal{P}_T\right)}{\partial t} \quad + \quad & \frac{\partial \rho u_i \mathcal{P}_T}{\partial x_i} = -\frac{\partial}{\partial h}\left\langle\left(\frac{Dp}{Dt} + \tau_{ij}\frac{\partial u_i}{\partial x_j} - \frac{\partial q_i}{\partial x_i} + \rho u_i f_i\right)\mathcal{P}_T\right\rangle + \\ - \quad & \frac{\partial}{\partial Y_k}\left\langle\left(-\frac{\partial j_{ki}}{\partial x_i} + \dot{S}_k\right)\mathcal{P}_T\right\rangle \end{aligned} \tag{5.85}$$

where the enthalpy h and the component mass fraction Y are introduced as variables describing the thermal dimension of the PDF. The components of the heat flux are described by the term q_i and the component of the diffusion mass flux of the component k are given by j_{ki}. The f_i are the components of external forces.

Without entering in the details, the previous equation describes the change of the PDF in physical space (the first term is the time variation of the PDF and the second term is the convective transport) and in the thermal space (the third and forth term on the right hand side).

The convective transport can be split into an averaged convection term and a turbulent convection term after splitting of the velocity u_i:

$$\frac{\partial}{\partial x_i}\left(\rho u_i \mathcal{P}_T\right) = \frac{\partial}{\partial x_i}\left(\rho U_i \mathcal{P}_T\right) + \frac{\partial}{\partial x_i}\left(\rho u_i' \mathcal{P}_T\right) \tag{5.86}$$

The turbulent convection requires a closure since the PDF doesn't contain any information about velocity fluctuation.

Part of the derivatives of the second and third terms, namely

$$\frac{\partial}{\partial h}\frac{\partial q_i}{\partial x_i} + \frac{\partial}{\partial Y_i}\frac{\partial j_{ki}}{\partial x_i}$$

under the assumption of unity Lewis number, can be rearranged into the following:

$$\begin{aligned}\frac{\partial}{\partial x_i}\left(\rho D \frac{\partial \mathcal{P}_T}{\partial x_i}\right) + \frac{\partial}{\partial x_i}\left(D\mathcal{P}_T \frac{\partial \rho}{\partial x_i}\right) + \\ -\rho \frac{\partial}{\partial \Psi_l}\frac{\partial}{\partial \Psi_m}\left[\left\langle D \frac{\partial \Psi_l}{\partial x_i}\frac{\partial \Psi_m}{\partial x_i}\right\rangle \mathcal{P}_T\right]\end{aligned} \tag{5.87}$$

where Ψ is the vector with components the temperature and the mass fractions. The first term in the previous equation represent the molecular diffusion, and the third is the turbulent diffusion, describing the turbulent mixing at the molecular level. This last term, together with the source term due to chemistry are of fundamental importance. As for the previous term the molecular diffusion requires a closure.

It is of fundamental importance to notice that the source term

$$\frac{\partial}{\partial Y_k}\left(\dot{S}_k \mathcal{P}_T\right)$$

is in closed form. The other terms, namely the compressibility term, the dissipation term and the external mass forces are small and usually can be neglected.

For the sake of completeness, it is worth recalling that the definition space for the PDF is not necessary formed by the temperature and the components as it has been done in the previous Sections. If the fluctuations of the components are not affecting the process, a PDF for the temperature T as a only variable can be used. Other thermal variables (for example the mixture fraction) being function of the temperature and the composition, can be used as a definition space for a PDF and appropriately transport equations can be formulated.

An other option for the space for the definition of PDF can be assumed. The whole set of thermal variables can be used together with the velocity. In such an approach the PDF serves as a closure for the thermal variables, describing the interaction between chemistry and turbulence, and serves as a closure for the momentum equation as well, describing the turbulence models. The composition *PDF* transport equation is derived the from the Navier-Stokes equations [281]:

$$\begin{aligned}\frac{\partial}{\partial t}(\rho\mathcal{P}) + \quad \tfrac{\partial}{\partial x_i}(\rho U_i \mathcal{P}) \quad + \frac{\partial}{\partial \psi_k}(\rho S_k \mathcal{P}) = \\ = \quad -\frac{\partial}{\partial x_i}\left[\rho \langle u_i'' | \psi \rangle \mathcal{P}\right] + \frac{\partial}{\partial \psi_k}\left[\rho \left\langle \frac{1}{\rho}\frac{\partial J_{i,k}}{\partial x_i}\middle| \psi \right\rangle \mathcal{P}\right]\end{aligned} \tag{5.88}$$

where ρ is the mean fluid density, U_i is the Fevre mean fluid velocity vector, S_k stands for reaction rate for species K, ψ is composition space vector, $v_i^{''}$ is the fluid velocity fluctuation vector and $J_{i,k}$ is the molecular diffusion flux vector. The notation of $\langle \dots \rangle$ denotes expectations, and $\langle A|B \rangle$ is the conditional probability of event A, given the event B occurs.

In Equation 5.88 the terms on the left-hand side are closed, while those on the right-hand side are not and require modeling. The first term on the left-hand side is the unsteady rate of change of the PDF, the second term represents convection by the mean velocity field, and the third term is the reaction rate. The principal strength of the *PDF* transport approach is that the highly-non-linear reaction term is completely closed and requires no modeling. The two terms on the right-hand side represent scalar convection by turbulence (turbulent scalar flux), and molecular mixing/diffusion, respectively. The turbulent scalar flux term is not closed, and can be modeled by the gradient-diffusion assumption:

$$-\frac{\partial}{\partial x_i}\left[\rho\langle u_i^{''}|\psi\rangle P\right] = \frac{\partial}{\partial x_i}\left(\frac{\mu_t}{\rho Sc_t}\frac{\partial P}{\partial x_i}\right) \tag{5.89}$$

5.8. The Eddy-Dissipation Model

The models previously described require intensive computation and for many applications quicker models must be applied even if further assumptions are needed in in many cases they are not strictly verified.

The interaction between turbulence and chemistry is assumed to be well described using the concept of Magnussen et al. [102, 225]. In order to react, fuel and oxidizer must be mixed at the molecular level. The smallest scales (eddies) in the turbulent spectrum are responsible for the mixing at the molecular level. Inside these eddies (called *fine structures*) the gas is well mixed and the structure can be viewed as a well-stirred reactor. Inside the fine structures the turbulence has no effect. When the fine structure is destroyed (by the turbulence), then the mixture inside them is released into the surrounding fluid.

The turbulence influences the overall process in several ways:

1. The turbulence is an intrinsic fluctuating process that can mix two neighboring regions of different temperatures and compositions. A model must take into consideration the possibility that a volumetric region must interact with other regions of different properties changing the conditions for the combustion.

2. In a diffusion flame turbulence is the most effective process that is able to mix the reactants and the products at the molecular level. The process of combustion and the process of mixing compete and various scenarios occur depending on the relationship between these two processes.

A phenomenological model has been firstly derived by [351] and then successively refined in [225] and [224]. The underlying idea is the splitting of a macroscopically well mixed control volume into microscopically well mixed reactors called fine structures and surrounding. Only in the fine structures, well mixed at the molecular level, volumetric chemical reactions are effective. The sources for a given quantity in the control volume is then the net exchange per unit of time between the surrounding and the fine structure. The characteristic time scale of the fine structure is calculated from a model of turbulent energy cascade as [224]:

$$\tau^* = \left(\frac{C_2}{3}\right)^{1/2}\sqrt{\frac{\nu}{\epsilon}} \tag{5.90}$$

and the ratio of the fine structure mass to the total mass is:

$$\gamma^* = \left(\frac{3C_2}{4C_1^2}\right)^{3/4} \left(\frac{\nu\epsilon}{k^2}\right)^{3/4} \tag{5.91}$$

where

ν	-	viscosity of the fluid
ϵ	-	turbulent dissipation
k	-	turbulent kinetic energy
C_1 and C_2	-	model constants

The mass transfer between the fine structure and the surroundings is given by:

$$\dot{m} = \rho\frac{\gamma^*}{\tau^*} = A\left(\frac{\nu\epsilon}{k^2}\right)^{1/4}\frac{\epsilon}{k} \tag{5.92}$$

with the constant A given by the relation:

$$A = \frac{3}{4C_1}\left(\frac{12C_2}{C_1^2}\right)^{1/4} \tag{5.93}$$

For the two constants, it was found empirically that $C_1 = 0.135$ and $C_2 = 0.5$, giving for the constant A the value of 23.66.

The Eddy Break Up (*EBU*) model [225] assumes that the reaction rate is equal only to the turbulent mass transfer between fine structure and surroundings (see [64, 65]):

$$\dot{S}_f = \dot{m}Y_f \tag{5.94}$$

where Y_f is the fuel mass fraction. The above equation calculates the maximum rate of combustion and it equals the combustion rate if the chemistry is quick compared to the turbulent mixing time scale. From the stoichiometry equations it is possible to derive a required rate of consumption of oxygen:

$$\dot{S}_{req} = \sum_f s_f \dot{S}_f \tag{5.95}$$

where s_f are the oxygen requirement for the fuel f. The maximum rate of combustion, due to the presence of the oxygen is:

$$\dot{S}_{O2} = \dot{m}\rho Y_{O2} \tag{5.96}$$

Equation 5.96, together with Equation 5.95, are used to create a limit for the rate of reaction R_f if $\dot{S}_{req} > \dot{S}_{O2}$:

$$\dot{S}_{f\ used} = S_f \cdot \frac{\dot{S}_{O2}}{\dot{S}_{req}} \tag{5.97}$$

These approach are correct only in the limit of combustion rate controlled by the turbulence. The chemical kinetic effects are not taken into considerations and the reactants immediately react to completion as soon as they mix.

For low temperatures or for relatively low reactions this approach over predicts the reaction

rates. In order to consider the limitation introduced by the kinetics (not taken entirely into account in the model aforementioned), small changes must be introduce. The total reaction process can be seen as a chain of two serial processes, the mixing with a rate $\dot{S}_{mix}$ and the reactions with a rate R_{kin}. Both rates can be considered together after application of the law of the serial processes:

$$\frac{1}{\dot{S}} = \frac{1}{\dot{S}_{mix}} + \frac{1}{\dot{S}_{kin}} \tag{5.98}$$

Another approach based on the *EBU* model can be also found in the literature. The net rate of production or consumption of species i is given by the smaller of the two expressions below:

$$\dot{S}_{i,r} = \nu'_{i,r} M_{w,i} A \rho \frac{\epsilon}{k} \min_{\mathcal{R}} \left(\frac{Y_{\mathcal{R}}}{\nu'_{\mathcal{R},r} M_{w,\mathcal{R}}} \right) \tag{5.99}$$

$$\dot{S}_{i,r} = \nu'_{i,r} M_{w,i} A B \rho \frac{\epsilon}{k} \frac{\sum_P Y_P}{\sum_j^N \nu''_{j,r} M_{w,j}} \tag{5.100}$$

where Y_P is the mass fraction of any product species and $Y_{\mathcal{R}}$ is the mass fraction of a particular reactant. The parameter A is an empirical constant equal to 4.0 and B is an empirical constant equal to 0.5. The second expression takes into consideration a limitation due to the absence of the products. Both version of the *EBU* model are suitable for global reactions only, where the chemistry is assumed fast in comparison to the mixing rate.

The Eddy Dissipation Concept (*EDC*) is an extension of the *EBU* model described in [224]. The reaction rate is given by:

$$\dot{S}_i = \rho \frac{\gamma^*}{\tau^*} (Y_i^o - Y_i^*) \xi \tag{5.101}$$

In the above equation Y_i^o is the mass fraction of species i in the surrounding entering the fine structure, and Y_i^* is the final composition in the fine structure. The factor ξ can be considered to limit the fraction of the fine structure that really reacts. Usually, it is near 1 and in many implementations of the *EDC* model its influence is ignored. The composition of the two regions can be related to provide the mean composition in the control volume:

$$Y_i = \gamma^* \xi Y_i^* + (1 - \gamma^* \xi) Y_i^o \tag{5.102}$$

Combining the last two equations, the rate of combustion can be written in terms of mean mass fraction and fine structure mass fractions:

$$\dot{S}_i = \frac{\gamma^*}{\tau^*} (Y_i - Y_i^*) \frac{\xi}{1 - \gamma^* \xi} \tag{5.103}$$

The fine structure composition can be calculated using both an equilibrium approach or a chemical kinetics model. In the last case the fine structure can be simulated as a well-stirred reactor [223, 66] or a plug flow reactor, both with a residence time given by the time scale given in 5.90. It is worth noticing that the several possibility are not equivalent. For example if flames near the stability limit are investigated, different conclusions can be derived since the ignition time in a well mixed reactor is shorter than the ignition time in a plug flow reactor and in the equilibrium calculations there is no ignition times.

A more theoretical derivation of the *EBU* model can be done using the PDF method [271, 112]. In the BML model [60, 62] already presented in Section 5.6 the following density function

for the progress variable c can be assumed:

$$\mathcal{P}(c) = \alpha\delta(c) + \beta\delta(1-c) + \gamma F(c) \tag{5.104}$$

with the normalization relation $\alpha + \beta + \gamma = 1$. Under $Da \gg 1$ an intermittent behavior of the progress variable is predicted therefore the reaction is not yet started ($c = 0$) or is already completed ($c = 1$). Under those circumstances, using a balance equation for $c(1-c)$, the reaction rate can be related to the the scalar dissipation rate of the progress variable:

$$\dot{S} = \frac{2}{2c_m - 1}\overline{\rho D \frac{\partial c}{\partial x_i}\frac{\partial c}{\partial x_i}} \tag{5.105}$$

A transport equation for the scalar dissipation rate may be written and solved, or one may postulate a linear relaxation of the fluctuations generated by micromixing leading to:

$$\overline{\rho D \frac{\partial c}{\partial x_i}\frac{\partial c}{\partial x_i}} = \frac{\overline{\rho c'^2}}{\tau} \tag{5.106}$$

where τ is the characteristic time of the integral length scales of the turbulent Ì„field $\tau = \frac{k}{\epsilon}$. Under the BML assumption it can be calculated as:

$$\dot{S} = \frac{2}{2c_m - 1}\frac{\rho\overline{c}(1-\overline{c})}{\tau} \tag{5.107}$$

5.9. The mixture fraction approach

The definition of the mixture fraction f is the following:

$$f(x) \equiv \frac{Z(x) - Z_o}{Z_f - Z_o} \tag{5.108}$$

where
- Z - mass fraction of a species at position (x)
- Z_f - mass fraction of the same species in the fuel stream
- Z_o - mass fraction of the same species in the oxidizer stream

The mixture fraction, defined in Equation 5.108, is, under the aforementioned assumptions, independent from the species considered. On the basis of the information provided in Table 5.1, one may assume that all the effective diffusivities are equal for all the species since the most efficient diffusion process is the diffusion due to turbulence. The molecular diffusivity (different for all the species) is less important than turbulence one, equal for all the species.

In gaseous combustion, the mixture fraction is a conserved scalar and its transport equation has no source. [5] The significance of the mixture fraction is in eliminating the chemistry source and sink from the species equation.

[5] The absence of the source term is not the reason for which the mixture fraction is useful. If oil or coal combustion are simulated with the mixture fraction approach then in the gas streams there is no fuel. The evaporation of the droplets or the devolatilization process bring inside the continuity equation terms of production of the mixture fraction.

The transport equation for the mixture fraction is explicitly written below:

$$\frac{\partial(\rho f)}{\partial t} + \nabla(f\vec{U}\phi) = \nabla(\Gamma_f \nabla\phi) \tag{5.109}$$

where

$$\Gamma_f = \rho\frac{D}{Pr_f}$$

with D being the effective diffusivity and Pr_f is the turbulent Prandtl number for the mixture fraction f.

The energy equation can also be simplified if the diffusivities are taken to be equal. If also the Lewis number Le, defined by:

$$Le_i = \frac{k}{\rho\, Cp D_{i,m}} \tag{5.110}$$

is equal to unity, the energy equation 4.31 simplifies to:

$$\frac{\partial}{\partial t}(\rho E) + \nabla\cdot(\vec{v}(\rho E + p)) = \nabla\cdot\left(k_{eff}\nabla T - \sum_j h_j\vec{J}_j + (\overline{\overline{\tau}}_{eff}\cdot\vec{v})\right) + S_h \tag{5.111}$$

The interaction with turbulence can be calculated using a probability density function $\mathcal{P}(f)$ in the same way as explained in Section 5.7. In the case of the probability density function for the mixture fraction f, the general transport equation 5.88, can be simplified further because f has no source terms and the dimensionality of the $\mathcal{P}$ is reduced to only two terms: the mixture fraction f and the temperature T.

The calculation of the $\mathcal{P}(f)$ using a transport equation is still too expansive for most of the industrial applications. A less expensive method is to use a *presumed* PDF like the β-function is used which is mathematically defined as:

$$\beta_{a,b}(f) = C(f)^{a-1}(1-f)^{b-1} \tag{5.112}$$

where C is the constant that assures the normalization. The two parameters a and b are linked to the first and the second moment of the PDF. If moreover the dimensionality is further reduced, considering the $\mathcal{P}$ only a function of the mixture fraction f, the parameter a and b are calculated using the mean value of mixture fraction f and the mixture fraction variance f'^2:

$$a = f\left(\frac{f(1-f)}{f'^2} - 1\right) \tag{5.113}$$

$$b = (1-f)\left(\frac{f(1-f)}{f'^2} - 1\right) \tag{5.114}$$

The mean mixture fraction equation was already written in equation 5.109. The conservation equation for the mean mixture fraction variance, f'^2 is:

$$\frac{\partial}{\partial t}\left(\rho f'^2\right) + \nabla\cdot\left(\rho\vec{v}f'^2\right) = \nabla\cdot\left(\frac{\mu_t}{\sigma_t}\nabla f'^2\right) + C_g\mu_t\left(\nabla^2 f\right) - C_d\rho\frac{\epsilon}{k}f'^2 \tag{5.115}$$

The constants σ_t, C_g, and C_d take the values 0.85, 2.86, and 2.0, respectively.

The influence of temperature on the chemistry (the terms $\phi(f)$ and $\rho(f)$ in the equation

above) is taken into consideration through the enthalpy h, calculated together with the flow field.

From the definition of the *PDF* it is possible to derive the mean and the variance for all the other variables. The model uses the mean of the species and the mean of the density only:

$$\overline{\phi}(h) = \int_0^1 \beta(f)\phi(f,h)df \tag{5.116}$$

$$\frac{1}{\rho}(h) = \int_0^1 \beta(f)\frac{1}{\rho(f,h)}df \tag{5.117}$$

Chemistry (components and temperature) is calculated when a link between the mixture fraction f and each component Y_i is established. In combustion theory the following three approaches are usually mentioned [278]:

- Stoichiometric calculation;
- Chemical Equilibrium approach;
- Flamelets utilization;
- Conditional Moment Closure models.

The modeling based on stoichiometric calculations is never applied since its accuracy is poor. It is worth noticing that the aforementioned link between the mixture fraction and the components is mostly independent from the details of the flow and it can be calculated before the CFD calculation and it can be stored in a table, saving time for complex chemistry calculations.

5.9.1. The equilibrium approach

For any given mixture fraction f and enthalpy h, the function $\phi(f,h)$ in 5.116 can be univocally calculated assuming chemical equilibrium at constant enthalpy and constant pressure. This method doesn't require the knowledge of any chemical mechanism, it is quick and easy to implement. Its drawback lays in the inability to predict correctly chemical effects like flame strain, stretching and quenching.

The accuracy of the solution is related to the achievement of equilibrium in the flow. For high temperature industrial applications (usually based on combustion) the accuracy can be acceptable but it decreases as the process temperature decreases (usually in gasification). Chemical equilibrium is never acceptable in the case of pollutant calculation (like nitric oxide) and in the case of rich flame. In the second case, the problem can be mitigated assuming for higher mixture fraction frozen chemistry or (linear) interpolation to the point $f = 1$.

5.9.2. The flamelet model

If the combustion is near equilibrium but chemical kinetic effects cannot be omitted (in the case of quenching for example) some other variable must be taken into consideration. The flamelet concept views the turbulent flame as an ensemble of thin, laminar, locally one-dimensional flamelet structures embedded within the turbulent flow field. As already pointed out in Section 5.4, once ignition has taken place, chemistry accelerates as the temperature increases due to heat release. When the temperature reaches values that are of the order of magnitude of those of the close-to-equilibrium branch the reactions that determine fuel consumption become very

fast. For methane combustion, for example, the rate determining reaction in the fuel consumption layer is the reaction of CH_4 with the H-radical. Since the chemical time scale of this reaction is short, chemistry is active only within a thin layer, namely the fuel consumption or inner layer. If this layer is thin compared to the size of a Kolmogorov eddy, it is embedded within the quasi-laminar flow field of such an eddy and the assumption of a laminar flamelet structure is justified.

Following [268, 270, 61] it is possible to calculate the structure of the flamelets considering another scalar, named the scalar dissipation χ as a parameter. The balance equations for the energy and for the components are firstly written only using the normal coordinate to the flamelet surface. The resulting simplified equations are then written using the mixture fraction (here Z) as a independent variable, resulting in the following relations:

$$\frac{\partial Y_k}{\partial t} = \frac{\chi}{2Le}\frac{\partial^2 Y_k}{\partial Z^2} + \frac{\dot{S}_k}{\rho} \tag{5.118}$$

$$c_p\frac{\partial T}{\partial t} = \frac{\chi}{2Le}\frac{\partial^2 h}{\partial Z^2} - \sum_{k=1}^{N} h_k\left\{\frac{\chi}{2}\frac{\partial^2 Y_k}{\partial Z^2} + \frac{\dot{S}_k}{\rho}\right\} \tag{5.119}$$

where the χ is the scalar dissipation at the stoichiometric condition. The above equations are assumed to be independent of the specific geometrical conditions and they can be solved for particular suitable configurations.

If the time dependency at the first term can be discarded, the model is described as steady laminar flamelet in opposition to the time dependent unsteady laminar flamelet models. The influence of the other two coordinates can be considered taking into account of the curvature effects as a secondary parameter.

A common laminar flame used to represent a flamelet in a turbulent flow is a counterflow diffusion flame consisting of two opposed, axisymmetric jets of fuel and oxidizer. As the distance between the jets decreases or the velocity of the jets increases, the flame is strained and increasingly departs from chemical equilibrium until it is eventually extinguished [271, 206]. In the laminar counterflow flame, the mixture fraction f decreases monotonically from unity at the fuel jet to zero at the oxidizer jet. If the species mass fraction and temperature along the axis are mapped from physical space to mixture fraction space, they can be uniquely described by two parameters: the mixture fraction and the strain rate (or, equivalently, the scalar dissipation ξ). Hence, the chemistry is reduced and completely described by the two quantities.

A characteristic strain rate for an opposed-flow diffusion flamelet can be defined as $a_s = \frac{v}{2d}$, where v is the velocity of the fuel and oxidizer jets, and d is the distance between the jet nozzles. Instead of using the strain rate to quantify the departure from equilibrium, it is common to use the scalar dissipation χ, defined as:

$$\chi = 2D\left|\nabla Z\right|^2 \tag{5.120}$$

where D is the molecular diffusion coefficient.

For the counterflow geometry, the flamelet strain rate can be related to the scalar dissipation at the position where f is stoichiometric by:

$$\chi_{st} = \frac{a_s}{\pi}\exp\left(-2(erfc^{-1}(2f_{st}))^2\right) \tag{5.121}$$

where f_{st} is the stoichiometric mixture fraction and $erfc^{-1}$ is the inverse complementary error function.

In addition, the laminar flamelet model is suited to predict moderate chemical non-equilibrium states in turbulent flames due to aerodynamic straining by the turbulence. The chemistry, however, is assumed to respond rapidly to this strain, so as the strain relaxes, the chemistry relaxes

to equilibrium. Physically, as the flame is strained, the width of the reaction zone diminishes, and the gradient of f at the stoichiometric position increases. The instantaneous stoichiometric scalar dissipation, χ_{st} , is used as the essential non-equilibrium parameter. In the limit $\chi_{st} \longrightarrow 0$ the chemistry tends to equilibrium, and as χ_{st} increases due to aerodynamic straining, the non-equilibrium increases. Local quenching of the flamelet occurs when χ_{st} exceeds a critical value.

The coupling between the flamelets and the turbulence is done through the *PDF* . The function $\mathcal{P}$ is now a function of two variables, the mixture fraction and the scalar dissipation. The mean scalar dissipation is calculated in the following way [278]:

$$\overline{\chi}_{st} = \frac{C_\chi f^{'2}}{k} \tag{5.122}$$

with the constant C_χ equals 2. The variance of the scalar dissipation is neglected and the $\mathcal{P}(\chi)$ becomes a δ-function in χ.

5.9.3. Conditional Moment Closure model

It has been observed that in combustion experiments (confirmed by DNS calculations) the fluctuations of a quantity near its mean conditioned to a given mixture fraction are relatively narrow. In the limit of fluctuations around the conditional mean being negligible the conditional source term can be closed:

$$\left\langle S(\phi) \,|f\right\rangle = S(\left\langle \phi \,|f\right\rangle) \tag{5.123}$$

where the operator $Q(f;x,t) \equiv \left\langle \phi \,|f\right\rangle$ is the conditional average of the quantity ϕ for a given mixture fraction f.

In Conditional Moment Closure models (CMC) equations for the conditional moments $Q(f;x,t)$ are solved [41, 181]:

$$\left\langle \rho \,|f\right\rangle \frac{\partial Q}{\partial t} + \left\langle \rho U_i \,|f\right\rangle \frac{\partial Q}{\partial x_i} = \frac{1}{2}\left\langle \rho\chi \,|f\right\rangle \frac{\partial^2 Q}{\partial f^2} + \left\langle S(\phi) \,|f\right\rangle \tag{5.124}$$

For simple chemistry the conditional moment Q can be found by interpolation between the two extreme cases, unreacted mixture and equilibrium (see [112] for some examples). A more accurate method is the formulation of a transport equation that depend explicitly on turbulent quantities. In practice, the mixture fraction is discretized in a number of bins and the conditional average is the average value in each bin. The conditional quantities are computed by solving transport equations in sample space. These CMC transport equations present additional unclosed terms, such as the conditional velocity, the conditional turbulent flux and conditional chemical source term. A key assumption of CMC is that fluctuations about the conditional mean are small therefore first order CMC hypothesis is often used to close the chemical source term as in equation 5.123, that is the scalar variance about the conditional average is negligible and the conditional averaged chemical source terms are closed by conditional averaged scalars.

First order closure may not be appropriate when the effects of conditional fluctuations are expected to be significant, as near flame quenching or extinction. The second order CMC approach may be preferred in these cases, as it provides better predictions for auto igniting cases and in the context of flames characterized by extinction/reignition.

If the conditional means together with a presumed PDF of the mixture fraction are known then the unconditional averaged source can be computed:

$$\left\langle S(\phi)\right\rangle = \int S(Q(f;x,t))\mathcal{P}(f;x,t)df \tag{5.125}$$

as in the Multiple Mapping Conditioning (MMC) model [180].

Another model that uses conditional averages to achieve closure of the chemical reaction source term is the Conditional Source-term Estimation (CSE) approach [72]. CSE uses the same CMC hypothesis for closing chemical source terms, where the conditional average of the chemical source term is determined by first order averages. However in the CSE approach the conditional averages are assumed to be homogeneous within a known ensemble of points (computational cells). Thus, conditional values are obtained by inverting an integral equation instead of solving transport equation (as in CMC).

The Conditional Moment Closure is related with the flamelet model but their mathematical derivations slightly differ. Even if it is possible to observe that those two models are consistent with each other [181], it has not yet bin assessed in which region the model can be safety applied.

5.10. Reactions in LES modeling

Large Eddy Simulation does not intend to numerically resolve all turbulent length scales, but only a fraction of the larger energy containing scales within the inertial subrange (see Section 4.4). Modeling is then applied to represent the smaller unresolved scales which contain only a small fraction of the turbulent kinetic energy. Therefore the computed flows are usually less sensitive to modeling assumptions. The reason why LES provides substantial advantages for modeling turbulent combustion is that the scalar mixing process is of importance in chemical conversion and LES modeling try to simulate a larger part of the process than a RANS approach does. Non-reactive and reactive system studies show that LES predicts the scalar mixing process and dissipation rates with improved accuracy compared to RANS, especially in complex flows. Detailed comparisons for industrial applications (see for example the calculation presented in Section Section 16.5.1) show that, irrelevant from the details, RANS modeling is capable of catching many of the characteristics of a reactor.

6. Modeling of Drying and Devolatilization

In this chapter several models for drying, pyrolysis and devolatilizations are discussed. The modeling of the conversion of the formed char is discussed in the next chapter.

6.1. Vaporization

As already explained in Section 2.4, drying is the first process undertaken by solid fuels as soon as particles enter an hot environment. The transfer of water from the particle to the bulk is accomplished by two processes, the vaporization and the boiling. For small solid particle the vaporization is the most important and it will be described below.

Modeling of vaporization (for moisture release from wet particles or for vaporization of multicomponent particles) requires the modeling of the following process: heat transfer by convection and radiation, kinetic rates modeling for the detachment of gaseous molecules from the liquid phase and mass transfer of the vaporized gas from the particle internal pores to the external surface and, last, to the bulk. For most industrial application the rate of detachment is much higher than the rate of the other two processes therefore local thermodynamic equilibrium at the particle surface can be assumed with high accuracy.

Following [336] the modeling of wet particle heating can be subdivided into the following groups in order of increasing complexity:

1. Models based on the assumption that the droplet surface temperature is uniform and does not change with time;
2. Models based on the assumption that there is no temperature gradient inside droplets (infinite thermal conductivity of liquid);
3. Models taking into account finite liquid thermal conductivity, but not the re-circulation inside droplets (conduction limit);
4. Models taking into account both finite liquid thermal conductivity and the re-circulation inside droplets via the introduction of a correction factor to the liquid thermal conductivity (effective conductivity models);
5. Models describing the re-circulation inside droplets in terms of vortex dynamics (vortex models);
6. Models based on the full solution of the Navier-Stokes equation for the liquid inside the particle.

Models belonging to the first group allow the reduction of the dimension of the system via the complete elimination of the equation for droplet temperature but even if interesting from the analytical point of view in combination with CFD calculations, their accuracy is too low. Models belonging to the last two groups have not yet been implemented due to their complexity. In the

following sections, models based on the second group will be described. For a review of the other approaches see [307].

The simplest model for vaporization assumes that at the particle surface thermodynamic equilibrium between the liquid and the gaseous phase is established. The rate of vaporization is then governed by diffusion through the boundary layer and by convection (Stephan flow). If the boundary layer is thin in comparison to the dimension of the particle, plane geometry can be assumed and the stationary mass balance equation for a general vaporizing component i and the total mass balance are expressed by the following two equations:

$$\rho U \frac{dY_i}{dx} = \frac{d}{dx}\left(\rho D \frac{dY_i}{dx}\right) \tag{6.1}$$

$$\rho U A = \dot{m} \tag{6.2}$$

where $\dot{m}$ is the constant (and unknown) mass evaporated from the surface per unit of time and U is the radial velocity of the evaporated component. From the second equation, assuming constant density in the boundary layer, it follows that the velocity U is a constant. The first equation can be then integrated once:

$$\rho U Y_i - \rho D \frac{dY_i}{dx} = \frac{\dot{m}_i}{A} \tag{6.3}$$

The the total mass flow for the non evaporating species (whose mass fraction is denoted Y_2) vanishes at steady state, $\dot{m}_2 = 0$. Since $Y_1 + Y_2 = 1$, from equation 6.3 the solution for the mass flow $\dot{m}$ can be derived:

$$\dot{m} = \frac{\rho D}{l} \ln(1 + B_m) \tag{6.4}$$

where the Spalding number sdefinwed by:

$$B_m = \frac{Y_0 - Y\infty}{1 - Y_0} \tag{6.5}$$

has been introduced. The mass fractions Y_0 and Y_∞ represent the mass fraction at the surface and in the bulk respectively.

If the boundary layer is not small in comparison with the dimension of the particle, the balance equations must be solved in spherical coordinates in which the stationary mass balance equation for the component i is written as follows:

$$\rho U \frac{dY_i}{dr} = \frac{1}{r^2}\frac{d}{dr}\left(r^2 \rho D \frac{dY_i}{dr}\right) \tag{6.6}$$

with U the radial velocity and D the binary diffusion coefficient. The total mass balance equation impose that the mass flow is a constant:

$$\rho U A = \dot{m} \tag{6.7}$$

with $A = \pi D_p^2$ the external surface of a sphere with diameter D_p. If the relation 6.6 is applied to the non evaporating component Y_2, a zero flow rate can be imposed at infinity and at the droplet surface. Since $Y_1 = 1 - Y_2$, assuming as before constant density, a solution for the mass fraction can be written:

$$Y = Y_0 + (Y_\infty - Y - 0)\left[\frac{e^{\overline{m}(1-\frac{1}{r})} - 1}{e^{\overline{m}} - 1}\right] \tag{6.8}$$

with the following non dimensional parameters:

$$\overline{m} = \frac{\dot{m}}{4\pi D_p \rho D} \tag{6.9}$$

$$\overline{r} = \frac{r}{D_p} \tag{6.10}$$

This relation will be used later, in Section 8.8, for the determination of the delay of char reactions in the presence of pyrolysis.

The evaporation rate $\dot{m}$ is given, in the case of spherical geometry, by the same relation derived in the case of planar geometry:

$$\dot{m} = \frac{\rho D}{D_p} \ln(1 + B_m) \tag{6.11}$$

If the Stephan flow is negligible, the Spalding number is small, $B_m \ll 1$, and after expansion of both, equation 6.4 and equation 6.11 in Taylor series, a linear relation is obtained:

$$\dot{m} = \frac{\rho D}{D_p} (Y_o - Y_\infty) \tag{6.12}$$

It is worth noticing that the previous equations can be written as well in term of partial pressures p', mole fractions x or concentration $[i]$. The fraction Y_0 of vapor at the droplet surface is evaluated by assuming that the partial pressure of vapor at the interface is equal to the saturated vapor pressure, p_{sat}, at the particle droplet temperature, T_p. This assumption is usually very accurate since the molecular interactions responsible for kinetic effects between phases are much faster than the following mass transfer rate.

The previous equations are valid if the droplets are at rest with respect to the surrounding fluid, since the molecular diffusivity D has been used. In applications where vaporization takes place, the particle are transported by the flow and a velocity difference (usually a small difference) is present. To take this forced diffusion into consideration the diffusion coefficient D is replaced by a more general mass transfer coefficient k calculated from the Sherwood number correlation:

$$Sh_{RM} = \frac{k_c d_p}{D_m} = 2.0 + 0.6 Re_d^{1/2} Sc^{1/3} \tag{6.13}$$

	D_m	diffusion coefficient of vapor in the bulk	$\frac{m^2}{s}$
where:	Sc	the Schmidt number,	$\frac{\mu}{\rho D_{i,m}}$
	D_p	particle diameter	m

There are many other correlations available [42], but all these correlations are an extension or modification of correlations presented in [286]. More modern theories introduce the influence of the turbulent intensity directly into the correlation for the Schmidt number after the observation that turbulence intensity enhances droplet vaporization rates compared to a laminar forced convective flow. The following correlation has been proposed [429]:

$$Sh_{turb} = Sh_{RM} \cdot \frac{0,74}{Da_t^{0.115}} \tag{6.14}$$

where $Da_t = \frac{\tau_{ed}}{\tau_v}$, $\tau_{ed} = \frac{(d_P^2 L)^{1/3}}{u'}$ and $\tau_v = \frac{\delta}{V}$ are the vaporization Damköhler number, the turbulent flow characteristic timescale based on the droplet initial diameter and the droplet vaporization timescale, respectively, The vapor film thickness, δ, and vapor blowing Stephan flow velocity, V, are calculated using the droplet boundary film theory [4]. For even more advanced models see [307, 308].

This simple approach can be improved if some of the assumptions used by the previous derivation are relaxed [308]. Among the most important improvement the following can be cited:

1. The conductivity of the liquid is not infinite, creating a temperature gradient inside the droplets;
2. The surface temperature is not anymore equal to the averaged temperature (usually solved by the CFD solvers, see Section 10.3);
3. An increase of the droplet dimensions due to a finite expansion coefficient lead to an increase of the initial evaporation rate through an increase of the external surface.

Further improvements of the models led to the introduction of corrections due to the finite thicknesses of thermal boundary layers. In spherical coordinates the balance equation of the enthalpy leads to:

$$\rho U c_p \frac{dT}{dr} = \frac{1}{r^2}\frac{d}{dr}\left(\lambda \frac{dT}{dx}\right) \tag{6.15}$$

that is practically identical to equation 6.6. This leads to the introduction of the the Spalding heat transfer number;

$$B_T \equiv \frac{c_P(T_g - T_s)}{L} \tag{6.16}$$

with L the specific heat of evaporation [1]. The final correlations for the Schmidt and the Nusselt numbers suggested in [336] are the following:

$$Sc = 2\left(1 + 0,3\frac{Re^{1/2}Sc^{1/3}}{F(B_M)}\right) \tag{6.17}$$

$$Nu = 2\frac{\ln(1+B_T)}{B_T}\left(1 + 0,3\frac{Re^{1/2}Pr^{1/3}}{F(B_T)}\right) \tag{6.18}$$

with $F(x) = (1+x)^{0,7}\frac{\ln(1+x)}{x}$.

In vaporization of pure liquid particles without expansion the diameter changes following the d^2 law if the vaporization rate is a constant. The mass conservation for the droplets is:

$$\dot{m} = \rho \cdot V = \frac{\pi}{6} D_p^3 \rho \tag{6.19}$$

and after derivation with respect to time:

$$D_p^2 \frac{d}{dt} D_p = \frac{2}{\pi\rho} \cdot \frac{d}{dt}\dot{m} \tag{6.20}$$

[1] If the Lewis number $Le = 1$ Both Saplding numbers are equal:

$$B_m = B_T$$

During devolatilization of more general solid fuels the d^2-law is not anymore valid and, in general, the law for the diameter change depends on the amount of humidity the particle posses. For the evaporation of slurry, where the concentration of solid particle is small, the d^2 law can be a fairly approximation. In the case of partially dried coals or biomass (usually fired in boilers), the amount of water contained trapped inside the porous structure is limited and the diameter can be considered constant.

6.2. Devolatilization

The process of devolatilization is usually very fast. Although the time needed to complete the process is short if compared with the residence time of the fuel inside the reactor, it affects strongly not only the structure of the flame, but, as already seen in Section 2.7, also the internal structure of the remaining char as well as its properties and its reactivity.

Devolatilization consists of three different steps:

1. pyrolysis, the decomposition of the solid structure;
2. volatile transport through the pores;
3. secondary reactions that can alter the chemical structure of the gases or can cause deposition of the gases on the pore walls.

The decomposition of the solid structure is an intrinsic chemical process determined by the temperature and by the internal pressure of the gas. The transport through the pore structure determines the internal pressure and the rate of the gas release if the pore resistance is high. Light gas is not affected by transport limitation as much as tar release.

There are a number of properties, different for each fuel, on which the devolatilization process depends on [347] and those properties must be taken into consideration if the description of the complex chemical processes together with the underling mass transport phenomena must be satisfactory described:

1. Elemental composition;
2. Functional group composition;
3. Plasticity;
4. Size of aromatic ring cluster;
5. Molecular weight of tars;
6. Variations in bridging materials;
7. Porosity;
8. Hydrogen bonding;
9. Catalytic constituents;
10. Material (usually hydrocarbons) not chemically bound.

While these properties affect the composition of the gas and the tars as well as the reactivity of the formed char, they do not affect directly the chemical decomposition rate of the fuels and they can be largely discarded as soon as the speed of decomposition alone is required.

The various models used for the mathematical description of devolatilization can be divided into the following categories:

1. One step global models;
2. One-stage multi-reactions models;
3. Two stage semi-global models;
4. Detailed models.

Many models try to simplify the complexity of the devolatilization process introducing a pseudo global rate. Using this rather crude phenomenological approach the devolatilization steps are usually condensed in the following global mechanism:

$$\text{solid} \xrightarrow{\text{k}} \text{volatile} + \text{char} \tag{R 6.1}$$

In this approach tar and light gases are treated as a unique species for which thermodynamic properties and kinetic rates for further homogeneous reaction must be defined. If information about the split between tar and gases are available then the global mechanism can be replaced by the following

$$\text{solid} \xrightarrow{\text{k}} \text{gas} + \text{tar} + \text{char} \tag{R 6.2}$$

where the splitting is a functions of thermodynamic quantities T and p. It is worth recalling that the split just defined is not based on any chemical rate: gases and tars are released at the same time.

6.2.1. Constant devolatilization model

The simplest assumption for the global reaction R 6.1 or R 6.2, is to calculate the mass loss using the following equation:

$$\frac{dm_p}{dt} = -k(1 - f_v)m_{p,0} \tag{6.21}$$

where the kinetic constant k is not temperature or pressure dependent. The fraction of volatile f_v is kept constant during the process therefore the mass loss predicted by 6.21 is linear in time. In quick pyrolysis of many coals usually this is not a drawback (see the example in section Section 6.3).

The model is successful in predicting the behavior of the solid fuels only if the parameters k and f_v are calculated by fitting experiments in the exact conditions used in the modeling.

It is worth noticing that in equation 6.21 the parameter f_v is usually a fixed parameter that must be obtained from measurements. No models have been developed from equation 6.21 with a temperature dependent f_v in order to simulate the temperature dependent yield.

6.2.2. Single-kinetic rate model

If the kinetic rate k is allowed to be a function of the temperature, the mass loss can be written as:

$$\frac{dm_p}{dt} = -K(1 - f_v)m_{p,0} \tag{6.22}$$

The kinetic constant K is expressed using an Arrhenius rate form:

$$K = AT_p^b \, e^{-\frac{E}{RT_p}} \tag{6.23}$$

As is the previous model, the devolatilization process is assumed single step. Although this model has a rate dependent on the particle temperature, for a fixed temperature the mass loss is constant.

The yield is not temperature dependent and must be derived from measurements.

6.2.3. Linear devolatilization model

If the rate is proportional to the volatile released, the mass loss can be expressed in the following form [15]:

$$\frac{dm_p}{dt} = -K(m_p - f_v m_{p,0}) \tag{6.24}$$

The kinetic constant K is expressed using an Arrhenius rate form:

$$K = AT_p^b \, e^{-\frac{E}{RT_p}} \tag{6.25}$$

The pyrolysis rate depends on temperature and on the content of gas. Still the final yield must be specified and the composition of the volatile is not known. The exponential form of the mass loss derived by equation 6.24 is suitable for predicting rates for most of the coals and can be safety applied to biomasses as well with reasonable accuracy.

The parameters needed for this model must be derived using dedicated experiments with conditions similar to those used in the modeling. In Section 11.3 it will be shown that using a single experiment the parameters are not unique.

6.2.4. Multi-kinetic rate model

The equations for the multi-kinetic rate model are similar to the equations of the mass loss of the previous model, but this model allows more than one reaction to be active in the process. The global mass loss is then given by:

$$\frac{dm_p}{dt} = -\sum_i K_i(m_p - f_{v,i} m_{p,0}) \tag{6.26}$$

with the sum extended over each reaction used to describe the devolatilization process.

The kinetic constants K_i are expressed using an Arrhenius rate form:

$$K_i = A_i T_p^{b_i} \, e^{-\frac{E_i}{RT_p}} \tag{6.27}$$

This scheme allows the prediction of products distributions based on kinetics when each product is described by a different kinetic reaction, as in the following list:

$$\text{solid} \xrightarrow{\text{k}_1} \text{H}_2\text{O} \tag{R 6.3}$$

$$\text{solid} \xrightarrow{\text{k}_2} \text{CO}_2 \tag{R 6.4}$$

$$\text{solid} \xrightarrow{\text{k}_3} \text{CH}_4 \tag{R 6.5}$$

$$\text{solid} \xrightarrow{\text{k}_4} \text{CO} \tag{R 6.6}$$

$$\text{solid} \xrightarrow{k_5} H_2 \tag{R 6.7}$$

$$\text{solid} \xrightarrow{k_5} \text{tar} \tag{R 6.8}$$

As pointed out in Section 2.5 the time history of some light species is better predicted if more than one reaction is used. As an example, using the multi-reaction approach, the global reaction R 6.4 can be split into the following three reactions:

$$\text{solid} \xrightarrow{k_{2a}} CO_2 \tag{R 6.9}$$

$$\text{solid} \xrightarrow{k_{2b}} CO_2 \tag{R 6.10}$$

$$\text{solid} \xrightarrow{k_{2c}} CO_2 \tag{R 6.11}$$

Similar scheme can be applied to other components as in [345] and in Table 6.1 the values used for the kinetic parameters are reported. It is worth noticing that the values given in the table, must be used together with a distribution of the activation energy (see the section Section 6.2.5) and they are here given as an example only.

Applied to biomass conversion, this approach allows the split of the fuel into its three main components, cellulose, hemicellulose and lignin:

$$\text{biomass} = \text{cellulose} + \text{hemicellulose} + \text{lignin} \tag{R 6.12}$$

and the reaction rates follow the scheme:

$$\text{cellulose} \xrightarrow{k_a} \text{products} \tag{R 6.13}$$

$$\text{hemicellulose} \xrightarrow{k_b} \text{products} \tag{R 6.14}$$

$$\text{lignin} \xrightarrow{k_c} \text{products} \tag{R 6.15}$$

For this model the rates are temperature dependent and a dependency on the content of gas is also present. While the composition is directly calculated, the total amount of volatile must be still derived from experiments. The advantage of having multiple reactions for each species is described in the following paragraph.

6.2.5. Distributed Activation Energy

The single kinetic model performs well only when the model is used in applications with similar heating rate than the one used for the derivation of the parameter (usually a curve fitting procedure). Following [345] it is possible to show that a unique single kinetic rate is not able to fit properly both the data at law and high heating rate. This happens because pyrolysis is a complex process in which many competitive reactions with different activation energies are involved. If a system with distributed activation energies is fitted with a single kinetic rate, an unreasonably low value of the activation energy is obtained. A simplified model known as distributed activation energy model (DAEM) for determining kinetic parameters for complex reactions such as coal pyrolysis reaction has been firstly proposed in [245, 246]. This model assumes a set of irreversible first-order reactions that have different activation energies. The distribution is often assumed to be a Gaussian function:

$$W(E) = \frac{W_0}{\sigma_i \sqrt{2\pi}} e^{-(E-E_0)^2/2\sigma^2} \tag{6.28}$$

The model has the same performance as the single kinetic rate model, with the advantage

Gas	FG	A	E	σ
CO_2 extra loose	carbonyl	0.56 E+15	30000	$\pm$1500
CO_2 loose	carbonyl	0.65 E+17	33850	$\pm$1500
CO_2 tight		0.11 E+16	38315	$\pm$2000
H_2O loose	hydroxyl	0.22 E+19	30000	$\pm$1500
H_2O tight	hydroxyl	0.17 E+14	32700	$\pm$1500
CO ether loose		0.14 E+19	40000	$\pm$6000
CO ether light	ether O	0.15 E+16	40500	$\pm$1500
HCN loose		0.17 E+14	30000	$\pm$1500
HCN tight		0.69 E+13	42500	$\pm$4750
NH_3		0.12 E+13	27300	$\pm$3000
CH_x aliphatic	H(al)	0.84 E+13	30000	$\pm$1500
CH_4 extra lose	methoxy	0.84 E+13	30000	$\pm$1500
CH_4 loose	mathyl	0.34 E+12	30000	$\pm$2000
H aromatic	H(al)	0.1 E+15	20500	$\pm$6000
CO extra light	ether O	0.2 E+14	45500	$\pm$1500

Table 6.1.: Kinetic rate used in the FG-DVC model for devolatilization of coal [345]

that its applicability can be enlarged at high heating rates even if the fitting has been done with measurements taken at lower heating rates. The disadvantage of the Gaussian distribution is its symmetry, whereas the reactivity distributions inferred from measurements tend to be asymmetric [71]. The asymmetry can be accounted for by replacing the Gaussian distribution with other distributions, for example the one used in [194]:

$$W(E) = \frac{\lambda}{\eta} y^{\lambda-1} e^{-y^{\lambda}} \tag{6.29}$$

with $y = \frac{E-\gamma}{\eta}$, λ is the shape parameter, η is the width parameter, and γ is the activation energy threshold.

The mass loss is given by the following equation:

$$\frac{dm_p}{dt} = -\int A \cdot W(E) T_p^b \, e^{-\frac{E}{RT_p}} (m_p - f_{v,i} m_{p,0}) dE \tag{6.30}$$

A drawback of the model is the necessity to solve a double integral and this mathematical operation can slow down the calculations. Several simplification have been proposed, based on asymptotic expansion for the integral [277, 237].

The distribution of the activation energy is not restricted to a single gaussian function. A double-Gaussian model was developed in [85] assuming that the pyrolysis process occurs in two steps with different kinetic behaviors, the tar and light hydrocarbon gas formation during the primary pyrolysis and the char condensation, cross-linking reactions, and a further gas production during the secondary pyrolysis. In [319] a model in which the pyrolysis is divided into three steps has been also proposed. The first corresponds to the breakage of light bonds and the release of some molecules, the second is the primary pyrolysis, and the third is the secondary pyrolysis. This model has been applied successfully to coals as well to biomass conversion.

6.2.6. Two competing kinetic rates model

A simple model for the description of the temperature dependent yield has been given in [182]. The fuel decomposition is governed by competing reactions having different volatile yields with the reactions contributing to the higher yields have the higher activation energies since an increase in temperature produce an increase in amount of volatiles released.

A mechanism that might show such behavior is the primary decomposition of coal to intermediates that either decompose further to form volatile compounds or form char by a combination of cross-linking, addition and condensation reactions. The decomposition reactions leading to the volatile formation have a higher activation energy than the condensation reactions leading to char formation.

The simple model proposed in [182] consist of two competing reactions, for which the mass losses can be calculated from the differential relation:

$$\frac{dm_1}{dt} = \dot{\mathcal{R}}_1 \alpha_1 m_p = A_1 e^{-(E_1/RT_p)} \alpha_1 m_p \tag{6.31}$$

$$\frac{dm_2}{dt} = \dot{\mathcal{R}}_2 \alpha_2 m_p = A_2 e^{-(E_2/RT_p)} \alpha_2 m_p \tag{6.32}$$

where $\dot{\mathcal{R}}_1$ and $\dot{\mathcal{R}}_2$ are two competing rates active in two different temperature ranges. Both reactions produce volatile and char as product but with two different split. The first reaction is assumed to be dominant at relatively low temperatures leading to the asymptotic volatile yield α_1 and char 1-α_1. At high temperatures the second reaction is assumed to become faster than the first one, requiring that E_2 is larger than E_1, The asymptotic behavior of the second reaction results in larger volatile yields. The total mass loss rate is governed by the following differential equation:

$$\frac{dm_p}{dt} = \frac{dm_1}{dt} + \frac{dm_2}{dt} = \left(\alpha_1 \dot{\mathcal{R}}_1 + \alpha_2 \dot{\mathcal{R}}_2\right) \cdot m_p \tag{6.33}$$

For a constant temperature an analytical solution exist and it is given by:

$$\frac{m_p(t)}{m_{p,0} - m_a} = \int_0^t \left(\alpha_1 \dot{\mathcal{R}}_1 + \alpha_2 \dot{R}_2\right) e^{\left(-\int_0^s \dot{\mathcal{R}}_1 + \dot{R}_2\right) dz} ds \tag{6.34}$$

Little physical significance should be given to the constants in the model. It should be noted, that the model reduces to a single reaction at relatively low temperature where the second reaction is negligibly slow. Therefore kinetic parameters for the first reaction are uniquely specified under relatively low temperature conditions. This allows the utilization of available kinetic parameters based on a single reaction model for the first reaction leaving two parameters to be evaluated at higher temperatures.

6.2.7. Multi-steps model (IFRF model)

The multi-steps model developed by the IFRF [408] is an example of the family of pyrolysis models in which kinetic effects are discarded and the gas released during devolatilization is only a function of the particle temperature. The model predicts the yield of devolatilization Ψ_v in the following way:

$$\Psi_v = F(T_p) \tag{6.35}$$

where the choice of IFRF has been to use for the function $F(T_p)$ a two steps piecewise linear function:

$$\Psi_v(T_p) = \begin{cases} 0 & T_p \leq T_l \\ \Psi_{ig} + \frac{T_p - T_l}{T_{ig} - T_l} & T_l \leq T_p \leq T_{ig} \\ \Psi_{ig} + (\Psi_h - \Psi_{ig}) \frac{T_p - T_{ig}}{T_h - T_{ig}} & T_{ig} \leq T_p \leq T_h \\ \Psi_{HT} & T_p \geq T_h \end{cases} \tag{6.36}$$

The temperatures T_l T_{ig}, and T_h are typically independent from the fuels. The yield at the ignition temperature T_{ig} is calculated following the relation:

$$\Psi_{ig} = \frac{E_{ig}}{LCV_{vol}} \tag{6.37}$$

where E_{ig} is the volatile energy at ignition and LCV_{vol} is the Low Calorific Value of the Volatile. The volatile energy at ignition is obtained from fuel characterization experiments.

The model is implemented into a CFD solver using the mass loss per unit of time. From equation 6.35 it is possible to derive the following equation:

$$\frac{dm_p}{dt} = \frac{dF(T_p)}{dT_p} \cdot \frac{dT_p}{dt} \tag{6.38}$$

where the differential mass loss is linked to the heating rate of the particle. The calculation of the heating rate $\frac{dT_p}{dt}$ is presented in equation Section 10.3.

The IFRF model is easy to implement and it works properly in pulverized coal combustion applications. Its main objective is a rate temperature dependent with a final yield that is also temperature dependent.

6.2.8. Semi-global pyrolysis models

Models belonging to the semi-global group, try to predict the behavior of the solid fuels using more fundamental steps in order to minimize the amount of fuel specific parameters. The complexity of the mathematical description is therefore increased.

The application of this idea to coal devolatilization has been successfully performed in [349] where each specific fuel is considered a linear combination of several reference fuels, namely pure carbon, and two reference coals: a lignite with high oxygen content ($coal_3$) and a reference coal without oxygen and particularly rich in hydrogen ($coal_1$). A third reference coal ($coal_2$) has been selected close to a number of bituminous coals. These reference coals can be described by three lumped or equivalent monomer structures which stand for reference configurations, saving the elemental C/H/O composition. The reference monomers which represents $coal_1$ is ($C_{12}H_{11}$), the one for $coal_2$ is ($C_{14}H_{10}O$) and for $coal_3$ ($C_{12}H_{12}O_5$). The $coal_1$ is considered as a 50/50 mol mixture of ($C_{12}H_{10}$) and ($C_{12}H_{12}$). The monomers from $coal_1$ to $coal_3$ are richer in side chains and posses less and less aromatic structures. The multi-step kinetic model describes the pyrolysis of these reference coals.

At low temperatures (or low heating rates), the reference coals initially form char and volatile species (tar^* and gas^*), which still are in the condensed phase. The tar^* in the condensed phase can be released from the fuel or can interact with the char structure in cross-linking reactions, which increase the residual char and produce further gas.

The following reactions are typical for many fuels [349]:

$$\mathrm{coal}_1 \longrightarrow 5\,\mathrm{char_H} + 0.1\,\mathrm{char_C} + 0.2\,\mathrm{H_2} + 0.9\,\mathrm{CH_4} + \mathrm{C_{2-5}} \tag{R 6.16}$$

$$\mathrm{coal_1} \longrightarrow \mathrm{tar_1^*} \tag{R 6.17}$$

$$\mathrm{tar_1^*} \longrightarrow \mathrm{tar_1} \tag{R 6.18}$$

Light hydrocarbon gases are H_2, CH_4 and a mixture of C_2-C_5 hydrocarbons lumped as a single pseudo-components with the equivalent formula (CH_2). as well as oxygenated products CO, CO_2 and H_2O. The other oxygenated species, namely formaldehyde, methanol, (both lumped into O_xC) ketene, and acetic acid (lumped into BTX group) are produced in smaller concentrations [2]. A typical example:

$$\mathrm{tar_1^* + char_H} \longrightarrow 5.3\,\mathrm{char_H} + 3\,\mathrm{char_C} + 2.55\,\mathrm{H_2} + 0.4\,\mathrm{CH_4} \tag{R 6.19}$$

$$\mathrm{tar_1^* + char_C} \longrightarrow 4.3\,\mathrm{char_H} + 4\,\mathrm{char_C} + 2.55\,\mathrm{H_2} + 0.4\,\mathrm{CH_4} \tag{R 6.20}$$

Lignite coals ($coal_3$) first move through an activate state in the condensed phase and then undergo a real decomposition reaction:

$$\mathrm{coal_3} \longrightarrow \mathrm{coal_3^*} \tag{R 6.21}$$

$$\mathrm{coal_3^*} \longrightarrow 1.5\,\mathrm{char_H} + 0.82\,\mathrm{char_C} + 2.08\,\mathrm{CO} + .25\,\mathrm{O}_x\mathrm{C} + ... \tag{R 6.22}$$

The hydrocarbon gases and pseudo-species trapped in the metaplast are all released with the same rate.

One of the first study of semi-global pyrolysis model applied to biomass has been proposed in [178] who studied in particular detail the thermal degradation of cellulose. The Author proposed that a general biomass fuel can be represented into the following form

biomass = α cellulose + β lignin + γ hemicellulose

As a consequence, the devolatilization mechanism is expressed in the following way:

$$\mathrm{cellulose} \longrightarrow \mathrm{anydrocellulose} \tag{R 6.23}$$

$$\mathrm{anhydrocellulose} \longrightarrow \mathrm{gas} + \mathrm{char} \tag{R 6.24}$$

$$\mathrm{cellulose} \longrightarrow \mathrm{tar} \tag{R 6.25}$$

The decomposition starts at around $\theta \approx 200°\mathrm{C}$ with endothermic internal water elimination to produce anhydrocellulose. At higher temperature cellulose decompose in tar while the anhydrocellulose decompose to form lighter gas and char as a remnant.

A similar decomposition scheme for cellulose has been proposed in [59], where the place of anhydrocellulose has been taken by a more general active cellulose group of molecules. The mechanism is divided into two main paths. The first path is active at low temperatures, and involves reduction in the degree of polymerization by bond rescission, appearance of radicals,

[2] formaldehyde: 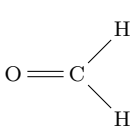 methanol: 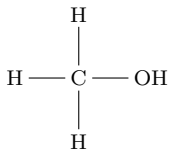 ketene: 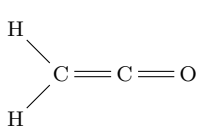 acetic acid: 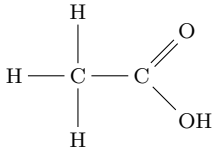

elimination of water and formation of gas and char. As soon as temperature increases, the tar formation reactions became more an more important.

$$\text{cellulose} \longrightarrow \text{active cellulose} \tag{R 6.26}$$

$$\text{active cellulose} \longrightarrow \text{tar} \tag{R 6.27}$$

$$\text{active cellulose} \longrightarrow \text{gas} + \text{char} \tag{R 6.28}$$

Both cited mechanisms predicts a temperature dependence for the char formation, with the amount of char decreasing with the increase of the temperature.

In [5] a different mechanism was proposed:

$$\text{cellulose} \longrightarrow \text{gas} \tag{R 6.29}$$

$$\text{cellulose} \longrightarrow \text{tar} \tag{R 6.30}$$

$$\text{cellulose} \longrightarrow \text{char} \tag{R 6.31}$$

based on the observation that the yield of gas and char are linked in the same way to the temperature and therefore the ratio is temperature independent.

For lignin, in [11] the following mechanism has been proposed:

$$\text{lignin} \longrightarrow \text{gas} + \text{char} \tag{R 6.32}$$

$$\text{lignin} \longrightarrow \text{tar} \tag{R 6.33}$$

$$\text{lignin} \longrightarrow \text{gas} + \text{reactive vapors} \tag{R 6.34}$$

where low temperature processes, producing gas and char, are active at low temperature.

In general, for all the model previously described, secondary reactions describe the cracking and the repolymarization of tar into lighter gas and char.

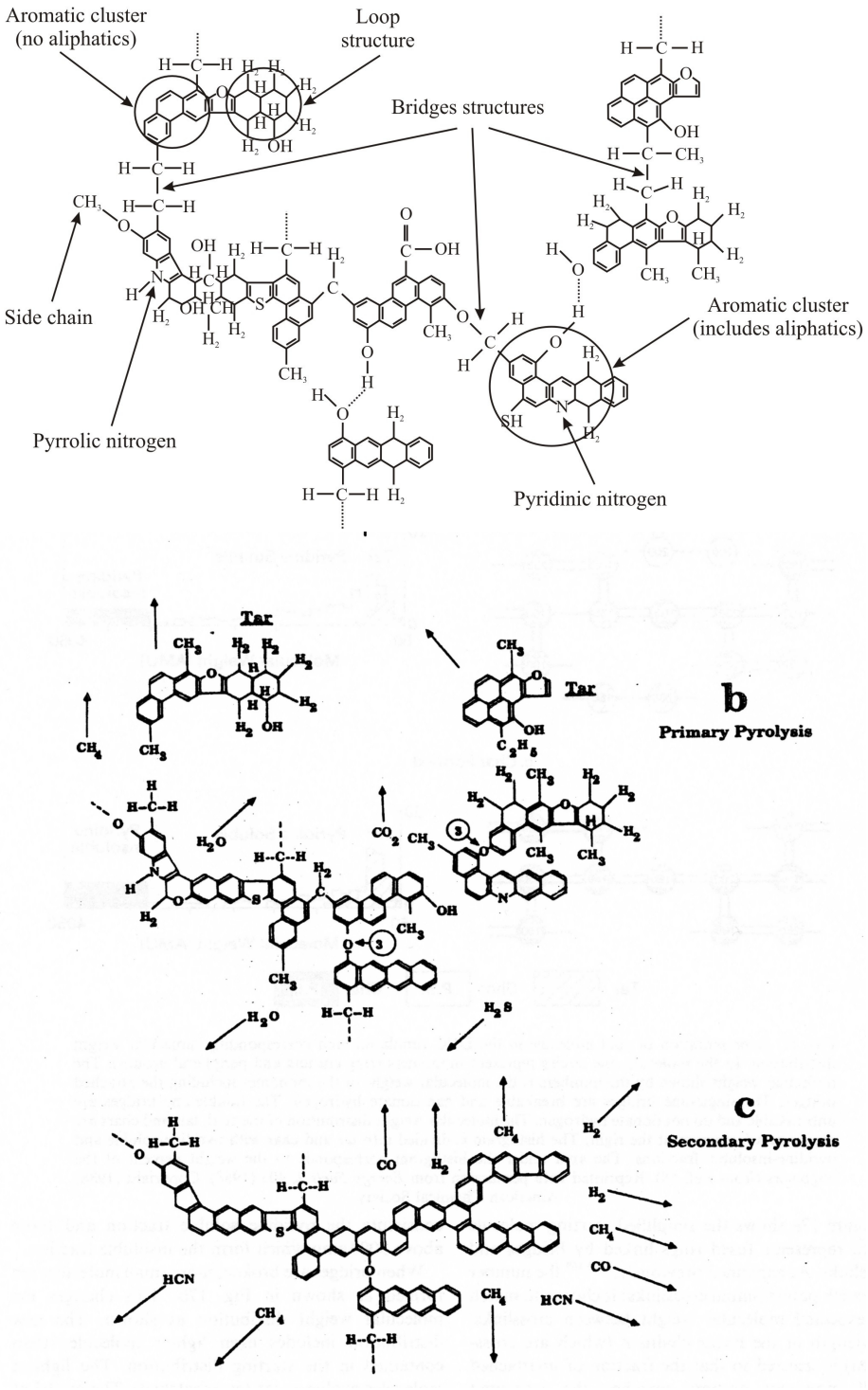

Figure 6.1.: Fuel structure and devolatilization steps as assumed in [111]

6.2.9. Detailed pyrolysis models

The most detailed theories for pyrolysis and devolatilization have the purpose of being able to predict light gas, char and tars fractions as well as their compositions (light molecules for the light gases and a molecular distribution for the tar fraction). They attempt to cover a wide spectrum in operating conditions (temperature, heating rate and pressure) for most of the fuels available for industrial applications. These models assumes that the variations among fuels are caused by the different chemical structure while the chemistry is coal independent.

The most known detailed models for pyrolysis are:

- The Chemical Percolation Devolatilization (CPD) model [132]
- The distributed-energy chain statistics (DISCHAIN) model [259]
- The Functional Gropus Devolatilization Vaporization Conversion (FG-DVC) model [344]

The CPD model uses percolation theory [3] and it has the capability of predicting total volatiles and tar yields on the base of heating rate, temperature, pressure and coal type. It consists of five principal components:

1. Description of the parent fuel structure;
2. Bridge reaction mechanism with associated kinetics;
3. Percolation lattice statistics to determine the relationship between bridge breaking and detached fragments (these fragments are tar precursor);
4. Vapor-liquid equilibrium mechanism to determine the fraction of liquids that vaporize;
5. Cross-linking mechanism for high molecular weigh tar precursors to reattach to the char.

The fuel is represented by a lattice of four generic structural components: aromatic nuclei, labile bridges, char links, and side chains as shown in Figure 6.1 Aromatic nuclei are non reacting units with the characteristics of the hypothetical aromatic cluster based on 13C NMR analysis. Except for HCN production from their nitrogen, nuclei are immutable. Nuclei are interconnected by two types of linkages: labile bridges or char links. Labile bridges contain all the oxygen, sulfur, and aliphatic carbon, but no aromatic components. Char links are non reacting completely aromatic with no heteroatoms. Peripheral groups are the remnants of broken bridges having the same composition. Attached to the rings, side chains are responsible for the chemical stabilization of the rings. From the chemical point of view the fuel is seen as an ensemble of functional groups that are organized into tightly bound aromatic ring clusters and are connected by bridges. Reaction rates are different for each functional groups but are relatively insensitive on the rank of the fuel.

Modeling of bridges reactions and the generation of light gas, char, and tar precursors is described by the scheme shown in Figure 6.2. where the variable $\pounds$ represents the original population of labile bridges in the lattice. Upon heating, these bridges become the set of reactive bridges. For the reactive bridges $\pounds^*$, two competing paths are available. In one path, the bridges react to form side chains, δ_i. The side chains may detach from the aromatic clusters to form light gases, $g_{1,i}$. As bridges between neighboring aromatic clusters are broken, a certain fraction of the coal becomes detached from the coal lattice. These detached aromatic clusters are the heavy-molecular-weight tar precursors that form the metaplast. The metaplast vaporizes to form

[3] The percolation theory is a branch of the mathematics that describes the properties of connected clusters in a random graph using statistical methods.

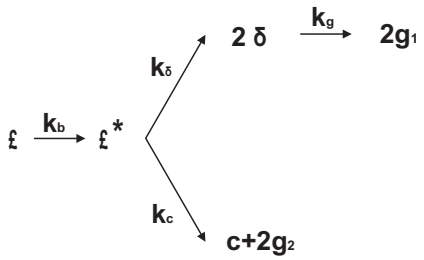

Figure 6.2.: Scheme of the coal behavior during devolatilization process as a simplified network of chemical bridges [111]

coal tar. While waiting for vaporization, the metaplast can also reattach to the coal lattice matrix (crosslinking). In the other path, the bridges react and become a char bridge, c, with the release of an associated light gas product, $g_{2,i}$. The total population of bridges in the coal lattice matrix can be represented by the variable p, where $p = \pounds + c$.

Given this set of variables that characterizes the coal lattice structure during devolatilization, reaction rates can be defined for the following processes:

1. formation of a reactive bridge intermediate from a labile bridge (k_b is reaction rate)
2. formation of a char bridge and gas from the reactive intermediate (k_c is reaction rate)
3. formation of a side-chain from the reactive intermediate (k_δ is reaction rate)
4. conversion of side chains into light gases ($k_{g,i}$ are reaction rates)

With the assumption that the reactive bridges are destroyed at the same rate at which they are created $\pounds^* = \pounds \frac{k_b}{k_\delta + k_c}$ the equations are written as:

$$\frac{d\pounds}{dt} = -k_b \pounds \tag{6.39}$$

$$\frac{dc}{dt} = k_b \frac{\pounds}{\rho + 1} \tag{6.40}$$

$$\frac{d\delta_i}{dt} = [2\rho k_b \cdot \frac{\pounds}{\rho + 1}] - k_{g,i}\delta_i \tag{6.41}$$

$$\frac{dg_{1,i}}{dt} = k_{g,i}\delta \tag{6.42}$$

$$\frac{dg_2}{dt} = 2\frac{dc}{dt} \tag{6.43}$$

where the rate constants for bridge breaking and gas release steps, k_b and $k_{g,i}$, are expressed in Arrhenius form with a distributed activation energy:

$$k = A \cdot \exp\left(-(E \pm E_\sigma)/RT\right) \tag{6.44}$$

The parameters A, E, and E_σ are, respectively, the pre-exponential factor, the activation energy, and the distributed variation in the activation energy; R is the universal gas constant, and T is the temperature and $\rho = \frac{k_\delta}{k_c}$ A total of 19 first-order, distributed-energy rate expressions for the release of various light gases have been provided [172]. It is not practical, however, to extend this kind of comprehensive approach for gas release to the production of tar with its very large

number of unique molecular species. Thus, tar production is modeled as a single first-order, distributed-energy rate expression with chain statistics and with lattice statistic.

It is worth noticing that the N_2 is released during primary devolatilization in two ways [122]. Firstly nitrogen contained in the aromatic clusters is transported away as large aromatic tar molecules escape the lattice (this is often the primary mode of nitrogen release during devolatilization). Additional nitrogen can be released as HCN and NH_3 after the rupture of aromatic rings. Nitrogen is first released as HCN for most coals, with some primary NH_3 from low-rank coals and biomass. Additional NH_3 can also be formed from subsequent reactions with H_2 in the char. In this model nitrogen is released primarily with tars and the kinetics of HCN and NH_3 are described using by first order kinetic with distributed activation energy [4]. In [258] an extra variable η is introduced. This variable monitors the average mole of N per aromatic cluster. Its change reproduces the measured effect of reduced HCN in large aromatic clusters present in high rank coals. The simple first order reaction, even with the distributed activation energy, is not able to reproduce the amount of stable nitrogen remaining into the char. This quantity is coal dependent and is strongly affected by heating rate dependent chemistry taken into account with correlations (see [122] for more results).

The fuel structure parameters, must be expressed as functions of coal mass changes and related release of volatile products. The fractional change in the coal mass as a function of time is divided into three parts: light gases ($f_{gas,i}$), tar precursor fragments (f_{frag}), and char (f_{char}). The variables given in the above differential equations may be related now to the mass of the individual sites and bridges. The masses on a per lattice site basis are expressed as follows [132]. The total mass is expressed by:

$$m_{total}(t) = m_a + m_b \cdot (1 - c_0)(\sigma + 1)/2 \tag{6.45}$$

where m_a and m_b are the averaged mass of a cluster and the mass of the bridges, respectively [5]. The mass of the gas released up to time t is expressed by [6]:

$$m_{gas,i} = m_b \cdot g_i \cdot \frac{\sigma + 1}{4} \tag{6.46}$$

Finally the total mass of tar clusters of size n is given by:

$$m_{frag,n}(t) = \left[n \cdot m_a + (n-1) m_b \left(\frac{\pounds}{p} + \tau \cdot m_b \left(\frac{\delta}{4}(1-p) \right) \right) \right] Q_n(p) \tag{6.47}$$

where $Q_n(p) = \frac{F_n(p)}{n}$ is the number of n-site clusters, expressed on a per site basis and p is the fraction of still intact bridges. The first term take into account the average molecular weight of the n-sites in a cluster. The second term gives the molecular weight for the mass of the bonds still intact as labile bridges multiplied by the fraction of intact labile bridges. The third term gives the molecular weight of side chains to be released as gas and is calculated from the fraction of side chains times the number of broken bridges tau. The total tar mass is obtained by summing over

[4] In [24] it has been observed that in slow heating rates experiments production of NH_3 is relevant and the production of HCN proceed the production of NH_3. It has been proposed that only HCN is produced from the coal structure and only in the pores HCN reacts heterogeneously to NH_3.

[5] The $\frac{\sigma+1}{2}$ term is the ratio of bridges to sites and converts a bridge parameter such as $1 - c_0$ into a site quantity

[6] The fraction of bridges that have been released as gas must be converted into a site variable by the factor $\frac{\sigma+1}{2}$ and an additional factor of is inserted to convert the mass of the bridges m_b into the half-bridge mass assigned to the average mass of side chains and of light gases released

the various finite clusters:

$$m_{frag}(t) = \Phi m_a F(p) + \Omega m_b K(p) \tag{6.48}$$

and it is accomplished by relationships obtained using percolation lattice statistics.

The variables Φ, Ω, $F(p)$ (total fraction of sites with p is the fraction of intact bridges), and $K(p)$ are the statistical relationships related to the cleaving of bridges based on the percolation lattice statistics, and are given by the following equations:

$$\Phi = 1 + r\left[\frac{\pounds}{p} + \frac{(\sigma-1)\delta}{4(1-p)}\right] \tag{6.49}$$

$$\Omega = \frac{\delta}{2(1-p)} - \frac{\pounds}{p} \tag{6.50}$$

$$F(p) = \left(\frac{p'}{p}\right)^{\frac{\sigma+1}{\sigma-1}} \tag{6.51}$$

$$K(p) = \left[1 - \left(\frac{\sigma+1}{2}\right)p'\right]\left(\frac{p'}{p}\right)^{\frac{\sigma+1}{\sigma-1}} \tag{6.52}$$

r is the ratio of bridge mass to site mass, m_b/m_a, and:

$$m_b = 2M_{\delta_i} \tag{6.53}$$

$$m_a = M_{cl} - (\sigma+1)M_{\delta_i} \tag{6.54}$$

M_δ and M_{cl} are the side chain and cluster molecular weights respectively; $\sigma+1$ is the lattice coordination number (alkyl groups and oxygen functional groups) which is determined from solid state Nuclear Magnetic Resonance (NMR) measurements related to coal structure parameters, and p' is the root of the following equation in p (the total number of intact bridges in the coal lattice matrix):

$$p'(1-p')^{\sigma-1} = p(1-p)^{\sigma-1} \tag{6.55}$$

The mass fraction of gas $f_{gas}(t) \equiv \frac{m_{gas}}{m_{total}}$, fragments $f_{frag} \equiv \frac{m_{frag}}{m_{total}}$ and char can be expressed as a function of the dynamic variables:

$$f_{gas,i}(t) = \frac{r(g_{1,i}+g_{2,i})(\sigma+1)}{4+2r(1-c_0)(\sigma+1)} \tag{6.56}$$

$$f_{frag}(t) = \frac{2}{2+r(1-c_0)(\sigma+1)}\left[\Phi F(p) + r\Omega K(p)\right] \tag{6.57}$$

$$f_{char}(t) = 1 - f_{gas}(t) - f_{frag}(t) \tag{6.58}$$

In accounting for mass in the metaplast (tar precursor fragments), the part that vaporizes is treated in a manner similar to flash vaporization, where it is assumed that the finite fragments undergo vapor/liquid phase equilibration on a time scale that is rapid with respect to the bridge reactions [7]. Tar is generated when the fragments become small enough to vaporize into the

[7] The phenomenology invokes an analogy between coal devolatilization and the steam distillation of petroleum. When steam is bubbled through a barrel of crude oil, the lightest fractions pass into the vapor and are transported away with bubbles breaking through the surface of the petroleum. But the material with high molecular weight remains in the liquid phase and condenses into coke if the temperature exceeds a certain threshold value. The role of the steam is played by the noncondensable gases produced whenever aliphatic components are partially converted into stable char

escaping noncondensible gases. Char forms by crosslinking among heavier fragments in the condensed phase, whose further depolymerization is suppressed whenever labile connections are converted into stable char links. Noncondensible gases are produced as a by-product of charring. All this chemistry occurs in the condensed phase, so no redeposition from the gas phase is involved.

As an estimate of the vapor/liquid that is present at any time, a vapor pressure correlation based on a simple form of Raoult's Law is used. The vapor pressure treatment is largely responsible for predicting pressure dependent devolatilization yields. For the part of the metaplast that reattaches to the coal lattice, a cross-linking rate expression given by the following equation is used:

$$\frac{dm_{cross}}{dt} = m_{frag} A_{cross} e^{-(E_{cross}/RT)} \tag{6.59}$$

where m_{cross} is the amount of mass reattaching to the matrix, m_{frag} is the amount of mass in the tar precursor fragments (metaplast), and A_{cross} and E_{cross} are rate expression constants.

In [123] a non linear correlation has been developed allowing the calculation of the structural parameters needed as model inputs as a function of the ultimate composition of the parent coal. This more complex model explain both, the observed heating rate dependencies and those pressure dependent.

Thermal history effects Thermal history effects are based on the heterogeneity of the fuels namely on the structure of the lattice. A distribution of activation energies for the depolymerization chemistry is responsible for the broad thermal response of the fuel, and explains why asymptotic volatiles yields are dependent on the pyrolysis temperature. But competitive char formation chemistry is needed to explain the proportions of tar and gas from coals of different rank [260]. Heating rate also affects the rate, yields, and composition of volatiles. As the heating rate is increased, the onset of devolatilization moves to higher temperatures and the devolatilization rate increases in rough proportion to the heating rate. Rapid heating enhances yields at lower pressures by delaying the generation of primary fragments until higher temperatures are achieved, where more of the heavier fragments are expelled as tar. Consequently, tar becomes more abundant and heavier as heating rates are accelerated and gas yields decrease because the additional tar shuttles away precursors to noncondensibles. But at elevated pressures, the heavier tar fragments cannot vaporize so the heating rate enhancements diminish. Some of the fragment mass is retained in the char, while the rest is released as noncondensible gases.

According to the flash distillation analogy, the phase equilibrium shifts to retain a larger portion of the lighter fragments in the condensed phase as the pressure is increased. Consequently, tar prepared at higher pressures becomes lighter and the tar yield diminishes. The fragments retained in the char also contain precursors to noncondensible gases which are eventually released, so gas yields increase as the pressure is elevated, but not by enough to compensate for the retention of tar precursors.

6.2.10. Summary

In Table 6.2 the capabilities of each model previously analyzed are summarized. The important properties needed in an accurate CFD calculation are the following:

1. Temperature dependent rate;

2. Conversion dependent rate;

links.

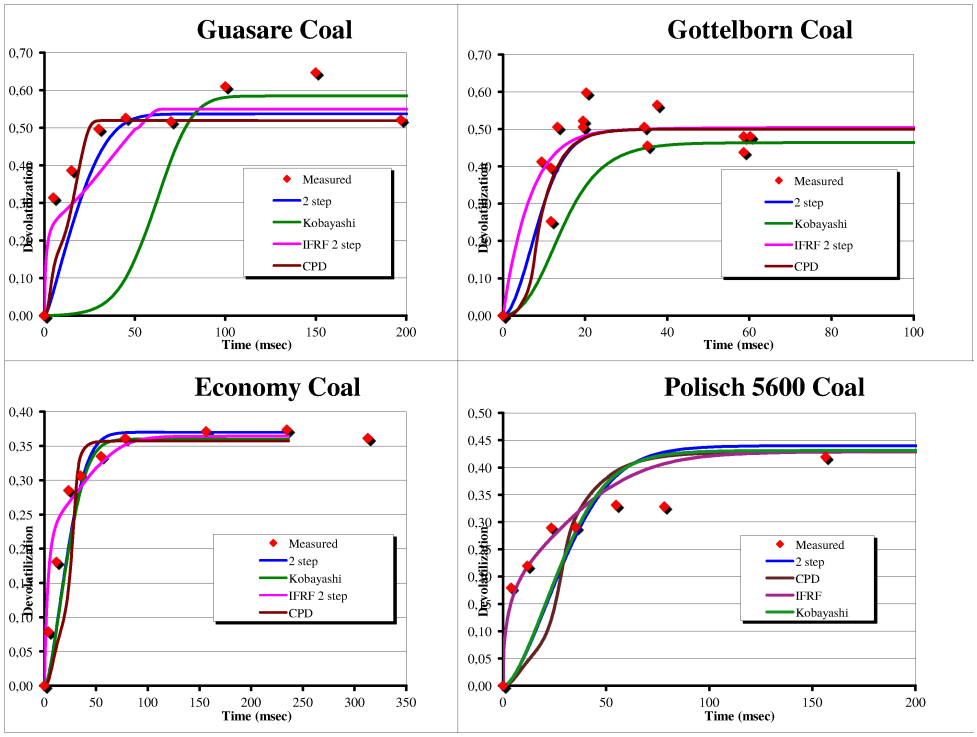

Figure 6.3.: Examples of fitting results for the devolatilization of four different coals

3. Yield temperature dependent;
4. Splitting between light gases and tars;
5. Composition of products;

Model		Rate(T)	Conversion(T)	Yield(T)	Tar	Gas Composition
constant	Section 6.2.1	No	No	No	No	No
Single	Section 6.2.2	No	Yes	No	No	No
Linear	Section 6.2.3	Yes	Yes	No	No	No
Competing	Section 6.2.6	Yes	Yes	Yes	No	No
IFRF	Section 6.2.7	Yes	Yes	Yes	No	No
Semi-global	Section 6.2.8	Yes	Yes	Yes	Yes	No
CPD	Section 6.2.9	Yes	Yes	Yes	Yes	Yes

Table 6.2.: Summary of the properties of several devolatilization models

6.3. Some examples

The fitting of several devolatilization experiments using models explained in this Chapter are shown below..

Mass loss In Figure 6.3 the fitted curves are compared with devolatilization experiments taken at the IFRF drop tube (see Chapter 11 for the description of the fitting method). The following models are used for the fitting:

1. a pure kinetic model (see Section 6.2.2);
2. a two competing reaction models (the Kobayashi model, see Section 6.2.6);
3. the CPD model (see Section 6.2.9);
4. the 2-steps model developed at the IFRF (see Section 6.2.7).

All the models predict fairly well the devolatilization history of all the coals but few comments must be added:

1. The experimental data at early times are not corrected from the uncertainty explained in Section 11.4.4. The higher mass loss due to the cooling produces in the experiments is the cause of the under-prediction at the early measurements points shown by almost all the models. Only the model used at the IFRF has the capability to predict high yield at low temperature.
2. For the fittimg of the Guasare coal, the Kobayashi model has been used taking both activation energies constant, as given in the original paper [182]. The comparison with the measured data shows that those activation energies are too high and the predicted devolatilization rate too low. In the aforementioned paper, the experiments from which the activation energies are derived have been performed with a relative low heating rate, explaining the lower devolatilization rate. If the activation energies are allowed to change (as in Section 11.4.2) the competing rate is able to predict variations with the devolatilization temperature.

Gas-tar splitting Predicted [121] and measured mass loss and Tar yields (reported by [430]) are reproduced in Table 6.3. The coal selected belong to a set with a broad range of carbon content. The comparison shows that the trend of both, the mass loss and the tar yield are well reproduced by the model.

Effects of the heating rate In Figure 6.4 predictions of the pyrolysis product distribution as a function of the heating rate for Göttelborn coal (high volatile bituminous coal with 80 % C) are shown. The calculations have been performed using the CPD model. Increasing the heating rate the amount of char decreases and the amount of tar increases. It is worth noticing that in the case of Göttelborn coal the measurements performed at the IFRF gave the following values for the yield: Char 51.2%; Volatiles 48.8%.

The total pressure dependency is shown in Figure 6.5 [172]. Increasing the pressure, tars release decreases while the amount of char increases. The model predict well this dependency.

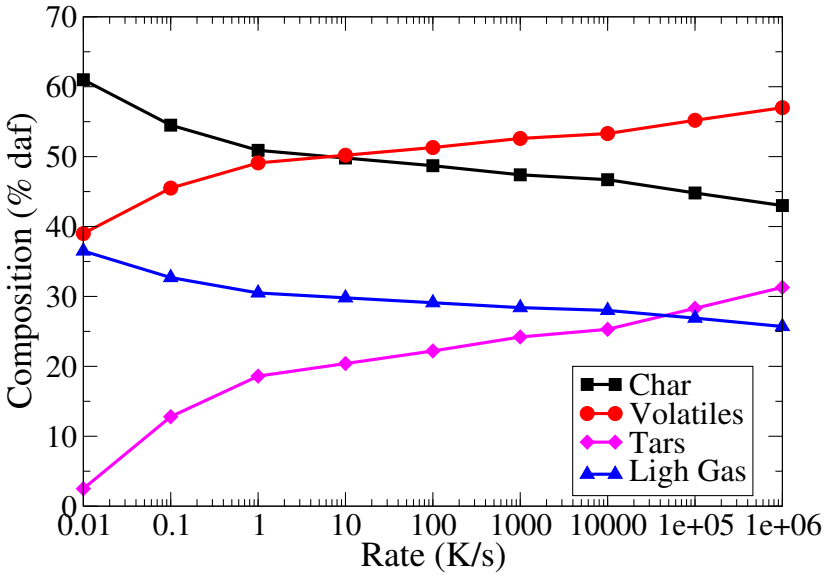

Figure 6.4.: Prediction of the product distribution as a function of the sample heating rate in the case of Göttelborn coal (hvb)

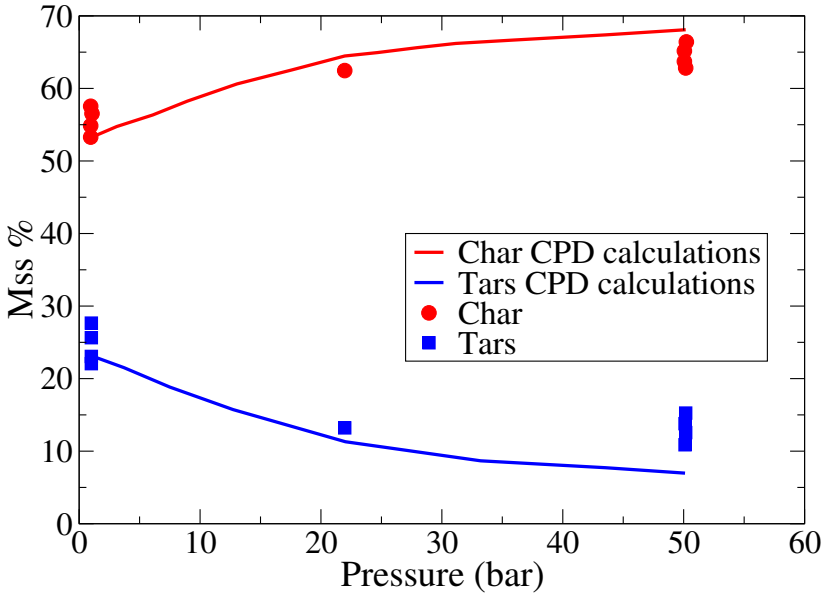

Figure 6.5.: Effect of pressure on the char and tar yields from Illinois No. 6 coal [172]

	Mass release		Tar yield	
coal	experimental	CPD	experimental	CPD
Yallourn	51.0	51.2	19.9	15.8
Rhein Braun	52.5	48.6	22.1	18.4
Morwell	55.5	51.1	25.6	14.8
Velva	48.5	53.0	17.9	15.0
Soyakoishi	49.0	50.5	20.9	16.6
South Beulah	47.0	54.2	16.8	17.0
Colowyo	41.5	50.2	19.3	16.2
Taiheiyo	53.0	47.7	29.6	24.6
Millmerran	51.5	46.4	29.8	24.4
Wandoan	52.0	51.0	27.9	25.5
Hunter Valley	38.0	50.1	21.9	22.0
Liddell	39.5	47.5	22.2	26.0
Newvale	35.5	46.8	19.4	24.2
Yubari Shinko	38.0	37.6	22.0	20.8
Vicary Creek	24.5	23.5	11.7	8.0
Keystone	17.0	12.8	8.1	3.7
Hongay	6.0	4.4	2.6	2.1

Table 6.3.: Comparison gas and tar yield from measurements [430] and calculations [121]

7. Modeling of fuel structure

Since solid fuels are porous materials, the macromolecular structure and its development during devolatilization and the following char reactions are as important as the chemical processes that are causing the fuel conversion. In this Chapter, several approaches used to describe the fuels pore structure and its development during conversion are described.

7.1. The pore structure

During pyrolysis, the porosity, the surface area and the density of the coal particle change significantly, which in turn influence the heterogeneous reaction rate of the char and the ash formation. All these properties are important for both, pyrolysis and char combustion. Below the modeling relevant to pyrolysis will be summarized, leaving to Chapter 8 a further discussion about aspects relevant to char reactions. For correct predictions of fuel conversion in a broad range of conditions, it is imperative that those properties can be adequately predicted and to this sake, several models for particle pore structure have been developed:

Isolated pore models [373, 419] in which all pores are identical cylinders extending through all the particle. The pores are randomly oriented, but they do not intersect. This restriction prevents the possibility to describe the evolution of the internal surface area as a function of the particle burnout with sufficient accuracy.

Random pore models [144, 145, 118, 119, 35, 36] are similar to the previous models but they take into account the interaction between different pores. The internal surface area and the mass transport inside the pores are obtained using the single pore model with the effects of pore interactions taken into account by integration over a distribution function for the pore dimensions. In [118] and in [35] the distribution is a known function while in [144] the distribution is not known and the closure is achieved using the momentum method. The random pore models are quite successful in the prediction of the evolution of the internal area as a function of the burnout, but they do not consider that pores are connected into a specified branching sequence which permits the gas to diffuse from one pore to the others.

Lattice models The lattice pore model account for a specified branching sequence which allows diffusion from one pore to the other [143]. This kind of models, however, are successful if the pore size distribution is narrow. In the case of coal and biomass, where the distribution is broad [327], several parameters must be inserted into the model to have a better prediction of the internal area evolution.

Pores tree models The pore tree model has been developed in [329] and [334]. It is basically a random pore model where a single pore is not described by a standard cylindrical geometry, but it is described by a structure leading to smaller pore attached to it.

The models mentioned above are used to describe the static pore structure. During conversion the following physical mechanisms drive changes and the structure evolution must be considered into the mathematical modeling [331, 330]:

Bulk growth The existing pores grow because of the breaking of the bonds of the solid structure;

Combination The destruction of small pores (and eventually the generation of large pores) due to the growing of larger pores into materials containing smaller pores;

Exposure Formation of small pores due to the opening of closed pores;

Generation Creation of small pores due to the release of solid matter.

Among all solid fuels, the pore structure of lignite coals changes in a different way [210]. During devolatilization, most particles become plastic and swell. However, because the content of metaplast in the particle of lignite during pyrolysis is small, the diameter of lignite changes little during pyrolysis with no thermoplastic deformation and some kinds of lignites are classified as nonswelling coals.

Particle porosity increases during pyrolysis because of mass release and the opening of closed pores while surface area changes little with mass release up to about 30%. For higher mass losses both, porosity and surface are strongly increased. With the maximum particle temperature increasing from 900 to 1200 K, it is observed that the predicted porosity of char formed during pyrolysis increases. However, with further increase of the maximum particle temperature, the predicted porosity and area change little. The influence of heating rate and ambient pressure on the change of pore structure during pyrolysis is small and the initial coal structure alone significantly influences the final pore structure of the char.

7.1.1. The single pore model

Aromatic clusters and bridges surround the closed pores. When the bridges are broken, the closed pores are opened and become part of open pores. The following linear relationship [210] describes the enlargement of the porosity caused by the opening of the closed pores:

$$\theta_{opening} = f_{PC}^{0}(1-\theta_0)\left(1-\frac{p}{p_0}\right) \tag{7.1}$$

where f_{PC}^{0} represents the initial volume fraction of closed pores, θ_0 represents the initial porosity of the coal particle, and p and p_0 represent the fraction of intact bridges and its initial value, respectively.

The following two equations describe the porosity expansion caused by the generation of gas and tar:

$$\theta_{gas} = f_{gas}(1-\theta_0)(1-f_{PC}^{0})\left(1-a_{dry}\right) \tag{7.2}$$

$$\theta_{tar} = f_{tar}(1-\theta_0)(1-f_{PC}^{0})\left(1-a_{dry}\right) \tag{7.3}$$

where f_{gas} and f_{tar} represent the yield of gas and tar on a dry ash-free basis, respectively, and a_{dry} represents ash content on a dry basis (see equations 6.56, 6.57 and 6.58).

The internal surface S_{int} is the surface available to molecules adsorbed in a single layer during adsorption. They can be N_2 or CO_2 as in the case of measurements or O_2, CO_2 and H_2O in the case of conversion. The following relation expresses the surface S_{int}:

$$S_{int} = S_a N_A n_a \tag{7.4}$$

where S_a represents the adsorption cross-section of the adsorbing species, N_A is the Avogadro's number, and n_a represents the moles of adsorbed molecules. During pyrolysis, the positions in

the macromolecular array originally occupied by volatile molecules are emptied and transformed into pores. However, not all the spaces left by volatiles can increase the surface area. Only the spaces on the surface of solid that are big enough for adsorbates to come in can be measured in the monolayer molecular adsorption. Therefore each space left in the particle by the gas after stabilization of a broken side chain (g_2) is filled by a char bridge and is not big enough to adsorb molecules. Differently, the light molecules g_1 are big enough for one adsorbent molecule to move in. The quantity of g_1 spaces attached to each aromatic cluster is given by:

$$N_{cluster}^{g_1 space} = \frac{g_1}{2}(\sigma + 1) \tag{7.5}$$

Considering that the fraction of pores from light gas spaces is estimated as:

$$f_{g_1} = \frac{g_1}{g_1 + \delta} \tag{7.6}$$

it follows that the quantity of pores consisting of two g_1 spaces that can adsorb, per aromatic cluster, is calculated as follows:

$$N_{cluster}^{ap} = \frac{g_1^2(\sigma + 1)}{4(\delta + g_1)} \tag{7.7}$$

Considering that tar is created when all the light bonds around it are broken, this process creates light molecules g_1 therefore the amount of available space for pores has been already included into 7.7. Extra spaces is anyway accounted for, being the tar molecules bigger that the g_1 spaces:

$$N_{cluster_{coal}} = (1 - a_{dry}) \left(\frac{1}{M_{cl}} - N_{cluster_{tar}} \right) m_p^0 \tag{7.8}$$

where $\frac{1}{M_{cl}}$ is the initial population of clusters per mass of dry ash-free coal, $N_{cluster_{tar}}$ represents the population of clusters removed out of the particle by evaporation of tar per mass of dry ash-free coal, and m_p^0 is the initial mass of the dry coal particle.

The final specific surface area can be derived after balancing the available volume in the particle, and it is given by[210]:

$$S_{int} = \frac{S_a N_A N_{cluster}^{ap} N_{cluster_{coal}} + s_{particle}^{t_0}}{(1 - f_{tar} - f_{gas})/(1 - a_{dry}) + a_{dry}} \tag{7.9}$$

7.1.2. Lattice model

In this model the development of the internal area A_i as a function of the burnout, is calculated assuming that the pores possess a geometrical lattice distribution inside the solid particle. Let us consider a cubic particle of side L whose pores are cylinders orthogonal to each face. There are N pores on each side, and the diameter of the pore be δ. The Volume V_p of the pore is:

$$V_p = 3N^2\delta^2 L - 2N^3\delta^3 \tag{7.10}$$

The porosity ε of the particle, defined by $\varepsilon = \frac{V_p}{L^3}$ can be written:

$$\varepsilon = 3Z^2 - 2Z^3 \tag{7.11}$$

where:

$$Z = \frac{N^3\delta^3}{L^3} \tag{7.12}$$

The internal surface of the pores S_p is:

$$S_p = 12\delta N^2 (L - \delta N) \tag{7.13}$$

and the internal surface per unit of volume $A_i = \frac{S_p}{L^3}$:

$$A_i = \frac{12}{\delta} Z^2 (1 - Z) \tag{7.14}$$

Each solid material usually has a distribution of pores dependent on its length L and its diameter δ. The equation 7.11 and the equation 7.14 must be changed using an integration:

$$\varepsilon = \int dL \int d\delta \left(3Z_{L,\delta}^2 - 2Z_{L,\delta}^3\right) \frac{L^3}{D^3} \tag{7.15}$$

$$A_i = \int dL \int d\delta \left(\frac{12}{\delta} Z_{L,\delta}^2 \left(1 - Z_{L,\delta}\right)\right) \frac{L^3}{D^3} \tag{7.16}$$

where D is the dimension of the particle.

Let us consider, as an example, a pore distribution piked on a macro-pores δ_M over a really law background V_ϵ. Moreover, to simplifying the calculations, let have pore with a unique length L. The differential distribution of the volume of the pore (quantity usually measured) is:

$$\frac{d}{d\delta} V_\delta = L^3 Z_\delta^2 (3 - 2Z_\delta) \tag{7.17}$$

that solved for Z_δ for $\delta \neq \delta_M$:

$$Z_\delta = \sqrt{\frac{V_\epsilon}{3L^3}} \tag{7.18}$$

The porosity is then calculated:

$$\varepsilon = \int \frac{V_\delta'}{D^3} d\delta \tag{7.19}$$

$$= \frac{V_\epsilon}{D^3} \delta_{max} + \frac{V_M}{D^3} \tag{7.20}$$

$$= \frac{L^3}{D^3} Z_M^2 (3 - 2Z_M) \tag{7.21}$$

The surface per unit of volume:

$$A_i = 4 \frac{V_\epsilon}{D^3} \ln \frac{\delta_{max}}{\delta_{min}} + \frac{L^3}{D^3} \frac{12}{\delta_M} Z_M^2 (1 - Z_M) \tag{7.22}$$

7.1.3. Random-pore models

According with the model [35, 36], the internal surface is created by a set of overlapping cylindrical pores of size distribution $f(r)$, where the function $f(r)$ identify the length distribution of the cylinders per unit of volume. The total length L_E, the total surface area S_E and total enclosed

volume V_E of the non-overlapped cylindrical system are described by the following equations:

$$L_E = \int f(r)\, dr \tag{7.23}$$

$$S_E = 2\pi \int r f(r)\, dr \tag{7.24}$$

$$V_E = \pi \int r^2 f(r)\, dr \tag{7.25}$$

A balance equation for the size of the growing cylinders can be written:

$$\frac{\partial f(r)}{\partial t} + \frac{\partial}{\partial} \left(f(r) \frac{\partial r}{\partial t} \right) = 0 \tag{7.26}$$

with the only assumption that pores are neither created nor destroyed.

The solution of this equation is linked to a specific model for the char reaction (and consequently for the surface accretion), and it will be further described in Section 8.6.3.

7.1.4. Pores-tree models

In [331, 330] the pore structure has been treated statistically, described by a collection of pore trees with a continuous size distribution and branching sequence. The pore tree model assumes that pores at the surface are the base of a structure that develops deep inside a particle. The dimensions of a single tree range from micro-scales of the order of $r_{min} \approx 0.1$ nm to macro-scale that is a significant fraction of the particle radius. The radius of the largest pore r_{max} is related to the particle radius R_p by the relation:

$$r_{max} = \frac{2}{3} \frac{R_p \cdot \varepsilon^{1/3}}{K_0} \tag{7.27}$$

where ε is the porosity, $K_0 \approx 5$ is an integration constant and R_p is the radius of the particle. The integration constant relates statistically the pore length l_p to its radius r_p:

$$l_p = K_p \frac{r_p}{\varepsilon^{1/3}} \tag{7.28}$$

The radius r_{min} of the smallest pore is given by:

$$r_{min} = 2 \frac{\varepsilon}{\beta \rho_s S_p} \tag{7.29}$$

where S_p is the internal specific area,

$$\beta = \ln \frac{r_{max}}{r_{min}} \tag{7.30}$$

and $\rho_s = 2,21 \frac{gram}{cm^3}$ is the density of the non-porous material.

Inside a single particle, the pores have several diameter r_p distributed between the minimum and the maximum diameter following a distribution function called $g(r_p)$ given by:

$$g(r_p) = \frac{\varepsilon}{2\pi} \frac{1}{r_p^3} \tag{7.31}$$

The radius r_p and the number of pores n are a function of the depth of the pore x. It has been shown that [331]:

$$n(x) = \left(\frac{r_t}{r_p(x)} \right)^2 \tag{7.32}$$

where r_t is the initial radius of the pore tree and the coordinates x is related to the radius by:

$$\frac{dr_p}{dx} = -\frac{r_p}{l_t} \tag{7.33}$$

The porosity and the internal surface area are $2\pi r_p^2$ and $4\pi r_p$ moments of the distribution $g(r)$, respectively.

It can be shown [331] that during pyrolysis the distribution $g(r) \sim \frac{1}{r^3}$ remain valid for all times, leading to the relation:

$$r_p = r_p(0) \left(\frac{\theta}{\theta(0)} \right)^{1/3} \tag{7.34}$$

$$l_p = l_p(0) \tag{7.35}$$

for all pores, indicating that the pore trees evolve in a self similar way.

In [335, 329] a differential equation for the distribution function $g(r)$ has been developed and information on the specific rates of pore formation and destruction has been inferred.

As expected, the theory predicts that the internal surface area is several order of magnitude larger than the area of the pores of the largest radius and that the volume is only a factor 10 larger than the volume of the largest pore.

The description of the diffusion of reactant inside the tree can be performed considering the usual differential equation for the concentration $[C]$. The diffusion inside n pores of radius r_p must be balanced by its reaction on the surface of the tree:

$$\frac{d}{dx} \left(n \rho_g D \pi r_p^2 \frac{d\,[C]}{dx} \right) = 2\pi n r_p k_g \tag{7.36}$$

where k_g is the reaction rate of the reactant with the solid structure and D is the diffusion coefficient. As in Section 8.5 the total amount of reactant reacted inside the pore tree must be equal to the diffusion of reactant at the $x = 0$:

$$\dot{M}_t = -\rho_g D \pi r_p^2 \left. \frac{d\,[C]}{dx} \right|_s \tag{7.37}$$

The reactant diffusion equation given by 7.36 must be solved for each tree and then integrated over all trees. The intrinsic reaction rate k is given by a adsorption desorption mechanism as described in Section 3.2 and the pore diffusion is given by the effective diffusivity model described in 8.5.1.1.

Analytical solutions have been obtained only in the limit of absorption kinetic for which $k \sim [C]$ and for Knudsen diffusion and are discussed further in Section 8.6.4.

7.2. Gas transport across the structure

The flash distillation analogy explained in Section 6.2.9 does not include any finite-rate transport mechanisms. Instead, the escape rate of gases is set equal to their rate of production from the chemical reaction mechanism, under the assumption that a bulk convective flow of gases can be established by a nominally infinitesimal pressure gradient across the particle; hence, internal and ambient pressures are equal and all transport resistances are negligible.

Following the model presented in [330], the gas released from the solid walls at a rate $\dot{m}_w$ must obey a continuity equation of the form

$$\frac{d}{dy} n \rho_g U \pi r_p^2 = n \dot{m}_w \tag{7.38}$$

where n is the number of the branches of radius r_p presented in the solid structure. The mass removed at the walls must be determined by the development of the pore structure:

$$\dot{m}_w = 2\chi \pi r_p \rho_s \frac{dr_p}{dt} \tag{7.39}$$

with $\chi = \frac{2}{3}$ a shape factor calculated by the model.

The change of the radius r_p is related to the change of the pore structure presented previously in Section 7.1:

$$\frac{dr_p}{dt} = \frac{r_p}{3\theta} \frac{d\theta}{dt} \tag{7.40}$$

and the development of the porosity is related to the intrinsic devolatilization reaction by:

$$\frac{d\theta}{dt} = k \left(\theta_f - \theta \right) \tag{7.41}$$

The model can reconstruct the pressure distribution inside each pore (detailed are given in [332]) assuming a limiting process for the diffusion. Usually, Knudsen diffusion limits the flow in small pores while for the largest tree choked flow can be achieved.

At high devolatilization rates, the fluid mechanics retard the release of gas out of the particle because a part of the gas stagnates at extremely high pressures inside the small pores. This stagnation at high pressure has an impact on secondary reactions.

7.3. Particle swelling during devolatilization

Coal can swell upon heating, resulting in larger particle size. This effect is stronger in an inert environment or under reducing conditions. The swelling factor, which is the ratio of the swollen coal particle to its original dimension, can range from about 1.3 (under oxidative conditions) to about 4 (in an inert environment). Swelling introduces thin-walled cenospheres, which can produce a sudden decrease in the particle size when burned and a density increase during burn off.

More generally, solid fuels can be divided into several classes regarding their ability to swell:

1. non-swelling;
2. fusion;
3. swelling;

4. cenospheres;

5. mixed.

Modeling thermal-plastic behaviors of solid particles are challenging because of uncertainties of the physical properties of fuels upon heating. A few attempts have been made to model the swelling of coal particles. In [343] a first single bubble model has been developed, where the swelling was assumed to be due to the pressure of trapped evolved gases against viscosity forces.

Following the single bubble approach, a multi-bubble model was proposed [262], which describs more accurately the bubble behaviors, including the bubble growth, coalescence, and transport to the surface. A most recent model [322] has been developed for the transient swelling of coal particles on the basis of a single bubble and porous shell assumptions, and volatile release was predicted using the advanced chemical percolation devolatilization model [348]. The formation, growth, and rupture of the bubble and the swelling and shrinking of the particle were modeled in detail. However, these processes have not been justified due to the lack of experimental observations. This model is only suitable to those coals tending to form cenospherical chars.

To avoid the complexity of a more detailed modeling, a phenomenological relation is assumed:

$$\frac{d}{d_0} = \left(\frac{m_p}{m_0}\right)^n \tag{7.42}$$

where n is a parameter determines using experiments.

8. Modeling of Char Conversion

In Chapter 3 the basics of heterogeneous kinetic rates have been underlined and various mechanisms leading to several expressions for the reaction rates have been discussed. The main conclusion of the Chapter was that heterogeneous reactions take place on activated sites, on the internal surface, and the rates of intrinsic heterogeneous reactions are affected by the following three parameters:

1. the type of the activated sites;

2. the amount of activated sites;

3. the availability of gaseous reactants.

Type and amount of activated sites are directly influenced by the past thermal history of the solid fue. Therefore the char reactivity is dependent on the way the char is formed (devolatilization). The availability of gases (oxygen, water, carbon dioxide) is affected by the structure of the particle into which reactants must diffuse.

CFD applications need an expression for the mass loss of the fuel particle $\frac{dm_p}{dt}$ to calculate the sources due to conversion reactions, and therefore this Chapter aims to present several approaches and assumptions to obtain the mass loss as a function of all the relevant thermodynamic quantities. Most of the models here presented have been developed in the case of char oxidation but their validity remain unaltered also for other kinds of reactions and the extension to gasification reactions are straightforward.

In the case of char oxidation simplifications in the description of the complex heterogeneous chemical reactions mechanism will be adopted and a stoichiometric global reaction is considered. The reaction is written as follows:

$$\mathrm{Char} + s \ \ \mathrm{O_2} \longrightarrow x \ \ \mathrm{CO} + y \ \ \mathrm{CO_2} \tag{R 8.1}$$

The splitting of the product between CO and CO_2 is a function of the temperature and is given in section Section 9.1 (see equation 9.3). The stoichiometric coefficient s can be related to a measurable quantity, named the oxygen requirement ζ defined as the kg of O_2 required to burn 1 kg of char. Char can be assumed to be pure carbon with the consequence that the stoichiometry $\zeta = 2.667\,\mathrm{kg_{O2}/kg_C}$ and the low calorific value $LCV = 32\,\frac{\mathrm{MJ}}{\mathrm{kg}}$. Most of the time those values are good approximations but a better approximations is to consider char as a macromolecule $C_aO_bH_c$ with the values of a, b and c calculated from the fuel and char analysis.

The gasification reactions are written in the simple stoichiometric form:

$$\mathrm{C} + \mathrm{CO_2} \longrightarrow 2\,\mathrm{CO} \tag{R 8.2}$$

and

$$\mathrm{C} + \mathrm{H_2O} \longrightarrow \mathrm{CO} + \mathrm{H_2} \tag{R 8.3}$$

.

8.1. A general model for char conversion

A general model for the conversion of the char could be written in the following form:

$$\frac{dm_p}{dt} = f(T_p)g(B)h(D_p) \tag{8.1}$$

where $f()$, $g()$ and $h()$ are functions dependent on the temperature of the particle T_p, the burnout of the particle B and on the diameter of the particle D_p. This approach is usually not used for several reasons:

1. The model described by equation 8.1 do not give any information on the the physical process taking place in the particle and therefore it is not scientifically satisfactory;
2. In the models described by equation 8.1 there is a need for extensive experimental data to reduce the infinite degree of freedom still present.

Although its phenomenological basis, such an approach has been used in the past. An example of coal-char combined gasification and oxidation reaction mechanisms has been given in [226] as a function of the variable $\tau = \frac{t}{\tau_{1/2}}$. The model predicts directly the burnout B using the following correlation:

$$B = a\tau + b\tau^2 + c\tau^3 \tag{8.2}$$

with the values of the parameters given in Table 8.1.

Reactant	a	b	b
Air	0.317	0.367	-0.182
CO_2	0.436	0.189	-0.122
H_2O	0.375	0.276	-0.148
H_2	0.349	0.283	-0.144
All	0.368	0.277	-0.147

Table 8.1.: Parameters for the unified reactions of coal char oxidation and gasification

The correlation is valid until $B \approx 70 - 80\%$. To be predictive, the model needs the knowledge of half-bornout time $\tau_{1/2}$.

8.2. Diffusion model

Two different approaches, leading to the same final model, can be considered for a more physical description of thermal conversion of solid fuels. The two approaches are described bx the two following two processes:

1. Diffusion of reactants through the boundary layer;
2. Chemical reactions with the macromolecular structure.

and they will be discussed in the following sections. We decided to start considering the diffusion of reactants as a first step to create the final char reaction model.

Using mass conservation, the amount of reactant participating in the conversion reaction inside the particle has to be equal to the amount of reactant diffused through the boundary layer of the particle. As soon as that amount is calculated, the reaction rate can be also calculated.

In vectorial form the steady-state diffusion equation for the reactant concentration $[C]$ can be derived by the conservation of the mass and is written in the following form [1]:

$$\nabla \cdot (D_c \nabla [C]) = \dot{S}_c \tag{8.3}$$

	D_c	-	diffusion coefficient	in $\frac{\mathrm{m}^2}{\mathrm{s}}$
where:	$[C]$	-	concentration of the reactant	in $\frac{\mathrm{kg}}{\mathrm{m}^3}$
	$\dot{S}_c$	-	Source term for the reactant c	in $\frac{\mathrm{kg}}{\mathrm{m}^3}$

This equation must be solved in the space outside the particle. To simplify the mathematical formulation, it is assumed that the problem posses spherical symmetry. In spherical symmetry (no dependencies on the angles ϑ and φ) and expressed in spherical coordinates, the previous equation becomes:

$$\frac{1}{r^2}\frac{\partial}{\partial r}\left(r^2 D(c,r)\frac{\partial}{\partial r}[C]\right) = \dot{S}_c(c,r) \tag{8.4}$$

Since no heterogeneous reactions are present in the boundary layer, the sources in the balance equation is zero and the diffusion equation 8.4 reduces to:

$$\frac{1}{r^2}\frac{\partial}{\partial r}\left(r^2 D(c,r)\frac{\partial}{\partial r}[C]\right) = 0 \tag{8.5}$$

Integrating the equation once, the mass flow rate j_c (in $\frac{\mathrm{kg}}{\mathrm{m}^3\,\mathrm{s}}$) can be calculated:

$$j_c \equiv -D_c \frac{d}{dr}[C] = \frac{K}{r^2} \tag{8.6}$$

with K a constant to be determined. Integrating a second time:

$$-\frac{K}{r}\bigg|_{R_p}^{\infty} = -D_c [C]_{R_p}^{\infty} \tag{8.7}$$

It follows:

$$\frac{K}{R_p} = D_c \left([C]_\infty - [C]_s\right) \tag{8.8}$$

from which it is possible to calculate the unknown constant K:

$$K = \frac{D_c}{R_p}([C]_\infty - [C]_s) \tag{8.9}$$

The total reaction rate $\dot{M}_c$ of the char is related to the reactant diffusing into the particle:

$$\dot{M}_c \equiv \frac{dm_p}{dt} = \frac{1}{\zeta} A_p j_c \tag{8.10}$$

where A_p is the external surface of the particle. For a spherical particle:

$$A_p = \pi D_p^2 \tag{8.11}$$

[1] The same equation can be also derived on mole basis but the results are the same.

The previous derivation assumed a non-moving particle with the diffusion coefficient D_c being the molecular diffusion coefficient of the reactant in the mixture. In practical application, this assumption is never valid, and more general correlations must be used. The flux j_c is more generally expressed as a function of the pressure difference between the bulk pressure p_∞ and the surface pressure p_s. From the ideal gas law:

$$p_c M_c = [c]\, RT \tag{8.12}$$

Introducing into equation 8.6 the value of K from equation 8.8 and expressing the concentration $[c]$ as a function of partial pressure from 8.12 the flux can be expressed as follows:

$$j_c = \frac{D_c M_c}{R_p\, R} \left(\frac{p_\infty}{T_\infty} - \frac{p_s}{T_s} \right) \tag{8.13}$$

The proportionality between the flux and the pressure difference is maintained and the proportionality coefficient h_m is introduced. The mass diffusion coefficient h_m is expressed in $\frac{m}{sec}$. The expression of the flux is then written in the following form:

$$j_c = h_m \frac{M_{ox}}{RT_e} \left(p_\infty - p_s \right) \tag{8.14}$$

In the above formula the temperature T_e is an effective temperature and can be calculated in several ways. The most common way is to assume an arithmetical averaged temperature between the bulk temperature and the particle temperature:

$$T_e = \frac{T_p + T_\infty}{2} \tag{8.15}$$

Using the equation 8.14, the reaction rate given in 8.10 can be rearranged in the following form:

$$\dot{M}_c = A_p \frac{M_{Carb}}{RT_e} \frac{h_m}{\zeta} \left(p_\infty - p_s \right) \tag{8.16}$$

The partial pressure of the reactant at the surface p_s is unknown. If the diffusion across the boundary layer is much slower than the reaction with the char structure, it is possible to assume that the partial pressure at the surface is negligible with respect the bulk partial pressure. The reaction rate is then given by:

$$\dot{M}_c = \frac{\pi D_p^2}{\zeta} \frac{M_{Carb}}{RT_e} h_m p_\infty \tag{8.17}$$

The diffusion coefficient h_m The diffusion coefficient h_m can be determined from the *Sherwood* number Sh, defined as:

$$Sh = \frac{h_m D_p}{D_c}$$

where D_p is the diameter of the particle. From empirical correlation for Sh as a function of the Re number. In the previous equation D_c is the diffusivity of the reactant in the gas around the char particle. If the Lewis number (defined as the ratio between the heat and mass diffusivity) $Le \equiv \frac{\alpha}{D_c} = 1$ then the Nusselt number Nu and Sh are equal and correlations for Nu can be used as well as for Sh. In the correlation the Prandlt number Pr has to be replaced by the the Schmidt number Sc, describing the ratio between momentum and mass diffusivity:

$$Sc = \frac{\mu}{\rho D_c}$$

Some useful correlations are the following:

Ranz-Marshall correlation [286] expressed by:

$$Sh = 2 + 0.6\sqrt{Re}Sc^{1/3} \tag{8.18}$$

Renksizbulut-Hayoowood correlation expressed by:

$$Sh = (2 + 0.57\sqrt{Re}Sc^{1/3})(1 + B)^{0.7} \tag{8.19}$$

Faeth correlation expressed by:

$$Sh = 2 + \frac{0.555\sqrt{Re}Sc^{1/3}}{1 + 1.23/\sqrt{ReSc^{4/3}}} \tag{8.20}$$

Free convection correlation expressed by:

$$Sh = 2 + 1.066Gr^{0.52} \tag{8.21}$$

The diffusion of the reactant through the boundary layer into the particle can be described by fitting of experimental data and mathematically can be expressed by (D_c is in $\frac{m^2}{sec}$):

$$D_c = C_o \left(T_p + T_\infty\right)^{1.75} \tag{8.22}$$

C_o = $9.54 \cdot 10^{-10}$ (in the case of oxygen)

with: T_p - Temperature of the particle

T_∞ - Bulk temperature

More accurate relations can be used. The Chapman-Enskog equation uses kinetic theory of gases to compute the diffusion coefficient in a binary mixture and it is given by:

$$\left[C_f\right] \mathcal{D}_{ij} = \frac{3}{16}\sqrt{\frac{2RT}{\pi}\left(\frac{1}{M_i} + \frac{1}{M_j}\right)}\frac{1}{N_A \sigma_{i,j}^2 \Omega_{D,ij}} \tag{8.23}$$

	$[C]_f$	concentration	in $\frac{\text{kg}}{\text{m}^3}$
	R	Universal gas constant	in $\frac{\text{kJ}}{\text{kmol}}$
	T	Temperature	in K
where:	M_x	Molecular mass	in $\frac{\text{kg}}{\text{kmol}}$
	N_A	Avogadro's number	
	σ	is the collision diameter	in m
	Ω	is the collision integral.	

Making use of the ideal gas law (reducing the applicability of the following equation only to low pressures) the previous equation simplifies:

$$\mathcal{D}_{ij} = 0.0018583\sqrt{T^3\left(\frac{1}{M_i}+\frac{1}{M_j}\right)}\frac{1}{p_{abs}\sigma_{i,j}^2\Omega_{D,ij}} \tag{8.24}$$

where now p_{abs} is the absolute pressure in atm and the collision diameter σ is in Å. For a binary mixture, σ_{ij} is calculated as the average of the individual σs:

$$\sigma_{ij} = \frac{1}{2}(\sigma_i + \sigma_j) \tag{8.25}$$

The collision integral Ω_D, which is a measure of the interaction of the molecules, is a function of the quantity T_D^*, where:

$$T_D^* = \frac{T}{(\epsilon/k_B)_{ij}} \tag{8.26}$$

k_B is the Boltzmann constant, which is defined as the gas constant R, divided by Avogadro's number. $(\epsilon/k_B)_{ij}$ for the mixture is the geometric average:

$$(\epsilon/k_B)_{ij} = \sqrt{(\epsilon/k_B)_i(\epsilon/k_B)_j} \tag{8.27}$$

The ϵ is the maximum energy of attraction between two unbounded molecules [2]. The relation for Ω follows:

$$\Omega_{D,ij} = \frac{1.06036}{T^{*0.15610}} + \frac{0.19300}{\exp(0.47635T^*)} + \frac{1.03587}{\exp(1.52996T^*)} + \frac{1.76474}{\exp(3.89411T^*)} \tag{8.29}$$

[2] ϵ and σ are parameters used in the Lennard-Jones description of the potential between two molecules:

$$V_{LJ} = 4\epsilon\left[\left(\frac{\sigma}{r}\right)^1 2 + \left(\frac{\sigma}{r}\right)^6\right] \tag{8.28}$$

and are tabulated.

8.3. Pseudo-chemical models

In the previous Section, relations for the conversion rate have been derived based on the rate of diffusion of the reactants across the boundary layer. In this Section, the conversion rate will be described based on expressions for the kinetic rates.

The starting point for the model of char reaction is the formulation of the reaction rates for heterogeneous reactions:

$$\frac{dm_p}{dt} = \frac{M_{reac}}{\zeta} A_p k_C \left[C\right]_S^n \tag{8.30}$$

where:

ζ	-	stoichiometric coefficient	in kg_f/kg_{char}
M_{reac}	-	Oxygen molecular weight	in $kg_f/kmol_f$
A_p	-	external particle surface	in m^2
k_c	-	reaction rate constant	in $\frac{m}{s}$ only if $n = 1$
$[C]_S$	-	reactant molar concentration at the surface of the particle	in kg_f/m^3
n	-	reaction order	-

It is important to notice that in the above equation the reaction is given as a function of the external surface that, with the approximation of spherical particles, is given by $A_p = \pi D_P^2$.

The kinetic rate constant k_c describes the kinetic of a *pseudo reaction*. It does not refer to any real kinetic reaction between reactant molecules and the char structure, but includes several phenomena not explicitly written in such a way that equation 8.30 is the definition for k_c. Usually, all the phenomena collected inside k_c are taken to be a function of the particle temperature only and the reaction rate constant is expressed in an Arrhenius form:

$$k_i(T_p) = A_c T^b e^{-\frac{E_c}{RT_p}} \tag{8.31}$$

In equation 8.30 the concentration of the reactant at the surface is not known. It can be assumed that the chemical reactions are slower than the diffusion of reactant to the particle surface (due to molecular diffusion through the particle boundary layer). The reactant is then always available at the surface and its concentration is equal to the concentration in the bulk:

$$\left[C\right]_S = \left[C\right]_\infty \tag{8.32}$$

This assumption is the opposite of the one made in the previous section describing the situation in which the bulk diffusion rate is slower than the kinetic rate. With the present assumption in equation 8.30, the pseudo kinetic model can be written in its final form:

$$\frac{dm_p}{dt} = \frac{M_{reac}}{\zeta} A_p k_C \left[C\right]_\infty^n \tag{8.33}$$

8.4. Kinetic-limited model

Equation 8.30 for the kinetic reaction rate and equation 8.14 for the diffusive flux can be coupled together. Before doing that, let us rewrite the equations in a more compact way. The general

equation for the reactant diffusion given by 8.14 can be written

$$\dot{M}_c = K_D \left(p_\infty - p_S \right) \tag{8.34}$$

where all the variables are condensed into the single coefficient K_D:

$$K_D = A_p \frac{M_f h_m}{R T_e \zeta} \tag{8.35}$$

In the same way equation 8.30 can be written using the partial pressure:

$$\dot{M}_c = K_C p_S^n \tag{8.36}$$

where the kinetic coefficient K_C is expressed as:

$$K_C = \left(\frac{M_f}{R T_p} \right)^n \frac{A_p k_c}{\zeta} \tag{8.37}$$

The unknown pressure at the surface can be extracted from equation 8.34 and inserted into equation 8.36 to give the final (implicit) rate:

$$\dot{M}_c = K_C \left(p_\infty - \frac{\dot{M}_c}{K_D} \right)^n \tag{8.38}$$

This is a non-linear equation for the variable $\dot{M}_c$. If the reaction order n equals unity, equation 8.38 can be analytically solved to give the reaction rate of the kinetically-limited model:

$$\dot{M}_c = \frac{K_D K_C}{K_D + K_C} p_\infty \tag{8.39}$$

8.5. Pore models

Most of the solid fuels are porous materials, and therefore heterogeneous reactions take place mostly on the internal surface, more extended than the external one. The availability of reactants and active sites must then be known as a function of the particle radius. Models able to describe the internal pore structure and its development are required to achieve a better prediction and a more satisfactory understanding of the overall conversion rate.

If the pore structure is not allowed to change, the effective diffusivity and the pore diameters remain constant and the pore models and the macroscopic models are equivalent. This approximation cannot describe the conversion of chars where changes in internal structure are relevant.

The division among different pores models, already proposed in Section 7.1, is also valid for char conversion models as the explanation below will clarify.

8.5.1. Isolated-pore models

The reactions between reactant and char structure take place directly on the internal surfaces of the porous particle. The reaction rate for the particle is written, without approximations, in the following form:

$$\dot{M}_c = \int q_v([C])\, dV \tag{8.40}$$

where $q_v([C])$ (in $\frac{\text{kg}}{\text{m}^3\,\text{s}}$) is the reaction rate per unit of volume and its dependency on the availability of reactant is explicitly expressed. The integration has to be performed all over the entire volume of the particle. The quantity q_v can be related to the more physical q_s, the reaction rate per unit of (internal) surface (in $\frac{\text{kg}}{\text{m}^2\,\text{s}}$):

$$q_v = \dot{q_c}\frac{S_T}{V} = \dot{q_c}A_i \tag{8.41}$$

The equation 8.40 can be rearranged as:

$$\dot{M_c} = \int \dot{q_c}([C])\frac{S_T}{V}\,dV = \int \dot{q_c}([C])A_i\,dV \tag{8.42}$$

The internal reaction rate $\dot{q_c}$ can be now expressed using an Arrhenius form:

$$\dot{q_c} = M_{Carb}\frac{k_i}{\zeta}\,[C]^n = \frac{1}{\zeta}\,[C]^n\,A\,T^b e^{\left(-\frac{E}{RT}\right)} \tag{8.43}$$

The reaction constant k_i in the previous equation should not be confused with the reaction rate k_C defined previously in equation 8.30. The rate k_C is an effective char reaction rate while the rate k_i is the rate of the reactions taking place at internal surfaces of the pores and is usually expressed in Arrhenius form:

$$k_i = A_i T_p^{b_i} e^{-\frac{E_i}{RT_p}} \tag{8.44}$$

The rate constant k_i is called the *intrinsic reaction constant*.

The expression 8.42, can be rewritten in the following way:

$$\dot{M_c} = -M_{Carb}\,4\pi r^2\frac{D_c}{\zeta}\frac{d}{dr}\,[C]\Big|_s = -M_{Carb}4\pi R_p^2\frac{D_c}{\zeta}\frac{d}{dr}\,[C]_s \tag{8.45}$$

For the determination of $\dot{M_c}$ the derivative $\frac{d}{dr}\,[C]_s$ must be found. This derivative is a function of the position inside the particle. To calculate this function, the diffusion equation of the reactant inside the particle has to be solved. If the concentration is not constant inside the particle, the reaction rate has to be written in the following way:

$$\frac{dm_p}{dt} = M_{Carb}\int dV_p\,\frac{A_i}{\zeta}k_i\,[C]^n \tag{8.46}$$

where:

ζ	-	stoichiometric coefficient	in $\text{kg}_\text{C}/\text{kg}_\text{char}$
M_{Carb}	-	molecular weight	in $\text{kg}_\text{C}/\text{kmol}_\text{C}$
A_i	-	internal particle surface per unit of Volume	in $\frac{\text{m}^2}{\text{m}^3}$
k_i	-	reaction rate constant	in $\frac{\text{m}}{\text{s}}$ only if $n = 1$
$[C]$	-	reactant molar concentration	in $\text{kmol}_\text{C}/\text{m}^3$
n	-	reaction order	-

The equation for the reactant diffusion inside a spherical particle was already written in

equation 8.4:

$$\frac{1}{r^2}\frac{\partial}{\partial r}\left(r^2 D([C],r)\frac{\partial}{\partial r}[C]\right) = S_c([C],r) \tag{8.47}$$

where the source term $S_c([C],r)$, expressed in $kmol_c/s/m^3$, is given by the following relation, after the definition given in equation 8.46:

$$S_c([C],r) = A_i k_i [C]^n \tag{8.48}$$

The final form of the equation for a reacting spherical particle for which the effective diffusivity $D([C],r) = D_{eff}$ is not dependent on the variable r, is the written below:

$$\frac{1}{r^2}\frac{\partial}{\partial r}\left(r^2\frac{\partial}{\partial r}[C]\right) = \frac{1}{D_{eff}} A_i k_i [C]^n \tag{8.49}$$

The boundary conditions are written at the center of the particle ($r = 0$) and at the surface of the particle ($r = R_p$):

$$\begin{cases} [C](R_p) &= [C]_s \\ \frac{d}{dr}[C](0) &= 0 \end{cases} \tag{8.50}$$

With the change of variables defined by:

$$\begin{array}{c} f = \frac{r}{R_p}\frac{[C]}{[C]_s} \\ x = \frac{r}{R_p} \end{array} \tag{8.51}$$

The relation 8.49 can be rewritten in the following way:

$$\frac{df^2}{d^2x} = [C]_s^{n-1} R_p^2 \frac{k_i}{D_{eff}} A_i \frac{f^n}{x^{n-1}} = A\frac{f^n}{x^{n-1}} \tag{8.52}$$

with the boundary conditions:

$$\begin{cases} f(1) &= 1 \\ \frac{d}{dx}\left(\frac{f}{x}\right)(0) &= 0 \end{cases} \tag{8.53}$$

The constant A is then defined by:

$$A = [C]_s^{n-1} R_p^2 \frac{k_i}{D_{eff}} A_i \tag{8.54}$$

8.5.1.1. The intrinsic model

The equation 8.52 can be analytically solved only in the case of $n = 1$ when it reduces to:

$$\frac{d^2 f}{dx^2} = Af \tag{8.55}$$

with the constant A defined by:

$$A = R_p^2 \frac{k_i}{D_{eff}} A_i \tag{8.56}$$

Using the given boundary conditions, the final solution reads:

$$f = \frac{\sinh\left(\sqrt{A}\, x\right)}{\sinh\left(\sqrt{A}\right)} \tag{8.57}$$

end in term of the reactant concentration:

$$[C] = [C]_s \frac{R_p}{r} \frac{\sinh\left(\sqrt{A}\, \frac{r}{R_p}\right)}{\sinh\left(\sqrt{A}\right)} \tag{8.58}$$

The species diffusion flux j_c in $\frac{\mathrm{kg}}{\mathrm{m}^2\,\mathrm{s}}$, is defined as:

$$j_c = -D_{eff} \frac{d}{dr} [C] \tag{8.59}$$

The amount of gas reacting inside the particle is equal to the the amount of gas flowing through the surface ($r = R_p$), and, according to the previous results, it is given by:

$$j_c = [C]_s \frac{D_{eff}}{R_p} \left(1 - \frac{\Phi}{\tanh \Phi}\right) \tag{8.60}$$

with:

$$\Phi = \sqrt{A} = R_p \sqrt{\frac{k_i}{D_{eff}} A_i} \tag{8.61}$$

Using the results previously derived:

$$\dot{M}_c = -M_{Carb} 4\pi R_p [C]_s \frac{D_{eff}}{\zeta} \left(\frac{\Phi}{\tanh \Phi} - 1\right) \tag{8.62}$$

With the definition of the Thiele modulus Φ:

$$\Phi = R_p \sqrt{\frac{A_i k_i}{D_{eff}}} \tag{8.63}$$

it is possible to write the reaction rate for the intrinsic model in the following final form:

$$\dot{M}_c = -4\pi R_p M_{Carb} [C]_s \frac{D_{eff}}{A_i k_i R_p^2} \frac{R_p^2 A_i k_i}{\zeta} \left(\frac{\Phi}{\tanh \Phi} - 1\right) \tag{8.64}$$

and using the definition of Φ in the right hand side:

$$\dot{M}_c = -\frac{4}{3}\pi R_p^3 M_{Carb} \frac{A_i k_i}{\zeta} [C]_s \frac{3}{\Phi^2} \left(\frac{\Phi}{\tanh \Phi} - 1\right) \tag{8.65}$$

Recognizing in the factor $\frac{4}{3}\pi R_p^3 A_i$ the total area A_T available for reaction, we have:

$$\dot{M}_c = -A_T M_{Carb} \frac{k_i}{\zeta} [C]_s \eta \tag{8.66}$$

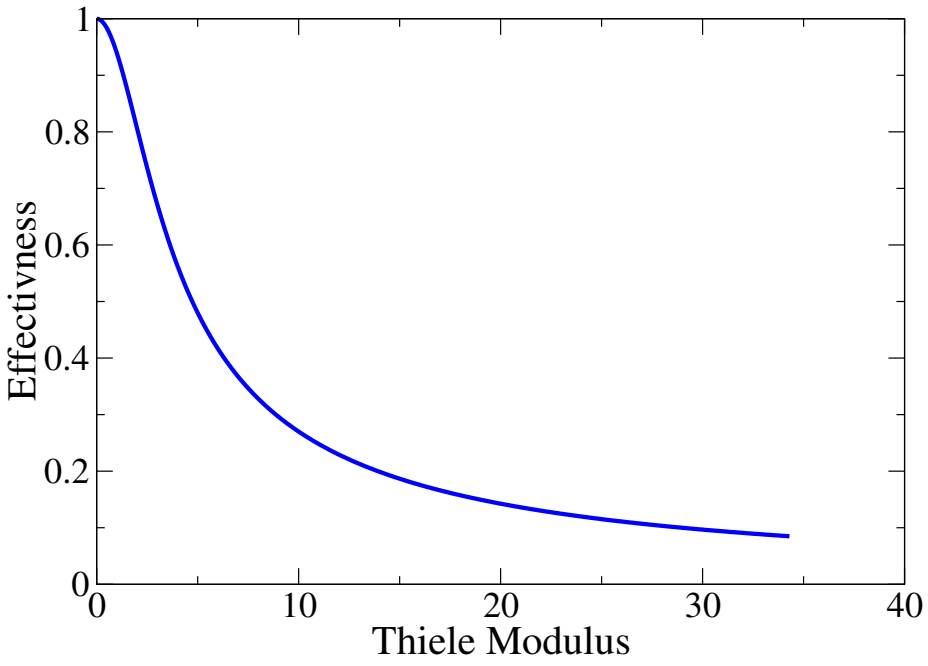

Figure 8.1.: Effectiveness as a function of the Thiele modulus for a spherical geometry

with η the effectiveness of the reactions inside the particle due to reactant diffusion:

$$\eta = \frac{3}{\Phi^2}\left(\frac{\Phi}{\tanh\Phi} - 1\right) \tag{8.67}$$

In equation 8.66 the concentration at the surface $[C]_S$ is not known. The method shown in Section 8.4 can then be applied to the case of intrinsic reaction as well.

The highest rate at a given temperature would occur when reactions take place on the entire surface and this conditions is satisfied when enough oxygen is able to diffuse into the entire particle. The effectiveness η is a number lass than unity that limit the maximum rate kinetic, and it can be indifferently seen as the amount of internal surface available to the oxygen.

Figure Figure 8.1 presents the graph of the effectiveness η given in equation 8.67 as a function of the Thiele modulus Φ. For small values of Φ the diffusion of the oxygen inside the particle is quicker than the reaction rates, and therefore most of the surface is involved in the reactions. The effectiveness η is then unity. As the Thiele Modulus increases and the diffusion becomes slower than the reactions, the effectiveness decreases reaching small values in the limit of very large Thiele numbers.

Considering the expression of the Thiele number as in equation 8.63, it becomes evident that the three parameters that characterize Φ are:

1. The pore radius;
2. The temperature;
3. The radius of the particle

A small pore radius decrease the effective diffusivity D_{eff} (see the next paragraph) increasing the Thiele modulus. The small pores are associated usually with an high internal surface,

but finally are responsible for decreasing of the overall reaction rate. A contrary effect have the particle dimension, represented, in equation 8.63, by the particle radius R_p. Large particles react with a rate limited by pore diffusion. FinaÃ¶lly the influence of the temperature is clear since an increase in T_p leads to an exponential increase of the kinetic rate with a consequent increase in Thiele number. Also at high temperature the conversion of particles is pore diffusion controlled.

In the case of diffusion controlled conversion, when the Thiele number is much larger than one, the expression of the effectiveness η can be asymptotically expanded:

$$\eta \longrightarrow \frac{3}{\Phi} \tag{8.68}$$

In this limit, the overall reaction rate in equation 8.66 can be adjusted as follow:

$$\dot{M}_c = -\frac{4}{3}\pi R_p^3 M_{Carb} \frac{A_i k_i}{\zeta} [C]_s \frac{3}{\Phi} = -4\pi R_p^2 M_{Carb} \frac{A_i k_i}{\zeta} [C]_s \cdot \sqrt{\frac{D_{eff}}{A_i k_i}} \tag{8.69}$$

and finally:

$$\dot{M}_c = -4\pi R_p^2 \frac{M_{Carb}}{\zeta} [C]_s \sqrt{D_{eff}} \cdot \sqrt{A_i k_i} \tag{8.70}$$

Two important observations must be made about the result expressed by this equation:

1. The factor $4\pi R_p^2$ represents the *external area* of the particle. In the limit of reactions largely dominated by pore diffusion, reactions take place on a small volume near the external surface of the particle.
2. The factor $\sqrt{k_i} = \sqrt{A_i} \cdot \exp\left(-\frac{E_i}{RT} \cdot \frac{1}{2}\right)$ shows that the activation energy in this limit is half of the intrinsic activation energy.

The effective diffusivity To determine the effective pore diffusion, two effects have to be taken into consideration :

1. The bulk molecular diffusion described by the diffusion coefficient D_c;
2. The interaction between the walls of the pore and the molecules of reactant, described by the diffusion coefficient D_{kn} (the Knudsen diffusion);

The diffusion in a single pore is written in the following way:

$$\frac{1}{D_i} = \frac{1}{D_c} + \frac{1}{D_{kn}} \tag{8.71}$$

The Knudsen diffusion D_{kn} is given as a function of the particle temperature T_p and pore radius r_p:

$$D_{kn} = 97.0\, r_p \sqrt{\frac{T_p}{M_{ox}}} \tag{8.72}$$

The mean pore radius δ_p are expressed in the following form:

$$r_p = 2\frac{\varepsilon\sqrt{\tau}}{A_i} \tag{8.73}$$

In the previous equation the tortuosity τ and the porosity ε are introduced.

To calculate the effective diffusivity for the entire particle, a simplified model is used, in which a porous layer contains non-intersecting cylindrical capillaries. The mass flux can be modeled using an effective diffusivity:

$$j_e = -D_e \frac{d}{dx}[C] \tag{8.74}$$

or using a summation over the diffusion in each pore [3]:

$$j_p = -D_p \frac{d}{dl}[C] = -\frac{1}{\tau}\frac{d}{dx}[C] \tag{8.75}$$

The total amount of mass has to be diffused through the same effective surface containing N_p pores of diameter δ_p:

$$A_e j_e = \pi \frac{\delta_p^2}{4} N_p j_p \tag{8.76}$$

giving the relation:

$$D_{eff} = \pi \frac{\delta_p^2}{4} \frac{N}{\tau A_e} D_p \tag{8.77}$$

The number of pores is related to the porosity ε by:

$$N = \frac{A_e \varepsilon}{\pi \frac{\delta_p^2}{4} \tau} \tag{8.78}$$

obtaining for the effective diffusivity the final relation:

$$D_{eff} = \frac{\varepsilon}{\tau^2} D_p \tag{8.79}$$

Using the model previously described, the length of the pore and the diameter can be calculated from measured quantities.

$$V_g = N L_P \pi \frac{\delta_p^2}{4} \tag{8.80}$$

$$A_g = N \pi \delta_p L_p \, f(1-\varepsilon) \tag{8.81}$$

where A_g and V_g are the specific internal surface area (in $\frac{m^2}{kg}$) and the specific pore volume (in $\frac{m^3}{kg}$). Solving both relations for δ_p and L_p, we obtain:

$$\delta_p = \frac{4f}{\rho_{app} A_g} \varepsilon (1-\varepsilon) \tag{8.82}$$

$$L_p = \frac{V_g \tau}{A_e \varepsilon} \tag{8.83}$$

The factor f is a roughness factor and for non-intersecting pore:

$$f\,(1-\varepsilon) = 1 \tag{8.84}$$

obtaining back the relation 8.73.

[3] The tortuosity is used to change coordinate along the pore with the coordinate vertical to the surface.

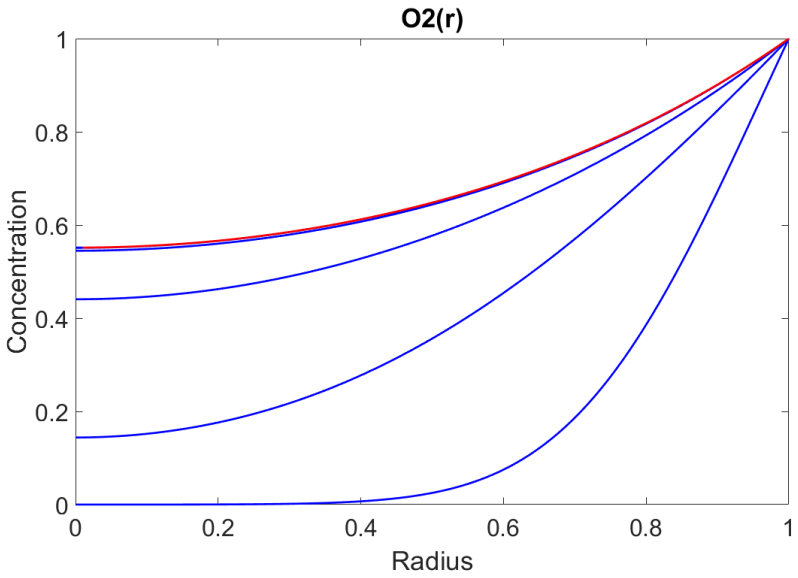

Figure 8.2.: Comparison of reactant concentration using a non steady model (blue curve) and a steady model (red curve) after a time $\tau = 1$

Assumption of the model All the model presented in the previous paragraphs contain the assumption of steady state. Conversion of single particles is intrinsically a non steady process. Before discussing more advanced char reaction models, it is worth analyzing the effects of the this major assumption considering the model intrinsic model just presented.

The unsteady equation for the reactant diffusion inside a spherical particle written as follow:

$$\frac{\partial [C]}{\partial t} + \frac{1}{r^2}\frac{\partial}{\partial r}\left(r^2 D([C], r)\frac{\partial}{\partial r}[C]\right) = S_C([C], r) \tag{8.85}$$

must be accompanied with an equation for the carbon density $\rho_C(r)$ inside the particle :

$$\frac{\partial \rho_C(r)}{\partial t} = -\xi S_C([C], r) \tag{8.86}$$

with, as before, the source term $S_C([C], r)$ is given by:

$$S_c([C], r) = k_a A_i [C]^n \tag{8.87}$$

and ξ is here the inverse of the stoichiometric coefficient.

Unsteady effects originates by two phenomena:

1. Oxygen needs time to diffuse inside the particle;

2. The local internal area A_i is a function of the local burnout $B(r)$ and, consequently it is a function of the time.

To analyze the impact of those two phenomena, properties are assumed constant and, as done for the intrinsic model, the equations are reduced in non dimensional form. The resulting

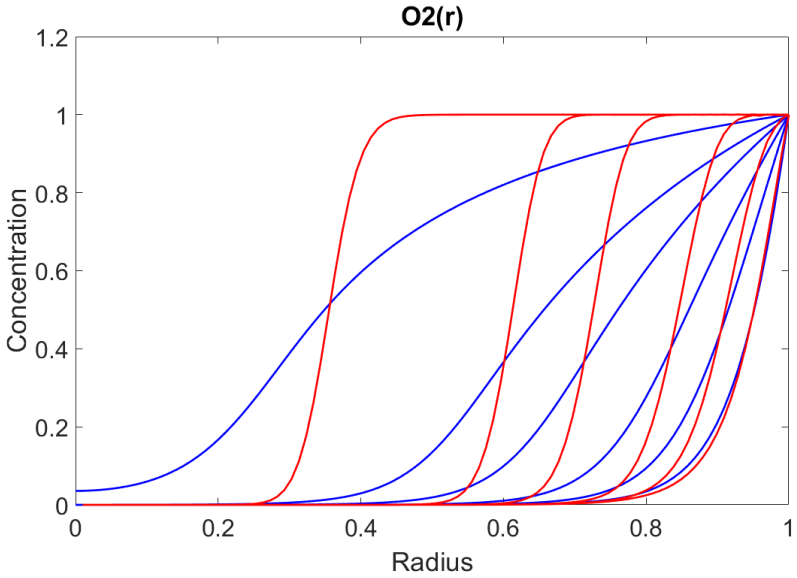

Figure 8.3.: Comparison of The numerical solution of the system 8.88 (blue curve) with the prediction of the intrinsic model (red curve) for different times in the case of a unitary Thiele modulus

system of partial differential equations is the following:

$$\begin{cases} \frac{\partial [C]}{\partial \tau} + \frac{1}{x^2}\frac{\partial}{\partial x}\left(x^2([C],x)\frac{\partial}{\partial x}[C]\right) = A_i k_i (1-B)\cdot[C] \\ \frac{\partial B}{\partial \tau} = \xi \frac{\rho_g}{\rho_C} A_i k_i (1-B)\cdot[C] \end{cases} \tag{8.88}$$

In the previous equation the time has been scaled using the diffusion time scale:

$$\tau^* = \frac{R_p^2}{D} \tag{8.89}$$

In the second equation in the system 8.88 it is important to notice the factor $\frac{\rho_g}{\rho_C} \sim \frac{1}{1000}$ that multiply the source term for the burnout. As a consequence, the concentration $[C]$ of the gaseous reactant changes following the time scale τ^* that in the reduced system 8.88 becomes $\tau = 1$. If the Thiele modulus is equal unity or smaller than unity, chemical reactions do not change this time scale, and the concentration adjust to the changes in burnout with time scale similar to τ^* ($\tau = 1$ in the reduced system).

The variation of the burnout follows a time scale that is a factor $\frac{\rho_g}{\rho_C} \sim \frac{1}{1000}$ slower. The gaseous reactants have plenty of time to arrange themselves to the variation of B and as shown in Figure Figure 8.3 the assumption of steady state condition for each burnout is correct.

If the local internal area is considered as a function of the local burnout, the analytical solution used for the derivation of the intrinsic model is not anymore valid. The numerical solution of the system 8.88 is compared with the prediction of the intrinsic model in Figures Figure 8.3 and Figure 8.4. The intrinsic model is calculated considering an averaged burnout all over the particle. Figure Figure 8.3 shows that the local burnout differs between the two models but the averaged one doe not. The intrinsic model can be still used with accuracy to calculate the averaged burnout of a particle.

It is interesting to notice that for small Thiele modulus (see Figure Figure 8.4) the differ-

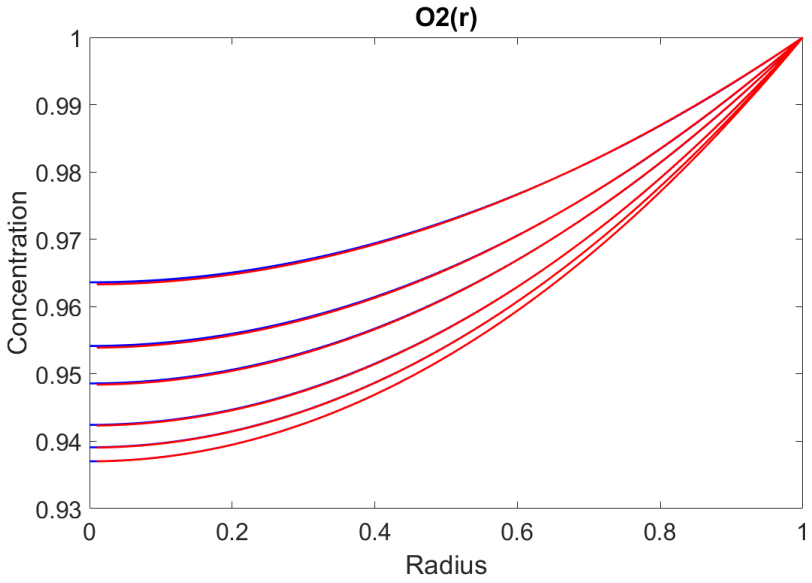

Figure 8.4.: Comparison of The numerical solution of the system 8.88 (blue curve) with the prediction of the intrinsic model (red curve) for different times in the case of a small Thiele modulus

ences between the two models disappear also in the prediction of the local burnout.

8.5.1.2. General reaction order

For a general reaction order $n \neq 1$ there is no closed solution for the transport equation given by equation 8.4. An approximate solution is given by the same reaction rate given in equation 8.66:

$$\dot{M}_c = -A_T M_{Carb} \frac{k_i}{\zeta} [C]_s \eta \tag{8.90}$$

$$\eta = \frac{3}{\Phi^2}\left(1 - \frac{\Phi}{\tanh \Phi}\right) \tag{8.91}$$

with the following definition of a generalized Thiele number:

$$\Phi = R_p \sqrt{\frac{n+1}{2} \frac{A_i k_i}{D_{eff}} [C]_S^n} \tag{8.92}$$

8.5.1.3. General geometries

The geometry of a coal particle is in general non-spherical. For a general geometry of the particle, there is no closed solution for the transport equation given in equation 8.4. An approximate solution is given by the same reaction rate in 8.66:

$$\dot{M}_c = -A_T M_{Carb} \frac{k_i}{\zeta} [C]_s \eta \tag{8.93}$$

$$\eta = \frac{3}{\Phi^2}\left(1 - \frac{\Phi}{\tanh \Phi}\right) \tag{8.94}$$

with the following definition of a generalized Thiele number:

$$\Phi = R_{eff}\sqrt{\frac{n+1}{2}\frac{A_i k_i}{D_{eff}}[C]_S^n} \tag{8.95}$$

where the *effective* radius R_{eff} is given as a function of the volume of the coal V_p and its external surface S_p:

$$R_{eff} = \frac{V_p}{S_p} \tag{8.96}$$

8.5.1.4. Langmuir reaction rate

If the reaction rate is expressed using the Langmuir form

$$\dot{R} = \frac{k_1 \cdot [C]}{1 + k_2 \cdot [C]} \tag{8.97}$$

a correction factor for the effectiveness given in equation 8.67 must be considered [156]:

$$f_c = \left(1 + \frac{\sqrt{1/2}}{2\Phi^2 + \frac{1}{2\Phi^2}}\right)^{0.5(1-n_{obs})^2} \tag{8.98}$$

where Φ is the Thiele number and the observed reaction order n_{abs} is defined as a function of the concentration at the surface $[C]_s$ by:

$$n_{obs} = \frac{1}{1 + k[C]_s} \tag{8.99}$$

The Thiele number must be also modified and its expression is written below:

$$\Phi = R_p\sqrt{\frac{A_i k_1}{D_{eff}}}\left(\frac{k_2 \cdot [C]_s}{1 + k_2 \cdot [C]_s}\right)\sqrt{\frac{1}{k_2 \cdot [C]_s - \ln(1 + k_2 \cdot [C]_s)}} \tag{8.100}$$

8.6. Surface development

The considerations of the previous Section focused on the dependencies between diffusion and reaction rate. They point out that the development of the internal surface plays an important role. The single-pore model presented in Section 8.5.1 assumed a dependency of the internal area with the burnout B of the form:

$$A_i = A_v \cdot \rho_p = A_v \cdot \rho_{p,0} \cdot (1 - B) \tag{8.101}$$

with the specific surface A_v assumed to be constant and the initial particle density given by $\rho_{p,0}$.

Since the pores are not isolated, this assumption can be questionable and indeed is not anymore correct for high burnouts, where the particles become more porous. The forthcoming sections show how the development of the internal area can be taken into account.

8.6.1. Lattice model

In this model, following the description of Section 7.1.2, the development of the internal area A_i as a function of the burnout, is calculated assuming that the pores possess a geometrical lattice distribution inside the solid particle.

The the internal surface per unit of volume A_i is calculated by the model with the relation 7.14, rewritten below:

$$A_i = \frac{12}{\delta} Z^2 (1 - Z)$$

where:

$$Z = \frac{N^3 \delta^3}{L^3}$$

and the porosity ε of the particle must be written using 7.11:

$$\varepsilon = 3Z^2 - 2Z^3$$

The variable Z is linked to the porosity that is linked to the burnout:

$$B = \tag{8.102}$$

in such a way that:

$$B = 1 \Longrightarrow Z = 1 \tag{8.103}$$

The internal area increase for $Z < \frac{1}{2}$ and decrease towards zero for $Z > \frac{1}{2}$.

8.6.2. Bimodal pore structure

From the simple lattice analysis presented in the previous section, it can be observed that the porosity is a function of the macropores distribution while the internal surface is a function of the micropores distribution. The pore structure is assumed to be bimodal in [118, 215] and this approach allows the Authors to derive a dependency of the internal surface from the burnout similar to the derivation using the random pore model theory (see next Section Section 8.6.3). The predicted particle structure parameters based on the initial surface area and porosity of macropores and micropores in the particle showed a reasonable agreement with the experimental extraction from both CO_2 gasification and air combustion. The predicted reaction rates, using this modified random pore model, agreed well with the experimental measurements under various conditions.

8.6.3. Random-pore models

According to the model shortly described in Section 7.1.3 the balance equation for the size of the growing cylinders can be written (see 7.26):

$$\frac{\partial f(r)}{\partial t} + \frac{\partial}{\partial t}\left(f(r)\frac{\partial r}{\partial t}\right) = 0$$

with the only assumption that pores are neither created nor destroyed.

If the rate of reaction on the actual surface is proportional to the total surface area (scaling as r^2), the rate of change of the pore diameter can be expressed as a function of the reactant concentration $[C]$:

$$\frac{dr}{dt} = -k_s [C]^n \tag{8.104}$$

Using equation 8.104 into equation 7.26 the following partial differential equation for the distribution $f(r)$ is obtained:

$$\frac{\partial f(r)}{\partial t} = -k_s \left[C\right]^n \frac{\partial}{\partial t} f(r) \tag{8.105}$$

with the boundary conditions $f(0) = 0$ and $f(\infty) = 0$. After multiplication by power of r and integration the following relation can be derived:

$$\frac{d}{dt} L_E = 0 \tag{8.106}$$

$$\frac{d}{dt} S_E = 2\pi k_s \left[C\right]^n L_E \tag{8.107}$$

$$\frac{d}{dt} V_E = k_s \left[C\right]^n S_E \tag{8.108}$$

The solution of the previous system of differential equations is given by:

$$S_E = \sqrt{(S_E^0)^2 + 4\pi L_E^0 (V_E - V_E^0)} \tag{8.109}$$

$$V_E = V_E^0 + S_E^0 k_s \left[C\right]^n t + \pi L_E^0 (k_s \left[C\right]^n t)^2 \tag{8.110}$$

The quantities presented in the previous equations must be related to the corresponding properties of the actual (overlapped) surface. The change in volume of overlapped surfaces is only a small fraction of the change of the actual volume enclosed by the non-overlapped surface V and this fraction is equal to $1 - V$. Therefore:

$$dV = (1 - V) dV_E \tag{8.111}$$

After considering that $V \to 0$ as $V_E \to 0$, this equation can be integrated to give V as a function of V_E:

$$V = 1 - e^{-V_E} \tag{8.112}$$

Under the same assumptions used until here, a relationship between the overlapped surface S_E and the non-overlapped surface S can be derived:

$$S = S_E (1 - V) \tag{8.113}$$

The change in the total length of the pores due to additional intersections may be written as:

$$dL = -\frac{L}{1 - V} dV \tag{8.114}$$

Considering that non-overlapping is possible as $V_E \to 0$, the integral relation follows:

$$L = L_E (1 - V) \tag{8.115}$$

Combining 8.112, 8.113 and 8.115 the final relations for the actual internal surface and the actual volume can be achieved:

$$\frac{S}{S_0} = \frac{1 - V}{1 - V_0} \sqrt{1 - \frac{4\pi L_0 (1 - V_0)}{S_0^2} \ln\left(\frac{1 - V}{1 - V_0}\right)} \tag{8.116}$$

$$\frac{1 - V}{1 - V_0} = \exp\left(-\frac{k_s \left[C\right]^n t}{1 - V_0} \left(S_0 + k_s \left[C\right]^n t\right)\right) \tag{8.117}$$

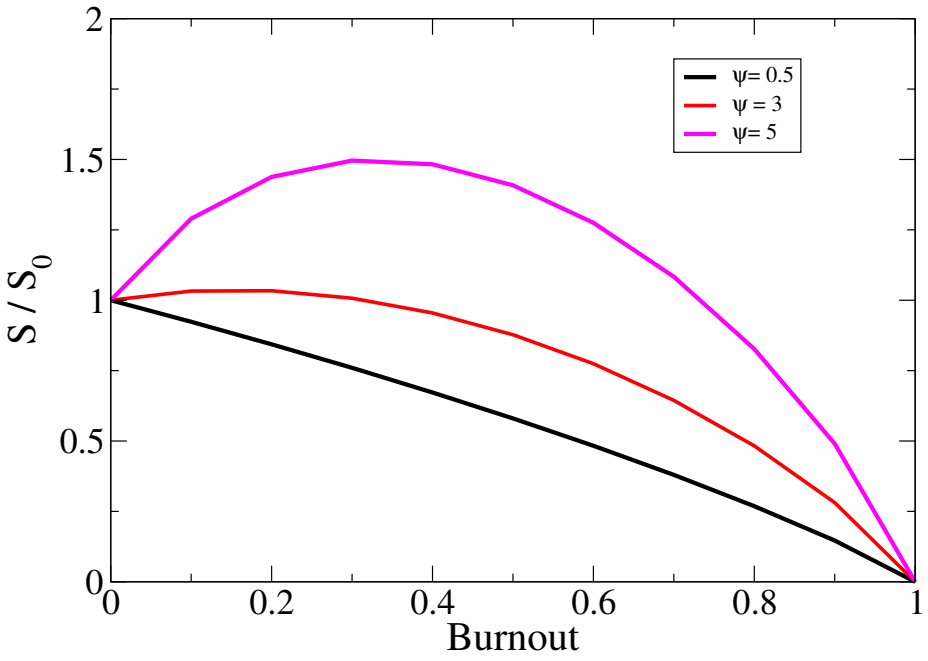

Figure 8.5.: Ratio between the initial internal surface and the internal surface available as a function of burnout B predicted by the random pore model. The curve are given for different values of the parameter ψ

For a spherical particle in the reaction controlled regime, the burnout can be calculated as:

$$1 - B = \frac{1 - V}{1 - V_0} \left(1 - \frac{k_s \left[C\right]^n t}{R_0} \right)^3 \tag{8.118}$$

where R_0 is the initial particle radius. This relation leads to the following formula for the internal surface development:

$$\frac{S}{S_0} = \frac{1 - B}{(1 - \frac{\tau}{\sigma})^3} \sqrt{1 - \psi \ln \left(\frac{1 - B}{1 - \frac{\tau}{\sigma})^3} \right)} \tag{8.119}$$

where $\tau = \frac{k_s \left[C\right]^n t}{1 - \epsilon_0}$ is the dimensionless time, $\sigma = \frac{R_0 S_0}{1 - \epsilon_0}$ the particle size parameter. $\psi = \frac{4\pi L_0 (1 - \epsilon_0)}{S_0^2}$ the structural parameter, and ϵ_0 the initial porosity.

After devolatilization, many chars have already a well developed internal surface and the parameter $\sigma \gg 1$. In this approximation the final form of the internal surface development can be written as in [35]:

$$\frac{S}{S_0} = (1 - B) \sqrt{1 - \psi \ln(1 - B)} \tag{8.120}$$

Figure Figure 8.5 show three typical curve representing the changes of the internal surface with increasing burnout B. All the curves decrease for large burnout, but if the structural parameter ψ is large enough, then the internal surface increase at the beginning of the conversion as in the case of coal combustion. If the structural parameter is lower than the critical parameter the internal surface will decreases for during the entire conversion as in the case observed during

conversion of of biomasses.

If among the products of the heterogeneous reactions solid remnants are present, the concentration of reactant $[C]_i$ at the interface must be calculated from the concentration in the bulk of the pore [36]. The layer of non-reacting remnants causes extra resistance to diffusion. Assuming a linear concentration gradient in the diffusion layer of thickness Δ a material balance for the reactant provides the following equation:

$$D_r \frac{[C] - [C]_i}{\Delta} = \frac{k_s [C]_i \zeta \rho}{M} \tag{8.121}$$

with D_r the molecular diffusivity of the reactant across the layer, M the molecular weight of the reactant an a the stoichiometry coefficient of the reaction

$$\mathrm{C(s)} + \zeta \mathrm{R(g)} \longrightarrow \mathrm{pP(g)} + \mathrm{qR(s)} \tag{R 8.4}$$

.

An equation for the thickness Δ can be obtained using mass balance for the solid phase and can be written:

$$\Delta = \frac{2Z(1-\epsilon_0)}{\psi S_0} \left(\sqrt{1 - \psi \ln(1-B)} - 1 \right) \tag{8.122}$$

where Z is the ratio of volume of solid phase after reaction to that before reaction.

Combining 8.120, 8.122 and 8.121 the equation for the mass loss of the particle reads:

$$\frac{dB}{dt} = \frac{k_s S_0 [c] (1-B) \sqrt{1 - \psi \ln(1-B)}}{(1-\epsilon_0) \left(1 + \frac{\beta Z}{\psi} (\sqrt{1 - \psi \ln(1-B)} - 1) \right)} \tag{8.123}$$

where $\beta = \frac{2K_s \zeta \rho (1-\epsilon_0)}{M D_r S_0}$ is a modified Biot modulus.

8.6.4. Pores-tree models

The pore tree model described in Section 7.1.4 assumes that pores at the surface are the base of a structure that develops deep inside a particle.

As described in the section previously mentioned, a balance equation for the size of the growing cylinders can be written as 7.26:

$$\frac{\partial f(r)}{\partial t} + \frac{\partial}{\partial r} \left(f(r) \frac{\partial r}{\partial t} \right) = 0$$

with the only assumption that pores are neither created nor destroyed.

In this approximation

$$k = k_i p_g [C] \tag{8.124}$$

and the absorption rate constant is a function only of the temperature:

$$k_i = \frac{k_1 k_2}{K' + k_2} \tag{8.125}$$

In the values of the Arrhenius rates are given in [331] and [209] by the correlations:

$$k_1 = 900e^{-19000/T} \tag{8.126}$$
$$k_2 = 90e^{-19000/T} \tag{8.127}$$
$$K = 200k_1k_2e^{-3500/T} \tag{8.128}$$

If the diffusion is dominated by wall interactions (Knudsen diffusion) then

$$D = \frac{2}{3}\overline{V}r_p \tag{8.129}$$

where $\overline{V} = \sqrt{\frac{8RT}{\pi M}}$ is the mean thermal velocity of the gas.

The solution under the previous conditions can be written as:

$$\dot{m}_t = ptr_t^2c_0\left(\frac{3}{4}k_ip_g\rho_g\overline{V}\right)^{1/2}\left(\frac{e^{2k}-1}{e^{2k}+1}\right) \tag{8.130}$$

with:

$$k = \sqrt{\frac{3k_ip_g}{\rho_g\overline{V}}}\left(\frac{S_t(r_t)}{2\pi r_t^2}\right) \tag{8.131}$$

The reaction rate obtained from the solution of the general equation written in 7.36 must then be summed up over all the pores distribution, with the result that several regimes can be identified:

- $r_{min} < r_t < r_1$: The reactions rate $\dot{m}_{KL}$ is kinetically controlled;
- $r_1 < r_t < r_2$: The reactions rate $\dot{m}_{KD}$ is controlled by Knudsen diffusion;
- $r_2 < r_t < r_{max}$: The reactions rate $\dot{m}_{BD}$ is controlled by bulk diffusion.

where the values for r_1 and r_2 are obtained imposing the continuity for the reaction rates.

In order to be used, the model needs the determination of the initial porosity ε_0 and the initial internal surface that in [334] is assumed to vary as:

$$s_p = 100 \cdot \varepsilon_0 \frac{m^2}{g} \tag{8.132}$$

It is important to remark here that in equation 8.131 and in equation 8.63 the pore radius produces different effects. In the definition of the Thiele modulus 8.63 smaller pore produce larger ϕ and therefore, following the single-pore model, combustion is diffusion limited. In the pore-tree model, small pore structures (trees) have bigger k (the pore-tree radius r_t is in the denominator) and therefore they are chemically controlled.

8.7. Phenomenological models

The starting point for the phenomenological (effective) models is the pseudo-kinetic equation given in 8.30:

$$\frac{dm_p}{dt} = \frac{1}{\zeta}A_pk_C\left[C\right]_S^n \tag{8.133}$$

The biggest drawback of this models is the lack of accuracy in the prediction of the last part of the burnout fraction because from experiments it is known that the combustion rates decrease at higher burnout (see also Section 2.10 and Section 8.8).

Instead of describing more details of the physics involved in the char combustion, the phenomenological models apply corrections to the above equation that takes into account the behavior mentioned above. Analytically the equation is as follows:

$$\frac{dm_p}{dt} = \frac{1}{\zeta} A_p k_C \left[C\right]_S^n f(B) S(B) \tag{8.134}$$

The functions $f(B)$ and $S(B)$ describe the chemical inhibition of the char at high burnout and the changes of the relative internal surface. They must be derived from experiments.

8.7.1. The Field's model

In [108] empirical expressions for the description of particle diameter as well as apparent density changes during the burnout have been defined in the following way:

$$d = d_0 \cdot (1 - B)^{\alpha} \tag{8.135}$$

$$\rho_a = \rho_{a,0} \cdot (1 - B)^{\beta} = \rho_{a,0} \cdot (1 - B)^{1 - 3 \cdot \alpha} \tag{8.136}$$

The exponents α and β are empirical parameters. After taking into account the dependency between the diameter and density of the particle by the use of mass conservation, the parameters α and β have to satisfy at every instance the following equation:

$$1 = \beta + 3 \cdot \alpha \tag{8.137}$$

Which combustion regime, the particle is burning at, is described by the exponent α.

1. In the case of diffusion-controlled combustion, the particle would burn with changing diameter and constant density ($\alpha = 0.333$, $\beta = 0$);

2. For kinetically-controlled combustion, the particle diameter would be constant, whereas density of the particle would continuously decrease ($\alpha = 0$, $\beta = 1$);

3. Some other specific cases can be distinguish:
   - For $\alpha = 0.5$ the surface area is constant and burnout increases linearly with time,
   - For $\alpha = 1$ the surface area is linearly decreasing and this results in an exponential expression for the burnout over the time (IFRF approach);
   - For $\alpha > 1$ the surface area is hyperbolically decreasing.

Applying the α parameter of Field into the description of the specific surface area leads to:

$$\frac{S_a(B)}{S_{a,0}} = (1 - B)^{2 \cdot \alpha} \tag{8.138}$$

The burnout for any $\alpha \neq 0.5$ can be calculated as:

$$B(t) = 1 - \sqrt[1-2\cdot\alpha]{1 - (1 - 2 \cdot \alpha) \cdot q_0 \cdot S_{a,0} \cdot t} \tag{8.139}$$

8.7.2. Extended approach for cenospherical particles

Smith [339] presented an extension of the Field model which takes into account more adequately the behavior of bituminous coals in the course of combustion. Char of these coals plasticizes during devolatilization and often forms an inflated sphere with one or more large internal voids (so-called cenosphere). For those particles, considering the simplified radial mass distribution inside the cenospherical particle results in a better model than describing the particle as a homogeneous sphere.

Smith improve the Field equations for particle diameter (8.135) and apparent density (8.136) with a diameter ratio C_d:

$$C_d = \frac{d_{external}}{d_{internal}} \tag{8.140}$$

$$d = d_0 \cdot (1 - B + B \cdot C_d^3)^{0.333} \tag{8.141}$$

$$\rho_a = \rho_{a,0} \cdot \frac{(1-B)}{(1 - B + B \cdot C_d^3)} \tag{8.142}$$

8.7.3. Unreacted shrinking-core model

The unreacted shrinking coal model assumes that quick chemical reactions take place in a thin layer around the particles while the reactant does not have time to diffuse towards the internal regions. Solid remnants may increase the resistance at higher burnout if they do not detach from the original solid structure. The surface available for the reaction is proportional to the external surface of the core that is a function of the core radius r_c:

$$\frac{dm_p}{dt} = 4\pi r_c^2 k_s \left[\mathrm{O_2}\right]_s^n \tag{8.143}$$

The concentration at the surface $\left[\mathrm{O_2}\right]_s^n$ must be calculated after application of the mass balance relation considering diffusion thorough the gas film and the diffusion thorough the external remnants:

$$\frac{D_e}{\frac{1}{R_p} - \frac{1}{r_c}} \left(\left[\mathrm{O_2}\right] - \left[\mathrm{O_2}\right]_s\right) = 4\pi r_c^2 k_s \left[\mathrm{O_2}\right]_s^n \tag{8.144}$$

The solution of the previous equation has been already discussed in Section 8.4.

8.7.4. The IFRF-97 model

The IFRF model (IFRF is an acronym for Intenational Flame Research Foundation) considers the decreasing of the reactivity at high burnout to be proportional to the burnout itself. The reaction rate is then written:

$$\frac{dm_p}{dt} = \frac{1}{\zeta} A_p k_C \left[C\right]_S^n (1 - B) \tag{8.145}$$

In 1997 Haas [138] extended the IFRF model considering two major effects on the normalized surface area:

- influence of the ash (f_1),
- influence of the temperature (f_2).

According to the model the normalized surface area is given by:

$$\frac{S_a}{S_{a,0}} = (1-B)\cdot f_1(B,a,P_D)\cdot f_2(B,T,\varepsilon_{max}) \tag{8.146}$$

When $f_1 = f_2 = 1$ equation 8.146 simplifies to the equation proposed at the foundation.

The burnout rate is given by:

$$\frac{dB}{dt} = q_0 \cdot S_{a,0} \cdot (1-B)\cdot f_1 \cdot f_2 \tag{8.147}$$

The first term, q_0, is a combustion rate derived from the pseudo–kinetic model and it is calculated from the initial char properties (d_0, ρ_0).

The aforementioned correction terms, f_1 and f_2, consider the nonlinear behavior of the surface area. The first correction, given by f_1, considers the non-linear effect of the ash content increasing for higher burnouts. By the high burnout level the ash content in the rest of char grain is more than 90%. This influence of the non-combustible phase on the burnout is calculated as follows:

$$f_1 = \left(\frac{1-a}{1-a_0}\right)^{P_D} \tag{8.148}$$

where a and a_0 are instantaneous and initial ash content in the particle, respectively. The fraction $\left(\frac{1-a}{1-a_0}\right)$ represents the instantaneous over the initial fraction of combustible matter and is assumed to be proportional to the instantaneous combustible surface area. With increasing the burnout degree the non-combustible surface of ash in the rest grain rises and passivates the char. In the case that ash also forms a resistance for diffusion of the reactant inflow, the passive parameter P_D increases. For the $P_D = 0$ no effect of the ash on burnout is observed and f_1 is a constant. Adjustment to the measurements has shown that for most of the coals P_D has a value $0 \div 1$ (however, the value 1 is not the upper limit).

The second correction term, given by f_2, takes into account the effect of the temperature on the normalized surface area. When the temperature is low, the total surface area of pores (inside the particle) can be used for the reaction. Otherwise, when the temperature is high, the C concentration on the outer surface of the particle is near zero. Therefore the maximum of the available reaction surface depends on the temperature and is defined as:

$$\frac{S_{a,max}}{S_{a,0}} = [1+B_{max}]^{\left(\frac{k_D}{k_c}\right)} \tag{8.149}$$

The exponent $(\frac{k_D}{k_c})$ describes how big is the ratio of reaction to the diffusion rate. When $(\frac{k_D}{k_c}) > 1$, the diffusive transport is much bigger than reaction rate, and reactant has enough time to penetrate the particle. In this case, the reaction surface area will be maximum. For very small values of $(\frac{k_D}{k_c}) < 1$ the exponent approaches zero and $\frac{S_{a,max}}{S_{a,0}} \to 1$, because no reactant reaches the inner surface area and the combustion takes place only on the outer surface area.

Photos of different chars from electron microscope have shown the typical evolution of the pore structure. The surface of the char particle burns and it gives access to the internal pore structure of the particle. The available surface area increases and can be accessed by reactant. If the partial pressure of C at the outer surface is not zero, it reacts at the pore walls resulting with growing of the porosity. At the maximum possible porosity particle starts to defragment and pores coalescence. Due to this effect, the total available surface area decreases. A first approximation for this phenomena is that the available pore surface area grows linearly until reaches the maximum value, then declines linearly:

For $B < B_{max}$:

$$f_2 = \frac{S_a}{S_{a,0}} = \frac{\frac{S_{a,max}}{S_{a,0}} - 1}{B_{max}} \cdot B + 1 \tag{8.150}$$

For $B \geq B_{max}$:

$$f_2 = \frac{S_a}{S_{a,0}} = \frac{1 - \frac{S_{a,max}}{S_{a,0}}}{1 - B_{max}} \cdot B + \frac{\frac{S_{a,max}}{S_{a,0}} - B_{max}}{1 - B_{max}} \tag{8.151}$$

where $S_{a,max}$ is the maximum surface area at the state of maximum porosity and B_{max} is the burnout degree X at which the maximum porosity is reached. It is derived from the expression for the entire particle volume:

$$V_p \cdot (1 - \varepsilon) = V_{ash} + V_c \tag{8.152}$$

where ε is the particle porosity. Assuming that the volume of carbon, V_c, changes proportionally with the carbon mass, B_{max} can be calculated:

$$B_{max} = \frac{\rho_c}{\rho_{a,0}} \cdot \frac{1}{1 - a_{0,char}} \cdot (\varepsilon_{max} - \varepsilon_0) \tag{8.153}$$

The carbon density is set to 2000 $\frac{\text{kg}}{\text{m}^3}$, whereas ε_{max} and ε_0 are the maximum and initial porosity of the particle, respectively. The initial value of the porosity can be calculated as follows:

$$\varepsilon_0 = 1 - \frac{\frac{\rho_c}{\rho_{a,0}} \cdot (1 - a_{0,coal}) \cdot HVM}{C_{sw}^3} \tag{8.154}$$

HMV is the high volatile matter yield and C_{sw} is the swelling coefficient (the diameter ratio of char to coal). The maximum achievable porosity ε_{max} depends on the initial char properties, and it is a specific parameter for each coal. Generally, the later the maximum porosity is reached, the higher increase of surface area will be.

The passivation parameter P_D is set arbitrary, the maximum porosity is determined by normalizing the reaction rate to the initial reaction rate and assuming that the change of reactivity is only due to the change of specific surface area.

8.8. Char deactivation

Many of the aforementioned models are not able to describe the deactivation of the solid structure reactivity at higher burnouts [441]. A model has been proposed [49] where non-active sites are converted at high temperature into further reacting active sites. The final rate is the following:

$$\dot{R} = \frac{k\,[C]}{1 + b\,[C]}\chi + k_I\,[C]\,(1 - \chi) \tag{8.155}$$

where χ is the fraction of active sites and k_I is the rate coefficient of the conversion into inactive sites.

According to the model of Hurt [160], the sites in a char deactivate by a first-order thermal process and are assumed to have a common pre-exponential factor and a distribution of activation energies for annealing. The parameters for the untreated chars are corrected by the deactivation ratio. Using this approach the untreated char reactivity can be back-calculated and used as an intrinsic reactivity determined for every single fuel.

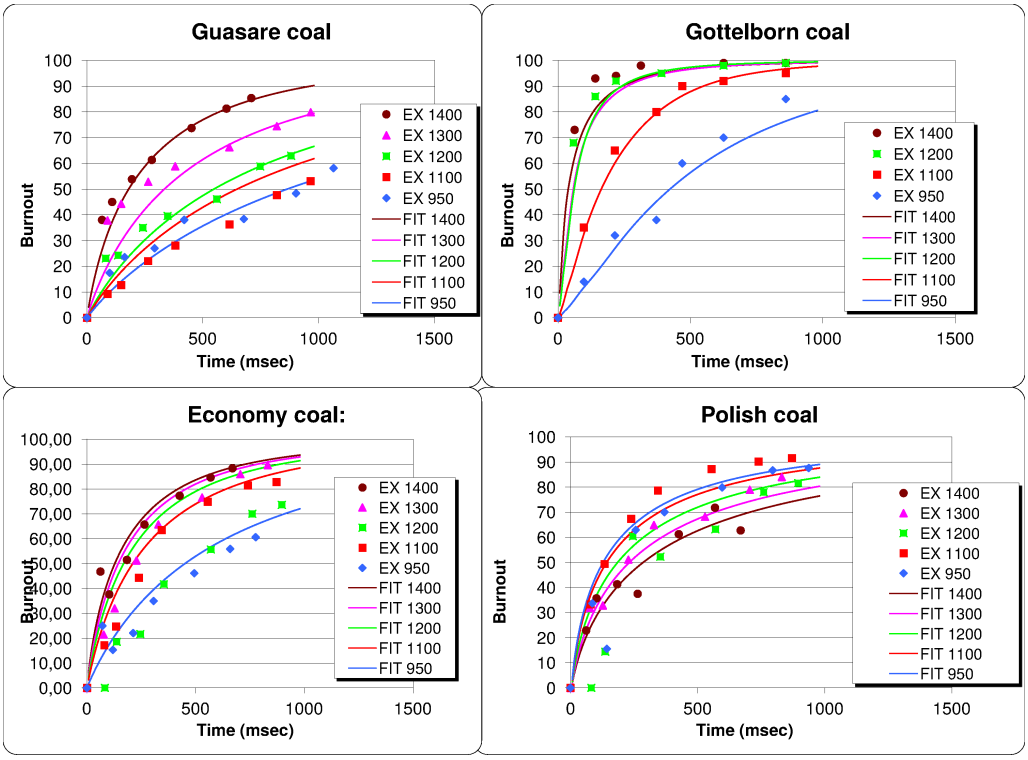

Figure 8.6.: Examples of fitting results for the char combustion of four different coals

8.9. Some examples

Fitting curves of measured burnout for four coals against residence time are presented in this paragraph. See Chapter 11 for the description of the fitting method.

In Figure 8.6 the fitting has been performed for the combustion models described in section Section 8.4 by the equation 8.38 (the kinetic-limited model) using the single pore model described in section Section 8.5. The model is a kinetic-limited model with non-unity reaction order where bulk diffusion is taken into consideration. The kinetic constant is calculated using the intrinsic model based on a single pore model with correction for the reaction order.

As shown in the Figure, the agreement is excellent for almost all the coals, and the fitting is quite well for all the temperatures taken into consideration.

9. Pollutants

Because of the chemical complexity of solid fuels, many unwanted components are generated during its thermal conversion [423]. It is possible to distinguish them into three different types of compounds:

1. compounds coming from the fuel;
2. by-products of combustion;
3. compounds due to incomplete combustion.

The compounds that belong to the first category are also the most harmful. To this group belong the $Fuel\ \ NO$, sulfur compounds, minerals, unburned particles.

Due to incomplete combustion, CO, soot, volatile organic compounds (VOC) and polycyclic aromatic hydrocarbons (PAH) are released into the atmosphere. Smaller quantities of other pollutants such as trace metals, hydrogen halides, unburnt hydrocarbons, non-methane volatile organic compounds and dioxins may also be emitted.

In this Chapter, only CO and NO emissions will be taken into consideration. The mechanism leading to the formation and destruction of both molecules will be underlined and the fundamentals of several modeling approaches will be presented. The exact prediction of CO emission is essential since this unburned molecule carries out a certain amount of energy reducing the thermal efficiency of the plants. Among the NO_x components, the NO_2 is the most harmful. It causes lungs irritation, and it leads to low blood pressure. In the presence of water, it forms nitric acid which is one of the most common components of acid rains. It is also a greenhouse gas. In high temperature processes NO_2 is thermodynamically disfavored and NO becomes the principal molecules to be considered.

9.1. CO emissions

CO emission is a result of the balance between its formation and its oxidation. In fact, CO is always formed during oxidation of hydrocarbons and during conversion of solid fuels, but its further oxidation is slowed down since the OH radicals, responsible for CO and hydrocarbon oxidation, prefer to react with hydrocarbons than with the carbon monoxide.

During conversion of solid carbonaceous particles, the following processes are responsible for the formation mechanism of the carbon monoxide:

1. Homogeneous formation from oxidation of hydrocarbons;
2. Formation during pyrolysis and devolatilization;
3. Heterogeneous oxidation of Char structure;
4. Heterogeneous gasification of Char structure due to the Boudoir reaction;
5. Homogeneous Water Gas Shift reaction ($CO_2 + H_2 \longrightarrow CO + H_2O$);
6. Heterogeneous Water Gas Shift reaction ($C(s) + H_2O \longrightarrow CO + H_2$).

Homogeneous CO formation CO oxidation is usually the last oxidation step of hydrocarbons (see [434]). Long hydrocarbons chains break down into CO, and only afterward the CO oxidation takes place. Usually, the reactions involving hydrocarbons cracking are much faster than carbon monoxide oxidation.

The formation of CO is almost entirely due to the reactions of HCO radical:

$$\mathrm{HCO + H_2O \rightleftharpoons H + CO + H_2O} \quad \text{(R 9.1)}$$

$$\mathrm{HCO + O_2 \rightleftharpoons HO_2 + CO} \quad \text{(R 9.2)}$$

$$\mathrm{HCO + OH \rightleftharpoons H_2O + CO} \quad \text{(R 9.3)}$$

$$\mathrm{HCO + M \rightleftharpoons H + CO + M} \quad \text{(R 9.4)}$$

A smaller amount of CO is formed in reactions involving directly higher radicals:

$$\mathrm{CH_3 + O \rightleftharpoons H + H_2 + CO} \quad \text{(R 9.5)}$$

$$\mathrm{CH_2 + O \rightleftharpoons H_2 + CO} \quad \text{(R 9.6)}$$

$$\mathrm{CH_2 + O_2 \rightleftharpoons OH + H + CO} \quad \text{(R 9.7)}$$

$$\mathrm{CH_2 + CO_2 \rightleftharpoons CO + CH_2O} \quad \text{(R 9.8)}$$

$$\mathrm{CH + O \rightleftharpoons H + CO} \quad \text{(R 9.9)}$$

$$\mathrm{HCCO + O_2 \rightleftharpoons 2\,CO + OH} \quad \text{(R 9.10)}$$

Formation during pyrolysis During pyrolysis, bonds are disrupted, and a gas composed of several light molecules are released. Pyrolysis models are responsible for the prediction of the concentration of CO in those gas.

In the case of the CPD model developed in [121] and described in Section 6.2.9, a look-up table is used to determine the composition of each light gas released from a coal as a function of the extent of the total volatile release, interpolating the values from several measured coals.

In Figure 9.1 (Up) the predicted composition of light gases for a range of coals is presented. The amount of carbon monoxide is almost constant, lying in the range 10 to 20 (volume %) and it is higher for low carbon content coals. It is interesting to notice from the Figure, how heavy molecules (usually undetected) are pyrolyzed in the case of coals with high carbon content.

In Figure 9.1 (Bottom) the history of the composition of the light gas is presented (mass % of the parent coal) for the Gïttelborn (hvb coal with 80 % C) for an heating rate $10^5 \frac{\mathrm{K}}{\mathrm{s}}$. Few results presented in the Figure are worth to be mentioned here:

1. The release of the tars start at relatively low temperatures and is completed below T =900 °C;
2. The release of the gas is bimodal with a second peak around T =900 °C;
3. The CO release is the last process starting well above T =600 °C and is completed at the highest temperature reached by the sample.

Heterogeneous CO formation route Carbon monoxide is formed during char conversion, during both oxidation processes and in the gasification processes:

$$\mathrm{C} + \gamma\ \mathrm{O_2} \longrightarrow 2\,(1-\gamma)\,\mathrm{CO} + 2\,(\gamma - \frac{1}{2})\ \mathrm{CO_2} \quad \text{(R 9.11)}$$

$$\mathrm{C + CO_2 \longrightarrow 2\,CO} \quad \text{(R 9.12)}$$

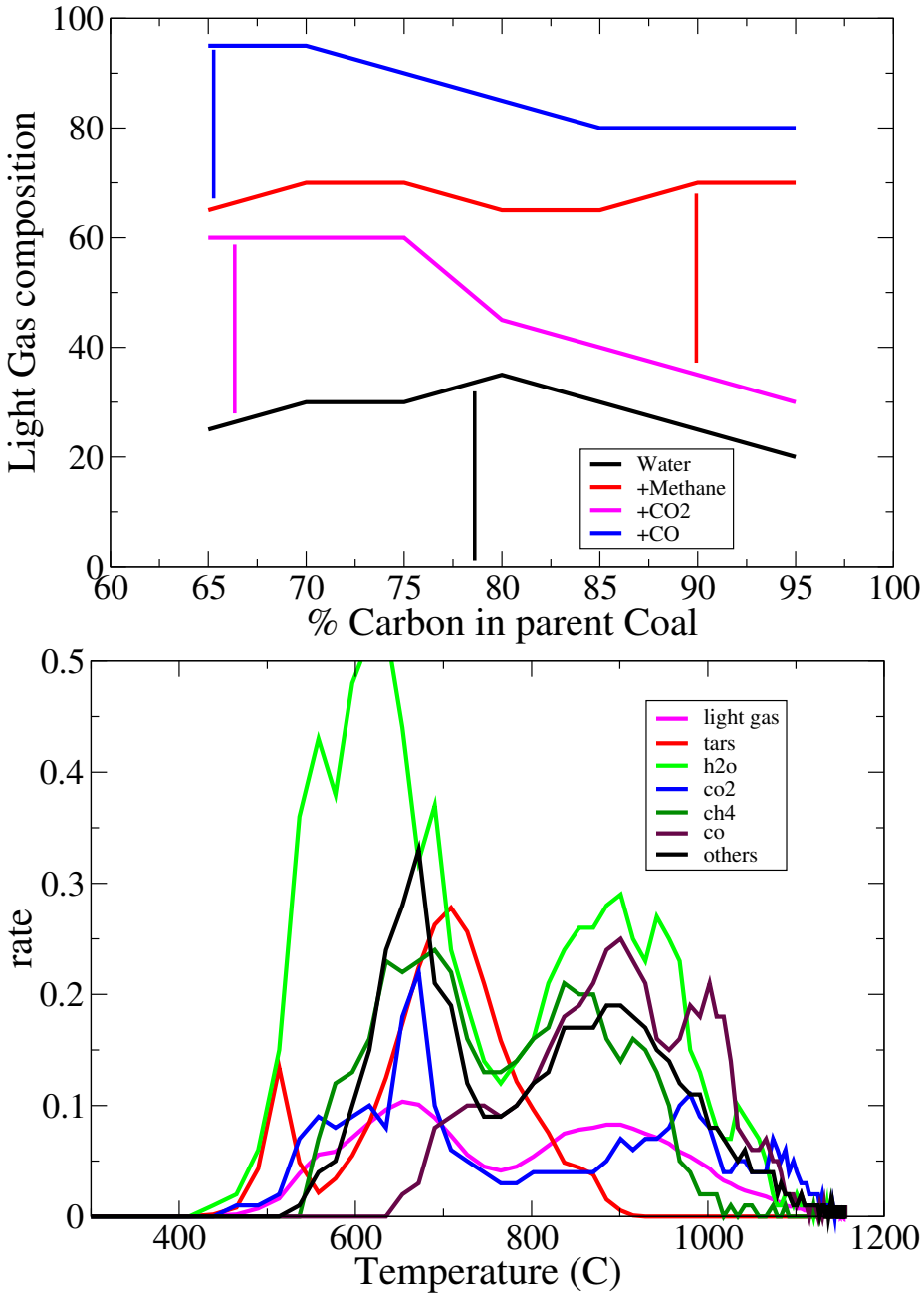

Figure 9.1.: Light Gas composition (volume %) predicted by the CPD model for several coals (Left) Release history for light gases in the case of Göttelborn coal (Right))

$$C + H_2O \longrightarrow CO + H_2 \qquad \text{(R 9.13)}$$

The CO/CO_2 ratio described by the splitting factor γ in R 9.11 depends on the temperature and oxygen concentration and can be calculated following several correlations. For oxygen mole

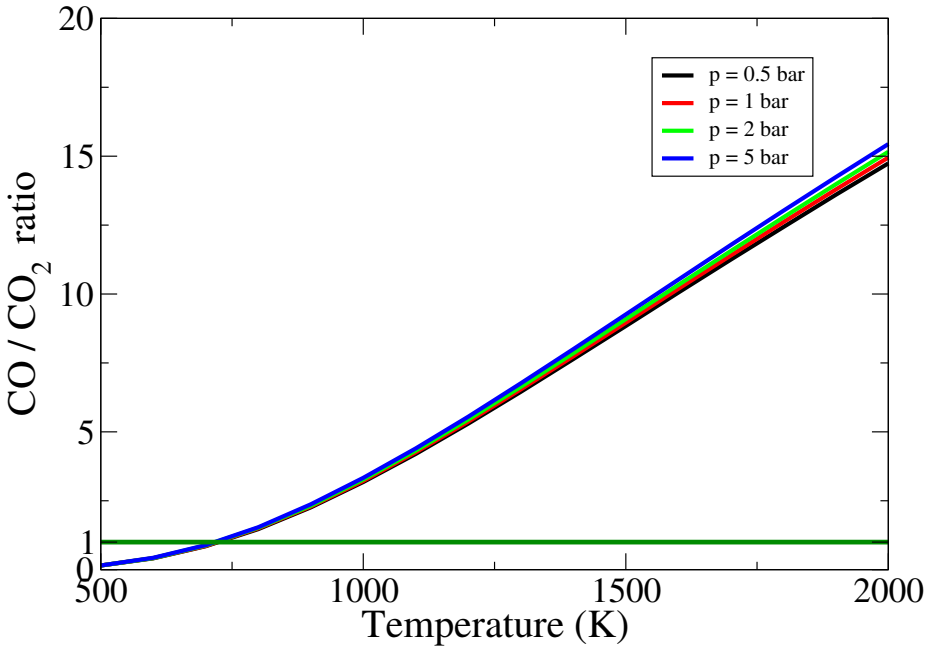

Figure 9.2.: CO to CO_2 ratio as a function of the temperature of a char particle. The values are calculated using the correlation 9.3)

fractions not larger than around 21%, the CO/CO_2 ratio is [13]:

$$\frac{CO}{CO_2} = 2512 \cdot exp(-\frac{6244}{T_p}) \tag{9.1}$$

The stoichiometric coefficient γ of the global reaction R 9.11 is, for a given temperature, calculated as follows:

$$\gamma = (1 + 0.5\frac{CO}{CO_2})/(1 + \frac{CO}{CO_2}) \tag{9.2}$$

The Arthur relation 9.1 was determined experimentally using both artificial graphite and coal char made from Warwickshire coal (the Ryder Seam) and 1-2.83 mm particles were examined in the 753-1173 K temperature range. Experiments of Tognotti et al. [377] were carried out using 180-250 µm Spherocarb char particles in the 670-1670 K temperature range and, for 20% oxygen content in nitrogen, the following relationship was obtained:

$$\frac{CO}{CO_2} = 69.39 \cdot exp(-\frac{3070}{T_p}) \tag{9.3}$$

The dependency on oxygen concentration has been introduced into the pre-exponential constant in the following way:

$$A = 69.39 \cdot (p_{O2})^n \tag{9.4}$$

where p_{O2} is in atmosphere and $n = 0.02$.

Figure Figure 9.2 plots the correlation from equation 9.3. For temperatures higher than $T = 850Kelvin$ most of the products are in form of CO. This trend is favored by an increase in pressure, but the effect is of lessen importance.

Shaddix et al. [320] have re-examined the experiments from Tognotti and concluded that

the relationship 9.3 is accurate if the particle temperature does not exceed 1250 K. In a previous article [120] the same Author gave a theoretical basis for the phenomenological analysis of Tognotti [1]. The results suggest that the CO_2/CO production ratio may be considerably lower than that estimated with existing power-law correlations for oxygen partial pressures less than 10 kPa and surface temperatures higher than 1600 K.

CO oxidation CO oxidation can proceed in two different ways, depending on the presence of H components. The *dry* route is initiated by the reactions:

$$\mathrm{CO + O_2 \rightleftharpoons CO_2 + 2\,O} \tag{R 9.14}$$

$$\mathrm{CO + O + M \rightleftharpoons CO_2 + M} \tag{R 9.15}$$

These reactions are slow and their contribution to CO_2 formation is negligible in most of combustion systems. However, they contribute to the creation and destruction of O radicals.

If water is present then the *wet* route is initiated with the formation of H radicals from the following reactions:

$$\mathrm{H_2O + O \rightleftharpoons 2\,OH} \tag{R 9.16}$$

$$\mathrm{H + O_2 \rightleftharpoons OH + O} \tag{R 9.17}$$

If H_2 is also present, the following additional reactions take place:

$$\mathrm{H_2 + O \rightleftharpoons OH + H} \tag{R 9.18}$$

$$\mathrm{H_2 + OH \rightleftharpoons H_2O + H} \tag{R 9.19}$$

The radical OH then quickly reacts with the CO:

$$\mathrm{CO + OH = CO_2 + H} \tag{R 9.20}$$

In the initial stage of CO oxidation, the high concentration of HO_2 can make the following reaction competitive with the above ones:

$$\mathrm{CO + HO_2 \rightleftharpoons CO_2 + OH} \tag{R 9.21}$$

Two remarks should be made on the CO oxidation mechanism:

1. The most important reaction is Reaction R 9.20. It proceeds through a four atoms activation complex and the Arrhenius plot shows that it cannot be considered as a simple molecular reaction.

[1] The global model suggested is the following:

$$\mathrm{2\,C() + O_2 \longrightarrow 2\,C(O)}$$
$$\mathrm{C + C() + O_2 \longrightarrow CO + C(O)}$$
$$\mathrm{\delta C() + C + C(O) + O_2 \longrightarrow CO_2 + C(O) + \delta C()}$$
$$\mathrm{C() + C + C(O) + O_2 \longrightarrow CO + 2\,C(O)}$$
$$\mathrm{C + C(O) \longrightarrow CO + C()}$$
$$\mathrm{C + 2\,C(O) \longrightarrow CO_2 + 2\,C()}$$

where C() denotes a free, active surface site, C symbolizes an inactive carbon atom in the char surface or underneath an active site.

2. The fate of the hydroxyl radical is important. As shown in Table 9.1 the competitive routes of OH destruction by attacking hydrocarbons are faster than Reaction R 9.20. That suggests, as already pointed out, the inhibition of CO oxidation in the presence of hydrocarbons.

Reaction	at 1000 K	at 2000 K
$C_3H_8 + OH$	$5.0 \cdot 10^{12}$	$1.6 \cdot 10^{13}$
$H_2 + OH$	$1.6 \cdot 10^{12}$	$6.0 \cdot 10^{12}$
$CO + OH$	$1.7 \cdot 10^{11}$	$3.5 \cdot 10^{11}$

Table 9.1.: Rate constant (k) of specific OH reactions (from [128])

It is evident that in the wet route the entire H_2 reaction paths has an important influence. The complete mechanism must be linked to the mechanisms described in Section A.1.1.

9.1.1. Modeling of homogeneous CO formation and oxidation

As already pointed out in other chapters, a reduced global scheme valid for all the conditions is not available. The following derivation of a two steps global mechanism for the wet route is presented for a heuristic purpose. The derivation is taken from [298]. The skeletal mechanism to be reduced is formed by the following reactions, where the numbers of the reactions refers to the number used in the aforementioned reference:

1:	$O_2 + H \xrightarrow{k_1} OH + O$	2:	$O_2 + H \overset{k_2}{\rightleftharpoons} OH + O$
3:	$H_2 + O \xrightarrow{k_3} OH + H$	4:	$OH + H \xrightarrow{k_4} H_2 + O$
5:	$H_2 + OH \xrightarrow{k_5} H_2O + H$	6:	$H_2 + H \xrightarrow{k_6} H_2 + OH$
7:	$OH + OH \xrightarrow{k_7} H_2O + O$	8:	$H_2O + O \xrightarrow{k_8} OH + OH$
9:	$H + H + M \xrightarrow{k_9} H_2 + M$	11:	$H + OH + M \xrightarrow{k_{11}} H_2O + M$
15:	$H + O_2 + M \xrightarrow{k_{15}} HO_2 + M$	17:	$HO_2 + H \overset{k_{17}}{\rightleftharpoons} OH + OH$
19:	$HO_2 + H \xrightarrow{k_{19}} H_2 + 02$	21:	$HO_2 + H \xrightarrow{k_{21}} H_2O + O$
23:	$HO_2 + O \xrightarrow{k_{23}} OH + 02$	25:	$HO_2 + OH \xrightarrow{k_{25}} H_2O + O_2$
38:	$CO + OH \xrightarrow{k_{38}} CO_2 + H$	39:	$CO_2 + H \xrightarrow{k_{39}} CO + OH$
46:	$CHO + H \xrightarrow{k_{46}} CO + H_2$	54:	$CHO + O_2 \xrightarrow{k_{54}} CO + HO_2$
56:	$CHO + M \xrightarrow{k_{56}} CO + H + M$	57:	$CO + H + M \xrightarrow{k_{57}} CHO + M$

CO oxidation The full numerical integrations shows that the species HO_2, OH and HCO are in steady state for all temperatures above roughly 600K. The OH equilibrium in the reaction H_2 + OH = H_2O + H, (reaction R A.9), together with the wet route for CO consumption CO + OH = CO_2 + H, (reaction R 9.20), results in a global reaction for the water gas shift reaction:

$$CO + H_2O \rightleftharpoons CO_2 + H_2 \qquad \text{(R 9.22)}$$

which neither creates nor destroys reaction intermediaries.

With a steady-state for HO_2 and with reactions $H + O_2 + M \longrightarrow HO_2 + M$ (reaction R A.13) and HO_2 + OH $\longrightarrow$ H_2O + O_2 (reaction R A.17) assumed to be dominant in the HO_2 kinetics, the overall recombination reaction is obtained:

$$2\,H + M \longrightarrow H_2 + M \tag{R 9.23}$$

If a steady-state for O atoms is also introduced and H_2 + O $\rightleftharpoons$ OH + H, (reaction R A.8) is assumed to maintain partial equilibrium, then the overall radical-production, oxygen-consumption process is found to be the following:

$$O_2 + 3\,H_2 \rightleftharpoons 2\,H_2O + 2\,H \tag{R 9.24}$$

This completes the definition of the three-step mechanism [2].

The stated steady-states and partial equilibrium relations yield for the concentrations of intermediates functions of the main components:

$$[OH] = \frac{k_5}{k_6}[H]\frac{[H_2O]}{[H_2]} \tag{9.5}$$

$$[H] = \frac{k_4}{k_3}[H]\frac{[OH]}{[H_2]} \tag{9.6}$$

$$[HO_2] = \frac{k_{15}}{k_{25}}[H]\frac{[M][O_2]}{[OH]} \tag{9.7}$$

$$[HCO] = [H]\frac{k_{57}[CO][M]}{k_{56}[M] + k_{46}[H]} \tag{9.8}$$

The reaction rates for the resulting three steps (denoted I, II, III) can be directly calculated from the reaction rates present in the detailed mechanism:

$$R_I = R_{38} \tag{9.9}$$

$$R_{II} = R_{15} + R_9 + R_4 - R_{57} \tag{9.10}$$

$$R_{III} = R_2 + R_{17} + R_{21} \tag{9.11}$$

A simple relation for the reaction rates can be derived if R_{21} is neglected:

$$R_I = \frac{\mathrm{k_6\,k_{38}\,[H]}}{\mathrm{k_5\,[H_2]}} \cdot (\mathrm{[CO][H_2O] - K_I\,[CO_2][H_2]}) \tag{9.12}$$

$$R_{II} = \mathrm{[M](k_{15}[O_2] + k^*_{57}[M][CO])[H]} \tag{9.13}$$

$$\tag{9.14}$$

where:

$$k^*_{57} = \frac{k_{57}}{1 + k_{56}[M]}\frac{1}{k_{46}[H]}$$

[2] Quoting directly from the Authors in [298]: from the numerical integrations it is found that the steady state for O is inaccurate below about 1100K, that partial equilibrium for steps H_2 + OH = H_2O + H and (especially) H_2 + O $\rightleftharpoons$ OH + H are inaccurate, and that step HO_2 + H $\longrightarrow$ OH + OH rather than step HO_2 + OH $\longrightarrow$ H_2O + O_2 is the main depletor of HO_2. An H steady state is found to be slightly more accurate than an O steady state throughout most of the flame. Despite those limitations, the results are qualitatively correct and the deviations from the prediction of the detailed mechanism are small.

the constant K_I is the equilibrium constant for the water gas shift reaction given by:

$$K_I = \frac{k_{39}k_5}{k_{38}k_6}$$

and K_{OH} is equilibrium constant for the reaction $H + O_2 + H_2O \rightleftharpoons 3\,OH$ given by

$$K_{OH} = \frac{k_1 k_3 k_6}{k_2 k_4 k_5}$$

The manipulation of a detailed mechanism to obtain rates for global reactions shows clearly a complex temperature dependency. The fitting into an Arrhenius form works in a limited range of temperatures only.

If also the radical H is assumed to be in equilibrium the following two steps mechanism can be recovered:

$$CO + \frac{1}{2}O_2 \longrightarrow CO_2 \tag{R 9.25}$$

$$H_2 + \frac{1}{2}O_2 \longrightarrow H_2O \tag{R 9.26}$$

The reaction rates for this two-steps mechanism are written in the following way:

$$R_I = R_{38} \tag{9.15}$$

$$R_{II} = R_5 + R_7 + R_{17} + R_{21} + R_4 \tag{9.16}$$

The concentration of the intermediates are expressed by algebraic non-linear equations and without any further simplifications they cannot be expressed in an explicit form [273].

CO formation The formation of CO is more difficult to predict since the concentration of the radicals and the concentration of the HCO is strongly dependent on the type of fuel used. Therefore as shown in [273] and references herein, each fuel requires a different global mechanism. In the case of CH_4 the following 4 steps mechanism has been derived:

$$CH_4 + 2\,H + H_2O \rightleftharpoons CO + 4\,H_2 \tag{R 9.27}$$

$$CO + H_2O \rightleftharpoons CO_2 + H_2 \tag{R 9.28}$$

$$H + H + M \rightleftharpoons H_2 + M \tag{R 9.29}$$

$$O_2 + 3\,H_2 \rightleftharpoons 2\,H + 2\,H_2O \tag{R 9.30}$$

and similar mechanisms have been found appropriate also for light hydrocarbons, where only the first reaction must be changed:

$$C_2H_n + O_2 \rightleftharpoons 2\,CO + nH_2 \tag{R 9.31}$$

and for propane:

$$C_3H_8 + O_2 + H_2O + 2\,H \rightleftharpoons 3\,CO + 6\,H_2 \tag{R 9.32}$$

The expression of the reaction rates and the radical concentration differ from case to case (see [273]).

9.2. NO emissions

The combustion products usually contain two kinds of nitrogen components: NO and NO_2, but others, such as N_2O, N_2O_3, N_2O_5 may appear in very small quantities. The most abundant in hot combustion environment is the NO. The NO_2 is usually only a few percents of the concentration of NO removed (usually not exceeding 5%) but in favorable conditions (for example in high-pressure turbines) its concentration can become significant.

As for the oxidation process, NO_x formation can be described by a chain of reactions where many stable species and radicals are involved. As for the primary oxidation process, the mechanism described in such a way is too complex to be used in conjunction with *CFD* calculations. For that reason, several sub-mechanisms for NO formation and destruction have been identified [242, 127, 67] and they are reviewed below:

- The *thermal* NO is characterized by the splitting of N_2 molecules due to attack of an O radical;
- The *prompt* NO is characterized by the splitting of N_2 molecules due to the attack of CH_i radicals;
- The N_2O path is characterized by the splitting of N_2 molecules (from the attack of O radical) through the formation of a N_2O molecule;
- The NNH path is characterized by the splitting of N_2 molecule (from the attack of H radical) through the formation of a NNH molecule;
- The *fuel* NO is characterized by the oxidation of N-containing radicals released during the decomposition of the fuel;
- The *reburning* of NO is the reaction back to N_2 by reactions with several radicals.

9.2.1. Thermal NO

The mechanism known as the *thermal* or *Zeldovich* mechanism is the reaction of the N_2 present in the air with O_2. The molecular nitrogen can be present in the natural gas (few percents), but the most important source is the combusting air in which it is the largest component. The first step of thermal NO formation is the dissociation of N_2:

$$\mathrm{N_2 + O \overset{k_1}{\rightleftharpoons} NO + N} \tag{R 9.33}$$

The N radical then reacts to form NO:

$$\mathrm{N + O_2 \overset{k_2}{\rightleftharpoons} NO + O} \tag{R 9.34}$$

$$\mathrm{N + OH \overset{k_3}{\rightleftharpoons} NO + H} \tag{R 9.35}$$

The N_2 molecule is a stable one (the two nitrogen atoms are linked with a triple bond) and can be dissociated only at high temperatures. If the temperature of the gas is lower than $1700\ K$ the dissociation is ineffective and Reaction R 9.33 creates both NO and N radicals at a low rate. The other two reactions are faster than the first, but overall, the mechanism is slow in comparison to the hydrocarbon oxidation rates. The time required to achieve equilibrium is, depending on the

conditions, between 3 $seconds$ and 15 $seconds$[3]. Usually, this time is longer than the residence time inside the region where the temperature is high enough. Hence the thermal NO formation is a chemically-controlled process, and the final NO concentration may be far from the equilibrium value.

Because of the difference in time scales between the first and the other two reactions, it is possible to assume that all the N radicals produced by Reaction R 9.33 immediately form NO. That observation implies that the N radicals are in a quasi-steady state and are given by:

$$[N] = \frac{k_1[N_2][O] + k_{-2}[NO][O] + k_{-3}[NO][H]}{k_{-1}[NO] + k_2[O2] + k_3[OH]} \tag{9.17}$$

To calculate the rate of formation of NO in a *CFD* software, the concentrations of the radicals need to be evaluated as a function of the main species[4].

Simple approach Using Equation 9.17 to estimate the concentration of N radicals together with the equilibrium of the following reaction:

$$\mathrm{H} + \mathrm{O_2} \rightleftharpoons \mathrm{OH} + \mathrm{O} \tag{R 9.36}$$

to eliminate the H radicals, it is possible to write the NO reaction rate as a function of the temperature T, the main species concentration [N_2], [O_2] and the [O] and [OH] radicals:

$$\frac{d}{dt}[NO] = 2k_1[O][N_2]\frac{1 - \frac{[NO]^2}{K[N_2][O_2]}}{1 + \frac{k_{-1}[NO]}{k_2[O_2]+k_3[OH]}} \tag{9.18}$$

where $K = \frac{k_1}{k_{-1}}\frac{k_2}{k_{-2}}$ is the equilibrium constant for the global reaction $N_2 + O_2 \rightleftharpoons NO + NO$.

If it is assumed that the oxygen dissociation reaction:

$$\mathrm{O_2} + \mathrm{M} \overset{\mathrm{k_o}}{\rightleftharpoons} \mathrm{O} + \mathrm{O} + \mathrm{M} \tag{R 9.37}$$

is in equilibrium, then it is possible to write the O radical concentration in terms of the oxygen concentration:

$$[O] = \sqrt{\frac{k_o}{k_{-o}}}[O_2] \tag{9.19}$$

In the same way it is possible to assume equilibrium for the reaction:

$$\mathrm{O} + \mathrm{H_2O} \overset{\mathrm{k_{oh}}}{\rightleftharpoons} \mathrm{OH} + \mathrm{OH} \tag{R 9.38}$$

[3]The time required to reach equilibrium can be estimated using the correlation derived by Rejzer and Zeldovich:

$$\tau_{eq} = \frac{2.06 \cdot 10^{-13}}{\sqrt{C_{N_2}}} \exp\left(\frac{53750}{T}\right)$$

where C_{N_2} is the concentration of molecular nitrogen in $\frac{mole}{liter}$, and the time is in seconds.

[4]In the *PDF* mixture fraction approach the radicals are quickly evaluated, and the calculation of the NO_x formation rate does nor require any other assumption.

and derive the following relation for the OH radicals:

$$[OH] = \sqrt{\frac{k_{oh}}{k_{-oh}}}\sqrt{[O][H_2O]} \tag{9.20}$$

It has been shown [186, 100, 81] that Reaction 9.19 under-estimates the value of O atoms. One way to correct for this imperfection is to still use the same equations 9.19 and 9.20 with different parameters. The equations for the concentrations $[O]$ and $[OH]$ are the following (in $\frac{\mathrm{g}}{\mathrm{m^3\,s}}$):

$$[O] = 36.64T^{1/2}[O_2]^{1/2}e^{-27123/T} \tag{9.21}$$
$$[OH] = 2.129\times10^{2}T^{-0.57}e^{-4595/T}[O]^{1/2}[H_2O]^{1/2} \tag{9.22}$$

Advanced approach A more theoretical approach for the calculation of the radicals [397] is to assume steady state for the following reactions:

$$\mathrm{O_2 + H \rightleftharpoons O + OH} \tag{R 9.39}$$
$$\mathrm{OH + H_2 \rightleftharpoons H_2O + H} \tag{R 9.40}$$
$$\mathrm{O + H_2 \rightleftharpoons OH + H} \tag{R 9.41}$$

and this results in the following expressions for the concentrations of the O, OH and H radicals:

$$[O] = K_o\frac{[H_2][O_2]}{[H_2O]} \tag{9.23}$$
$$[H] = K_h\frac{[H_2]\sqrt{[H_2][O_2]}}{[H_2O]} \tag{9.24}$$
$$[OH] = K_{oh}\sqrt{[H_2][O_2]} \tag{9.25}$$

with the constants K given by:

$$K_o = \frac{k_o}{k_a}\frac{k_{-o}}{k_{-a}} \tag{9.26}$$
$$K_h = \frac{k_a}{h_{-a}}\sqrt{\frac{k_o}{k_{-o}}\frac{k_b}{k_{-b}}} \tag{9.27}$$
$$K_{oh} = \sqrt{\frac{k_o}{k_{-0}}\frac{k_b}{k_{-b}}} \tag{9.28}$$

9.2.2. Prompt NO

The prompt mechanism is the formation of NO in fuel reach regions near the flame front. This mechanism is initiated by the presence of CH_i radicals generated via the dissociation of the fuel. The mechanism takes place only in a small region of the flame and therefore the fraction of NO generated is relatively small and it decreases as the thermal input (flame temperature) increases. The initiating reactions are:

$$\mathrm{CH + N_2 \rightleftharpoons HCN + N} \tag{R 9.42}$$

$$CH_2 + N_2 \rightleftharpoons HCN + NH \quad \text{(R 9.43)}$$

There are also other radicals that can participate in the prompt mechanism. For example, C_2H and C_2 radicals may participate in the formation of the NCO molecule vie the reactions:

$$C_2H + N_2 \rightleftharpoons HCN + CN \quad \text{(R 9.44)}$$

$$C_2 + N_2 \rightleftharpoons 2\,CN \quad \text{(R 9.45)}$$

$$CN + O_2 \rightleftharpoons NCO + O \quad \text{(R 9.46)}$$

It has been established [148] that the prompt mechanism is proportional to the volumetric concentration of C atoms. In such a way, the above reactions are not primary contributors to the NO formation because is unlikely that C_2 or C_2H are produced from CH_4 with an efficiency higher than 0.5 or from C_3H_x molecules with an efficiency higher than 0.3.

The HCN generated in the above reactions reacts further. In a reducing environment, the following reactions take place:

$$HCN + M \rightleftharpoons CN + H + M \quad \text{(R 9.47)}$$

$$HCN + H \rightleftharpoons CN + H_2 \quad \text{(R 9.48)}$$

$$HCN + CN \rightleftharpoons C_2N_2 + H \quad \text{(R 9.49)}$$

In a partially oxidizing environment, other elementary reactions take place, with O and OH radicals as reactants:

$$HCN + O \rightleftharpoons CN + OH \quad \text{(R 9.50)}$$

$$HCN + O \rightleftharpoons NCO + H \quad \text{(R 9.51)}$$

$$HCN + O \rightleftharpoons NH + CO \quad \text{(R 9.52)}$$

$$HCN + OH \rightleftharpoons CN + H_2O \quad \text{(R 9.53)}$$

$$HCN + OH \rightleftharpoons HNCO + H \quad \text{(R 9.54)}$$

In an oxidizing environment, the cyanogen CN undergoes the following reactions:

$$CN + OH \rightleftharpoons HCN + N \quad \text{(R 9.55)}$$

$$CN + O \rightleftharpoons CO + N \quad \text{(R 9.56)}$$

$$CN + O_2 \rightleftharpoons NCO + O \quad \text{(R 9.57)}$$

The radicals formed up to this point undergo further oxidation (mainly to NH and NO):

$$NCO + O \rightleftharpoons NO + CO \quad \text{(R 9.58)}$$

$$NCO + H \rightleftharpoons NH + CO \quad \text{(R 9.59)}$$

$$NCO + H_2 \rightleftharpoons HNCO + H \quad \text{(R 9.60)}$$

$$HNCO + H \rightleftharpoons NH_2 + CO \quad \text{(R 9.61)}$$

At the end of this long chain of reactions, a part of the nitrogen-containing molecules is converted to NO (Reaction R 9.58 and Reaction R 9.60) but a part is also converted to amine radicals, specified in Reaction R 9.59 and Reaction R 9.61 [5].

[5] These radicals are processed in parallel to ammonia. The NH_3 molecules originate directly from the fuel N. At flame

The NH_2 molecule originates from the group of $N-C-H-O$ molecules which contains HCNO, NOCN and HNCO. The group is generated in the NO reburning path. The NH_2 molecules undergo the following reactions:

$$NH_2 + O \rightleftharpoons OH + NH \quad \text{(R 9.62)}$$

$$NH_2 + H \rightleftharpoons H_2 + NH \quad \text{(R 9.63)}$$

$$NH_2 + OH \rightleftharpoons H_2O + NH \quad \text{(R 9.64)}$$

$$NH_2 + O \rightleftharpoons HNO + H \quad \text{(R 9.65)}$$

$$NH_2 + O_2 \rightleftharpoons HNO + OH \quad \text{(R 9.66)}$$

The NH formed from the NH_2 and from the NCO can react to water and hydrogen:

$$NH + H \rightleftharpoons N + H_2 \quad \text{(R 9.67)}$$

$$NH + OH \rightleftharpoons N + H_2O \quad \text{(R 9.68)}$$

or further to NHO:

$$NH + O \rightleftharpoons NO + H \quad \text{(R 9.69)}$$

$$NH + H \rightleftharpoons HNO + H \quad \text{(R 9.70)}$$

$$NH + O_2 \rightleftharpoons HNO + O \quad \text{(R 9.71)}$$

The HNO reacts finally to NO:

$$HNO + M \rightleftharpoons NO + H + M \quad \text{(R 9.72)}$$

$$HNO + H \rightleftharpoons NO + H_2 \quad \text{(R 9.73)}$$

$$HNO + OH \rightleftharpoons NO + H_2O \quad \text{(R 9.74)}$$

$$HNO + O \rightleftharpoons NO + OH \quad \text{(R 9.75)}$$

The path with the amine radicals is faster than the one in which HCN is involved [6]. In Figure Figure 9.3 the complete path is clearly shown.

Modeling in a CFD calculation In the *CFD* calculations, two approaches for the prediction of the NO produced by the prompt mechanism are considered (without the solution of the aforementioned chains of elementary reactions). The first approach which is due to De Soete [86], provides the following rate of NO formation:

$$R_{pr} = f_{pr} C \left(\frac{RT}{P}\right)^{1+b_1} [O_2]^{b_1} [N_2][Fuel] \exp\left(-\frac{E}{RT}\right) \quad (9.29)$$

temperatures, the bigger molecules break off into smaller ones. Their reactions achieve partial equilibrium:

$$NH_3 + O \rightleftharpoons NH_2 + OH$$
$$NH_3 + H \rightleftharpoons NH_2 + H_2$$
$$NH_3 + OH \rightleftharpoons NH_2 + H_2O$$

In the natural gas, there are no relevant amounts of N linked directly to the fuel. Thus, the presence of NH_3 is not important, and the entire path will start from NH_2.

[6] Usually in solid particle combustion the HCN path is more important than the NH path. In fact the NH radical concentration is much smaller than the HCN one.

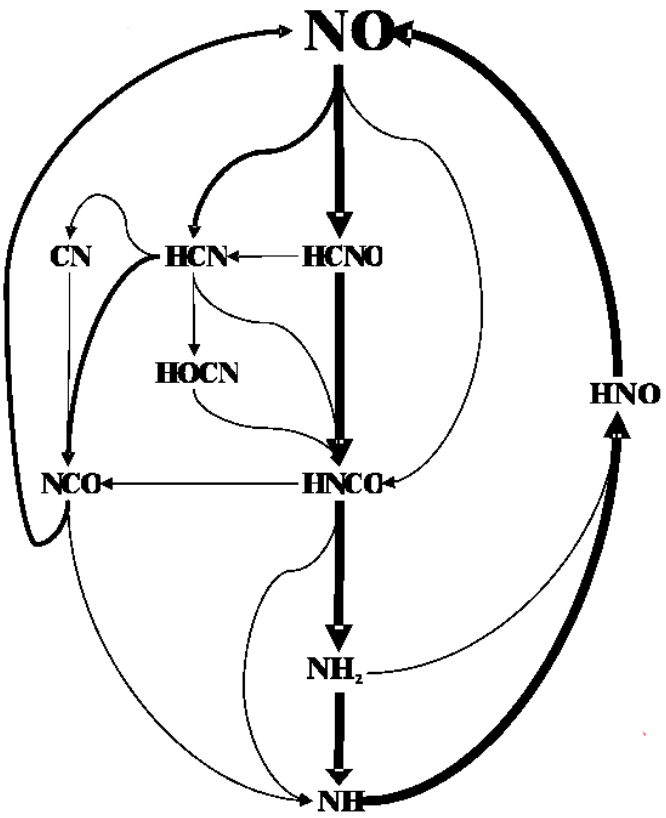

Figure 9.3.: Reaction path diagram for NO formation. The arrows indicate the direction of all the reactions that involve the two species. Their thickness is proportional to the net intensity of formation or destraction of the species involved.

	R_{pr}	-	reaction rate in $\frac{\text{mol}}{\text{cm}^3\,\text{s}}$
	C	-	pseudo pre-exponential factor $= 6.4\,10^6\ \frac{1}{\text{s}}$
where	E	-	pseudo-activation energy $= 72.5\,10^3$ cal/mol
	f_{pr}	-	correction factor
	b_1	-	oxygen reaction order

The correction factor and the oxygen reaction order are given by (X_{O2} is the molar fraction of oxygen in the mixture):

$$f_{pr} = 4.75 + 0.0819N_c - \frac{23.2}{\lambda} + \frac{32.0}{\lambda^2} - \frac{12.2}{\lambda^3} \tag{9.30}$$

$$b_1 = \frac{1}{1+\exp(-3.93(4.9+c))} \tag{9.31}$$

$$c = \ln X_{O2} \tag{9.32}$$

where λ is the local stoichiometry and N_c is the number of carbon atoms in the fuel.

The second approach is based on Reaction R 9.42 and the rate of NO formation can be written as:

$$\frac{d}{dt}[NO] = 2k_{p1}[CH][N_2] \tag{9.33}$$

with an analytical evaluation of the CH radicals. In natural gas combustion, usually the fuel is composed mainly of methane CH_4 and ethane C_2H_6. The cracking path for the methane is the following:

$$CH_4 \longrightarrow CH_3 \longrightarrow CH_2 \longrightarrow CH$$

and for ethane is:

$$C_2H_6 \longrightarrow C_2H_5 \longrightarrow C_2H_4 \longrightarrow C_2H_3 \longrightarrow C_2H_2 \longrightarrow CH_2 \longrightarrow CH$$

As in reference [186], CH_3 and methylene are assumed to be the direct precursors to the CH_2 radicals following the reactions:

$$\mathrm{CH_3 + H \overset{k_{p7}}{\rightleftharpoons} CH_2 + H_2} \tag{R 9.76}$$

$$\mathrm{CH_3 + OH \overset{k_{p8}}{\rightleftharpoons} CH_2 + H_2O} \tag{R 9.77}$$

$$\mathrm{C_2H_2 + O \rightleftharpoons CH_2 + CO} \tag{R 9.78}$$

The CH_3 radical concentration is calculated assuming that the following two reactions are in partial equilibrium:

$$\mathrm{CH_4 + H \overset{k_{p2}}{\rightleftharpoons} CH_3 + H_2} \tag{R 9.79}$$

$$\mathrm{CH_3 + O \overset{k_{p3}}{\rightleftharpoons} CH_2O + O} \tag{R 9.80}$$

and is given by the equation:

$$[CH_3] = k_{p2}\frac{[CH_4][H]}{k_{p2}[H_2] + k_{p3}[O]} \tag{9.34}$$

The CH_2 radical is formed from CH_3 and C_2H_2 in the way described by Reaction R 9.76, Reaction R 9.77 and Reactions R 9.78. The C_2H_2 radical is formed directly from ethane:

$$\mathrm{C_2H_6 + H \overset{k_{p4}}{\rightleftharpoons} C_2H_5 + H_2} \tag{R 9.81}$$

followed by these reactions, that bring all the C_2H_5 molecules to C_2H_2:

$$\mathrm{C_2H_5 + M \rightleftharpoons C_2H_4 + H + M} \tag{R 9.82}$$

$$\mathrm{C_2H_4 + R \rightleftharpoons C_2H_3 + RH} \tag{R 9.83}$$

$$\mathrm{C_2H_3 + R \rightleftharpoons C_2H_2 + RH} \tag{R 9.84}$$

where R is a generic radical. Finally the CH_2 radical is consumed by the reactions:

$$\mathrm{CH_2 + O \overset{k_{p5}}{\rightleftharpoons} Products} \tag{R 9.85}$$

$$\mathrm{CH_2 + O_2 \overset{k_{p6}}{\rightleftharpoons} Products} \tag{R 9.86}$$

Considering the above CH_2 formation and destruction mechanisms, the equation for the CH_2 radical concentration reads:

$$[CH_2] = k_{p4}[C_2H_6][H] + \frac{k_{p7}[H] + k_{p8}[OH]}{k_{p5}[O] + k_{p6}[O_2]} \tag{9.35}$$

The CH radical concentration can be estimated by taking into consideration the following formation reactions:

$$\mathrm{CH_2 + H \overset{k_{p9}}{\rightleftharpoons} CH + H_2} \tag{R 9.87}$$

$$\mathrm{CH_2 + OH \overset{k_{p10}}{\rightleftharpoons} CH + H_2O} \tag{R 9.88}$$

$$\mathrm{CH_2 + O \overset{k_{p11}}{\rightleftharpoons} CH + OH} \tag{R 9.89}$$

and the destruction paths:

$$\mathrm{CH + H_2O \overset{k_{p12}}{\rightleftharpoons} CH_2O + H} \tag{R 9.90}$$

$$\mathrm{CH + O_2 \overset{k_{p13}}{\rightleftharpoons} Products} \tag{R 9.91}$$

$$\mathrm{CH + O \overset{k_{p14}}{\rightleftharpoons} CO + H} \tag{R 9.92}$$

$$\mathrm{CH + H \overset{k_{p15}}{\rightleftharpoons} C + H_2} \tag{R 9.93}$$

$$\mathrm{CH + OH \overset{k_{p16}}{\rightleftharpoons} HCO + H} \tag{R 9.94}$$

The calculations give the following estimation for the CH radical concentration:

$$[CH] = \frac{[CH_2]\left(k_{p9}[H] + k_{p10}[OH] + k_{p11}[O]\right)}{k_{p12}[H_2O]k_{p13}[O_2] + k_{p14}[O] + k_{p15}[H] + k_{p16}[OH]} \tag{9.36}$$

In Equations 9.34, 9.35 and 9.36 the O, OH and H radicals are calculated using Equations 9.23, 9.24 and 9.25.

In [141] the previous mechanism has been reduced using the Quasi-Steady State (QSS) method. The procedure followed in [265] can be summarized in the following steps, typical for a QSS reduction approach:

1. Determination of main reaction paths;
2. Elimination of redundant species;
3. Elimination of redundant reactions;
4. Identification of irreversible reactions;
5. Elimination of non-selective irreversible reaction channels;
6. Identification of species in steady state;
7. Identification of reactions in partial equilibrium.

As a result, NO, HCN NH_3 and N_2 only must be considered as independent species while C_2N_2, NCN, NO_2, H_2NO, HONO and N_2H_2 can be completely discarded. The other components, CN, HOCN, HNCO, NCO, NH_2, NH, and N are calculated in steady state.

The reduced model showed very good agreement with the detailed chemical kinetic model for conditions similar to those in a pulverized coal flame.

9.2.3. The N_2O path

In low-temperature combustion (below 1500 K) of lean mixtures of hydrocarbons (or at pressures higher than the atmospheric) a mechanism, in which the N_2O molecule is the intermediary becomes important [239]. The reaction involved in the formation of the N_2O molecule is the following:

$$\mathrm{N_2 + O + M \overset{k_{n1}}{\rightleftharpoons} N_2O + M} \tag{R 9.95}$$

This reaction is a limiting rate for the N_2O molecules that are converted into NO by the following reactions:

$$\mathrm{N_2O + O \overset{k_{n2}}{\rightleftharpoons} NO + NO} \tag{R 9.96}$$

$$\mathrm{N_2O + O \overset{k_{n3}}{\rightleftharpoons} N_2 + O_2} \tag{R 9.97}$$

$$\mathrm{N_2O + H \overset{k_{n4}}{\rightleftharpoons} NO + NH} \tag{R 9.98}$$

$$\mathrm{N_2O + H \overset{k_{n5}}{\rightleftharpoons} N_2 + OH} \tag{R 9.99}$$

$$\mathrm{N_2O + OH \overset{k_{n6}}{\rightleftharpoons} N_2 + H_2O} \tag{R 9.100}$$

This mechanism is still under investigation, and most of the rates in high-temperature conditions must be extrapolated from laboratory experiments at lower temperatures. It is the case for Reaction R 9.100 for which the reaction rate at 500^oC is known. Since Reaction R 9.95 is slower than the others, the concentration of N_2O is assumed to be in a quai-steady state:

$$[N_2O] = \frac{k_{n1}[N_2][O][M] + k_{n2}[NO]^2}{(k_{n2} + k_{n3})[O] + (k_{n4} + k_{n5})[H]} \tag{9.37}$$

Assuming that the NH radical is converted to NO, the rate of NO formation is:

$$\frac{d}{dt}[NO] = 2[N_2O]\left(k_{n2}[O] + k_{n4}[H]\right) \tag{9.38}$$

The above equation predicts accurately the rate above $1900\ K$ but strongly over-predicts it at lower temperatures. This is due to the over prediction of $[O]$ and $[H]$ radicals at lower temperatures as previously discussed (see [186]).

9.2.4. The NNH path

This mechanism of relatively little importance includes the following two reactions (see [58]):

$$\mathrm{N_2 + H} \overset{\mathrm{k}_{h1}}{\rightleftharpoons} \mathrm{NNH} \tag{R 9.101}$$

$$\mathrm{O + NNH} \overset{\mathrm{k}_{h2}}{\rightleftharpoons} \mathrm{NO + NH} \tag{R 9.102}$$

Assuming a partial equilibrium, the NNH concentration is:

$$[NNH] = k_{h2}[N_2][H] \tag{9.39}$$

Assuming that the NH radical is converted later into NO, the NO formation rate can be written as:

$$\frac{d}{dt}[NO] = 2k_{h2}[NNH][O] \tag{9.40}$$

Expression 9.40 is also valid for temperatures higher than $1900\ K$.

9.2.5. The Fuel NO

If nitrogen is linked to the structure of a fuel, the disruption of the bounds during pyrolysis, oxidation or gasification, releases automatically radicals containing the N atoms, mainly HCN or NH_3. Therefore modeling the fuel-NO_x formation requires the detailed description of the release of the nitrogen from the fuel, including both the rate of release and the form or species in which N is released.

The form of N-atoms in the fuel determines which species are released during each conversion process. The N atoms bonded to the fuel (usually N atoms are bounded directly in the ring structures) start to be released into the gas phase as soon as the fuel itself starts to decompose during pyrolysis, and the release continues during the subsequent conversion of the char structure. The radicals formed by the bonds CN, NO and NH react into stable species, mainly hydrogen cyanide HCN, ammonia NH_3, NO and a small amount of cyanogen CN in the form of dicyanogen $(CN)_2$. The HCN is formed primarily from the tars and nitrogen bound in aromatic rings, and the NH_3 is formed primarily from the amines in the coal. Heterocyclic compounds of pyridine, quinoline, pyrrole, and benzonitrite are mostly pyrolyzed to HCN at typical combustion temperatures.

The amount of the respective compounds is a function of the fuel and the stoichiometry. In the case of very rich mixture non-oxidized components, NH_3 and HCN are present while for stoichiometric flames both components are present in trace and mainly HCO and NO appear. For slightly under stoichiometric condition the maximum amount of fuel bounded N is transformed directly into N_2. More HCN has been observed from bituminous coals, but more NH_3 was formed from sub-bituminous and lignite coals and this is consistent with the observation that the number of aromatic rings in coal decreases with coal rank, and the number of molecular cyclic structures increases. Measurements have not generally confirmed this difference in industrial applications. In that conditions usually, solid fuels are transported using air, creating an under-stoichiometric condition at the beginning of the devolatilization process and therefore HCN prevails.

The details of the mass loss depend, as in the case of pyrolysis, on the heating rate and temperature of the solid particle. All the details are still not clear but the following behaviors have been observed (see [153] and reference herein):

- Devolatilization studies show that nitrogen leaves the coal at a rate proportional to, but somewhat higher than the rate of coal weight loss.
- Coal nitrogen loss is less dependent on coal type than is coal mass loss.
- Nitrogen evolution is more sensitive to temperature than is the coal mass devolatilization.
- Nitrogen is emitted more slowly than the coal mass at lower temperatures and more rapidly at higher temperatures.
- Typically, low-rank coals release a larger fraction of nitrogen in the light gases, and a lower fraction in the tars, compared to medium-rank coals.

The subsequent chemistry of the formed compounds follows the description given in Section 9.2.2 and the one given in Section 9.2.6.

Various global reaction rates have been proposed, for example [86], [54] and [244]. An example, with more details, will be given in Chapter 14.

9.2.6. Reburning of NO

The amount of NO already present in the gaseous phase can be reduced by its interaction with CH_i radicals (homogeneous reduction) or with its interaction with C atoms (heterogeneous reduction).

At relatively high temperatures the presence of CH_i radicals can initiate reactions that may reduce NO as follows:

$$NO + CH \rightleftharpoons HCN + O \quad \text{(R 9.103)}$$

$$NO + CH \rightleftharpoons NCO + H \quad \text{(R 9.104)}$$

$$NO + CH \rightleftharpoons HCO + N \quad \text{(R 9.105)}$$

$$NO + CH_2 \rightleftharpoons HCN + OH \quad \text{(R 9.106)}$$

$$NO + CH_2 \rightleftharpoons HCNO + H \quad \text{(R 9.107)}$$

$$NO + CH_2 \rightleftharpoons HNCO + H \quad \text{(R 9.108)}$$

$$NO + CH_3 \rightleftharpoons H_2CN + OH \quad \text{(R 9.109)}$$

$$NO + CH_3 \rightleftharpoons HCN + H_2O \quad \text{(R 9.110)}$$

$$\mathrm{NO} + \mathrm{C_2H} \rightleftharpoons \mathrm{HCN} + \mathrm{CO} \quad \text{(R 9.111)}$$

$$\mathrm{NO} + \mathrm{HCCO} \rightleftharpoons \mathrm{HCNO} + \mathrm{CO} \quad \text{(R 9.112)}$$

$$\mathrm{NO} + \mathrm{N} \rightleftharpoons \mathrm{N_2} + \mathrm{O} \quad \text{(R 9.113)}$$

The main compounds formed from the reburning process are $N-C-H-O$ molecules, NCH and HCN. Inside the $N-C-H-O$ group several reactions are important:

$$\mathrm{HNCO} + \mathrm{O} \rightleftharpoons \mathrm{NCO} + \mathrm{OH} \quad \text{(R 9.114)}$$

$$\mathrm{HOCN} + \mathrm{H} \rightleftharpoons \mathrm{HNCO} + \mathrm{H} \quad \text{(R 9.115)}$$

$$\mathrm{HCNO} + \mathrm{H} \rightleftharpoons \mathrm{HNCO} + \mathrm{H} \quad \text{(R 9.116)}$$

$$\mathrm{HCNO} + \mathrm{H} \rightleftharpoons \mathrm{HCN} + \mathrm{OH} \quad \text{(R 9.117)}$$

$$\mathrm{HCNO} + \mathrm{H} \rightleftharpoons \mathrm{NH_2} + \mathrm{CO} \quad \text{(R 9.118)}$$

At the end the HNCO molecule is converted to NH_2:

$$\mathrm{HNCO} + \mathrm{OH} \rightleftharpoons \mathrm{NH_2} + \mathrm{CO_2} \quad \text{(R 9.119)}$$

Several approaches have been used to calculate the rate of NO reburning. In the first approach, a global simplified reaction scheme is used [65, 266]:

$$\mathrm{NO} + \mathrm{Fuel} \longrightarrow \mathrm{HCN} + ... \quad \text{(R 9.120)}$$

$$\mathrm{HCN} + \mathrm{O_2} \longrightarrow \mathrm{NO} + ... \quad \text{(R 9.121)}$$

$$\mathrm{HCN} + \mathrm{NO} \longrightarrow \mathrm{N_2} + ... \quad \text{(R 9.122)}$$

The reaction rate for Reaction R 9.120 is given by [77] in $\frac{mole}{sec\ m^3}$:

$$R_{NO-HCN} = 2.68 \cdot 10^6 [Fuel][NO] \exp(-\frac{9517}{T}) \tag{9.41}$$

The reactions rates for HCN are given by [86] in $\frac{mole}{sec\ m^3}$:

$$R_{HCN-NO} = 10^{10} \left(\frac{RT}{P}\right)^b [HCN][O_2]^b \exp(-\frac{33738}{T}) \tag{9.42}$$

$$R_{HCN-N2} = 3 \cdot 10^{12} \left(\frac{RT}{P}\right) [HCN][NO] \exp(-\frac{30213}{T}) \tag{9.43}$$

with (X_{OO} is the mole fraction of oxygen):

$$b = \frac{1}{1 + \exp(-3.93(4.9 + c))} \tag{9.44}$$

$$c = \ln X_{O2} \tag{9.45}$$

The second approach, as for the prompt NO, takes into consideration the individual reactions with the radicals CH_i:

$$\mathrm{CH} + \mathrm{NO} \xrightarrow{\mathrm{k}_{r1}} \mathrm{HCN} + \mathrm{O} \quad \text{(R 9.123)}$$

$$\mathrm{CH_2} + \mathrm{NO} \xrightarrow{\mathrm{k}_{r2}} \mathrm{HCN} + \mathrm{OH} \quad \text{(R 9.124)}$$

$$CH_3 + NO \xrightarrow{k_{r3}} HCN + H_2O \quad \text{(R 9.125)}$$

The rate constants for these reactions are expressed in m^3/gmol-sec (from [55]):

$$k_{r1} = 1 \times 10^8 \quad (9.46)$$
$$k_{r2} = 1.4 \times 10^6 e^{-550/T} \quad (9.47)$$
$$k_{r3} = 2 \times 10^5 \quad (9.48)$$

The NO depletion rate due to the reburning is expressed as:

$$\frac{d[NO]}{dt} = -k_{r1}[CH][NO] - k_{r2}[CH_2][NO] - k_{r3}[CH_3][NO] \quad (9.49)$$

The concentrations of the radicals CH_i are taken from Equations 9.34, 9.35 and 9.36.

NO_x can be heterogeneously reduced by C(s)+NO $\longrightarrow$ N_2. The reaction rates are different for different chars with bio-chars being the less reactive [440]. Experiments showed that the reaction rate for NO reduction in oxygen-free experiments was lower by a factor of about 10 compared to that from char combustion experiments. The main reasons for this difference were thermal deactivation, increasing surface area during char combustion, producing reactive surface intermediates, and presence of gases such as CO, which can promote the NO reduction.

The reduction of NO_x on the surface of the solid phase is interpreted by the following reactions [342]:

$$O_2 + 2\,C \longrightarrow 2\,C(O) \quad \text{(R 9.126)}$$
$$C(O) \longrightarrow CO + \text{free carbon site} \quad \text{(R 9.127)}$$
$$2\,C(O) \longrightarrow CO_2 + (C) + \text{free site} \quad \text{(R 9.128)}$$
$$O_2 + C + C(N) \longrightarrow C(O) + C(NO) \quad \text{(R 9.129)}$$
$$C(NO) \longrightarrow NO + C \quad \text{(R 9.130)}$$
$$NO + C \longrightarrow \frac{1}{2}\,N + C(O) \quad \text{(R 9.131)}$$
$$NO + C(NO) \longrightarrow N_2O + C(O) \quad \text{(R 9.132)}$$
$$N_2O + C \longrightarrow N_2 + C(O) \quad \text{(R 9.133)}$$

where (C), C(O), C(N) and C(NO) are active carbon site, not covered by oxygen, active sites covered by oxygen, nitrogen sites and an oxygen-covered nitrogen site respectively. The reaction R 9.131 is the sum of the two consecutive reactions NO + 2 C $\longrightarrow$ C(O) + C(N) and 2 C(N) $\longrightarrow$ N_2 + 2 C.

The Authors were able to estimate the reaction constants from experimental data and solving the set of equations derived from the previous scheme, they pointed out the importance of the N_2O molecules during NO reduction mainly at high temperatures where conversion of char-nitrogen into N_2O increases with combustion temperature. Moreover around $T = 1000$K, only a small part of the NO (20%) is converted into N_2 while a major part of N_2O (40 to 80%) is reduced to N_2. A major part of the molecular nitrogen released originates from N_2O reduction (typically 60%), rather than from NO reduction (typically 40%). They concluded that reduction of NO thus occurs preferentially via the intermediate formation of nitrous oxide.

9.2.7. The formation of NO_2

Thermodynamic equilibrium strongly disfavors at high temperatures the formation of NO_2 against the NO, the last usually being more than 95% of the total NO_x. The H radicals diffuse from the flame zone and react with oxygen:

$$\mathrm{H} + \mathrm{O_2} + \mathrm{M} \rightleftharpoons \mathrm{HO_2} + \mathrm{M} \tag{R 9.134}$$

At high temperatures, a competitive reaction reabsorbs the H radicals:

$$\mathrm{H} + \mathrm{O_2} \rightleftharpoons \mathrm{OH} + \mathrm{O} \tag{R 9.135}$$

At the same time NO also diffuses from the reacting zone and interacts with the peroxide:

$$\mathrm{NO} + \mathrm{HO_2} \rightleftharpoons \mathrm{NO_2} + \mathrm{OH} \tag{R 9.136}$$

Parallel to this reaction the dissociation of NO_2 takes place:

$$\mathrm{NO_2} + \mathrm{H} \rightleftharpoons \mathrm{NO} + \mathrm{OH} \tag{R 9.137}$$

$$\mathrm{NO_2} + \mathrm{O} \rightleftharpoons \mathrm{NO} + \mathrm{O_2} \tag{R 9.138}$$

9.3. Interaction with turbulence

As previously discussed, the reactions leading to NO formation are substantially slower than fuel oxidation reactions. Moreover, the NO kinetics is usually slower even in comparison to the turbulence time scales. However, turbulence fluctuations usually play a decisive role because of the high non-linearity of the NO reaction rates.

Two models are used for the turbulent chemistry interaction: an *Eddy Dissipation Concept* and a *Probability Density Function*. The first model has been already described in section Section 5.8. The *PDF* method differs slightly from the one explained in section Section 5.7 and applied to the prediction of the main species and therefore is described below in some detail.

The reaction rates of the mechanisms discussed in section Section 9.2 are assumed to be valid for a given Temperature T and a given gas composition x_i. The fluctuations change both the temperature and the composition. If the *PDF* of those variables are known, then it is possible to calculate the averaged reaction rate easily $\overline{R}_{nox}$ using:

$$\overline{R}_{nox} = \int P(T, x_i) R(T, x_i)\, dT dx_i \tag{9.50}$$

where $P(T, x_i)$ is the *PDF* and $R(T, x_i)$ is the total NO_x reaction rate for a specific temperature and a specific composition. Usually, it is assumed that the fluctuations of the temperature and the species are independent, simplifying the numerical calculation of the integrals greatly. Moreover, only the following combinations are taken into consideration:

- fluctuations of temperature: $P(T, x_i) = P(T)$;
- fluctuations of the temperature and one species: $P(T, x_i) = P_T(T) P_a(x)$;
- fluctuations of two independent species: $P(T, x_i) = P_a(x) P_b(y)$.

As in the case of the mixture fraction (see section Section 5.7), the β function is used as the PDF of the temperature, expressed by the following relation:

$$P(T) = \beta_{a,b}(T)$$

The coefficients a and b are a function of the mean temperature $\overline{T}$ and its variance σ:

$$a = \overline{T}\left(\frac{\overline{T}(1-\overline{T})}{\sigma^2} - 1\right) \tag{9.51}$$

$$b = (1-\overline{T})\left(\frac{\overline{T}(1-\overline{T})}{\sigma^2} - 1\right) \tag{9.52}$$

The averaged temperature $\overline{T}$ is calculated from the solution of the averaged energy equation. For the calculation of the variance, a transport equation for the σ^2 can be written:

$$\frac{\partial}{\partial t}\left(\rho\sigma^2\right) + \nabla\cdot(\rho\vec{v}\sigma^2) = \nabla\left(\frac{\mu_t}{\sigma_t}\nabla\sigma^2\right) + C_g\mu_t(\nabla\overline{m})^2 - C_d\rho\frac{\epsilon}{k}\sigma^2 \tag{9.53}$$

where the constants σ_t, C_g and C_d take the values 0.85, 2.86, and 2.0, respectively. The above equation is identical to Equation 5.115 derived in Section 5.7. If the mixture fraction *PDF* model is used, then the equation 9.53 is already solved.

Assuming equal rates of production and of dissipation of the variance, an analytical estimation for σ^2 is obtained:

$$\sigma^2 = \frac{\mu_t}{\rho}\frac{k}{\epsilon}\frac{C_g}{C_d}(\nabla\overline{T})^2 \tag{9.54}$$

The limits of the integration are taken to be equal to T_u and T_b where the unburned temperature T_u is set to be $T_u = 300\ K$ and the burned temperature T_b is set to the local adiabatic equilibrium temperature. The value for the unburned temperature is not important because the source term is small (see [266]) at that temperature.

In the case of fluctuation of reacting gases, a β-PDF can also be used and similar equations can also be formulated in this case.

10. Implementation in a CFD software

In the previous Chapters, it has been described how the thermochemical processes of solid particles can be mathematically implemented into the frame of reactive turbulent fluid dynamics. To complete this overview other three points must be addressed:

1. Modeling of the motion of the particle;
2. Modeling of the temperature of the particle;
3. Modeling of the particles interaction with the radiation field.

In this Chapter, a brief description of these last three points is presented.

10.1. Multi-phase flow tracking

The multiphase fluid flow analysis is used to simulate the behavior of a mixture of phases and their interactions. Simulations of solid particles conversion processes are an intrinsically multiphase calculation. Many kinds of multiphase flow exist, depending on the mass ratio, the volume ratio, the geometrical arrangements (also considering the gravity direction) and many other [63]. Multiphase flow regimes can be generally divided into four categories:

1. gas-liquid or liquid-liquid flows;
2. gas-solid flows;
3. liquid-solid flows;
4. three-phase flows.

For some of the simpler flows, such as those in vertical or horizontal pipes, a substantial number of investigations have been conducted to determine the dependence of the flow pattern from the flow conditions. The results are often displayed in the form of a flow regime map that identifies the flow patterns occurring in various parts of a parameter space defined by the component flow rates. An example of such a flow regime map for gas-liquid mixture in a vertical flow is shown in Figure 10.1 (here the the Hewitt and Roberts map is shown, similar the the old and standard Baker map [19]), presenting several ways, the two-phase can be classified. The axis are both labeled using each phase momentum G to the density ρ ratio.

The following regimes are typical for gas-liquid or liquid-liquid flows:

- Bubbly flow: This is the flow of discrete gaseous or fluid bubbles in a continuous fluid.
- Droplet flows: This is the flow of discrete fluid droplets in a continuous gas.
- Slug flow: This is the flow of large bubbles in a continuous fluid.
- Stratified/free-surface flow: This is the flow of non-miscible fluids separated by a clearly-defined interface.

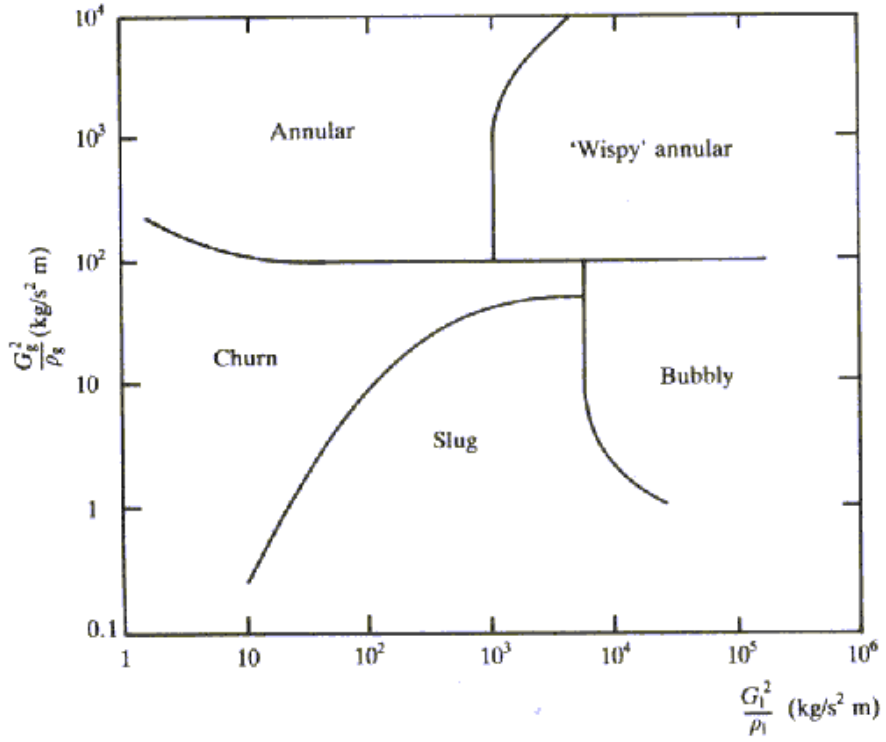

Figure 10.1.: Example of a flow regime map for a multiphase flow in a vertical pipe (Hewitt and Roberts map [19])

In the case of a gas-solid mixture, the following regimes are typical of gas-solid flows:

- Particle-laden flow: This is a flow of discrete particles in a continuous gas.
- Pneumatic transport: This is a flow pattern that depends on factors such as solid loading, Reynolds numbers, and particle properties. Typical patterns are dune flow, slug flow, and homogeneous flow.
- Fluidized bed: This consists of a vertical cylinder containing particles, into which a gas is introduced through a distributor. The gas rising through the bed suspends the particles. Depending on the gas flow rate, bubbles appear and rise through the bed, intensifying the mixing within the bed.
- Packed bed.

If the volume fraction of the solid phase is high enough, the particles are packed, and the freedom of movement is limited. Decreasing the packed ratio, the solid particles become to experience a relative motion in the fluidized bed regime, in which still the interaction between single particles are still determinant for the motion. In the extreme limit of low solid phase volume fraction, the particles are so diluted inside the gas that the interactions among them do not influence the flow. This is the regime of discrete particles in which the solid-solid interactions can be completely neglected: this regime is the only interesting regime taken into consideration in this thesis. In practice, discrete phase must be present at a reasonably low volume fraction,

usually less than 10-12% (the limitation is done on the volume fraction, while the mass loading of the discrete phase may greatly exceed 10-12%).

The solid phase can be described following the two general approaches:

1. Lagrangian reference frame;
2. Eulerian reference frame.

In the Eulerian reference frame, the same approach presented in Chapter 4 for the description of the gaseous phase is also used for the second phase. Using this method, the particles are regarded as a continuous phase for which conservation equations (continuity, momentum, and energy) are solved in a similar way to gas flow field. This approach is the most general, applicable for all the flow regimes, particularly suitable for denser suspensions when particle-particle interactions are important and the particle effects on the flow is too large to be neglected. The Eulerian reference frame approach posses drawbacks due to its difficult convergence behavior.

Taking advantage of the fact that interactions among particles in the second phase are neglected, the analysis in a Lagrangian frame can be carried out. Conservation equations are written for each particle (in a Lagrangian frame), and they are then solved iteratively one after the other from their injection inside the domain until they leave the domain (or some other criteria is fulfilled).

10.2. Particle tracking in Lagrangian frame

In the Lagrangian discrete phase model, the fluid phase is treated as a continuum by solving the time-averaged Navier-Stokes equations, while the dispersed phase is solved by tracking a large number of particles, bubbles, or droplets through the calculated flow field. The dispersed phase exchanges momentum, mass, and energy with the fluid phase.

The particle or droplet trajectories are computed individually at specified intervals during the fluid phase calculation. This makes the model appropriate for the modeling of spray dryers, coal and liquid fuel combustion, and some particle-laden flows, but inappropriate for the modeling of liquid-liquid mixtures, fluidized beds, or any application where the volume fraction of the second phase is not negligible.

The dispersion of the second phase is simulated in a Lagrangian frame. For each particle position $\vec{X}_p$ and velocity $\vec{u}_p$ are calculated solving the following equations [56, 402, 57, 211]:

$$\frac{d\vec{X}_p}{dt} = \vec{u}_p \tag{10.1}$$

$$\frac{d\vec{u}_p}{dt} = \vec{a}_d + \left(1 - \frac{\rho}{\rho_p}\right)\mathbf{g} \tag{10.2}$$

with $\vec{a}_d$ and $\vec{g}$ are the acceleration due to drag force and the acceleration due to gravity. The particles are assumed to be spherical therefore the drag acceleration is written as:

$$\vec{a}_d = \frac{18\mu}{d_p\rho_p^2}\frac{C_D Re_p}{24}\left|u_{rel}\right|\vec{u_{rel}} \tag{10.3}$$

where $\vec{u_{rel}} = \vec{u} - \vec{u}_p$ is the relative velocity of the particle respect to the actual velocity of the gas $\vec{u}$.

In Equation 10.3 the particle Reynolds number Re_p is defined by:

$$Re_p = \frac{\rho d_p u_{rel}}{\mu} \tag{10.4}$$

and the drag coefficient, C_D, taken from [251]:

$$C_D = a_1 + \frac{a_2}{Re_p} + \frac{a_3}{Re_p^2} \tag{10.5}$$

A more generally valid equation has been proposed in [236] where the forces together with the gravity force, the force due to the fluid pressure gradient, inertia force of added mass, the viscous and pressure drag force and the viscous force due to unsteady relative acceleration (also known as the Basset history term) are taken into consideration. If the particle Reynolds number Re_p is small (it has been proved [101] that the most restrictive condition is $Re_p < 0.5$) the Stokes approximation is allowed for the viscous and pressure drag force. Due to this Stokes approximation, no lift force is present in the equation. All those forces can be neglected and the proposed equation 10.2 is obtained back when the density of the dispersed particles is much bigger than the density of the Eulerian fluid.

The driving velocity in equation 10.3 is the instantaneous velocity of successive fluid particles that cross the solid particle trajectory. In RANS models that detailed information is lost since averaged quantities are calculated only. The actual velocity of the gas $\vec{u}$ can be reconstructed from the Favre averaged gas velocity $\vec{U}$ adding a random contribution from the turbulent fluctuations (the Eddy Interaction Model, or EIM) [129]:

$$u_i = U_i + \xi\sqrt{u_i'^2} \tag{10.6}$$

where ξ a normally distributed random number. If the assumption of homogeneous turbulence is used as in the k-ε and k-ω models the previous equation is simplified into the following:

$$\vec{u} = \vec{U} + \widehat{n}\sqrt{2k} \tag{10.7}$$

where $\widehat{n}$ is a random generated unit vector.

The equations of motion 10.1 and 10.2 are solved in a given instance of the turbulence for a characteristic lifetime of the eddy defined by

$$\tau_e = 2C_L\frac{k}{\varepsilon} \tag{10.8}$$

with the constant $C_L = 0.15$ for the k-ε model and $C_L = 0.3$ for the RSM. To increase the accuracy of the model, the equations for each droplet are integrated several times and the results averaged before passing them to the solver for the gas phase.

The aforementioned model, with the isotropic turbulence assumption, can be accurately employed as long as particles are outside the woll boundary layer. If particles move inside the layer the velocity fluctuations present strong inhomogeneities and modifications for each component must be taken into account. As an example, the modification proposed in [93, 94] are

obtained by data fitting from DNS calculations [1]:

$$u^{'+} \equiv \frac{\sqrt{\overline{u'^2}}}{U} = \frac{0.40y^+}{1+0.0239y^{+\,1.496}} \tag{10.9}$$

$$w^{'+} \equiv \frac{\sqrt{\overline{w'^2}}}{U} = \frac{0.19y^+}{1+0.0361y^{+\,2.421}} \tag{10.10}$$

where u and w are the components parallel and normal to the wall.

Models that take into consideration in more detail the correlation function (in space as well as in time) can be derived using stochastic equations. Three kinds of models are available in literature:

1. The Thomson models [375], in which the velocity is considered a stochastic variable and is given by the following equation:

$$du_i = a_i \cdot dt + b_{i,j} \cdot dW_j \tag{10.11}$$

   where $a_{i,j}$ and dW_j are the diffusion tensor and the infinitesimal increment of a vector Wiener process, with Gaussian distribution with mean zero and variance dt and its successive values are uncorrelated. The vector a and the tensor b can be expressed as a function of the Lagrangian auto-correlation function (see [193] for more details).

2. The Sawford model [305], an acceleration-based stochastic Lagrangian model in which the acceleration is a stochastic variable given by the equation:

$$da_i + \alpha_1 a_i \cdot dt + \alpha_2 \int_0^t a_i(t')dt' \cdot dt = \sqrt{2\alpha_1\alpha_2\sigma_u^2} \cdot dW_j \tag{10.12}$$

3. The Reynolds model [290] that improve the Sawford model to obtain non-Gaussian distribution by using an instantaneous dissipation rate modeled by an independent stochastic equation.

10.3. Modeling of particle temperature

The temperature of the particle T_p must be calculated using the energy balance for a single particle. If the fuel particles are small enough, the Biot number Bi of the particle is smaller than one. The thermal resistance due to conduction is negligible in comparison with the effective heat transfer coefficient (h_{eff} takes into consideration radiation and convection) and the temperature of the particle can be assumed uniform.

Heat transfer to the particle during the devolatilization process includes contributions from convection, radiation, and the heat consumed during each process.

$$m_p c_p \frac{dT_p}{dt} = hA_p(T_\infty - T_p) + \epsilon_p A_p \sigma(\theta_R^4 - T_p^4) + f_h H_{reac}\frac{dm_p}{dt} \tag{10.13}$$

[1] In the original paper modification to the turbulent viscosity and to the turbulent energy dissipation have been also proposed.

	m_p	mass of the particle	kg
	c_p	heat capacity of the particle	$\frac{\text{J}}{\text{kg K}}$
	A_p	surface area of the particle	m^2
where:	T_∞	local temperature of the continuous phase	K
	h	convective heat transfer coefficient	$\frac{\text{W}}{\text{m}^2\,\text{K}}$
	ϵ_p	particle emissivity	-
	θ_R	radiation temperature,	$(\frac{G}{4\sigma})^{1/4}$ K

H_{reac} is the heat released by each process. In the case of devolatilization that energy is negligible. Only a portion $(1 - f_h)$ of the energy produced by the surface reaction appears as a heat source in the gas-phase energy equation: the particle absorbs a fraction f_h of this heat directly. For coal combustion, it is recommended that f_h be set at 1.0 if the char burnout product is CO and 0.3 if the char burnout product is CO_2.

The heat transfer coefficient, h, is evaluated using the correlation of Ranz and Marshall [286] (other relations can be used as well):

$$Nu = \frac{hd_p}{k_\infty} = 2.0 + 0.6Re_d^{1/2}Pr^{1/3} \tag{10.14}$$

	d_p	particle diameter	m
	k_∞	thermal conductivity of the continuous phase	W m K
where:	Re_p	Reynolds number (based on the particle diameter)	
		and the relative velocity	
	Pr	Prandtl number of the continuous phase	-

10.4. Radiative Properties of Particles

The evaluation of the radiative properties of pulverized coal, char and fly ash particles requires knowledge of their size and complex index of refraction [131, 130, 436, 134]. The size typically ranges from a few hundred to tens of μm, and may be even smaller, of the order of one micron.

The contribution of particles to the radiative intensity field is calculated during Lagrangian particle tracking. The particles absorption coefficient inside a certain control volume is calculated by summing up the contribution of all particle classes inside the volume. [74]

$$a_p = \sum_{n=1}^{N} Q_{abs,n} \cdot \frac{A_{p,n}}{V_{CV}} \tag{10.15}$$

where $Q_{abs,n}$ is the absorption efficiency of the nth particle, $A_{p,n}$ is the particle's projected area,

and V_{CV} is the cell's volume. A similar expression holds for the scattering coefficient

$$\sigma_p = \sum_{n=1}^{N} Q_{sca,n} \cdot \frac{A_{p,n}}{V_{CV}} \tag{10.16}$$

where $Q_{sca,n}$ is the scattering efficiency of the nth particle. The particle volume fraction in each cell f_V can be calculated using the relation:

$$f_V = \sum_{n=1}^{N} \frac{V_{p,n}}{V_{CV}} \tag{10.17}$$

If the volume fraction becomes sufficiently large, i. e. the distance between the particle is so small that scattering does not take place on single droplets but on a cluster of particles, e. g. for further details see [247], and the calculation scheme taking this effect into account becomes very involved.

The radiative properties of the particles depend on their shape, size parameter, complex index of refraction, and clearance to wavelength ratio. Soot particles, pulverized coal particles, char, and fly-ash are generally assumed to be spherical, as far as thermal radiation is concerned. The particle size parameter is defined as $x = 2\pi a/\lambda$, where a is the radius of the particle, and λ the wavelength of the incident radiation. The complex index of refraction, which depends on the material of the particle, is defined as $m = n - ik$, where n is the refractive index and k the absorptive index. The influence of the clearance to wavelength ratio, defined as the ratio of the distance between the particles to the wavelength of the incident radiation, may be neglected for most combustion problems. In such a case, the scattering is referred to as independent.

The radiative properties of a spherical particle may be determined using Mie's theory [247]. This theory is based on the solution of the Maxwell equations for the scattering of an electromagnetic wave incident on a homogeneous spherical particle, and it requires the knowledge of the complex index of refraction. The refractive index of coal varies little with the wavelength in the infrared region of the spectrum and is weakly sensitive to the type of coal, while the absorptive index exhibits much larger variations. The absorptive index of fly ash is about 1.5, and its refractive index varies significantly. Typical values of the complex refractive index of coal, char, and fly-ash may be found in [232] and [247].

Once the complex index of refraction is available, Mie theory may be used to determine the radiative properties of a spherical particle.

In order to perform Mie calculations for the efficiencies as well as phase function, certain values have to be defined. The absorption efficiency factor is defined as the ratio between absorption cross section C_{abs} and the geometric projected area A_p

$$Q_{abs} = \frac{C_{abs}}{A_p} \tag{10.18}$$

while the scattering efficiency is the ratio between scattering cross section C_{sca} and A_p

$$Q_{sca} = \frac{C_{sca}}{A_p} \tag{10.19}$$

The sum of both efficiency is called the extinction efficiency Q_{ext}

$$Q_{ext} = \frac{C_{ext}}{A_p} = \frac{C_{abs} + C_{sca}}{A_p} = Q_{abs} + Q_{sca} \tag{10.20}$$

These values generally depend on the size parameter $x = \pi \cdot D \cdot \eta$ and the complex index of refraction m. For details on the calculation of efficiencies, the reader is referred to [247, 386]. After calculating the efficiencies for one diameter, the gray values are calculated according to

$$Q_i = \frac{\int_0^\infty Q_{i,\eta} \cdot I_{\eta,b} \cdot \mathrm{d}\,\eta}{I_b} \tag{10.21}$$

where $I_{\eta,b}$ is the spectral blackbody intensity given through Planck's law and I_b is the total blackbody emissive power given by the Stefan-Boltzmann law. Subscript i stands either for absorption (abs) or scattering (sca). Figure 10.2 shows the result of the Planck averaged efficiencies as a function of diameter calculated at different temperatures. With increasing temperature the contribution of absorption decreases while the one of scattering increases. From Figure 10.2 it can be seen that at large diameter the sum of the contributions of scattering and absorption exceeds unity which is due to diffraction, also known as the extinction paradox [386]. In CFD calculations, the effect of diffraction is neglected [247] in such a way that it is assumed that half of the extinction is due to diffraction and, therefore, the scattering coefficient in Eq (10.16) is simply

$$Q_{sca} = 1 - Q_{abs} \tag{10.22}$$

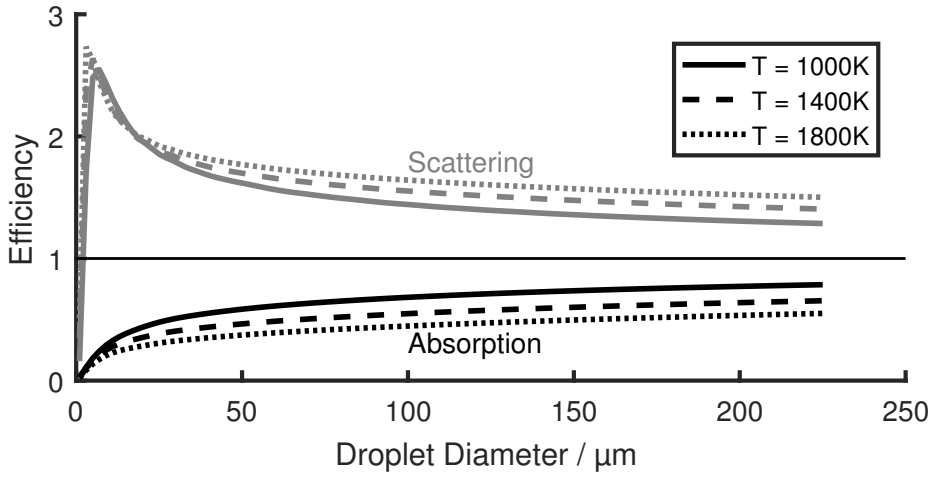

Figure 10.2.: Scattering and absorption coefficients as a function of particle diameter at different temperatures. Calculated using Mie theory [386, 247] with glycol properties using measurements of Sani and Dell' Oro [303].

The radiative properties of a cloud of particles may be determined from those of the individual particles if the particle size distribution is known and the scattering is independent. In such a case, the spectral absorption, scattering and extinction coefficients of a cloud of particles are

given by

$$\begin{aligned} \kappa_\lambda &= \int_0^\infty C_{abs}(a)\, n(a)\, da \\ \sigma_{s\lambda} &= \int_0^\infty C_{sca}(a)\, n(a)\, da \\ \beta_\lambda &= \int_0^\infty C_{ext}(a)\, n(a)\, da \end{aligned} \tag{10.23}$$

where C_{abs}, C_{sca} and C_{ext} are the absorption, scattering and extinction cross sections, respectively, which are defined as the ratio of the radiative power of the incident radiation beam that is absorbed, scattered or extinguished by the particle, respectively, to the radiative energy flux of the incident radiation beam and $n(a)$ is the particle radius distribution function, i.e., $n(a)da$ is the number of particles per unit volume with radius in the interval between a and $a + da$. The scattering phase-function of a cloud of particles is given by

$$\Phi_\lambda(\Theta) = \frac{1}{\sigma_{s\lambda}} \int_0^\infty C_{sca}(a)\, \Phi(a, \Theta)\, n(a)\, da \tag{10.24}$$

where Θ is the angle between the incoming and the outgoing radiation beams.

In [68] the Mie theory is applied to homogeneous spherical particles for a wide range of complex index of refraction and particle size distributions. It has been found ([68]) that the spectral absorption and extinction coefficients of a cloud of spherical particles normalized by the corresponding coefficients for the small particle limit, which are given by Rayleigh theory, are approximately independent of the particle size distribution, and depend only on the mean particle diameter and the index of refraction. The Planck-mean and the Rosseland-mean absorption and extinction coefficients were calculated from the spectral results, and the following correlations

were proposed:

$$\begin{aligned}
\frac{\kappa_P}{f_A} &= \left[\left(0.0032\phi\left(1+\left(\frac{\phi}{725}\right)^{1.65}\right)\right)^{-3/2}+\left(\frac{13.75}{\phi^{0.13}}\right)^{-3/2}\right]^{-2/3} \\
\frac{\kappa_R}{f_A} &= \left[\left(0.0032\phi\left(1+\left(\frac{\phi}{650}\right)^{2.3}\right)\right)^{-25/22}+\left(\frac{15.65}{\phi^{0.143}}\right)^{-25/22}\right]^{-22/25} \\
\frac{\beta_P}{f_A} &= \left[\left(0.0032\phi\left(1+\left(\frac{\phi}{355}\right)^{1.9}\right)\right)^{-6/5}+\left(\frac{10.99}{\phi^{0.02}}\right)^{-6/5}\right]^{-5/6} \\
\frac{\beta_R}{f_A} &= \left[\left(0.0032\phi\left(1+\left(\frac{\phi}{485}\right)^{1.75}\right)\right)^{-6/5}+\left(\frac{10.99}{\phi^{0.02}}\right)^{-6/5}\right]^{-5/6}
\end{aligned} \tag{10.25}$$

where

$$\begin{aligned}
\phi &= \bar{a}T \\
\bar{a} &= \frac{3f_v}{4f_a} \\
f_a &= \int_0^\infty \pi a^2 n\left(a\right) da
\end{aligned} \tag{10.26}$$

The mean particle radius, $\bar{a}$, is expressed in μm. The expressions above correlate the experimental data for different coals within 30% in the temperature range from 500 to 2500 *K*. They can be used as approximations if no more accurate data are available for the coal under consideration.

If the particles can be assumed as very large spheres such that the size parameter $x >> 1$ and $x|m-1| >> 1$, then the geometric optics theory is applicable. If, in addition, the particles are opaque, grey and reflect diffusely, then the absorption efficiency, defined as the ratio of the absorption cross-section to the projected area of the particle (πa^2), is equal to the emissivity of the surface, ε. Similarly, the scattering efficiency, defined as the ratio of the scattering cross section to the projected area of the particle, is equal to the reflectivity of the surface, ρ. Under these conditions, the spectral absorption and scattering coefficients of a cloud of particles are given by:

$$\begin{aligned}
\kappa_\lambda &= \pi\varepsilon\int_0^\infty a^2 n\left(a\right) da \\
\sigma_{s\lambda} &= \pi\rho\int_0^\infty a^2 n\left(a\right) da
\end{aligned} \tag{10.27}$$

This procedure has been used, e.g., in [435]. Its accuracy can be questionable, particularly in the

case of fly ash, which is semi-transparent in the spectral range of importance of thermal radiation in combustion. Notice that due to the assumption of grey particles, the spectral coefficients in Eq. 10.27 become independent of the wavelength.

Coal particles exhibit a highly forward scattering behavior. Although the Mie theory may be used to determine the scattering phase function, it is often advantageous to rely on relatively simple approximate phase functions, e.g., either a Henyey-Greenstein phase function or a linear anisotropic delta-Eddington phase function. Marakis et al. [232] claim that neglecting scattering is a reasonable approach for atmospheric coal combustion, while anisotropic scattering should be taken into account for pressurized pulverized coal combustion. The approximation of isotropic scattering was found to yield poorer results than neglecting scattering [232] .

Combustion of biomass produces particles very similar to those of coal combustion. Soot, fly ash and char are the main particles in biomass combustion. Bahador and Sundén [17] observed that the chemical composition of fly ash from coal and biomass combustion is similar, and so they assumed that the complex refractive indices are also similar. The Mie theory can be used to determine the radiative properties of single spherical particles, and Eqs. 10.23 and 10.24 employed to calculate the spectral radiative properties of a cloud of particles. According to [17], the absorption effects of fly ash are important and can increase the radiative heat source and wall heat fluxes. However, for prescribed fly ash volume fractions, the effect of scattering by particles on the radiative heat source and radiative heat flux to the wall is not so important [17].

Radiative properties of particles may be considered by accounting for the transparency in the infrared or by assuming that the particles are grey opaque spheres. This last approximation has been used, for example, in [16], for the modeling of thermal radiation from droplets in light fuel oil spray combustion. Under this approximation, the absorption and the scattering coefficients are determined using Eq. 10.27.

In the first approach the transparency of the droplets is taken into account, and therefore it is more rigorous, but not so computationally efficient. A simplified model for radiation absorption by semi-transparent diesel fuel droplets is reported in Dombrovsky et al. [91]. It was found that this model is more accurate than the previous one, based on the assumption of opaque droplets. However, the grey medium approach used by may lead to important errors in non-isothermal media. An improved spectral model is described in [90]. In this work, the spectral absorptive index was experimentally determined for several Diesel fuels, while the spectral refractive index was theoretically obtained. Approximate equations to calculate the absorption and scattering efficiencies were reported. The radiative properties were obtained using these approximations and compared with those calculated using the more general Mie theory. It was concluded that the accuracy of the simplified approach is sufficient for practical applications in the visible and infrared ranges, for various types of Diesel fuels, and for droplet radii in the range from 5 to 50 μm. Further information on radiative properties of droplets may be found in [89].

Part III.

Applications

11. Fuel Characterization

The application of the models described in the previous chapters, requires the estimation of several parameters whose values have to be calculated from specifically designed experiments. The influence of those parameters on the accuracy of the results can be high and therefore great care must be taken in both, design of the experiments and the successive mathematical analysis.

Since each fuel has different composition and different chemical structure, the details of the conversion rates remain fuel dependent. Consequently, experiments must be designed and performed individually for each fuel. In the past, several attempts have been published with the aim to generalize reactions rates and correlations to be able to predict fuels conversion rates without the use of extensive experiments. The idea behind the intrinsic model for char combustion [339], for example, is based on the separation between the intrinsic chemical rate, equal for all the chars, and the effect of pore structures that is char dependent. Even if those attempts have been surmounted with some success, fuel specific effects are still observable and only with tuned parameters high predictive models can be expected to meet the requirements of science and technology.

There is a second reason why parameters and experiments are fuel dependent. Correlations are generated only for a narrow range of fuels (coals, wood, biomass) and they cannot be applied with confidence to any fuel. In the last decades, many different fuels have been used in industry and even more out of specification fuels will be used. It becomes clear that parameters used until now cannot be anymore utilized in modeling many of the existing industrial processes.

Considering the vast variety of solid fuels, many kinds of techniques and experiments have been developed for the extraction of data for the modeling. In fact, there are dependencies among parameters and thermodynamical quantities (temperature, pressure, gas concentrations), and the parameters itself are also related to other chemical processes (char reactivity depends on how devolatilization is conducted).

In this Chapter, some of the methodologies used to derive the unknown parameters are presented. Few experiments are presented in more detail together with the mathematical approach used for the analysis.

11.1. Basic analysis

Few properties are fundamental as a preliminary characterization. These properties are listed below:

Ultimate analysis provides the amount of C, H, O, N, S and sometimes Cl in the fuel.

Proximate analysis provides the amount of moisture, volatile matter, fixed carbon, and ash in the fuel.

Heating value provides the heat released by the reactions. The measurements are performed in calorimeters. These instruments usually consist of a calorimetric vessel containing the fuel sample, with the vessel surrounded by a shield and an external thermostat. In isothermal calorimeters, the vessel is placed in a large bath held at a constant temperature, and the heat released by chemical reactions occurring in the sample is determined by measuring

the heat dissipated to the environment. In adiabatic calorimeters, the heat generated by fuel oxidation is not transferred to the environment, and is then calculated by measuring the temperature rise within the vessel.

The analysis mentioned above is performed for the fuel as received and for the char after conversion. Knowing the characteristics of the coal as received and that of the char, as a difference, the averaged, global characteristics of the volatilized gases can also be calculated.

Additional analyzes can be performed in view of special applications. Among them:

- Particle size distribution;
- Density (usually apparent and with the knowledge of the porosity also the true density can be derived);
- Specific heat of the solid;
- Thermal conductivity of the solid;
- Swelling, shrinking and fragmentation phenomena;
- Ignition delay time;
- Grindability;
- Ash analysis (Si, Al, Fe, Ca, K... content);
- Ash fusion tests;
- Morphological analysis (shape and distribution of pores);
- Maceral analysis (Inertite, Liptinite, Vetrinite, for coals);
- Nuclear Magnetic Resonance (NMR) analysis;
- Chemical analysis (Cellulose, Hemicellulose, lignin, for biomasses);
- Merceological analysis (main fractions in wastes and residues).

The knowledge of the morphological structure of a solid porous material is relevant for a proper applications of some models as already pointed out in Chapter 7 and in Chapter 8. Without their knowledge (internal surface, pore diameters, and their development with the conversion) it is not possible to extract chemical parameters from the experimental data and the applications to other regimes may lead to wrong rates (see Chapter 13). Ash analysis is of fundamental importance for applications to slagging and fouling phenomena [29].

Since each model has a different mathematical formulation based on different physical and chemical phenomena, the need of parameters remains model dependent. In oxidation and gasification, using the intrinsic rate given in Arrhenius form, the following data are usually required:

1. The activation energy;
2. The pre-exponential factor;
3. The reaction order for the reactants.

In the case of devolatilization experiments with the single kinetic rate the following parameters are searched:

1. The amount of volatiles released;
2. The activation energy;
3. The pre-exponential factor;
4. The composition of the gas released.

11.2. Methods for solid fuel conversion characterization

The required modeling parameters are extracted from specifically designed experiments where mass loss as a function of time is measured in a controlled environment (temperature, pressure, gas composition). The most common techniques for the characterization are listed below (see also [275]):

Heated grid experiments In this kind of experiments a thin layer of particles have been heated up using electrically heated wire. Weight loss has been obtained by weighting the char after quick cooling of the sample. The tar, as well as the gas, can be collected and analyzed. Secondary reactions cannot be eliminated but using efficient cooling, they can be reduced. Using heated grid experiments, time can be accurately measured, and balances can be adequately closed. The main disadvantage of this technique is that the temperature cannot be easily estimated or measured. Moreover, the heating rate is moderately high (being $\sim 10^3 \frac{K}{sec}$) still far from those encounter in industrial applications.

Entrained flow reactors In this techniques, solid fuel is injected into a preheated stream of gas. Residence time can be controlled known the velocity distribution inside the reactor. High heating rates together with high final temperatures can be achieved, but difficulties arise in measuring or calculating the particle temperature accurately. Secondary reactions are present and their influence cannot be easily estimated. To avoid the difficulties related to the particle temperature determination, gas and fuel can be heated up together inserting them into a reactor tube with constant wall temperature (electrically controlled). To further reduce the inaccuracy for the particle temperature determination, the preheated gas and the fuel stream are inserted into a transparent wall reactor. This solution opens the possibility to control the particle paths with non-intrusive techniques. As a disadvantage, the wall temperature cannot be as high as in the previous reactors. Moreover due to heat transfer through the walls the system is not anymore isotherm. A well-mixed reactors can also be used. Strong mixing reduces the uncertainties of temperature but increases the difficulties of extrapolating good kinetics due to different particle residence times.

TGA Thermogravimetric (TG) balance consists in slowly heating up the sample and recording the rate of change in weight as functions of time in a controlled atmosphere. The thermogravimetry analysis can easily obtain differential thermogravimetry (DTG). Analysis of the released gases can be performed using chromatography or FTIR techniques. However temperatures and heating conditions are far from those of large-scale furnaces, so data and parameters obtained with this analysis should be considered as a first level in the characterization of the fuels. Difficulties arise in extrapolating the kinetic from low heating rates to high heating rates experienced in many industrial furnaces. Besides, as already explained in other chapters, yields are different (as a strong function of the temperature), kinetics can be different and mainly tar amount (drastically increasing with the heating rate) and composition are different. The maximum temperature is generally around $1000°\mathrm{C}$, the maximum heating rate can be $100\frac{°\mathrm{C}}{\mathrm{min}}$. The sample is inserted in appropriate crucibles (of

different materials depending on the final temperature), and the maximum amount can be on the order of some tenths of milligrams, typically ranging from $1\mathrm{mg}$ to $50-100\mathrm{mg}$. The residence time depends on the thermal program and can be on the order of some minutes or more. The sample weight and temperature are continuously monitored, and the accuracy is generally high. The weighing sensitivity is on the order of $0.1\mu\mathrm{g}$, while the temperature precision is on the order of $0.1°\mathrm{C}$. Small amounts of sample ($5\mathrm{mg}$ or less) should be used for obtaining the devolatilization kinetics and avoiding the heat transfer limitation during the test. At least three runs (under different heating rates) should be programmed to elaborate the intrinsic kinetics by using iso-conversional methods. Larger amounts of sample (for example 1 or 2 g) can be used for studying the gas products (by coupling the TG balance with a gas analyzer, e.g., FTIR or MS-GC). This method is accurate and, most of all, it gives the weight loss curve directly as a function of the time. As a drawback the measurements are slow and only one sample per time can be analyzed. TGA is inadequate if the sample is inhomogeneous. More capable reactors must be built, and problems in determining the temperatures accurately and the homogeneity of conditions inside the probe may arise.

Radiative heating In this type of experiments particles are heated up by laser or flash lamps. Extremely high heating rates with high accuracy in heat flux measurements can be achieved with the possibility to control secondary reactions. In many devices, there is the possibility to have optical access to the sample. The possibility of temperature gradients effects must be accounted as a drawback of the method. Moreover the accuracy of the temperature estimation relay on optical properties of char (eventually soot present around the particle). The combination of laser heating and electrodynamic balance can be used for monitoring the weight losses continuously.

Fluidized and fixed beds The method of using a fluidized and fixed bed in devolatilization experiments is applicable in retrieving the volatile yield in particular condition, but they are usually not designed for calculating kinetics rate or detailed mechanisms, due to the difficulty to determine residence time and particle temperatures. The technique is primarily used to study the behavior of relatively big particle and to study secondary reactions of tars [252, 187, 147]. Detailed mass and energy transport calculation must be performed to analyze the data, and this difficulty limits the accuracy of the predictions.

Shock tubes The sample is quickly heated up by a shock wave and rapidly cooled down by the rarefaction wave. High temperature and high heating rates can be achieved, but a precise determination of the particle temperature is difficult to be obtained.

Mass spectrometry Pyrolysis experiments have been performed at the inlet of a mass spectrometer. The sample is slowly heated up in the vacuum and the products after an ionization zone are analyzed by a mass spectrometer. The technique is useful in studying the compositions of tars before they undergo secondary reactions.

Drop tubes The reactor is generally formed by a vertical tube inserted in a furnace. The fuel is fed at the top section generally with a pneumatic transport with a primary gas. A secondary gas can be introduced too. Electrically heated elements along the internal wall of the furnace provide the heat to the gas/solid mixture along the tube. The appropriate set up of these resistances can give an isothermal profile inside the tube. A gas burner can be inserted in the top section to give a transport gas at high temperature. In this kind of reactors conditions similar to the ones prevalent in large-scale plants can be achieved and therefore they are suitable for the analysis of the remnants after the devolatilization. As for drawbacks it must be mentioned that interpretation of the raw data still creates some inaccuracy

and mainly the balances are hardly closed. To regain accuracy for the devolatilization kinetic at high heating rates, experiments in drop furnaces must be coupled with detailed mathematical analysis of the sample.

Differential thermal analysis The Differential Thermal Analysis (DTA) technique an old method in which the solid sample is slowly heated up, and the temperature is continuously measured. The rate of reaction is calculated after comparison of the recorded temperature with the temperature of a similar inert sample.

Two general remarks must be made at the end of this list. The determination of particle temperature is a crucial factor in interpreting correctly every experiment for kinetic parameter determination and its inaccuracy estimation can lead to inaccurate kinetic parameters. When high particle temperatures have been measured at a high rate it is likely that the measured temperatures at the surface is different than the temperatures inside the particle [345]. Direct measurements of particle temperature require the knowledge of spectral radiation properties. If the radiation properties can be assumed to be gray, by measurements at a single frequency of the radiation intensity emitted or using different colors, it is possible to compare the amplitudes emitted at several wavelengths estimating the temperature.

Mass balance can be closed with an inaccuracy of 5% in those experiments where direct measurements are possible. In entrained flow experiments, in fluidized beds, in radiative tubes as well as in shock tubes the inaccuracy in mass balance can be higher. In devolatilization experiments, it is not possible to achieve perfect mass balance better than 5-10% (coal mass basis), due to the difficulties of collecting material with big molecular weight [345].

11.3. Parameter calculations

The calculation of the parameters values from the experimental data is a step involving the knowledge of the mathematical expression of the model and the knowledge of the details of the experiments. Generally, the experiments used can be divided into the following three categories:

1. Isothermal experiments, in which the temperature of the sample is kept constant;
2. Non-isothermal experiments with a constant heating rate, in which the temperature increase of the sample is controlled and kept constant;
3. Non-isothermal experiments with a non-constant heating rate are the most common.

Two mathematical methodologies can be applied to any of the experiments mentioned above:

1. Integral methods;
2. Differential methods.

Integral methods are based on relations that arise after integration of the differential equations and require calculation of integrals from the measured data while differential methods use relation based on differentiation of measured quantities. Generally, both mathematical approaches are appropriate, and if applied to idealized conditions they result in the same estimation of the parameters. As shown in [405] both methods, when correctly applied in the case of a synthetic conversion rate, estimate the correct parameters. Each method behaves differently when applied to real experiments, where uncertainties are presented in both, the measured quantities and the assumed mathematical model.

Differential methods are based on a mathematically ill-posed operator [1] (the derivative) and the uncertainties in the data and the model are usually amplified. To overcome this difficulty methods for the solution of *inverse problems* can be applied [376].

Integral methods are based on a well-posed operator (the integration) that cannot generally be expressed in a closed analytical form and they require therefore numerical integration.

11.3.1. Isothermal experiments

The easiest expression for the mass loss can be reformulated in the following expression (see Section 8.3):

$$\frac{d\alpha}{dt} = k(T)p_x^n(1-\alpha)^q \tag{11.1}$$

where $\alpha = 1 - \frac{m_p}{m_0}$ is the reaction progress variable taking values from zero (no fuel converted) to one (full conversion) and p_x is the partial pressure of the reactant (in the case of devolatilization that term is not present and the reaction order is $n = 0$). The goal of the mathematical analysis is the calculation of the activation energy E and the pre-exponential factor A, both present in the rate constant k expressed in Arrhenius form:

$$k(T) = Ae^{-\frac{-E}{RT}}$$

Integral methods Integral methods use the integral form of equation 11.1. Experiments deliver a certain set of conversions $\alpha_{i,j}$ (i is the index of the measurement point for the temperature with index j) measured at time $t_{i,j}$. The first step for the calculation of the unknown parameters A, E, (see as an example [401]) is the determination of the reaction rate constant $k_j(T)$. A fitting procedure follows after analytical integration of the equation 11.1. If $q = 1$, after integration:

$$\ln(1-\alpha) = -k(T)p_x^n \cdot t \tag{11.2}$$

and if $q \neq 1$:

$$\big(1-\alpha(t)\big)^{(1-q)} = (q-1)\left(k(T)p_x^n \cdot t + 1\right) \tag{11.3}$$

Both equations can be used as a fitting function for the set of measured pairs $\alpha_{i,j};\ t_{i,j}$ (index i) for each experiment at temperature T_j. A plot of $\ln k_j$ versus $\frac{1}{T_j}$ provides the activation energy and the pre-exponential factor since:

$$\ln k(T) = \ln A + \frac{E}{RT} \tag{11.4}$$

Only experiments at two different temperatures are needed to obtain both parameters, but at least a third experiment must be used to validate the linearity of the derived relation. More temperatures can be used to reduce the numerical uncertainties of the fitting algorithm.

As stated in [401] this procedure of obtaining the parameters does not contain any mathematical ambiguity. The accuracy of determining E and A is determined both by the quality of the experimental data and the accuracy of the least square fit. The correlation coefficient of the regression procedure used is a good indicator of its accuracy.

[1] A well-posed problem has the properties that (following Hadamard):

1. a solution exists;
2. the solution is unique;
3. the solution's behavior changes continuously with the initial conditions.

Problems that are not well-posed in the sense of Hadamard are termed ill-posed.

It is worth noticing that, as explained later in section Section 11.3.4, a non-linear multivariate fitting can be used. Instead of fitting the function 11.2 (if $q = 1$) or 11.3 (if $q \neq 1$) for each single experiment at temperature T_j, the measured points are fitted simultaneously $\alpha_{i,j};\ t_{i,j}$, obtaining directly the unknown parameters E and A, bypassing the calculation of the constant k_j. This both methods are mathematically equivalent, giving the same parameters in the case of synthetic generated fuel. The non-linear method, in conjunction with an appropriate solver, returns values with less statistical uncertainties.

Differential method Direct utilization of equation 11.1 can also be used for the calculation of the reaction rate constant, but this method is usually less accurate than integral methods.

If the equation 11.1 is used the reactant reaction order n is calculated after fitting $\ln \frac{d\alpha}{dt}$ versus $\ln(p_x)$. The reaction order q is obtained fitting $\ln \frac{d\alpha}{dt}_{i,j}$ versus $\ln(1 - \alpha_{i,j})$ since:

$$\ln \frac{d\alpha}{dt} = \ln k + q \cdot \ln(1 - \alpha) + n \cdot \ln p_x \tag{11.5}$$

The extrapolated derivative $\frac{d\alpha}{dt}(t = 0)$ at the beginning of the conversion can also be used for the parameter calculation, but this method is usually affected by larger uncertainties since it is more difficult to know the exact conditions that must be applied for the fitting (mostly temperature and composition of the gas).

11.3.2. Constant heating rate

The use of non-isothermal experiments is usually motivated by the necessity to save time (non-isothermal experiments are generally quicker than isothermal ones). Moreover, a non-isothermal behavior of the sample is natural in devolatilization and pyrolysis experiments since thermal decomposition cannot be avoided as in the case of char reaction by the utilization of non-reactive mixture.

In non-isothermal experiments, the sample is heated with a predetermined rate $m = \frac{dT}{dt}$ and typically remains constant throughout the experiment. The relation given by the equation 11.1 can be recast in term of the temperature T

$$\frac{d\alpha}{dT} = \frac{A}{m} e^{-\frac{-E}{RT}} p_x^n (1 - \alpha)^q \tag{11.6}$$

The integral form of this equation cannot be expressed with analytical functions, and, using the variable $x = \frac{E}{RT}$ it can be written as follows:

$$-\ln(1 - \alpha) = \frac{AE}{mR} \int_x^\infty \frac{e^{-\zeta}}{\zeta}\, d\zeta \equiv \frac{AE}{mR} p(x) \tag{11.7}$$

It is worth noticing that in the previous equation the upper bound of the integration has been replaced with ∞ with the assumption that at the beginning of the experiment the initial temperature (usually the room temperature) is too low to have some conversion already in place.

There exist a large number of methods for extracting both the activation energy and the pre-exponential factor from the non-isothermal experiments and as in the isothermal experiment case those methods can be grouped onto both integral methods and differential methods.

Integral methods In integral methods the equation 11.7 is used to fit the experimental data obtaining the unknowns parameters. The function $p(x)$ is related to the exponential integral

$Ei(x)$ by the relation:

$$p(x) = \frac{e^{-x}}{x} - Ei(-x) \tag{11.8}$$

In several mathematical software the exponential integral $Ei(x)$ is implemented with high accuracy, but direct approximations of the function $p(x)$ itself have also been derived. The simplest approximation is the one developed by [255] (originally used for $x > 15$):

$$p(x) \simeq \frac{e^{-x}}{x^2} \tag{11.9}$$

Inserting this equation into 11.7:

$$\ln\left(-\frac{1-\alpha}{T^2}\right) = \ln\left(\frac{AR}{mE}\right) - \frac{E}{RT} \tag{11.10}$$

and when m is given, A and E can be determined from the intercept and the slope of a plot $\ln\left(-\ln\frac{1-\alpha}{T^2}\right)$ versus $\frac{1}{T}$. A linear approximation for the logarithm of $p(x)$ has been given in [92]:

$$\ln p(x) \simeq -0.4567 \cdot x - 2.315 \tag{11.11}$$

In [80] the following approximation has been proposed:

$$p(x) \simeq \frac{e^{-x}}{x^2}\left(1 - \frac{2}{x}\right) \tag{11.12}$$

leading to a non-linearfitting:

$$-\ln(1-\alpha) = \frac{AR}{mE}T^2 \exp\left(-\frac{E}{RT}\right)\left(1 - 2\frac{RT}{E}\right) \tag{11.13}$$

The previous non-linearfitting can be reduced to a linear one after taking the logarithm of both sides:

$$\ln\left(-\frac{\ln(1-\alpha}{T^2}\right) = \ln\left[\frac{AR}{mE}\left(1 - 2\frac{RT}{E}\right)\right] - \frac{E}{RT} \tag{11.14}$$

and assuming constant the first term on the right side. This is a valid approximation if $x \gg 2$.

An other approximation has been derived in [318] leading to the following non-linearfitting:

$$p(x) \simeq \frac{e^{-x}}{x^2}\frac{x^4 + 18x^3 + 86x^2 + 96x}{x^4 + 20x^3 + 120x^2 + 240x + 120} \tag{11.15}$$

Differential methods As for the isothermal case, differential methods use directly the expression given by 11.6 as basis for a non-linearfit. From the pairs $\alpha_i;\ t_i$ (assuming one single experiment) the derivative $\frac{d\alpha_i}{dT_i}$ must be calculated before the application of the fitting procedure. Several experiments at different (but similar) heating rate can be performed to increase the accuracy.

A second differential method is based on the search for the maximum of the rate $\frac{d\alpha}{dT}$, leading to the following relation (again assuming one single experiment):

$$\frac{E}{RT_{max}^2} = \frac{q\left.\frac{d\alpha}{dT}\right|_{max}}{1 - \alpha_{max}} \tag{11.16}$$

requiring the determination of pair α_{max}; T_{max} at which the gradient of the conversion curve $\frac{d\alpha}{dT}$ has a maximum (denoted $\left.\frac{d\alpha}{dT}\right|_{max}$).

All the approximations and the derived fitting methods have been compared in [401]. A synthetic coal with typical parameters for char oxidation experiments given by $E = 123.3\,\frac{\mathrm{kJ}}{\mathrm{mol}}$ and $A = 16\,647.24\,1/\mathrm{s}$ and a biomass with pyrolysis given by the kinetic parameters given by ($E = 30.0\,\frac{\mathrm{kJ}}{\mathrm{mol}}$ and $A = 0.02\,1/\mathrm{s}$) have been used.

The conclusions in [401] can be summarized as follows:

1. In all of the cases considered, all the integral methods have provided an excellent visual fit to the synthetic data but they returned different values for the parameters (see also Section 11.3.4 for an explanation).

2. Reliability of the methods examined is directly related to accuracy in approximating the Arrhenius integral. Experiments on pyrolysis and oxidation of solid fuels are typically conducted in the x ratio ($x = E/R/T$) range from 2 to 50. The formula from Senum [318] given by equation 11.15 approximates the Arrhenius integral with accuracy better than 0.05% over the whole x ratio range.

3. The integral method based on the approximations from Doyle [92] given by 11.11 is unreliable.

4. The approximation from [80] given by Redfern 11.12 has resulted in 23% the activation error in energy and 350% error in the pre-exponential factor.

5. The integral method based on the approximation from Murray [255] given by 11.9 has identified the activation energy E within 4% error from the exact value, however the error in determining the pre-exponential factor A is around 40%.

6. The differential method has identified the activation energy within 5% margin from the exact value, however the error in the pre-exponential factor has reached almost 50%.

7. The integral method based on the approximation from Senum [318] given by 11.15 has provided both kinetic parameters within 0.5% error from the exact values.

The application of the differential method to experimental data of the integral type such as mass loss data in TGA reveals a critical disadvantage caused by the need of using numerical differentiation for estimating $\frac{d\alpha}{dt}$. The procedure dramatically amplifies the noise present in experimental data. For this reason, numerical differentiation has to be combined with smoothing. Integral methods do not suffer from this drawbacks.

11.3.3. Iso-conversional methodology

The iso-conversional methodology is a generalization of the above given approaches. It is based on the assumption that the effects of temperature and the effects of the conversion can be separated as given in the following equation:

$$\frac{d\alpha}{dt} = k(T) \cdot g(\alpha) \tag{11.17}$$

The iso-conversional method is an useful procedure to extract the activation energies only. Further mathematical procedures are required to extract other information.

Using the integral method, after separation of variables and integration of equation 11.17 the following expression can be written:

$$\int_0^{\alpha} \frac{d\alpha}{g(\alpha)} = \int_0^{t} k(T)dt \tag{11.18}$$

According to the iso-conversional methodology, the unknown integral on the right side is a constant for any given α. If several heating rates experiments are used, the same conversion α (and consequently the same integral on the right of 11.18) will be reached at different temperatures. The activation energy can be then estimated with a subsequent fitting procedure. If the heating rate is a constant, the temperature integral $I(E,T) = \int_{T_0}^{T} k(T_0 + mt)dt$ must be approximated and the same approximations shown in Section 11.3.2 can be used.

A better way of deriving the parameter E is based on the observation that if $g(\alpha)$ does not depend on the temperature program then the following equation holds:

$$g(\alpha) = \frac{A}{m_i} I(E_\alpha, T_i) \tag{11.19}$$

for each measurement point i. As a consequence (see [390] and reference herein) the expression:

$$\Phi(E_\alpha) = \sum_i \sum_{j \neq i} \frac{m_j I(E_\alpha, T_i)}{m_i I(E_\alpha, T_j)} \tag{11.20}$$

has a minimum equal to $\Phi_{min} = N(N-1)$, with N being the number of different heating rates.

It has been proved (see [391]) that the minimization of 11.20 is practically not affected by the uncertainties in the measurements, mainly in the range of small $x = \frac{E}{RT} < 30$. As explained in [390] this method has further advantages in comparison with the standard method based on fitting:

- In the standard method the lower boundary of the temperature integral is set to $T = 0$ instead of a finite T_0. The use of the function Φ solves the problem. This modification also allows the application of the iso-conversional methods on process occurring on cooling (like crystallization) rather than on heating.
- If the sample temperature is not equal to the measured furnace temperature, the temperature integral cannot be used. The function Φ allows the integral to be evaluated on time.
- The activation energy E is a mean value between conversion from $\alpha = 0$ to α. If non-constant activation energy describes the process, this procedure leads to unsealable values. The function Φ can instead be evaluated dividing the range of conversion in smaller intervals and assuming constant activation energy for each of them. This modification opens up the possibility to use a better algorithm for the evaluation of the integrals, increasing the accuracy and reducing the computing time (see for more details [390]).

The estimation of the pre-exponential factor A and the function $g(\alpha)$ can be achieved in two ways. The kinetic part can be rearranged into the function:

$$\ln\left(\frac{1}{g(\alpha)\frac{d\alpha}{dt}}\right) = \ln A(\alpha) - \frac{E(\alpha)}{RT} \tag{11.21}$$

showing the linear dependency between $\ln A(\alpha)$ and $E(\alpha)$ for a given α. The parameters of the

linear correlation can be derived by fitting data from a single heating rate experiment. Introducing the previously derived value of the activation energy $E(\alpha)$ into the linear relation 11.21 a value for the exponential function $A(\alpha)$ is found. An estimation of the function $g(\alpha)$ is achieved after numerical integration:

$$g(\alpha) = m\frac{d\alpha}{dt}\frac{A(\alpha)}{\exp\left(-\frac{E(\alpha)}{RT}\right)} \tag{11.22}$$

In applications of iso-conversional methods to the study of solid fuel conversion, two main assumptions must be taken into account:

1. The rate equation can be split into a part temperate dependent and a part conversion dependent. In other words, the method is based on the possibility to reach the same conversion α at a given temperature T regardless of the detail of the experiment (usually the temperature history).
2. Since the iso-conversional method is based on the repetition of experiments, the methodology applies to processes that are not altered by the parameters of the experiments.

In solid fuel conversion methods, both assumptions are not valid for pyrolysis and questionable for oxidation and gasification. For pyrolysis, it is well known that the heating rate influence strongly the outcome of the experiments in such a way that multiple parallel kinetics are invoked for better fitting.

11.3.4. The general case

If more complex models for devolatilization and char burnout are used, reaction rates cannot be easily estimated from the measured data, and the aforementioned methods cannot be applied. Several difficulties cause extensions of an easy model like the one expressed by the equation 11.1:

- The mathematical relation 11.1 is not accurate since other physical and chemical effects play a role. More complex models have been already presented and discussed in Chapter 6 and in Chapter 8.
- The assumption of constant temperature is never valid in the case of pyrolysis and must be verified in the case of char conversion. In both cases, exothermic and endothermic reactions change the temperature of the sample.
- The temperature of the sample is not directly measured, and it must be calculated using heat transfer calculations, introducing further differential equations that must be solved together with the conversion.
- Constant heating rate is an assumption that often is not valid, mainly when the experiments are performed near the limits of the device.
- Single chemistry in pyrolysis (and probably also in char conversion) is not a valid assumption. In a simplified mathematical expression, the assumption of a constant value of activation energy is implicit but many times not correct.
- Diffusion of reactants into the sample change the value of the reactant concentration. Consequently, the surface available for the reactions and the local temperature of the sample differs from the averaged values. Also, in this case, supplementary differential equations must be solved to obtain the unknown values.

More general relations for the description of particle conversion (including both pyrolysis and char conversion) can be written in the following mathematical form:

$$\frac{d\alpha}{dt} = F(T, [X], \alpha, p) \tag{11.23}$$

where now a general model is described by the function F, where the sample temperature T and the reactant concentration $[X]$ are dependent variables. The vector p is the vector of all parameters to be determined, namely the activation energy E, the pre-exponential factor A, the reaction order n and many others that the specific model requires. If the sample temperature and the concentration of reactant are unknown, equation 11.23 can be coupled with additional differential equations. For example in the case of dispersed particle temperature (needed in plug flow reactor experiments), the already written relation 10.13:

$$m_p c_p \frac{dT_p}{dt} = hA_p(T_\infty - T_p) + \epsilon_p A_p \sigma(\theta_R^4 - T_p^4) + f_h H_{reac} \frac{dm_p}{dt}$$

can be used. The particle conversion is then described by a system of ordinary differential equations of the form:

$$\begin{aligned} \frac{d\alpha}{dt} &= F(T, [X], \alpha, p) \\ \frac{dT}{dt} &= G(T, [X], \alpha, p) \\ \frac{d[X]}{dt} &= H(T, [X], \alpha, p) \end{aligned} \tag{11.24}$$

The parameters vector p must be then determined after fitting the curves representing the solutions of the system 11.24 to the experimental values for α. Since now in the equation for α unknowns parameters appear (local temperature and reactant concentration, for example), differential methods cannot be applied, and the system of ODE must be numerically solved.

A multivariate optimization method must be used to determine the reaction order and the kinetic parameters [175, 174, 22, 254]. For least-squares based optimization, the objective function is defined as:

$$f = \sum_{i,j} \left(B_{ij,c} - B_{ij,m}\right)^2 \tag{11.25}$$

where the index i and j refers to the i-th measurements into the j-th series. The fitting procedure is performed using a non-linear least squares problems as the Levenberg-Marquardt procedure [208, 234].

The method discussed is mathematically more expensive than a $\log$-diagram fitting but it posses several advantages:

1. Its application is not limited to purely Arrhenius rate, but can be applied to the most complex expressions like the Langmuir-Hinshelwood form of the reaction rate Section 3.1;

2. The method can be applied to non-isothermal conditions and non-constant heating rates;

3. The method can take into consideration a measured diameter distribution (several models have an intrinsic diameter dependency and a mono-dispersed distribution is practically impossible to be realized during a single experiment);

4. The method takes advantage of the possibility to fit different curves (representing different experimental conditions) using the same kinetic parameters, increasing the accuracy of the

parameters consequently.

As an example of what has been previously explained, the kinetic parameters for the South African Char from Kleinkopje will be presented. Kleinkopje colliery is an open-pit mine situated in South Africa, 8 km south of Witbank in Mpumalanga and forms part of the South African Coal Estates Complex. The Char has been produced at the IFRF (the International Flame Research Foundation) in the plug flow reactor and then characterized in the same device (see Section 11.4 for a similar device). The reaction order has been previously determined to be $n = 1$ (without showing here the results). The fitting for evaluation of the Activation energy E and of the pre-exponential function A will be presented hereafter.

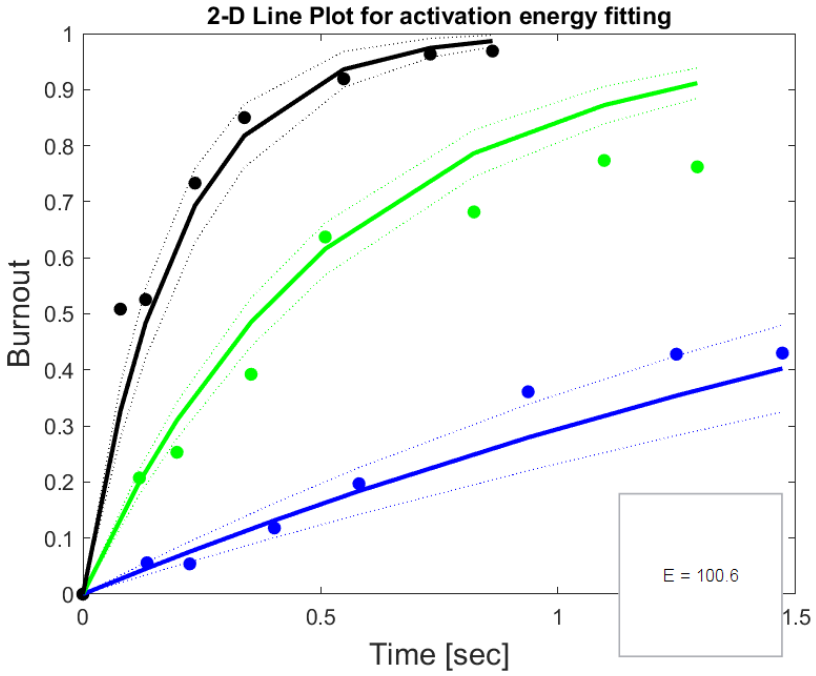

Figure 11.1.: Fitting of isothermal experiments for a South African coal for the determination of the activation energy E

In Figure 11.1 the results of the fitting of the burnout B at three different temperatures ($\vartheta_1 = 950\,°\mathrm{C}$, $\vartheta_2 = 1200\,°\mathrm{C}$, $\vartheta_3 = 1400\,°\mathrm{C}$) is presented. The open circles are the measured burnouts as a function of residence times. The solid lines represent the calculated burnouts for the optimal parameters together with the prediction at 1-σ confidence level. The simple kinetic model given by:

$$\frac{dB}{dt} = Ae^{-\frac{E}{RT}} \cdot p_{O2}$$

has been used, and the three curves have been fitted together. The obtained values are $E = 99\,\frac{\mathrm{MJ}}{\mathrm{kg}}$ (uncertainty $\Delta E = 3\,\frac{\mathrm{MJ}}{\mathrm{kg}}$) and $A = 5900\,\frac{\mathrm{kg\,bar}}{\mathrm{s}}$ (uncertainty $\Delta A = 1800\,\frac{\mathrm{kg\,bar}}{\mathrm{s}}$). It is interesting to mention that the fitting is not visually perfect, as also the value of the $\chi^2 = 0,98$ mathematically suggest. A second approach to the fitting procedure is to fit separately every single temperature with the reaction constant $k(T)$ as a parameter and then using a $\log$-diagram fitting to extract the parameters A and E. This algorithm produces the following vales for the parameters: $E = 90.2\,\frac{\mathrm{MJ}}{\mathrm{kg}}$ (uncertainty $\Delta E = 18.5\,\frac{\mathrm{MJ}}{\mathrm{kg}}$) and $A = 2800\,\frac{\mathrm{kg\,bar}}{\mathrm{s}}$ (uncertainty

$\Delta A = 4800\ \frac{\mathrm{kg\,bar}}{\mathrm{s}}$). Both results are consistent but the second procedure has larger uncertainties.

The multivariate optimization method highlights the fact that there is a range of combinations of parameters which can represent adequately the measurements (see also [22, 175]). Figure 11.2 reports the values of objective function in the (A, E) space, in which the two parameters are scaled around the optimum values A_{opt} and E_{opt} using exponential functions in the following way:

$$\begin{aligned} A &= A_{opt} \cdot e^{f_A} \\ E &= E_{opt} \cdot e^{f_E} \end{aligned}$$

With this rescaling the optimum values are in the point $(f_A = 0; f_E = 0)$. It is possible to note from Figure 11.2 that near the minimum point an elongated valley with steep walls is present. Along the valley, it is possible to find a family of points giving the value of the objective function not dissimilar than the optimum value. This characteristic makes difficult a visual assessment of the goodness of the fit since all pairs of E and A on the button of the valley produce small values of the objective function even if their values differ significantly.

11.3.5. Comments on the objective function

In the previous paragraph the objective function has been defined by the relation 11.25:

$$f = \sum_{i,j} \left(B_{ij,c} - B_{ij,m}\right)^2$$

The underlying meaning of this expression is that the weight of each single measurements point is the same. In reality, for many applications, a better prediction of the high burn out region is of importance and many times the best fitting of many conversion models is not able to predict the last 10% of the conversion curve correctly. The calculation of the burnout in pulverized solid fuel-fired boilers is a typical example (see the prediction in Chapter 14).

The other negative effect of the mathematical approach adopted in the previous paragraph can be seen when the model is not able to predict the measured conversion for each temperature correctly, as in the case of the test shown in Figure 11.1. The optimized parameters, when used to simulate the combustion of those conditions, predict values of the burnout that minimize the total discrepancy, but they do not predict correctly any of the burnout curves. In such conditions, it is preferable that the model correctly predicts the measured burnout at higher and at lower temperatures, while with more uncertainties for the intermediate temperatures.

A similar drawback appears in applications without significant temperature variations in the combustion region. Also, in this case, more importance can be given at the prediction of those models with temperatures near the operating temperature.

In both this circumstances the formula 11.25 is (often arbitrarily) written in the following form:

$$f = \sum_{i,j} W_{i,j} \left(B_{ij,c} - B_{ij,m}\right)^2 \tag{11.26}$$

where a weighting function $W_{i,j}$, for each point in each curve is introduced.

11.3.6. Sensitivity analysis

Since measurements are affected by errors and uncertainties, it is worth investigating how much those errors affect the fitted parameters. The burnout history of synthetic coal with effective

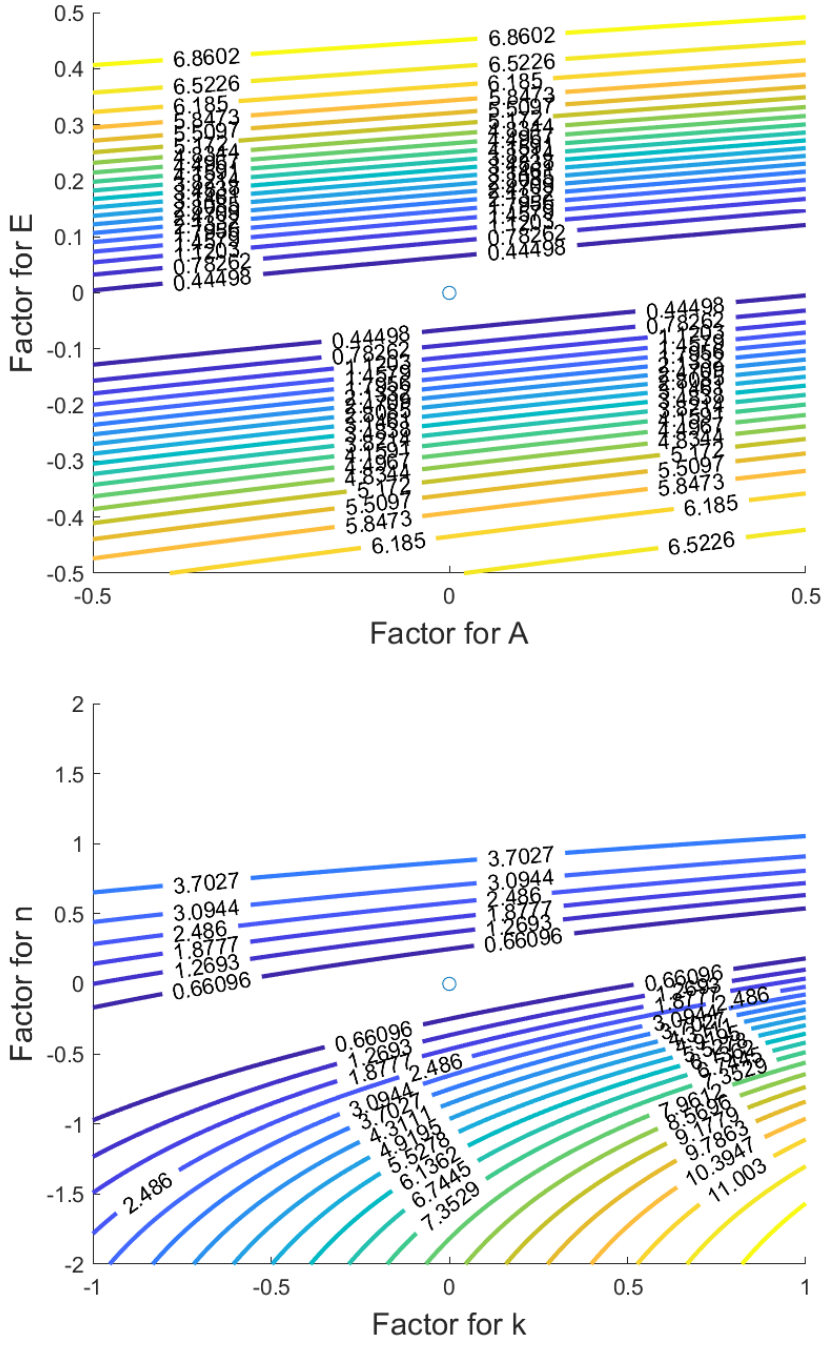

Figure 11.2.: Contour diagram of the apparent pre-exponential factor and apparent activation energy of a South African coal char with a fixed apparent reaction order of 1.0. The values indicated on the contours correspond to the values of the objective function. The minimum is marked with a filled circle

reaction rate given by the kinetic law (without pore or bulk diffusion limitation) is given by:

$$\frac{dm}{dt} = -Ae^{-\frac{E}{T}} p_{\mathrm{O}_2}^n \cdot m$$

and it is generated in simulated isothermal experiments. Only the uncertainties on temperature, burnout (reflecting uncertainties in the measured mass loss) and oxygen concentration will be analyzed.

Systematic errors Measurement errors can be divided into two components: random errors and systematic errors. Systematic errors are errors that are not determined by statistics but are introduced by an inaccuracy (involving either the observation or measurement process) inherent to the system.
In Figure 11.3 the errors (in %) associated with the fitting of the activation energy E, the pre-exponential factor A and the reaction order n are presented. The errors are generated by a systematic error ΔT in the determination of the temperature of the sample (the temperature is constant since the simulated experiments are isothermal) for two (real) activation temperatures, namely for $\frac{E_{real}}{R} = 8000\mathrm{K}$ (Top) and $\frac{E_{real}}{R} = 12000\mathrm{K}$ (Bottom). The following conclusion can be drowned by the results shown in the Figure:

1. Both the values of E and A are overestimated if the temperature is underestimated and the errors decrease with an increase of ΔT;
2. Underestimating the temperature ($\Delta T < 0$) produces larger error than an overestimation of the temperature T;
3. If the real activation energy E is higher, also the errors (in %) are larger;
4. The errors associated with the reaction order n are smaller than the ones associated with the activation energy E and they are larger for larger activation energies;
5. Underestimating the temperature ($\Delta T < 0$) produces smaller values of the reaction order.

In Figure 11.4 the error generated by an uncertainty Δp in the determination of the reactant partial pressure (here oxygen) are presented. The activation energy is not as much affected by the uncertainties as the reaction order is. If the partial pressure is underestimated then both the activation energy and the reaction order are overestimated. The dependency with the activation energy is also shown by the comparison between the results for the $\frac{E_{real}}{R} = 8000\mathrm{K}$ (Left in the figure) and $\frac{E_{real}}{R} = 12000\mathrm{K}$ (Right in the figure). The errors decrease with an increase of E, but the effect is not very pronounced.

The errors estimation presented here cannot be used as a general rule since the results are dependent on how the error is calculated. In the previous results, a constant error (for example ΔT in Figure 11.3) is assumed for all the experiments. If the systematic error is then calculated proportional to the measured value, then the following is observed.

1. A systematic proportional error on the temperature affects neither the reaction order nor the pre-exponential factor, but strongly deteriorate the uncertainties on the activation energy as shown in top part of Table 11.1.
2. An underestimation of the temperature causes a larger overestimation of the activation energy;
3. The relative error on the activation energy is not dependent on the value of the real activation energy.

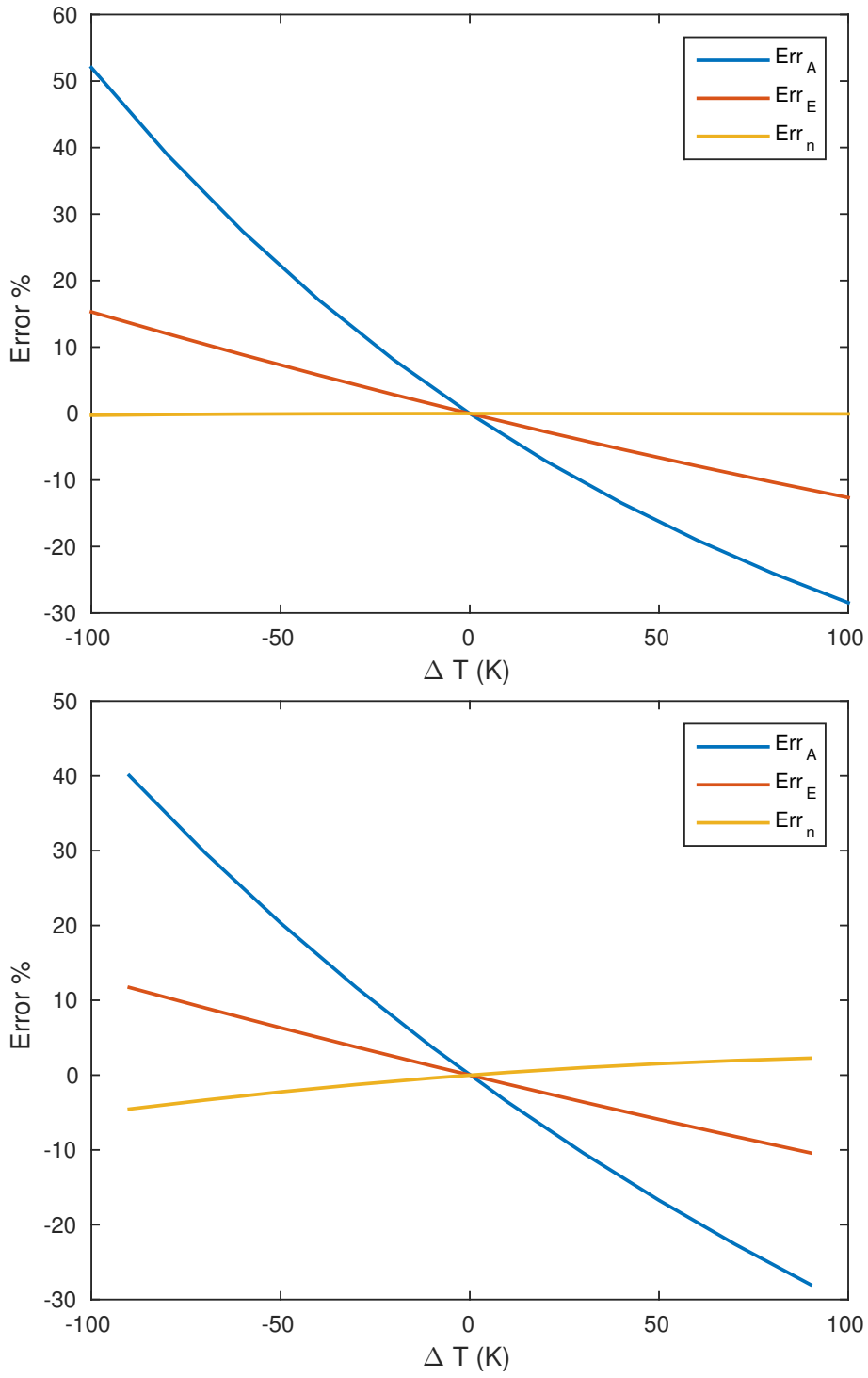

Figure 11.3.: Errors in % calculated as a function of the temperature uncertainty (in K) for $E_{real} = 8000\text{K}$ (Top) and $\frac{E_{real}}{R} = 12000\text{K}$ (Bottom)

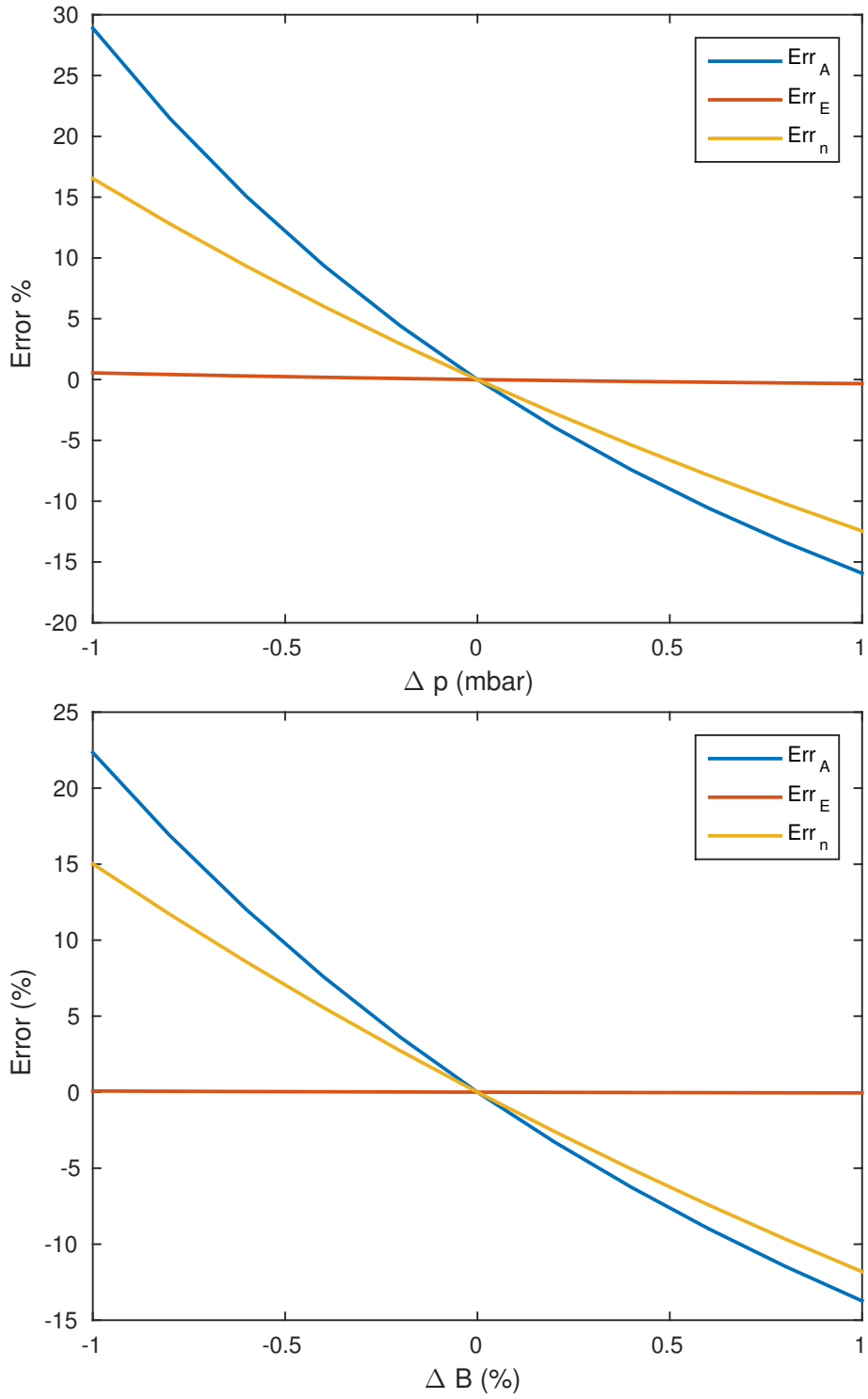

Figure 11.4.: Errors in % calculated as a function of the partial pressure uncertainty (in mbar) or $E_{real} = 8000\text{K}$ (Top) and $\frac{E_{real}}{R} = 12000\text{K}$ (Bottom)

4. A proportional error on the partial pressure affects only the pre-exponential factor but neither the activation energy nor the reaction order. The results are presented in the bottom part of Table 11.1.

Quantity	**Changes**	**Exact** $\cdot 10^{-3}$	**Results**	**Deviation**
ΔT	-10%	$\frac{E}{R} = 8$	ΔE	+11.11%
ΔT	-5%	$\frac{E}{R} = 8$	ΔE	+5.26%
ΔT	-2%	$\frac{E}{R} = 8$	ΔE	+2.04%
ΔT	+2%	$\frac{E}{R} = 8$	ΔE	-1.96%
ΔT	+5%	$\frac{E}{R} = 8$	ΔE	-4.76%
ΔT	+10%	$\frac{E}{R} = 8$	ΔE	-9.09%
ΔO_2	-10%	$A = 2$	ΔA	-8.08%
ΔO_2	-5%	$A = 2$	ΔA	-4.02%
ΔO_2	-2%	$A = 2$	ΔA	-1.60%
ΔO_2	+2%	$A = 2$	ΔA	+1.59%
ΔO_2	+5%	$A = 2$	ΔA	+3.98%
ΔO_2	+10%	$A = 2$	ΔA	+7.92%

Table 11.1.: Errors of the activation energy E and of the pre-exponential factor A as function of proportional systematic errors on the temperature T (Top) and on the partial pressure p (Bottom)

In Figure 11.5 the errors generated by a systematic proportional error ΔB in the determination of the Burnout are presented. As for the previously presented results, two (real) activation temperatures are taken into consideration, namely $\frac{E}{R} = 8000$K (Top) and $\frac{E}{R} = 12000$K (Bottom). In this case, both the errors of the activation energy and the ones of the reaction order are small and do not change much if the real activation energy is increased. An underestimation of the burnout produces smaller values for both, the activation energy E and the reaction order n.

Random errors Random errors are errors in measurements that lead to different values every time a quantity is measured and are described by random variables. A random variable x is distributed following a probability density function $P(x)$ from which the mean μ and the variance σ of the fluctuating variable x can be calculated. As a consequence of the existence of random fluctuations in an input variable x, the results of the operation $\mathcal{F}$ will be distributed following a probability density function G. Since the operator $\mathcal{F}$ is not generally a linear operator it is expected that $\mu(y = \mathcal{F}(x)) \neq \mathcal{F}(\mu(x)$.

As an example, only random errors on the measurement of the burnout curve are considered for the case in which the real activation temperature is $\frac{E_{real}}{R} = 8000$K and $n_{real} = 0.8$. The calculations are performed with errors calculated using a normal distribution of mean 0 and variance 5% of the real burnout:

$$B_i = B \cdot (1 + N(\mu = 0; \sigma = 0.05 \cdot B_i))$$

In Figure 11.6 the histograms distribution of the Activation energy and of the reaction order are fitted with a Normal distribution (in red). The statistical analysis of the fitting procedure gives

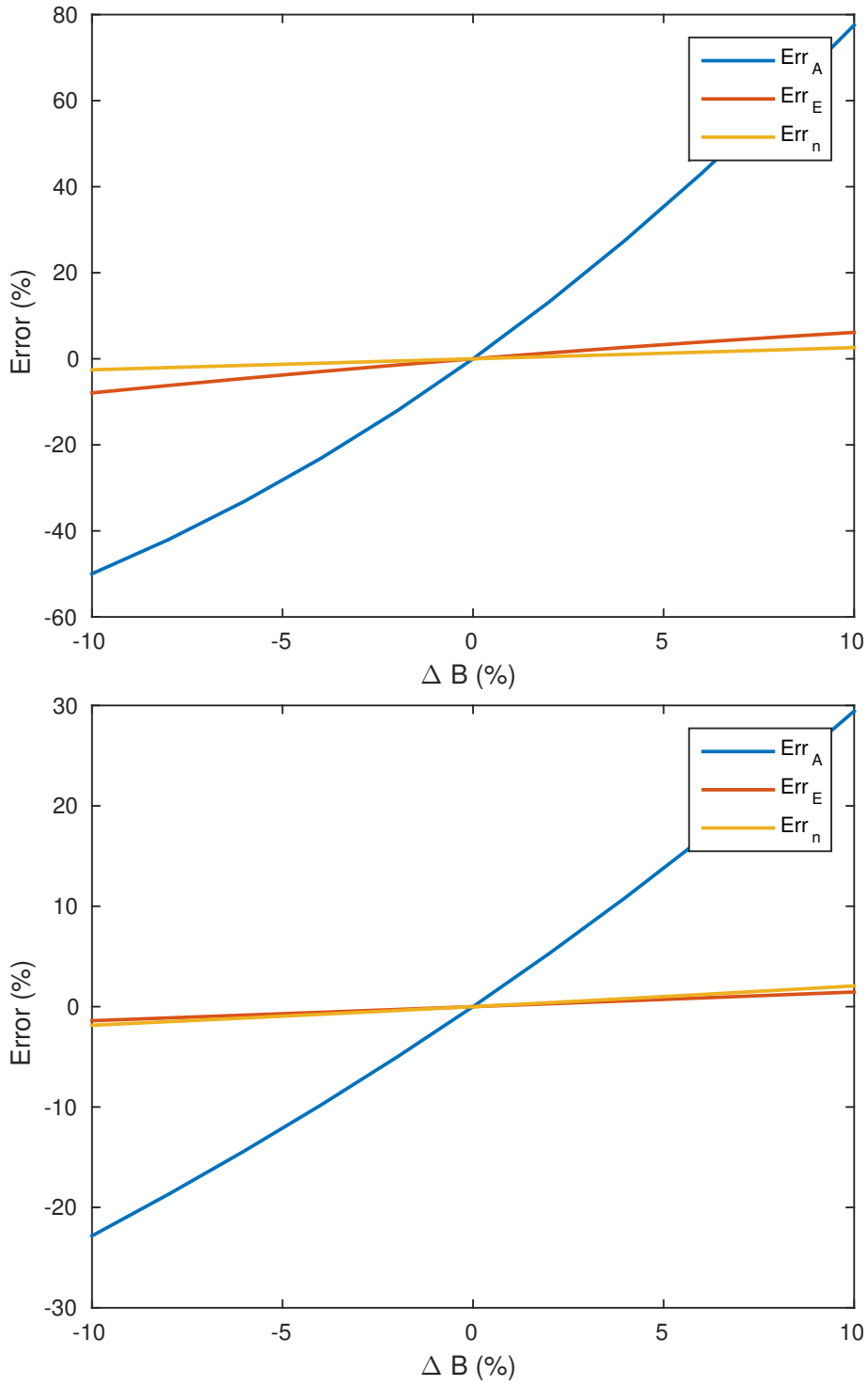

Figure 11.5.: Errors in % calculated as a function of the Burnout uncertainty (in %) for $E = 8000\text{K}$ (Top) and $\frac{E}{R} = 12000\text{K}$ (Bottom)

the following two averaged values:

$$\begin{aligned} \frac{E}{R} &= 7997 \pm 111\text{K} \\ n &= 0.80 \pm 0.02 \end{aligned}$$

Further analysis, which results are not presented here, have shown that:

1. If the real activation energy increases the distribution is wider. In the case of $\frac{E_{real}}{R} = 12000\text{K}$, a statistical analysis of the distribution of the results gives the following:

$$\begin{aligned} \frac{E}{R} &= 12006 \pm 203\text{K} \\ n &= 0.80 \pm 0.05 \end{aligned}$$

2. Statistical analysis of experiments with $E_{real} = 8000\text{K}$ and measurement scattering of 10%, gives the results:

$$\begin{aligned} \frac{E}{R} &= 8006 \pm 226\text{K} \\ n &= 0.80 \pm 0.04 \end{aligned}$$

showing a nearly linear relation between the uncertainty of the burnout and the uncertainty of the calculated parameters.

11.4. Fuel Characterization in IPFR

In this paragraph, the Isothermal Plug Flow Reactor (IPFR) method is analyzed in detail using the reactor of the Institute for Energy Process Engineering and Fuel Technology (IEVB, from the German name Institut für Energieverfahrenstechnik und Brennstofftechnik) at the Technical University of Clausthal, in Lower Saxony.

The IPFR allows investigating of devolatilization and char burnout phenomena, carried out as two separate experiments. The main advantage of this approach is a possibility of carrying out investigations with conditions close to industrial pulverized fuel (PF) fired boilers, namely high temperatures and high heating rates (around $10^5 \frac{\text{K}}{\text{s}}$). The IPFR is characterized by the flat profiles of the temperature and oxygen along the furnace length. This ensures that the fuel particles experience the same condition on the whole length of the reactor. The facility has generally been used for research purposes to obtain kinetic data of both devolatilization and char burnout processes.

11.4.1. Experimental setup

The experimental rig is divided into four main sections (as shown in the Figure 11.7):

- **The gas preheater**: allows the heat up of the gas mixture before entering the reactor, ensuring high heating rates.
- **The fuel feeding system**: consists of a screw feeder, which provides the fuel to an injector, where it is mixed with the transport gas. From the injector, the fuel-gas mixture is transported pneumatically to the feeding, water-cooled probe, which can be mounted in several openings along of the reactor.

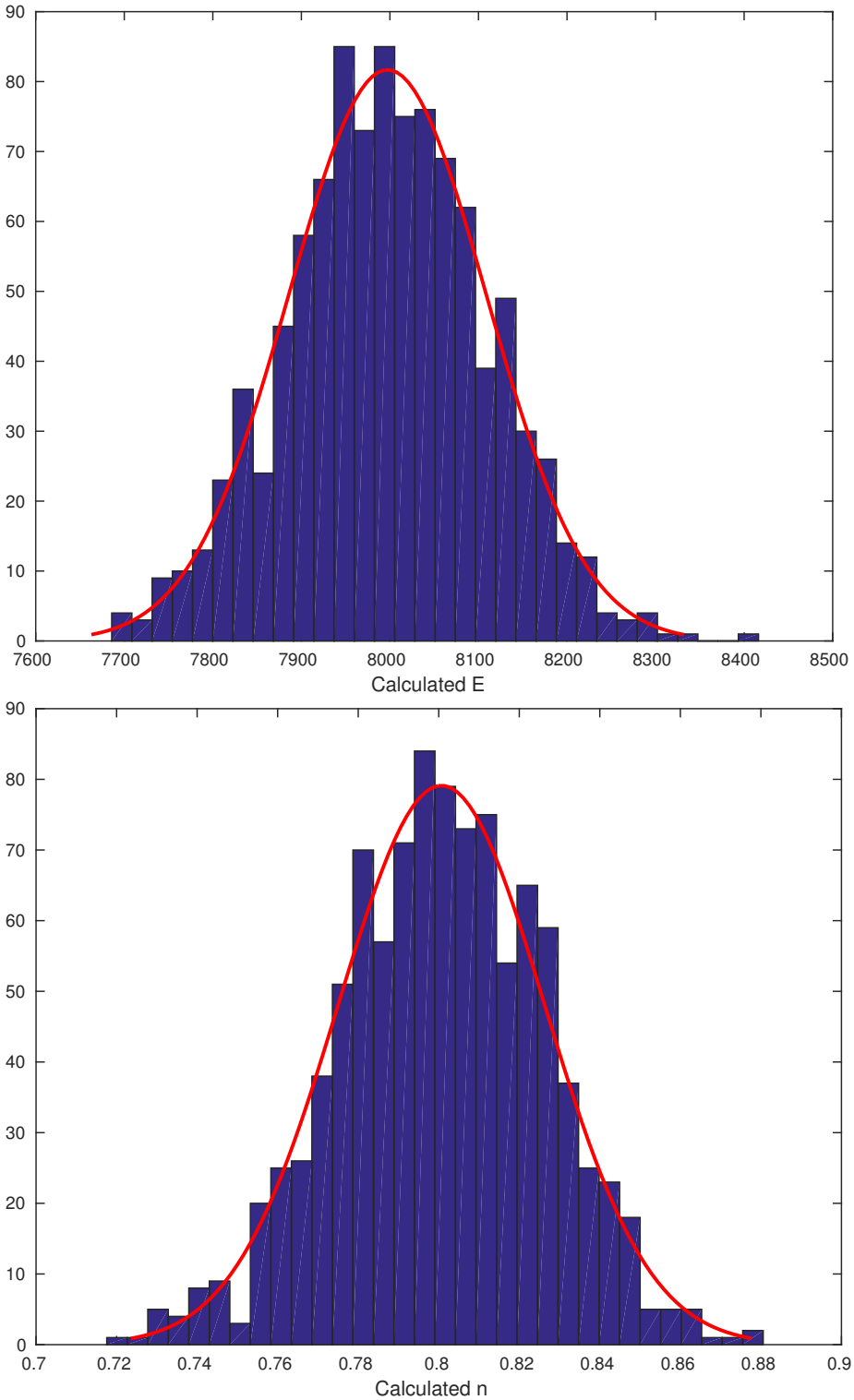

Figure 11.6.: Histograms for the distribution of the calculated activation energy E (Top) and the reaction order n (Bottom) fitted with a Normal distribution (red)

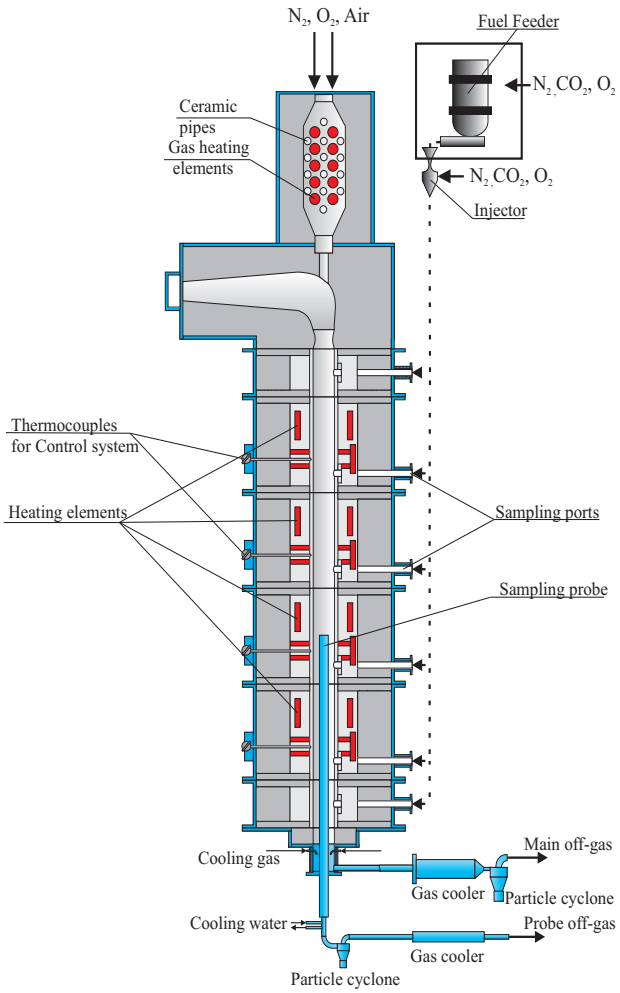

Figure 11.7.: Schematic view of IPFR facility

- **The combustion chamber**: is a vertical, cylindrical ceramic tube with 0.12 m diameter and total length of 3.1 m, which contains six modules.The main part of the reactor is 2 m long and contains four electrically heated elements–one for each segment, giving 20 kW of total heat power. The first and the last module are 0.25 m high, and both are not heated. All segments are thermally isolated and enclosed in a metal casing. The access to the ports is possible after every 0.25 m of reactor length.

- **The particle collecting system**: it is divided into two parts for the main off-gas, and off-gas sucked through the sampling probe.

During the experiments, the particle collecting system is used in two different configurations, for measurements of devolatilization or measurements of char burnout. In this second mode, the reactor can also work as a reactor for char production. For devolatilization experiments a movable, water and nitrogen cooled vertical sampling probe is used. The probe is installed at the bottom part of the reactor and moved along the furnace length allowing to achieve different residence time in a range from 20 to 250 ms. The gas flowing through the probe is passing

the cyclone to separate particles for further analysis. For the char burnout/production, only the mainline is used. In this case, the cyclone is installed close to the reactor outlet to maximize the sampling efficiency.

The outcome of the reactor is to provide partially converted particles at different distances from the particle injection system. Information about the process rate is extrapolated from the collected probe (see Chapter 12) and this information are mathematically analyzed to get the unknown model parameters. The fitting procedure requires the knowledge of the conversion as a function of time at several known conditions and these data must be extracted using a calculated mean velocity for the gas. Therefore the whole procedure is based on the following assumptions:

1. The velocity of the gas at the probe position is known;
2. The interaction of the particles with turbulence does not alter the time history previously determined;
3. The temperature of the particles is known;
4. The reactant concentration in the gas is known;
5. The presence of the injection probe and the collector device do not alter the quantities previously determined;
6. The reactions are quenched in such an effective way that the time previously calculated is a representative quantity for the conversion.

To answer all these questions, a detailed CFD simulation of the reactor together with the conversion process has been performed and the results are summarized in the Section 11.4.4.

11.4.2. A typical char combustion experiment

A typical experiment for characterization of a solid fuel consist of several standard steps:

1. Proximate and ultimate analysis;
2. Particle size distribution determination;
3. Devolatilization experiments;
4. Char generation;
5. Char characterization (oxidation or gasification).

An example of the procedure and some results are given below. Two fuels are chosen for investigation: the South African Middelburg coal and leaves of sugar beets, counted as a biomass fuel. The coal fired in our experiments is identical to the one used in [404]. The properties of both fuels are given in Table 11.2.

Particle Size distribution Both biomass and coal fuels have been investigated in pulverized form. The measured particle size distribution fitted with the Rosin-Rammler [2] and it's parameters

[2] The Rosin-Rammler distribution is given in its comulatiove form by the folloowing equation:

$$p = \exp\left(-\left(\frac{D_p}{\sigma}\right)^n\right)$$

where D_p is the particle diameter.

	Property	Unit	Coal	Biomass	Method
ultimate analysis	C	wt. %	66,2	40,4	DIN 51721
(as received)	H	wt. %	4,1	5,4	DIN 51721
	N	wt. %	1.7	1,4	DIN 51722
	S	wt. %	0,9	0,2	DIN 51724
	O	wt. %	11,1	38,9	by difference
proximate analysis	moisture	wt. %	6,1	8,5	DIN 51718
(as received)	Volatile	wt. %	30,4	71,2	DIN 51720
	ash	wt. %	10,0	5,3	DIN 51719
	Fixed Char	wt. %	53,5	15,1	by difference
calorific data	LCV	MJ/kg	25,3	14,1	DIN 51900

Table 11.2.: Proximate and ultimate analysis and calorific data of the fuels

(the mean particle size D_{mean} and spread parameter n) are shown in Figure 11.8. From the data, 80% of coal sample is smaller than 150 µm, which is typical for such coals. Biomass is characterized with coarser fraction, where only 60% is smaller than 150 µm.

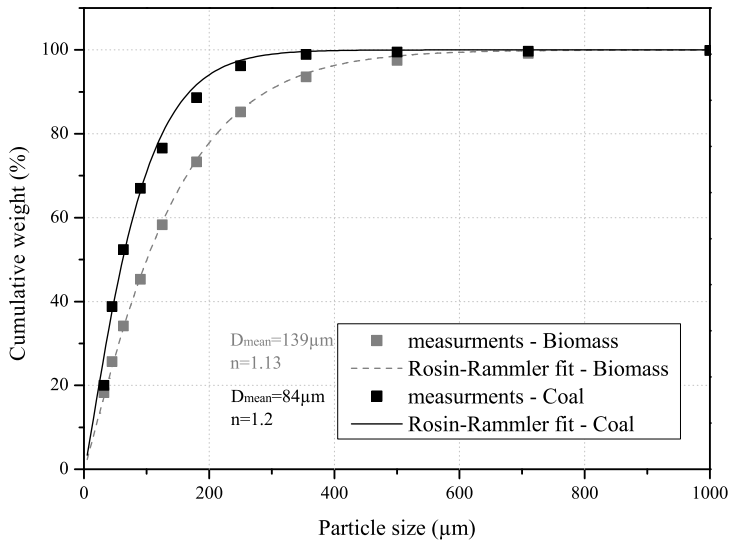

Figure 11.8.: Particle size distribution of biomass and coal fuel

Devolatilization The devolatilization experiments were conducted at two typical temperatures, 1000 °C and 1200 °C. Pure nitrogen was used as an inert purge gas to prevent sample oxidation and thus reducing the secondary reaction effects within the hot particles. The residence times between 10 and 250 ms were covered, with reactor chamber velocity of 3 $\frac{m}{s}$. Two ports, 7 and 8 for feeding probe were used and the residence time was regulated by changing the position of the sampling probe. The feeding rate of the sample was kept in a range of 100 $\frac{g}{h}$. The

samples obtained in the small cyclone at the end of the sampling probe were investigated for an ash content and the mass loss M has been calculated via ash tracking method, simply as:

$$M = 1 - \frac{a_0}{a} \tag{11.27}$$

where a_0 is the ash content of the initial coal and a the ash content of the sample, both in wt. % , so that the mass loss M has no dimension.

The plot of the mass loss against residence time is presented in Figure 11.9 in the case of the coal and in Figure 11.10 in the case of the biomass and the results of the fitting are presented in Table 11.3 for both fuels. The model used is the two competing kinetic rate model presented in Section 6.2.6.

Parameter	Symbol	Unit	**Coal**	**Biomass**
First rate				
Pre-exponential Factor	A_1	kg/(m^2 s)	200	260
Activation Energy	E_1	kJ/mol	7.8	3
Weighting factor	α_1	-	0.28	0.31
Second rate rate				
Pre-exponential Factor	A_2	kg/(m^2 s)	3×10^7	2.6×10^7
Activation Energy	E_2	kJ/mol	62	70
Weighting factor	α_2	-	0.98	0.97

Table 11.3.: Parameters for single kinetic rate model

For both temperatures, the volatiles are released in the first 60 – 70 ms. As expected, more volatile matter is released at higher temperatures. A higher devolatilization yield than the value measured by the proximate analysis is observed. For biomass fuel 95 % at 1200 °C and 88 % at 1000 °C is achieved, a value to be compared with 71,2 % from the proximate analysis. Also in the case of the coal a value of 37 % at 1200 °C must be compared with the value of 30.4% from the proximate analysis.

The results for the coal devolatilization show that volatiles are released at almost the same time as in the case of biomass devolatilization. This is specific to the coal used, and it cannot be generalized. In the case of a German sub-bituminous Hambach coal whose devolatilization experiments are presented in Figure 11.11, the time required for devolatilization is in the range 90 – 130 ms. It has to be noted that volatile yield at higher heating rates amounts to around 60 % (compared with 45.8 % from the standard analysis).

Char production Char was produced at 1200 °C in pure nitrogen atmosphere. Fuel was injected at the maximum possible mass flow rate of approximately 300 $\frac{\mathrm{g}}{\mathrm{h}}$ into the reactor in Port 6, with a reactor chamber velocity of 3 $\frac{\mathrm{m}}{\mathrm{s}}$. The produced char was collected in the large cyclone in the exhaust line (no sampling probe was used). After the production phase, the char samples were analyzed. Results of the proximate and ultimate analysis are summarized in Table 11.4. This data is used further to calculate the burnout rate and to determine the concentration of nitrogen oxides.

11.4.3. Char Burnout

The oxidation rate of the generated coal char is determined using the same IPFR reactor, operated with a carrier gas containing N_2/O_2 mixtures and the oxygen content taking values of 5%, 10%,

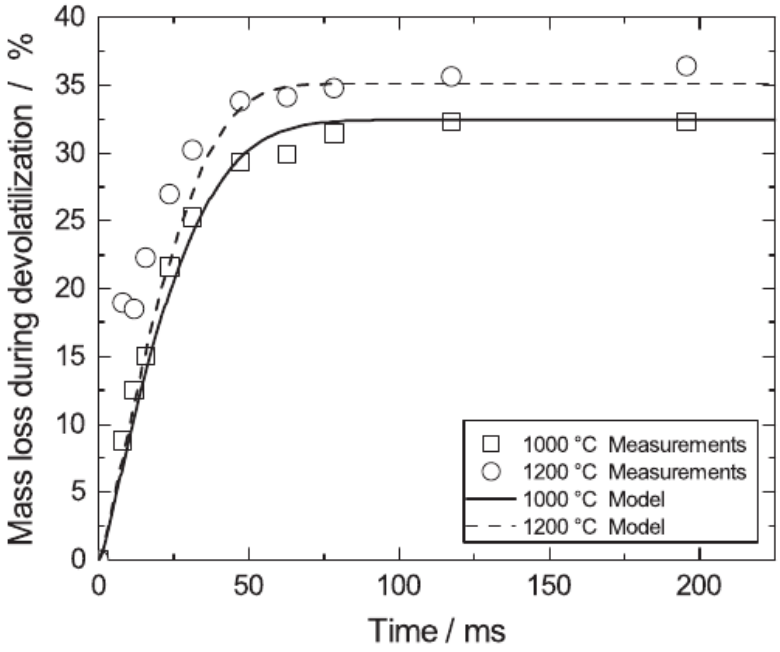

Figure 11.9.: Devolatilization of Middelburg coal at two temperatures, 1000 °C and 1200 °C

	Property	Unit	Coal	Biomass	Method
ultimate analysis	C	wt. %	86,67	-	DIN 51721
(as recevied)	H	wt. %	0,86	2	DIN 51721
	N	wt. %	0,6	0,95	DIN 51722
	S	wt. %	0,57	-	DIN 51724
	O	wt. %	1,89	-	by difference
proximate analysis	moisture	wt. %	0	0	DIN 51718
(as recevied)	Volatile	wt. %	4,07	7,73	DIN 51720
	ash	wt. %	9,16	54,17	DIN 51719
	Fixed Carbon	wt. %	86,77	38,1	by difference

Table 11.4.: Proximate and ultimate analysis of char

and 15% in volume. Three temperatures has been chosen, 900 °C, 1000 °C and 1200 °C. In the case of biomass, the bio-Char Burnout experiments were conducted with a gas temperature of 1000 °C and with an oxygen concentration (10 vol. %). The gas velocity has been chosen in such a way, that the highest possible residence times could be achieved, without overheating the gas preheater. The residence times were changed by changing the position of the feeding probe. Mass flow rates of the chars were chosen in such a way, that the oxygen concentrations at the outlet of the reactor deviated maximally within 10 % from the desired set point. The samples were collected with the same device used for the char production and investigated for the ash content. Char burnout was obtained through ash tracking method, comparing the ash content in

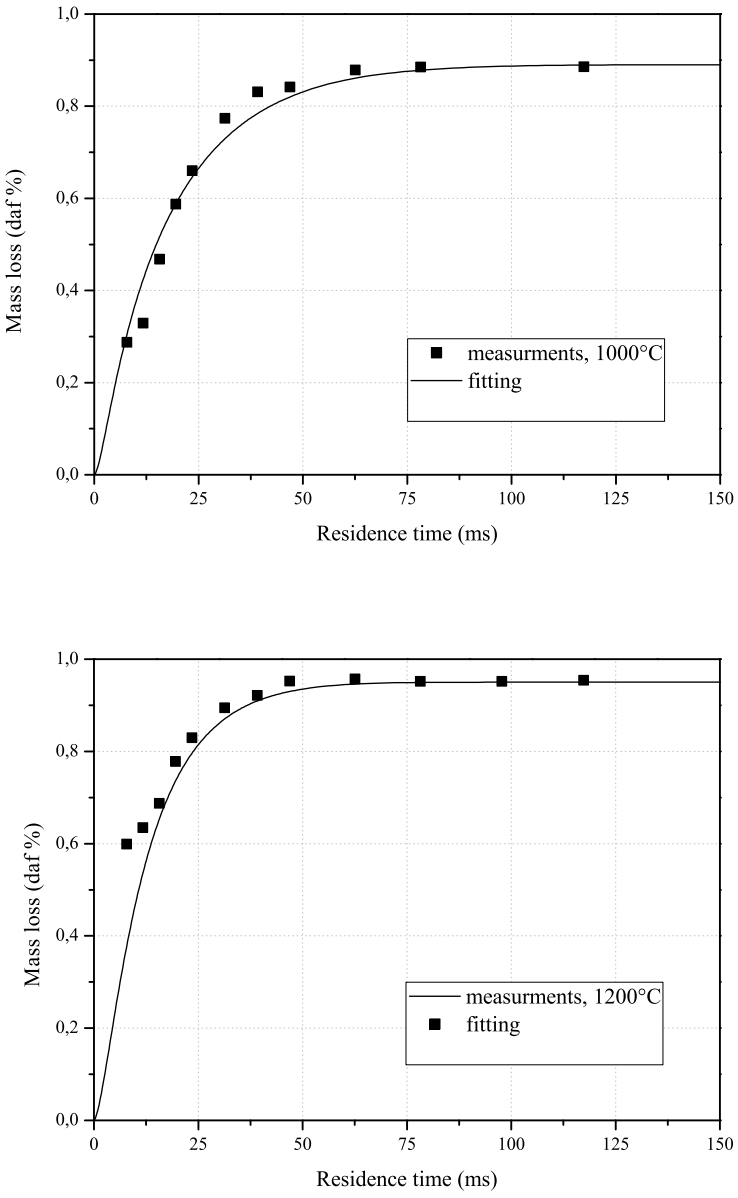

Figure 11.10.: Devolatilization of biomass at two temperatures, 1000 °C and 1200 °C

burned char with the original ash content in char:

$$B = \frac{1 - \frac{a_0}{a}}{1 - a_0} \tag{11.28}$$

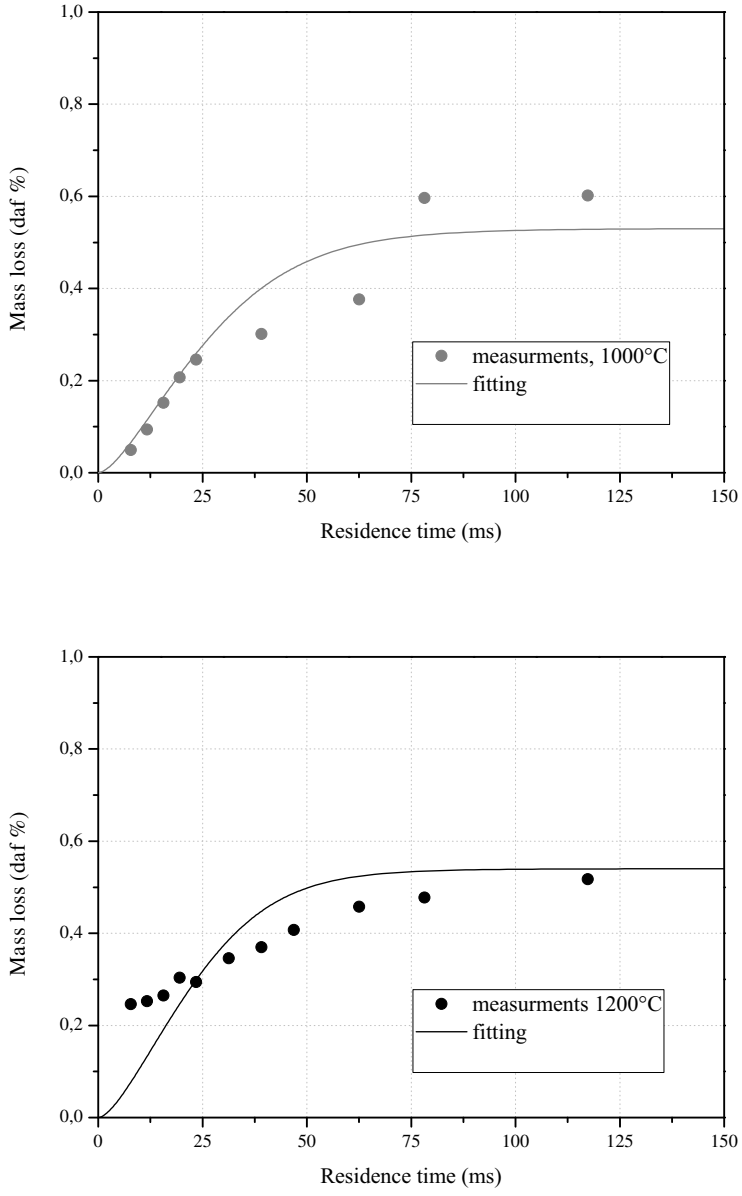

Figure 11.11.: Devolatilization of German sub-bituminous Hambach coal at two temperatures, 1000 °C and 1200 °C

where B is the burnout, a_0 ash content in the original char and A is the ash content of the sample, both in wt. % .

The results for the fitting of char burnout is shown in Figure 11.12 for the case of coal-char and in Figure 11.13 for the case of biochar. In both cases, the intrinsic model is used (see 8.5.1.1). The obtained parameters are shown in Table 11.5

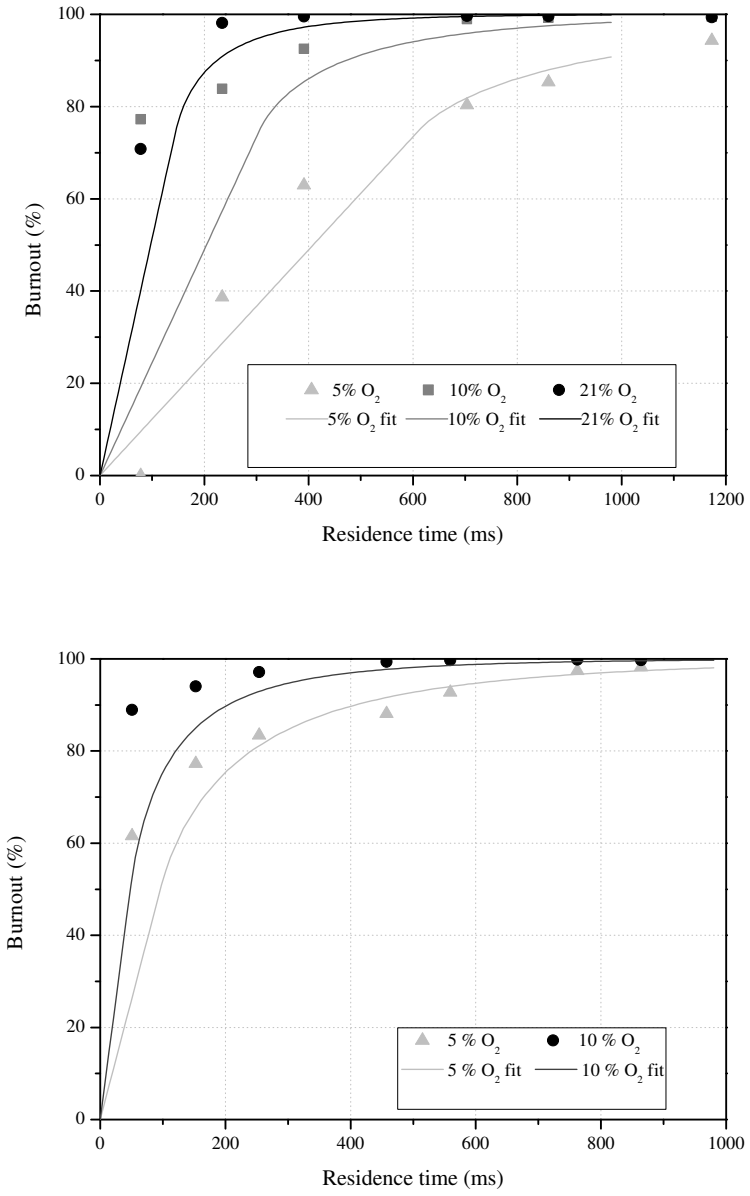

Figure 11.12.: Burnout of coal at 1000 °C and at 1200 °C and different concentration of oxygen

11.4.4. Analysis of the IPFR measurements

It has been already mentioned that the fitting procedure requires the knowledge of the conversion as a function of time at several known conditions. It is important to remark that the previously described procedure is based on the following assumptions, already listed in Section 11.4.1:

1. The velocity of the gas at the probe position is known;

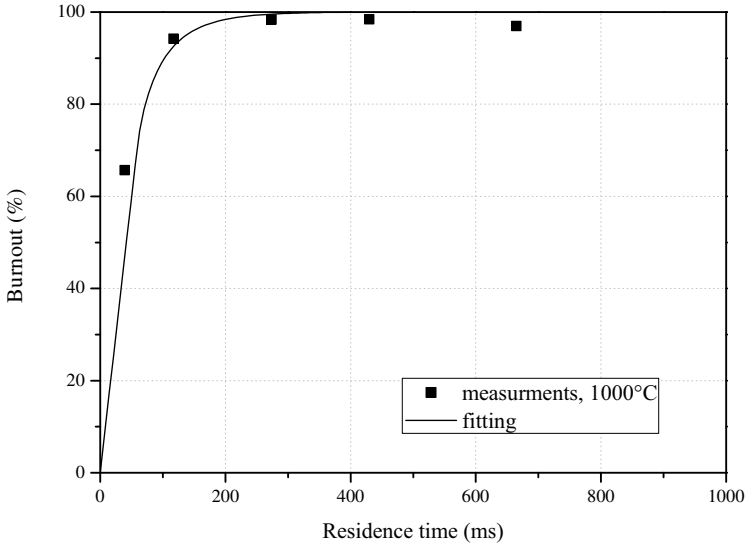

Figure 11.13.: Burnout of biomass at 10 % of oxygen concentration and 1000 °C

Table 11.5.: Parameters for intrinsic model

Parameter	Symbol	Unit	Case A	Case B
Mass Diffusion-Limited Rate Constant	C_1	$m^3/(K^{0.75}\ s)$	5.5×10^{-12}	10
Pre-exponential Factor	A_i	$kg/(m^2\ s)$	4	8
Activation Energy	E_i	J/kmol	1.55×10^8	1×10^{13}
Char Porosity	θ	-	0.5	0.5
Mean Pore Radius	r_p	m	6×10^{-7}	6×10^{-7}
Specific Internal Surface Area	A_g	m^2/kg	3×10^5	3×10^5
Tortuosity	τ	-	1.41	1.41
Burning Mode, alpha	–	–	0	0

2. The interaction of the particles with turbulence does not alter the time history previously determined;

3. The temperature of the particles is known;

4. The reactant concentration in the gas is known;

5. The presence of the injection probe and the collector device do not alter the quantities previously determined;

6. The reactions are quenched in such an effective way that the time previously calculated is a representative quantity for the conversion.

To check if these assumptions are correct, a series of detailed CFD simulations of the re-

actor (see Figure 11.14) together with the conversion process have been performed [3]. The CFD analysis has been performed to study both, the devolatilization experiments and the char reaction experiments. The following conclusions can be drawn:

1. The maximum gas velocity at the axis of the reactor is different from the averaged velocity. Since the fuel is injected on the axis of the reactor, a correction factor must be applied to the averaged velocity to obtain the correct particle residence time.

2. Turbulence produces a scattering in residence time of the order of 10%, depending on the distance between the injection probe and the particle collector. The utilization of the mean residence time appears to cause no deterioration of the prediction.

3. In the case of char conversion experiments, the temperature of the particles is practically identical to the gas temperature. Only for small particles, due to intense reactions, the gas and the particles temperatures significantly differ. Taking into consideration this discrepancy, the reliability of the predictions increases.

4. In the case of Char reaction experiments, the oxygen diffusion into the reacting particle stream is fast enough, that each particle sees the same oxygen concentration.

5. In the case of Devolatilization experiments, large differences have been found in the case of sampling at a low residence time. Both the temperature and the particle residence time show differences than the ones calculated using averaged quantities. The utilization of properly computed temperatures, lower than the ones assumed based on averaged calculations, are of importance for a better agreement between predictions and measurements.

6. At higher residence times the aforementioned effects don't play anymore an important role also in the case of devolatilization experiments.

7. A proper quenching system after the collector probe is important to stop the reactions at the wanted residence times. In the case of the quenching system installed at the IEVB corrections must be implemented only in the case of devolatilization.

11.5. Fuel Characterization in TGA

The application of the TGA method to coal combustion and gasification has been analyzed in [38] and some results published in [39]. In these studies, several aspects have been taken into consideration [4] with the goal to improve the reliability of the measurements:

The choice of crucible is important since mass transfer rates may be affected by it. In [38] a platter crucible made of Al_2O_3 since the platter crucible facilitates the access of gas, flowing from TGA bottom, to the sample surface.

[3] The chemical parameters are not exactly known during the CFD analysis therefore firstly some assumptions have to be made, and some preliminary kinetic parameters are derived. The CFD calculations will provide a proof of consistency and possible correction factors to adjust the fitting algorithm. This interaction between experiments and modeling is a practical example of the synergy between them: the experiments give data, parameters, and measurements for validation for the modeling and the mathematical modeling gives detailed information of the extracted data from the experiments. A well-validated model from well-performed experiments is a necessary and essential tool for applications to science and industrial processes.

[4] For more literature on the subject, the reader is referred to the literature cited in [38]

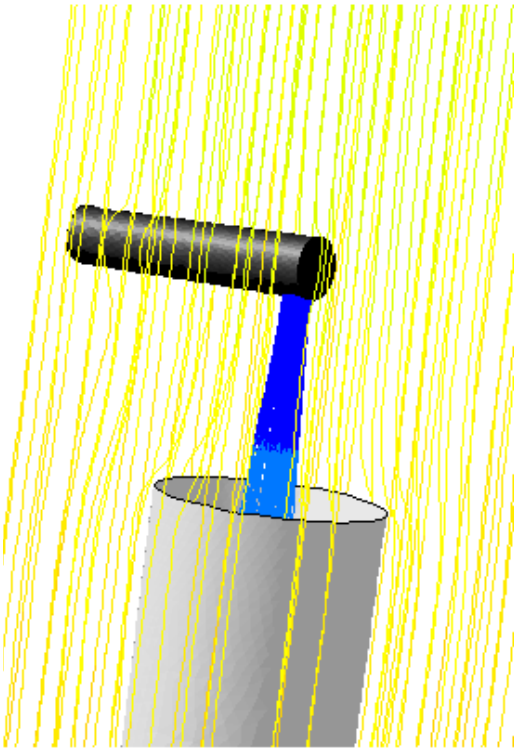

Figure 11.14.: Detail of sketch of the 3D geometry of the IPFR as used in the CFD calculation. The horizontal feeding system and the collector probe are shown together with the stream lines (yellow) and the solid fuels particles paths (blue)

The amount of fuel put into the crucible plays an important role due to two factors. Firstly the amount of fuel affects the diffusion of oxygen into the probe directly, and secondly, self-heating or self-cooling can be present if the sample is too large. In [38], the sample of a size of m=8 mg has been used and the particles have been uniformly distributed on the plate. This small amount has been chosen as a compromise between negative effects and accuracy of the device.

The particles size is important since pore resistance can affect the measurements if the particles are too large. Bigger particles offer resistance to the reactant diffusion as explained in Section 8.5 therefore, to facilitate rapid mass transfer rate, the char particles are sieved to the particles diameters $\leq 0.25\,\mathrm{mm}$. Additionally, small particles also help to maintain an equal temperature in the entire particle volume, which is crucial, when measurements are used for the determination of kinetic parameters.

The gas mixture volumetric flow rate The use of protective gas is mandatory (for the device used in [38] the requested value was $\dot{m} = 10\,\frac{\mathrm{mL}}{\mathrm{min}}$) therefore the flow of nitrogen must be higher than the required value. In addition O_2, CO_2 or steam must be considered, giving

a range in which optimum and stable value can be achieved [5].

The heating rate has to be correctly chosen. From the numerical analysis point of view the optimal heating rate must be chosen based on the conversion rate for the specific fuel. If the heating rate is too low, the conversion will practically be analyzed at low and almost constant temperature, decreasing the temperature range and consequently the accuracy for the activation energy. If the rate is too high, the conversion will occur only at the highest temperature, again reducing the temperature range and the accuracy of the activation energy. Of no lesser importance, the actual heating rate must remain constant during the whole experiment. At high heating rates and higher temperatures, the device can deviate from the ideal conditions (usually the heating rate lowers in those conditions) influencing and biasing the subsequent mathematical analysis.

The final temperature has to be properly chosen. The spanned temperatures during the experiments must represent well the temperatures of the processes. As previously discussed, if the final temperature is too low for both, devolatilization and conversion experiments, part of the information is lost, and the mathematical procedure is not able to recover the correct parameters. If on the contrary, the temperature is too high, the heating elements can have difficulty in maintaining a constant heating rate. From the chemical point of view, high temperatures are not required since diffusion processes (and not chemical reactions) will determine the measured mass loss.

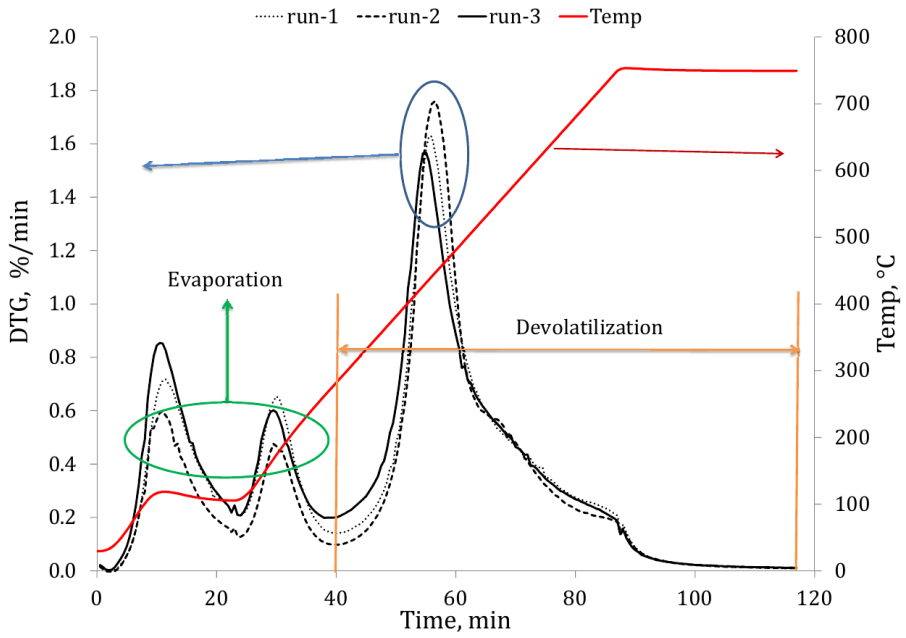

Figure 11.15.: Relative mass loss rate (black lines) and temperature (red line) of the sample during devolatilization in TGA; atmosphere - nitrogen [38]

TGA measurements for pyrolysis are intrinsically non-isothermal, but oxidation or gasification measurements can be carried out as isothermal or non-isothermal. As pointed out in [38], in non-isothermal experiments, firstly, the char is heated up to the required temperature in an inert

[5] In the case of the measurement done in [38] the gas flow rate has been chosen to be $\dot{m} = 80\ \frac{\text{mL}}{\text{min}}$

atmosphere. Only after reaching the required temperature, the reactive gas flow is initiated and the mass loss as a function of time can be recorded.

Nevertheless, non-isothermal experiments have the following advantages over isothermal ones:

- Non-isothermal experiments are quicker since temperature is allowed to reach a maximum, which implies that for each run the sample will react;
- Non-isothermal experiments require (theoretically) only one single run for the determination of the activation energy;
- Non-isothermal experiments allow the investigation of heating rates effects on the sample;
- Non-isothermal experiments allow the investigation of overlapping effects (for example pyrolysis and char reactions since it is known that a cooling of the char sample can change the reactivity of the char, as demonstrated in [166, 82, 38]);
- Non-isothermal analysis is overall cheaper since fewer experiments are required.

The main disadvantage of non-isothermal experiments has been already discussed in Section 11.3.2 and it is related to the difficulty to obtain an accurate and robust fitting. A second disadvantage appears considering the impossibility to isolate a single process (gasification, for example), since usually all thermal conversion processes overlap. In isothermal experiments, times can be freely adjusted (as previously discussed) but in non-isothermal experiments, times are dictated only by the heating rates. Even if the overlapping is small (in mass and rate) the fitted parameters are in both cases different. Therefore non-isothermal experiments must be fitted considering all the processes taking place inside the investigated temperature range.

In Figure 11.15 an example of the relative mass loss rate and the temperature rise (taken from [38]) are presented. The fuel examined is the Polish coal Janina, and a non-isothermal TGA is applied to investigate the pyrolysis. The temperature control of the device tries to keep a constant heating rate of $1\ \frac{^\circ\mathrm{C}}{\mathrm{K}}$. AT the beginning of the process the sample temperature has a plateau at 100 °C which is clearly due to the evaporation of the water present in the sample. For higher temperatures, the heating rate is constant until the maximum temperature is reached which for this measurement run has been set to 750 °C. Regions, where drying and pyrolysis are present, are clearly shown in the diagram. It is worth noticing that the water release is divided into two different processes, the evaporation of the water present at the surface (first peak at $T = 100\,^\circ\mathrm{C}$) and the water present inside the pores (second peak at higher temperatures). The devolatilization starts around $T = 250\,^\circ\mathrm{C}$ but an evident overlapping is shown by the data.

11.5.1. Analysis of the TGA Measurements

CFD analysis has been performed to clarify if the following uncertainties cause errors in the fitted parameters:

1. Diffusion of reactants into the sample;
2. Correct heating up of the sample;
3. Limitations due to particles dimensions.

An example of this kind of analysis can be found in [314] in which a TGA experiment of CO_2 gasification of Rhenish coal has been investigated. The Authors recognize that diffusion of CO_2 and the Stephan flow generated by the products of the homogeneous reactions are the

only responsible mechanisms for providing reactants into the crucible. In certain conditions a gradient of reactant concentration can be established, limiting the local availability of CO_2. With this knowledge, a model for species and heat transfer within the crucible has been developed and used in the fitting procedure. For the Boudouard reaction of char, the activation energy was calculated to be 126.9 $\frac{\text{kJ}}{\text{mol}}$ instead of the 118.4 $\frac{\text{kJ}}{\text{mol}}$ taken from the original fitting of the data. The discrepancy in the reaction order is more pronounced. The reaction order increases from 0.67 for the initial fitting to 0.74 for the fitting with adjusted reactant diffusion.

In other simulations (see [69]), the behavior of TGA experiments for the Janina coal (not char) gasification has been investigated with a CFD unsteady model. It has been found that the cooling due to the endothermic gasification reactions cause a change of local temperature of around −20 K for the higher heating rate. The temperature difference decreases if the heating rate decrease. When this difference is not taken into consideration, following the uncertainties analysis done in section Section 11.3.6, the activation energy is overestimated with an error about 20%.

11.6. Measurements of surface structure evolution

As already pointed out in Chapter 8, the description of the growth of the internal area is as important as the knowledge of the intrinsic kinetic rate. The evolution of A_g affects directly the changes in the conversion rate, and it is responsible for the reduction in conversion at the last 10-20% of the conversion history (see [138]). The following characteristics are important, and they must be well reproduced by every model of internal surface evolution:

1. The evolution of the internal surface is fuel dependent;
2. The initial value of A_g depends on the (previous) thermal history;
3. The evolution of the internal surface is temperature and conversion (burnout) dependent.

In Figure 11.16 the measured evolution of the internal surface (from [138]) together with its fitting by the random pore model (see Section 8.6.3) is presented. The measurements have been taken during oxidation in a PFR at three different temperatures, namely T =950 °C, 1200 °C and 1400 °C. It is important to notice that the evolution is different for each thermal conditions. At low temperature, an increase of the internal surface is observable, while for higher temperatures this increase is less pronounced and disappear at the highest temperature. For all of the temperatures at higher burnout the internal surface decrease steady towards lower values. The predicted evolution using the random pore model represents quite well the observed tendency.

Also in [38] the random pore model has been used. The model requires the knowledge of several char dependent quantities that have to be measured, namely the total specific intrusion volume $V_{pore,0}$ (in $\frac{\text{m}^3}{\text{g}}$), the total specific pore area $S_{m,0}$ (in $\frac{\text{m}^2}{\text{g}}$), the median pore diameter $d_{pore,av,0}$ (in nm), the apparent density $\rho_{app,0}$ (in $\frac{\text{kg}}{\text{m}^3}$), and the total porosity ϵ_0 (in $\text{m}^3{}_\text{g}/\text{m}^3$). In addition to those quantities the other quantities needed by the model can be calculated, namely the real density ρ_{true} (in $\frac{\text{kg}}{\text{m}^3}$), the average pore diameter calculated as $4\frac{V_{pore,0}}{S_{m,0}}$ (in $\frac{\text{m}^3}{\text{g}}$) volumetric pore length $L_{V,0}$ in ($\frac{\text{m}}{\text{m}^3}$), pore structural parameter ψ, initial volumetric internal surface area $S_{V,0}$ ($\frac{\text{m}^2}{\text{m}^3}$) and pore tortuosity τ.

In the previously cited work, two different chars have been generated from the Polish coal Janina. The first char (called TGA Char) has been generated in a TGA run of the original coal. The second char (called GTB Char) has been generated by heating up a 5 mm size coal particle. Both chars have been successively milled to similar diameter classes. The results of Mercury

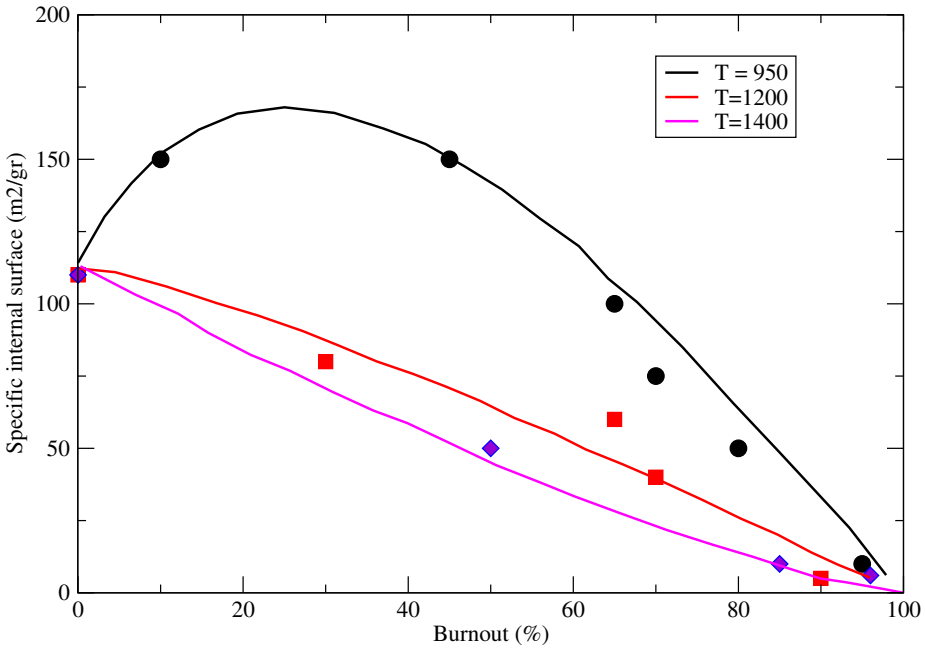

Figure 11.16.: Measured [138] and fitted evolution of the specific internal surface at three different temperatures

porosimetry measurements for the two chars are reported in Table 11.6 and they clearly reveal different char structures.

This kind of results shows that it is possible to significantly influence the char reactivity by changing the coal devolatilization rate, due to modification of the specific surface area and porosity. The first parameter is responsible for the surface available for the reactions, and the second one for the modeling of the gas diffusion inside a char particle.

Parameter	GTB Char	TGA Char
Parameters obtained directly from Mercury porosimetry software		
$V_{pore,0}$ (in $\frac{m^3}{g}$)	0.270	0.166
$S_{m,0}$ (in $\frac{m^2}{g}$)	26.8	15.8
$d_{pore,av,0}$ (in nm)	40.2	41.9
$\rho_{app,0}$ (in $\frac{kg}{m^3}$)	1163	1257
ϵ_0 (in $\frac{m^3}{m^3}$)	0.286	0.191
Parameters calculated from the previous quantities		
ρ_{true} (in $\frac{kg}{m^3}$)	1628	1554
$L_{V,0}$ in ($\frac{m}{m^3}$)	2.47×10^{14}	1.51×10^{14}
ψ	2.28	3.88
$S_{V,0}$ ($\frac{m^2}{m^3}$)	3.11×10^7	1.99×10^7
τ	1.20	1.19

Table 11.6.: Parameters obtained from Mercury porosimetry [38]

12. Validation

The kinetic data obtained using the methods presented in Chapter 11 are applied here to independent experiments, with the goal to show how accurate CFD modeling is in predicting combustion phenomena in real furnaces. In this work, the CFD method is validated using two experiments, a small scale experiment (20 kW) performed at the IEVB (see Section 12.1) and a semi-industrial scale experiment (2.5 MW) performed in Furnace number 1 of the IFRF (see Section 12.2).

The validation procedure requires the following steps to be performed:

1. Check that the calculated mass and the elemental balances are closed. The calculated final composition must be compared with the measurements available at the furnace outlet. Comparison with stoichiometry calculations or equilibrium calculations (at constant temperature and constant pressure) are usually useful. The balance should be as close as possible since elemental balance tells nothing about the conversion process (no CFD calculations are required for the prediction of the elemental composition of the flue gases). In modeling conversion of solid fuels three effects can lead to elemental imbalance, and they must be carefully analyzed:

   1.1. In-leakage of uncontrolled external air;

   1.2. Incomplete conversion of the solid, in which case the remnants must be added to the balance;

   1.3. Incorrect elemental composition of the solid, since the ultimate and proximate analysis are affected by uncertainties;

   In the case of temperature dependent yield of the devolatilization (a feature that any implemented advanced model should have as explained in section Section 6.2.9) a further problem can arise. The elemental composition of the volatiles plus the elemental composition of the char must be equal to the elemental composition of the fuel as received. Since the initial elemental composition of the fuel is unchanged, the other two compositions must be consequently both temperature dependent. A fixed composition of released gases and chars together with a temperature dependent devolatilization yield lead to inconsistent elemental balance.

2. Check that the calculated energy balance is closed. The energy balance (usually an enthalpy balance) is based on two different steps:

   2.1. Energy balance;

   2.2. Radiative energy balance.

   The energy balance can be performed indifferently using the total enthalpy or the physical enthalpy. Agreement with the measured furnace exit temperature must be as good as possible. Since the energy transferred to the charge, or loss through the walls, cannot be estimated with a high accuracy without the utilization of CFD calculations (see Section 4.9), the exit temperature cannot be estimated correctly before performing the calculation. Therefore, no perfect agreement can be expected. The comparison between the calculated exit temperature and the measured one is a direct indication that the calculation can be further verified using detailed in-flame measurements. The correct balance of

the RTE (radiative energy emitted or absorbed by the gas must be equal to the net radiative energy transferred through the walls) is a further indication of the correctness of the calculations.

3. Comparison of the flow field. Velocities (mean velocity and its fluctuations if available) must be compared with the measured values. Flow pattern must be considered and analyzed. The correctness of the momentum balance is more difficult to be checked since more terms must be evaluated. A lot of experience is required to determine if the flow pattern is correct (reasonable) or not. The correctness of the solution of the Navier-Stoked equations can be validated using in-furnace measurement only.

4. The temperature field must be analyzed. The calculated temperatures must be compared with the in-furnace measured temperatures. As in the case of velocity, experience is also in this case required. Global energy balance is needed for judging the correctness of the calculation but it is not a sufficient requirement since different flame shapes can end-up in similar exit temperatures (and closed energy balance). Comparison with local (in each cell) equilibrium calculations at constant enthalpy and constant pressure can be useful. Equilibrium calculations do not allow a direct method for validations, but they are essential as a reference.

5. The species fields must be analyzed, starting from the fuel and oxygen, followed by the CO, the other products and finally (if available) several radicals (the radical OH is usually measured to give a hint about position and structure of the flame). Reactions are temperature dependent. Therefore, a connection between components and temperature must be recognizable.

6. Solid fuel conversion and solid particle tracking must be finally analyzed.

From the theoretical point of view, a sophisticated and traversal method like computational fluid dynamics must be firstly evaluated in each single components. To validate a single component, specific care and measurements must be adopted to reduce the number of parameters that can have an influence in the process under investigation that cannot be directly controlled. The calculation of the radiative heat transfer can be used as an example (see also Appendix C for some results). Since temperature and components distribution play an important role in the determination of the radiative intensity, the validation of modeling assumption using data of a real industrial furnace is difficult since an eventual inaccuracy of the radiative fluxes can be caused by inaccuracy of the combustion module altering the temperature or the components distribution. In this context, validation of a specific sub-model should be better performed using a synthetic flame when a better mathematical model is available (see for example Chapter 3 in [385]).

In this work, we implicitly assume that each module or sub-model has been already separately and successfully validated. The amount and the quality of the results presented the literature is so extensive that no strong doubts can arise about the prediction capabilities of every single sub-model. There is indeed room for improvements, but our goal here is to show the ability of CFD to be able to predict industrial processes. An example of this kind of validation applied to the calculation of the absorption coefficient for the gas is presented in Appendix C. Without entering into the details (see also [385] and [229]), the main conclusion of the Appendix is that, even if the Weighted Sum of Grey Gas (WSGG) model can be improved, a more accurate radiative property model does not improve neither the temperature nor the radiation intensity field since a small rearrangement of the wall temperature masks the improvements of the better model. In this case, the sub-model for the absorption coefficient cannot be validated using real in-flame data, and the comparison with the measurements shows that (in the calculated condition) the model of the absorption coefficient is *good enough*.

A more subtle subject to be discussed is the validation of the CFD calculations with small laboratory flames like the ones from [1] for validation of industrial-scale flames. In those lab-scale experiments, the inputs are entirely controlled, and not intrusive measurements are performed. Moreover, the flames are near the unstable point in such a way that chemistry and mixing become a decisive factor for the prediction of the flame. The problem with lab-scale experiments is that the results are difficult to be scaled up to industrial scales for several reasons.

It has been observed (see [398] for more details) that disparity between the in-flame temperatures measured in lab-scale and in large-scale flames can be as large as 100-200 K due to different measurement techniques used. In lab-scale experiments, one observes a strong interaction between turbulence and chemistry and the measured data is sensitive to small alterations to burner inputs and boundary conditions. The sensitivity disappears at large-scales since the convective mixing is the dominant (the slowest) mechanism. In other words, different effects are seen at small- and large-scales and different mechanisms are controlling.

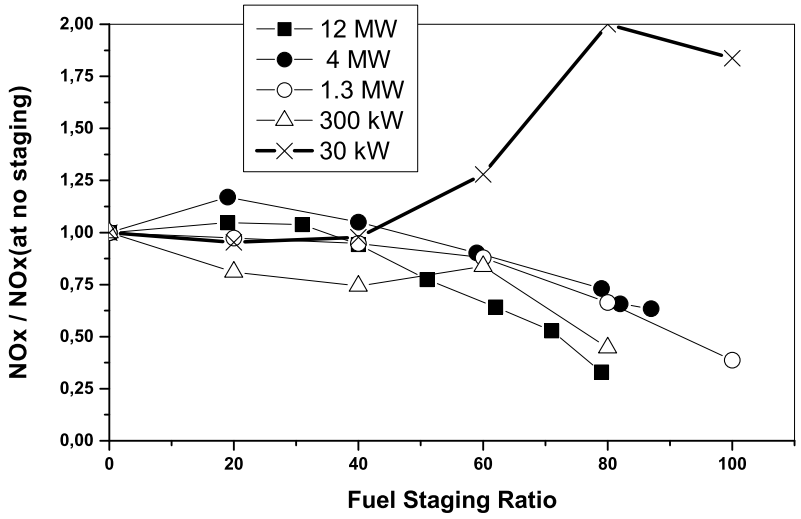

Figure 12.1.: The Scaling 400 data concerning performance of the burner at fuel staging (low NO_x) conditions. [398]

The Scaling-400 natural gas burner [398] is used here to show an unexpected change to the flames issued from the burner during the scaling trials. The burner had the possibility to operate at different thermal inputs, namely 30 kW 300 kW, 1.3 MW, 4 MW and 12 MW. The burners could be operated in standard (high-NO_x) mode where all the fuel (natural gas) was injected through the central fuel injector located at the centerline while, by injecting the fuel via eight staged fuel pipes, the NO_x emissions could be lowered reaching the lowest values at 80% or 100% staging (0% staging corresponded to the situation when all the fuel was injected via the central injector while 100% staging means that all the fuel was injected by the eight injectors equidistantly spaced on the circumference).

Figure 12.1 shows the NO_x emissions dependence on fuel-staging at different thermal inputs indicating that the dependency was reproduced at all considered burner scales but the smallest (30 kW) burner size. Although attempts have been made to explain this unexpected behavior

observed in the 30 kW experiments, it is perhaps fair to say that the reasons for the departure remain unknown.

Indeed, a universal model possessing perfect physics should work at all scales. We don't have this model yet. And since the scaling challenge is not part of this work, validation using lab-scale experiments is not further discussed.

12.1. Small scale experiments

The Down Fired Combustion Chamber (DFCC) facility at the IEVB has been used as a first step for the validation of the CFD modeling approach. The DFCC is a vertical furnace of 20 kW thermal input. Solid fuel is introduced from the top through a burner. The reactor is divided into three main parts (see Figure 12.2):

- **burner** installed axis-symmetrically and characterized by a stable performance in a broad range of conditions and very well determined outflows aerodynamic. Two burner configurations are used, different for biomass and for coal fuel as shown in Figure 12.2.

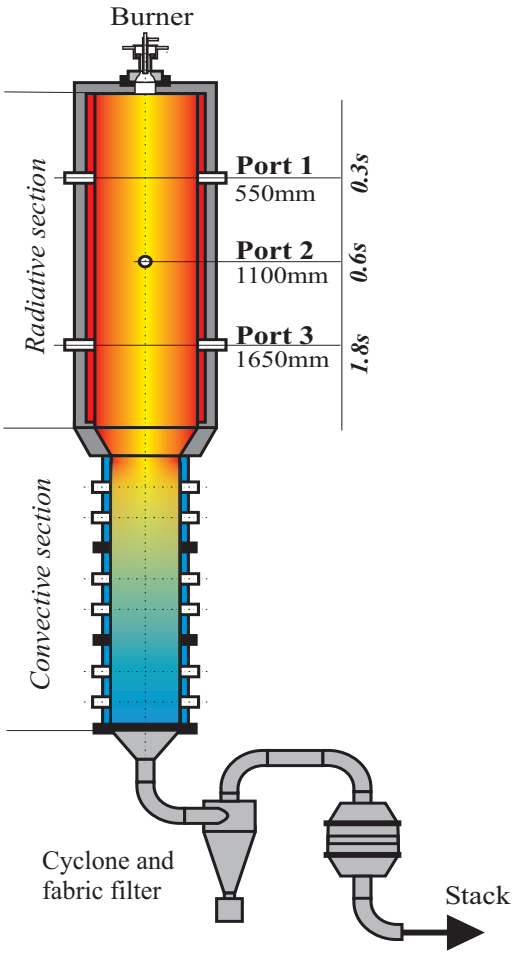

Figure 12.2.: Schematic view of DFCC facility

- **radiative section** electrically heated 2.2 m long ceramic tube with inner diameter of 0.3 m ensures high temperatures and minimize heat loses from flame region.This section includes three ports for temperature and gas composition measurement and for sampling probes for burnout determination.
- **convective section** The convective section is 1.8 m long and is made out of 0.2 m diameter steel pipe. In this section the flue gases are cooled down to around 200 °C to protect the down stream equipment. Downstream of the convective section the particle collecting system is situated and consists of a cyclone and a fabric filter for the capture of fine particles.

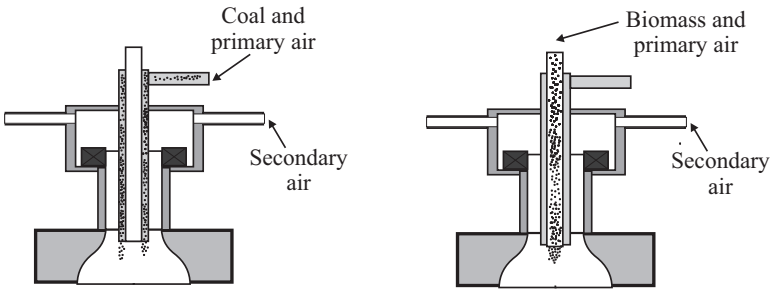

Figure 12.3.: Burner configurations for coal (left) and biomass (right)

Boundary	Property	Unit	Coal	Biomass
primary air	$\dot{m}$	kg/h	11.16	6.41
	v	m/s	5	6
	T	°C	25	25
	ε	–	0.9	0.9
	d_h	m	0.016	0.008
	turbulent int.	%	20	20
	w_{O_2}	wt. %	0.23	0.23
secondary air	$\dot{m}$	kg/h	10.44	40.97
	T	°C	250	25
	ε	–	0.9	0.9
	d_h	m	0.36	0.36
	turbulent int.	%	20	20
	w_{O_2}	wt. %	0.23	0.23
fuel inlet	$\dot{m}$	kg/h	2.37	3.81
	v	m/s	30	30
	T	°C	25	25
	ε	–	0.9	0.9
wall	T	°C	1200	950
	ε	–	0.9	0.9

Table 12.1.: Boundary conditions for the experiment at DFCC

Three openings, which are marked in Figure 12.2 as ports 1, 2 and 3, are used for the measurements. At each port, the temperature is measured using a suction pyrometer. The flue

gas composition (for NO, SO_2, CO_2, CO, O_2) is measured using a gas sampling probe and a set of gas analyzers. Another, specially designed, sampling probe allows for the measurements of carbon burnout.

Two different measurement sets will be compared with CFD calculations. Solid fuel has been used in both experiments. In the first run, Rhine coal at stoichiometry $\lambda = 1.2$ has been used, while in the second experiment Biomass at stoichiometry $\lambda = 2.5$ has been used. Both fuels have previously been fully characterized using the IEVB drop tube furnace (see Section 11.4). Neither air nor fuel is preheated during biomass combustion, while the secondary air for coal combustion is preheated to 250 °C. The inputs used in both experiments and the boundary conditions for the modeling are reported in Table 12.1.

12.1.1. Results for coal combustion

12.1.1.1. Flow pattern

In Figure 12.4 stream functions [1] (up) and the contour plot of the gas velocity in m/s (down) and along the chamber are presented.

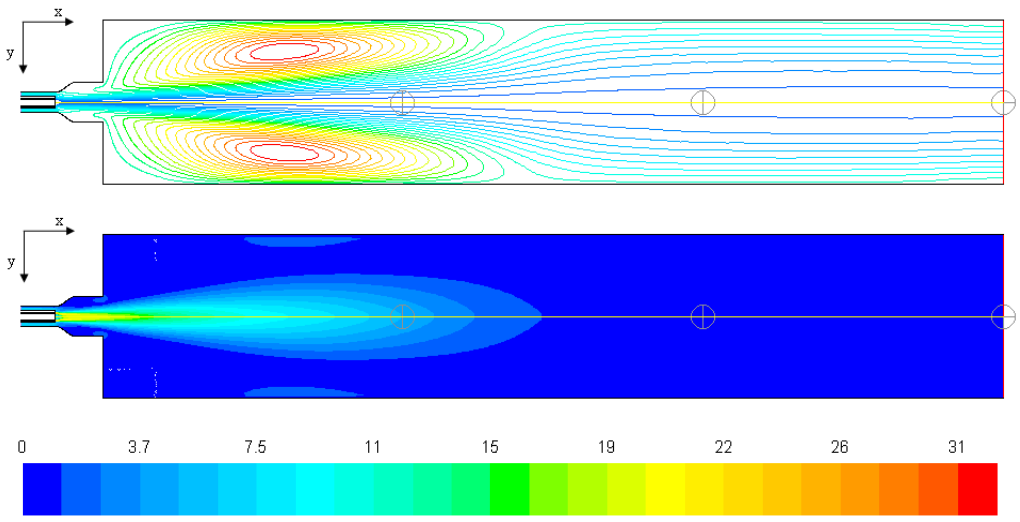

Figure 12.4.: Contours of stream function (up) and velocity (down) - Coal combustion

Since velocity vectors are tangent to a streamline, a streamline plot shows the trajectory of fluid particle inside the reactor. As it can be observed from the Figure, the high-velocity fuel jet merges quickly the combustion (secondary) air and a recirculation zone is formed by the momentum of both merged jets.

The amount of gas recirculated is an essential parameter in furnace design since the stability of a flame, the dilution of the jet, the maximal temperature inside the flame or the amount of

[1] In 2 dimension the stream function at a point P can be defined [25] as the the mass flux through the curve connecting the point P with a reference point A. The point A is a reference point defining where the stream function is zero: a shift of A results in adding a constant to the stream function. Since streamlines are tangent to the flow velocity vector of the flow, the value of the stream function is constant along a streamline. Following those properties, the streamlines are used for:

1. a quick visual representation of the flow and its structures;
2. the representation of the mass distribution and eventual mass recirculation.

thermal NO_x are examples of important quantities directly affected by the amount of gas recirculated. Its value can be obtained after integration of the mass flux j over an appropriate surface. In the case of the flame discussed in this section the amount of gas recirculated is 3.4 times the amount of gas injected with the burner (transport air plus comburent air).

Since jets are typical configurations for solid fuels burner, the features shown present in the DFCC can be found in many applications. The entrainment of a free jet allows a better mixing between fuel and air streams and its features (length, turbulent intensity, temperature) are of fundamental importance in flame stabilization, fuel ignition, and furnace optimization (see es an example the MILD combustion with its application to boilers in Chapter 14 and in Chapter 15).

12.1.1.2. Temperature Field

The calculated temperature field along the combustion chamber is presented in Figure 12.5. As it can be observed, the pulverized coal ignites in the close vicinity of the burner, and most of the combustion is completed by the first measurement port, which is located 0.55 m away from the burner. The highest temperatures of the flame have been reached before port-1 and the peak value of around 1500 °C has been calculated. Downstream port-1 the temperatures gradually decrease along the reactor until around 1200 °C, representing the temperature of the heated lateral walls.

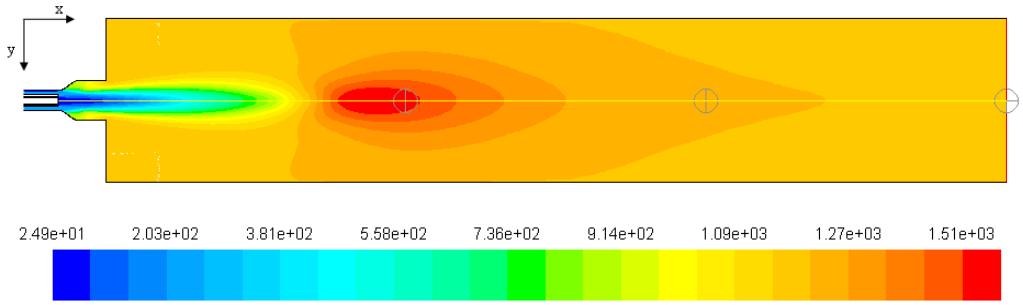

Figure 12.5.: Contours of temperature field in °C- Coal combustion

In Figure 12.6 the calculated temperatures along the reactor axis are plotted against the measured values. No significant difference between the model predictions and measurements can be observed, except for the region near the port-1, where the calculated temperatures overpredict the measured ones about 130 °C (for a similar difference see the predictions in [31] obtained in the same reactor but with different coal). The model well predicts the temperature values in port-2 and port-3, and the difference between measured and simulated data is in the range 15 to 25 °C.

12.1.1.3. Profile of species concentration

Oxygen and carbon dioxide concentration In Figure 12.7 and Figure 12.8 the calculated O_2 and CO_2 concentration profiles are presented. The O_2 concentration at the inlet has the highest value, while the oxidation reactions are not yet started. O_2 decrease gradually and conversion of volatiles and char to CO_2 take place.

The comparison between the measured concentrations and the calculated ones are presented in Figure 12.9 The computed concentrations are in good agreement with the experimental values. However, both, O_2 and CO_2 concentrations, are slightly higher than measured values in the last two ports. From experiments, values in range 3.8 to 3 % for O_2 and 15.4 to 16 % for CO_2 are

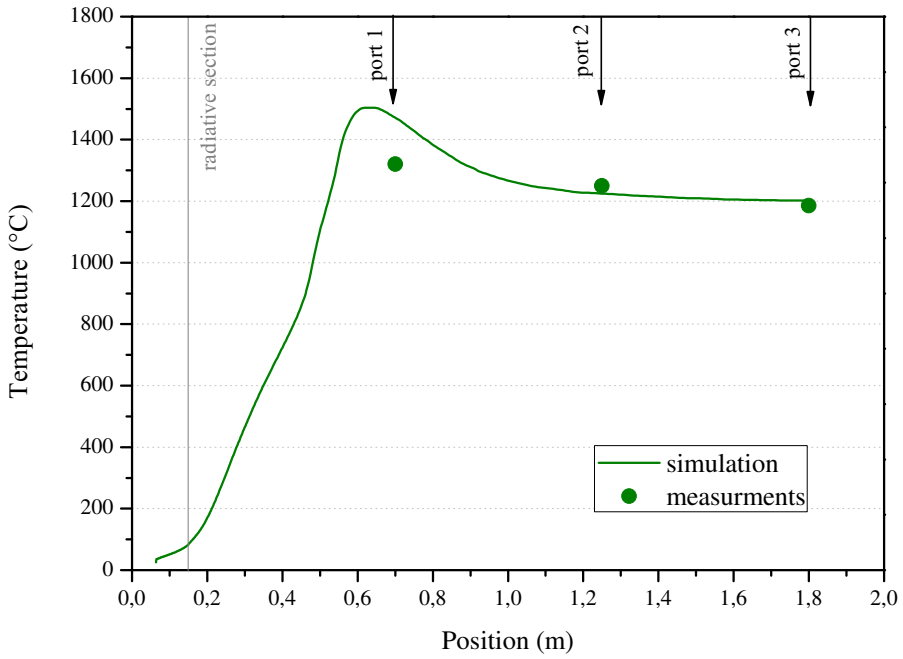

Figure 12.6.: Temperature profile along the center line - Coal combustion

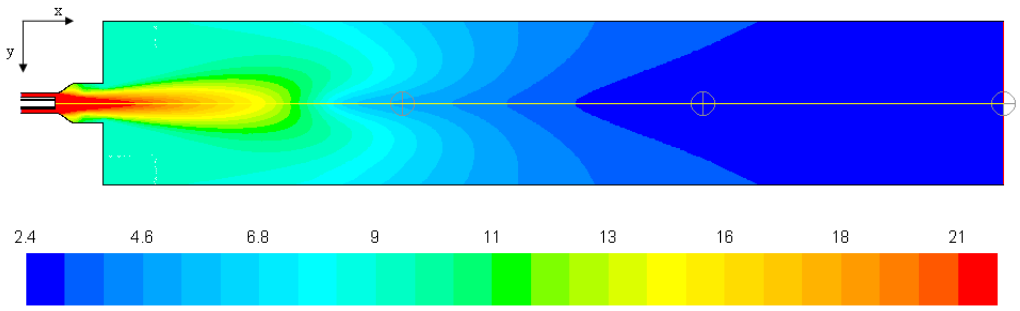

Figure 12.7.: Contours of O_2 concentration in vol. % - Coal combustion

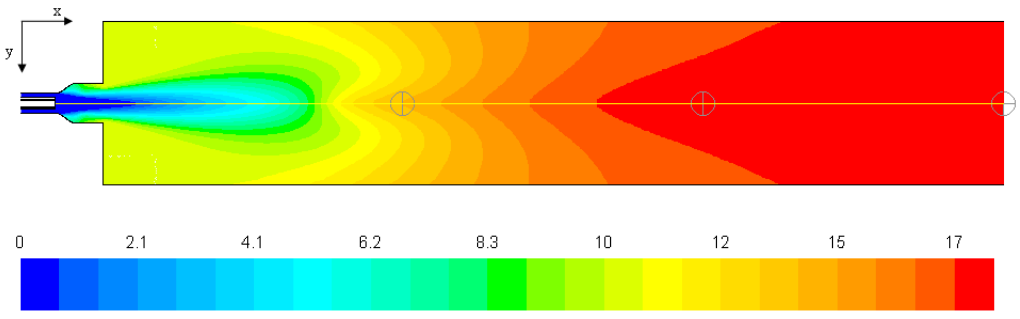

Figure 12.8.: Contours of CO_2 concentration in vol. % - Coal combustion

determined, while the calculated results vary from 5.21 to 2.55 % and 13.9 to 17.2 % , respectively for O_2 and CO_2. According to the simulations, combustion still takes place nearby port-1, because oxygen is predicted correctly (and carbon dioxide is produced in proper concentrations).

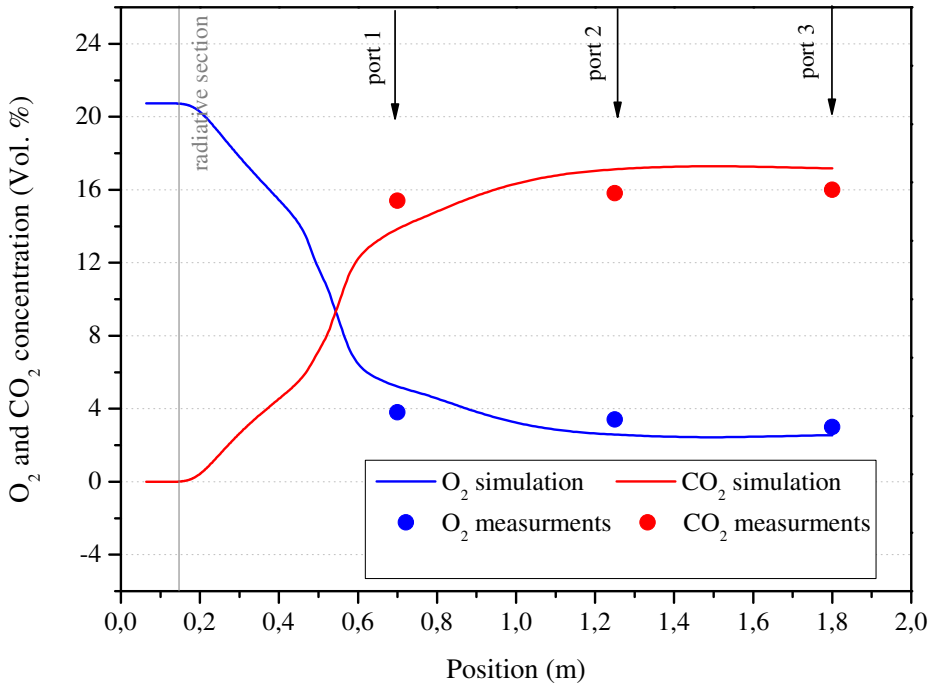

Figure 12.9.: O_2 and CO_2 concentration along the center line - Coal combustion

Carbon monoxide concentration The contours of CO concentration are shown in Figure 12.10. The highest CO concentration is achieved in the ignition region, and then it quickly decreases due to further oxidation. At the end of the radiative zone, CO is almost completely burnt, and nearly a zero value is predicted. The simulated concentration peak reaches about 13 000 vol. – ppm and is located at 0.45 m from the front wall of the radiative section. This value is too high, in comparison to measured 2000 vol. – ppm , as shown at Figure 12.11. In port-2 and port-3 a good agreement with experiments is achieved.

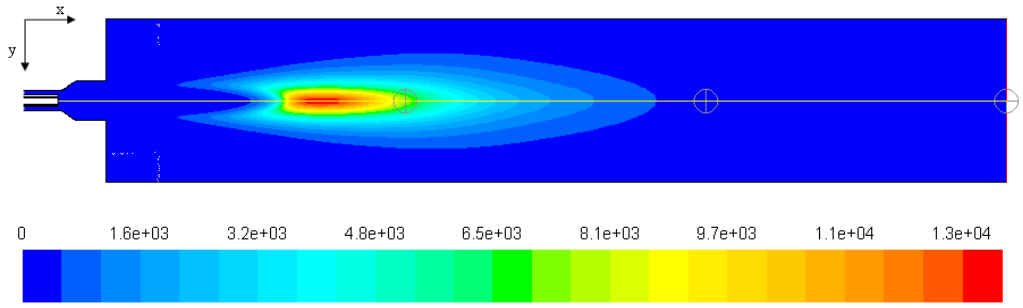

Figure 12.10.: Contours of CO concentration in vol. – ppm - Coal combustion

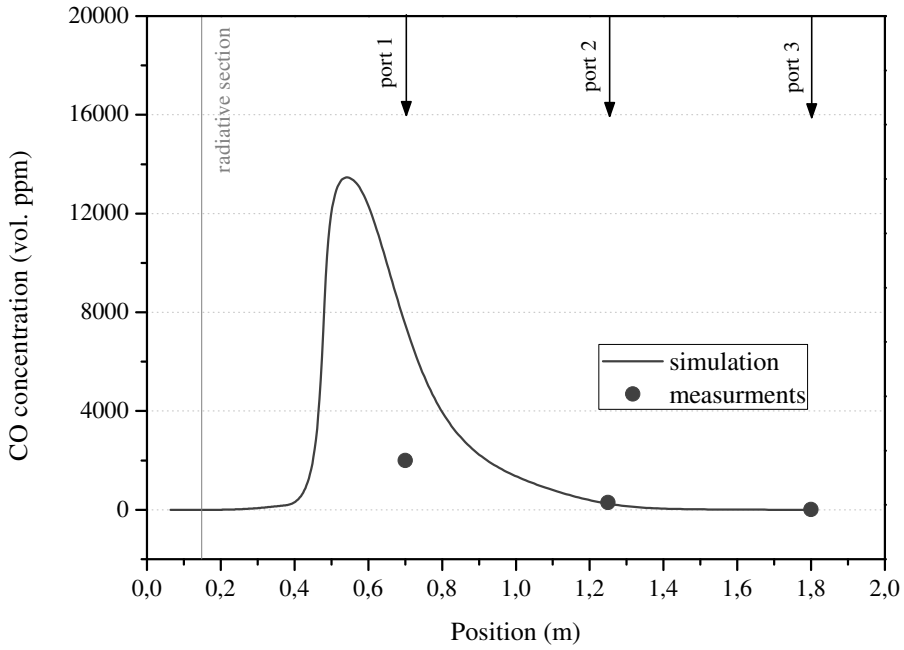

Figure 12.11.: CO concentration along the center line - Coal combustion

Nitric oxide concentration In Figure 12.12 the computed contours of the NO_x concentration are presented. Even if the thermal, the prompt and the fuel NO mechanism path formations are taken into consideration, in the present calculation the fuel-NO is the most important mechanism accounting for 90% of the formed NO. NO is formed within the flame front, after the intermediates (NCO in the case of coal combustion) are generated and oxidized and its concentration remains approximately constant along all the furnace.

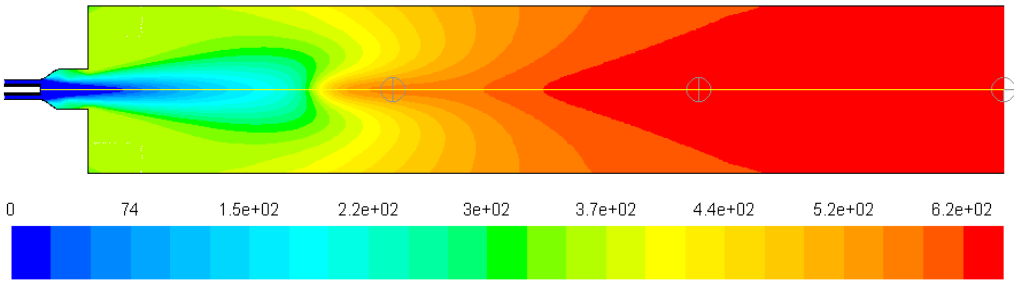

Figure 12.12.: Contours of NO_x concentration in vol. – ppm - Coal combustion

The measured values are compared with the calculated ones in Figure 12.13. The calculated peak value is in order of 620 vol. – ppm and is located in port-2, while the measured peak of 650 vol. – ppm has been reached already in port-1. In port-2 and 3 constant values of around 600 vol. – ppm are measured. Ignoring a small discrepancy near port-1, the agreement is excellent.

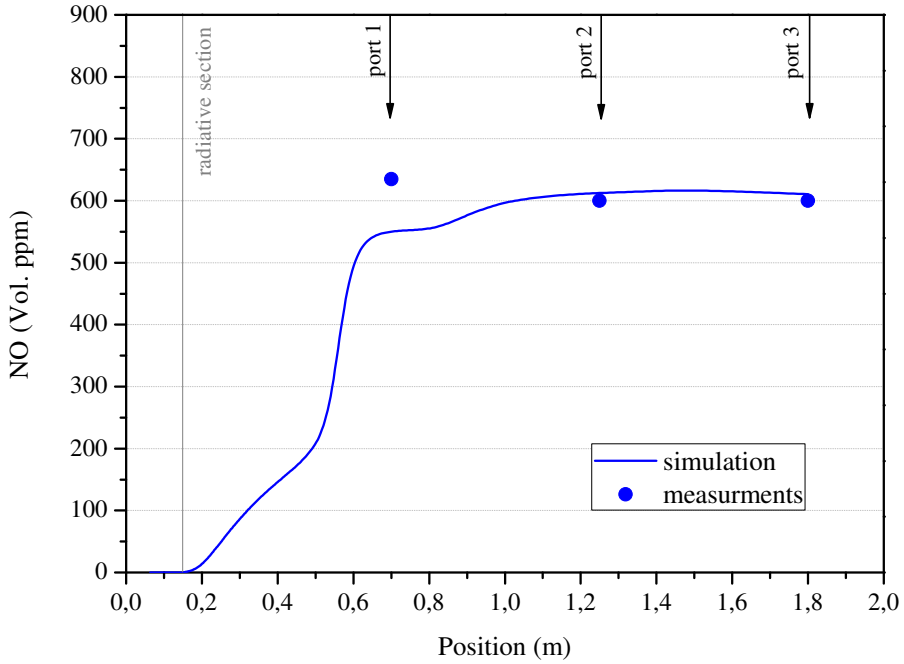

Figure 12.13.: NO_x concentration along the axis in vol. – ppm - Coal combustion

12.1.1.4. Discrete-phase

In Figure 12.14 two coal trajectories colored by residence time are shown. The injected particles have two diameters, the smaller having $D_p = 50\,\mu m$ and the bigger $D_p = 200\,\mu m$. The smaller particle achieves longer residence time, up to 16 s than the bigger particle (2.6 s). Due to the heavier weight, the bigger particles move directly to the bottom of the reactor while the smaller and lighter particles are scattered around by the turbulence and are easily recirculated in the top part of the reactor.

In Figure 12.15 the trajectories of the same particles are again presented (on the top the trajectories of smaller particles 50 µm and the bottom the trajectories of bigger particles 200 µm) with the color representing a different thermo-chemical process. The Blue color represents simple heating or cooling, the Yellow represents the devolatilization, and Red color represents the char oxidation.

Smaller particles reach the devolatilization temperature quicker and devolatilize faster than the bigger particles. For those particles, char burnout occurs earlier. For bigger particles, both processes are shifted down into the radiative section. However, considering the particle size distribution of this coal, around 10 % (in mass) of the particles are represented than particles with the diameter bigger than 200 µm while approximately 70 % are represented by particles with the diameter smaller than 100 µm. Hence most of the devolatilization takes place before port-1 and most of the char oxidation in the surrounding of this port.

The averaged burnout of 5000 particles calculated at each port is shown in Figure 12.16. In calculating the burnout, only particles in the close vicinity of the axis has been taken into consideration since experimental sampling is also carried out in the middle of the reactor. High burnout has been achieved, and the calculated values reproduce quite well the measurements. The burnout of heavier particles is low as it has been previously seen while burnout of smaller particle

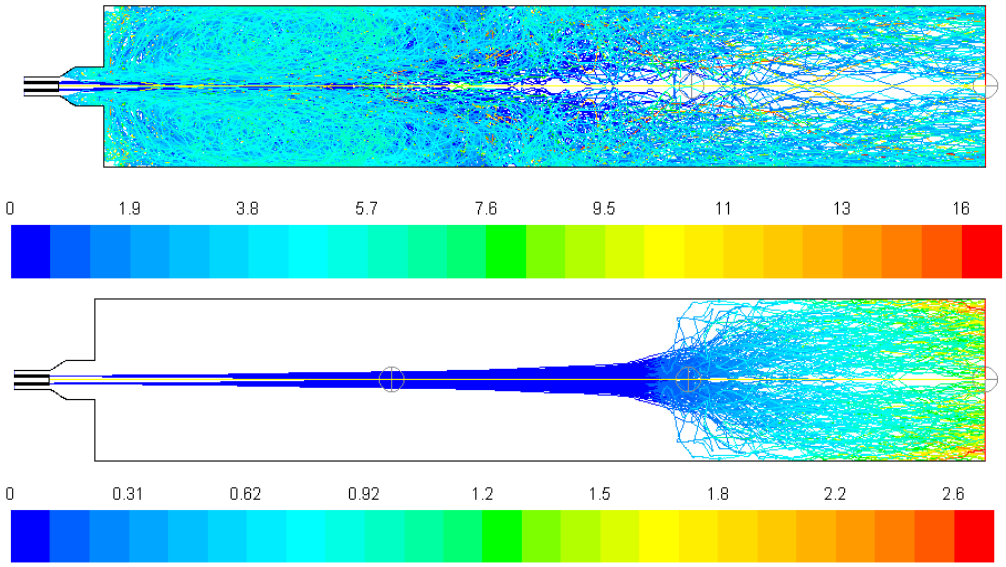

Figure 12.14.: Trajectories colored by residence time for 50 µm coal particle (Top) and 200 µm coal particles (Bottom) - Coal combustion

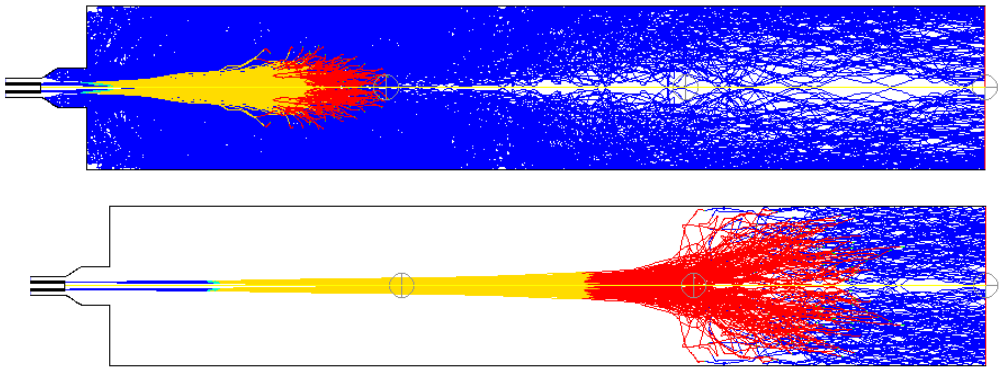

Figure 12.15.: Contours of particle law index of 50 µm (top) and 200 µm (bottom) particles - Coal combustion

is higher due to quicker reactions and due to higher residence times (also due to the presence of smaller particle that after being trapped inside the recirculation zone reach the sampling probe with almost complete burnout.

12.1.2. Results for biomass combustion

The calculation of the biomass combustion in the DFCC has been compared with the measured values. The results are presented in this Section.

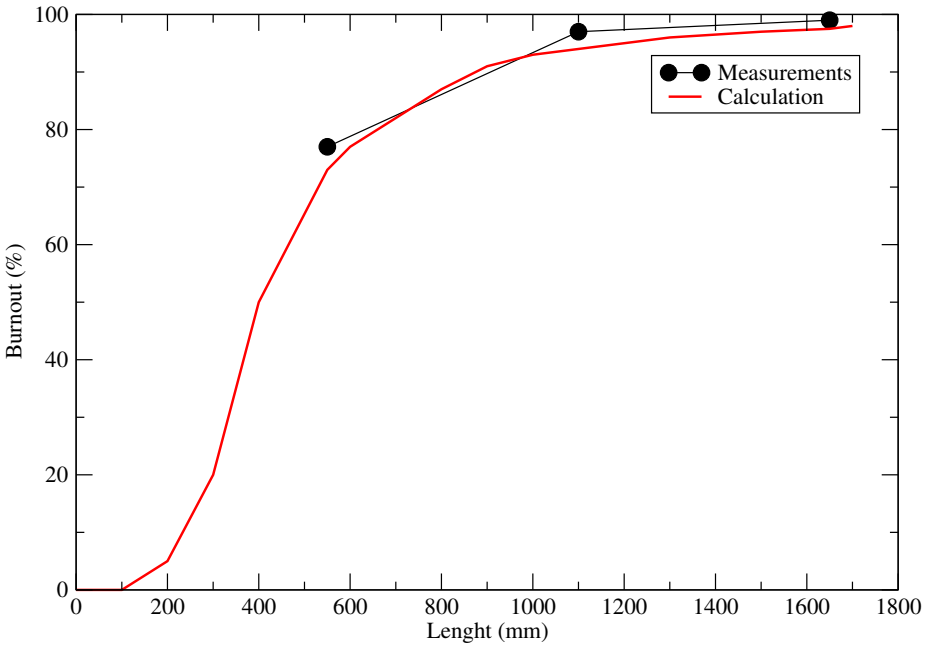

Figure 12.16.: Calculated and measured char burnout in each port - Coal combustion

12.1.2.1. Flow pattern

In Figure 12.17 the contours of the gas velocity in m/s (down) and the stream function (up) are presented. The profile of the stream functions profile is similar to the profile obtained in the case of coal combustion. Entrainment of the recirculated gas into the combustion air is observed and a constant decrease in velocity is achieved. The values of the calculated velocity for the fuel stream and secondary air at the inlet are 30 $\frac{m}{s}$ and 13.7 $\frac{m}{s}$, respectively.

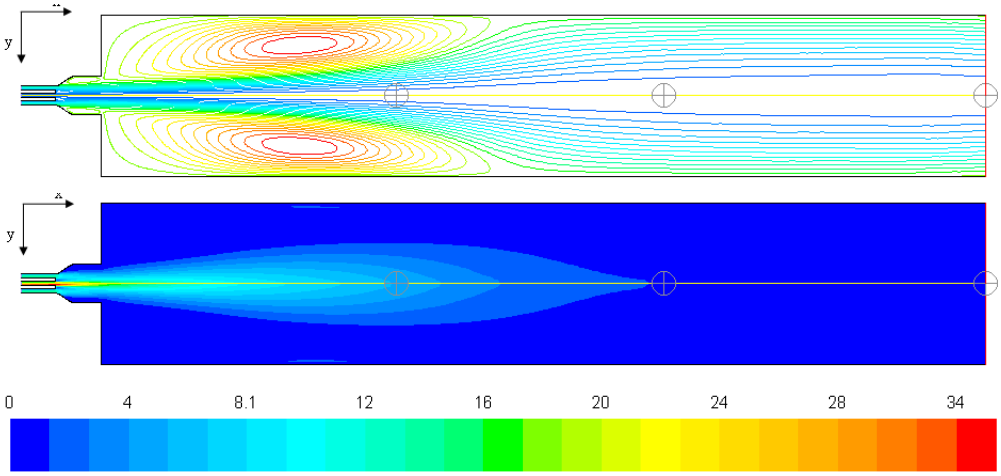

Figure 12.17.: Contours of stream function (up) and velocity (down) - Biomass combustion

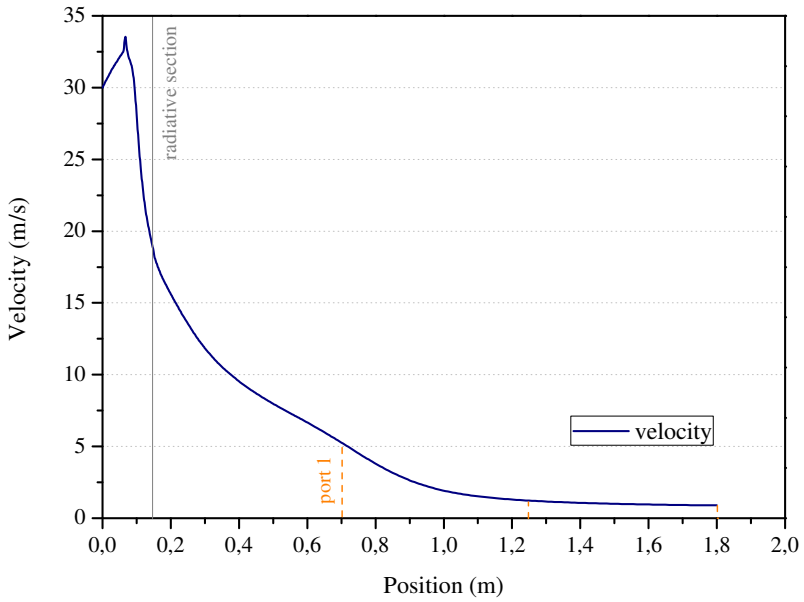

Figure 12.18.: Velocity profile along the center line - Biomass combustion

In Figure 12.18 the velocity is plotted along the reactor center line. As it can be observed, the velocity increases near the burner to a value of 33 $\frac{m}{s}$ and downstream a constant decrease is observed. At port-1 the velocity reach 5 $\frac{m}{s}$ and decrease to 1.3 $\frac{m}{s}$ in port-2. After that the profile is almost flat and values lower than 1 $\frac{m}{s}$ are computed.

12.1.2.2. Temperature Field

The contours of the temperature field are given in Figure 12.19. As it can be seen, the flame is created somewhere between port-1 and port-2 and its temperature increase from 900 to 1070°C, reaching a peak value of 1040 °C, close to the port-2, far downstream in the radiant section. Due to the high excess ratio ($\lambda = 2,5$) lower temperatures are achieved.

In Figure 12.20 the measured values are reported against the simulated ones. In the comparison, the temperature profile is well predicted by the model. The temperature in port-1 is calculated to be 673 °C, while the measured value is higher and reach 750 °C. In port-2, a value of 1400 °C is predicted in comparison to 990 °C from the measurements. In port-3, the measured value is about 20 °C lower than the measured value and it reach 1020 °C.

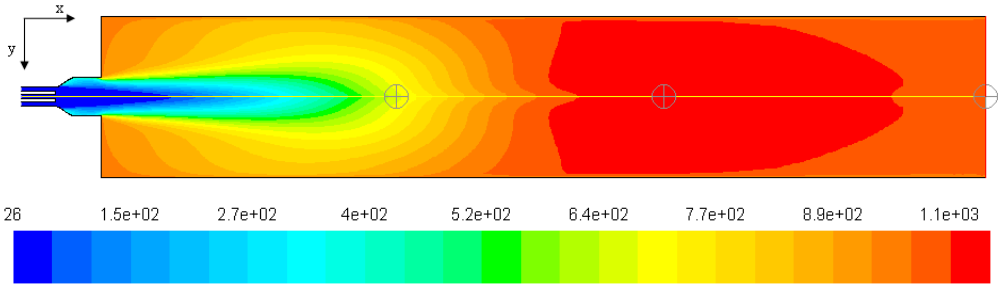

Figure 12.19.: Contours of temperature field in °C- Biomass combustion

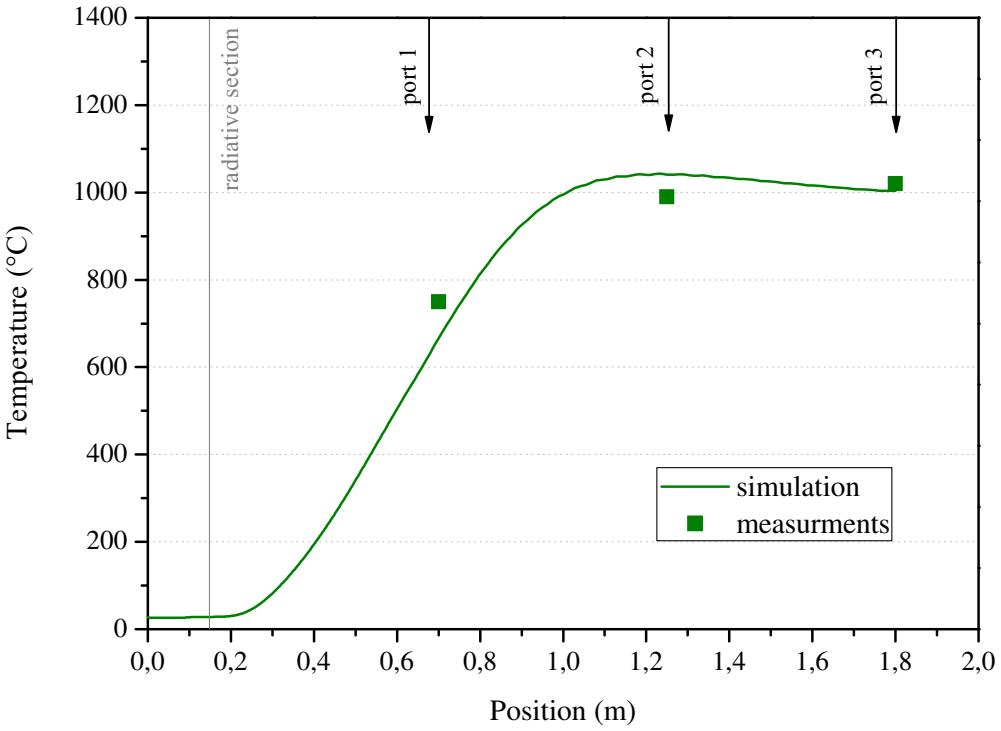

Figure 12.20.: Temperature profile along the center line - Biomass combustion

12.1.2.3. Profile of species concentration

Oxygen and carbon dioxide concentration In Figure 12.21 and Figure 12.22 the molar concentrations of O_2 and CO_2 are plotted. Generally it can be observed, that combustion extends far into the reactor and near port-2, 1.1 m into the radiative section, still oxygen is consumed.

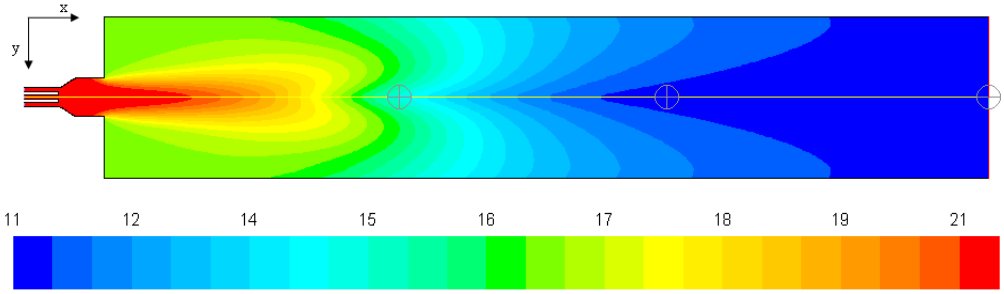

Figure 12.21.: Contours of O_2 concentration in vol. % - Biomass combustion

In Figure 12.23 the measured data are reported against the results of the simulation. Both species concentration are in good agreement with the experiments. The difference between the simulated values of O_2 and the measured one varies in range 0.7 to 2.9 vol. %. As it can be seen, CO_2 concentration are computed with greater accuracy, and only 0.5 to 0.12 vol. % difference is achieved. While in port-1 17.6 vol. % have been measured, simulation gives a value of 14,6 vol. %. From those discrepancies, it is possible to infer that the simulated combustion

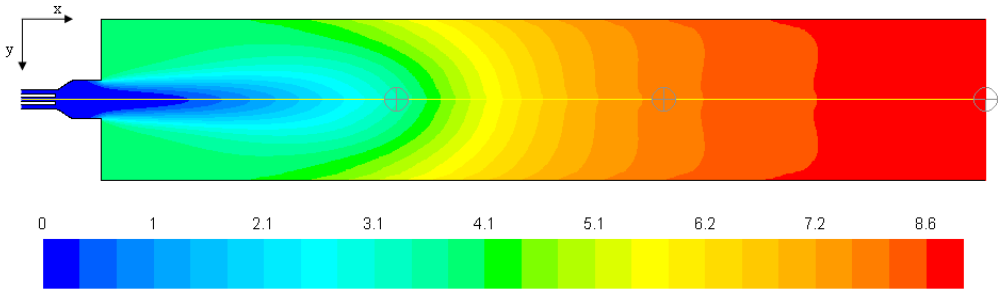

Figure 12.22.: Contours of CO_2 concentration in vol. % - Biomass combustion

proceed slightly faster, in comparison to the combustion taking place inside the reactor chamber.

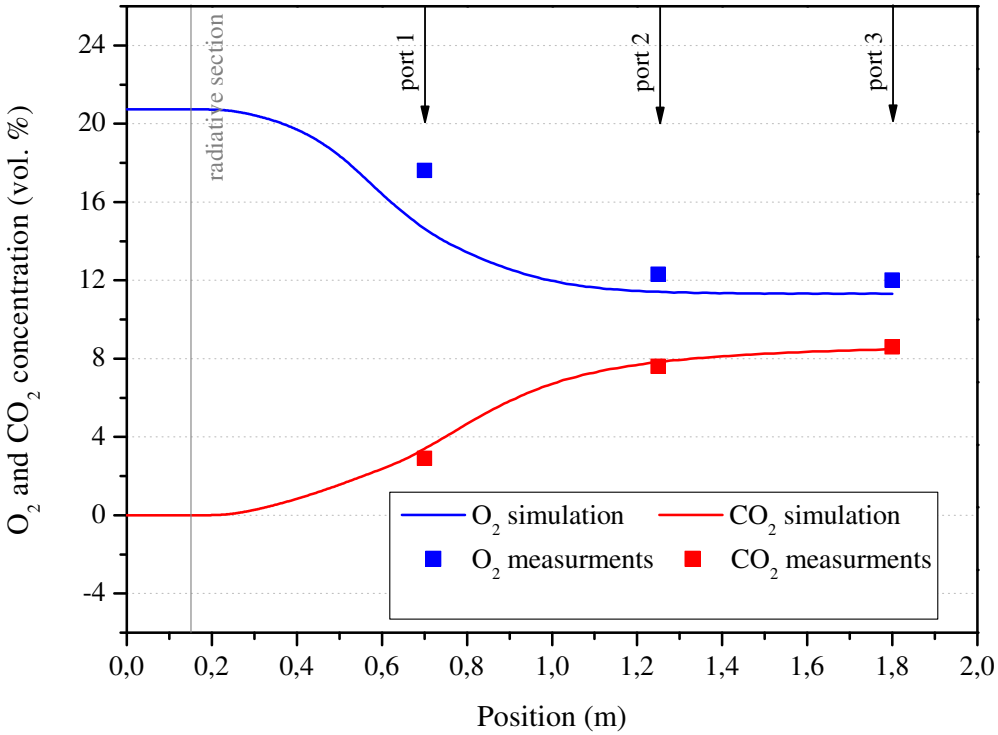

Figure 12.23.: O_2 and CO_2 concentration along the center line - Biomass combustion

Carbon monoxide concentration The Figure 12.24 presents the contours of the CO concentration. The CO level remains high along the whole radiative section. The simulated peak value reach about 26 000 vol. – ppm and is located in the vicinity of port-1 (Figure 12.25). The measured value at this position is only 10 700 vol. – ppm . Also at port-2 and 3, the computed values are higher, ending with a CO concentration of 3480 vol. – ppm . The obtained differences underline the difficulties to achieve a reasonable prediction of the CO emission in solid fuel combustion.

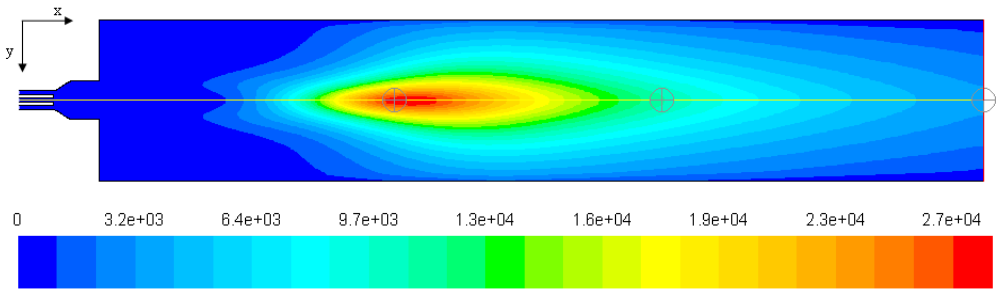

Figure 12.24.: Contours of CO concentration in vol. – ppm - Biomass combustion

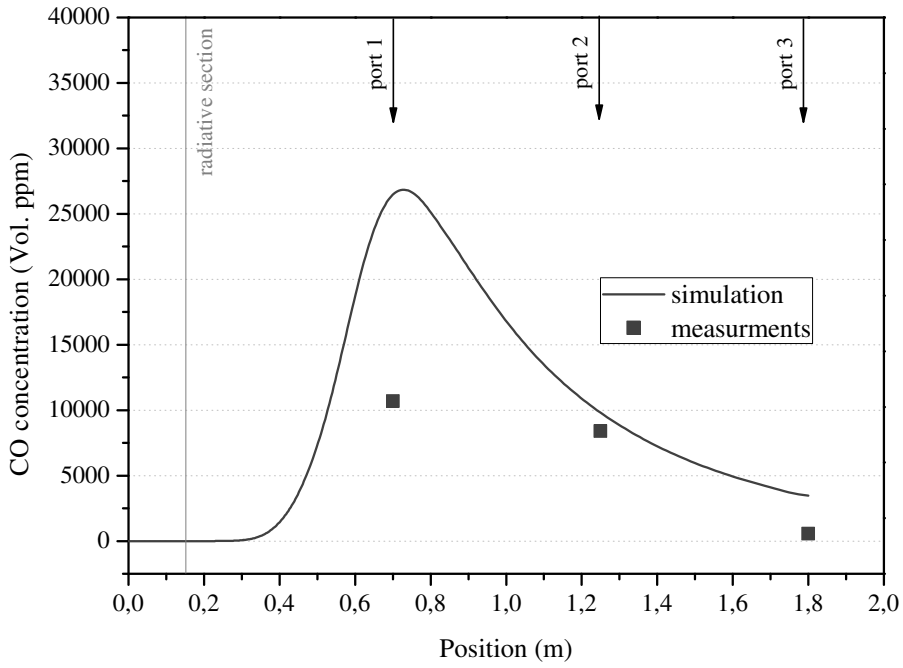

Figure 12.25.: CO concentration along the center line - Biomass combustion

Nitric oxide concentration Because of the fairly low temperature (950 °C) present in the chamber, only Fuel NO was taken into consideration. In the case of biomass, as mentioned in Section 9.2.5, all the nitrogen, both from char and volatiles is firstly converted to NH_3, and the ammonia reacts further to NO. The contours of NO concentration are shown in Figure 12.26.

The trend of NO concentration is not correctly predicted as clearly appears in Figure 12.27 where the plot of the measured values and the predicted ones is shown. Especially at the port-2 and 3, a discrepancy is evident. The outlet NO concentration should be 830 vol. – ppm while only a level of about 200 vol. – ppm has been computed.

For this simulation, the NO formation follows the path indicated in Figure 12.28. According to this mechanism, nitrogen from the Volatile Matter can either directly reacts to NO, or it can be converted to NH_3. The fraction of N directly converted to NO is not known for this biomass. In Figure 12.29 the values of the NO concentration calculated at port-1 and 3 are plotted against the fraction of N directly converted into NH_3. Decreasing the fraction, the level of NO in port-3

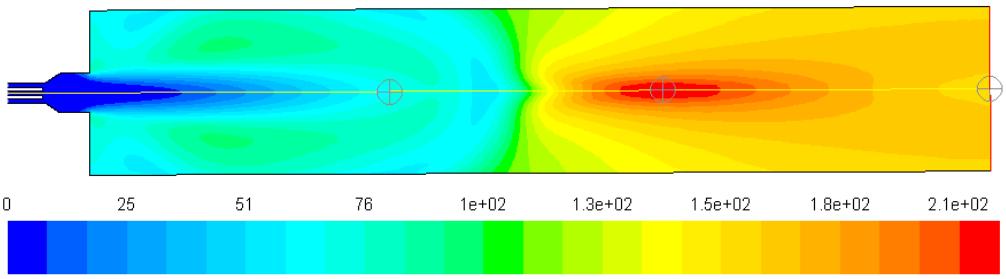

Figure 12.26.: Contours of NO_x concentration in vol. – ppm - Biomass combustion

increases but the level in port-1 increases steeper, and reach values (1400 ppm) not compatible with the measurements before the measured value in port-3 is achieved.

The impossibility to obtain a correct NO_x level in all the three measurement points indicate the inadequacy of the model adopted. It is worth recalling that the similar model used for coal in 12.1.1.3, in which NH_3 was replaced by HCN, can reproduce the NO emissions quite well in the whole reactor.

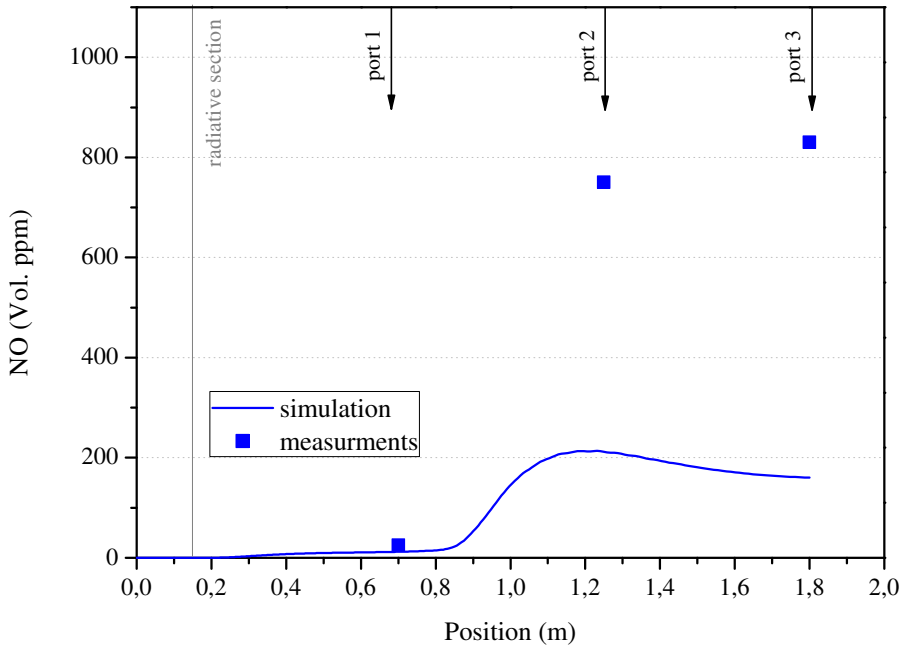

Figure 12.27.: NO_x concentration along the axis in vol. – ppm - Biomass combustion

12.1.2.4. Discrete phase

In Figure 12.30 particle tracks colored by low index for smaller (top) and bigger (bottom) particles is given. The meaning of the colors is as described previously in 12.1.1.4.

Due to the higher velocity at the inlet, a shorter residence time for both particle sizes is calculated if compared to the residence time obtained in the coal combustion experiments presented

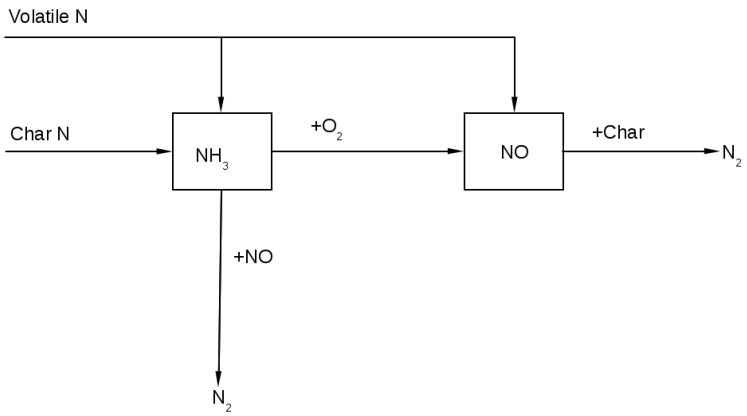

Figure 12.28.: Fuel NO path adopted in the simulation for Biomass combustion

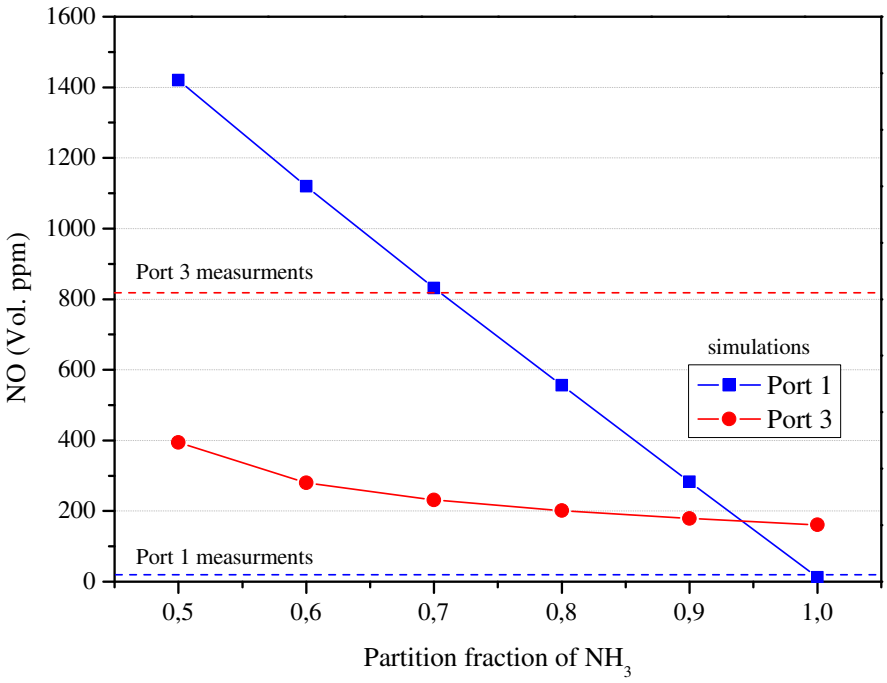

Figure 12.29.: NO_x concentration predicted in the Biomass combustion experiment by changing NH_3 partition in fuel NO path

in 12.1.1.4. Particles with the diameter of 50 µm remain in the reactor up to the 12 s scattered by the turbulence, while the biggest particles of 500 µm spend less than 0.3 s in the chamber.

As expected, devolatilization plays a dominant role in biomass combustion while char burnout is responsible for only about 5% of the mass loss.

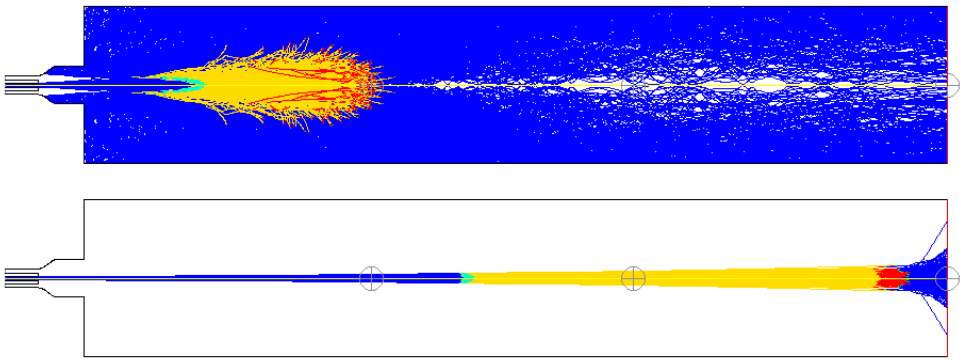

Figure 12.30.: Contours of particle law index of 50 µm (top) and 200 µm (bottom) particles - Biomass combustion

In Figure 12.31 the calculated burnout is compared with the measured values from the samples extracted in all three ports. Significant differences between measured and calculated values in port-1 are observed, while a better agreement is achieved in port-3. The computed values are 14,8%, 58,8% and 93% against the measured 64,6%, 87,1% and 98,2%, for port-1, 2 and 3 respectively.

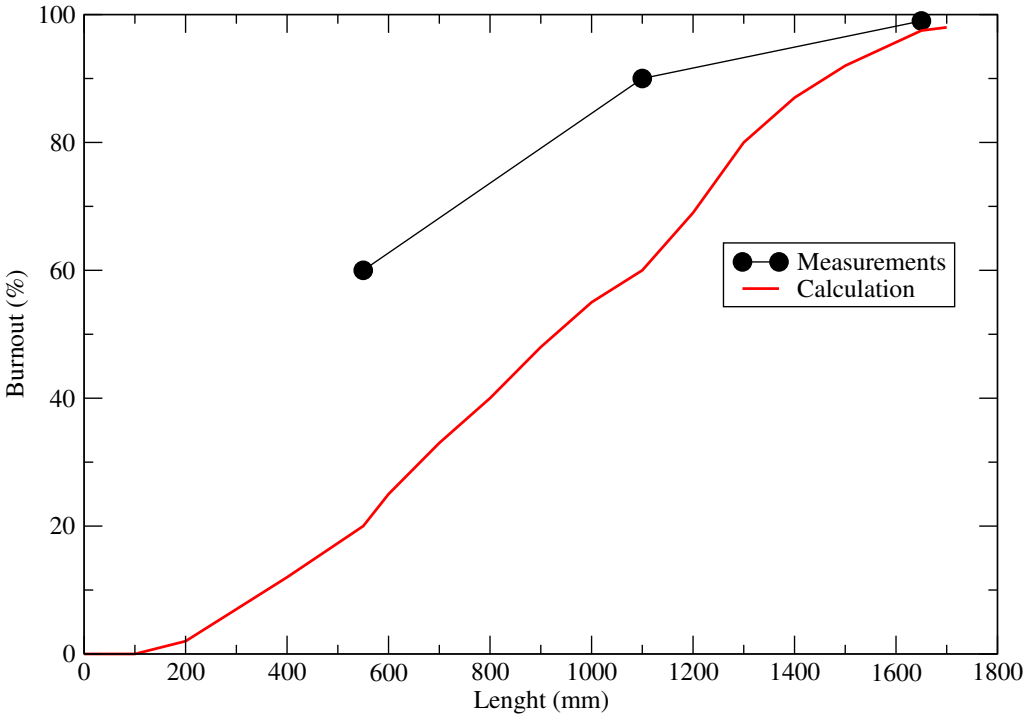

Figure 12.31.: Simulated char burnout in each port - Biomass combustion

12.2. Semi-industrial scale

In the previous section, examples of the applicability of the CFD method to small flames has been given. In these Sections, the same method will be applied to the prediction of a semi-industrial swirled coal flame taken also into account in [267]. In the MMF5-2 investigation executed at the IFRF, an unstaged (therefore high-NO) coal flame was generated in the old IFRF furnace no.1 shown in Figure 12.32 using the experimental aerodynamically air staged burner shown in Figure 12.33. In-flame temperatures, chemical species concentrations, and coal burnout were measured at seven traverses using standard IFRF sampling probes. The measured chemical species are O_2, CO, CO_2, NOx-precursors (HCN and NH_3), N_2O and NO_x. Velocity and turbulence measurements were performed at four traverses using an LDV technique, with the coal particles used as the scattering source. Radiative heat fluxes near the furnace refractory wall, the heat extraction of the seven cooling loops and flue gas chimney values were also measured. The coal fired was a Saarcoal: Gottelborn hvBb. For more details about the coal and the inputs, see [267].

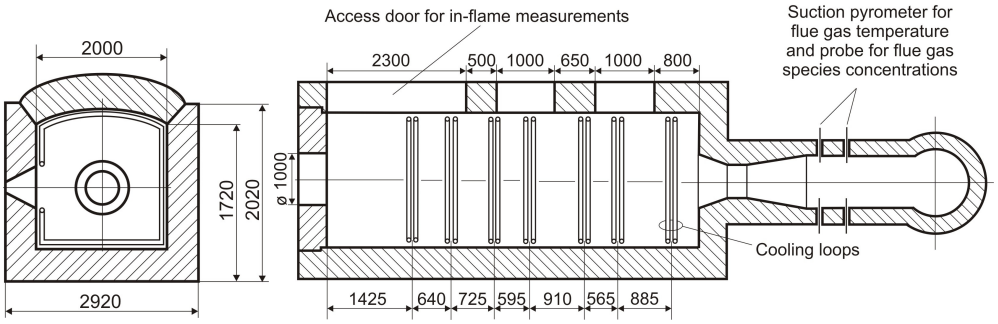

Figure 12.32.: Sketch for the old IFRF Furnace number 1 used in the MMF5-2 investigation [267]

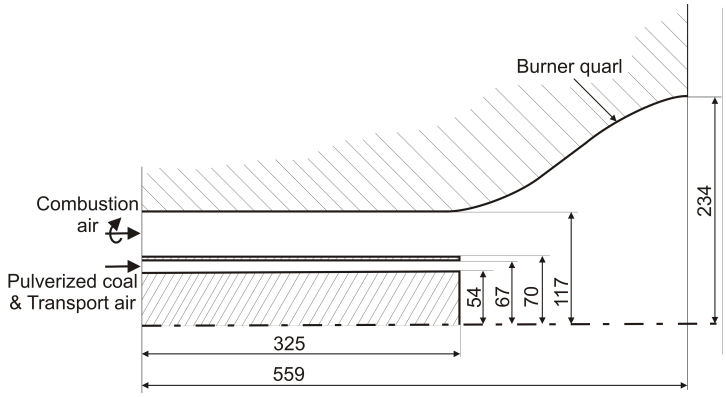

Figure 12.33.: Sketch of the aerodynamically air staged burner used in the MMF5-2 investigation [267]

Contrary to previous examples that have been considered in detail, in this Section, only a few general characteristics of the modeling will be presented. The flame generated by the burner is a high swirled unstaged flame and has two recirculation zones, an internal recirculation zone surrounded by the flame and an external recirculation zone due to the penetration of the flame inside the combustion chamber. Due to the acceleration the flame is closed, and a typical bulb is formed, while for higher tangential velocity the flame assumes the form of an open tulip.

The Authors in [267] describing the results of the modeling, show that the CFD can predict the near-burner zone axial and tangential velocities and their root-mean-square values with a good accuracy (applying the standard k-ϵ turbulence model). The overall agreement between predicted and measured carbon monoxide, oxygen, and carbon dioxide concentrations in the flame zone have also been found to be good.

The MMF5-2 burner is axis-symmetric and has been modeled accordingly using a two-dimensional cylindrical coordinate system. However, the whole combustion chamber is not axial-symmetric for two reasons:

1. The shape of the chamber section is a square with the roof slightly curved;
2. The burner is not situated in the center of the burner-wall but 20 cm below (see Figure 12.32).

The calculation presented in reference [267] has been performed with the version 3,0 of the software FLUENT. The flame has been predicted to be closed, in accordance with the experimental observation. Later, with new software versions, better numeric in the solver, finer mesh discretization, and faster computers, the flame has always been predicted open. During the first several thousand iterations the flame remains closed, and with the progress of the solution through the external recirculation zone, the flame shortens until it opens up and become entirely stable. In the present section it is shown that after imposing an additional symmetry, the wrong flow field pattern is calculated.

In Figure 12.34 the stream-lines for the axial symmetric simulation are presented. The flow field is predicted with several recirculation zones:

1. A first internal recirculation zone (experimentally observed);
2. A second internal recirculation zone where the flame open up (experimentally NOT observed);
3. A first external recirculation zone along the furnace (experimentally observed);
4. A second and a third recirculation zones near the burner (experimentally NOT observed).

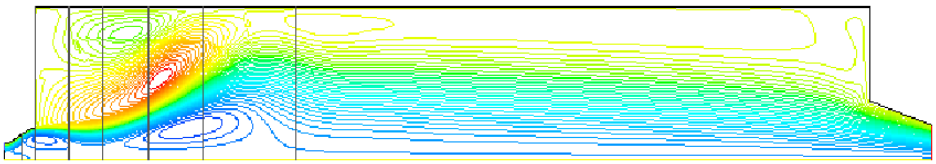

Figure 12.34.: Stream-lines of the MMF5-2 flame calculated imposing axial symmetry

The position and the intensity of the recirculation zones can be seen from the axial and swirl velocities measured. In Figure 12.35 the axial velocity calculated by the CFD model has been compared with the data obtained by the LDV measurements. Three cases are reported in the Figure:

Case 1: Simulation after 20k iterations with a closed flame (realizable k-ϵ turbulence model);

Case 2: Simulation after 50k iterations with an open flame (realizable k-ϵ turbulence model);

Case 3: Simulation after 50k iterations with an open flame (RSM turbulence model).

Two aspects are worth noticing. At the first reported traverse, with an axial distance of 0.234 m still inside the divergent part of the burner, measurements indicate a weak internal recirculation zone since the axial velocity is roughly U = $-2\,\frac{m}{s}$. This velocity is well predicted by the model when the flame remain closed, (model 1) while as soon as the flame opens up (model 2 and 3), the internal recirculation zone moves downstream and the modeled velocity at the first traverse increases and it is predicted to be about U = $-20\,\frac{m}{s}$. At the traverses 0.734 m and 1.084 m from the burner, the not well-predicted position of the velocity peak is an indication that the flame is open (case 2 and case 3). Moreover in the same traverses, near the center of the furnace, the predicted negative axial velocity shows the presence of the second internal recirculation zone, clearly not present in the measurements. As a last observation, the opening of the flame is independent on which turbulence model has been used and which parameters for the combustion sub-models have been adopted (many variations, not presented in this section, have been performed without changes in the quality of the predictions).

Since the whole furnace doesn't have any axial symmetry full 3D calculations has been performed, with results shown in the following table:

Run	Geometry	Roof	Burner	Flame
R-1	cylindrical	-	Center	**Open**
R-2	rectangular	Flat	Center	**Open**
R-3	rectangular	Curved	Center	**Open**
R-4	rectangular	Flat	Down	**Closed**
R-5	rectangular	Curved	Down	**Closed**

Those calculations demonstrated that the correct position of the burner (together with the correct numeric) is essential for the good prediction of the flame form. In Figure 12.36 the axial and the swirl velocities predicted by the model R-5 are presented. In Figure 12.37 the temperature and the CO concentration predicted by the same R-5 model are presented. A good accuracy between measured and calculated values is achieved. The position of the internal recirculation is better predicted than the 2D model together with the CO level. The temperature inside the burner remains underpredicted, a consequence of the low predicted reaction intensity.

12.2.1. LES Simulation

For the sake of comparison, it is worth noticing that in [294] the same flame has been simulated using an LES approach. The furnace has been simulated with a quadratic section, and the burner has been placed in the center. Although the RANS model predicts, in the same conditions, as that the flame open up, the performed LES predicts a closed flame as shown in Figure 12.38.

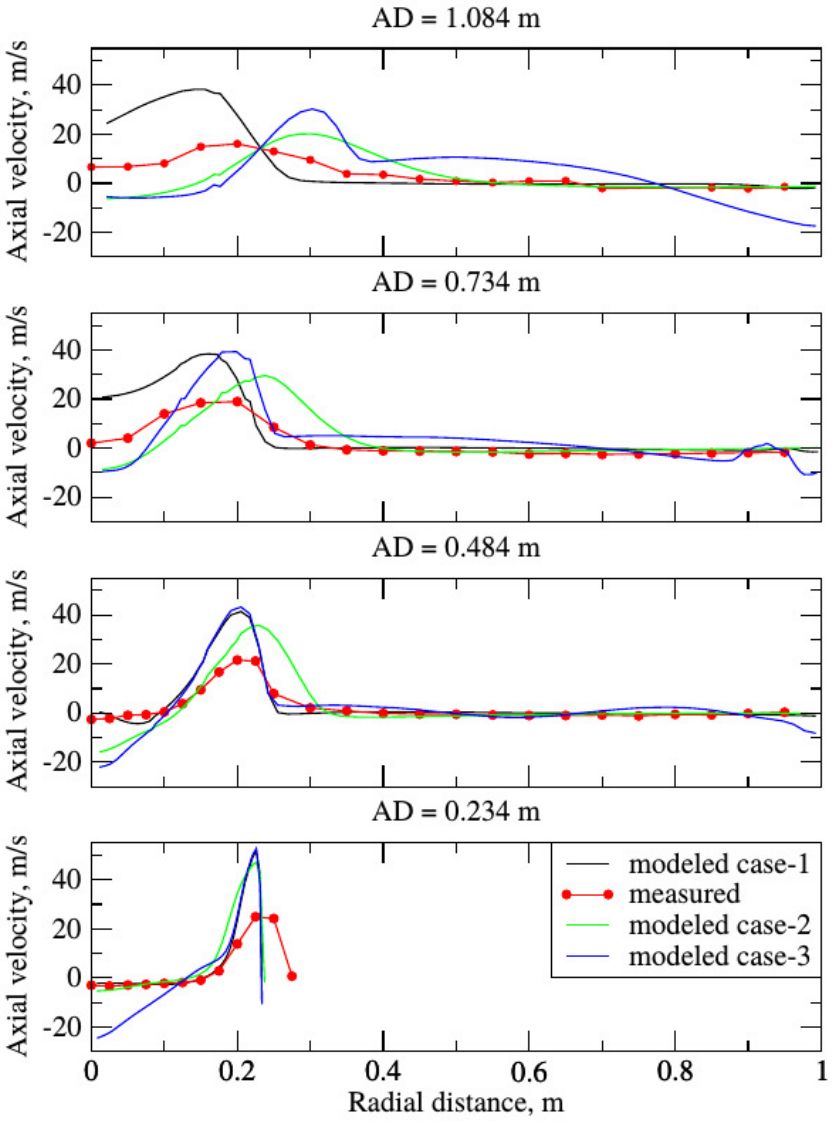

Figure 12.35.: Axial velocity of the MMF5-2 flame calculated imposing axial symmetry

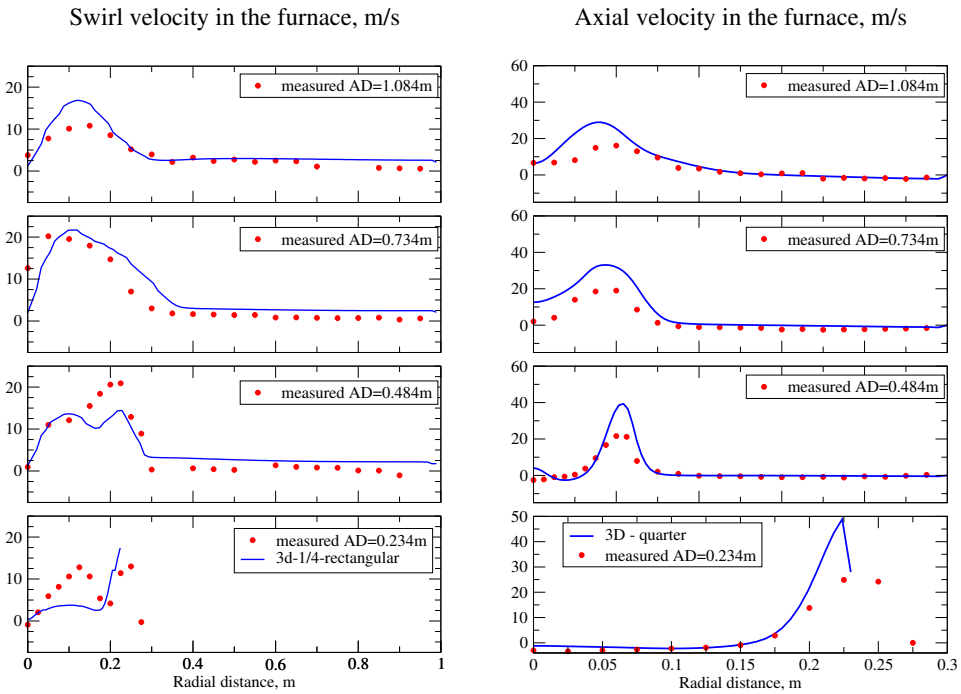

Figure 12.36.: Axial and Swirl velocities of the MMF5-2 flame calculated using RANS modeling. The geometry is a full 3D with asymmetrical position of the burner (run R-5)

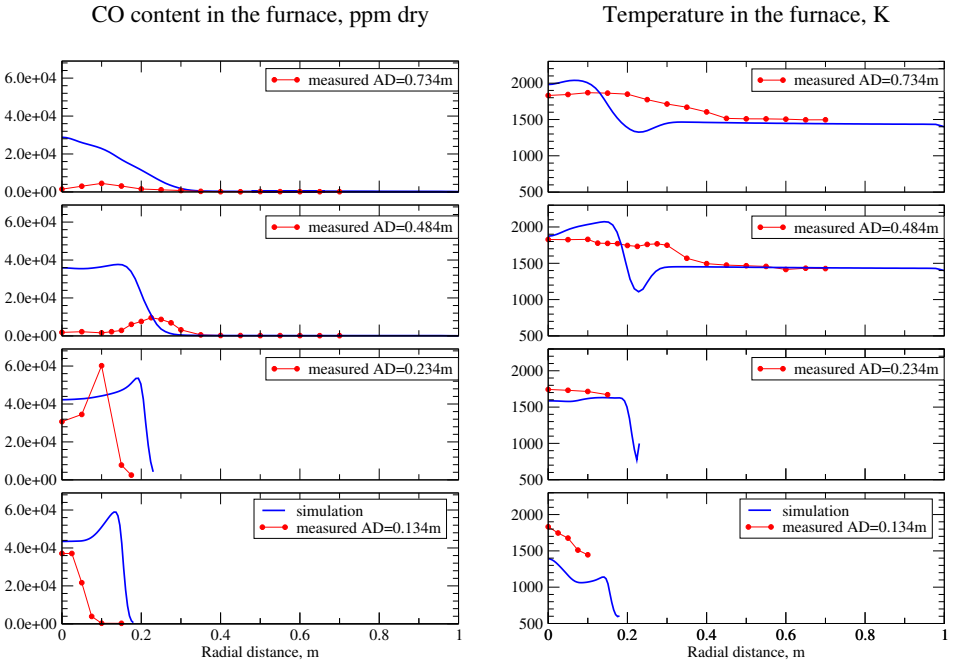

Figure 12.37.: Temperatures and CO mole fraction of the MMF5-2 flame calculated using RANS modeling. The geometry is a full 3D with asymmetrical position of the burner (run R-5)

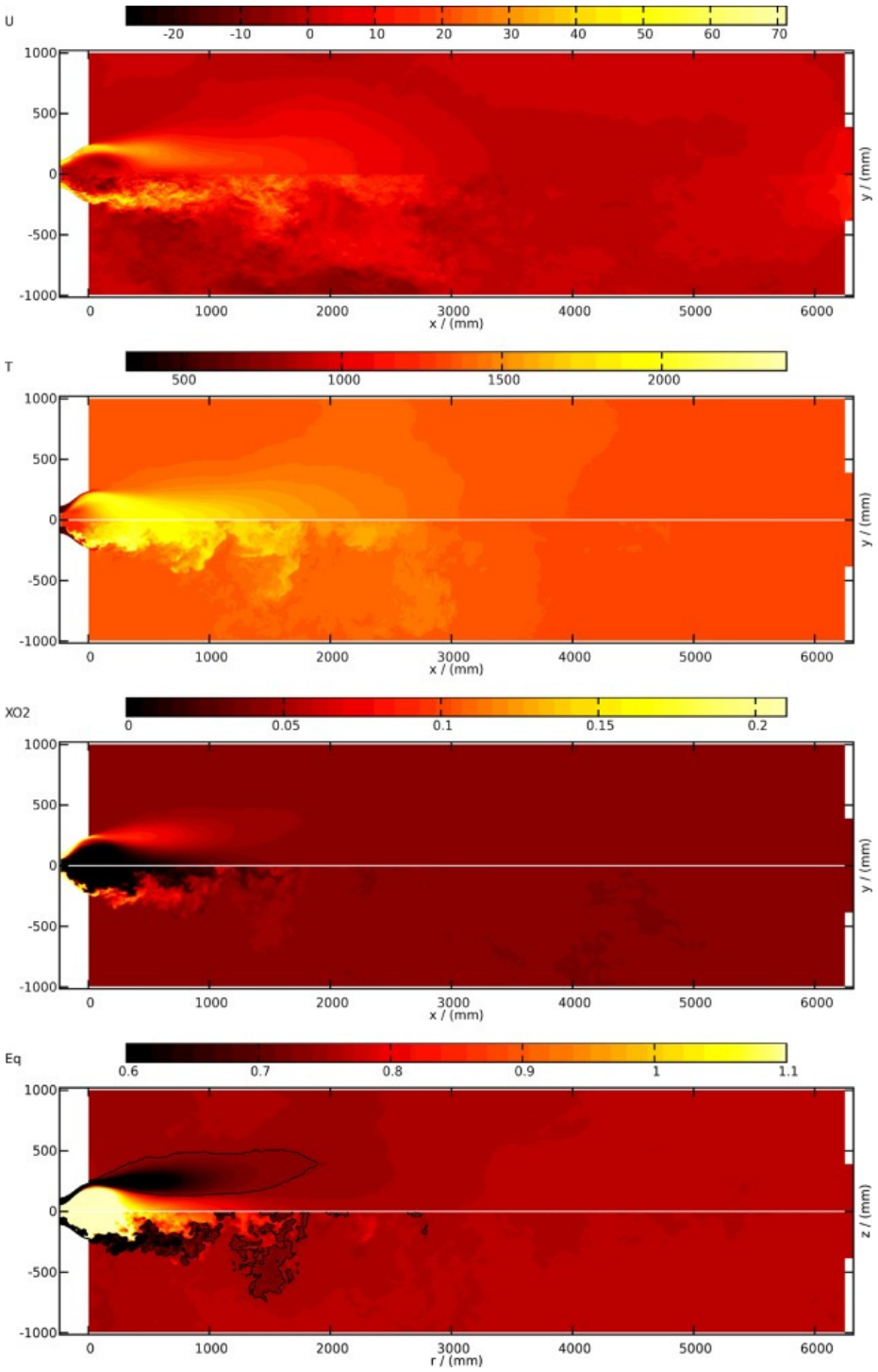

Figure 12.38.: Contours of the MMF5-2 flame calculated using LES modeling [294]

13. Oxidation of large particles

Predicting combustion rates of char particles is an important issue since such information is required during designing pulverized coal boilers, fluidized bed combustors, fixed bed combustors, and gasifiers. In pulverized coal boilers, fuel is usually introduced into the combustion chamber in small particles for which the methods of determining the conversion kinetic have been explained in the previous Chapters. In some applications like packed bed reactors or fluidized bed reactors, the fuel is introduced in millimeter size or even centimeter size particle. The question, if the intrinsic reactivity together with the proper determination of structural changes inside the particles is enough for the determination of the overall rates, is of importance. An affirmative answer to that question implies that adequate knowledge of the fuel at laboratory conditions allows the prediction of conversion rates at more difficult operating conditions. In [30] a detailed CFD simulation has been carried out to answer the question. The results are taken from that work which should be consulted for more details.

The aforementioned work was concerned with the combustion of a 5.2 mm coal-char particle in a stream of hot air. During the particle combustion, an ash layer has been formed which inhibits the oxidation rate. In the paper, a CFD based mathematical model has been compared with measurements. The model calculates the development of the oxidation front within the particle and predicts the ash layer development. It will be shown that the model replicates well the experiment and the slow-down of the oxidation process, occurring during the last 20 % burnout, is also well reproduced.

13.1. Experiments

Bibrzycki et al. [39, 38] have reported a series of measurements concerning oxidation rates of char particles. In [30], experimental run No. 1 is considered (see Table 2 in [39]) where a char particle of 5.2 mm diameter is oxidized in a stream of hot air T =1069 K approaching the particle with 3.3 $\frac{\mathrm{m}}{\mathrm{s}}$ velocity. The mass loss of the particle has been recorded every second using an analytical balance while the surface temperature has been recorded, every three seconds using an infrared camera as shown in Figure 13.1.

The composition of the char has been determined to be the following:

moisture	= 1.5%
fixed carbon	= 78.0%
volatiles	= 7.7%
ash content	= 12.8%

At the end of the oxidation process ($\sim$300 s), the remnants are equal to the initial ash mass. The infrared images show that in experimental run No. 1 the particle diameter stays approximately constant because the ash remains on the particle.

Mercury porosimetry has been used to determine the true particle density, the volumetric pore length, the porosity, the pore structural parameter, the initial internal volumetric surface area and the pore tortuosity (see Tables 3 and 4 in [39]). The measured values are reported below:

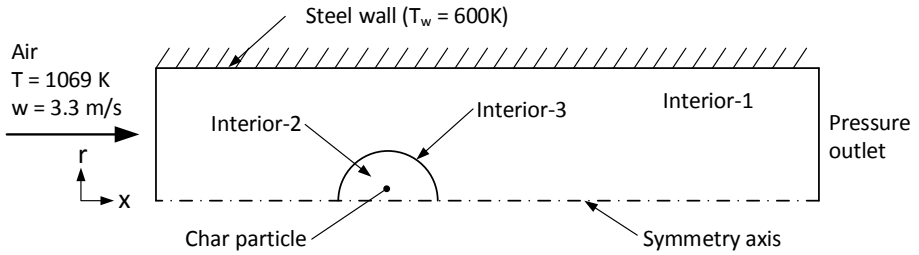

Figure 13.1.: Simplified representation of the experiment [39, 38]: computational domain and boundary conditions [30]

particle true density	ρ_{true}	1628 $\frac{\mathrm{kg}}{\mathrm{m}^3}$
volumetric pore length	L_{V}	$2.47 \cdot 10^{14}\,\frac{\mathrm{m}}{\mathrm{m}^3}$
porosity	ε	0.286
pore structural parameter	ψ	2.28
initial internal volumetric surface area	S_{V_0}	$3.11 \cdot 10^7\,\frac{\mathrm{m}^2}{\mathrm{m}^3}$
pore tortuosity	τ_{pore}	1.20

The intrinsic kinetics for the char considered have been determined using TGA operated in an isothermal mode to eliminate both the complexity and ambiguity in deriving the kinetic parameters at non-isothermal operation (see Section 11.3 and [401]). Assuming that the char consists of ash and carbon only, the char oxidation is described by the following stoichiometric equation:

$$\mathrm{C} + \gamma\mathrm{O_2} \longrightarrow (\,2\,\gamma\text{-}1)\,\mathrm{CO_2} + (\,2 - 2\,\gamma)\,\mathrm{CO} \tag{R 13.1}$$

where the CO/CO_2 ratio is taken to be temperature dependent [13]

The pre-exponential factor and the activation temperature of the Arrhenius expression

$$k_{\mathrm{int}} = A_{\mathrm{int}} \cdot \exp\left(-\frac{E_{\mathrm{a,int}}}{R \cdot T}\right) \tag{13.1}$$

for Reaction (R 13.1) have been determined to be $A_{\mathrm{int}} = 4.04 \cdot 10^3\ \frac{\mathrm{m}}{\mathrm{s}}$ and $E_{\mathrm{a,int}}/R = 15\,450\mathrm{K}$ [39]. The latter corresponds to a 128 $\frac{\mathrm{kJ}}{\mathrm{mol}}$ activation energy which is lower than typically quoted values of around 140 $\frac{\mathrm{kJ}}{\mathrm{mol}}$ [105] or 160 $\frac{\mathrm{kJ}}{\mathrm{mol}}$ [339]. The pre-exponential factor and the activation temperature for oxidation of the same char in carbon dioxide (Boudouard reaction)

$$\mathrm{C} + \mathrm{CO_2} \longrightarrow 2\,\mathrm{CO} \tag{R 13.2}$$

have been determined to be $A_{\mathrm{int}} = 2\,775\ \frac{\mathrm{m}}{\mathrm{s}}$ and $E_{\mathrm{a\,int}}/R = 26\,177\,\mathrm{K}$ [39]. Thus, a 218 $\frac{\mathrm{kJ}}{\mathrm{mol}}$ activation energy [150, 216] has been measured. The ratio of CO_2 gasification to oxidation rate at 1063 K is then $3.13 \cdot 10^{-5}$ which aligns well with typical values (see Table 2 in [150]). In the experimental determination of the above kinetic constants, reactions (R 13.1) and (R 13.2) are taken to be first order.

13.2. Two-dimensional char combustion model

A CFD based mathematical model has been formulated describing the time-dependent char oxidation process. The model describes the flow around the particle with the homogeneous reactions as well as the reactant transport and heterogeneous reactions inside the coal structure (see also [103]). No turbulence must be taken into account since the oxidizer flow is laminar (flow Reynolds number ≈ 465) and the particle Reynolds number is 140 so that the boundary layer around the particle is also laminar and a time-dependent wake is formed on the downwind side. The model must reproduce the alterations to the particle structure and shows the build-up of the ash layer with time. It is assumed that heterogeneous reactions (R 13.1) and (R 13.2) take place inside the particle (on the walls of the particle pores) and on the external particle surface. The reactions produce both CO and CO_2 and, if oxygen is available, CO can be further oxidized to CO_2 in the particle voids and in the air flow.

The computational domain is shown in Figure 13.1. It is divided into the gas-flow region (Interior-1) and the porous particle (Interior-2 and Interior-3). In Interior-1 the laminar incompressible Navier-Stokes equations have been solved together with equations for the energy balance, the total gas mass balance and the mass balance for each component. The following species are taken into consideration, CO, CO_2, H_2O, N_2 and O_2. Only CO oxidation is present, with the consumption rate calculated as [96]:

$$\begin{aligned} \frac{\mathrm{d}[\mathrm{CO}]}{\mathrm{d}t} &= -2.239 \cdot 10^{12} \cdot \exp\left(-\frac{20\,157}{T}\right) \cdot [\mathrm{CO}] \cdot [\mathrm{O_2}]^{0.25} + \\ &+ 5 \cdot 10^{8} \cdot \exp\left(-\frac{20\,157}{T}\right) \cdot [\mathrm{CO_2}] \end{aligned} \tag{13.2}$$

For the porous particle (Interiors-2 and -3) the continuity equation is written separately for the gas present in the particle voids:

$$\frac{\partial(\rho_{\mathrm{g}} \cdot \varepsilon)}{\partial t} = \dot{S}_{\mathrm{g}} \tag{13.3}$$

and for solids:

$$\frac{\partial(\rho_{\mathrm{true}} \cdot (1-\varepsilon))}{\partial t} = \dot{S}_{\mathrm{C}} \tag{13.4}$$

where the gas-phase mass source $\dot{S}_{\mathrm{g}}$ and the solid-phase source $\dot{S}_{\mathrm{C}}$ are calculated as:

$$\dot{S}_{\mathrm{g}} = -\dot{S}_{\mathrm{C}} = \dot{S}_{\mathrm{r,oxy}} + \dot{S}_{\mathrm{r,B}} \tag{13.5}$$

In the above equations the source terms $\dot{S}_{\mathrm{g}}$ and $\dot{S}_{\mathrm{C}}$ are calculated using $\dot{S}_{\mathrm{r,oxy}}$ and $\dot{S}_{\mathrm{r,B}}$ which represent the overall carbon consumption rates (in $\frac{\mathrm{kg}}{\mathrm{m^3\,s}}$) in reaction (R 13.1) and in Boudouard reaction (R 13.2), respectively.

The mass balance for the i^{th} species present in voids of the particle are calculated by solving the following transport equation:

$$\frac{\partial(\rho_{\mathrm{g}} \cdot \varepsilon \cdot Y_i)}{\partial t} = \nabla \cdot (\rho_{\mathrm{g}} \cdot \varepsilon \cdot D_{\mathrm{eff\,i}} \cdot \nabla Y_i) + \dot{S}_{\mathrm{g\,i}} + \dot{R}_i \cdot \varepsilon \tag{13.6}$$

where the source terms $\dot{R}_i$ is the source due to homogeneous CO oxidation while the source terms $\dot{S}_{\mathrm{g\,i}}$ are due to heterogeneous conversion of carbon. No convection term is present in the above equation, and reactants transport inside the particle is due to molecular and Knudsen diffusion only as explained in Section 8.5.1.

The energy equation has been derived assuming thermal equilibrium between the gas and

the solid structure:

$$\frac{\partial}{\partial t}(\varepsilon \cdot \rho_{\mathrm{g}} \cdot h_{\mathrm{g}} + (1-\varepsilon) \cdot \rho_{\mathrm{true}} \cdot h_{\mathrm{s}}) = \dot{S}_{\mathrm{e}} + \dot{S}_{\mathrm{er}} + \dot{S}_{\mathrm{he}} \cdot \varepsilon + \nabla \cdot (\lambda_{\mathrm{eff}}) \cdot \nabla T \tag{13.7}$$

The S_{e}-source represents the heterogeneous reactions. The term S_{er} is present in Interior-3 only, and it takes into account the radiation exchange between the particle and the surroundings.

The variation of the porosity (ε) with time and space has been calculated according to the random pore models described in Section 8.6.3 in which the internal surface area is given by:

$$S_{\mathrm{V}} = S_{\mathrm{V}_0} \cdot (1-X) \cdot \sqrt{1 - \psi \cdot \ln(1-X)}$$

13.3. Model predictions

Among all the results presented in [30], only the ones describing the capability of the method to predict conversion of large particles will be here shown. A few seconds after initialization of the calculations, the flow field shown in Figure 13.2 has been formed. The flow is close to the classical laminar flow around a sphere with stagnation on the upwind side and a wake (with a recirculation zone) on the downstream side.

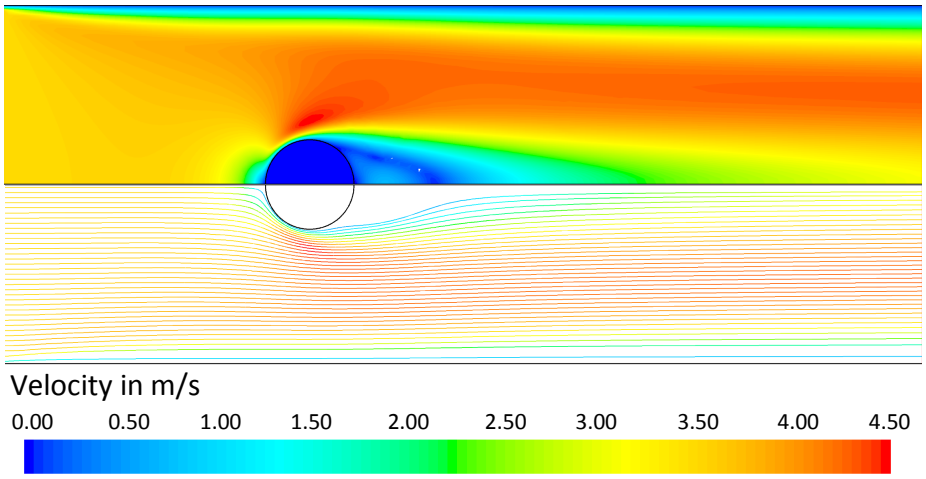

Figure 13.2.: Axial velocity profiles (top) and streamlines (bottom) at 60 s. The air flows from left to right. [30]

In Figure 13.3 and Figure 13.4, the contours of the temperature field and the CO concentration are reported at four different conversion times. In those figures, the black contour-line shows the particle boundary so that the region outside the particle, the ash layer and the reacting core can be identified. A thin high-temperature reacting layer moves inward to the particle center, and the reacting layer temperature remains approximately constant at around 2000 K. At 60 s, the temperature inside the particle is already high, indicating rapid heat conduction.

Carbon monoxide is present inside the particle already in early times, produced by heterogeneous reactions in the reacting layer. Diffusion towards the center of the particle explains the presence of CO in all the shrinking core. The carbon monoxide leaving the reacting surface towards the particle surface is then oxidized to carbon dioxide, and the oxidation is completed already within the ash layer. It is worth noticing that both Figures indicate an asymmetrical carbon oxidation process due to differences in oxygen transport rates.

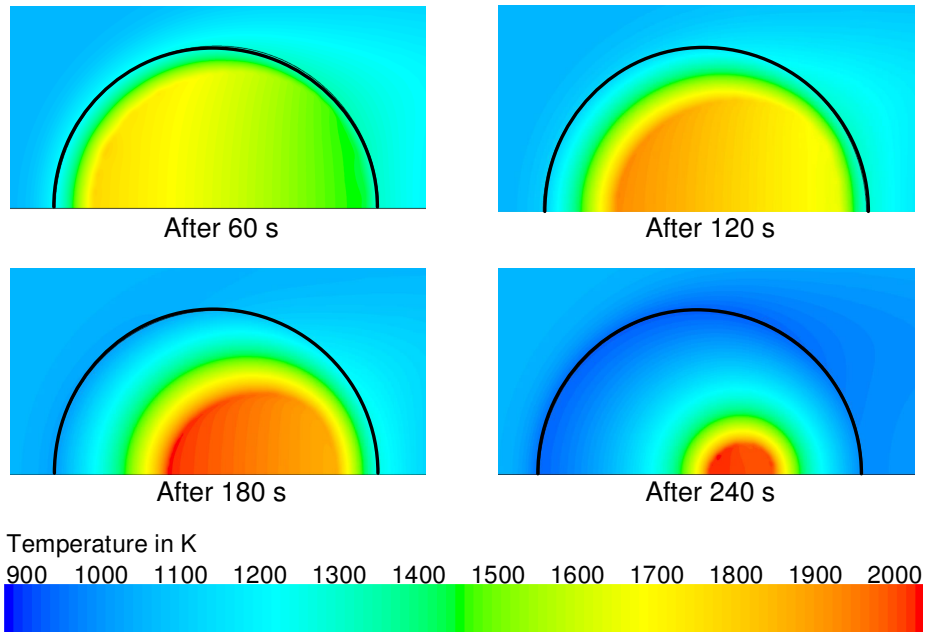

Figure 13.3.: Temperature in the particle and in its vicinity. [30]

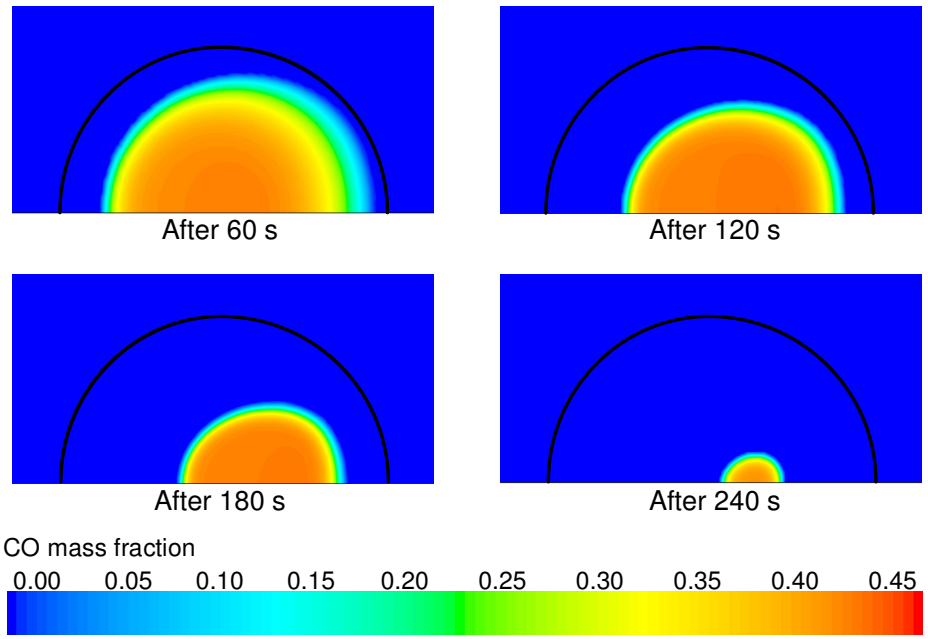

Figure 13.4.: Carbon monoxide mass fraction in the particle and in its proximity. [30]

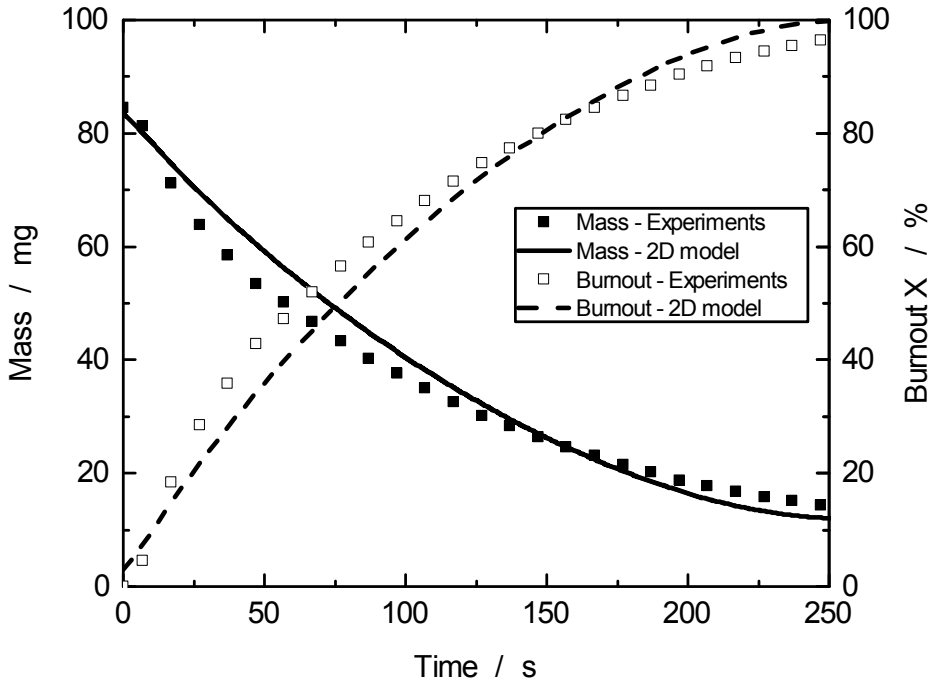

Figure 13.5.: Measured [38] and computed particle mass loss

In Figure 13.5 the measured and the calculated particle mass loss are compared. It is evident that the mass loss predictions agree well with the measured data during all the oxidation time. It is important here to remind that no corrections to the mathematical model are needed to slow-down the char conversion rates at the end of the process since the decreased conversion rates at high burnouts are due to the decreased reacting layer volume and generally due to alterations to the particle morphology.

Also, the comparison between measured and calculated particle surface temperature presented in Figure 13.6, indicate a good agreement with the computed temperature. The CFD predictions are slightly higher than the averaged temperature of about 50 K [1]. At around 50 s the hemisphere-averaged particle surface temperature reaches a maximum at around 1300 K and afterward, since the char reaction front moves gradually inside the particle, the surface temperature decreases due to convective and radiative heat losses.

A further analysis has been presented in [30], exploring deeper the mechanisms underling the oxidation of large particles. The carbon conversion rates, $\dot{S}_{\mathrm{r,oxy}}$ and $\dot{S}_{\mathrm{r,B}}$ for the direct oxidation and for the Boudouard reaction, respectively, are presented in Figure 13.7. At around 130 s the rates are equal indicating a preference of the carbon structure to reacts with oxygen. At a successive conversion stage, the carbon is primarily consumed in the Boudouard reaction, and oxygen reacts mainly to the formed carbon monoxide. This explanation underlines the importance of both the Boudouard reaction and the CO_2 diffusion inside the particle in predicting oxidation of large particles.

[1] The value indicated by the camera is affected by uncertainties and variation of the surface emissivity. The shown temperatures are calculated using a fixed value for the emissivity, and no attempt has been made to improve the predictions (see [30]).

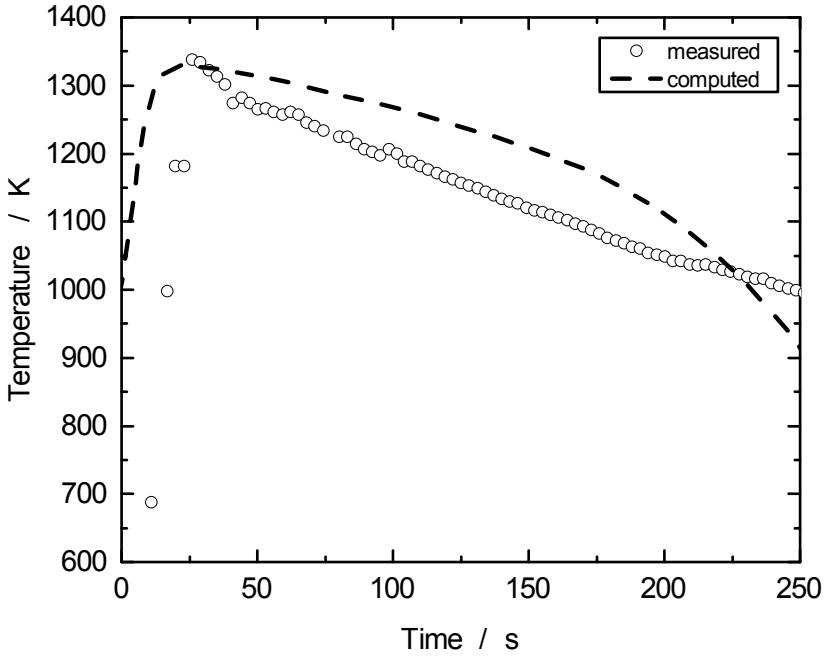

Figure 13.6.: Computed and measured [38] surface mean particle temperature on the downwind side [30]

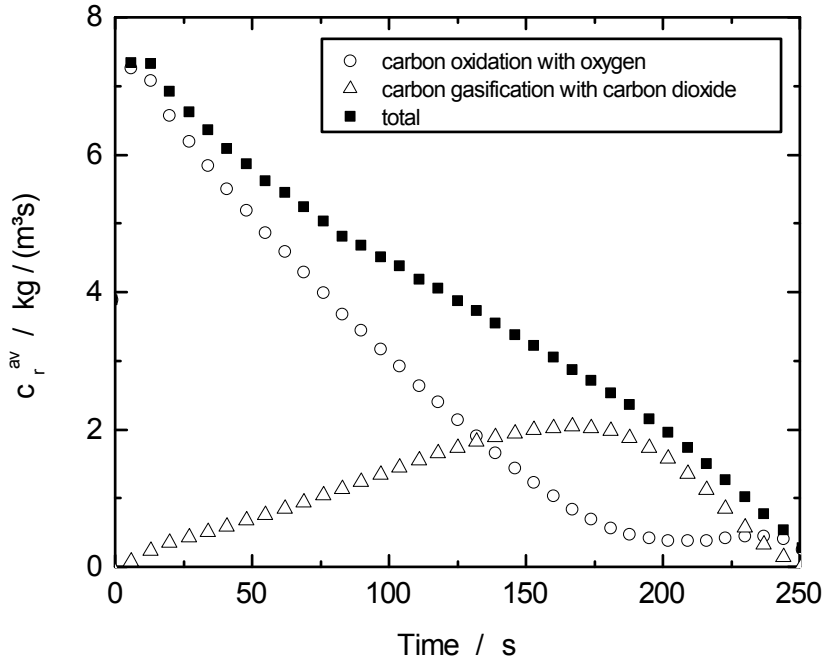

Figure 13.7.: Calculated char conversion rates due to heterogeneous reactions [30]

14. Mild combustion

The exhaust gases from most industrial processes contain considerable enthalpy. To save energy, it is essential to recover as much as possible of this wasted henthalpy or in other words to lower the final exhaust temperature at which the combustion products are released to the atmosphere. In most cases, one avoids lowering the temperature below the dew point to prevent condensation.

There are several ways of implementing heat recovering. The first method consists in preheating the load. On continuous furnaces, for example, an added unfired preheat suction can preheat the load with free heat that would otherwise have been discharged up to the stack. Other examples include a long inlet tunnel on a conveyor furnace, an economizer on a boiler, a preheat added to a cement kiln. A second possibility is to recirculate the exhaust energy, preheating the air using heat exchangers. This method (see the detailed information in Section 14.1) has the promising advantage to increase the furnace efficiency and reduce the fuel consumption, but as a drawback, the emissions (mainly of NO_x) increase dramatically with the increase of the preheat.

A new technology named initially HTAC (an acronym for High-Temperature Air Combustion) has been developed with the goal of maintaining the high degree of preheat and reducing the emissions [228]. This technology is also known by different names, namely MILD combustion (Moderate or Intensive Low-oxygen Dilution) (often written merely as mild combustion) and even FLameless Oxidation (FLOX). The combustion characteristics of the MILD applications differs considerably from the one encountered in standard combustion therefore considerable efforts have been made to investigate the capability of the CFD approach to predict those distinctive characteristics.

In the first part of this chapter a short introduction about energy balances in furnaces is presented, and successively, the MILD method for increasing the efficiency of the plant is discussed and finally results of the application of the solid fuel conversion modeling to MILD combustion experiments are presented.

14.1. Mild combustion

MILD is a combustion technology which essence is having the fuel oxidized in an environment that contains a substantial amount of inert (flue) gases (see [228, 310]). Several technological realizations achieve this result, and two, perhaps the most common ones, are shortly described here. In the first method, the combustion air is provided by a central, strong (high-momentum) air jet that is surrounded by a number of weak (low-momentum) fuel jets (in industrial applications typically two jets are used). These weak fuel jets are positioned away from the central air jet to inject the fuel into recirculated combustion products and, by doing so, to dilute the fuel before it mixes with the combustion air stream.

The second method can be characterized by a central fuel jet and some air jets positioned in the relative vicinity of the central fuel jet. In both realizations, little combustion occurs within the natural gas jets and the temperature rise along the fuel is almost exclusively due to the entrainment of hot combustion products. A similar process undergoes the oxidizer jets. The process taking place within both jets can be named *preconditioning* of the fuel and it results in a mixture containing a significant amount of hot combusted gases diluting the fuel and the oxidizer. The

fuel does not ignite until it merges into the oxidizer jet. For clean gaseous fuels that do not contain any fuel-bounded nitrogen, this results in very low NO_x emissions even if the combustion air stream is preheated to temperatures more than 1000 °C. Chemical reactions take place in almost the entire volume of the combustion chamber and uniformity of both the temperature and the chemical species fields are characteristics of this technology [230]. Low gradients of the relevant scalars are present and induce a smaller impact of turbulent fluctuations than for conventional combustion.

14.1.1. Furnace energy balance

To quantify the characteristics of MILD combustion, a simple approach based on a global energy balance is here presented. The furnace efficiency η can be generally written in the following way:

$$\eta \equiv \frac{\dot{Q}_{used}}{\dot{H}_{input}} = 1 - \frac{\overline{c_p}(T_{out})(T_{out} - T_0)}{\overline{c_p}(T_{ad})((T_{ad} - T_0)} \tag{14.1}$$

where the outlet temperature T_{out} and the adiabatic temperature T_{ad} are used. The two mean specific heats $\overline{c_p}$ cannot be in general simplified because they are function of two different temperatures. If the temperature T_{out} is high, then its dependency from T is not anymore so pronounced and it can be assumed that $\overline{c_p}$ at both temperatures T_{out} and T_{ad} are equal, leading to the final (but approximated) relation for the efficiency of a combustion chamber:

$$\eta = 1 - \frac{T_{out} - T_0}{T_{ad} - T_0} \tag{14.2}$$

In Figure 14.1 the efficiency η is plotted against the furnace exit temperature for three different fuels (blast furnace gas, coke oven gas and Gröningen Natural gas) for two different stoichiometries. As shown in the Figure, for higher furnace exit temperatures, the efficiency drops, particularly in processes where high temperature is achieved. The thermal energy contained in the exhaust gases can be recirculated back into the combustion chamber preheating the comburent air. Using this method, the efficiency of the whole process (furnace plus the heat exchangers) increases for two reasons:

1. The adiabatic temperature increases, increasing the furnace efficiency;
2. The heat is recirculated, increasing the efficiency of the whole process (furnace plus heat recirculation).

14.1.2. Increase of the adiabatic temperature

The adiabatic temperature is calculated from the equation:

$$h_{in} = (1 + \lambda \cdot L) \int_{T_0}^{T_{ad}} c_{p,out}(T)\, dT = (1 + \lambda \cdot L) h_{ad} \tag{14.3}$$

where L is the air requirement at the stoichiometric condition (in kg_{air}/kg_{fuel}) and λ is the stoichiometric ratio. Both specific enthalpies can be explicitly written as a function of the mean specific heat $\overline{c_p}$:

$$LCV + \lambda \cdot L\overline{c_p}(T_A)(T_A - T_0) = (1 + \lambda \cdot L)\overline{c_p}(T_{ad})(T_{ad} - T_0) \tag{14.4}$$

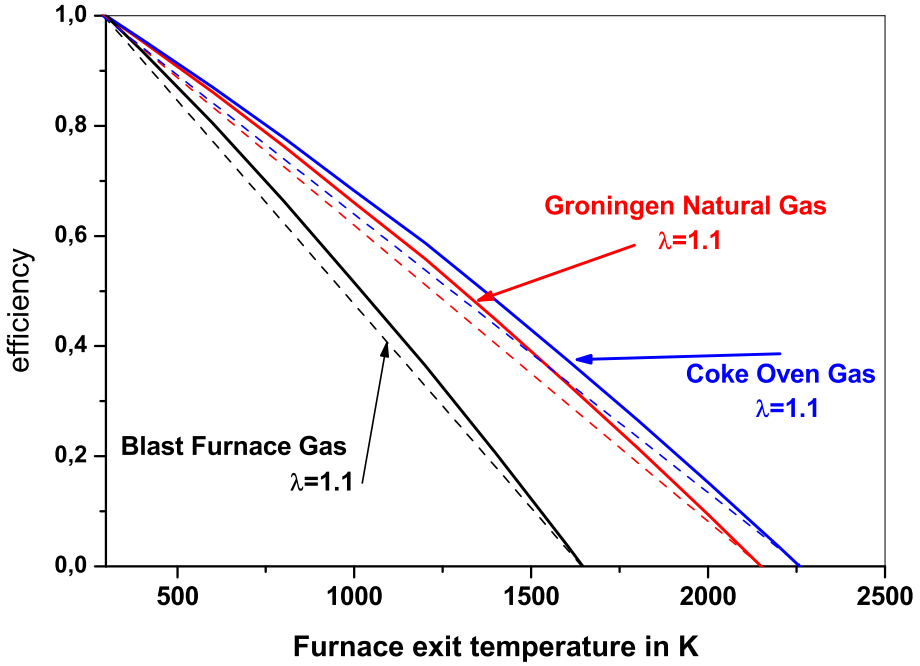

Figure 14.1.: Furnace efficiency η plotted against the furnace exit temperature for three different fuels (blast furnace gas, coke oven gas and Gröningen Natural gas) for two different stoichiometries

and consequently, the adiabatic temperature can be derived:

$$T_{ad} = T_0 + \frac{LCV + \lambda \cdot L\overline{c_p}(T_A)(T_A - T_0)}{((1 + \lambda \cdot L)\overline{c_p}(T_{ad})} \tag{14.5}$$

From the previous equation it is evident that the adiabatic temperature T_{ad} increases with the increase of the preheat temperature T_A. In Figure 14.2 the adiabatic temperature is plotted versus the temperature of the comburent for several oxygen concentrations. The same figure is used to argue that, while a reduction of thermal NO_x can be achieved by reducing the local adiabatic temperature, the reduction of local oxygen concentration also helps in decreasing the local temperature. With a preheat of 1500K, 8% (in mass) oxygen concentration in the comburent, is required to reduce the adiabatic temperature to the level of conventional combustion (no preheat and 23% oxygen in air).

The following expression gives the efficiency of the combustion chamber:

$$\eta = 1 - \frac{(1 + \lambda \cdot L)\, h_{out}}{LCV + \lambda \cdot Lh_A} \tag{14.6}$$

14.1.3. Heat recirculation

The efficiency of the whole process (furnace plus recirculation) increases after recirculating part of the energy contained in the exhaust gases back to the combustion air. Because preheating

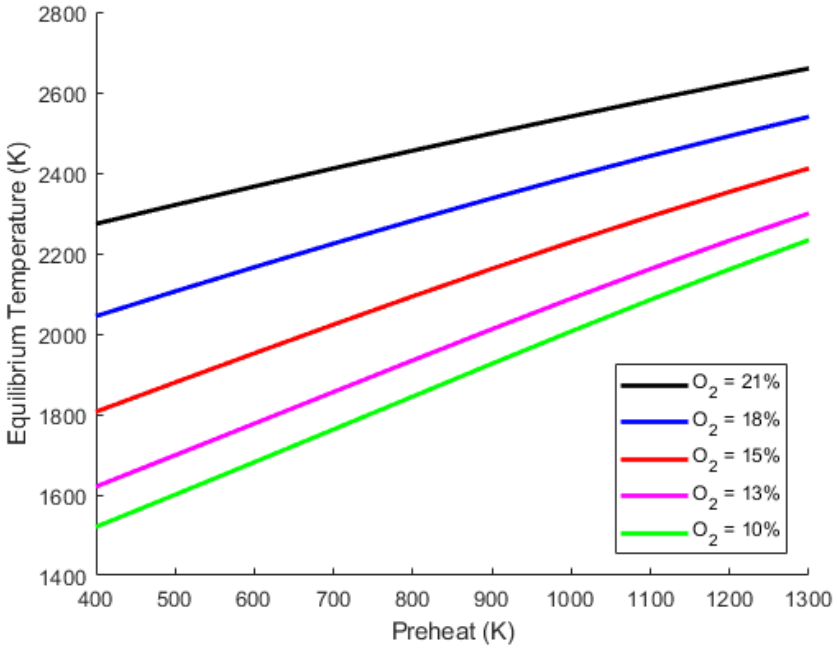

Figure 14.2.: Adiabatic temperature as a function of the preheat temperature for several O_2 concentration

the fuel is energetically not so efficient as preheating the comburent, from now on in all the equations the physical enthalpy of the fuel will be dropped [1]. The air can be preheated using two heat exchanger type:

- Regenerators for preheat up to medium level;
- Recuperator for a high degree of preheat temperatures.

The efficiency of the process can now be calculated considering a control volume comprehensive of the recirculating heat. The efficiency is then calculated by the formula:

$$\eta = 1 - \frac{(1 + \lambda \cdot L)\, h_{out}}{LCV} \tag{14.7}$$

where now h_{out} is the specific enthalpy of the exhaust gases after the heat exchangers.

14.1.4. Fuel savings

The same results can be seen in term of fuel savings FS defined as:

$$FS = 1 - \frac{\dot{m}_{F,preheat}}{\dot{m}_{F,No-preheat}} \tag{14.8}$$

[1] The preheat of the fuel has two drawbacks. Fuel at high temperature is not safe due to problems related to self-ignition. Secondly, because the maximum preheat temperature must be equal to the exhaust gas temperature the amount of heat recirculated is lower than in the case of air preheating due to the factor $\lambda \cdot L$.

Introducing the mass flow of the fuel from the equation ($\dot{Q}$ is the amount of used heat into the process and this quantity must remain constant):

$$\dot{m}_F = \frac{\dot{Q}}{LCV + h_F + \lambda \cdot Lh_A - (1 + \lambda \cdot L)h_{out}} \tag{14.9}$$

into the Equation 14.8, the equation for the fuel saving can be obtained:

$$FS = 1 - \frac{LCV - (1 + \lambda \cdot L)h_{out}}{LCV - (1 + \lambda \cdot L)h_{out} + \lambda \cdot Lh_A} \tag{14.10}$$

Considering now that the efficiency of a furnace without preheat is given by equation 14.7, after some algebra Equation 14.10 can be written in its final form:

$$FS = 1 - \frac{\eta_{not,P}}{\eta_{not,P} + \frac{h_A}{LCV}} \tag{14.11}$$

In Figure 14.3 the fuel savings (in %) are reported as a function of the Air preheat for several Furnace exit temperatures. The regions in which regenerators (heat transfer efficiency between 0.2 and 0.5) and recuperators (heat transfer efficiency between 0.8 and 0.95) work are also marked. The figure shows clearly that the potential for fuel savings increase with the Air preheat and it is more pronounced if the furnace exit temperature is high (even for the same level of Air preheat). The high level of the savings in the high-temperature process forces every furnace to be equipped with a system of energy recirculation.

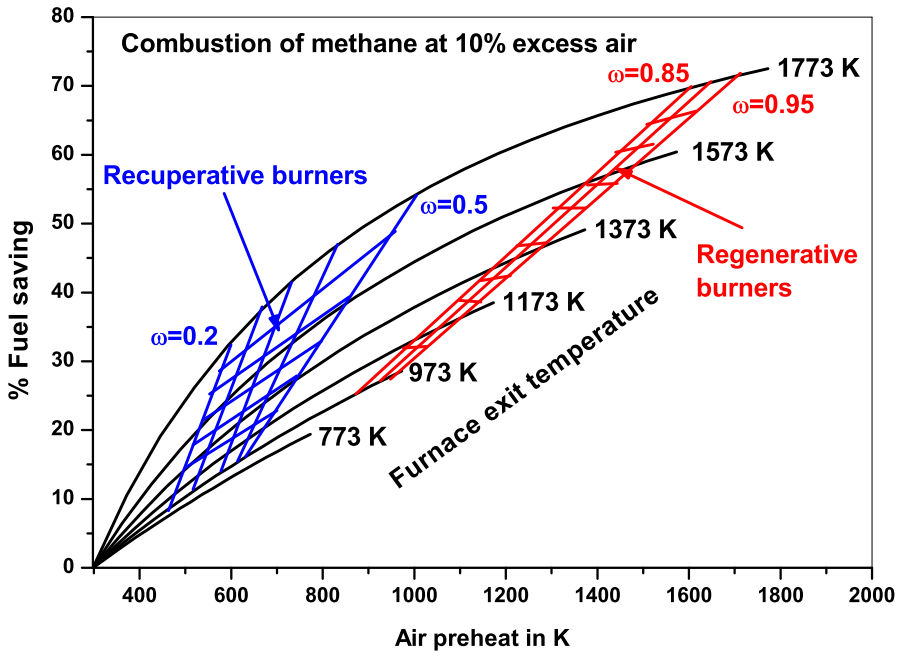

Figure 14.3.: Fuel savings as a function of the Air preheat for several Furnace exit temperatures

14.2. Validation of the CFD model

In the following sections a complete program for the validation of the CFD tool in semi-industrial scales experiments of a realization of the MILD combustion is presented. The results of the calculations are taken from [310] and [311].

The International Flame Research Foundation (IFRF) in the 90's carried out experiments on the applicability of the MILD combustion concept to gas, oil and pulverized coal firing [264, 410, 400]. In the test of pulverized coal combustion, a high volatile coal (1.4% N) was combusted with high-temperature air and the lowest NO_x emissions were in the range 160-175 ppm (at 3% O_2) indicating a high NO_x reduction potential of this technology also for nitrogen-containing fuels (see Table 14.1).

Fuel	NO_x IN	NO_x out	Δ
Gas	110	140	30
LFO	90	95	5
HFO (0.4 % N)	70	215	145
Coal (1.4 % N)	110	220	110

Table 14.1.: Input-output NO_x measurements in the IFRF HTAC (MILD) experiments

Among the experiments carried out by the IFRF, only the experiments with coal as fuel will be presented below (see also [310]).

14.2.1. The experimental setup

The MILD experiments [400, 410] were carried out in a refractory lined IFRF furnace schematically shown in Figure 14.4. The furnace has a square cross section of 2 m times 2 m and its length is 6.25 m. It consists of 11 water-cooled segments. The wall temperatures of all segments were monitored using thermocouples located at the top and sidewalls of the furnace. The furnace heat extraction was monitored by measuring the volumetric flow rate and the temperature rise of the cooling water circulating in each segment.

The burner consisted of a central 125 mm diameter pipe supplying the oxidizer and two 27.3 mm coal injectors (pipes), which were located at 280 mm away from the burner center. The burner operated at 0.58 MW fuel input and the vitiated air temperature was 1623 K. The vitiated air stream contained 22% (wet, by weight) oxygen and 89 *ppm* (wet, by weight) NO_x. The vitiated air and the fuel streams were supplied into the furnace with injection velocities of 65 and 26 $\frac{\mathrm{m}}{\mathrm{s}}$, respectively. The fuel is a high volatile bituminous coal. Its ultimate and proximate analysis, as well as its volatilization velocity and the char reaction rate were experimentally determined to obtain the parameters needed for the mathematical modeling.

The measurements were taken at several traverses in a horizontal plane cutting through the burner centreline (see Figure 14.4). In-flame measurements included mean and rms axial velocities, gas temperature, gas composition (CO_2, O_2, CO, NO_x, C_nH_m), burnout, solids concentration, total irradiation and total radiative fluxes at the furnace wall. The velocity measurements were performed using the IFRF water cooled Laser Doppler Velocimetry (LDV) probe. In-flame temperatures were measured using a suction pyrometer equipped with a type B thermocouple (Pt-6%Rh/Pt-30%Rh). Local in-flame gas compositions were measured using a gas sampling probe. The measurements of total irradiation and total radiative heat fluxes were performed using a standard IFRF narrow-angle radiometer and an ellipsoidal radiometer, respectively. A detailed description of these measurements can be found in [264, 410].

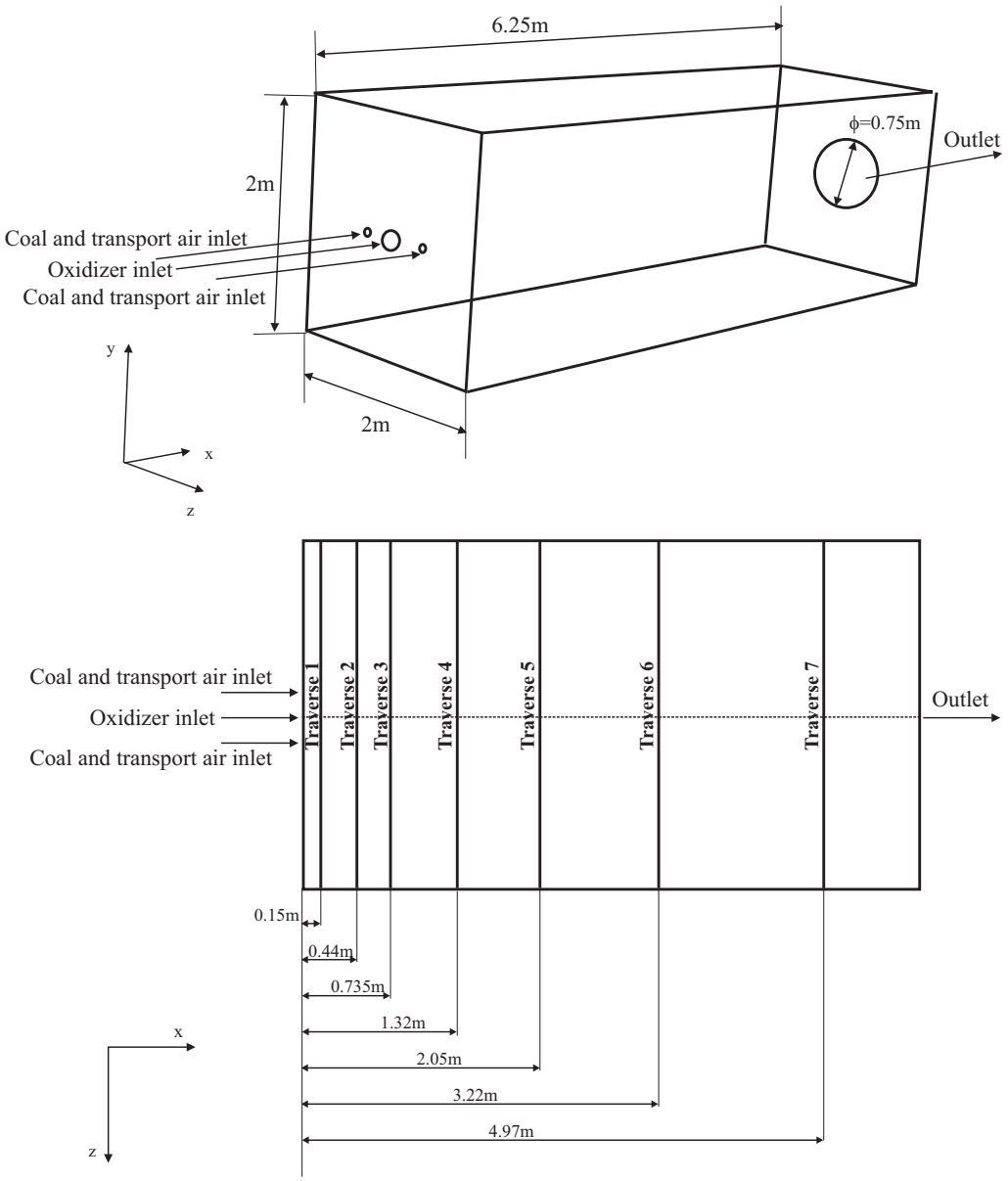

Figure 14.4.: Geometry of the MILD Experiment at IFRF [310]

The input conditions are summarized in Table 14.2.

	Mass flow $\frac{kg}{h}$	Vel. $\frac{m}{s}$	Temp. K	Enthalpy MW	Composition weight % wet
Coal	66	-	-	0.58	
Coal transport air	130	26	313	-	O_2 =23, N_2 =77
Oxidizer (vitiated air)	675	65	1623	0.30	O_2 =22, H_2O =9.5, CO_2 =12.5, NO =$89 \cdot 10^{-4}$, N_2 =56
Furnace exit	871	30	1503	0.36	O_2 =2.8, H_2O =11, CO_2 =31, NO =$250 \cdot 10^{-4}$, N_2 =55.2

Table 14.2.: Experimental conditions

14.3. The mathematical model

The equations used in modeling the IFRF experiment has been described with details in [310] to which we refer. Substantial efforts have been allocated into a proper numerical description of the coal combustion. To this end, several fuel specific subroutines have been developed. The Venezuelan bituminous Guasare coal was combusted [264] which, according to the ASTM classifications it is a high volatile bituminous A coal. The proximate and ultimate analysis of Guasare coal are given in Table 14.3 and Table 14.4, respectively.

composition	**wt%**
moisture (105 °C)	2.9
volatile matter	37.1
fixed carbon	56.7
ash	3.3
LCV	31.74 $\frac{MJ}{kg}$

Table 14.3.: Guasare coal proximate analysis

composition, wt% daf	**coal**	**char**	**volatiles**
C	81.6	92.6	72.51
H	5.5	1.3	9.10
N	1.5	1.7	1.3
O	10.7	4.0	16.3
S	0.6	0.4	0.8

Table 14.4.: Guasare coal ultimate analysis (dry, ash free basis)

The Rosin-Rammler distribution function with the mean diameter of 42 µm and the spread

of 1.36 represents the measured data nicely, and it is shown in Figure 14.5.

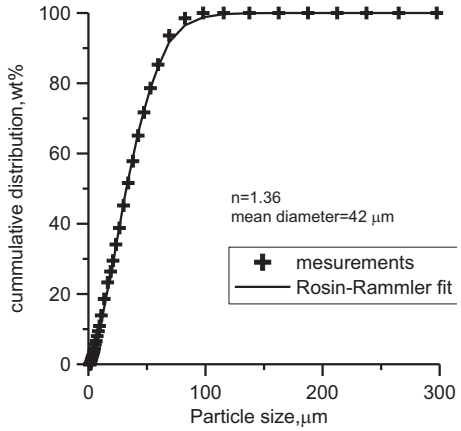

parameter	value	unit
mean diameter	42	μm
max. diameter	300	μm
min. diameter	10	μm
spread parameter	1.36	

Figure 14.5.: Guasare coal particle distribution (left) and distribution parameters (right)

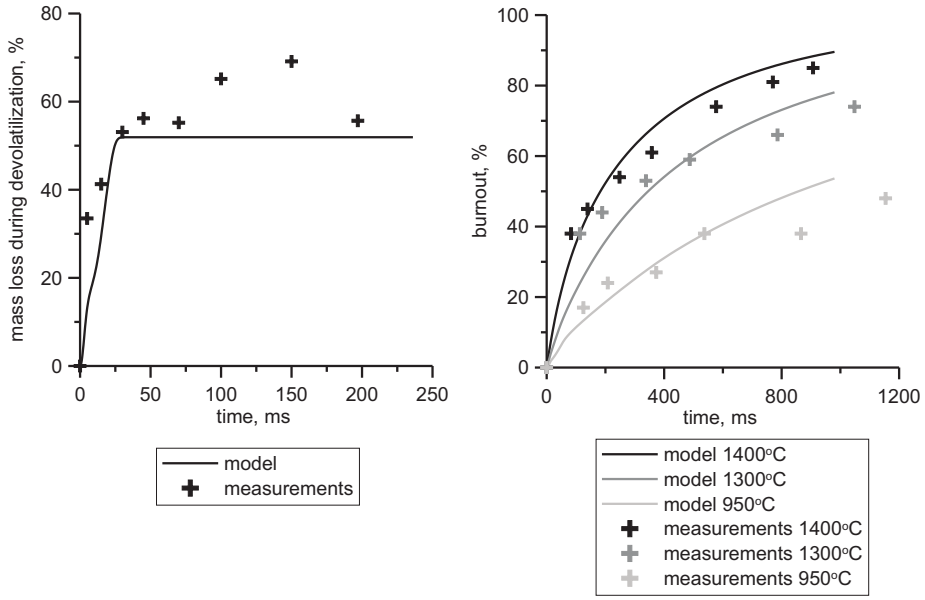

Figure 14.6.: Devolatilization and burnout measurements [369] with the CPD (left) and the intrinsic (right) model fittings for Guasare coal

The rate of the devolatilization process has been modeled using the CPD model described in Section 6.2.9. The parameters have been derived using the IFRF experimental data [369] on the characterization of both devolatilization and char combustion of Guasare coal. Figure 14.6 (left) shows the devolatilization curve obtained using the IFRF Isothermal Plug Flow Reactor (IPFR) operated at a 1200 °C temperature. The particle heating rate of these experiments is in the range $10^5 \div 10^6 \frac{\mathrm{K}}{\mathrm{s}}$ depending on the particle size. Under such rapid heating conditions, a 55% high-temperature yield is measured as opposed to 37% ASTM volatiles. The obtained values of the CPD parameters after the fitting are listed in Table 14.5 while the CPD model devolatilization

curve is shown in Figure 14.6 (left) using a solid line. The volatiles are represented in the CFD predictions as $C_{1.20}H_{4.48}O_{0.44}$ which provides the stoichiometric coefficient of 1.5 (see R 14.1).

parameter	symbol	value	unit
Initial Fraction of Bridges in Coal Lattice	p_0	0.5	-
Initial Fraction of Char Bridges	c_0	0	-
Lattice Coordination Number	$\Sigma + 1$	5	-
Cluster Molecular Weight	M_{cl}	300	$\frac{\text{kg}}{\text{kmol}}$
Side Chain Molecular Weight	M_{del}	30	$\frac{\text{kg}}{\text{kmol}}$

Table 14.5.: The derived parameters for the CPD devolatilization model of Guasare coal used in [310]

parameter	symbol	value	unit
Mass Diffusion-Limited Rate Constant	C_1	$5 \cdot 10^{-12}$	$\frac{m^3}{K^{0.75} \cdot s}$
Pre-exponential Factor	A_i	$1 \cdot 10^{-3}$	$\frac{kg}{m^2 s}$
Activation Energy	E_i	50	$\frac{\text{MJ}}{\text{kmol}}$
Char Porosity	Θ	0.74	-
Mean Pore Radius	$\overline{r_p}$	$1 \cdot 10^{-7}$	m
Specific Internal Surface Area	A_g	$2.5 \cdot 10^4$	$\frac{m^2}{kg}$
Tortuosity	τ	$\sqrt{2}$	-

Table 14.6.: The parameters for the intrinsic char combustion model of Guasare coal used in [310]

The intrinsic model for char burnout has been used (see 8.5.1.1). The adaption of the char combustion model to the Guasare coal has been achieved using again the IFRF measurements [369] of Guasare char burnout as a function of time for temperatures of 950 °C, 1300 °C and 1400 °C, see Figure 14.6 (right). These measurements were carried out at 4% oxygen volume fraction. The char morphology data were also measured: the apparent char density equal to 339 $\frac{\text{kg}}{\text{m}^3}$ and porosity equal to 74%. Fixing the mass diffusion-limited rate constant (C_1) at a value of $5 \cdot 10^{-12}$ $\frac{m^3}{K^{0.75} \cdot s}$, the char porosity at the 74%, and the specific surface area at $2.5 \cdot 10^4$ mater^2/kg we optimize values of the kinetic parameters A_i and E_i and n to obtain a proper fit to the IFRF data, as shown in Figure 14.6 (right). The optimization results in the values given in Table 14.6. During the simulation the initial particle diameter remains unaltered through the char combustion processes while the rate of char oxidation is calculated using 8.66. The char density is changing during the char burnout process according to the conservation of the mass law.

The other models used in the simulation are quickly listed below:

- The $k - \varepsilon$ model (see section 4.3.1.3) for the turbulence;

- The EDC model (see Section 5.8) for the turbulence-chemistry interaction;
- The DPM model (see Section 10.2) for the tracking of the coal particles;
- The DO model (see Section 4.8) for the solution of the Radiative heat transfer equation with the gas absorption coefficient from the WSGGM described in [340];
- The fuel, thermal, prompt and N_2O paths as well as NO reburning have been considered, as shown in Figure 14.7 (see for the detail of the model Section 9.2). It is assumed in [311] that all fuel nitrogen, both from volatiles and char, is converted into HCN that can undergo reduction or formation of NO. The source term for the NO specie is then given by the sum of the six following terms:

$$\begin{aligned} S_{NO} &= S_{NO,fuel} + S_{NO,hom.reburn} + S_{NO,het.reburn} \\ &\quad + S_{NO,thermal} + S_{NO,propmpt} + S_{NO,N2O} \end{aligned} \tag{14.12}$$

  corresponding to the NO_x path taken into consideration.

Combustion of the volatiles has been simplistically represented by two overall reactions (see for more details about the impact of this simplification in [2]):

$$\mathrm{C_{1.2}H_{4.48}O_{0.44}} + 1.5\,\mathrm{O_2} = 1.2\,\mathrm{CO} + 2.24\,\mathrm{H_2O} \tag{R 14.1}$$

$$\mathrm{CO} + 0.5\,\mathrm{O_2} = \mathrm{CO_2} \tag{R 14.2}$$

The particle-radiation interaction was taken into account assuming that the particles are very large opaque and gray spheres (implying that the geometric optics theory holds), which reflect diffusely. The absorption coefficient for the particles (a) is given by a constant value of 1.5 m^{-1} and kept constant through the furnace volume. The value has been derived using the narrow-angle radiance measured by the IFRF [264], see Section 14.4.

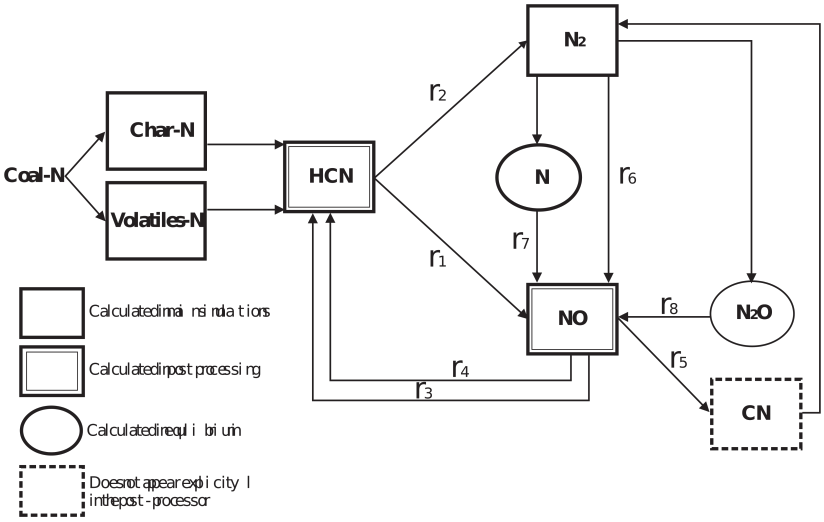

Figure 14.7.: Path of NO formation and reburning path modeled.

14.4. The results

Furnace outlet The temperature, oxygen, carbon oxides and nitric oxide concentrations and char burnout at the outlet of the furnace for calculations and measurements are summarized in Table 14.7. The furnace exit temperature is very close to the measured value and the difference is about 50 K which corresponds to 2.37% of the furnace thermal input.

parameter	**unit**	**experiment** [264]	**predictions** [311]
T	K	1503	1555
O_2	vol. % dry	3.1	2.52
CO	vol. ppm dry	<50	10
CO_2	vol. % dry	25.50	23.93
NO_x	vol. ppm dry	320	333
Char burnout	%	99.4	100
Carbon in ash	%	14.95	none

Table 14.7.: Computed and measured values at the furnace exit

Flow field and recirculation In Figure 14.8 the measured and calculated velocities along the seven traverses are shown. At the first traverse, the computed values correspond well with the measured velocities except for the comburent centerline velocities which were measured about 20 $\frac{\mathrm{m}}{\mathrm{s}}$ lower than the calculated values. At the first two traverses, the comburent jet can be clearly distinct from the coal jet. The coal jet merges into the comburent jet near the third traverse and downstream both jets merge and form one stream that can be observed at the next traverses. At a distance of 2m downstream of the furnace front wall (from the fifth traverse onwards) the velocity profile is flat. As shown in Figure 14.8 the size of the recirculation region formed in the furnace and its low magnitude (negative) velocities are well reproduced in the computation.

Temperature field and radiative heat fluxes The temperature profiles along the traverses are given in Figure 14.9. No substantial difference between the model predictions and the measurements can be seen with the exception of the fuel jet at the first traverse. The temperature level, as well as the temperature peaks, are reproduced well by the simulations. Ignition of the fuel jet takes place somewhere between the first and the second traverse so that the peak temperature of around 1800K occurs between the second and third traverses. This feature is again well reproduced in the numerical simulations. From the fourth traverse downwards, the temperature profile is flat since slow combustion proceeds downstream in the furnace, and the temperature level is everywhere around 1600K.

To obtain such a good accuracy of the temperature predictions, it is imperative that the value of the absorption coefficient appearing in the RTE 4.131 is properly selected. Following the method of Lallemant et al. [195] and Sayre et al. [306] the narrow angle radiance measured at the fifth traverse (2 05m) has been used for the calibration. Figure 14.10 shows that using a value of 1 5m which accounts for the soot and particles radiation, the predicted and measured radiation intensities are in good agreement. In the flame region, the predictions are better than in the recirculation zone, where the radiation intensity is over-predicted by about 10%.

The verification of the correctness of the radiative heat transfer procedure is demonstrated in Figure 14.11 showing very good agreement between the measured and the predicted total incident heat flux at the furnace wall. Flatness and high values of the radiative heat flux are

characteristics of mild combustion [407, 411]. The predicted wall temperature, calculated using a coupled heat transfer approach, has an excellent agreement with the measured values, while the radiative heat fluxes at the end of the furnace are under-predicted by most simple models. Most detailed model, based on the flamelet and the GRI mechanism (not shown here), has better accuracy, also at the end of the furnace, due to a better prediction of the flame temperature after the ignition point.

Carbon monoxide concentration field Carbon monoxide profiles are illustrated in Figure 14.12. The highest concentration of CO is about 6%, and it is located at the third traverse. The prediction of its peak value agrees entirely with the measurement. Downstream of the fifth traverse no considerable amount of carbon monoxide is detectable.

Nitric oxide concentration field NO_x concentration profiles are given in Figure 14.13 showing that the model reasonably well predicts its concentrations, not only qualitatively but also quantitatively. It can be observed that the NO formation begins upstream of the first traverse, however, most of the NO is formed upstream of the third traverse in the volatiles released zone. At the second traverse, the highest peak of 900 ppm has been measured. This peak is also well reproduced in the calculations. Downstream of the fourth traverse the nitric oxide profile is flat and of a low level (around 300 ppm). At the outlet 333 ppm NO was calculated and this value agrees very well with the measurements (320 ppm).

Among the six terms which appear in the source for the net NO formation rate (see equation 14.12), the fuel-NO path, the homogeneous NO-reburning path, and the heterogeneous NO-reburning path are significant. The fuel-NO source, $S_{NO,fuel}$, is of the order of $7.8 \cdot 10^{-4}\ \frac{\text{kmol}}{\text{m}^3\,\text{s}}$ while the homogeneous NO-reburning rate, $S_{NO,hom.reburn}$, is around $-2.7 \cdot 10^{-4}\ \frac{\text{kmol}}{\text{m}^3\,\text{s}}$ and the heterogeneous NO-reburning rate, $S_{NO,het.reburn}$, is of the order of $-2.0 \cdot 10^{-4}\ \frac{\text{kmol}}{\text{m}^3\,\text{s}}$. Thus, these three sources are of the same order of magnitude, and the in-flame NO-concentrations are determined by their balance which is then altered due to the NO advection and diffusion. The NO post-processor predicts a rapid reburning occurring already in the fuel jet where NO is formed directly from HCN decomposition.

Integration of the NO sources over the entire furnace volume provides further insight into the NO-mechanisms. The overall NO production rate through the fuel mechanism is calculated to be 18.5 mg_{NO}/s. The NO reburning rate is so that the net NO production rate in the furnace amounts to 7.0 mg_{NO}/s. This figure reproduces exactly the difference between the amount of NO at the furnace exit (11.0 mg_{NO}/s) and at the furnace inlet (4.0 mg_{NO}/s) Thus, only those two terms in the overall NO-balance are significant; the NO generation via the fuel mechanism and the NO reburning mechanism.

Char burnout Figure 14.14 shows both the measured and predicted char burnout along the centerline of the fuel jet. The char burnout predictions are in good agreement with the measured data up to 80% burnout. For higher degrees of burnout the model over-predicts the char oxidation rates, and at the furnace outlet, a complete burnout is predicted (see Table 14.7). This is a consequence of the fact that the parameters of the char combustion model have been derived using the measured data that extend up to 85% burnout. As can be seen in Figure 14.6, an extrapolation of the char model predictions to residence times of 5-6 seconds results in complete burnout. To predict the last stages of burnout, corrections to the char model are needed to slow down the rate as the char oxidation proceeds (see for example [267, 138]).

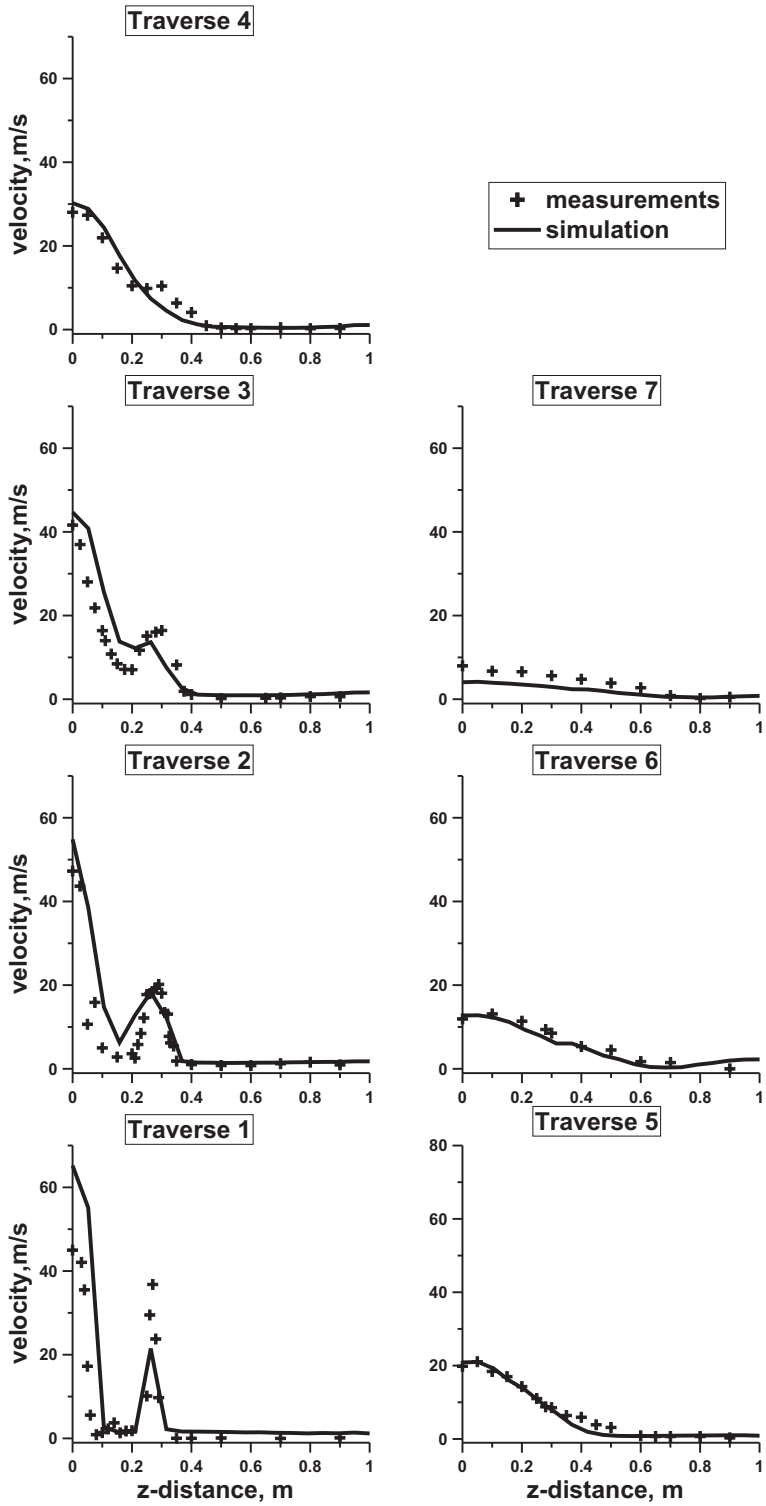

Figure 14.8.: Velocity profiles along the measurement traverses. The measured values taken from [264]. For location of the measurement traverses see Figure 14.4 [310]

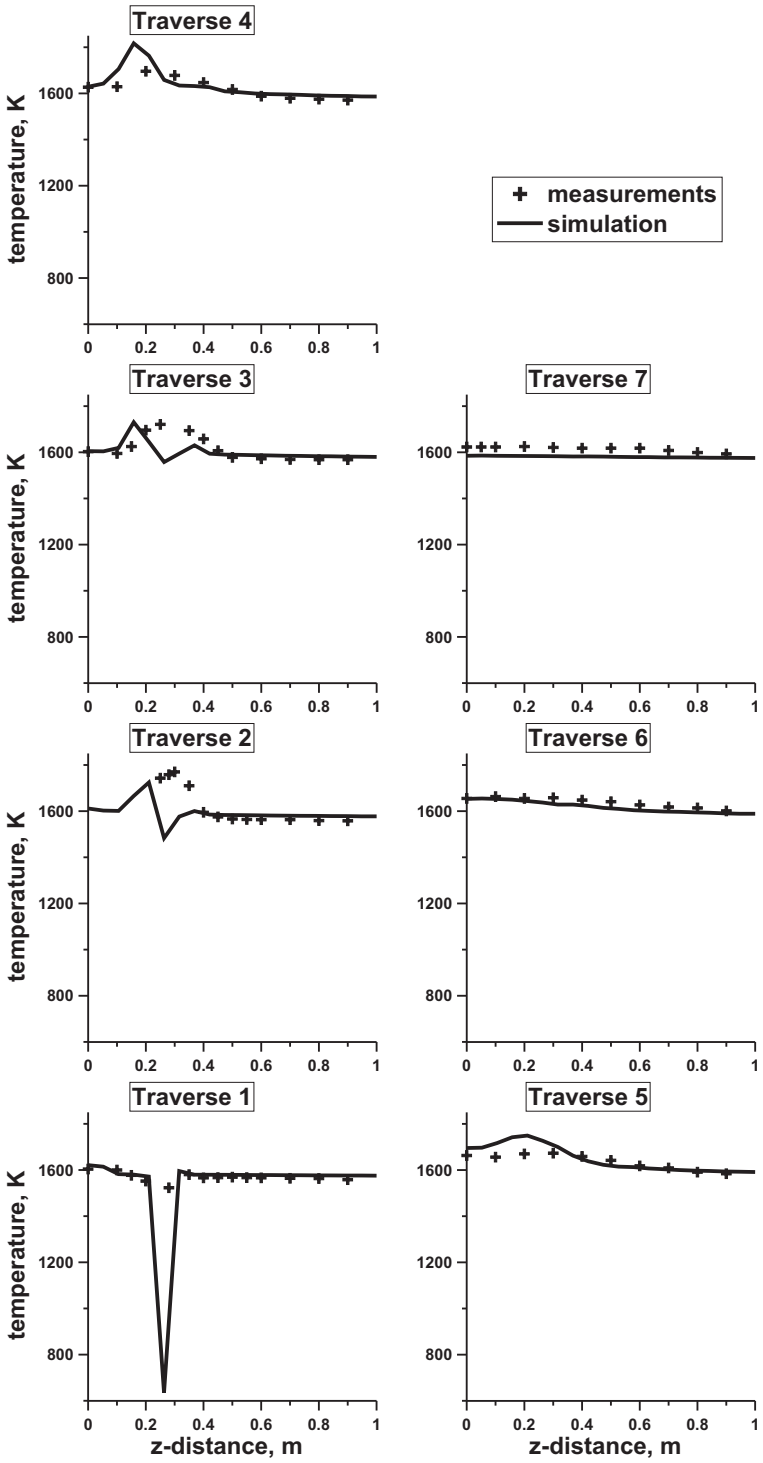

Figure 14.9.: Temperature profiles along the measurement traverses. The measured values taken from [264]. For location of the measurement traverses see Figure 14.4 [310]

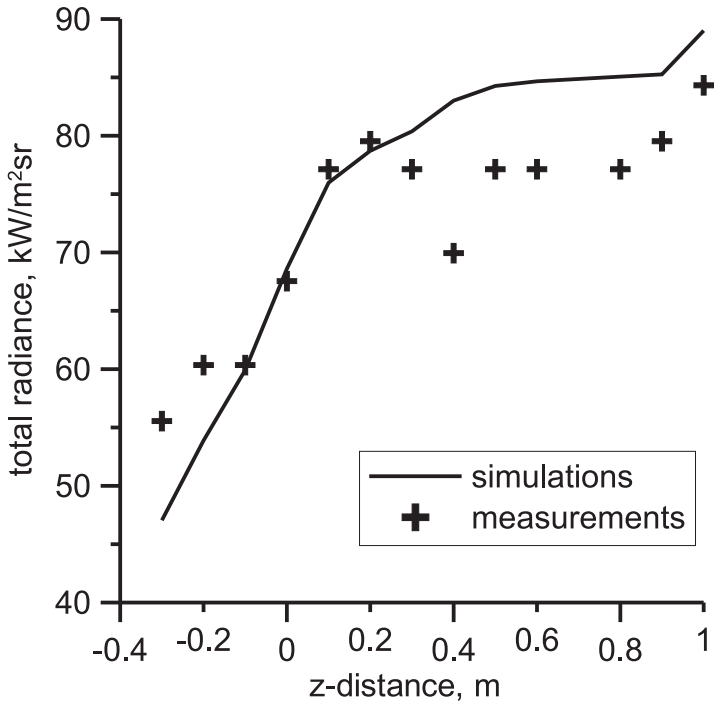

Figure 14.10.: Measured [264] and calculated total radiation intensity for a=1 51m

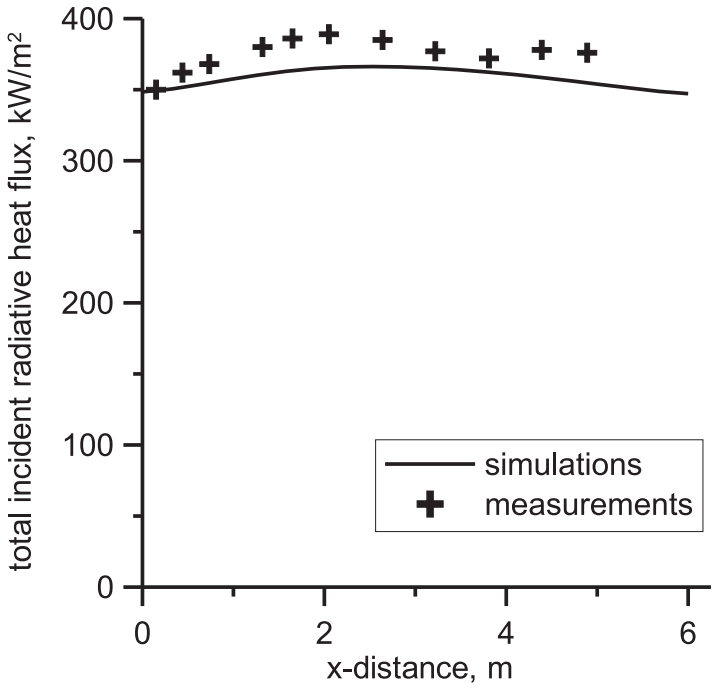

Figure 14.11.: Measured [264] and calculated total incident radiative heat flux [310]

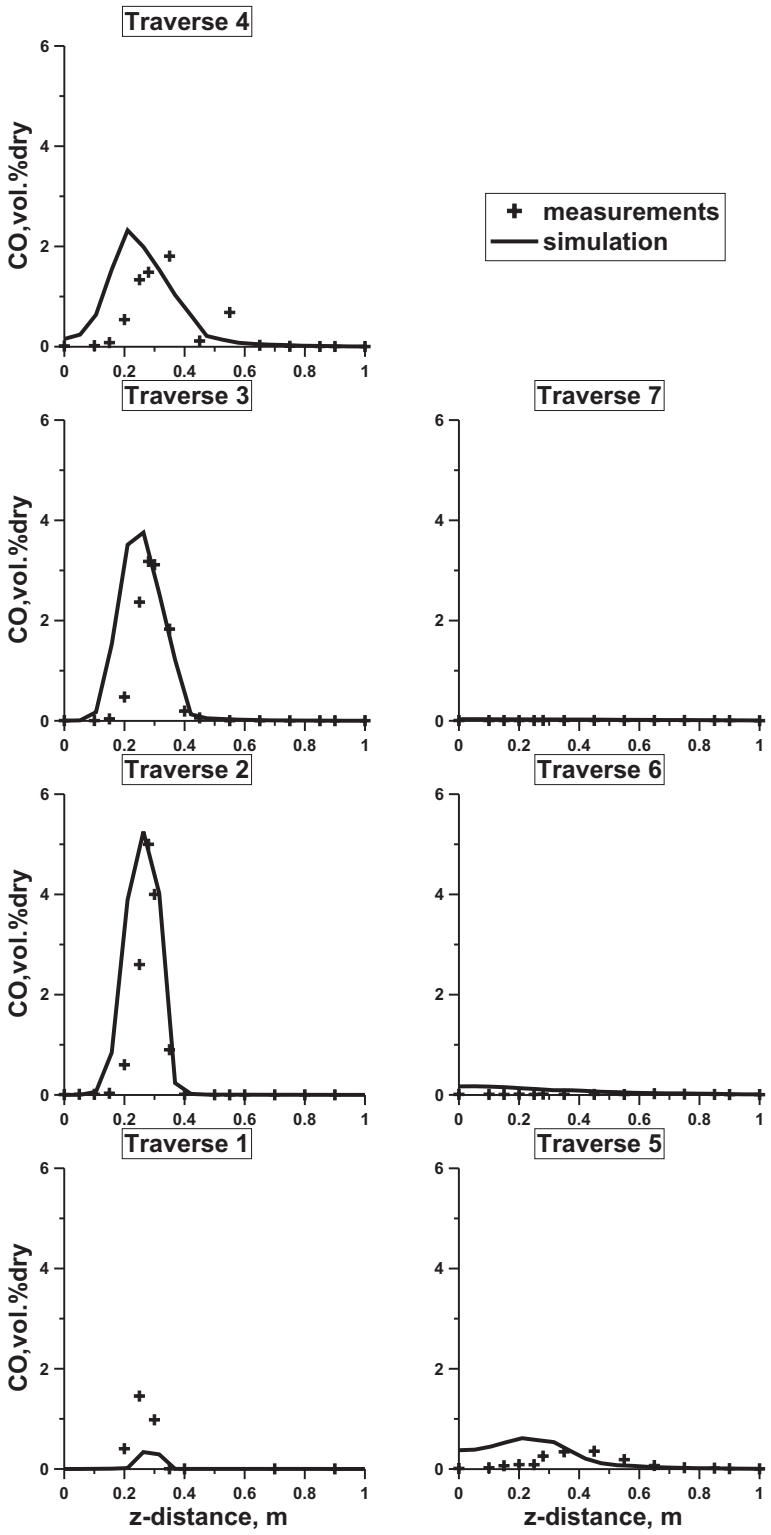

Figure 14.12.: Carbon monoxide concentration profiles along the measurements traverses [310]

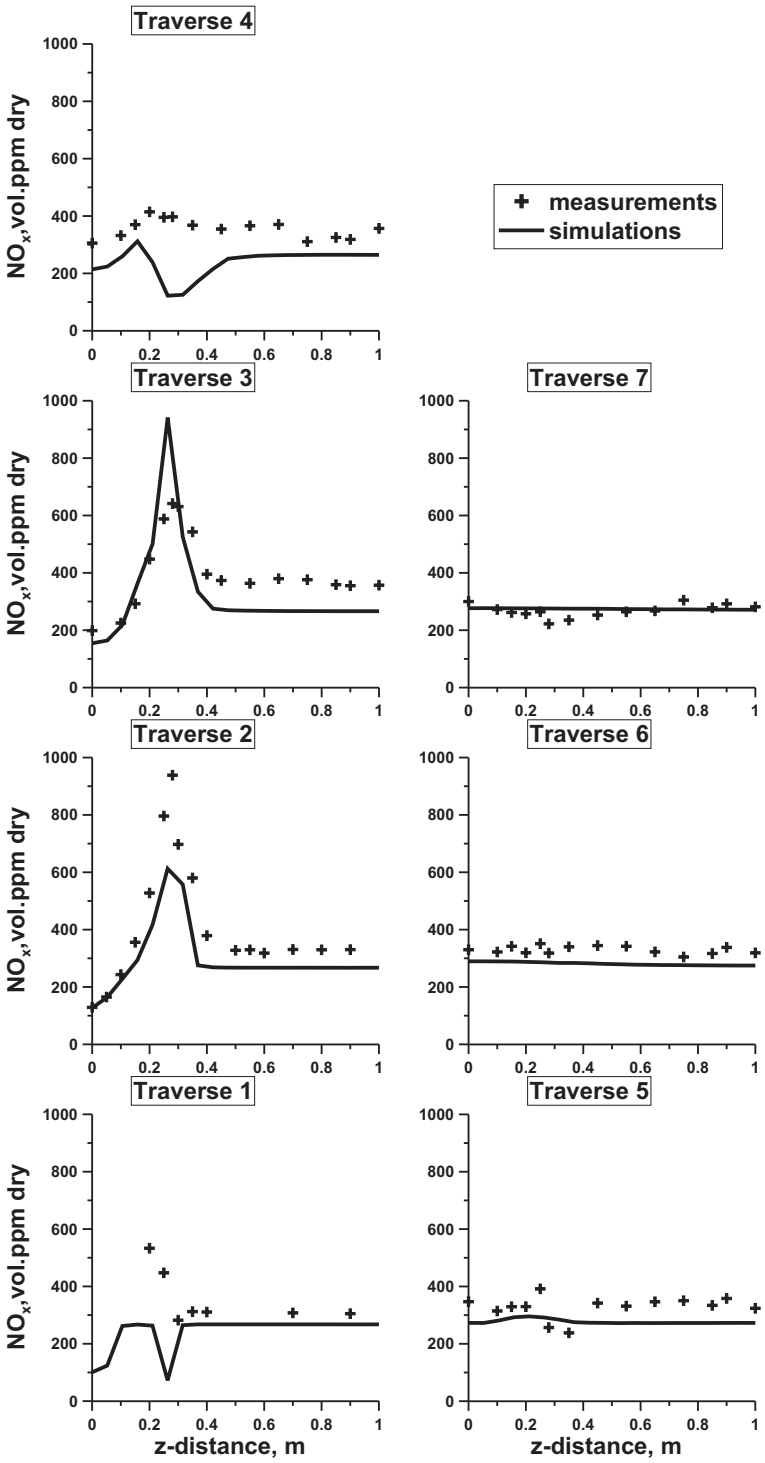

Figure 14.13.: Nitric oxide concentration profiles along the measurements traverses [310]

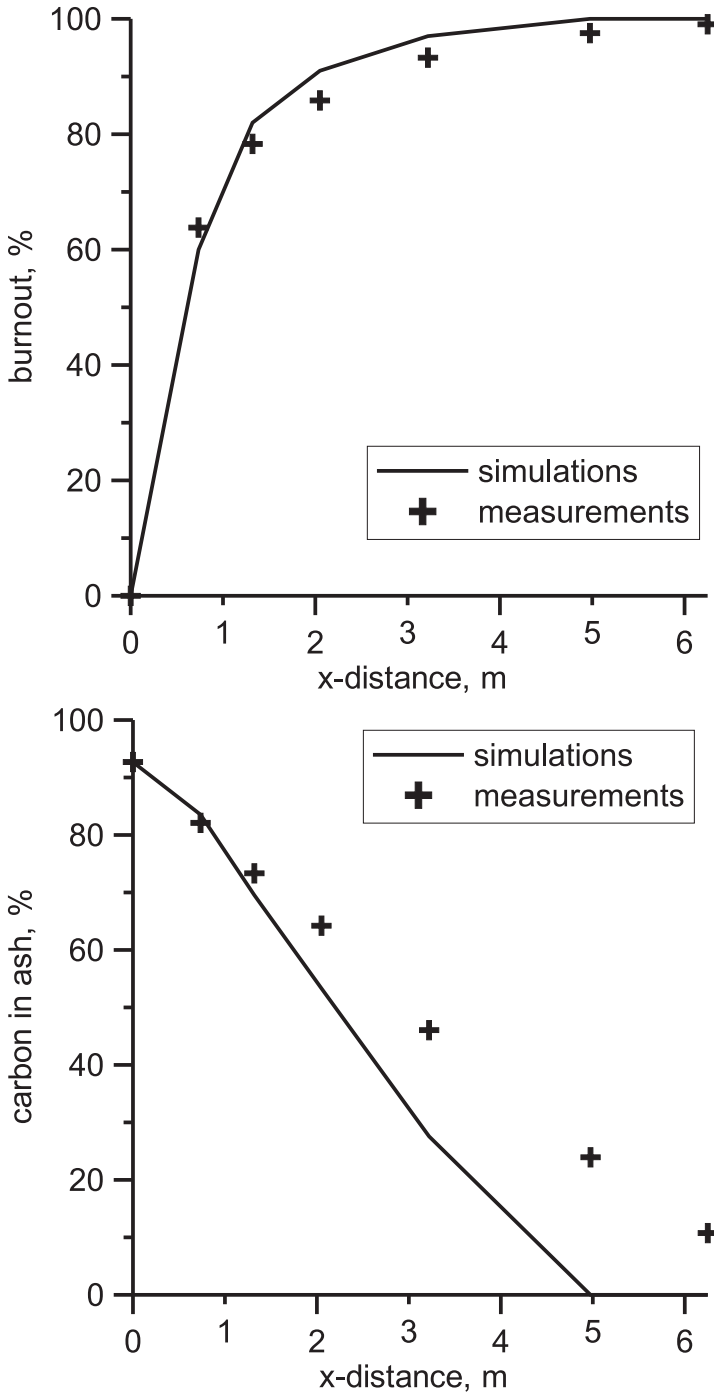

Figure 14.14.: Char burnout (Top) and carbon in ash (Bottom) along the centerline of the fuel jet. The measured values taken from [264]

15. Numerical simulation of boilers

The original application of the models for coal combustion is the numerical simulation of pulverized coal-fired boilers [399, 263, 70]. In those systems, the fuel, usually coal, is pulverized and then injected into the combustion chamber where it reacts with the oxygen present in the gaseous phase. The energy released by the exothermic reaction is usually transferred to a secondary external medium. In the case of boiler used in power plants, the second medium is water to generate steam and the steam, at high temperature and high pressure, is used to produce work.

The CFD method has advantages to other methods (see also Section 4.9) since in boilers, burners are designed to optimize the heat transfer (both heat transfer mechanisms are present, either radiation and convection) with the restriction that fuel must be completely converted. Since many years, boilers for power generation have been developed and optimized and nowadays their performances are so high that much effort and high accuracy is needed to achieve further improvements.

15.1. Boilers

The efforts of improving existing boilers performance are directed towards two challenges:

1. The utilization of alternative fuels, mainly biomass with a decrease in thermal efficiency.

2. The subsequent deterioration of the heat transfer process due to the increased slugging and fouling.

In facts, co-firing of alternative fuels with pulverized coal became very important in the last decade since resources protection and climate precaution became more important for the power industry. Unknown ash behavior and ash-related operational problems, such as the effects of the co-fired fuel on slagging and fouling in the system, are challenges in co-firing technology. Careless co-firing of difficult alternative fuels could lead to a reduction of boiler reliability and availability, and to unscheduled plant shut-downs.

The replacement of coal with biomass results in an increase of slugging and fouling in several parts of the boiler. Most importantly, as shown in Figure 15.1 fouling affects heat transfer on the superheater and accumulated material near the burners, altering the flow field and indirectly the combustion zone. Generally the accumulation of material in unwanted part of the boiler causes the following problem:

- Decreased efficiency;

- Unexpected shutdowns;

- Limited availability;

- Increased pollutant emissions;

- Increased production costs.

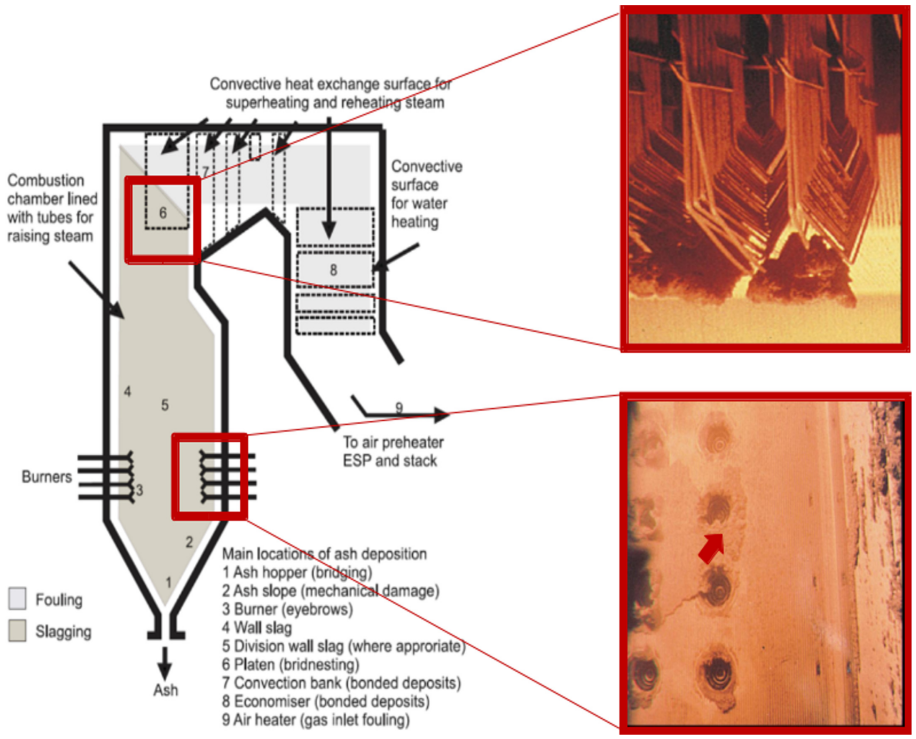

Figure 15.1.: Region of possible slugging and fouling effects inside a boiler [191]

The first step in tackling that challenge is the investigation of the distribution inside the boiler of the solid particles, the temperature field and finally the efficiency of the boiler. The CFD method presented in the previous Chapters does just that. In Figure 15.2 and in Figure 15.3 the temperature distribution and the particle paths are presented for a boiler fired with pulverized coal (Left) and in the same boiler where part of the coal is replaced with biomass (Right). Without entering into details, the differences shown by the calculations are evident.

The knowledge of the temperature distribution together with the other aforementioned thermodynamic quantities doesn't complete the task since the proper rate of fouling is still difficult to compute in real boiler geometries like the one shown here as an example. As the solid particles approach the surface where the impaction rate is required, (this information is provided by CFD calculations), the path through the boundary layer of the surface must be addressed, and the impaction rate must be calculated. Subsequently, not all the particles hitting the surface remain on the surface since physical and chemical processes cause the particle to be rebounded from or adhere the surface. In particular conditions, some of them stay bounded forming the slag material. Those two processes are commonly not addressed by CFD software.

In [190] blends of a South African bituminous Middleburg coal and alternative fuels (sewage sludge, saw-dust and refuse-derived fuel) have been tested to experimentally examine the effect of the added fuel on the slagging propensity of the mixtures. Substantial impact of sewage sludge has been observed. The initially formed deposits have become rapidly molten and they flow around the deposition probes, particularly when the sewage sludge fraction exceeds 15% by thermal input and the gas flow temperature exceeds the ash melting point. A 5% addition of the refuse-derived fuel (RDF) has increased the deposition rate by almost a factor of two. Large

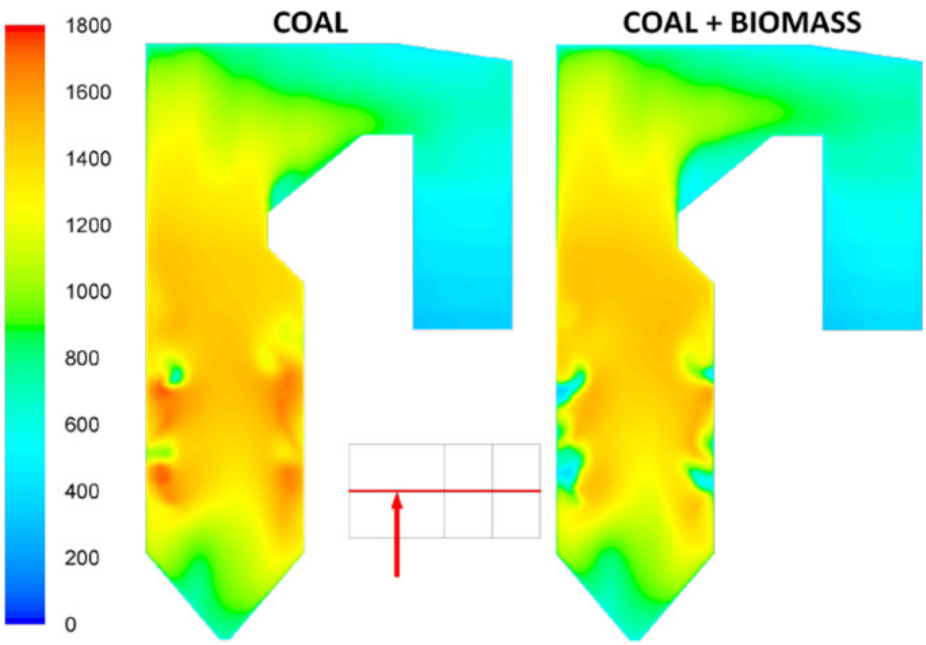

Figure 15.2.: Temperature distribution inside a boiler fired with pulverized coal (Right) and with a certain amount replaced by Biomasses (Left)

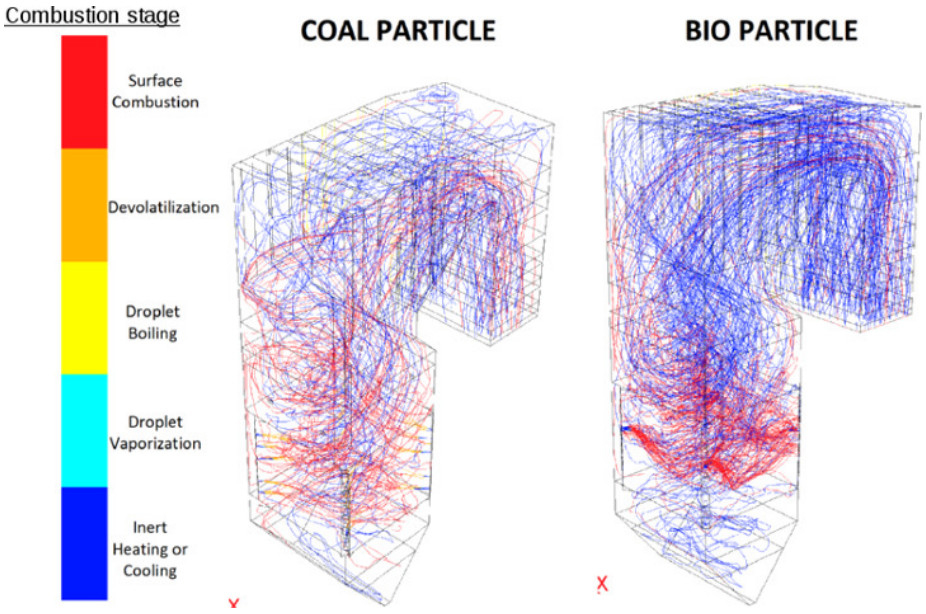

Figure 15.3.: Solid particle paths inside a boiler fired with pulverized coal (Right) and with a certain amount replaced by Biomasses (Left)

RDF ash particles have been observed in the deposits.

In [409, 406, 146] the requirements for accurate predictions of impaction efficiency on tubes using CFD approach (RANS in the first two articles and DNS in the third) have been identified. Flows which pass a cylinder have been computed using steady-state and time-dependent simulations with emphasis on related numerical errors, boundary layer, and turbulence modeling. Inertial impaction on the front face of the cylinder and eddy impaction on the rear face have been considered, and measures needed for accurate predictions of the particle arrival rate have been formulated. Accurate predictions of the impaction efficiency are obtainable only when the flow-field in the neighborhood of the deposition surface is accurately resolved. Those requirements include turbulence modeling choice and discretization of the boundary layer around the cylindrical probe.

In [31] the requirements derived in the previous studies have been applied to the prediction of ash deposition from a flame using RANS and compared with measurements of fly ash deposition in a 15 kW pulverized coal jet flame. The CFD-model predictions have been able to reproduce the measured dependencies after adjustments to the particle sticking sub-model.

For the details of those results we refer to the original papers, [409, 406, 31].

15.2. The MILD boiler

The aforementioned developments must satisfy the usual constraints of any combustion system, namely:

1. A stable flame;
2. The desired heat flux;
3. A minimum pollution.

These requirements are usually conflicting, and the goal of engineering modeling is to provide useful information to combine all at best [413]. In [311, 312] a new approach to the solution of the aforementioned problems has been taken, implementing the MILD technology (see [228] and Chapter 14) to boilers. The characteristics of a MILD combustion are summarized below:

1. Low NO and CO emissions;
2. Complete combustion in applications with short residence times;
3. High and uniform wall heat fluxes;
4. Flame stabilized without problem of ignition;
5. Simple burner construction.

Although most current applications are limited to industrial furnaces, MILD technology is expected to provide significant advantages when also applied to power station boilers. It is not clear if fuel can be saved since the method of external heat recirculation, due to the presence of ash in the flue gas, can cause slugging inside the heat exchangers but, since high radiative fluxes are expected, the boiler can be build more compact, opening the possibility for high steel quality to be used so that the cycle thermal efficiency is improved due to increased (superheated) steam parameters. A simple design of the burners and a very stable combustion process open up the possibility of using low-rank coals without decreasing the burnout at the exit.

A typical conventional boiler is composed of the radiative section and the convective section. An air preheater and an economizer are used to recover the waste heat of flue gases. In MILD combustion, the adiabatic flame temperature is much higher than that of a conventional

boiler and the heat transfer inside the boiler is dominated by radiation. Thus, it should be possible to design a boiler without the convective section and yet maintain the same thermal output. The removal of the convective heat transfer region will certainly lead to a significant reduction of boiler size and cost.

As already discussed, MILD combustion can be achieved by an intense recirculation of combustion products inside the chamber. This recirculation causes that both the combustion air stream and the fuel stream are diluted before the ignition occurs, causing the reduction of the temperature peaks. The challenge tackled [312] (see also [311]) is to study the possibility of generating a recirculation with the needed intensity in a combustion chamber smaller than the one available in furnaces.

The Author of [312] develop a conceptual 130 MW_{th} boiler fired with Venezuelan Guasare coal. The boiler posses a radiative section only with its design and layout guaranteeing operation in MILD combustion regime. Unconventional but simple burners characterized by a high momentum (strong) central (combustion air) jet and two (weak) coal jets provide the necessary mixture of fuel and oxidizer [310].

Numerical simulations have been performed to determine the shape of the boiler and to optimize some constructive features allowing the establishment of the MILD combustion regime. The boiler design procedure consists of the steps outlined below:

1. Boiler shape. Three shapes (A, B, C - see Figure 15.4 have been considered; see section Section 15.3.
2. Burner spacing. Configurations with five, three and one burner have been considered;
3. Burner Block Location. Up-fired and down-fired options have been considered; see Section 15.4;
4. Boiler Volume. Smaller, medium and larger volumes have been considered;

Results of the first and third optimization steps only will be reported in details below. The CFD-based mathematical model has been previously explained and their validation presented in Section 14.2 and, for more details, [310]. The main features of the CFD model used in the calculations are listed below:

1. Euler description of the gas-phase with turbulence described by the k-ε model;
2. Lagrangian formulation for the solid-phase (the pulverized coal);
3. A global 2-steps mechanism for the volatile matter combustion coupled with the Eddy Dissipation Concept for turbulent combustion;
4. Fuel, Thermal, Prompt and Reburning mechanism for the description of the NO chemistry.
5. DO model as a solver for the radiative transport equation with the WSGG model for the calculation of the gas absorption coefficient.

The coal used is the Guasare coal already described in Chapter 14. In that chapter, the char combustion model and the adopted parameters are also presented.

15.3. Boiler shape

The first challenge of the MILD boiler design project is to find a shape of the boiler appropriate for MILD technology. Calculations have been performed for three different boiler shapes which

are marked in Figure 15.4 as designs A, B, and C. The first two (A and B) designs are derived to resemble standard PC boilers. The third (C) boiler is an innovative concept (of the authors), invented to create a proper internal recirculation of the combustion products.

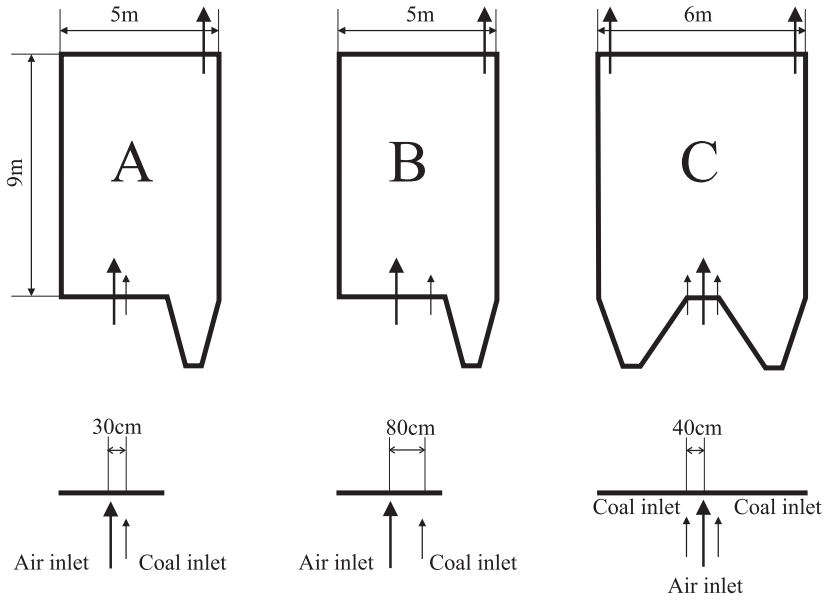

Figure 15.4.: Illustration of the considered combustion chamber forms configuration

As shown in Figure 15.5, the geometry of the boiler and the configuration of the inlets determine the recirculation pattern inside the boiler. The intensive recirculation created in the symmetric boiler results in a more uniform temperature field, lower temperature peaks, moderate oxygen concentrations, and complete burnout of the combustible gases and the char. Table 15.1 lists the calculated peak temperature and burnout for designs A, B, and C. The table also lists standard deviations of the predicted temperature and oxygen fields. The lower values for design C indicate the highest degree of homogeneity. As a result of the simulations, the symmetric boiler has been found to be the most suitable among the three considered designs, so further work focuses on this concept.

	A	B	C
Peak temperature, K	2618	2437	2106
Burnout, %	97	99	100
Standard deviation of the temperature, K	375	238	290
Standard deviation of the oxygen concentration, %	3	5	1

Table 15.1.: Results of the boiler shape determination

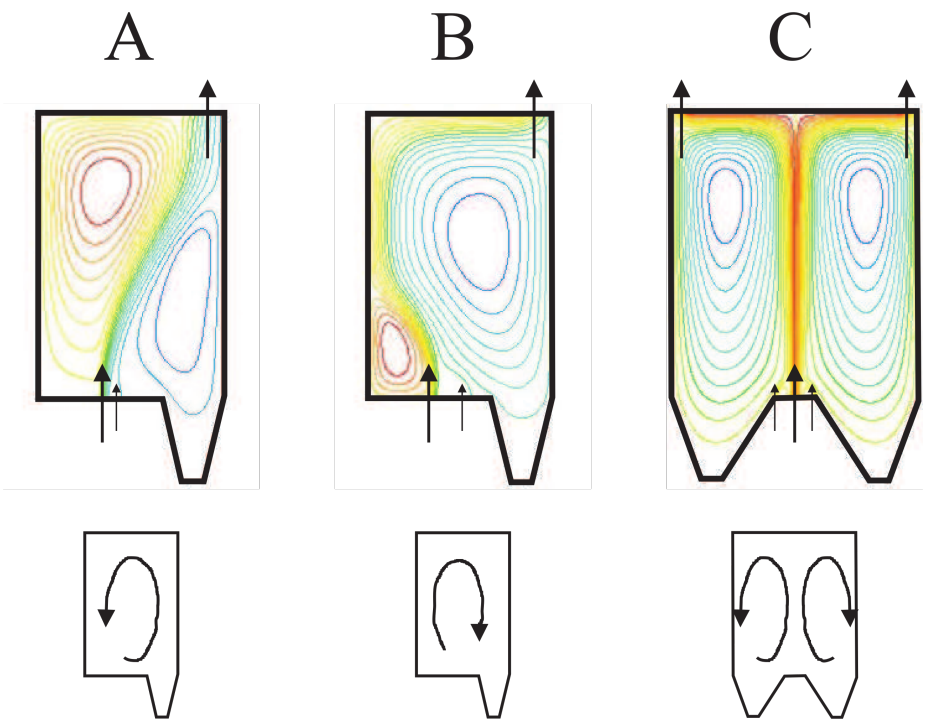

Figure 15.5.: Predicted recirculation zones inside the combustion chamber [310]

15.4. Location of the burner block

The third simulation series has been carried out to examine the down-fired configuration of the MILD boiler and to compare the results with the up-fired one. The down-fired configuration has been tested because of slagging problems and a risk of the burner destruction by the agglomerated ash, when the burner is located at the bottom. Several advantages of the down-fired boiler have been identified; the recirculation path is longer in the down-fired configuration than in the up-fired one resulting in a more intensive heat transfer (see Figure 15.6 and Table 15.2). So, lower flue gas temperatures are observed. Furthermore, the down-fired configuration features more uniform heat fluxes. Therefore, the down-fired configuration has been selected for further investigations.

	Up-fired	Down-fired
Heat transfer rate, $\frac{kW}{m^2}$	220	261
Outlet temperature, K	1722	1568

Table 15.2.: Results of the burners location determination

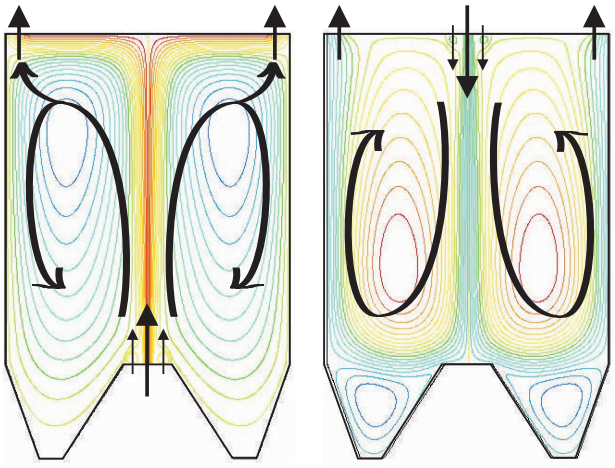

Figure 15.6.: Recirculation inside the up-fired boiler (left) and down-fired boiler (right) [310]

15.5. Final configuration of the MILD boiler

Based on the previous investigations (see in [310] the details of all the investigations), the final configuration of the MILD boiler was selected and it is presented in Figure 15.7. The boiler is 13 m high and has a 7 m times 6 m cross-section. It is equipped with a burner block that consists of five identical burners located at the top wall; thus the boiler is a down-fired one. The flue gas 1 m $\times$ 1 m square outlets are also located at the top, and they are symmetrically positioned on both sides of the burner block. Each of the five burners is equipped with a central injector of hot air and two coal guns positioned on both sides of the air injector. Pulverized coal is introduced into the furnace by nozzles of 140 mm diameter and the combustion air by 480 mm nozzles. The boiler is equipped with two ash hoppers. The combustion air is preheated to 1200 K and the coal together with its transport air is supplied at ambient temperature (300 K). The coal feeding rate is 3.2 $\frac{\text{kg}}{\text{s}}$, and its transport air is almost twice as high. The mass flow of combustion air is equal to 33.1 $\frac{\text{kg}}{\text{s}}$. The air jet is supplied at a high velocity (120 $\frac{\text{m}}{\text{s}}$), and the coal jet has the velocity of 30 $\frac{\text{m}}{\text{s}}$. The boiler is operated at 130 MW total thermal input. The fuel thermal input is equal to 100 MW so each burner operates at 20 MW fuel power. Both the combustion and the transport air streams contain 23% (wt) oxygen and 77% (wt) nitrogen. The wall temperature is constant in the final boiler design calculations and it is equal to 800 K.

The final boiler design possesses an intensive in-furnace recirculation and the dead zones are small, as can be observed in Figure 15.8. The whole volume of the chamber participates in the combustion process. The internal recirculation of the combustion products creates homogenous both the temperature and the chemical species concentration fields. Further, due to the dilution of the combustion air and fuel jets with the combustion products, coal ignition takes place in low oxygen concentration environment, and therefore the temperature peaks are suppressed.

The whole boiler is filled up with combustion products of 1600-2000 K temperatures while the furnace exit temperature is around 1400 K. As already mentioned, a way of using the exit gas enthalpy to preheat the combustion air must be developed to reach high efficiency for the whole process. This enthalpy must be recovered in a heat exchanger and utilized to preheat the combustion air. The oxygen concentration in the entire boiler is in a range of 3-5% while in the flue gas is equal to 3.4%. As a result of the strong recirculation inside the combustion chamber and as a consequence of the uniform temperature field, the heat fluxes are high and

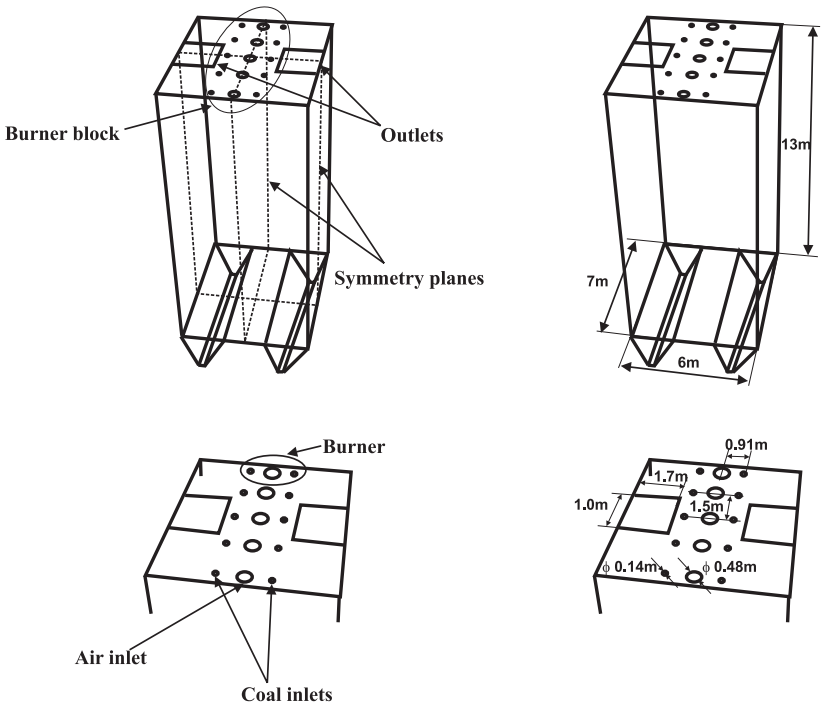

Figure 15.7.: Final geometry of the MILD boiler

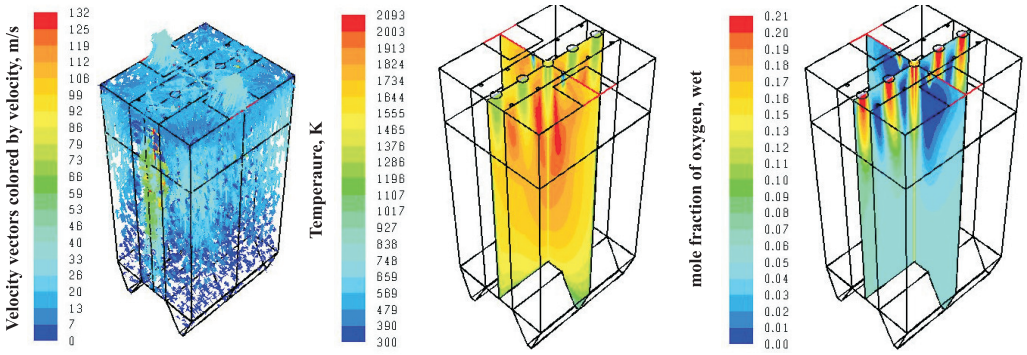

Figure 15.8.: Velocity vectors (left), temperature field (center) and oxygen concentration field (right) inside the MILD boiler

almost constant along the height of the MILD boiler (see Figure 15.9, right). For the sake of comparison typical heat flux profiles for fluidized bed boilers (see Figure 15.9, left [222]), and conventional wall-fired boilers (see Figure 15.9, center [222]) are also shown. The MILD boiler has two advantages: uniform heat fluxes along the boiler height (as in fluidized bed boilers) and high heat fluxes values (as in wall fired pulverized coal boilers). Heat transfer due to radiation is dominant; its share is 83% of the total heat transfer rate.

Most of NO is generated in the region between the burners. The NO concentration peak is equal to 1195 ppm while downstream of this region the nitric oxide concentrations are low, in a

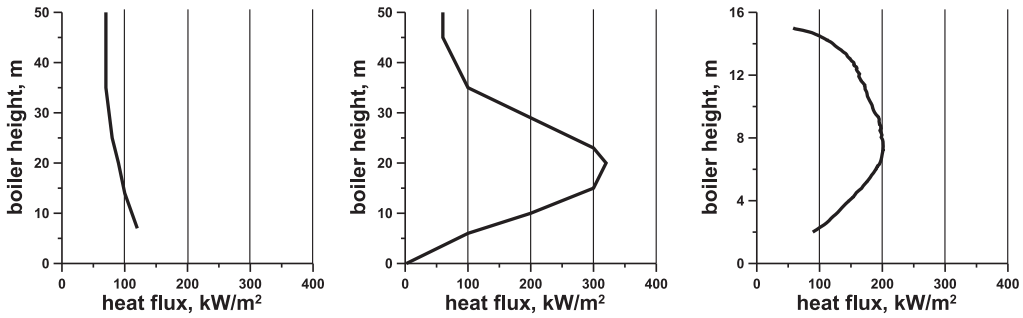

Figure 15.9.: Heat fluxes along height of a fluidized bed boiler (left), conventional pulverized coal boiler (center) and the simulated MILD boiler (right)

300-400 ppm range. In the MILD boiler, 98% of nitric oxide is formed via fuel mechanism, and the NO reburning mechanism plays an important role. As a result, the nitric oxide concentrations at the boiler outlet are low and equal to 298 ppm. (For a detailed discussion of the NO_x formation and destruction mechanisms the reader is referred to [310]). The large particles residence time and recursive recirculation of the combustion products improve the burnout of the CO, volatiles, and the char.

15.6. Effects of selected operating parameters

The impact of three important operating parameters has been further examined. For all calculations, the final MILD boiler geometry is retained and the same boundary conditions are applied.

1. The combustion air preheat has been decreased and the numerical simulations showed that the technology could also be realized without preheating the combustion air stream.

2. The combustion air jet velocity has also been decreased but the installation of a high momentum jet, creating an intense recirculation, has been found imperative for the realization of the MILD characteristics.

3. The air excess ratio has been decreased to $\lambda = 1.05$, and the mixing of oxygen with the fuel has been found enough to guarantee still complete combustion.

15.7. Steam cycle

From the point of view of steam parameters, pulverized coal fired power plants can be divided into [32]:

- sub-critical (under critical point of water [1]
- super-critical (over critical point of water; usually up to 24 MPa and 565^oC)
- ultra-super-critical (USC) (over super-critical conditions; usually 30 MPa and 600^oC)

[1] The critical point of water is 22.06 MPa and 375 °C; usually 19 MPa and 535 °C

In order to improve coal-fired power plant efficiencies the power industry must move from sub-critical to super-critical steam cycles. A super-critical design not only improves the efficiency by increasing the working fluid pressure (modern super-critical coal-fired power plants have efficiencies above 45%) but it allows super-heating of the steam to higher temperatures which provides a significant steam cycle efficiency improvement. The super-critical technology plays a dominant role in the newly built power plants, however, the installed technology is based predominantly on sub-critical steam cycles.

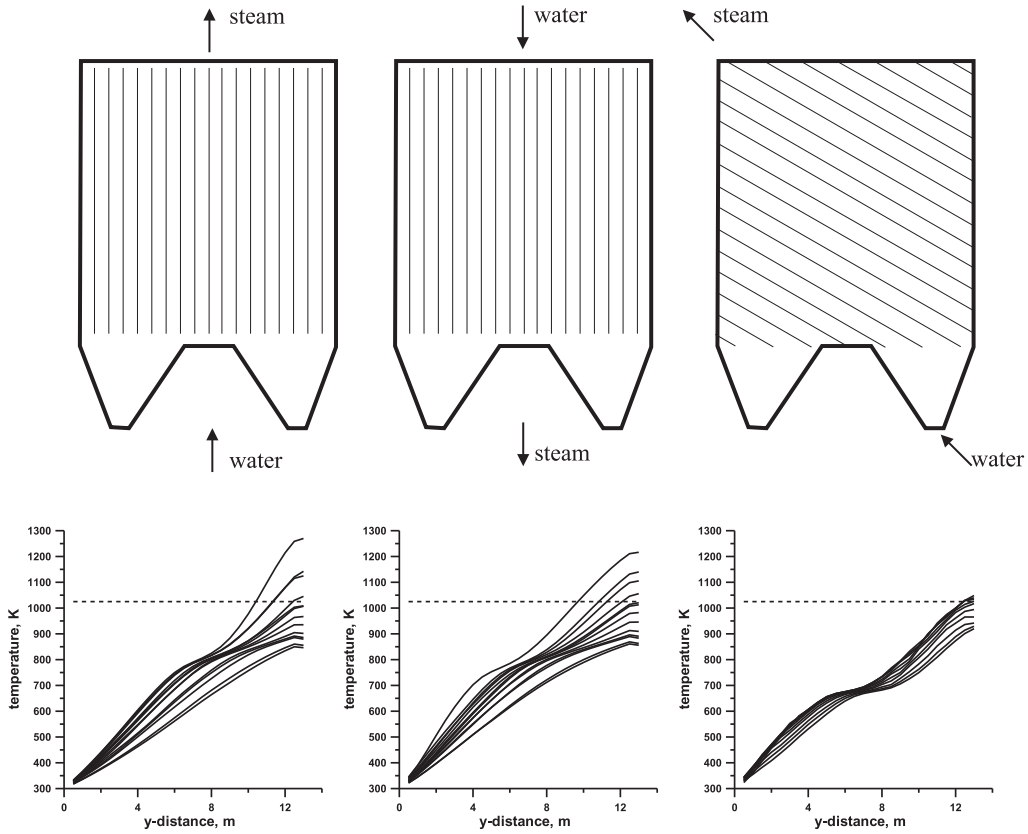

Figure 15.10.: Heat flux along the height of the boiler for the simulated tubes arrangements: vertical down-up (left), vertical up-down (center) and spiral (right) [310]

Boiler design procedures involve an examination of the combustion process as well as the steam cycle. Both issues are strongly coupled due to the heat transfer proceeding from the combustion products inside the chamber to the water/steam mixture inside the boiler tubes. In this simulation series, the coupling between the MILD boiler and the entire steam cycle is considered. The final boiler geometry, as well as the operating and boundary conditions, are the starting point for these calculations. The heat transfer rates per unit of height ($\dot{Q}_l$) of the membrane wall have been obtained in the CFD predictions of the combustion chamber. This heat is transferred to the boiler tubes and the working fluid. The heat conduction through the tube walls is neglected. At the beginning of the process, the working fluid is super-critical water which is then converted into ultra-superheated steam. The working fluid consists of the one phase only because of super-critical conditions of the process.

The heat transfer rate between the combustion products and the working fluid is described

by the following equation:

$$\frac{d\dot{H}}{dy} = \dot{Q}_l \tag{15.1}$$

Introducing into the above equation the mass flow of the medium one obtains:

$$\dot{m}\frac{dh}{dy} = \dot{Q}_l \tag{15.2}$$

where $\dot{Q}_l$ is the heat transfer rate per meter of the tube height, $\dot{H}$ stands for the total enthalpy rate of the medium, h is the medium specific enthalpy and $\dot{m}$ is the mass flow rate of the medium while y is the distance in y direction.

Solving equation 15.2 the specific enthalpy of the medium, represented by $h(y)$ is calculated, as a function of y distance. Furthermore, the temperature of the working fluid denoted as $T_s(y)$ is calculated using the steam tables. This temperature should be lower than 750°C which is assumed in this calculations as the maximum allowable temperature of the steel material. The steam pressure is assumed to be p=30 MPa and water/steam mass flow is equal to 17 $\frac{\text{kg}}{\text{s}}$. Additionally, the convective heat transfer coefficient α is computed along the tube at the side of the super-critical working fluid. The Nusselt function is calculated for the water/steam under super-critical conditions according to the formula of Yamagata et al. [432]. The efficiency of the fins is assumed to be equal to 1. As a result of these calculations, the temperature profiles at the boiler walls are obtained.

The MILD boiler is proposed as an ultra-super-critical boiler with the once-through type of the water circulation. Three commonly used configurations of the once-through boiler tubes were tested in this series of calculations: vertical down-up, up-down and spiral (see Figure 15.10, top). The most uniform temperature profile can be found in the boiler with the spiral tubing as can be found in Figure 15.10, bottom. Comparing the two vertical tubes arrangements, it can be noticed that the up-down configuration works worse than the down-up one. It was concluded that the spiral tubes configuration is the most suitable for the MILD boiler designed in this work. However, this configuration is technically most complicated. The Rankine cycle efficiency of the steam cycle coupled with the MILD boiler is calculated to be above 50%.

16. Entrained flow gasifier

In the last decade pyrolysis and gasification have become the main topic for industrial applications of solid fuel conversion. Following this tendency many basic and applied research projects came to stand to give support to industrial requirements.

The main idea of pyrolysis and gasification is to convert solid fuels into combustible gases that can be easily used in industrial processes. During pyrolysis solids are converted by thermal treatment and, during gasification, by heterogeneous reactions with special gases (mainly CO_2 and H_2O).

There are basically three kinds of gasifiers:

1. Entrained flow gasifiers (EFG)
2. Fixed bed gasifiers, either counter-current (up-draft) or co-current (down-draft)
3. Fluidized bed gasifiers (FBG), either circulating bed gasifiers (CBG) or non-circulating bed gasifiers.

In the entrained flow reactors, fuel is injected into the reactor as small particles or small droplets, creating a mixture in which the second phase can be considered as dispersed. Fluid dynamics drive the flow, and the mixing and small or no interactions among the particles are expected. In a fixed bed reactor, solid fuel particles are in contact with each other, and they are not free to move. Gasification medium can flow only between particles, and the mixing is limited. A fluidized bed reactor has properties lying between those of an entrained flow reactor and those of fixed bed reactors. Particles experience strong interactions among them, but they are still free to move and to mix with the gasification medium.

All the aforementioned forms of gasifiers have in common that part of the fuel must be combusted (exothermic reaction) to obtain high enough temperatures needed to sustain the endothermic gasification and pyrolysis reactions.

In Table 16.1 several characteristics for the gasifiers are summarized. The advantages and the disadvantages of each kind of gasifier are also presented. The entrained flow reactors have the advantage to produce a clean gas, with high thermal input but high technological requirements must be satisfied. The fuel must usually be of high quality, traditionally pulverized or atomized. Temperatures in an EFG are also higher than in the other technologies. On the contrary, the fixed bed technology doesn't have high requirements for the fuels, therefore, this is the best technologies to be applied in the case of difficult fuels. The drawbacks of the FBG lay in the relatively low quality of the gases.

In this chapter a CFD analysis of an entrained flow reactor is presented, with the goal to show how well the CFD tools can simulate those kinds of devices.

16.1. Introduction

At the Karlsruhe Institute of Technology (KIT) in Germany, a new process for handling low calorific biomass fuels has been developed, the bioliq® process [98]. Agriculture waste, highly decentralized, are thermally treated, and a slurry is formed with the obtained liquid and the

	Fixed bed		Fluidized bed		Entrained flow
	Parallel	Counter-current	stationary	circulating	
T in °C	700-1200	700-900	<900	< 900	1200-1500
Tars content g/Nm^3	0.1-2	10-100	2-50	1-20	0
Control	easy	easy	moderate	moderate	difficult
Power MW$_{th}$	<5	<20	10-100	>20	>100
Gas quality	gut	difficult	moderate	moderate	fine particles

Table 16.1.: Characteristics of gasifiers [189]

remaining bio-char. The slurry is then transported to central plants where it is gasified at high pressure.

The Helmholtz Virtual Institute of Gasification Technology (HVIGasTech) [165, 183] has been created with the goal to develop a well scientifically established numerical model for the bioliq® process. To reach this goal, several sub-processes have been addresses, namely the convective and the radiative heat transfer, the characteristics of the heterogeneous and the homogeneous reactions, the characteristics of the molten slag at the walls, the turbulent mixing inside the reactor, the atomization process of the liquid fuel. The final CFD model, incorporating every single sub-model, has been validated against in gasifier measurement of slurry and of model-fuel in reactors at atmospheric and high pressure. Ethylenglycol (IUPAC name: ethane-1,2-diol) has been chosen as model-fuel, and the REGA Facility at KIT serves as an atmospheric reactor.

In a three-part paper series [110, 229, 99] current experimental and modeling results concerning gasification of mono-ethylene-glycol (MEG) have been presented. In the first part [110] an experimental campaign is described. The second paper [229] reports on simulation of the campaign using RANS based CFD. The third paper [99] describes Large Eddy Simulation of the same REGA-glycol-T1 campaign.

In this Chapter, the results of the simulations of the atmospheric experiments will be presented. Following the results in [229] closely, the discussion will be based on the analysis of the REGA-glycol-T1 experiments.

16.2. Modeling

The models used in the simulations are summarized in the following list:

- Navier-Stokes equations have been solved using the RANS approach in Euler frame (see Section 4.1);
- Turbulence modeled using the RSM (see Section 4.3.3);
- The interaction with turbulence has been described by the EDC (see Section 5.8);
- The droplets of Glycol has been described using the DPM model (see Section 10.2);
- The radiative heat transfer equation is solved using the DO model Section 4.8;
- The thermodynamic properties has been taken from available measurements or calculated using the kinetic theory of gases.

As shown in more detail in [229] few other turbulence models have been tested (see Figure 16.8) to quantify their influence on the calculated quantities. The mixture fraction approach

with equilibrium chemistry (see Section 5.7) has also been used since it posses a few advantages that can be exploited especially in simulations of gasification. The model for the chemistry-turbulence interaction should possess the following features:

1. Good predictions of the micro-mixing process and consequently a good limitation mechanism for the kinetic rate of reaction;
2. Correct asymptotic behavior predicting chemical equilibrium (see below);
3. Usability, in terms of applicability to complex industrial gasification plants.

The first requirement is fulfilled by both models, the EDC and the PDF. Considering that exothermic reactions are expected to be fast, and consequently reaction rates are not everywhere kinetically controlled. Both chosen models can correctly predict the limitation of laminar reaction rates in turbulent flames. Generally, the description of the turbulent fluctuations and of the mixing provided by a PDF method is more accurate than the one given by the EDC since more details are retained by the PDF description while the EDC describes the turbulent fluctuations based upon two regions only. A drawback of the β-PDF used in the modeling is its inadequacy of simulating mixing of three streams. In REGA the stream of evaporating MEG is mixed with the gasification medium (enriched air) and with recirculated and partially converted syn-gas. Since evaporation is slower than the entrainment (mixing with the recirculated syn-gas), even if the recirculation is strong, the inaccuracy introduced should be small. This may not be correct in the near burner region where the atomization process governs the mixing.

The second requirement is related to the need to let the water gas shift reaction (WGSR) reach the equilibrium. In combustion problems, the WGSR is essential inside the flame hotspots only. In gasification systems, the WGSR equilibrium is reached at lower temperatures. The PDF method equipped with chemical equilibrium provides a way to reach equilibrium under any conditions. However, the EDC does not possess this property. In the EDC, the reaction rates are limited by the local turbulent time scales. Since the standard implementation of EDC is based on quantities locally calculated in each cell, there is no memory of previously achieved molecular mixing and when a local turbulent time scale increases, because of laminarization or natural turbulence decay as in convective regions, the chemical reactions do not have anymore the possibility to reach equilibrium in the gas phase. As a lemma of this analysis, models based only on turbulent mixing as the Eddy Break Up model [225] (see also Section 5.8), or the mixed-is-burned model, not implementing chemistry, do not reproduce accurately the reaction rates and they are inadequate for gasification modeling.

The advantage of the species transport model coupled with the EDC manifests itself in its adaptability to complex geometrical arrangements pertinent in industrial applications. The implementation of the PDF method discussed here is based on one single mixture fraction. One mixture fraction is enough for the simulation of the gasification of pure MEG as in this paper, but it is not enough for the simulation of for example slurry (oil + char) gasification. Increasing the number of mixture fractions is mathematically feasible, but the resulting model requires more computational power.

The last drawback of PDF model implemented for this calculation consists in the utilization of chemical equilibrium also in regions where finite rate chemistry could play a role.

16.2.1. Fuel decomposition and gas-phase reactions

The chemical reactions used in the EDC can be written in the following way:

$$\sum_{r}^{N} \nu_r M_r \leftrightarrows \sum_{p}^{N} \nu_p M_p \tag{16.1}$$

where the index r refers to the reactants and p to the products. The forwards and the backwards reaction rates are expressed using the Arrhenius form:

$$k = AT^b \exp\left(-\frac{E}{RT}\right) \tag{16.2}$$

The following reaction sequence is considered:

1. thermal decomposition of the MEG molecule. MEG droplets, after evaporation, decompose into a gas containing $CO, CO_2, CH_4, H_2, H_2O$ and hydrocarbons:

$$C_2H_6O_2 \longrightarrow CO, CO_2, CH_4, H_2, H_2O \tag{R 16.1}$$

2. reactions with O_2:

   b1) partial oxidation of MEG molecule in gas-phase

$$C_xH_yO_z + \zeta O_2 \longrightarrow \zeta_1\, CO + \zeta_2\, H_2 + \zeta_3\, CO_2 + \zeta_4\, H_2O \tag{R 16.2}$$

   b2) oxidation of decomposition products and syn-gas components

$$H_2 + 0.5\, O_2 \longrightarrow H_2O \tag{R 16.3}$$

$$CO + 0.5\, O_2 \longrightarrow CO_2 \tag{R 16.4}$$

$$CH_4 + 0.5\, O_2 \longrightarrow CO + 2\, H_2 \tag{R 16.5}$$

3. reforming / gasification reactions.

$$CO + H_2O \longleftrightarrow CO_2 + H_2 \tag{R 16.6}$$

$$CH_4 + H_2O \longrightarrow CO + 3\, H_2 \tag{R 16.7}$$

To describe the reactions mentioned above either detailed kinetic mechanisms or global kinetics may be applied. The detailed GRI3.0 mechanism has been chosen since it is validated for combustion of natural gas in a wide range of conditions with λ, the air ratio, from 0.2 to 10, temperatures from 1000 to 2500 K and pressure up to 10 atm [338]. The applicability of GRI3.0 for high-pressure partial oxidation of methane has been reported by Vegendla [387] and Rehm [288]. Tranter [379] has simulated reasonably well shock tube experiments of ethane oxidation and pyrolysis from 5 bar to 1000 bar and up to 1550 K using the GRI3.0.

Detailed mechanisms are less suitable for RANS simulation due to excessive computing time. Therefore a global mechanism for a) decomposition of MEG and b+c) combustion and gasification of decomposition products and syngas components applicable for entrained flow gasification conditions is needed. By reason that C1 to C3 hydrocarbon fuels are included, GRI3.0 is used as a reference for the reactions mentioned above.

A large number of global mechanisms for combustion and gasification of various fuels is available in the literature. The most frequently used global mechanisms for C1-C4 hydrocarbon combustion are given by Westbrook & Dryer [416] and Jones & Linstedt [169]. The more complex Jones and Linstedt Four-Step Mechanism contains the reaction R 16.5, R 16.6, and R 16.7 and has also been validated for moderately fuel rich methane-air flames [10]. The mechanisms reported by Biba [37] and Petersen [274] are derived for gasification of coal and sewage sludge, whereas [358] simulated moving bed coal gasification (10-60 bar, 1500-1600K) and Mann [231]

steam gasification of char at 915^oC. None of the above global mechanisms has been validated for gasification of MEG under EFG conditions, i.e., temperatures above 1500 K.

Different single reactions from literature have been compared with GRI3.0 simulation under appropriate concentration, stoichiometry, and temperature. Using Chemkin 4.1 [287], isothermal CSTR calculations were conducted under variation of residence time from 10^{-8} to 10 seconds and temperature from 800 to 1800^oC. In Figure 16.1 an example of such comparison is shown. Starting from a non-equilibrium mixture of WGS components (CO_2, H_2, CO, H_2O, and N_2) corresponding to REGA stoichiometry, the H_2 concentration in the WGS-reaction (R6) at 1400^oC as a function of reaction time is compared for different global mechanisms and the detailed mechanism GRI3.0. It is clearly seen that in comparison with the predictions of the GRI3.0 mechanism, the Sudiro [358] the Jones [169] (adopted into the HVI mechanism as reaction HVI5, see Table 16.2) and the Mann [231] reactions are too fast whereas Peterson [274] and Biba [37] are too slow. As none of the kinetic data from literature have shown sufficient conformity with the GRI3.0-reference at low and high temperatures, the Arrhenius parameters of the global kinetics has been adapted to give the best fit over the whole temperature range to be considered. The line in Figure 16.2 labeled HVI shows the results for the kinetic parameters derived via this procedure.

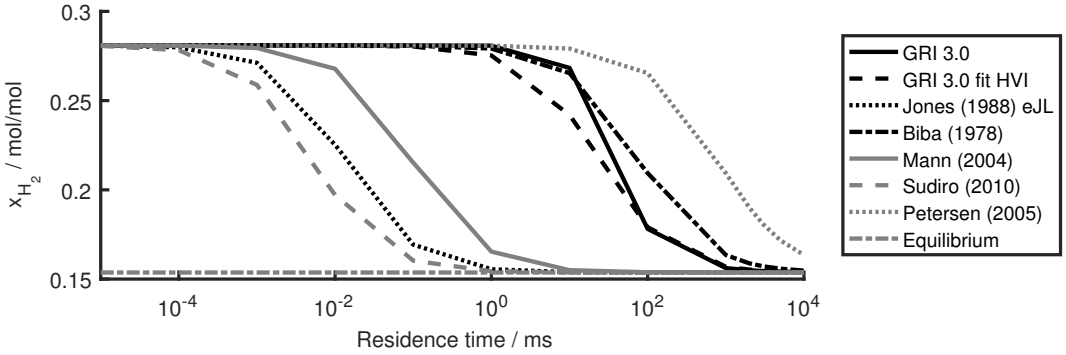

Figure 16.1.: H_2 concentration while reaching WGS Equilibrium at 1400^oC [304]

While the homogeneous gas phase reactions can be derived from literature or adapted to GRI3.0, the decomposition of the fuel needs separate modeling. In the absence of experimental and literature data for MEG decomposition products and global kinetics, reaction (R 16.1) has been adapted to a detailed mechanism for gasification of MEG. Rashidi et al. [139] developed this detailed high-temperature mechanism from a mechanism for ethanol combustion and used for simulations of previous REGA data [293]. Only the main products of the MEG decomposition (H_2, CO, H_2O and CH_4) are considered. In Figure 16.2 temperature and concentrations of MEG and main products are shown. The MEG decomposing is undertaken at a constant heating rate of 10^5 K/s, which is a typical value for EFG. The bold lines show the predictions using the detailed mechanism and the dashed lines the prediction using the adapted global decomposition reaction.

In Table 16.2 the parameters used in the final global mechanism called *HVI* mechanism are reported.

To ensure that the set of adapted kinetics works together as well as they work as the single reactions, the resulting complete global mechanism was tested (and further optimized) using Chemkin 4.1 for calculations of a 1D-PFR model of REGA with the temperature profile given by measurements and input data from several experimental set up (see [110]).

To show the influence of chemical reaction kinetics on CFD-modelling, an alternative mechanism was derived from the 4 step Jones-Linstedt mechanism [169], combined with reaction

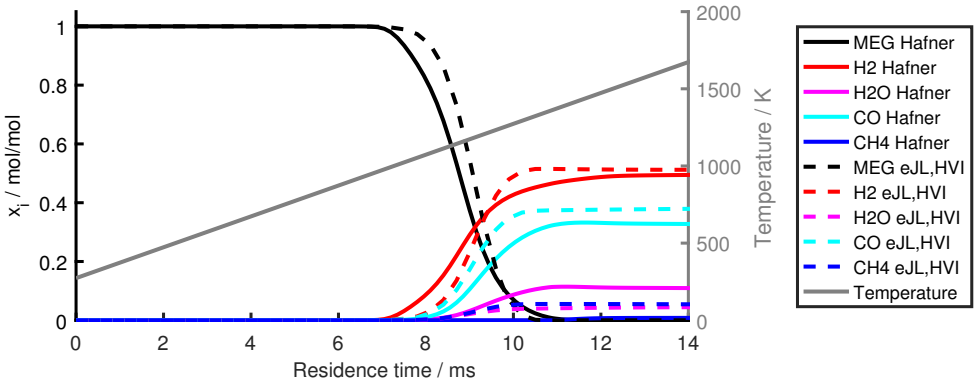

Figure 16.2.: Molar concentrations during decomposition of pure MEG at 10^5 K/s (constant) heating rate [304]

	Reaction	A kmol,meter,second	b	E / 10^8 $\frac{\text{J}}{\text{kmol}}$
HVI1	$4C_2H_6O_2 \rightarrow 9H_2 + 7CO + H_2O + CH_4$	9.31 10^{13}	0.0	2.684
HVI2	$CO + 1/2O_2 + H_2O \rightarrow CO_2 + H_2O$	3.1623 10^{11}	0.0	1.256
HVI3	$CH_4 + H_2O \rightleftarrows CO + 3H_2$	1.7 10^{10}	0.0	2.300
HVI4	$CH_4 + 1/2O_2 \rightarrow CO + 2H_2$	1.5811 10^{14}	0.0	2.512
HVI5	$CO + H_2O \rightleftarrows H_2 + CO_2$	8.5 10^9	0.0	2.040
HVI6	$H_2 + 1/2O_2 \rightarrow H_2O$	2.8464 10^{+14}	0.0	2.592

Table 16.2.: The HVI mechanism for MEG gasification

eJL2 (see Table 16.3) for direct combustion of MEG and with the same decomposition reaction of MEG (reaction eJL1 in the table mentioned above). The parameters of the adopted alternative global mechanism called *e-JL* mechanism are shown in Table 16.3.

	Reaction	A kmol,meter,second	b	E / 10^8 $\frac{\text{J}}{\text{kmol}}$
eJL1	$4C_2H_6O_2 \rightarrow 9H_2 + 7CO + H_2O + CH_4$	9.31 10^{13}	0.0	2.684
eJL2	$C_2H_6O_2 + O_2 \rightarrow 2CO + 2H_2O + H_2$	4.3975 10^{10}	0.0	1.256
eJL3	$CH_4 + H_2O \rightarrow CO + 3H_2$	3.0 10^8	0.0	1.256
eJL4	$CH_4 + 1/2O_2 \rightarrow CO + 2H_2$	4.4 10^{11}	0.0	1.256
eJL5	$CO + H_2O \rightleftarrows CO_2 + H_2$	2.75 10^9	0.0	0.838
eJL6	$2H_2 + O_2 \rightleftarrows 2H_2O$	2.5 10^{16}	-1	1.6747

Table 16.3.: The Extended Jones-Lindstedt (e-JL) mechanism for MEG gasification

Reaction JL1 represents the splitting of the gaseous MEG into H_2, CO, H_2O and CH_4 and it has been left unchanged in both mechanism. Reaction JL2 represents the oxidation of the MEG. Its rate has been taken from [169]. Reactions JL3 to JL6 describe the original mechanism presented by Lindstedt. In the original paper [169] two equations for the eJL6 rate has been

given. In this work the most accurate relation has been used:

$$\dot{R}_6 = k_6 \cdot \frac{[\mathrm{H_2}]^{0.5}[\mathrm{O_2}]^{2.25}}{[\mathrm{H_2O}]} \tag{16.3}$$

For a further verification purpose, both mechanisms have been used to calculate several typical zones in an EF gasifier like oxidation of hot recirculating syngas with oxygen or methane conversion in gasification zone. The following diagram (Figure 16.3) shows as an example of methane conversion of detailed (GRI3.0) and global (HVI and e-JL) mechanisms in a gasifying atmosphere at 1200^oC and 1400^oC resulting from isothermal PFR calculations.

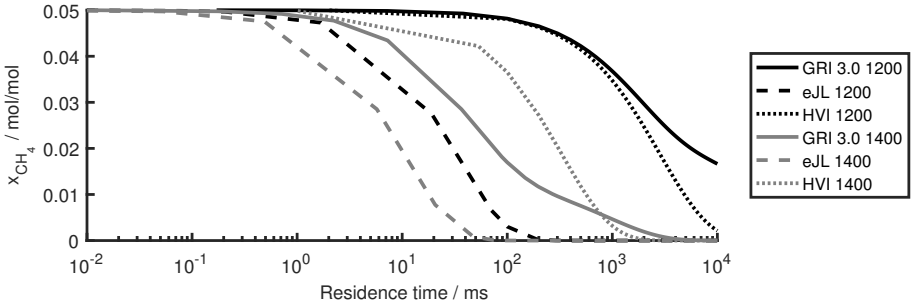

Figure 16.3.: Comparison of CH_4-concentration over residence time during CH_4 reforming in gasification zone at 1200^oC and 1400^oC between detailed and global mechanisms [304]

For typical temperatures in the REGA gasification zone (1200^oC) HVI mechanism shows excellent agreement with detailed mechanisms, while e-JL is too fast. For higher temperatures, e-JL reaches a better agreement with a detailed mechanism.

It is worth noticing here that the rate for the MEG decomposition (reaction HVI1 and reaction eJL1) is also calculated using the EDC. In this case, the EDC does not consider the mixing of different reactants (not needed for this kind of reaction) but takes into account the heating up of the MEG due to the turbulent mixing. With the assumption of the Lewis number equal to unity, the mathematical expression for the reaction rate does not differ from one of the other reactions.

A direct integration of the rate equations inside the fine structures has been adopted. Techniques of using tabulated values for the chemistry (for example the ISAT table) has not been used to avoid the introduction of other inaccuracies into the calculations.

16.3. Inlet and boundary conditions for the REGA-glycol-T1 campaign

The REGA test rig has been simulated using a 2D axisymmetric solver with a discretization of the computational domain using roughly 10^5 unstructured cells. Mesh sensitivity has been performed, and computational test using a structured mesh has been performed. The number of cells has been determined by the accuracy needed inside the flame where high steep gradients are present ($\Delta \sim 0.1$mm). The inputs of the model for the REGA-glycol-T1 run (see [110]) are summarized in Table 16.4.

Both air leaking into the reactor and the nitrogen purge are injected together with the atomizing medium, resulting in a flow of $\dot{m} = 18\frac{\mathrm{kg}}{\mathrm{h}}$. The oxygen represent 0.538 % in moles of the total flow.

		REGA-glycol-T1	
MEG	$\dot{m}$	12.56	$\frac{\mathrm{kg}}{\mathrm{h}}$
Air	$\dot{V}_A$	7.02	$\frac{\mathrm{Nm}^3}{\mathrm{h}}$
Oxygen	$\dot{V}_O$	4.98	$\frac{\mathrm{Nm}^3}{\mathrm{h}}$
Purge (N_2)	$\dot{V}_P$	0.514	$\frac{\mathrm{Nm}^3}{\mathrm{h}}$
	Leakage (air)	1.8	$\frac{\mathrm{Nm}^3}{\mathrm{h}}$

Table 16.4.: Inputs for the REGA-glycol-T1 simulation

The walls of the REGA has been electrically heated. For the heating elements a fixed temperature of $\vartheta_{he} = 1200^o$C has been assumed. The heating elements are placed inside the lateral wall at a depth of $\delta_w = 50$mm, and the heat transfer through this layer has been calculated using the Fourier law for a plane wall:

$$\dot{q}_w = k_w \frac{T_{he} - T_w}{\delta_w} \tag{16.4}$$

with $\dot{q}_w$ the specific heat flux through the wall, k_w the thermal conductivity of the refractory material and T_w the temperature of the internal surface.

The *no slip velocity* condition is assumed at the walls. This condition creates a boundary layer that requires fine cells near the walls to be adequately resolved. To avoid the exact solution of the near wall effects and consequently minimize the cell number requirement, the wall function approach is used (see Section 4.7.1). In the simulations, the smooth regime is always used, neglecting roughness effects. Since in the performed simulations the wall y^+ is smaller than 30 the two-layer model where the linear viscous region is resolved together with the logarithmic turbulent region and a blending function is used [173]. A similar approach using a law-of-the-wall has also been used to resolve the boundary layer for the enthalpy and for the species.

16.3.1. Inlet conditions for the spray modeling

The MEG droplets diameter distribution has been taken from measurements [165] and fitted using the Rosin-Rummler distribution (see Figure 16.4). In the Figure both mass based distribution and volume based distribution are presented. The parameters for the mass based Rosin-Rummler distribution have values of $D_{mean} = 100.9\mu m$ and $n = 1.776$.

Droplets are injected with a velocity of $U = 10\frac{m}{s}$ with injection directions distributed homogeneously in a cone of $\alpha = 10^o$ half angle.

16.4. Results of the REGA-glycol-T1 simulation

The calculated streamlines are reported in Figure 16.5. The streamlines for the HVI chemistry model are in the upper part, while those for the extended JL model are in the middle and those for the PDF model are reported in the lower part. The near burner region shows a strong recirculation zone where partially reacted gases are brought back to the burner and mixed both with the enriched air (the gasification medium) and the fuel from the burner inlets. All the models predict qualitatively the same pattern with similar figures for the total recirculated mass. The recirculation predicted by the HVI model has a strength of $\dot{m}_{rec} = 130\frac{\mathrm{kg}}{\mathrm{h}}$, corresponding to about 7 times the amount of air injected into the reactor (approximately 4.6 times the total mass flow injected

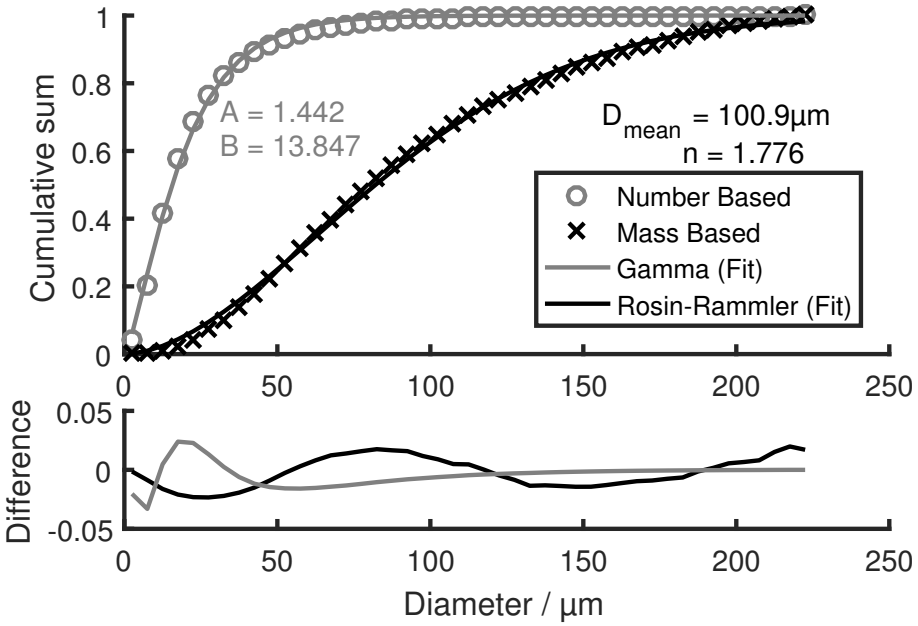

Figure 16.4.: Fitting of the droplet diameter distribution

into the reactor), and it extends up to $z = 840$mm distance from the burner. The extended JL model predicts the length of the recirculation to be $\Delta z = 910$mm. The PDF model predicts a stronger recirculation zone with a strength of $\dot{m}_{rec} = 135\frac{\text{kg}}{\text{h}}$ and a length of $\Delta z = 800$mm. The predictions of the PDF model also differ in the region downstream of the recirculation zone, where the streamlines are more open than in the predictions from the EDC based models.

The calculated temperatures, composition (CO, CO_2, H_2 and CH_4) and the droplet velocities have been compared with the measured values. The measurements have been taken in the radial direction at two distances from the burner, at $z = 300$mm (z_1) and $z = 682$mm (z_2). The Figure 16.6 shows contour of the CFD-calculated temperature (Bottom) and the temperature profile along the axis (Top). Results of the calculations of the EDC model with both chemical schemes and the PDF model are compared with measured values. The excellent agreement for all the calculations presented is an indication of the correctness of the adopted thermal boundary conditions.

In Figure 16.7 the gas temperatures (left) and the composition (right) are shown at five distances from the burner. All the models show the same general features while differences appear in details. Up to 150mm from the burner, a cold thin core is formed in the middle of the reactor, where glycol droplets are present. Around this cold core, a thin and hot flame is predicted by all the models. Both EDC models show a similar flame structure with the e-JL model predicting a longer flame while the HVI model is predicting a slightly hotter region. The predictions of the PDF model show substantial differences in the first 200 mm from the burner. The mixing between the streams is quicker, and it is accomplished within the first 50 mm from the burner (the figure predicted by the EDC models is more than 100 mm). As a consequence of the better mixing and the chemical equilibrium calculations, ignition takes place practically at the burner. The Figure 16.6 shows clearly the absence of a cold cone region in the PDF calculations. An immediate ignition of MEG vapors results in a high-temperature region also on the axis, and this high temperature drives further evaporation (endothermic process) with a subsequent decrease in temperature clearly seen in Figure 16.6.

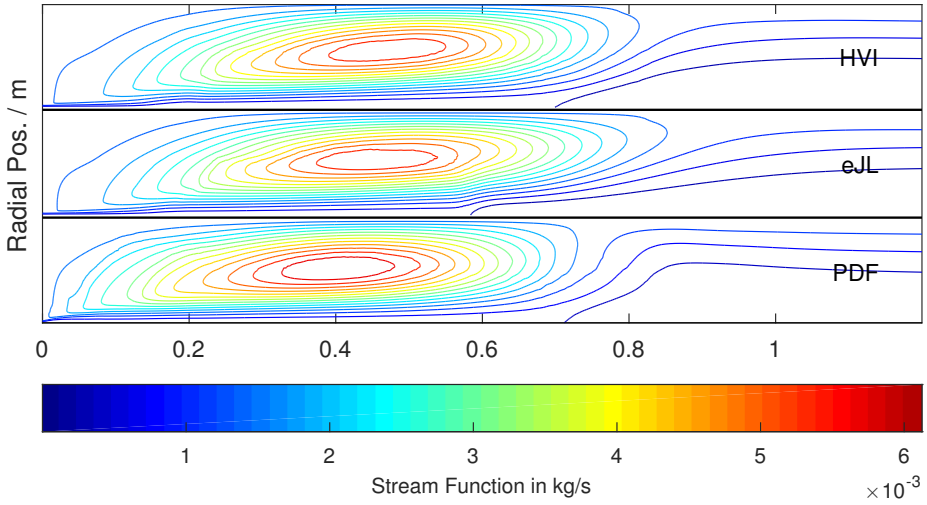

Figure 16.5.: Streamlines predicted by three different models [229]

The maximum temperature predicted by the HVI model is $\theta_{max} = 2867$ K while the e-JL model predicts $\theta_{max} = 2775$ K. Both temperatures are high for the absence of radicals in the mixture. Inside the flame, in the first 100 mm from the burner the PDF model, due to the coupling with chemical equilibrium calculations, predicts up to 2% of radicals, not taken into consideration in the global mechanisms. As a consequence the PDF model predicts the maximum temperature of $\theta_{max} = 2497$ K which is substantially lower than the predictions of the other two model.

From the comparisons presented in Figure 16.7 it is possible to see that both EDC models predict the temperature and all the composition very accurately at $z_2 = 680$ mm. The HVI mechanism overpredicts the methane concentration slightly at z_2, while at traverse $z_1 = 300$ mm is more accurate and predicts all the species reasonably well. All the calculations well reproduce the temperatures. The e-JL mechanism predicts higher temperature on the axis while the species concentrations are not as flat as the measurements indicate. It is worth noticing that the extended JL mechanism does not reproduce the CO to CO_2 ratio near the axis: the measurements indicate higher carbon monoxide than carbon dioxide concentration while the extended JL shows the opposite. This mechanism predicts a longer flame and at traverse $z_1 = 300$ mm the gas composition reflects more combustion than gasification.

16.5. Sensitivity Analysis

Because uncertainties, simplifications, and assumptions present in the model, needed for speeding up the calculations, a sensitivity analysis has been performed.

16.5.1. Turbulence models

The standard k-ϵ model, the realizable k-ϵ and the SST k-ω have been used in place of the more advanced RSM (see 4.3.1.3 for a short description).

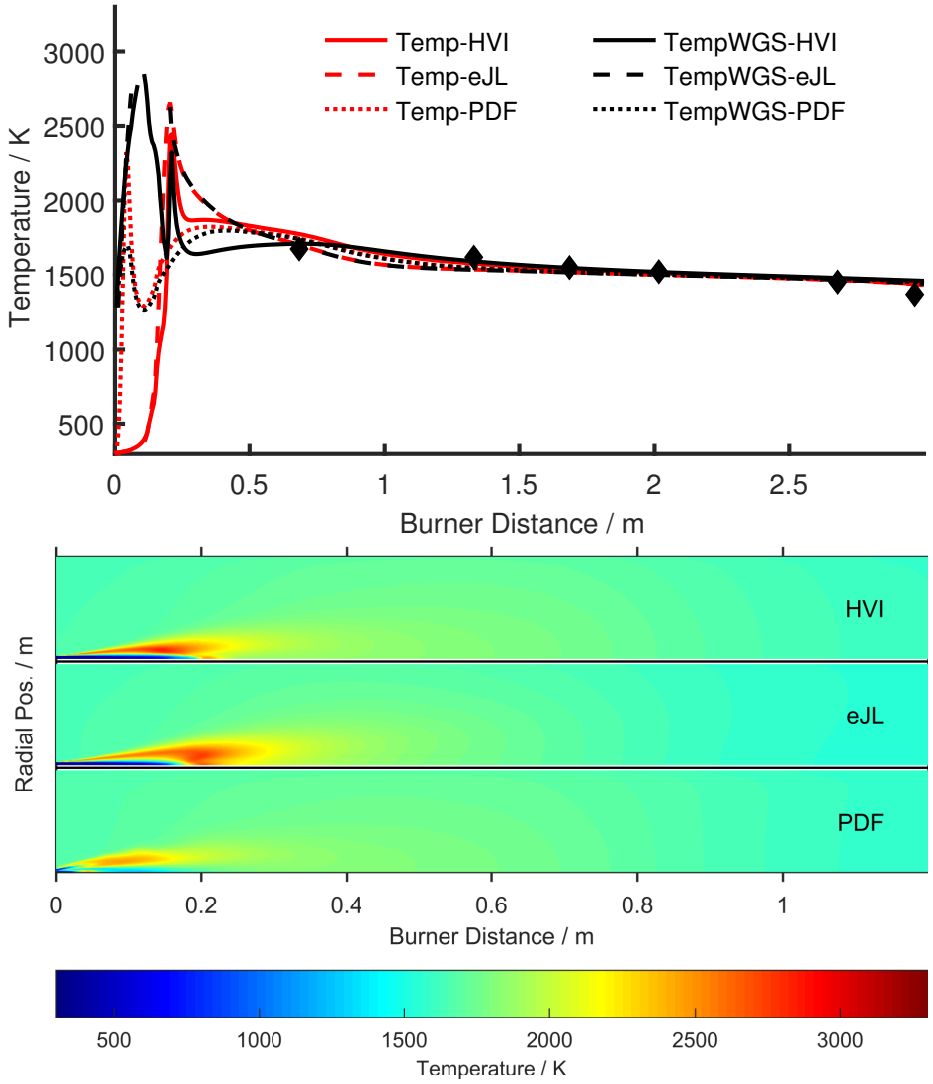

Figure 16.6.: Top: Measured and predicted gas temperature along the gasifier axis. Bottom: raster plot of the CFD-calculated temperatures [229]

In the k-ϵ models, the turbulent Reynolds stress tensor $\mathbf{T}$ is written using the turbulent viscosity hypothesis:

$$\mathbf{T} = -\mu_T \left(\frac{\partial U_i}{\partial x_j} + \frac{\partial U_j}{\partial x_i} \right) \tag{16.5}$$

with the turbulent viscosity μ_T expressed as a function of the turbulent kinetic energy k and its dissipation ϵ:

$$\mu_T = \rho C_\mu \frac{k^2}{\epsilon} \tag{16.6}$$

Only two extra equations are needed to close the model, namely the equation for the turbulent

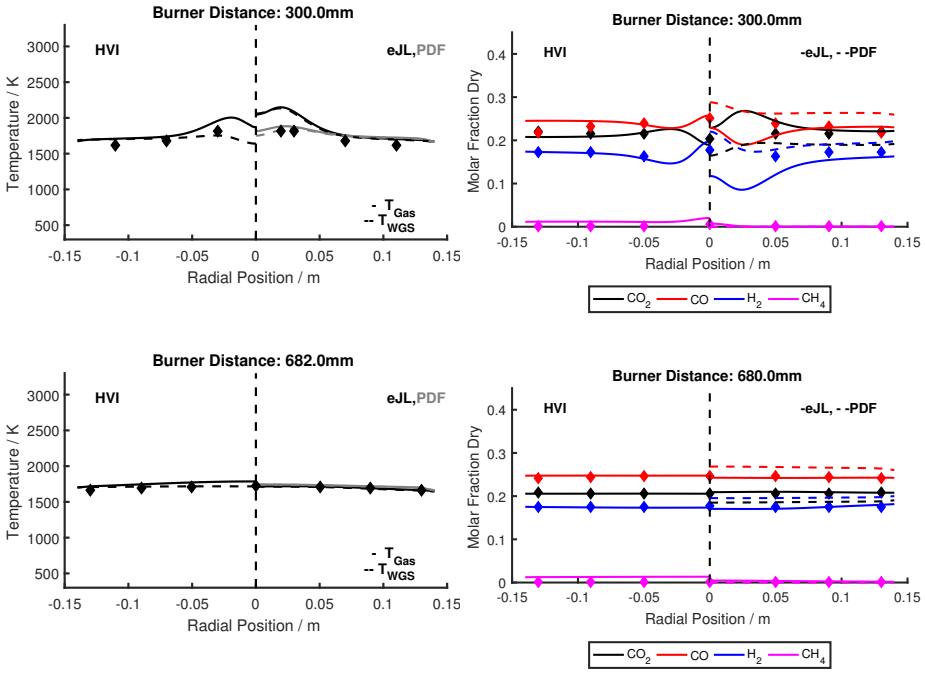

Figure 16.7.: Temperature (left) and Composition (right) radial profiles [229]

kinetic energy k and the equation for its dissipation ϵ. The standard and the realizable k-ϵ differ in the formulation for the turbulent viscosity and in a different transport equation for the dissipation rate, derived from an exact equation for the transport of the mean-square vorticity fluctuation.

Also, the SST k-ω model is a two-equation turbulence model that attempts to predict turbulent quantity using an equation for the kinetic energy and a second equation for the specific dissipation rate $\omega = \frac{\epsilon}{kC_\mu}$. The SST version (Shear Stress Transport) of the model combines the k-ω turbulence model and k-ϵ turbulence model such that the first one is used in the inner region of the boundary layer and switches to the second one in the free shear flow.

It is known that the standard k-ϵ model is weaker than other more advanced turbulence models in predicting the spread of free round (and planar) jet accurately. Both the realizable version of the k-ϵ and the k-ω model are superior in predicting this kind of flow structure.

Applied to the REGA reactor most of the differences can be seen in the flow field only. For all the simpler models the strength of the recirculation increases from $\dot{m} = 130$ to $\dot{m} = 144\ \frac{\mathrm{kg}}{\mathrm{h}}$; in the case of the standard k-ϵ model a wider jet is predicted from the comparison of the axial velocity at $z = 300$mm presented in Figure 16.8 (left). Despite of these differences the composition of the gas changes only slightly as also presented in the same figure (right). This effect can be understood comparing the time scale of the small eddies τ^* (see Eq (5.90)) and the fraction of the fine structure γ^* (see Eq (5.91)). Both quantities are functions of the turbulent k and ϵ and the differences inside both reaction zones are about 10%.

If the goal of the simulations is to predict the chemical composition of the syn-gas correctly the choice of the turbulence model is irrelevant.

As already mentioned before, particularly important is the determination of the molecular diffusion of vapor as a function of temperature, needed for the determination of the evaporation rate (see Eq. (6.11). Since a change in the diffusivity leads to a quicker or a slower evaporation,

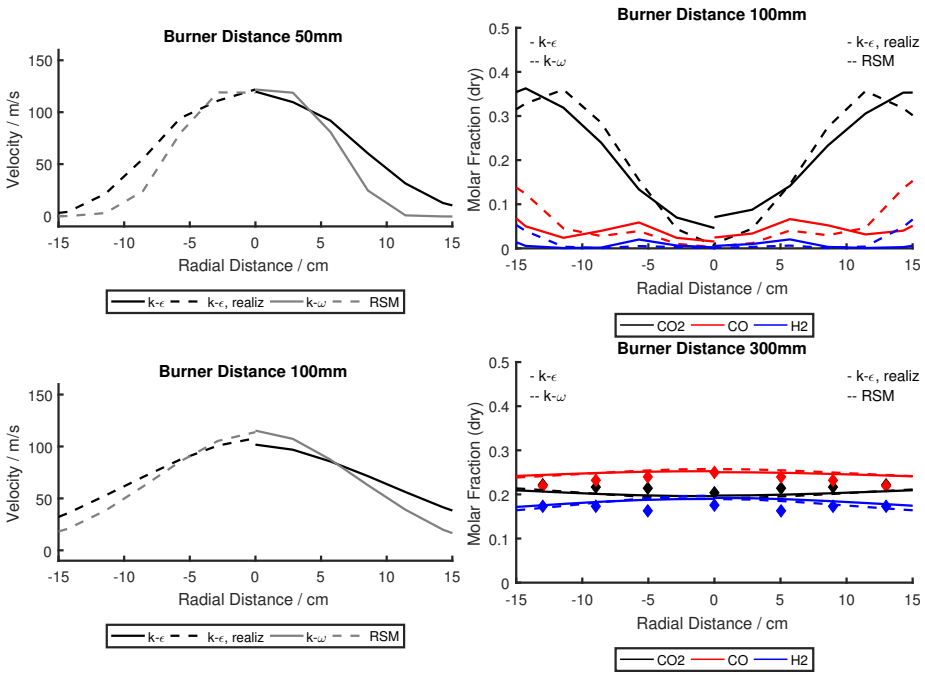

Figure 16.8.: Axial velocity (left) and composition (right) predicted using the RSM and three other simpler models. All the model use the HVI chemistry [229]

the consequences of using an inaccurate value are similar to the effects observed using smaller or bigger droplets.

17. Closure

The numerical simulation of solid fuels conversion is a part of the broader field of simulation of reactive systems, but it stands out because of its peculiar complexity. First of all, the process of conversion of solid materials involves many chemical reactions and physical processes that have not yet been completely clarified. As mentioned in the text, an enormous amount of experiments, measurements, and research has been made over several decades, but still more work is to come. This is so because solid fuels have a complex chemical structure that undergoes many changes when temperature increases. This complex behavior has been reviewed in this thesis with an attempt to explain it using, when possible, a unified view without losing sight of the individual processes.

This choice has been made for two reasons. Firstly, because solid materials are nowadays converted and processed in many ways with chemical and thermal changes going on in parallel and affecting and influencing each other. A unified description is more appropriate than a specific one for predicting the behavior of the solids in wider ranges without the need to introduce correction factors or ad hoc parameters. A second reason for a unified description is related to the large variety of available fuels. Despite the differences between them, some chemical and physical properties can be linked to more general and fundamental characteristics, reducing the arbitrariness of some assumptions.

The research in this field has not yet been completed since not all the many complexities are reduced to unified descriptions and, therefore, the use of experiments and measurements for a specific fuel is still necessary to close the gaps for the modeling. A drawback of a unified description of so many complex processes may be a loss of knowledge of each individual process. And this drift can be dangerous mainly for students. Due to the lack of experience, they can miss some correlations or some properties typical of each process. The consideration presented in this thesis combined both descriptions. The characteristics of each single process have been described, in conjunction with more advanced modeling that can highlight more general properties.

In this book, the subject has been presented in conjunction with CFD calculations since this is the natural mathematical environment for the field of non-equilibrium thermodynamics of reactive flows. Moreover, the CFD tools become more and more common among engineers and already are an essential steps in the industrial calculation and design. The possibility of applying such a sophisticated tool also brings limitations, disadvantages, and issues that are still open. The main challenge, present in almost all the described models, is the seek for simplicity of the mathematical description and is a typical feature of every CFD-based model. Without going into details, each model is a compromise between accuracy and calculability and the balance is a function of the computer performances. Aiming for this balance, several models have been presented, starting from the simplest ones (for which the accuracy and the applicability are limited) up to to the most complex and detailed models (for which the use in simulation of industrial processes is limited). Both approaches are, in my view, essential in modeling, in the same way as the description of single processes should be consistent with a unified description (as previously discussed).

The CFD method has been explained with the same philosophy, with emphasis focused on the RANS approaches. Several models for the treatment of unclosed terms have been presented and some of them have been discussed in more details. It is not correct to create the impression

on young students that everything done in the past is the result of mistakes, approximations or incorrect assumptions that no one would do today anymore. Even the simplest of the models is based on analyses that have been developed with the use of some mathematical tools (which therefore are scientific) from which the young student should learn a lot.

For space reasons, it has not been possible to provide comparisons between the different models presented even if in a didactic perspective such comparisons are of fundamental importance and interest. For the same reason, nothing has been written about the solution methods of the differential equations.

In the second part of the book, the experimental method adopted at the IEVB (an acronym for the German name: Institut für Energieverfahrenstechnik und Brennstofftechnik) for the analysis of solid fuels has been described and results of its application have been presented. The philosophy adopted, is based on three steps:

1. Collection of data for each fuel;
2. Extraction of the parameters needed in the modeling;
3. Validation of the resulting CFD model using simple flames up to semi-industrial scales.

One of the goals of this book (perhaps the main one) was to demonstrate to what extent the CFD method can predict in-flame measurements. Many examples of calculations where flames are well predicted are available in the literature, and some of them have been reported here. As a conclusion, CFD can predict accurately solid fuels conversion processes, with some limitations:

1. Small-scale flames are better predicted than industrial ones;
2. Accuracy deteriorates if details of the fuel are not known;
3. Some inaccuracies are still present in the predictability of CO and NO concentrations.

The limitations listed above become evident to modelers in everyday life when results and information are requested during designing industrial applications. It is unlikely that the first CFD run will give results in accordance with measurements. Usually, the excellent agreement presented in the literature is the results of many years of research, thorough investigations and uncertainties analysis. Therefore, there is also a list of conditions, experiments, flames, where the CFD fails to predict the measurements. Those cases are hidden in the drawers, also because no scientific journal would publish results that are contradicted by measurements.

Last but not least, the explanations, the modeling closures, and the approaches presented in this thesis are given having in mind applications to industrial processes. Alongside new models, examples of how CFD calculations produce information, useful in the development of new technologies, have been presented.

What is to come further? There is still a lot to do in the field of solid fuel modeling. In all aspects presented here:

- Many closures in the CFD sub-models are behind in development in comparison to the models designed for combustion of gaseous fuels. Accurate chemistry mechanisms that involve the relevant light-gas components as well as the tars, begin to be available but their reduction and implementation into a CFD is still in the infancy. For example, the analysis of the interaction between chemistry and turbulence based on the Low-Dimensional Manifolds idea works well for gaseous fuels but it has not been yet developed in the case of solid fuels conversion processes.

- There is still a lack of understanding of details in many solid fuels conversions. The rates of pyrolysis, combustion, and gasification at high pressures and high temperatures are seldom known and, mainly in the case of pyrolysis, the models predicting the dependency of the products on the thermodynamic parameters lack the required accuracy.
- The uncertainties in measurements must be reduced (in measurements of properties of the solids);

Is CFD the *final tool* in thermal-fluid science and thermal engineering?

CFD is an excellent tool, useful in many applications and it solves the basic equations for the non-equilibrium thermodynamics (invoking the assumption of a Local Thermodynamic Equilibrium). Theoretically, it could be employed in almost all industrial applications since there is almost always a fluid in motion. It's hard to say if it is the *ultimate one* since for the moment it has limitations in its reliability and its applicability. But the most important reason why I would say it cannot be the *final* tool (at least not in education) is its complexity. Students need understanding. They need to build their knowledge using smaller blocks until they master them to such a level that these blocks (sub-models) become distinguishable to them while incorporated in CFD codes.

Part IV.

Appendices

A. Detailed homogeneous combustion mechanisms

A.1. The reaction scheme

In this section detailed combustion mechanisms for few relevant molecules (hydrocarbons) are reviewed. Generally, the oxidation path can be divided into three main steps [383, 117]:

1. the fuel is attacked by H and O radicals and is converted in CH_i radicals and H_2. Hydrogen, in the presence of oxygen, is converted into water;
2. the CH_i radicals oxidize further to CO and H_2 that is later converted into water;
3. CO is oxidized to CO_2.

Considering the enthalpy of formation of the given species it is easy to show that about 25% of the energy of the process is released in the last step.

Typical behavior in a premixed flame front is shown in Figure A.1. Methane is the only fuel, and the oxidizer is air with $\lambda = 1.1$. The mixture is preheated to a temperature of 1500 K. In the figure, it is possible to recognize three regions.

Pre-ignition region: At the beginning, just after the pre-mixing, the gas needs a certain amount of time to start the reaction and ignite itself. The ignition time depends on the composition and the mixture temperature. For compositions near the ignition limits and temperatures near the ignition temperature, this time is longer, reaching a minimum near the stoichiometric conditions.

Combustion region: After ignition, the speed of reactions gradually increases. This region is a transition region where several reaction rates scales play an important role. The concentration of fuel (in the case of Figure A.1 only methane) and oxygen start to decrease, and the products are formed. Each fuel has a different kind of transition regions. For hydrocarbons in conventional combustion conditions, the transition is extremely fast: the radicals attack and quickly dissociate the hydrocarbon molecules. For CO and even for H_2 the transition is slower. The concentration of intermediate species (hydrogen in Figure A.1 is one of them) and the radicals, after ignition, can reach high peaks and then decrease towards equilibrium.

Post-combustion region: The reaction rates decrease in this region. The time dependence is lower, and almost all the species are near equilibrium.

The importance of these three regions has been reconsidered in Section 5.4, with regards to the interaction with turbulence since each model is based on assumptions valid only in one of the aforementioned regions.

Detailed mechanisms are formed by a large number of chain reactions in which stable molecules react with radicals. Chain reactions can be grouped into five main categories depending on the fate of the radicals involved:

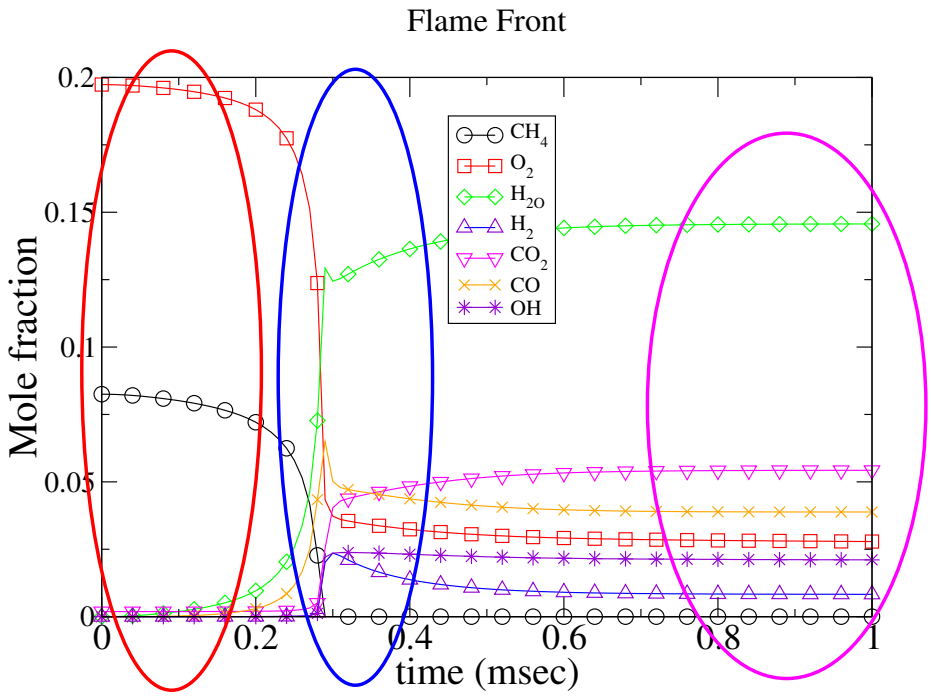

Figure A.1.: Premixed flame front for CH_4 and air in lean condition with inlet temperature of 1500 K. The circles point out the three different regions in which hydrocarbons combustion can be divided

1. Chain initiation, in which radicals are formed from stable molecules;
2. Chain branching, in an attack of a radical to a stable molecule, cause the number of radicals to increase;
3. Chain propagation, in which the number of radicals is left unchanged;
4. Chain inhibition, in which the number of radicals decreases;
5. Chain termination, in which radicals recombination to stable molecules let no free radicals available.

Every step is made up of different reactions depending on the temperature and pressure but also from the geometrical structure of the flame considered. In this chapter, several oxidation mechanisms for diffusion flames are shortly described.

A.1.1. The formation and destruction of H_2

The combustion of hydrogen is important since it is the last step of combustion for all the fuels containing H atoms. This section follows the review of [383] closely, but more extended reviews can be found in [434, 117, 401].

The formation of H_2 is due to the breaking of the hydrocarbon chains mainly following the reactions:

$$CH_4 + H \rightleftharpoons CH_3 + H_2 \quad \text{(R A.1)}$$

$$C_2H_4 + H \rightleftharpoons C_2H_3 + H_2 \quad \text{(R A.2)}$$

$$CH_3 + H \rightleftharpoons CH_2 + H_2 \quad \text{(R A.3)}$$

$$CH_2O + H \rightleftharpoons HCO + H_2 \quad \text{(R A.4)}$$

$$CH_3 + O \rightleftharpoons H + H_2 + CO \quad \text{(R A.5)}$$

The initiation reactions for the oxidation are[1]:

$$H_2 + O_2 \rightleftharpoons HO_2 + H \quad \text{(R A.6)}$$

followed by the reactions involving radicals:

$$H + O_2 \rightleftharpoons OH + O \quad \text{(R A.7)}$$

$$H_2 + O \rightleftharpoons OH + H \quad \text{(R A.8)}$$

$$H_2 + OH \rightleftharpoons H_2O + H \quad \text{(R A.9)}$$

$$O + H_2O \rightleftharpoons 2\,OH \quad \text{(R A.10)}$$

The chain-terminating reactions are the three body recombination reactions:

$$H + O + M \rightleftharpoons OH + M \quad \text{(R A.11)}$$

$$H + OH + M \rightleftharpoons H_2O + M \quad \text{(R A.12)}$$

together with the recombination of H and O into hydrogen and oxygen.

When the following reaction:

$$H + O_2 + M \rightleftharpoons HO_2 + M \quad \text{(R A.13)}$$

becomes active, then the reactions of the hydroperoxide radical (HO_2) follow:

$$HO_2 + H \rightleftharpoons 2\,OH \quad \text{(R A.14)}$$

$$HO_2 + H \rightleftharpoons H_2O + O \quad \text{(R A.15)}$$

$$HO_2 + O \rightleftharpoons O_2 + OH \quad \text{(R A.16)}$$

$$HO_2 + OH \rightleftharpoons H_2O + O_2 \quad \text{(R A.17)}$$

and the reactions of the hydrogen peroxide (H_2O_2):

$$HO_2 + HO_2 \rightleftharpoons H_2O_2 + O_2 \quad \text{(R A.18)}$$

$$HO_2 + H_2 \rightleftharpoons H_2O_2 + H \quad \text{(R A.19)}$$

and:

$$H_2O_2 + OH \rightleftharpoons H_2O + HO_2 \quad \text{(R A.20)}$$

$$H_2O_2 + H \rightleftharpoons H_2O + OH \quad \text{(R A.21)}$$

$$H_2O_2 + H \rightleftharpoons HO_2 + H_2 \quad \text{(R A.22)}$$

$$H_2O_2 + M \rightleftharpoons 2\,OH + M \quad \text{(R A.23)}$$

[1] The thermal dissociation of H_2 is important only at very high temperature

A.1.2. The formation and destruction of CO

This important mechanism has been already summarized in Section 9.1.

A.1.3. Oxidation of CH_4

At high temperature ($T \geq 1500\,\mathrm{K}$) the thermal decomposition of methane is the initiating step of the oxidation process:

$$\mathrm{CH_4 + M \longrightarrow CH_3 + H + M} \tag{R A.24}$$

With the presence of H radical (in stable diffusion flames), the oxidation process for the system H_2 - O_2 takes place quickly and the other reactions are more effective in extracting the hydrogen radical from the methane molecule:

$$\mathrm{CH_4 + H \longrightarrow CH_3 + H_2} \tag{R A.25}$$

$$\mathrm{CH_4 + OH \longrightarrow CH_3 + H_2O} \tag{R A.26}$$

The reaction with the OH radical is usually the fastest.

If the further oxidation of the ethyl radical is slow for example in the region of the flame where no oxygen is present, the recombination reaction to form ethane takes place:

$$\mathrm{CH_3 + CH_3 \longrightarrow C_2H_6} \tag{R A.27}$$

The ethane formed by the previous reaction has to be oxidized further as soon as oxygen is available.

Competing with the reaction R A.27, the most effective reaction is the following:

$$\mathrm{CH_3 + O_2 \longrightarrow CH_3O + O} \tag{R A.28}$$

The methoxy radical CH_3O decompose rapidly into formaldehyde:

$$\mathrm{CH_3O + M \longrightarrow H_2CO + H + M} \tag{R A.29}$$

The formaldehyde is attacked by radicals to give HCO:

$$\mathrm{H_2CO + H \longrightarrow HCO + H_2} \tag{R A.30}$$

$$\mathrm{H_2CO + O \longrightarrow HCO + OH} \tag{R A.31}$$

$$\mathrm{H_2CO + OH \longrightarrow HCO + H_2O} \tag{R A.32}$$

that reacts further to CO.

In Figure A.2, Figure A.3 and Figure A.4 the reaction path diagrams following C for $\lambda < 1$, $\lambda = 1$ and $\lambda > 1$ respectively are presented. The diagrams are created from the simulation of a opposite diffusion flame (flamelet) for methane and air at a strain of $\chi = 1\,\frac{1}{\mathrm{s}}$.

The following can be observed:

1. In under-stoichiometry conditions (figure Figure A.2) methane reacts to ethane and acetylene (the second being favored in this conditions). No CO is formed.

2. In stoichiometry conditions (figure Figure A.3) the main path through formaldehyde is active. Ethane has been already oxidized while the path through acetylene (to CO) is

still active. CO is now formed from HCO (from formaldehyde) and dissociation of CO_2 eventually formed in other reactions.

3. At higher stoichiometry (figure Figure A.4) CO is oxidized to CO_2.

In Figures Figure A.5, Figure A.6 and Figure A.7 the reaction path diagrams following H for $\lambda < 1$, $\lambda = 1$ and $\lambda > 1$ respectively are presented. Much more reactions are present in those diagrams but the paths identified from the previous analysis are still recognized. The main difference now is the presence o hydrogen, formed during radical reactions at sub-stoichiometry and stoichiometry conditions. Hydrogen will be slowly oxidized as soon as radicals recombine.

Globally the methane oxidation could better be described by the reaction:

$$\mathrm{CH_4 + O_2 \longrightarrow CO + H_2 + H_2O}$$

followed by oxidation of CO and H_2.

A.1.4. Oxidation of higher hydrocarbons

The importance of higher order hydrocarbons results not only from their substantial presence in the fuel composition but also, as already seen in the Section above, from the fact that methyl radicals recombine to give ethane.

In the absence of radicals the long hydrocarbon molecules split thermally and a $C-C$ bond is broken:

$$\mathrm{C_nH_{2n+2} + M \longrightarrow R' + R'' + M} \qquad \text{(R A.33)}$$

where R' and R'' are two radicals of lower order. Some of the $C-H$ bonds are also broken, leading to the formation of the H radical:

$$\mathrm{C_nH_{2n+2} + M \longrightarrow C_nH_{2n+1} + H + M} \qquad \text{(R A.34)}$$

Other low-temperature reactions can also be present as, for example, the low-temperature reaction with oxygen. The final result of these first steps is the formation of H radicals that can react with O_2 leading to the formation of a pool of radicals. After that pool is formed, the fuel is reduced following the reactions:

$$\mathrm{R{-}H + OH \longrightarrow R + H_2O} \qquad \text{(R A.35)}$$

$$\mathrm{R{-}H + X \longrightarrow R + H{-}X} \qquad \text{(R A.36)}$$

where R represent one of the alkyl radicals and X is mainly one of O, OH, H or CH_3 radicals with the reaction rates being dependent also on which H atom is abstracted.

The alkyl radical is usually highly unstable and dissociates into an olefin and a lower order radical or, in the case of the ethyl radical, into ethene and H.

Propane forms either n-propyle radical (the H abstracted was linked to a C atom at the end of the chain) or an iso-propyl radical (the H abstracted was attached to the central carbon atom of the chain). The two radicals form propene (from the iso-propyl radical) and ethene (from the n-propyl radical):

$$\mathrm{n\text{-}C_3H_7 + M \longrightarrow C_2H_4 + C_3} \qquad \text{(R A.37)}$$

$$\mathrm{i\text{-}C_3H_7 + M \longrightarrow C_3H_3 + H} \qquad \text{(R A.38)}$$

The reaction rate of the second path is higher than the first.

The H removed by alchene molecules is usually the one not linked to a double bonded C atom. Therefore all the higher hydrocarbons commonly present in the natural gas form ethene, before reacting to CO.

In the case of ethane oxidation, for the removal of the H atom the ethyl radical C_2H_5 can react directly with oxygen:

$$C_2H_5 + O_2 \longrightarrow C_2H_4 + HO_2 \quad \text{(R A.39)}$$

The primary attack on ethene is by the O radical:

$$C_2H_4 + O \longrightarrow CH_3 + HCO \quad \text{(R A.40)}$$

but other reactions can be involved, like:

$$C_2H_4 + O \longrightarrow CH_2 + H_2CO \quad \text{(R A.41)}$$

$$C_2H_4 + OH \longrightarrow CH_3 + H_2CO \quad \text{(R A.42)}$$

$$C_2H_4 + OH \longrightarrow C_2H_3 + H_2O \quad \text{(R A.43)}$$

$$C_2H_4 + H \longrightarrow C_2H_3 + H_2 \quad \text{(R A.44)}$$

The species formed up to now undergo mainly the following transformations:

$$C_2H_3 + M \longrightarrow C_2H_2 + H + M \quad \text{(R A.45)}$$

$$C_2H_3 + O_2 \longrightarrow C_2H_2 + HO_2 \quad \text{(R A.46)}$$

$$C_2H_2 + O \longrightarrow CH_2 + CO \quad \text{(R A.47)}$$

$$CH_2 + O \longrightarrow H_2CO + O \quad \text{(R A.48)}$$

A.1.5. The oxidation of aromatic compounds

The pyrolysis and the oxidation of aromatic compounds are both problematic processes to be generally described since many species are involved, and those species usually have very different chemical properties. The reaction of Benzene must be treated separately since no hydrocarbon radicals are attached to the ring, bat also Toluene has a proper reactivity that resembles the one of Benzene.

The aromatic ring interferes with the reactivity of the attached molecules changing the selectivity how carbon atoms react, but usually the side chains are converted before the ring itself since (at higher temperatures) the radicals react faster with the ring than the rate of thermal dissociation. Of importance is also the knowledge when the ring chemically opens or thermally decomposes changing the way the remaining molecules reacts.

In the case of benzene, experiments at high temperatures have shown a sequence of stable compounds following the order [128]: phenol, cyclopentadiene, vinyl acetylene, butadiene, ethene, and acetylene. The combustion of toluene (and higher alkylated aromatics) is remarkably similar to the oxidation of benzene. During the conversion, the ring remains stable until the molecules have reached the phenyl radical stage. From the C_6 stage, identical mechanisms follow.

Aromatic compounds have the property to react with other compounds, by electrophilic substitution reactions. The most important reactions are:

1. Halogenation, with the formation of Chlorobenzene;

2. Nitration, with the formation of Nitrobenzene;

3. Sulfonation, with the formation of Benzenesulfonic acid.

Those reactions open up the possibility that in solid fuel conversion, tars can react with the vapors from the ash evaporation.

A.1.6. Simplified combustion

In a *CFD* calculation, it is prohibitive to manage the chemistry calculation in such a detail as described in the previous Section. To simplify the chemistry calculation, several strategies are adopted.

Simplified mechanisms: Not all the species and not all the reactions are important in combustion. In such a way, several simplified mechanisms are considered. These mechanisms differ in the number of species and number of reactions. The reaction rates are given using an Arrhenius expression as for the complete mechanisms.

Reduced mechanisms: Only a small number of main species are resolved and the reaction mechanism is extremely simplified. To improve the generality of the schemes the reaction rates are not given in an Arrhenius form, but in other analytical forms, which are typically complex functions of temperature and main species concentration. The concentration of radicals generally is estimated using either the quasi-steady state approximation or the partial equilibrium approximation.

Global mechanisms: As in the reduced mechanisms, only the main species are taken, and only a few steps are resolved, but the reaction rates are given in an Arrhenius form. The parameters of the Arrhenius formula are usually derived either by fitting experimental data or by performing more detailed chemistry calculations. The effect of the radicals is omitted.

The combustion of natural gas can be modeled using the following mechanisms:

Two-step mechanism: The hydrocarbon mixture comprises of methane and a numerical fuel [2] that react following the two-step mechanism:

$$\mathrm{CH_4} + 1.5\,\mathrm{O_2} \longrightarrow \mathrm{CO} + \mathrm{H_2O} \tag{R A.49}$$

$$\mathrm{C}_x\mathrm{H}_y + 0.5\,(\mathrm{x} + 0.5\,\mathrm{y})\,\mathrm{O_2} \longrightarrow x\,\mathrm{CO} + 0.5\,y\,\mathrm{H_2O} \tag{R A.50}$$

$$\mathrm{CO} + 0.5\,\mathrm{O_2} \longrightarrow \mathrm{CO_2} \tag{R A.51}$$

The reaction rates are taken from Dryer [95].

Four-step mechanism: The mixture contains only methane and the reactions proceed as follows:

$$\mathrm{CH_4} \longrightarrow \mathrm{CH_3} + 0.5\,\mathrm{H_2} \tag{R A.52}$$

$$\mathrm{CH_3} + 0.5\,\mathrm{O_2} \longrightarrow 2\,\mathrm{CO} + 3\,\mathrm{H_2} \tag{R A.53}$$

$$\mathrm{CO} + 0.5\,\mathrm{O_2} \longrightarrow \mathrm{CO_2} \tag{R A.54}$$

$$\mathrm{H_2} + 0.5\,\mathrm{O_2} \longrightarrow \mathrm{H_2O} \tag{R A.55}$$

[2] A Numerical Fuel (NF) is a hypothetical fuel of the form $C_xH_yO_zN_t$ where the parameters x, y, z and t are calculated from the composition of the parent mixture. The molecular weight, the specific heat and the formation enthalpy can also be calculated from the parent fuel composition.

Four-step mechanism: The hydrocarbon mixture is represented by a numerical fuel (C_xH_y) only and the reaction mechanism scheme proposed by Jones and Lidestedt [169] is as follows:

$$\mathrm{C}_x\mathrm{H}_y + x\,\mathrm{H_2O} \longrightarrow x\,\mathrm{CO} + 0.5\,(\mathrm{y} + 2\,\mathrm{x})\,\mathrm{H_2} \quad \text{(R A.56)}$$

$$\mathrm{C}_x\mathrm{H}_y + x\,\mathrm{O_2} \longrightarrow x\,\mathrm{CO} + 0.5\,y\,\mathrm{H_2} \quad \text{(R A.57)}$$

$$\mathrm{CO} + \mathrm{H_2O} \longleftrightarrow \mathrm{CO_2} + \mathrm{H_2} \quad \text{(R A.58)}$$

$$\mathrm{H_2} + 0.5\,\mathrm{O_2} \longleftrightarrow \mathrm{H_2O} \quad \text{(R A.59)}$$

Nine-step mechanism: The mechanism of combustion is as follows, with a mixture of 9 species (derived from the Augmented Reduced Mechanism of Chen et al. [359, 360, 361]):

$$\mathrm{H_2} + \mathrm{O_2} \rightleftharpoons \mathrm{H} + \mathrm{OH} \quad \text{(R A.60)}$$

$$4\,\mathrm{H} + \mathrm{O_2} \rightleftharpoons \mathrm{H_2} + 2\,\mathrm{OH} \quad \text{(R A.61)}$$

$$\mathrm{H} + \mathrm{O} \rightleftharpoons \mathrm{OH} \quad \text{(R A.62)}$$

$$\mathrm{H_2} + 2\,\mathrm{O} + \mathrm{CH_3} \rightleftharpoons 4\,\mathrm{H} + \mathrm{OH} + \mathrm{CO} \quad \text{(R A.63)}$$

$$\mathrm{O} + \mathrm{CH_4} \rightleftharpoons \mathrm{OH} + \mathrm{CH_3} \quad \text{(R A.64)}$$

$$\mathrm{H} + \mathrm{OH} + \mathrm{CO} \rightleftharpoons \mathrm{H_2} + \mathrm{CO_2} \quad \text{(R A.65)}$$

$$\mathrm{H} + \mathrm{OH} \rightleftharpoons \mathrm{H_2O} \quad \text{(R A.66)}$$

$$5\,\mathrm{H} + \mathrm{NO} \rightleftharpoons 2\,\mathrm{H_2O} + \mathrm{OH} + \mathrm{N_2} \quad \text{(R A.67)}$$

$$\mathrm{O} + \mathrm{N_2O} \rightleftharpoons \mathrm{O_2} + \mathrm{N_2} \quad \text{(R A.68)}$$

14-step mechanism: The mechanism contain 19 species and 14 reactions (derived from the Augmented Reduced Mechanism of Chen et al. [359, 360, 361]) :

$$\mathrm{H} + 0.5\,\mathrm{O_2} \rightleftharpoons \mathrm{OH} \quad \text{(R A.69)}$$

$$\mathrm{H_2} + 0.5\,\mathrm{O_2} \rightleftharpoons \mathrm{H} + \mathrm{OH} \quad \text{(R A.70)}$$

$$\mathrm{HO_2} \rightleftharpoons 0.5\,\mathrm{O_2} + \mathrm{OH} \quad \text{(R A.71)}$$

$$0.5\,\mathrm{O_2} + \mathrm{H_2O_2} \rightleftharpoons \mathrm{OH} + \mathrm{HO_2} \quad \text{(R A.72)}$$

$$0.5\,\mathrm{O_2} + 0.5\,\mathrm{C_2H_2} \rightleftharpoons \mathrm{H} + \mathrm{CO} \quad \text{(R A.73)}$$

$$\mathrm{CH_3} + \mathrm{CO} + \mathrm{C_2H_4} \rightleftharpoons 0.5\,\mathrm{O_2} + \mathrm{CH_4} + 1.5\,\mathrm{C_2H_2} \quad \text{(R A.74)}$$

$$0.5\,\mathrm{O_2} + 2\,\mathrm{CH_3} \rightleftharpoons \mathrm{H_2} + \mathrm{CH_4} + \mathrm{CO} \quad \text{(R A.75)}$$

$$0.5\,\mathrm{O_2} + \mathrm{CH_4} \rightleftharpoons \mathrm{H} + \mathrm{CH_2O} \quad \text{(R A.76)}$$

$$0.5\,\mathrm{O_2} + \mathrm{CO} \rightleftharpoons \mathrm{CO} \quad \text{(R A.77)}$$

$$0.5\,\mathrm{O_2} + \mathrm{C_2H_6} \rightleftharpoons \mathrm{CH_4} + \mathrm{CH_2O} \quad \text{(R A.78)}$$

$$\mathrm{H} + \mathrm{OH} \rightleftharpoons \mathrm{H_2O} \quad \text{(R A.79)}$$

$$\mathrm{H} + \mathrm{CH_4} + \mathrm{NO} + \mathrm{HCN} \rightleftharpoons 0.5\,\mathrm{O_2} + 2\,\mathrm{CH_3} + \mathrm{N_2} \quad \text{(R A.80)}$$

$$\mathrm{H} + 0.5\,\mathrm{O_2} + \mathrm{CH_4} + \mathrm{HCN} \rightleftharpoons 2\,\mathrm{CH_3} + \mathrm{NO} \quad \text{(R A.81)}$$

$$0.5\,\mathrm{O_2} + \mathrm{CH_4} + \mathrm{NH_3} + \mathrm{HCN} \rightleftharpoons \mathrm{H_2O} + 2\,\mathrm{CH_3} + \mathrm{N_2} \quad \text{(R A.82)}$$

It is worth noticing that in the last two reduced mechanisms, NO production is considered within the principal mechanism itself and not as a post-processor.

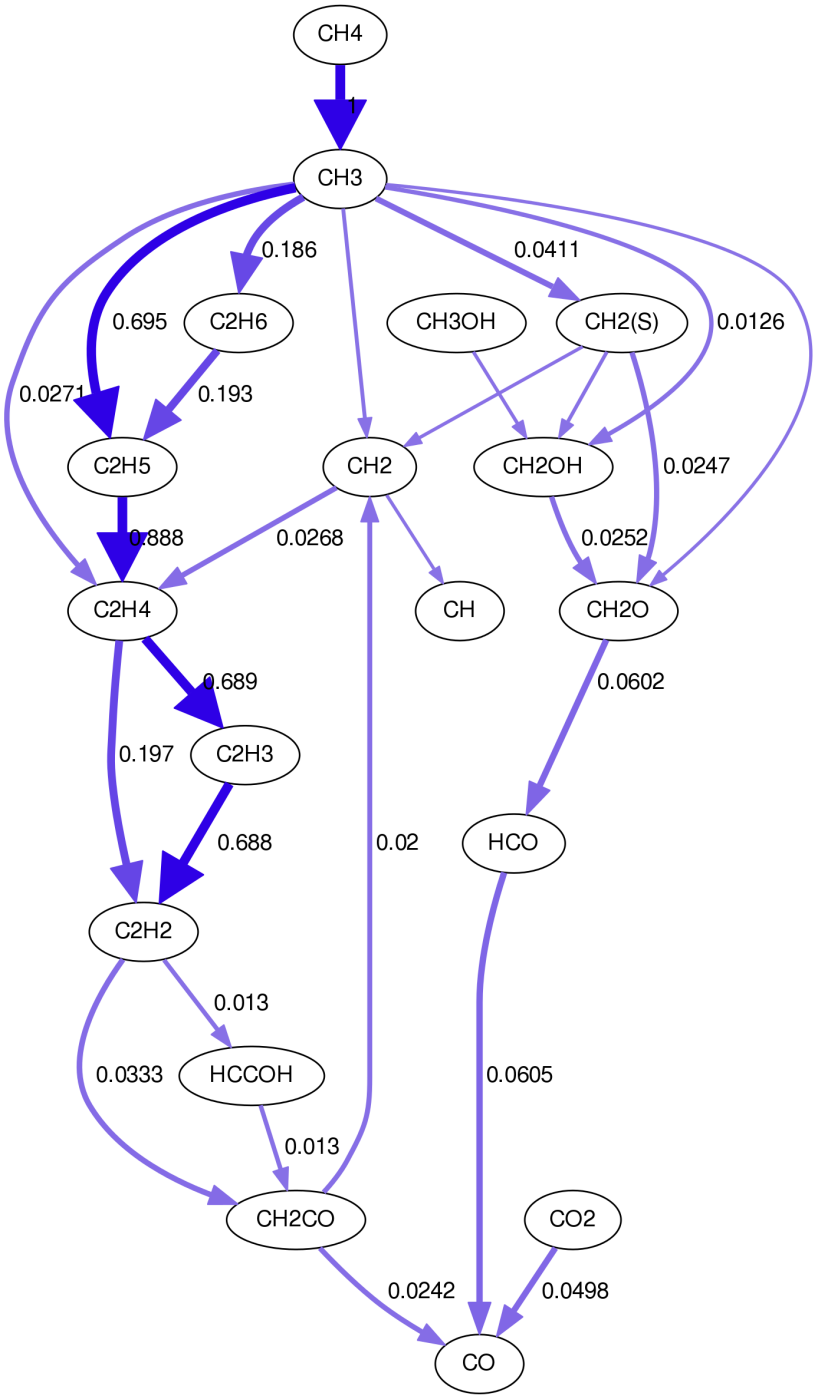

Figure A.2.: Reaction path diagram following C for $\lambda < 1$

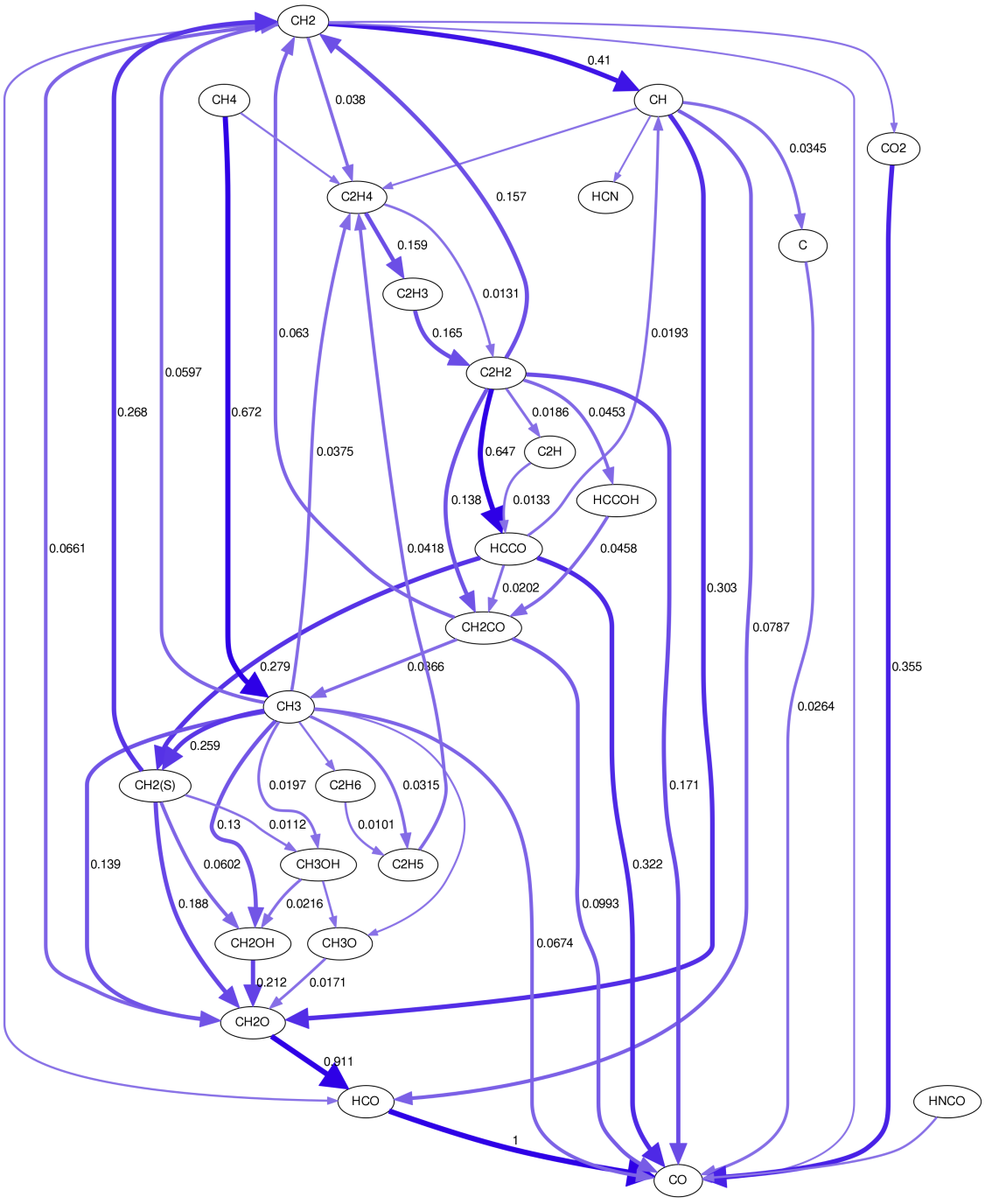

Figure A.3.: Reaction path diagram following C for $\lambda = 1$

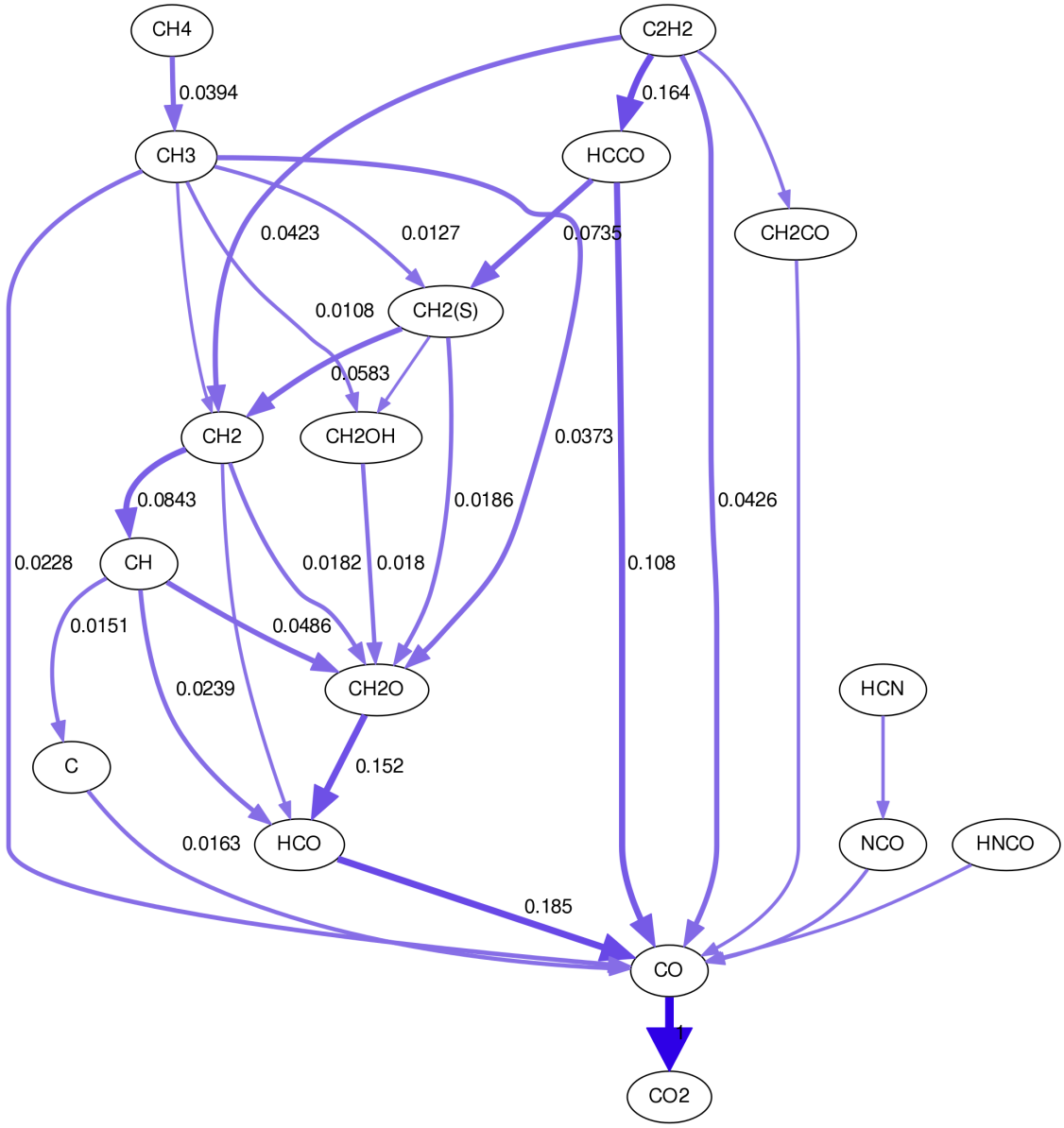

Figure A.4.: Reaction path diagram following C for $\lambda > 1$

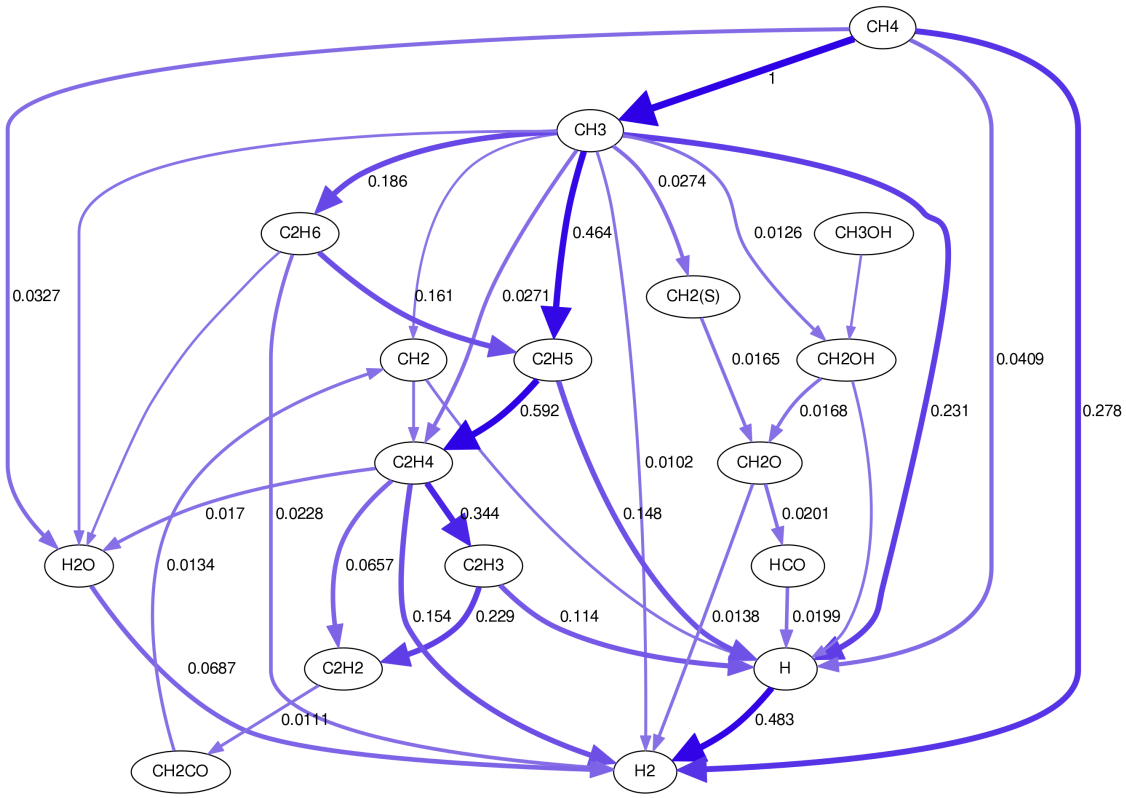

Figure A.5.: Reaction path diagram following H for $\lambda < 1$

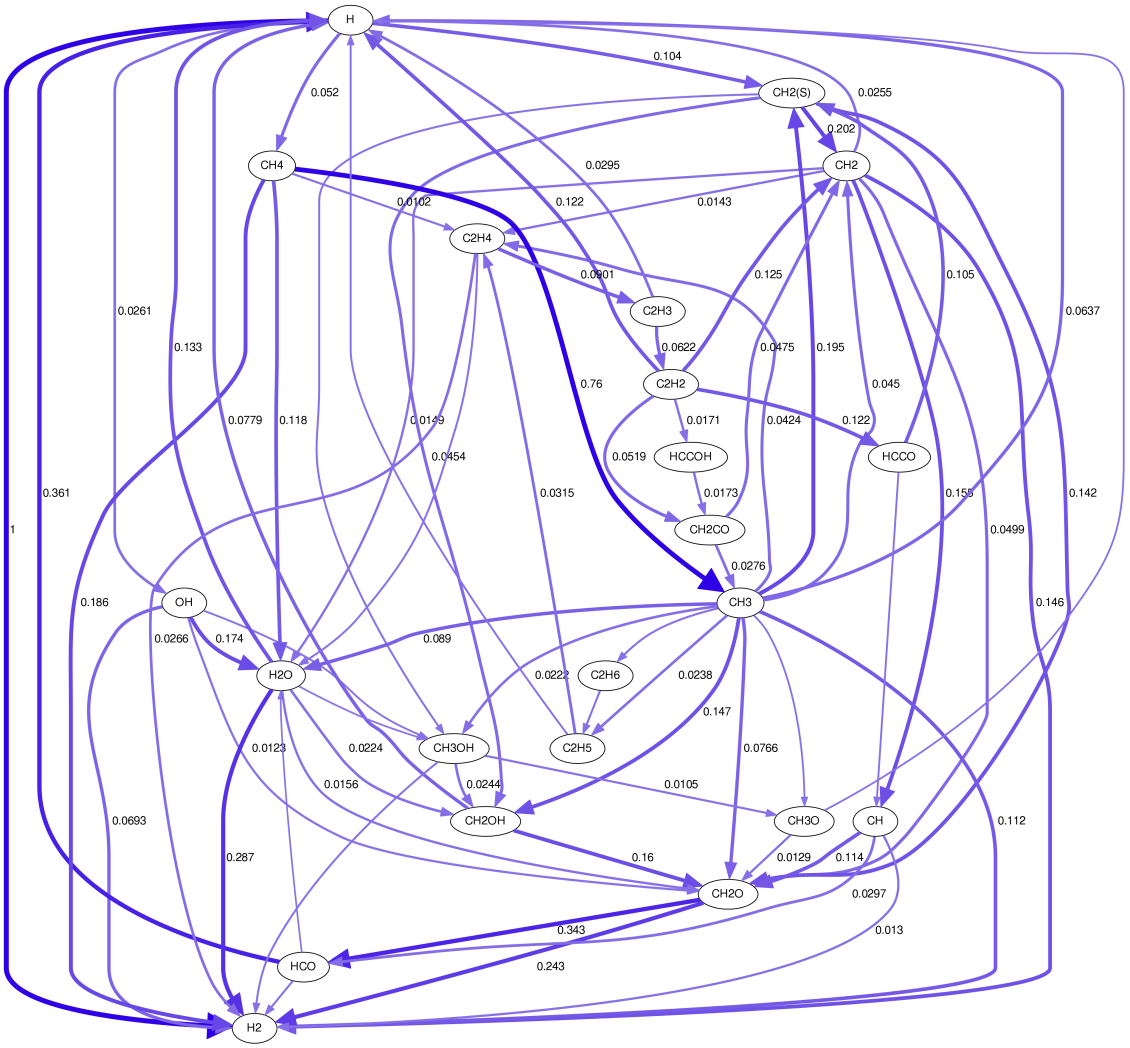

Figure A.6.: Reaction path diagram following H for $\lambda = 1$

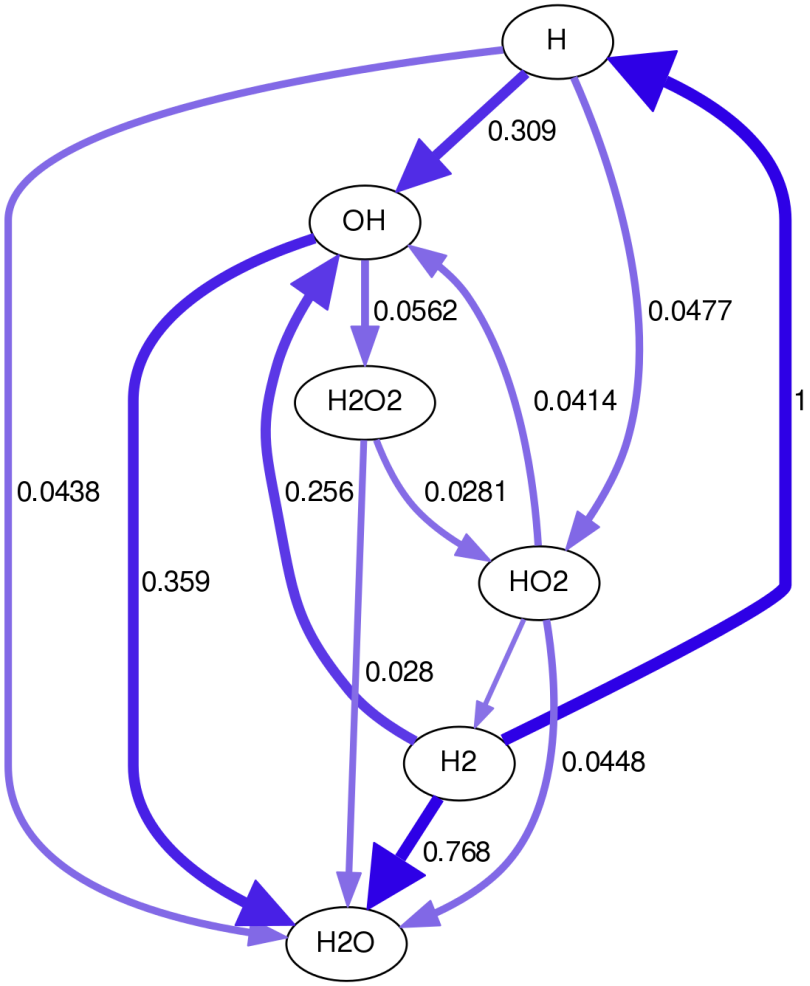

Figure A.7.: Reaction path diagram following H for $\lambda > 1$

B. Furnace energy balance

B.1. The energy balance

The steady-state energy balance of a combustion chamber is written in the following way:

$$\dot{H}_{in} = \dot{L} + \dot{Q} + \dot{H}_{out} \tag{B.1}$$

where: $\dot{H}_{in}$ is the total energy flow in inlet, $\dot{L}$ are the losses, $\dot{Q}$ is the heat transfer to the process and $\dot{H}_{out}$ is the enthalpy flow of the exhaust gas.

The total enthalpy flow in inlet is determined as the sum of the enthalpy of the fuel $\dot{H}_{in,F}$ plus the enthalpy of the comburent $\dot{H}_{in,A}$ and the enthalpy of the fuel is the sum of its chemical enthalpy and its physical enthalpy. Both enthalpy flows can be written in terms of the specific enthalpy h:

$$\dot{H}_{in,F} = \dot{m}_F \cdot (LCV + h_F(T_F)) \tag{B.2}$$

and when physical enthalpy is expressed in term of the specific heat of the fuel $c_{p,F}$:

$$\dot{H}_{in,F} = \dot{m}_F \cdot \left(LCV + \int_{T_0}^{T_F} c_{p,F}(T)\, dT \right) \tag{B.3}$$

The enthalpy of the comburent can be written in a similar way:

$$\dot{H}_{in,A} = \dot{m}_A h_A(T_A) \tag{B.4}$$

and in terms of the specific heat:

$$\dot{H}_{in,A} = \dot{m}_A \cdot \left(\int_{T_0}^{T_A} c_{p,A}(T)\, dT \right) \tag{B.5}$$

The enthalpy of the exhaust gas, considering complete combustion, does not contain any term for the chemical enthalpy and can be written:

$$\dot{H}_{out} = \dot{m}_{out} h_{out}(T_{out}) \tag{B.6}$$

and in terms of the specific heat:

$$\dot{H}_{out} = \dot{m}_{out} \cdot \left(\int_{T_0}^{T_{out}} c_{p,out}(T)\, dT \right) \tag{B.7}$$

It is worth noticing that in equations B.3, B.5 and B.7 the specific heat has to be determined from

the composition of the gas:

$$c_p(T) = \sum_i Y_i c_{p,i}(T)$$

where Y_i are the mass fractions of each species present in the gaseous mixture and $c_{p,i}$ are the specific heat of each specie. At high temperatures it is not possible to calculate the gas composition simply from a (complete combustion) stoichiometry calculation because dissociation of molecules is present. Therefore if equation B.7 is to be used, dissociation has to be taken into account. The same argument is valid also for the physical enthalpy of the gas and of the air but in this cases dissociation plays a minor role.

Together with the energy balance the mass balance must also holds:

$$\dot{m}_F + \dot{m}_A = \dot{m}_{out} \tag{B.8}$$

The ratio between $\dot{m}_F$ and $\dot{m}_A$ is fixed by the excess air ration λ:

$$\lambda = \frac{\dot{m}_A}{\dot{m}_{sto}} \tag{B.9}$$

where $\dot{m}_{sto}$ is the stoichiometric amount of air needed. This is a linear function of the mass flow of the gas:

$$\dot{m}_{sto} = \dot{m}_F \, L \tag{B.10}$$

The factor L determines the amount in kg of air per kg of fuel and is dependent only on the ultimate composition of the fuel. Using the relation B.9, the mass flow of the exhaust gas can be expressed as a function of the mass flow of the fuel:

$$\dot{m}_{out} = \dot{m}_F \, (1 + \lambda L) \tag{B.11}$$

The general form of the energy balance in a combustion chamber can be finally written with the help of the previous equations:

$$\dot{m}_F \cdot (LCV + h_F + \lambda L h_A) = \dot{L} + \dot{Q} + \dot{m}_F \cdot (1 + \lambda L) h_{out} \tag{B.12}$$

B.1.1. Furnace exit temperature

The left hand side of equation B.12 is often called as total thermal input (TTI) into the system:

$$TTI = \dot{m}_F \cdot (LCV + h_F + \lambda L h_A) \tag{B.13}$$

Dividing both sides of equation B.12 by $\dot{m}_F \cdot LCV$, and after some algebra one obtains:

$$\frac{\dot{Q} + \dot{L}}{\dot{m}_F \cdot LCV} = \frac{(1 + \lambda L) h_{out}}{LCV} + \frac{h_F}{LCV} + \frac{h_A}{LCV} \tag{B.14}$$

The ratio $\frac{\dot{Q}+\dot{L}}{\dot{m}_F \cdot LCV}$ is the fraction of the fuel thermal input that is extracted by the process (including heat losses). For a given fuel and a given preheat the ratio is a function of the excess air (λ) and the furnace exit temperature T_{out} only so that:

$$\frac{\dot{Q} + \dot{L}}{\dot{m}_F \cdot LCV} = f(\lambda, T_{out}) \tag{B.15}$$

It is worth observing that for $\dot{Q} + \dot{L} = 0$:

$$T_{out} = T_{ad} \tag{B.16}$$

If $T_{in} = T_0$ (no preheat) Equation B.14 simplifies further to:

$$X = \frac{\dot{Q} + \dot{L}}{\dot{m}_F \cdot LCV} = 1 - \frac{(1 + \lambda L)h_{out}}{LCV} \tag{B.17}$$

The ratio X is a fraction of the fuel thermal input that is available for the process and therefore it is often called in short **percentage available heat**.

B.2. Efficiencies

In order to quantify the performance of a furnace, heater, or an industrial plant a parameter called efficiency is used. In general it is defined as:

$$\eta = \frac{RESULT}{INPUT} \tag{B.18}$$

What is regarded as $RESULT$ and what as $INPUT$ (effort) depends on the engineer that formulates the question and therefore a number of efficiencies are in use. First of all one may consider the calculation of efficiency of a whole plant or a specific part of the plant. Usually, a furnace is just a part of an entire plant and therefore maximizing its efficiency is a task of the furnace operator.

To calculate an efficiency both the $RESULT$ and the $INPUT$ must be in the same units and must correspond to the same control volume. By the control volume, one means a fictitious boundary that encompasses the plant or its specific part for which we intend to calculate efficiencies. Usually, several energy (enthalpy) streams enter the control volume and one or more of them the engineer regards as the $INPUT$ (effort). Similarity several energy streams leave the control volume and here again the engineer has to decide which of them are seen as the $RESULT$.

Consider a simple furnace for continues heating of a charge. The enthalpy increase of the charge is $\Delta\dot{H}_C$. For the transport of the charge, a water-cooled transporter is used that also takes up the heat marked herewith as $\Delta\dot{H}_T$. The furnace heat loss is marked $\dot{L}$. The furnace is fired with the fuel of $\dot{H}_f$ enthalpy while the enthalpy of the combustion air stream is $\dot{H}_a$. The enthalpy of the combustion products leaving the furnace is $\dot{H}_{out}$.

The control volume for the energy balance of the furnace is marked using the dotted line. The energy balance for the control volume reads:

$$\dot{H}_f + \dot{H}_a = \dot{L} + \Delta\dot{H}_T + \Delta\dot{H}_C + \dot{H}_{out} \tag{B.19}$$

The sum $\dot{L} + \Delta\dot{H}_T + \Delta\dot{H}_C$ is the available heat ($\dot{Q}$) introduced previously while the ratio $X = \frac{\dot{Q}}{\dot{H}_f}$ represents the percentage available heat.

Several efficiencies can be easily defined. Let begin with the overall efficiency of the heating process of the charge:

Process efficiency

$$\eta_p = \frac{\Delta\dot{H}_C}{\dot{H}_f + \dot{H}_a} \tag{B.20}$$

Furnace efficiency

$$\eta_f = \frac{\dot{L} + \Delta\dot{H}_T + \Delta\dot{H}_C}{\dot{H}_f + \dot{H}_a} \tag{B.21}$$

Heat transfer efficiency

$$\eta_{ht} = \frac{\Delta\dot{H}_T + \Delta\dot{H}_C}{\dot{L} + \Delta\dot{H}_T + \Delta\dot{H}_C} \tag{B.22}$$

Heat transfer charge/transport elements

$$\eta_{htc} = \frac{\Delta\dot{H}_C}{\Delta\dot{H}_T + \Delta\dot{H}_C} \tag{B.23}$$

The process efficiency can be expressed as a product of specific efficiencies since:

$$\eta_p = \eta_f \cdot \eta_{ht} \cdot \eta_{htc} \tag{B.24}$$

If there is no preheat of the combustion air stream ($\dot{H}_a = 0$) the process efficiency (η_p) equals the fuel utilization efficiency (or percentage of available heat) showing the fraction (percentage) of fuel thermal input ($\dot{H}_f$) that is realized as the useful output of the furnace.

While formulating the energy balance and subsequently while deriving the efficiencies, we assumed that the latent heat of moisture in combustion products would not be utilized. However, if one insists on the correctness of the above formulation with the first law of thermodynamics, we should have used Gross (High) Calorific Value, as it has already been explained. A new trend in designing of industrial boilers for water heating and production of low-pressure steam is to condense the moisture. This, however, requires materials (steel with a ceramic coating) of high resistance to corrosion. For such boilers, the efficiency should be defined using a Gross Calorific Value (GCV) of the fuel otherwise efficiencies larger than 100% may occur.

With preheating of the air, the efficiency of a combustion chamber is generally defined as the heat used $\dot{Q}$ divided by the energy in input $\dot{H}_{in}$:

$$\epsilon = \frac{\dot{Q}}{\dot{H}_{in}} \tag{B.25}$$

The amount of heat $\dot{Q}$ needed for the process is independent of the combustion chamber because is only determined by the process itself. Eliminating $\dot{Q}$ using the energy balance the previous equation can be written:

$$\epsilon = 1 - \frac{\dot{L} + \dot{H}_{out}}{\dot{H}_{in}} \tag{B.26}$$

Explicitly written:

$$\epsilon = 1 - \frac{\dot{L} + \dot{m}_{out} h_{out}}{\dot{m}_F (LCV + h_F + \lambda L h_A)} \tag{B.27}$$

B.2.1. Fuel (utilization) efficiency

One of the most important efficiency that describes furnace (or plant) operation is fuel efficiency or fuel Utilization factor. The factor shows the fraction of the fuel energy (η_{fuel}) that is utilized as useful heat. Thus,

$$\eta_{fuel} = \frac{\Delta\dot{H}_C}{\dot{H}_f} \tag{B.28}$$

B.2.2. Plant efficiencies

For the evaluation of the performances of an entire plant, the control volume must include all the elements, facilities and mass or energy exchange among all the single systems. Plant fuel efficiency is:

$$\eta_{plant,fuel} = \frac{\Delta \dot{H}_C}{\dot{H}_f} \tag{B.29}$$

where $\dot{H}_f$ stands for chemical enthalpy of the fuel only.

The plant thermal efficiency (heating process efficiency) is defined as:

$$\eta_{plant,fuel} = 1 - \frac{\dot{H}_{out}}{\dot{H}_f} \tag{B.30}$$

where $\dot{H}_f$ is the chemical enthalpy of the fuel and $\dot{H}_{out}$ is the enthalpy of the combustion products leaving the plant.

B.2.3. Efficiency with no losses

Usually, the losses in a combustion chamber are only a few percents of the total thermal input inside the furnace. If they can be neglected, the expressions of the energy balance and the efficiency of the combustion chamber are simplified. The energy balance from the general equation B.12 now reads:

$$\dot{m}_F \cdot (LCV + h_F + \lambda L h_A) = \dot{Q} + \dot{m}_F \cdot (1 + \lambda L) h_{out}$$

from which the amount of fuel needed for the process can be calculated:

$$\dot{m}_F = \frac{\dot{Q}}{LCV + h_F + \lambda L h_A - (1 + \lambda L) h_{out}} \tag{B.31}$$

The efficiency given by the relation B.27 can be written:

$$\epsilon = 1 - \frac{\dot{m}_{out} h_{out}}{\dot{m}_F h_{in}} \tag{B.32}$$

where for compactness $h_{in} = LCV + h_F + \lambda L h_A$ With the help of equation B.11 the ratio between the mass flow of the fuel $\dot{m}_F$ and the total mass flow $\dot{m}_{out}$ can be expressed only as a function of fixed quantities:

$$\epsilon = 1 - \frac{(1 + \lambda L)\, h_{out}}{h_{in}} \tag{B.33}$$

The denominator in the previous expression can be expressed as a function of other fixed quantities, namely the adiabatic temperature T_{ad}. The definition of the adiabatic temperature follows from the energy balance B.12 with all the heat extracted equal zero:

$$\dot{H}_{in} = \dot{H}_{ad} \tag{B.34}$$

The total inlet enthalpy is already defined by the equations B.2 and B.4, while the total enthalpy

of the exhaust gas is defined in B.6 with the replacement $T_{out} = T_{ad}$:

$$H_{in} = \dot{m}_{out} \cdot \left(\int_{T_0}^{T_{ad}} c_{p,out}(T)\, dT \right) \tag{B.35}$$

The previous equation can also be simplified using equation B.11, eliminating the dependency from the amount of fuel:

$$\begin{aligned} h_{in} &= (1 + \lambda L) \int_{T_0}^{T_{ad}} c_{p,out}(T)\, dT \\ &= (1 + \lambda L) h_{ad} \end{aligned} \tag{B.36}$$

The expression of h_{in} derived in the previous equation can be inserted into equation B.33 and the efficiency can be written:

$$\begin{aligned} \epsilon &= 1 - \frac{h_{out}}{h_{ad}} = \\ &= 1 - \frac{\int_{T_0}^{T_{aut}} c_{p,out}(T)\, dT}{\int_{T_0}^{T_{ad}} c_{p,out}(T)\, dT} \end{aligned} \tag{B.37}$$

It has to be noted that in equation B.37 the specific heat c_p is the same in the denominator as well as in the nominator. The previous equation can be written as a function of the mean specific heat $\overline{c_p}$ defined by:

$$\overline{c_p}(T) = \frac{1}{T} \int_{T_0}^{T} c_p(s)\, ds \tag{B.38}$$

The relation B.37 becomes:

$$\epsilon = 1 - \frac{\overline{c_{p,out}}(T_{out})(T_{out} - T_0)}{\overline{c_{p,out}}(T_{ad})((T_{ad} - T_0)} \tag{B.39}$$

In the previous equation the two mean specific heats cannot be simplified in general because $\overline{c_p}$ is a function of the temperature. If the temperature T_{out} is relative high, then its dependency from T is not anymore so strong and it can be assumed that $\overline{c_p}$ at both temperature is equal, leading to the final (but approximated) relation for the efficiency of a combustion chamber:

$$\epsilon = 1 - \frac{T_{out} - T_0}{T_{ad} - T_0} \tag{B.40}$$

C. Radiation

Radiation is an important mechanism of heat transfer, especially in a furnace at higher temperatures. The complexities of solving the RTE in general geometries with participating media has been shortly summarized in Section 10.4 and in Section 4.8 and more details can be obtained from [247, 158, 385].

In this Appendix, two further aspects are considered of the modeling glycol gasification [229] already discussed in 16:

1. Calculation of the gas radiation properties;
2. Calculation of the absorption and scattering on solid particles;

will be analyzed. Two most advanced calculations will be used to derive parameters for two simplified models Those models will be applied to the simulation of the atmospheric gasifier presented in Chapter 16.

C.1. Gas radiation properties

As already stated, the RTE with constant absorption coefficient is valid for one single wavenumber only. In principle, the RTE must be solved for each wavenumber, and the spectral intensity must be integrated over the whole wavenumber range to yield the total intensity $I = \int I_\eta \cdot \mathrm{d}\,\eta$. In solid fuel conversion, the most important species participating in radiation are CO_2, H_2O, and CO whose spectra consists of several million individual spectral absorption lines. Several models to avoid integration over the whole spectrum exist and they differ in computing power and accuracy. The most accurate is the line-by-line model which considers each individual absorption line using spectral databases like HITEMP-2010 [299] with a typical resolution of $\Delta\eta = 0.01\,\mathrm{cm}^{-1}$.

A gray-gases model (WSGGM) [157] has also been developed based on accurate spectral line-by-line calculations using HITEMP-2010 database [299]. The RTE is solved for each gray band k separately and weighted by its temperature weighting function w_k. Assuming negligible scattering, the RTE can then be written for each gray gas [248]

$$\frac{\mathrm{d}\,I_k}{\mathrm{d}\,s} = -a_k \cdot I_k + w_k \cdot a_k \cdot I_\mathrm{b} \tag{C.1}$$

Summation over all gas contributions yields to the total intensity $I = \sum I_k$.

The same method, described in [9, 7, 8] has been used to calculate the absorption spectra as a starting point for the evaluation of the emissivity as a function of temperature for different pressure-path lengths $p_a \cdot L$ where p is the sum of partial pressures of all radiatively participating molecules and L is the optical path length. In the WSSGM the total emissivity is calculated using

$$\varepsilon^\mathrm{tot} = \sum_{k=0}^{N_g} w_k(T) \cdot \left[1 - \exp\left(-a_k \cdot p_a \cdot L\right)\right] \tag{C.2}$$

where N_g is the number of gray gases, w_k is the temperature scaling function of gas k, a_k is the pressure-based absorption coefficient of pseudo gas k, and $p_a \cdot L$ is again the pressure path-length.

An example of a fitted WSGGM using 5 gray gases (plus a clear gas) and a 6th degree polynomial for the weighting function is shown in Figure C.1. Emissivities calculated using the fitted WSGGM differ by $0.017\,\% \pm 1.272\,\%$ from the line-by-line calculated values.

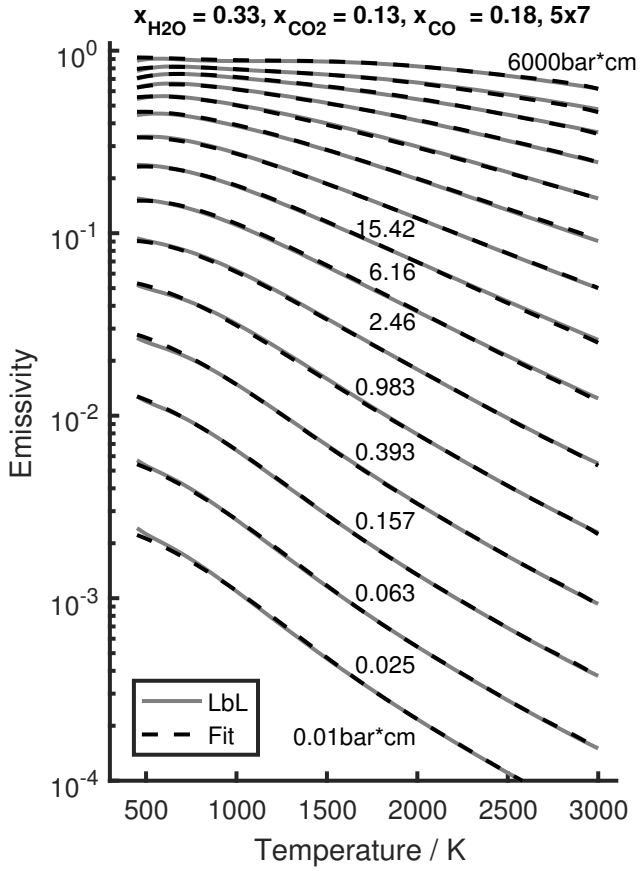

Figure C.1.: Example of a fitted WSGGM using 5 gray gases (plus a clear gas) and a 6th degree polynomial for the weighting function [6].

The produced sets of tabulated values have been implemented into the CFD solver and in each computational cell radiative properties are evaluated using the local composition. The radiation source is important since it contributes to the energy equation and, therefore, influences both the temperature field and the gas composition. The source term S is defined as the divergence of the radiative flux field $\vec{q}$ [247]:

$$S = -\nabla \cdot \vec{q} = -\nabla \cdot \int_{4\,\pi} I \cdot \vec{s} \cdot \mathrm{d}\,\Omega \tag{C.3}$$

The CFD calculations have been carried out using either a constant emissivity, determined using a typical gas composition inside the gasifier and a typical temperature, or WSGGM is used which facilitate a variable absorption. The constant absorption coefficient a for the DO solver is then calculated through the mean beam length L_{eq}:

$$a = -\frac{\ln\left(1-\varepsilon\right)}{L_{\mathrm{eq}}} = 0.53\,\mathrm{m}^{-1}$$

The calculation using the constant absorption coefficient is used as a reference case. The absorption coefficient in case of the WSGGM is an average value calculated using:

$$\overline{a} = p_a \cdot \sum_{k=0}^{5} w_k\left(T\right) \cdot a_k$$

The following conclusions can be drowned by the analysis of the results (see [110]):

1. The mean absorption coefficient is larger than the constant value 0.53 $\frac{1}{\mathrm{m}}$ almost throughout the whole domain.

2. The radiation flux incident on the walls, changes only slightly and most of the changes are in the near-flame region.

3. The radiation source changes especially in the flame region but, the effect on the temperature field is small since in this region the energy source due to the chemical reactions is much larger (around two orders of magnitude) if compared to the radiative contribution.

Figure C.2 shows the wall incident radiation, the radiative as well as total (radiation plus convection) heat flux to the inner tube wall of the REGA reactor, and the internal wall temperature. Due to the WSGGM, the surface incident radiation is increased in the near-flame region so that the wall temperature is slightly increased. As can be seen in Fig. Figure C.2, the radiative heat flux to the wall significantly increases whereas the total heat flux increases to a lesser extent since due to the higher wall temperature the convective heat transfer decreases. The total (radiation + convection) heat flux to the wall is 34.22 kW (reference case) and 36.17 kW (WSGGM), whereas for the radiative heat flux alone values of 26.41 kW (reference case) and 33.59 kW (WSGGM) are applicable so that in case of the WSGGM the contribution of radiation is more pronounced if compared to the convective part.

C.1.1. Absorption and Scattering on droplets

Besides the gas radiation properties, also the contribution of the droplets must be taken into account. In contrast to gaseous molecules, droplets do not only emit and absorb but also scatter the radiation intensity. Assuming spherical droplets, scattering coefficients can be calculated using the Mie-Lorentz theory [386, 247]; the emissivity or absorption also depends on the droplet diameter or more precisely on the diameter distribution.

The contribution of droplets to the radiative intensity field is calculated during Lagrangian particle tracking. The particles absorption coefficient inside a numerical control volume is calculated by summing up the contribution of all particle classes inside the volume: [74]:

$$a_p = \sum_{n=1}^{N} Q_{abs,n} \cdot \frac{A_{p,n}}{V_{CV}} \tag{C.4}$$

where $Q_{abs,n}$ is the absorption efficiency of the nth droplet, $A_{p,n}$ is the droplet's projected area, and V_{CV} is the cell's volume. A similar expression holds for the scattering coefficient:

$$\sigma_p = \sum_{n=1}^{N} Q_{sca,n} \cdot \frac{A_{p,n}}{V_{CV}} \tag{C.5}$$

where $Q_{sca,n}$ is the scattering efficiency of the nth droplet.

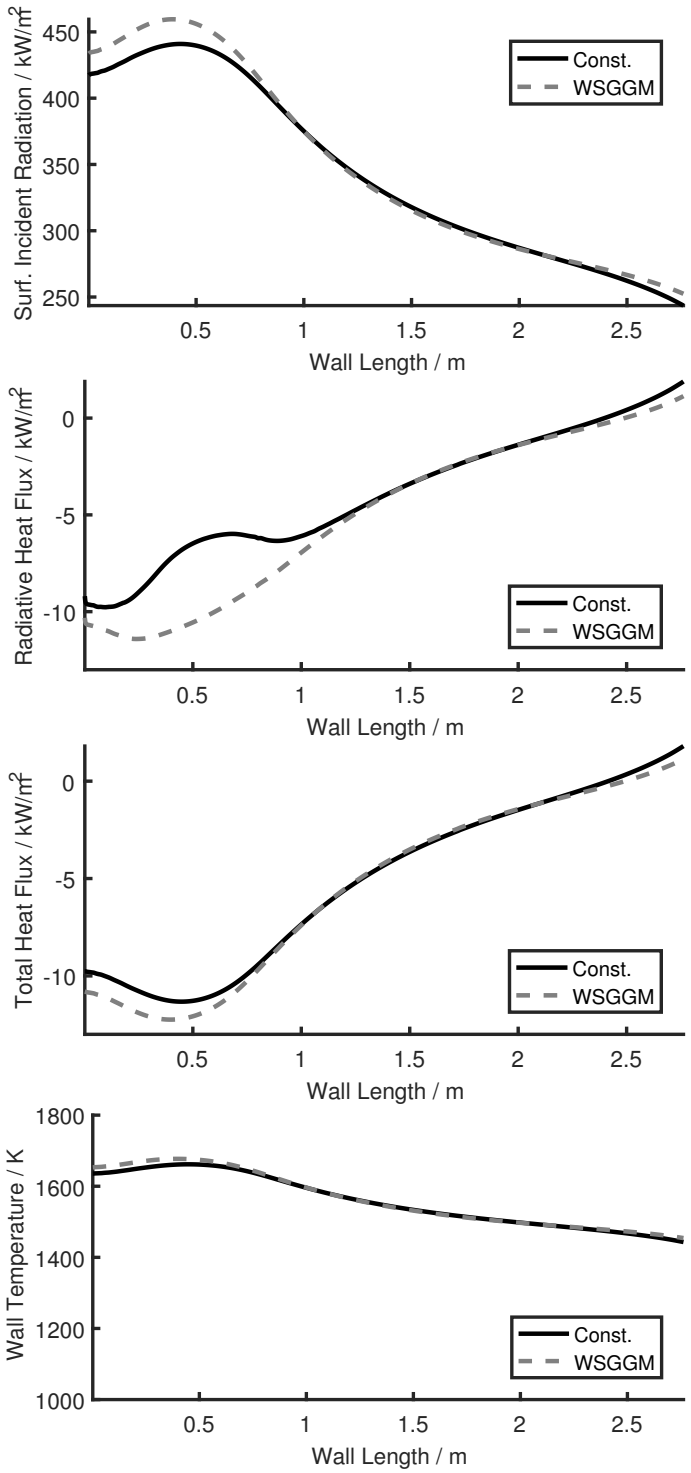

Figure C.2.: Effect of the WSGGM on the (i) wall surface incident radiation, the (ii) radiative as well as (iii) total (radiation + conduction) heat flux to the wall, and the (vi) wall temperature [110]

The calculations of the droplets volume fraction using the experimentally determined diameter distribution for REGA-1 conditions have shown that the value of the average distance between droplets is comparable with pulverized coal combustion [247] so that the scattering can be treated as independent.

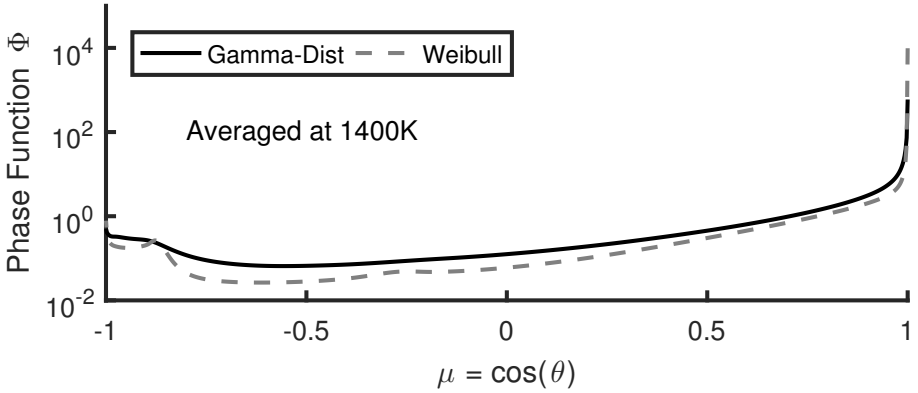

Figure C.3.: Diameter-Distribution-Averaged Phase function which has been further averaged using Planck's function at 1400 K temperature.

Figure C.3 presents an example of a diameter-distribution-averaged phase function which has been further averaged using Planck's function at 1400 K temperature.

The following conclusions can be derived for the application of the Mie scattering to CFD simulations:

1. The theory let the exact calculations of the absorption coefficient and the scattering coefficient based on the spectral data of the particle (in this case liquid Glycol);
2. It confirms the application of the geometrical optics for the droplets present in the REGA gasifier;
3. It confirms the weak diameter dependency of the characteristics mentioned above and therefore confirms the simple approach used in the standard model;
4. It shows that any of the important quantities in radiative transfer calculations are affected by the utilization of the exact theory.

Bibliography

[1] International Workshop on Measurement and Computation of Turbulent Nonpremixed Flames. http://www.sandia.gov/TNF/abstract.html, 2012.

[2] *Combustion of Pulverised Coal in a Mixture of Oxygen and Recycled Flue Gas*. Elsevier Ltd. All, 2015.

[3] Abdol-Hamid, K. S., Carlson J. R., and Rumsey C. L. Verification and validation of the k-kl turbulence model in fun3d and cfl3d codes. Technical report, NASA/TM-2015-218968, 2015.

[4] B. Abramzon and W.A. Sirignano. Droplet vaporization model for spray combustion calculations. *International Journal of Heat and Mass Transfer*, 32(9):1605 – 1618, 1989.

[5] R. K. Agrawal. Kinetics of reactions involved in pyrolysis of cellulose I. the three reactions model. *The Canadian Journal of Chemical Engineering*, 66(3):403–412, 1988.

[6] M. Alberti. *Modeling of the gas radiative properties at elevated pressures*. PhD thesis, Technical University of Clausthal, 2018.

[7] M. Alberti, R. Weber, and M. Mancini. Re-creating Hottel's emissivity charts for carbon dioxide and extending them to $40\,\mathrm{bar}$ pressure using HITEMP-2010 data base. *Combustion and Flame*, 162:597–612, 2015.

[8] M. Alberti, R. Weber, and M. Mancini. Re-creating Hottel's emissivity charts for water vapor and extending them to $40\,\mathrm{bar}$ pressure using HITEMP-2010 data base. *Combustion and Flame*, 169:141–153, 2016.

[9] M. Alberti, R. Weber, M. Mancini, A. Fateev, and S. Clausen. Validation of HITEMP-2010 for Carbon Dioxide and Water Vapour at high temperatures and atmospheric pressures in 450-7600 cm^{-1} spectral range. *Journal of Quantitative Spectroscopy & Radiative Transfer*, 157:14 – 33, 2015.

[10] J. Andersen, Ch. Lund Rasmussen, T. Giselsson, and P. Glarborg. Global combustion mechanisms for use in CFD modeling under oxy-fuel conditions. *Energy & Fuels*, 23(3):1379–1389, 2009.

[11] M.J. Antal. Biomass pyrolysis: A review of the literature part 2 - lignocellulose pyrolysis. *Advances in Solar Energy*, 3:175–255, 1985.

[12] D.B. Anthony, H.C. Howard, J.B. Hottel, and H.P. Meissner. Rapid devolatilization of pulverized coal. *15th Symp. (Int) on Combustion*, pages 1303–1317, 1975.

[13] J.R. Arthur. Reactions between carbon and oxygen. *Transactions of the Faraday Society*, 47:164–178, 1951.

[14] D. C. Astholz, J. Troe, and W. Wieters. Unimolecular processes in vibrationally highly excited cycloheptatrienes. I. thermal isomerization in shock waves. *J. Chem. Phys.*, 70:5107–5116, 1979.

[15] S. Badzioch and P.G.W. Hawksley. Kinetics of Thermal Decomposition of Pulverized Coal Particles. *Ind. Eng. Chem. Process Design and Development*, 9:521–530, 1970.

[16] S.W. Baek, H.S. Kim, M.J. Yu, S.J. Kang, and M.Y. Kim. Application of the extended weighted sum of gray gases model to light fuel oil spray combustion. *Combustion Science and Technology*, 174:37–70, 2002.

[17] M. Bahador and B. Sundén. Investigation on the effects of fly ash particles on the thermal radiation in biomass fired boilers. *International Journal of Heat and Mass Transfer*, 51(9-10):2411 – 2417, 2008.

[18] J.G. Bailey, A. Tate, C.F.K. Diessel, and T.F. Wall. A char morphology system with applications to coal combustion. *Fuel*, 69(2):225 – 239, 1990.

[19] O. Baker. Simultaneous flow of oil and gas. *Oil and Gas Journal*, 12:185–195, 2954.

[20] B. S. Baldwin and H. Lomax. Thin layer approximation and algebraic model for separated turbulent flows. *AIAA Paper*, 78(257), 1978.

[21] B.S. Baldwin and T.J. Barth. A One-Equation Turbulence Transport Model for High Reynolds Number Wall-Bounded Flows. Technical report, NASA TM 102847, 1990.

[22] J. Ballester and J. Santiago. Kinetic parameters for the oxidation of pulverised coal as measured from drop tube tests. *Combustion and Flame*, 142(3):210 – 222, 2005.

[23] A. F. Bartholomay. Stochastic models for chemical reactions: I. theory of the unimolecular reaction process. *Bull. Math. Biophys*, 20:175–190, 1951.

[24] R. Bassilakis, Y. Zhao, P. R. Solomon, and M. A. Serio. Sulfur and nitrogen evolution in the Argonne coals. Experiment and modeling. *Energy & Fuels*, 7(6):710–720, 1993.

[25] G. K. Batchelor. *An Introduction to Fluid Dynamics*. Cambridge Mathematical Library. Cambridge University Press, 2000.

[26] F. Battin-Leclerc. Development of kinetic models for the formation and degradation of unsaturated hydrocarbons at high temperature. *Physical Chemistry Chemical Physics*, 4(11):2072–2078, 2002.

[27] F. Battin-Leclerc. Detailed chemical kinetic models for the low-temperature combustion of hydrocarbons with application to gasoline and diesel fuel surrogates. *Progress in Energy and Combustion Science*, 34(4):440 – 498, 2008.

[28] F. Battin-Leclerc, E. Blurock, R. Bounaceur, R. Fournet, P.-A. Glaude, O. Herbinet, B. Sirjean, and V. Warth. Towards cleaner combustion engines through groundbreaking detailed chemical kinetic models. *Chemical Society Reviews*, 40(9):4762–4782, 2011.

[29] A. M. Beckmann. *Experiments and CFD Modeling of Pulverized Coal Flames with Emphasis on Fly Ash Deposition*. PhD thesis, TU Clausthal, 2016.

[30] A. M. Beckmann, J. Bibrzycki, M. Mancini, A. Szlęk, and R. Weber. Mathematical modeling of reactants transport and chemistry during oxidation of a millimeter-sized coal-char particle in a hot air stream. *Combustion and Flame*, 180(Supplement C):2 – 9, 2017.

[31] A.M. Beckmann, M. Mancini, R. Weber, S. Seebold, and M. Müller. Measurements and cfd modeling of a pulverized coal flame with emphasis on ash deposition. *Fuel*, 167:168 – 179, 2016.

[32] J.M. Beer. High efficiency electric power generation: The environmental role. *Prog. Energy Comb. Sci.*, 33:107–134, 2007.

[33] K.E Benfell, G.-S Liu, D Roberts, D.J Harris, J.A Lucas, J.G Bailey, and T.F Wall. Modeling char combustion: The influence of parent coal petrography and pyrolysis pressure on the structure and intrinsic reactivity of its char. *Symposium (International) on Combustion*, 28:2233, 2000.

[34] T. Beyer and D. F. Swinehart. Algorithm 448: number of multiply-restricted partitions. *Commun. ACM*, 16:379, 1973.

[35] S. K. Bhatia and D. D. Perlmutter. A random pore model for fluid-solid reactions: I. isothermal, kinetic control. *AIChE J.*, 26(3):379–386, 1980.

[36] S. K. Bhatia and D. D. Perlmutter. A random pore model for fluid-solid reactions: II. diffusion and transport effects. *AIChE J.*, 27(2):247–254, 1981.

[37] V. Bíba, J. Macák, E. Klose, and J. Malecha. Mathematical model for the gasification of coal under pressure. *Industrial & Engineering Chemistry Process Design and Development*, 17(1):92–98, 1978.

[38] J. Bibrzycki. *Investigations of Coal Particle combustion and gasification*. PhD thesis, Technical University of Clausthal, 2014.

[39] J. Bibrzycki, M. Mancini, and R. Weber. A char combustion sub-model for CFD-predictions of fluidized bed combustion - experiments and mathematical modeling. *Combustion and Flame*, 163:188 – 201, 2016.

[40] J. Bibrzycki and T. Poinsot. Investigation of Laminar Flame Speed of CH4/N2/O2 and CH4/CO2/O2 Mixtures Using Reduced Chemical Kinetic Mechanisms . *Archivium Combustionis*, 30(4):287–296, 2010.

[41] R. W. Bilger. Conditional moment closure for the turbulent reacting flow. *Phys. Fluids A*, 5:436, 1993.

[42] M. Birouk and I. Gökalp. Current status of droplet evaporation in turbulent flows. *Progress in Energy and Combustion Science*, 32(4):408 – 423, 2006.

[43] J. D. Blackwood. The kinetics of the system carbon-hydrogen-methane. *Aust. J. Chem.*, 15:397, 1962.

[44] J. D. Blackwood and F. McGrory. The carbon-steam reaction at high pressure. *Aust. J. Chem.*, 11(16), 1958.

[45] J.D. Blackwood and A.J. Ingeme. The reaction of carbon with carbon dioxide at high temperatures. *Aust. J. Chem.*, 13:194–209, 1960.

[46] C. Di Blasi. Modeling chemical and physical processes of wood and biomass pyrolysis. *Progress in Energy and Combustion Science*, 34(1):47 – 90, 2008.

[47] C. Di Blasi. Combustion and gasification rates of lignocellulosic chars. *Progress in Energy and Combustion Science*, 35(2):121 – 140, 2009.

[48] E. S. Blurock, Martin T., and Fabian M. Phase optimized skeletal mechanisms for engine simulations. *Combustion Theory and Modelling*, 14(3):295–313, 2010.

[49] G. Blyholder and H. Eyring. Kinetics of graphite oxidation. *The Journal of Physical Chemistry*, 61(5):682–688, 1957.

[50] G. Blyholder and H. Eyring. Kinetics of graphite oxidation II. *The Journal of Physical Chemistry*, 63(6):1004–1008, 1959.

[51] W. Boie. Fuel technology calculations. *Energietechnik*, 3:309–316, 1953.

[52] R. Borghi. Turbulent combustion modelling. *Prog. Energy Combust. Sci.*, 14:245–292, 1988.

[53] R. Borghi. Turbulent combustion modeling: an overview of current methods related to the structure of non premixed flames. In M. Onofri and A. Tesei, editors, *Fluid dynamics aspect of combustion theory*, pages 87–112. Logman Scientific & Technical, 1990.

[54] A.C. Bose, K.M. Dannecker, and J.O.L. Wendt. Coal composition effects on mechanisms governing the destruction of no and other nitrogenous species during fuel-rich combustion. *Energy & Fuels*, 2(5):301–308, 1988.

[55] C. T. Bowman. Chemistry of gaseous pollutant formation and destruction. In W. Bartok and A. F. Sarofim, editors, *Fossil Fuel Combustion*. J. Wiley and Sons, 1991.

[56] F. Boysan, W. H. Ayer, and J. Swithenbank. A fundamental mathematical modeling approach to cyclone design. *Transactions of the Institution of Chemical Engineering*, 60:222–230, 1982.

[57] F. Boysan, R. Weber, J. Swithenbank, and C. J. Lawn. Modeling coal-fired cyclone combustors. *Comb. and Flame*, 63:S. 73–86, 1986.

[58] J. W. Bozzelli and A. M. Dean. $O + NNH$: A possible new route for NO_x formation in flames. *Int. J. Che. Kin.*, 27:1097–1109, 1995.

[59] A. G. W. Bradbury, Y. Sakai, and F. Shafizadeh. A kinetic model for pyrolysis of cellulose. *Journal of Applied Polymer Science*, 23(11):3271–3280, 1979.

[60] K. N. C. Bray, M. Champion, and P. A. Libby. Mean reaction rates in premixed turbulent flames. *In Twenty-Second Symposium (International) on Combustion*, pages 763–769, 1988.

[61] K.N. Bray and N. Peters. *Turbulent Reacting Flows*, chapter Laminar Flamelets in Turbulent Flames, pages 63–114. Academic Press, 1994.

[62] K.N.C. Bray and J.B. Moss. A unified statistical model of the premixed turbulent flame. *Acta Astronautica*, 4:91–319, 1977.

[63] C. E. Brennen. *Fundamentals of Multiphase Flows*. Cambridge University Press, 2005.

[64] F. Breussin, N. Lallemant, and R. Weber. *User Manual to IFRF User Defined Subroutines to Fluent 4.5*. IFRF.

[65] F. Breussin, N. Lallemant, and R. Weber. Computing of oxy-natural gas flames using both a global combustion scheme and a chemical equilibrium procedure. *Combust. Sci. and Tech.*, 160:369–397, 2000.

[66] A. Brink, M. Hupa, F. Breussin, N. Lallement, and R. Weber. Modelling of oxy-natural gas combustion chemistry. *AIAA Journal of Propulsion and Power*, 16(4):609–614, 2000.

[67] A. Brink, P. Kilpinen, and M. Hupa. An improved description of the hydrocarbon combustion is the key to advanced NO modelling. In 12^{th} *IFRF Members Conference*, Noordwijkerhout, the Netherlands, May 6-8 1998.

[68] R.O. Buckius and D.C. Wang. Radiation properties for polydispersions: Application to coal. *J. Heat Transfer*, 102:99–103, 1980.

[69] RafaÅ, BuczyÅ„ski, Grzegorz Czerski, Katarzyna Zubek, Roman Weber, and PrzemysÅ‚aw Grzywacz. Evaluation of carbon dioxide gasification kinetics on the basis of non-isothermal measurements and CFD modelling of the thermogravimetric analyser. *Fuel*, 228:50 – 61, 2018.

[70] RafaÅ, BuczyÅ„ski, Roman Weber, and Andrzej SzlÄ™k. Innovative design solutions for small-scale domestic boilers: Combustion improvements using a cfd-based mathematical model. *Journal of the Energy Institute*, 88(1):53 – 63, 2015.

[71] A. K. Burnham and R. L. Braun. Global kinetic analysis of complex materials. *Energy & Fuels*, 13(1):1–22, 1999.

[72] W. Bushe and H. Steiner. Conditional moment closure for large eddy simulation of nonpremixed turbulent reacting flows. *Phys. Fluids*, 11:1896–1906, 1999.

[73] H.-Y. Cai, A.J. Güell, I.N. Chatzakis, J.-Y. Lim, D.R. Dugwell, and R. Kandiyoti. Combustion reactivity and morphological change in coal chars: Effect of pyrolysis temperature, heating rate and pressure. *Fuel*, 75(1):15 – 24, 1996.

[74] J. Cai, X. Zhao, M.F. Modest, and D.C. Haworth. Nongray Radiation Modellings in Eulerian-Lagrangian Methods for pulverized coal flames. In Americal Society of Therman and Fluids Engineers, editors, *Proceedings of the 1st Thermal and Fluids Engineering Summer Conference*, New York City, USA, 2016.

[75] S. M. Candel and T. J. Poinsot. Flame stretch and the balance equation for the flame area. *Combustion Science and Technology*, 70(1-3):1–15, 1990.

[76] Chao Chen, Jing Wang, Wei Liu, Sen Zhang, Jingshu Yin, Guangqian Luo, and Hong Yao. Effect of pyrolysis conditions on the char gasification with mixtures of CO2 and H2O. *Proceedings of the Combustion Institute*, 34(2):2453 – 2460, 2013.

[77] W. Chen. *A global reaction rate for nitric oxide reburning*. PhD thesis, Bringham Young University, 1994.

[78] C. Chevalier, W.J. Pitz, J. Warnatz, C.K. Westbrook, and H. Melenk. Hydrocarbon ignition: Automatic generation of reaction mechanisms and applications to modeling of engine knock. *Symposium (International) on Combustion*, 24(1):93 – 101, 1992.

[79] E.H. Chui and G.D. Raithby. Computation of radiant heat transfer on a nonorthogonal mesh using the finite-volume method. *Numerical Heat Transfer, Part B: Fundamentals*, 23(3):269–288, 1993.

[80] A. W. Coats and J. P. Redfern. Kinetic parameters from thermogravimetric data. *Nature*, 201:68–69, 1964.

[81] P.J. Coehlo and M.G. Carvalho. Mathematical Modeling of NO Formation in a Pawer Station Boiler. In 2^{nd} *Conference on Combustion Technology for Clean Environment*, pages 1093–1102, Lisbon, 1993.

[82] G. Czerski, K. Zubek, P. Grzywacz, and S. Porada. Effect of char preparation conditions on gasification in a carbon dioxide atmosphere. *Energy & Fuels*, 31(1):815–823, 2017.

[83] P. Dagaut and M. Cathonnet. The ignition, oxidation, and combustion of kerosene: A review of experimental and kinetic modeling. *Progress in Energy and Combustion Science*, 32(1):48 – 92, 2006.

[84] B. J. Daly and F. H. Harlow. Transport equations in turbulence. *Phys. Fluids*, 13:2634–2649, 1970.

[85] B. de Caprariis, P. De Filippis, C. Herce, and N. Verdone. Double-Gaussian Distributed Activation Energy Model for Coal Devolatilization. *Energy & Fuels*, 26(10):6153–6159, 2012.

[86] G.G. De Soete. Overall reaction rate of NO and N_2 formation from fuel nitrogen. *Symposium (International) on Combustion*, 15:1093–1102, 1975.

[87] M de Souza-Santos. *Solid Fuels Combustion and Gasification: Modeling, Simulation*. CRC Press, 2010.

[88] A. Demirbaş. Mechanisms of liquefaction and pyrolysis reactions of biomass. *Energy Conversion and Management*, 41(6):633 – 646, 2000.

[89] L. Dombrovsky and D. Baillis. *Thermal Radiation in Disperse Systems: An Engineering Approach*. Begell House, 2010.

[90] L.A. Dombrovsky, S.S. Sazhin, S.V. Mikhalovsky, R. Wood, and M.R. Heikal. Spectral properties of diesel fuel droplets. *Fuel*, 82(1):15 – 22, 2003.

[91] L.A Dombrovsky, S.S Sazhin, E.M Sazhina, G Feng, M.R Heikal, M.E.A Bardsley, and S.V Mikhalovsky. Heating and evaporation of semi-transparent diesel fuel droplets in the presence of thermal radiation. *Fuel*, 80(11):1535 – 1544, 2001.

[92] C. D. Doyle. Estimating isothermal life from thermogravimetric data. *J. Appl. Polym. Sci.*, 6:693–642, 1962.

[93] T. D. Dreeben. *PDF modeling of near-wall turbulent flows*. PhD thesis, Cornell University, 1997.

[94] T. D. Dreeben and S. B. Pope. Probability density function and Reynolds-stress modeling of near-wall turbulent flows. *Phys. Fluids*, 9(1):154–163, 1997.

[95] F.L. Dryer. *High temperature oxidation of CO and CH_4 in a Turbulent flow reactor*. PhD thesis, Aerospace and Mechanical Sciences Department, Princeton University, Princeton, New Jersey, 1972.

[96] F.L. Dryer and I. Glassman. High-temperature oxidation of CO and CH_4. *Symposium (International) on Combustion*, 14:987–1003, 1973.

[97] J. K. Dukowwicz and A. S. Dvinsky. Approximate factorization as a high-order splitting for the implicit incompressible flow equations. *Journal of Computational Physics*, 102:336–347, 1992.

[98] M. Eberhard, U. Santo, D. Böning, H. Schmid, B. Michelfelder, B. Zimmerlin, A. Günther, P. Weigand, M. Müller-Hagedorn, D. Stapf, and Thomas Kolb. Der bioliq-Flugstromvergaser: ein Baustein der Energiewende. *Chem. Ing. Tech.*, 2018.

[99] Georg Eckel, Patrick Le Clercq, Trupti Kathrotia, Alexander Saenger, Sabine Fleck, Marco Mancini, Thomas Kolb, and Manfred Aigner. Entrained flow gasification. part 3: Insight into the injector near-field by large eddy simulation with detailed chemistry. *Fuel*, 223:164 – 178, 2018.

[100] Eggels. NO-post calculation for flat laminar CH_4/air flames. In 2^{nd} *Conference on Combustion Technology for Clean Environment*, pages 10–14, Lisbon, 1993.

[101] S. Elghobashi and G.C. Truesdell. Direct simulation of particle dispersion in a decaying isotropic turbulence. *Journal of Fluid Mechanics*, 242:655–700, 1992.

[102] I. S. Ertesvag and B. F. Magnussen. The eddy dissipation turbulence energy cascade model. *Combust. Sci. and Tech.*, 159:213–135, 2000.

[103] Sima Farazi, Mohsen Sadr, Seongwon Kang, Martin Schiemann, Nikita Vorobiev, Viktor Scherer, and Heinz Pitsch. Resolved simulations of single char particle combustion in a laminar flow field. 201, 12 2016.

[104] P. P. Feistel, K. H. van Heek, and H. Jiintgen. Gasification of a German Bituminous Coal. With H2O, H2 and H2O-H2 Mixtures. *Am. Chem. Soc. Div. Fuel Chemistry Preprints*, 22(1):53, 1977.

[105] P.S. Fennell, J.S. Dennis, and A.N. Hayhurst. The order with respect to oxygen and activation energy for the burning of an antracitic char in O_2in a fluidised bed, as measured using a rapid analyser for CO and CO_2. *Symposium (International) on Combustion*, 32:2051–2058, 2009.

[106] J. Fermoso, M. V. Gil, A. G. Borrego, C. Pevida, J. J. Pis, and F. Rubiera. Effect of the pressure and temperature of devolatilization on the morphology and steam gasification reactivity of coal chars. *Energy & Fuels*, 24(10):5586–5595, 2010.

[107] J. Fermoso, C. Stevanov, B. Moghtaderi, B. Arias, C. Pevida, M.G. Plaza, F. Rubiera, and J.J. Pis. High-pressure gasification reactivity of biomass chars produced at different temperatures. *Journal of Analytical and Applied Pyrolysis*, 85(1):287 – 293, 2009. Pyrolysis 2008.

[108] M.A. Field, D. Gill, B. Morgan, and P. Hawskley. *Combustion of pulverized coal*. BCURA, 1967.

[109] W.A. Fiveland and A.S. Jamaluddin. Three-dimensional spectral radiative heat transfer solutions by the discrete-ordinates method. *Journal of Thermophysics and Heat Transfer*, 5(3):335–339, 1991.

[110] S. Fleck, U. Santo, C. Hotz, T. Jakobs, G. Eckel, M. Mancini, R. Weber, and T. Kolb. Entrained flow gasification part 1: Gasification of glycol in an atmospheric-pressure experimental rig. *Fuel*, 217:306 – 319, 2018.

[111] T.H. Fletcher, A.R. Kerstein, R.J. Pugmire, and D.M. Grant. Chemical Percolation Model for Devolatilization: 2. Temperature and Heating Rate Effects on Product Yields. *Energy and Fuels*, 4:54–60, 1990.

[112] R.O. Fox. *Computational Models for Turbulent Reacting Flows*. Cambridge University Press, 2003.

[113] B. Franzelli, E. Riber, M. Sanjos, and T. Poinsot. A two-step chemical scheme for kerosene-air premixed flames. *Combustion and Flame*, 157(7):1364 – 1373, 2010.

[114] C. G.von Fredersdorff and M. A. Elliott. *Coal Gasification*, chapter in Chemistry of Coal Utilization. Wiley, 1963.

[115] S. Fu, B. E. Launder, and M. A. Leschziner. Modeling strongly swirling recirculating jet flow with Reynolds-stress transport closures. In *Sixth Symposium on Turbulent Shear Flows*, Toulouse, France, 1987.

[116] P. J. Gans. Open first-order stochastic processes. *J. Chem. Phys.*, 33:691–694, 1960.

[117] W.C. Jr Gardiner and D. B. Olson. Chemical kinetics of high temperature combustion. *Annual Review of Physical Chemistry*, 31:377–399, 1980.

[118] G. R. Gavalas. A random capillary model with application to char. casification at chemically controlled rates. *AIChE J.*, 26:577, 1980.

[119] G. R. Gavalas. Analysis of char combustion including the effect of pore enlargement. *Comb. Sci. and Tech.*, 24(5):197, 1981.

[120] M. Geier, C.R. Shaddix, and F. Holzleithner. A mechanistic char oxidation model consistent with observed co2/co production ratios. *Proceedings of the Combustion Institute*, 34(2):2411 – 2418, 2013.

[121] D. Genetti. *An Advanced Model of Coal Devolatilization Based on Chemical Structure*. PhD thesis, Department of Chemical Engineering, Brigham Young University, 1999.

[122] D. Genetti and T. H. Fletcher. Modeling nitrogen release during devolatilization on the basis of chemical structure of coal. *Energy & Fuels*, 13(5):1082–1091, 1999.

[123] D. Genetti, T. H. Fletcher, and R. J. Pugmire. Development and application of a correlation of 13C NMR chemical structural analyses of coal based on elemental composition and volatile matter content. *Energy & Fuels*, 13(1):60–68, 1999.

[124] P. Gerlinger. *Numerische Verbrennungssimulation, Effiziente numerische Simulation turbulenter Verbrennung*. Springer-Verlag Verlag Berlin-Heidelberg-New York, 2005.

[125] R.C. Giberson and P.L.Jr Walker. Reaction of nuclear graphite with water vapor part I. Effect of hydrogen and water vapor partial pressures. *Carbon*, 3(4):521–525, 1966.

[126] M. M. Gibson and B. E. Launder. Ground Effects on Pressure Fluctuations in the Atmospheric Boundary Layer. *J. Fluid Mech.*, 86:491–511, 1978.

[127] P. Glarborg, N.I Lilleheie, S. Bigostoyl, B. Magnussen, P. Kilpinen, and M. Hupa. A reduced mechanism for nitrogen chemistry in methane combustion. *Symposium (International) on Combustion*, 24:889–898, 1992.

[128] Irvin Glassmann. *Combustion*. Academic Press, 3^{rd} edition, 1996.

[129] A. D. Gosman and E. Ioannides. Aspects of computer simulation of liquid fuelled combustors. *J. Energy*, 7:482–490, 1983.

[130] P. Graeser and M. Schiemann. Char particle emissivity of two coal chars in oxy-fuel atmospheres. *Fuel*, 183:405 – 413, 2016.

[131] P. Graeser and M. Schiemann. Emissivity of burning bituminous coal char particles - burnout effects. *Fuel*, 196:336 – 343, 2017.

[132] D.M. Grant, R.J. Pugmire, T.H. Fletcher, and A.R. Kerstein. Chemical Model of Coal Devolatilization Using Percolation Lattice Statistics. *Energy Fuels*, 3:175–186, 1989.

[133] D. Gray, J. Cogoli, and R. Essenhigh. *Problems in pulverized Coal and Char Combustion*, volume 131, chapter 7, pages 72–91. American Chemical Society, 1974.

[134] Tim Gronarz, Jan C. Schulze, Mischka Laemmerhold, Philipp Graeser, Jeanette Gorewoda, Vitali Kez, Martin Habermehl, Martin Schiemann, Jochen StrÃ¶hle, Bernd Epple, Viktor Scherer, and Reinhold Kneer. Quantification of the influence of parameters determining radiative heat transfer in an oxy-fuel operated boiler. 157:76 – 89, 03 2017.

[135] C. Guizani, F.J. Escudero Sanz, and S. Salvador. The gasification reactivity of high-heating-rate chars in single and mixed atmospheres of h2o and co2. *Fuel*, 108(Supplement C):812 – 823, 2013.

[136] Gunz. *Kurzes Handbuch der Brennstoff- und Feuerungstechnik*. Springer Verlag, 1962.

[137] Tennekes H. and Lumley J. *A First Course in Turbulence*. The MIT Press, Cambridge, Massachusetts,, 1972.

[138] J. Haas. *Experimentelle Untersuchungen der Reaktivität von Kohlenkoks zur Modellierung seines Verbrennungsverhaltens in Staubfeurungen*. PhD thesis, Faculty of Energy and Management, Clausthal University of Technology, 1999. (in German).

[139] S. Hafner, A. Rashidi, G. Baldea, and U. Riedel. A detailed chemical kinetic model of high-temperature ethylene glycol gasification. *Combustion Theory and Modelling*, 15(4):517–535, 2011.

[140] K. Hanjalic and B. E. Launder. Contribution towards a Reynolds-stress closure for low-Reynolds-number turbulence. *J. Fluid Mech.*, 74:593–610, 1976.

[141] S. Hansen and P. Glarborg. Simplified model for reburning chemistry. *Energy & Fuels*, 24(8):4185–4192, 2010.

[142] F.H. Harlow and P.I. Nakayama. Transport of turbulence energy decay rate. Technical Report LA-3854, Los Alamos Sience Lab, California (USA), 1968.

[143] M. Hartman and R. W. Coughlin. Reaction of sulfur dioxide with limestone and the grain model. *AIChE J.*, 22(3):490–498, 1976.

[144] K. Hashimoto and P. L. Silveston. Gasification: Part I. Isothermal, kinetic control model for a solid with a pore size distribution. *AIChE*, 19(2):259–268, 1973.

[145] K. Hashimoto and P. L. Silveston. Gasification: Part II. Extension to diffusion control. *AIChE J.*, 19(2):268–277, 1973.

[146] N. E. L. Haugen, S. Kragset, M. Bugge, R. Warnecke, and M. Weghaus. {MSWI} super heater tube bundle: Particle impaction efficiency and size distribution. *Fuel Processing Technology*, 106:416 – 422, 2013.

[147] H.D. Haustein, T. Kreitzberg, B. GÃ¶vert, A. Massmeyer, and R. Kneer. Establishment of kinetic parameters of particle reaction from a well-stirred fluidized bed reactor. *Fuel*, 158:263 – 269, 2015.

[148] A. N. Hayhurst and I. M. Vance. The origin and nature of *prompt* nitric oxide in flames. *Combust. Flame*, 50:41–57, 1983.

[149] D.O. Hayward. *Chemisorption*. BUTTERWORTHS & CO, 2nd edition, 1968.

[150] E.S. Hecht, C.R. Shaddix, A. Molina, and B.S. Haynes. Effect of CO_2 gasification reaction on oxy-combustion of pulverized coal char. *Symposium (International) on Combustion*, 33:1699–1706, 2011.

[151] R. A. W. M. Henkes, F. F. van der Flugt, and C. J. Hoogendoorn. Natural convection flow in a square cavity calculated with low-Reynolds-number turbulence models. *Int. J. Heat Mass Transfer*, 34:1543–1557, 1991.

[152] N. J. Higham. *Accuracy and Stability of Numerical Algorithms*. Society for Industrial and Applied Mathematics, 2002.

[153] S.C Hill and L. D. Smoot. Modeling of nitrogen oxides formation and destruction in combustion systems. *Progress in Energy and Combustion Science*, 26(4-6):417 – 458, 2000.

[154] C. N. Hinshelwood. On the theory of unimolecular reactions. *Proc. Royal Soc. A*, 17:230–233, 1926.

[155] E. Hippo and P. L. Walker. Reactivity of heat-treated coals in carbon dioxide at 900 Â°c. *Fuel*, 54(4):245 – 248, 1975.

[156] Jianhui Hong, William C. Hecker, and Thomas H. Fletcher. Improving the accuracy of predicting effectiveness factors for mth order and langmuir rate equations in spherical coordinates. *Energy & Fuels*, 14(3):663–670, 2000.

[157] H. Hottel and A. Sarofim. *Radiative Transfer*. McGraw-Hill, 1967.

[158] J.R. Howell, M.P. Mengüç, and R. Siegel. *Thermal Radiation Heat Transfer*. Taylor & Francis Group, 6 edition, 2016.

[159] Z. Huang, J. Zhang, Y. Zhao, H. Zhang, G. Yue, T. Suda, and M. Narukawa. Kinetic studies of char gasification by steam and CO2 in the presence of H2 and CO. *Fuel Processing Technology*, 91(8):843 – 847, 2010. Gasification: Fundamentals and application.

[160] R. Hurt, J. Sun, and M. Lunden. A kinetic model of carbon burnout in pulverized coal combustion. *Combustion and Flame*, 113(1-2):181 – 197, 1998.

[161] R. H. Hurt. Structure, properties, and reactivity of solid fuels. *Symposium (International) on Combustion*, 27(2):2887 – 2904, 1998.

[162] R. H Hurt and J. M Calo. Semi-global intrinsic kinetics for char combustion modeling. *Combustion and Flame*, 125(3):1138 – 1149, 2001.

[163] F. P. Incropera and D. P. DeWitt. *Introduction to Heat Transfer*. Willey, 2001.

[164] Singer M. J. and D. N. Munns. *Soils: An Introduction*. Upper Saddle River: Prentice Hall, 6th edition edition, 2005.

[165] T. Jakobs, N. Djordjevic, S. Fleck, M. Mancini, R. Weber, and T. Kolb. Gasification of high viscous slurry r&d on atomization and numerical simulation. *Applied Energy*, 93:449 – 456, 2012. (1) Green Energy; (2)Special Section from papers presented at the 2nd International Enery 2030 Conf.

[166] K. Jayaraman and I. Gokalp. Effect of char generation method on steam, CO2 and blended mixture gasification of high ash Turkish coals . *Fuel*, 153:320 – 327, 2015.

[167] D.A. Johnson and L.S. King. A mathematically simple turbulence closure model for attached and separated turbulent boundary layers. *AIAA Journal*, 23:1684–1692, 1985.

[168] J.F. Johnstone, C. Y. Chen, and D. S. Scott. Kinetics of the steam-carbon reaction in porous graphite tubes. *Ind. Engn. Chem.*, 44(194):1564, 1952.

[169] W.P. Jones and R.P. Lindstedt. Global reaction schemes for hydrocarbon combustion. *Combustion and Flame*, 73(3):233 – 249, 1988.

[170] J. Jovanovic. *The Statistical Dynamics of Turbulence*. Springer, 2004.

[171] W. H. Green Jr. Predictive kinetics: A new approach for the 21st century. In Guy B. Marin, editor, *Chemical Engineering Kinetics*, volume 32 of *Advances in Chemical Engineering*, pages 1 – 313. Academic Press, 2007.

[172] R. S. Jupudi, V. Zamansky, and T. H. Fletcher. Prediction of light gas composition in coal devolatilization. *Energy & Fuels*, 23(6):3063–3067, 2009.

[173] B. Kader. Temperature and concentration profiles in fully turbulent boundary layers. *Int. J. Heat Mass Transfer*, 24(9):1541–1544, 1981.

[174] O. Karlström, A. Brink, E. Biagini, M. Hupa, and L. Tognotti. Comparing reaction orders of anthracite chars with bituminous coal chars at high temperature oxidation conditions. *Proceedings of the Combustion Institute*, 34(2):2427 – 2434, 2013.

[175] O. Karlström, A. Brink, M. Hupa, and L. Tognotti. Multivariable optimization of reaction order and kinetic parameters for high temperature oxidation of 10 bituminous coal chars. *Combustion and Flame*, 158(10):2056 – 2063, 2011.

[176] L. S. Kassel. Studies in homogeneous gas reactions. ii. introduction of quantum theory. *J. Phys. Chem.*, 32:1065–1079, 1928.

[177] J. Keck and G. Carrier. Diffusion theory of nonequilibrium dissociation and recombination. *J. Chem. Phys.*, 43:2284–2298, 1965.

[178] F.J. Kilzer and A. Broido. Speculations on the nature of cellulose pyrolysis. *Pyrodynamics*, 2:151–163, 1965.

[179] J. Kim, P. Moinand, and R. Moser. Turbulence statistics in fully developed channel flow at low Reynolds number. *J. Fluid Mech.*, 177:133–166, 1987.

[180] A. Klimenko and S. Pope. The modeling of turbulent reactive flows based on multiple mapping conditioning. *Phys. Fluids*, 15:1907–1925, 2003.

[181] A. Y. Klimenko and Bilger R. W. Conditional moment closure for turbulent combustion. *Prog. Energ. Combust. Sci.*, 25(6):595 – 687, 1999.

[182] H. Kobayashi, J.B. Howard, and A.F. Sarofim. Coal devolatilization at high temperatures. *Symposium (International) on Combustion*, 16(1):411–425, 1977.

[183] T. Kolb, M. Aigner, R. Kneer, M. Müller, R. Weber, and N. Djordjevic. Tackling the challenges in modelling entrained-flow gasification of low-grade feedstock. *Journal of the Energy Institute*, 89(4):485–503, 2015.

[184] A.N. Kolmogorov. The local structure of turbulence in incompressible viscous fluid for very large Reynolds numbers. *Dokl. Akad. Nauk SSSR*, 30, 1941. Translated by V. Levin., Reprinted in Proc. R. Soc. London A 434, 1991.

[185] N.P. Komninos and C.D. Rakopoulos. Modeling HCCI combustion of biofuels: A review. *Renewable and Sustainable Energy Reviews*, 16(3):1588 – 1610, 2012.

[186] A. A. Konnov. NO formation rate in natural gas combustion. In *Proceedings of the* 4^{th} *International Conference on Technologies and Combustion for a Clean Environment*, volume II, July 1997.

[187] T Kreitzberg, H.D. Haustein, B Gävert, and R. Kneer. Investigation of Gasification Reaction of Pulverized Char Under N2/CO2 Atmosphere in a Small-Scale Fluidized Bed Reactor. *ASME. J. Energy Resour. Technol.*, 2016.

[188] I. M. Krieger and P. J. Gans. First-order stochastic processes. *J. Chem. Phys.*, 32:247–250, 1960.

[189] M. Kübel. *Teerbildung und Teerkonversion bei der Biomassevergasung: Anwendung der nassmechanischen Teerbestimmung nach CEN-Standard*. PhD thesis, TU Stuttgart, 2007.

[190] T. Kupka, M. Mancini, M. Irmer, and R. Weber. Investigation of ash deposit formation during co-firing of coal with sewage sludge, saw-dust and refuse derived fuel. *Fuel*, 87:2824–2837, 2008.

[191] T. Kupka, K. Zając, and R. Weber. Effect of fuel type and deposition surface temperature on the growth and structure of an ash deposit collected during co-firing of coal with sewage sludge and saw dust. *Energy & Fuels*, 23:3429–3436, 2009.

[192] J. Y.W. Lai, K. C. Lin, and A. Violi. Biodiesel combustion: Advances in chemical kinetic modeling. *Progress in Energy and Combustion Science*, 37(1):1 – 14, 2011.

[193] S. Lain1 and C. A. Grillo. Comparison of turbulent particle dispersion models in turbulent shear flows. *Brazilian Journal of Chemical Engineering*, 24(3):351–363, 2007.

[194] Chittur Chandrasekharan Lakshmanan and Noam White. A new distributed activation energy model using weibull distribution for the representation of complex kinetics. *Energy & Fuels*, 8(6):1158–1167, 1994.

[195] N. Lallemant, A. Sayre, and R. Weber. Evaluation of emissivity correlations for $H_2O - CO_2 - N_2/air$ mixtures and coupling with solution methods of the Radiative Transfer Equation. *Prog. Energy Combust. Sci.*, 22:543–574, 1990.

[196] S. H. Lam and D. A. Goussis. Understanding complex chemical kinetics with computational singular perturbation. In 22^{nd} *Symposium (International) on Combustion*, page 931. The Combustion Institute, Pittsburgh, PA, 1988.

[197] S.H. Lam and D.A. Goussis. Conventional assymptotics and computational singular perturbation for simplified kinetics modelling. Technical Report 1864(a)-MAE, Princeton University, USA., 1990.

[198] R. B. Langtry and F. R. Menter. Correlation-based transition modeling for unstructured parallelized computational fluid dynamics codes. *AIAA Journal*, 47(12):2894–1906, 2009.

[199] B. E. Launder. Second-moment closure: Present... and future? *Int. J. Heat Fluid Flow*, 10(4):282, 300 1989.

[200] B. E. Launder, G. J. Reece, and W. Rodi. Progress in the development of a reynolds-stress turbulent closure. *Journal of Fluid Mechanics*, 63:537–566, 1975.

[201] B. E. Launder and D. B. Spalding. *Lectures in Mathematical Models of Turbulence*. Academic Press, London, England, 1972.

[202] B.E. Launder. Second-moment closure and its use in modeling turbulent industrial flows. *International Journal for Numerical Methods in Fluids*, 9:963–985, 1989.

[203] B.E. Launder and N. Shima. Second-moment closure for the near-wall sublayer: Development and application. *AIAA Journal*, 27(10):1319–1325, 1989.

[204] B.E. Launder and D.B. Spalding. The numerical computation of turbulent flows. *Computer Methods in Applied Mechanics and Engineering*, 3:269–289, 1974.

[205] N.M. Laurendeau. Heterogeneous Kinetics of Coal Char Gasification and Combustion. *Prog. Energy Com. Sci.*, 4:221–270, 1978.

[206] C.K. Law. *Combustion Physics*. Cambridge Univ. Press, New York, 2006.

[207] T.W. Lester, W.R. Seeker, and J.F. Merklin. The influence of oxygen and total pressure on the surface oxidation rate of bituminous coal. *Proc Combust Inst,*, 18:1257–1265, 1981.

[208] K. Levenberg. A method for the solution of certain problems in least squares. *Quart. Appl. Math*, 2:164–168, 1944.

[209] P. F. Lewis and G. A. Simons. Char Gasification: Part II. Oxidation Results. *Combustion Science and Technology*, 20(3-4):117, 1979.

[210] S. Li, H. Yang, T. H. Fletcher, and M. Dong. Model for the evolution of pore structure in a lignite particle during pyrolysis. *Energy & Fuels*, 29(8):5322–5333, 2015.

[211] B. Liedmann, W. Arnold, B. Krġer, A. Becker, S. Krusch, S. Wirtz, and V. Scherer. An approach to model the thermal conversion and flight behaviour of refuse derived fuel. *Fuel*, 200:252 – 271, 2017.

[212] F. S. Lien and M. A. Leschziner. Assessment of turbulent transport models including non-linear RNG eddy-viscosity formulation and second-moment closure. *Computers and Fluids*, 23(8):983–1004, 1994.

[213] F. A. Lindemann, S. Arrhenius, I. Langmuir, N. R. Dhar, J. Perrin, and W. C. Lewis. Discussion on the radiation theory of chemical action. *Trans. Faraday Soc.*, 17:598–606, 1922.

[214] E. Lindner. Chemie für ingenieure. Lindner Verlag Karlsruhe.

[215] G. Liu, P. Beyon, K.E. Benfell, G.W. Bryant, A.G. Tate, R.K. Boyd, D.J. Harris, and T.F. Wall. The porous structure of bituminous coal chars and its influence on combustion and gasification under chemically controlled conditions. *Fuel*, 79:617–626, 2000.

[216] G. Liu, A.G. Tate, G.W.Bryant, and T.F. Wall. Mathematical modeling of char reactivity with co_2 at high pressures and temperatures. *Fuel*, 79:1145–1154, 2000.

[217] Gui-Su Liu and Stephen Niksa. Coal conversion submodels for design applications at elevated pressures. Part II. Char gasification . *Progress in Energy and Combustion Science*, 30(6):679–717, 2004.

[218] T. Loevas. Automatic generation of skeletal mechanisms for ignition combustion based on level of importance analysis. *Combustion and Flame*, 156(7):1348 – 1358, 2009.

[219] Liming Lu, Chunhua Kong, Veena Sahajwalla, and D.Harris. Char structural ordering during pyrolysis and combustion and its influence on char reactivity. *Fuel*, 81(9):1215 – 1225, 2002.

[220] T. Lu and C. K. Law. Toward accommodating realistic fuel chemistry in large-scale computations. *Progress in Energy and Combustion Science*, 35(2):192 – 215, 2009.

[221] J. L. Lumley. *Stochastic tools in turbulence*, volume 12 of *Applied Mathematics and Mechanics*. Academic Press, New York, 1970.

[222] R. Lundquist, A. Schrief, P. Kinnunen, K. Myohanen, and M. Seshamani. A Major Forward- The Supercritical CFB Boiler. In *Power-Gen International 2003*, Las Vegas, USA, 2003.

[223] H.C. Magel, U. Schnell, and K.R.G. Hein. Simulation of detailed chemistry in a turbulent combustion flow. *Symposium (International) on Combustion*, 26:67–73, 1996.

[224] B.F. Magnussen and I. R. Gran. A numerical study of a bluff-body stabilized diffusion flame. Part 2. Influence of combustion modeling and finite rate chemistry. *Combust. Sci. Tech.*, 119:191–217, 1996.

[225] B.F. Magnussen and B.H. Hjertager. On mathematical models of turbulent combustion with special emphasis on soot formation and combustion. In *In 16th Symp. on Combustion.*, volume 16, pages 719–729. The Combustion Institute, 1976.

[226] Om P. Mahajan, R. Yarzab, and P. L. Walker, Jr. Unification of coal-char gasification reaction mechanisms. *Fuel*, 57(10):643–646, 1978.

[227] A.K. Majumder, Rachana Jain, P. Banerjee, and J.P. Barnwal. Development of a new proximate analysis based correlation to predict calorific value of coal. *Fuel*, 87(13-14):3077–3081, 2008.

[228] M. Mancini. *Analysis of mild combustion of Natural gas with preheated air*. PhD thesis, Technical University of Clausthal, 2006.

[229] M. Mancini, M. Alberti, M. Dammann, U. Santo, G. Eckel, T. Kolb, and R. Weber. Entrained flow gasification. part 2: Mathematical modeling of the gasifier using rans method. *Fuel*, 225:596 – 611, 2018.

[230] M. Mancini, R. Weber, and U. Bollettini. Predicting NOx emissions of a burner operated in flameless oxidation mode. *Proceedings of the Combustion Institute*, 29(1):1155 – 1163, 2002. Proceedings of the Combustion Institute.

[231] M. D. Mann, R. Z. Knutson, J. Erjavec, and J. P. Jacobsen. Modeling reaction kinetics of steam gasification for a transport gasifier. *Fuel*, 83(11-12):1643–1650, 2004. Fundamental Mechanisms of Biomass, Pyrolysis and Oxidation.

[232] J.G. Marakis, C. Papapavlou, and E. Kakaras. A parametric study of radiative heat transfer in pulverised coal furnaces. *International Journal of Heat and Mass Transfer*, 43(16):2961 – 2971, 2000.

[233] R. A. Marcus and O. K. Rice. The kinetics of the recombination of methyl radicals and iodine atoms. *J. Phys. Coll. Chem.*, 55:894–908, 1951.

[234] D. Marquardt. An Algorithm for Least-Squares Estimation of Nonlinear Parameters. *A, SIAM J. Appl. Math*, 11:431–441, 1963.

[235] D. M. Mason and K. N. Gandhi. Formulas for calculating the calorific value of coal and coal chars: Development, tests, and uses. *Fuel Processing Technology*, 7(1):11–22, 1983.

[236] M.R. Maxey and J.J. Riley. Equation of motion for a small rigid sphere in a nonuniform flow. *Physics of Fluids*, 26(4):883–889, 1983.

[237] M.J. McGuinness, E. Donskoi, and D.L.S. McElwain. Asymptotic approximations to the distributed activation energy model. *Applied Mathematics Letters*, 12(8):27 – 34, 1999.

[238] J.P.and P. McKendry. Energy production from biomass (part 1): overview of biomass. *Bioresource Technology*, 83(1):37–46, 2002.

[239] P.C. Melte and D.T. Pratt. Measurement of atomic oxygen and nitrogen oxides in jet stirred combustion. *Symposium (International) on Combustion*, 15:1061–1070, 1974.

[240] M. Menster and S. Ergun. A study of the carbon dioxide-carbon reaction by oxygen exchange. *U.S. Bureau of Mines*, 1973.

[241] F. R. Menter. Two-equation eddy-viscosity turbulence models for engineering applications. *AIAA Journal*, 32(8):1598–1605, 1994.

[242] J. A. Miller and C. T. Bowman. Mechanism and modeling of nitrogen chemistry in combustion. *Progress in Energy and Combustion Science*, 15(4):287 – 338, 1989.

[243] A. Misdariis, O. Vermorel, and T. Poinsot. A methodology based on reduced schemes to compute autoignition and propagation in internal combustion engines. *Proceedings of the Combustion Institute*, 35(3):3001–3008, 2015.

[244] J.W. Mitchell and J.M. Tarbell. A kinetic model of nitric oxide formation during pulverized coal combustion. *AIChE Journal*, 28:302, 1982.

[245] K. Miura. A new and simple method to estimate f(e) and k0(e) in the distributed activation energy model from three sets of experimental data. *Energy & Fuels*, 9(2):302–307, 1995.

[246] K. Miura and T. Maki. A simple method for estimating f(e) and k0(e) in the distributed activation energy model. *Energy & Fuels*, 12(5):864–869, 1998.

[247] M. F. Modest. *Radiative Heat Transfer*. Academic Press, Burlington, 2003.

[248] M.F. Modest. The Weighted-Sum-of-Grey-Gases Model for arbitrary solution methods in radiative transfer. *J. Heat Transfer*, 113:650–656, 1991.

[249] E. Mokrzycki and A. Uliasz-Bochenczyk. Alternative fuels for the cement industry. *Applied Energy*, 74(1):95 – 100, 2003. Energex 2002 - New and Renewable Sources of Energy - Topic I.

[250] E. W. Montroll and K. E. Shuler. The application of the theory of stochastic processes to chemical kinetics. *Adv. Chem. Phys.*, 1:361–399, 1958.

[251] S. A. Morsi and A. J. Alexander. An investigation of particle trajectories in two-phase flow systems. *Fluid Mechanics*, 55(2):193–208, 1972.

[252] A. Mueller, H. D. Haustein, P. Stoesser, T. Kreitzberg, R. Kneer, and T. Kolb. Gasification kinetics of biomass- and fossil-based fuels: Comparison study using fluidized bed and thermogravimetric analysis. *Energy & Fuels*, 29(10):6717–6723, 2015.

[253] H.-J. Mühlen, K. H. van Heek, and H. Jüntgen. Kinetic studies of steam gasification of char in the presence of H2, CO2 and CO. *Fuel*, 64(7):944 – 949, 1985.

[254] J. J. Murphy and C. R. Shaddix. Combustion kinetics of coal chars in oxygen-enriched environments. *Combustion and Flame*, 144(4):710 – 729, 2006.

[255] P. Murray and J. White. *Trans. Br. Ceram. Soc.*, 54(204-237), 1955.

[256] J.Y. Murthy and S.R. Mathur. Finite volume method for radiative heat transfer using unstructured meshes. *Journal of Thermophysics and Heat Transfer*, 12(3):313–321, 1998.

[257] Z. M. Nikolaou, J.-Y. Chen, and N. Swaminathan. A 5-step reduced mechanism for combustion of $CO/H_2/H_2O/CH_4/CO_2$ mixtures with low hydrogen/methane and high H_2O content. *Combustion and Flame*, 160(1):56 – 75, 2013.

[258] S. Niksa. Flashchain theory for rapid coal devolatilization kinetics. 6. predicting the evolution of fuel nitrogen from various coals. *Energy & Fuels*, 9(3):467–478, 1995.

[259] S. Niksa and A. R. Kerstein. Flashchain theory for rapid coal devolatilization kinetics. 1. formulation. *Energy & Fuels*, 5(5):647–665, 1991.

[260] S. Niksa, G. Liu, and R. H. Hurt. Coal conversion submodels for design applications at elevated pressures. Part I. devolatilization and char oxidation . *Progress in Energy and Combustion Science*, 29(5):425–477, 2003.

[261] S. Niksa and G.-S. Liu. Detailed reaction mechanisms for coal-nitrogen conversion in pulverized fuel flames. *Symposium (International) on Combustion*, 29:2259–2265, 2002.

[262] M. S. Oh, W. A. Peters, and J. B. Howard. An experimental and modeling study of softening coal pyrolysis. *AIChE Journal*, 35(5):775–792, 1989.

[263] S. Orsino, F. Breussin, R. Weber, E. Perez, and F. Malaubier. A numerical study of down-fired boilers. In *Proceedings of the International Conference on Applied Computational Fluid Dynamics ACFD*, pages 682–689, Beijing China, 10 2000.

[264] S. Orsino, M. Tamura, P. Stabat, S. Costantini, O. Prado, and R. Weber. Excess enthalpy combustion of coal. Results of HTAC 99 trials. Technical Report IFRF Doc. No. F46/y/3, IFRF Research Report, IJmuiden, 2000.

[265] L. S. Pedersen, P. Glarborg, and K. D. Johansen. A reduced reaction scheme for volatile nitrogen conversion in coal combustion. *Combustion Science and Technology*, 131(1-6):193–223, 1998.

[266] A. A. F. Peters and R. Weber. Mathematical Modelling of a 2.25 MW Swirling Natural Gas Flame. Part 1: Eddy-Break-up Concept for Turbulent Combustion; Probability Density Function Approach for Nitric Oxide Formation. *Combust. Sc. and Tech.*, 110-111:67–101, 1995.

[267] A.A.F. Peters and R. Weber. Mathematical Modeling of a 2.4 MW_{th} Swirling Pulverized Coal Flame. *Combust. Sci. and Tech.*, 122:131–182, 1997.

[268] N. Peters. Laminar diffusion flamelet models in non premixed combustion. *Prog. Energy Combust. Sci.*, 10:319–339, 1984.

[269] N. Peters. Numerical and asymptotic analysis of systematically reduced reaction schemes for hydrocarbon flames. *Lect. Notes Phys.*, 241:90, 1985.

[270] N. Peters. Laminar flamelet concepts in turbulent combustion. *Symposium (International) on Combustion*, 21:1231–1250, 1986.

[271] N. Peters. *Turbulent Combustion*. Cambridge University Press, 2000.

[272] N. Peters. Multiscale combustion and turbulence. *Proceedings of the Combustion Institute*, 32(1):1 – 25, 2009.

[273] N. Peters and B. Rogg, editors. *Reduced Kinetic Mechanisms for Applications in Combustion Systems*, volume 15 of *Lecture Notes in Physics Monographs*. Springer Berlin Heidelberg, 1993.

[274] I. Petersen and J. Werther. Experimental investigation and modeling of gasification of sewage sludge in the circulating fluidized bed. *Chemical Engineering and Processing: Process Intensification*, 44(7):717–736, 2005.

[275] S. Pielsticker, S. Heuer, O. Senneca, F. Cerciello, P. Salatino, L. Cortese, B. Gövert, O. Hatzfeld, M. Schiemann, V. Scherer, and R. Kneer. Comparison of pyrolysis test rigs for oxy-fuel conditions. *Fuel Processing Technology*, 156:461 – 472, 2017.

[276] W. J. Pitz and Ch. J. Mueller. Recent progress in the development of diesel surrogate fuels. *Progress in Energy and Combustion Science*, 37(3):330 – 350, 2011.

[277] C.P. Please, M.J. McGuinness, and D.L.S. McElwain. Approximations to the distributed activation energy model for the pyrolysis of coal. *Combustion and Flame*, 133(1-2):107 – 117, 2003.

[278] T. Poinsot and D. Veynante. *Theoretical and Numerical Combustion*. R. T. Edwards, Inc., 2005.

[279] S. B. Pope. A Lagrangian two-time probability density function equation for inhomogeneous turbulent flows. *Phys. Fluids*, 26:3448–50, 1983.

[280] S. B. Pope. *Turbulent flows*. Cambridge University Press, 2000.

[281] S.B. Pope. PDF methods for turbulent reactive flows. *Prog. Energy Combust. Sci.*, 11:119, 1985.

[282] S.B. Pope. The evolution of surfaces in turbulence. *International Journal of Engineering Science*, 26(5):445 – 469, 1988.

[283] L. Prandtl. Über die ausgebildete Turbulenz. In *ZAMM*, volume 5, pages 136–139, 1925.

[284] M. M. Rahman, T. Siikonen, and R. K. Agarwal. Improved Low Re-Number One-Equation Turbulence Model. *AIAA*, 49(4), 2011.

[285] Pallares Ranz. *Unberned carbon in ash preciction in pulverized coal utility boilers*. PhD thesis, University of Zaragoza, 2007.

[286] W.E. Ranz and W.R. Marshall. Evaporation from drops: part II. *Chem Eng Prog*, 48:173–180, 1952.

[287] Reaction Design. Chemkin-pro 4.1, 2016.

[288] M. Rehm. *Numerische Strömungssimulation der Hochdruckvergasung unter Berücksichtigung detaillierter Reaktionsmechanismen*. Dissertation, Technische Universität Bergakademie Freiberg, Freiberg (DE), May 2010.

[289] Zhuyin Ren, Yufeng Liu, Tianfeng Lu, Liuyan Lu, Oluwayemisi O. Oluwole, and Graham M. Goldin. The use of dynamic adaptive chemistry and tabulation in reactive flow simulations. *Combustion and Flame*, 161(1):127 – 137, 2014.

[290] A. M. Reynolds. On the application of nonextensive statistics to lagrangian turbulence. *Physics of Fluids*, 2003.

[291] O. K. Rice and H. C. Ramsperger. Theories of unimolecular gas reactions at low pressures. *J. Am. Chem. Soc.*, 49:1617–1629, 1927.

[292] L. Richardson. *Weather Prediction by Numerical Process*. Cambridge University Press, 1922.

[293] Ridle. Ridle calculates rega.

[294] M. Rieth, F. Proch, M. Rabaçal, B.M. Franchetti, F. Cavallo Marincola, and A.M. Kempf. Flamelet {LES} of a semi-industrial pulverized coal furnace. *Combustion and Flame*, 173:39 – 56, 2016.

[295] D. G. Roberts and D. J. Harris. A kinetic analysis of coal char gasification reactions at high pressures. *Energy & Fuels*, 20(6):2314–2320, 2006.

[296] D. G. Roberts, D. J. Harris, and T. F. Wall. On the effects of high pressure and heating rate during coal pyrolysis on char gasification reactivity. *Energy & Fuels*, 17(4):887–895, 2003.

[297] M.M. Rogers and R. D. Moser. Direct simulation of a self-similar turbulent mixing layer. *Phys. Fluids*, 6:903–923, 1994.

[298] B. Rogg and F.A. Williams. Structures of wet CO flames with full and reduced kinetic mechanisms. *Symposium (International) on Combustion*, 22(1):1441 – 1451, 1989.

[299] L.S. Rothman, I.E. Gordon, R.J. Barber, H. Dothe, R.R. Gamache, A. Goldman, V.I. Perevalov, S.A. Tashkun, and J. Tennyson. HITEMP, the high-temperature molecular spectroscopic database. *Journal of Quantitative Spectroscopy and Radiative Transfer*, 111(15):2139 – 2150, 2010.

[300] P. J. Saffman. The large-scale structure of homogeneous turbulence. *J. Fluid Mech.*, 27:581, 1976.

[301] P. Sagaut. *Large Eddy Simulation for Incompressible Flows*. Springer, 2004.

[302] M. Sami, K. Annamalai, and M. Wooldridge. Co-firing of coal and biomass fuel blends. *Progress in Energy and Combustion Science*, 27(2):171–214, 2001.

[303] E. Sani and A. Dell'Oro. Optical constants of ethylene glycol over an extremely wide spectral range. *Optical Materials*, 37:36–41, 2014.

[304] U. Santo. Private communications, 2017. Karlsruhe Institute of Technologies, Institute of Technical Chemistry.

[305] B. L. Sawford. Reynolds number effects in lagrangian stochastic models of turbulent dispersion. *Physics of Fluids*, 1991.

[306] A. Sayre, N. Lallemant, J. Dugué, and R. Weber. Effect of radiation on nitrogen emissions from non-sooty swirling flames of natural gas. *Symposium (International) on Combustion*, 25:235–242, 1994.

[307] S. S. Sazhin. Advanced models of fuel droplet heating and evaporation. *Progress in Energy and Combustion Science*, 32(2):162 – 214, 2006.

[308] S.S. Sazhin, T. Kristyadi, W.A. Abdelghaffar, and M.R. Heikal. Models for fuel droplet heating and evaporation: Comparative analysis. *Fuel*, 85(12-13):1613–1630, 2006.

[309] S.C. and Saxena. Devolatilization and combustion characteristics of coal particles. *Progress in Energy and Combustion Science*, 16(1):55–94, 1990.

[310] N. Schaffel, M. Mancini, A. Szlek, and R. Weber. Mathematical modeling of mild combustion of pulverized coal. *Combustion and Flame*, 156(9):1771 – 1784, 2009.

[311] N. Schaffel-Mancini. *Ecological evaluation of the pulverized coal combustion in HTAC technology*. PhD thesis, Silesian University of Technology, 2010.

[312] N. Schaffel-Mancini, M. Mancini, Andrzej Szlek, and R. Weber. Novel conceptual design of a supercritical pulverized coal boiler utilizing high temperature air combustion (HTAC) technology. *Energy*, 35(7):2752 – 2760, 2010.

[313] R. Scholz, M. Beckmann, C. Pieper, M. Muster, and R. Weber. Consideration on providing the energy needs using exclusively renewable resources: Energiewende in germany. *Renewable ans Sustainable Energy Reviews*, 35:109–125, 2014.

[314] S. Schulze, P. Nikrityuk, Z. Abosteif, S. Guhl, A. Richter, and B. Meyer. Heat and mass transfer within thermogravimetric analyser: From simulation to improved estimation of kinetic data for char gasification. *Fuel*, 187:338 – 348, 2017.

[315] W.R. Seeker, G.S. Samuelsen, M.P. Heap, and J.D. Trolinger. The thermal decomposition of pulverized coal particles. *Symposium (International) on Combustion*, 18(1):1213–1226, 1981. Eighteenth Symposium (International) on Combustion.

[316] Y. Sekine, K. Ishikawa, E. Kikuchi, M. Matsukata, and A. Akimoto. Reactivity and structural change of coal char during steam gasification. *Fuel*, 85(2):122 – 126, 2006. Special Issue: The 21st Annual International Pittsburgh Coal Conference.

[317] O. Senneca, P. Salatino, and S. Masi. The influence of heat treatment and weathering on the gasification reactivity of montana lignite. *Symposium (International) on Combustion*, 27(2):2991 – 2999, 1998.

[318] G. I. Senum and R. T. Yang. Rational approximations of the integral of the arrhenius function. *J. Therm. Anal.*, 11:445–447, 1977.

[319] M. A. Serio, D.G. Hamblen, James R. Markham, and P.R. Solomon. Kinetics of volatile product evolution in coal pyrolysis: experiment and theory. *Energy & Fuels*, 1(2):138–152, 1987.

[320] C. Shaddix, F. Holtzleithner, M. Geier, and B.S. Haynes. Numerical assessment of Tognotti determination of CO2/CO production ratio during char oxidation. *Combust. Flame*, 160:1827–1834, 2013.

[321] J. T. Shaw. Theoretical work on reaction sequences in the gasification of coke by carbon dioxide and by steam in conditions remote from equilibrium. *Fuel*, 56:135, 1977.

[322] C. Sheng and J.L.T. Azevedo. Modeling the evolution of particle morphology during coal devolatilization. *Proceedings of the Combustion Institute*, 28(2):2225 – 2232, 2000.

[323] Y. Shi, L. Liang, H.-W. Ge, and R. D. Reitz. Acceleration of the chemistry solver for modeling DI engine combustion using dynamic adaptive chemistry (DAC) schemes. *Combustion Theory and Modelling*, 14(1):69–89, 2010.

[324] T.H. Shih, W. W. Liou, A. Shabbir, and J. Zhu. A new k-ϵ eddy-viscosity model for high Reynolds number turbulent flows: Model development and validation. *Computers Fluids*, 24(3):227–238, 1995.

[325] M. Shur, M. Strelets, L. Zaikov, A. Gulyaev, V. Kozlov, and A. Secundov. Comparative numerical testing of one- and two-equation turbulence models for flows with separation and reattachment. *AIAA Paper*, 95(0863), 1995.

[326] A. J. F. Siegert. On the approach to statistical equilibrium. *Phys. Rev.*, 76:1708–1714, 1949.

[327] J. Berger T. Siemieniewska and K. Tomkow. Development of porosity in brown-coal chars on activation with carbon dioxide. *Fuel*, 55(1):9–15, 1976.

[328] J. M. Simmie. Detailed chemical kinetic models for the combustion of hydrocarbon fuels. *Progress in Energy and Combustion Science*, 29(6):599 – 634, 2003.

[329] G. A. Simons. The Structure of Coal Char: Part II - Pore Combination. *Combustion Science and Technology*, 19(5-6):227–235, 1979.

[330] G. A. Simons. Coal pyrolysis I. pore evolution theory. *Combustion and Flame*, 53(1-3):83–92, 1983.

[331] G. A. Simons. The role of pore structure in coal pyrolysis and gasification. *Prog. Energy Combust. Sci.*, 9(4):269–361, 1983.

[332] G. A. Simons. Coal pyrolysis II. species transport theory. *Combustion and Flame*, 55(2):181–194, 1984.

[333] G. A . Simons and P. F. Lewis. *Mass transport and heterogeneous reactions in a porous medium*. The Combustion Institute, 1977.

[334] G. A. Simons and M. L. Finson. The Chemical Structure of Coal Tar and Char: Part I Pores Branching. *Comb. Sci. Tech.*, 19:217, 1979.

[335] G. A. Simons and M. L. Finson. The Structure of Coal Char: Part I - Pore Branching. *Combustion Science and Technology*, 19(5-6):217–225, 1979.

[336] W.A. Sirignano. *Fluid dynamics and transport of droplets and sprays*. Cambridge University Press, Cambridge, 1999.

[337] A. M. O. Smith and T. Cebeci. Numerical solution of the turbulent boundary layer equations. Technical report, Douglas aircraft division report DAC 33735., 1967.

[338] G. P. Smith, D. M. Golden, M. Frenklach, N. W. Moriarty, B. Eiteneer, M. Goldenberg, C. T. Bowman, R. K. Hanson, S. Song, Jr. W. C. Gardiner, V. V. Lissianski, and Z. Qin. GRI mechanism 3.0. Technical report, Sandia National Laboratories, http://www.me.berkeley.edu/gri_mech/, 2000.

[339] I. W. Smith. The combustion rates of coal chars: A review. *Symposium (International) on Combustion*, 19:1045–1065, 1982.

[340] T.F. Smith, Z.F. Shen, and J.N. Friedman. Evaluation of coefficients for the weighted sum of gray gases model. *J. Heat Transfer*, 104:602–608, 1982.

[341] L. D. Smoot. *Fundamentals of coal combustion for clean and efficient use*. Elsevier,Amsterdam-London-New York-Tokyo, 1993.

[342] G.G. De Soete, E. Croiset, and J.-R. Richard. Heterogeneous formation of nitrous oxide from char-bound nitrogen. *Combustion and Flame*, 117(1-2):140–154, 1999.

[343] P. G. Solomon and D. G. Hamblen. *Chemistry of coal conversion*, chapter 5. Plenum Press, New York, 1985.

[344] P. R. Solomon, D. G. Hamblen, R. M. Carangelo, M. A. Serio, and G. V. Deshpande. General model of coal devolatilization. *Energy & Fuels*, 2(4):405–422, 1988.

[345] P. R. Solomon, M. A. Serio, and E. M. Suuberg. Coal pyrolysis: Experiments, kinetic rates and mechanisms. *Progress in Energy and Combustion Science*, 18(2):133–220, 1992.

[346] P.R. Solomon and T. H. Fletcher. Impact of coal pyrolysis on combustion. *Symposium (International) on Combustion*, 25(1):463 – 474, 1994. Twenty-Fifth Symposium (International) on Combustion.

[347] P.R. Solomon and D.G. Hamblen. Finding order in coal pyrolysis kinetics. *Progress in Energy and Combustion Science*, 9(4):323–361, 1983.

[348] P.R. Solomon, M. A. Serio, Girish V. Despande, and Erik Kroo. Cross-linking reactions during coal conversion. *Energy & Fuels*, 4(1):42–54, 1990.

[349] S. Sommariva, T. Maffei, G. Migliavacca, T. Faravelli, and E. Ranzi. A predictive multi-step kinetic model of coal devolatilization. *Fuel*, 89(2):318 – 328, 2010.

[350] P. R. Spalart and S. R. Allmaras. A one-equation turbulence model for aerodynamic flows. *AIAA Paper*, 92(439), 1992.

[351] D.B. Spalding. Mixing and chemical reaction in steady confined turbulent flames. *Symposium (International) on Combustion*, 13, 1970.

[352] D.B. Spalding, H.C. Hottel, S.L. Bragg, A.H. Lefebvre, D.G. Shepherd, and A.C. Scurlock. The art of partial modeling. *Symposium (International) on Combustion*, 9(1):833 – 843, 1963.

[353] C. Speziale, R. Abid, and E. Anderson. Critical evaluation of two-equation models for near-wall turbulence. *AIAA Journal*, 30:324–331, 1992.

[354] C. G. Speziale. On non-linear $k - l$ and k-ϵ models of turbulence. *J. Fluid Mech.*, 178:459–475, 1987.

[355] C.G. Speziale, S. Sarkar, and T.B. Gatski. Modelling the pressure-strain correlation of turbulence: An invariant dynamical systems approach. *J. Fluid Mech.*, 227:245–272, 1991.

[356] G. N. Spokes and S. W. Benson. *Oxidation of a thin film of carbonaceous solid at pressure below* 10^{-4} *torr*, page 318. Academic press, New York, 1967.

[357] S. E. Stein and B. S. Rabinovitch. Accurate evaluation of internal energy level sums and densities including anharmonic oscillators and hindered rotors. *J. Chem. Phys.*, 58:2438–2444, 1973.

[358] M. Sudiro, M. Pellizzaro, F. Bezzo, and A. Bertucco. Simulated moving bed technology applied to coal gasification. *Chemical Engineering Research and Design*, 88(4):465–475, 2010.

[359] C.J. Sung, C.K. Law, and J.-Y Chen. An augmented reduced mechanism for methane oxidation with comprehensive global parametric validation. *Proc. Combust. Inst*, 27:295–304, 1998.

[360] C.J. Sung, C.K. Law, and J.-Y Chen. Further Validation of an Augmented Reduced Mechanism for Methane Oxidation: Comparison of Global Parameters and Detailed Structure. *Combust. Sci. Tech.*, 156:201–220, 2000.

[361] C.J. Sung, C.K. Law, and J.-Y. Chen. Augmented Reduced Mechanisms for NO Emission in Methane Oxidation. *Combust. Flame*, 125:906–919, 2001.

[362] E. M. Suuberg, W. A. Peters, and J. B. Howard. Product composition and kinetics of lignite pyrolysis. *Ind. Eng. Chem. Process Des. Dev.*, 17(1):37–46, 1978.

[363] E. M. Suuberg, M. Wojtowicz, and J. M. Calo. Reaction order for low temperature oxidation of carbons. *Proceedings of the Combustion Institute*, 22:79–87, 1988.

[364] E.M. Suuberg. Mass transfer effects in pyrolysis of coals: A review of experimental evidence and models. In R.H. Schlosberg, editor, *Chemistry of coal conversion*, page 67. Plenum Press, New York, 1985.

[365] E.M. Suuberg. Thermally induced changes in reactivity of carbons. In J. Lahaye, editor, *Fundamental issues in control of carbon gasification reactivity*, pages 269–305. Kluwer Academic Publishers, 1991.

[366] E.M. Suuberg, W.A. Peters, and J.B. Howard. Product composition and kinetics of lignite pyrolysis. *Proc. Combust. Inst,*, pages 1303–1317, 1979.

[367] I. Sykorova, W. Pickel, K. Christanis, M. Wolf, G.H. Taylor, and D. Flores. Classification of huminite ICCP System 1994 . *International Journal of Coal Geology*, 62(1-2):85–106, 2005. Marlies Teichmueller Symposium.

[368] Matthew B. T. and R. E. Mitchell. Coal and biomass char reactivities in gasification and combustion environments. *Combustion and Flame*, 162(9):3220 – 3235, 2015.

[369] M. Tamura. Data on characterization of Guasare coal, 2000. (unpublished).

[370] D. C. Tardy and B. S. Rabinovitch. Collisional energy transfer. thermal unimolecular systems in the low-pressure region. *J. Chem. Phys.*, 45:3720–3730, 1966.

[371] S. Tavularis and S. Corrsin. Experiments in a nearly homogeneous turbulence shear flow with a uniform mean temperature gradient. Part 1 . *J. Fluid Mech.*, 104:311–347, 1981.

[372] M. Teichmüller. The genesis of coal from the wiewpoint of coal petrology. *International Journal of Coal Geology*, 12:1–87, 1989.

[373] E. W. Thiele. Relation between catalytic activity and size of particle. *Ind. Eng. Chem.*, 31(7):916–920, 1939.

[374] Larry Thomas. *Coal geology*. John Wiley and Sons, Lt, 2013.

[375] D. J. Thomson. Criteria for the selection of stochastic models of particle trajectories in turbulent flows. *Journal of Fluid mechanics*, 1987.

[376] A. N. Tikhonov and V. Y. Arsenin. *Solutions of Ill-Posed Problems*. New York, Winston, 1977.

[377] L. Tognotti, J. Longwell, and A. Sarofim. The products of the high temperature oxidation of a single char particle in an electrodynamic balance. *Symposium (International) on Combustion*, pages 1207–1213, 1990.

[378] A. S. Tomlin, T. Turanyi, and M. J. Pilling. Chapter 4 mathematical tools for the construction, investigation and reduction of combustion mechanisms. In M.J. Pilling, editor, *Low-Temperature Combustion and Autoignition*, volume 35 of *Comprehensive Chemical Kinetics*, pages 293 – 437. Elsevier, 1997.

[379] R. S. Tranter, A. Raman, R. Sivaramakrishnan, and K. Brezinsky. Ethane oxidation and pyrolysis from 5 bar to 1000 bar: Experiments and simulation. *International Journal of Chemical Kinetics*, 37(5):306–331, 2005.

[380] J. Troe. Collisional energy transfer in thermal unimolecular reactions. *Ber. Bunsenges. Phys. Chem.*, 77:665, 1973.

[381] J. Troe and H. Gg. Wagner. Unimolekulare reaktionen in thermischen systemen. *Ber. Bunsenges. Phys. Chem.*, 71:937, 1967.

[382] T. Turanyi, A. S. Tomlin, and M. J. Pilling. On the error of the quasi-steady-state approximation. *The Journal of Physical Chemistry*, 97(1):163–172, 1993.

[383] S. R. Turns. *An Introduction to Combustion*. Mc Graw Hill, 3^{rd} edition, 2000.

[384] S. Umemoto, S. Kajitani, and S. Hara. Modeling of coal char gasification in coexistence of CO2 and H2O considering sharing of active sites. *Fuel*, 103(Supplement C):14 – 21, 2013.

[385] L. Vervisch und D. Roekaers, editor. *Best Practice Guide in Computational Fluid Dynamics of Turbulent Combustion*. ERCOFTAG, 2016.

[386] H.C. van de Hulst. *Light Scattering by Small Particles*. Dover Publications, Inc., 1981. Reprint of the John Wiley & Sons, Inc., New York, 1957 edition.

[387] S. N. P. Vegendla, D. Messig, S. Weise, and C. Hasse. Flamelet-based time-scale analysis of a high-pressure gasifier. *Energy & Fuels*, 25(9):3892–3899, 2011.

[388] H. Versteeg and W. Malalasekra. *An Introduction to Computational Fluid Dynamics: The Finite Volume Method*. 2007.

[389] D. Veynante and L. Vervisch. Turbulent Combustion Modeling. *Prog. Energy Combust. Sci.*, 28:193–266, 2002.

[390] S. Vyazovkin. *Isoconversional Kinetics of Thermally Stimulated Processes,*. Springer International Publishing Switzerland, 2015.

[391] S. Vyazovkin and D. Dollimore. Linear and nonlinear procedures in isoconversional computations of the activation energy of thermally induced reactions in solids. *J. Chem. Inf. Comp. Sci.*, 36:42–45, 1996.

[392] P.L. Walker, Jr., F. Rusinko, Jr., and L.G. Austin. Gas reactions of carbon. In P.W. Selwood D.D. Eley and Paul B. Weisz, editors, *Advances in Catalysis*, volume 11 of *Advances in Catalysis*, pages 133–221. Academic Press, 1959.

[393] T. F. Wall, G. Liu, H. Wu, D. G. Roberts, K. E. Benfell, S. Gupta, J. A. Lucas, and D.J. Harris. The effects of pressure on coal reactions during pulverized coal combustion and gasification. *Progress in Energy and Combustion Science*, 28(5):405–433, 2002.

[394] S. Wallin and A. V. Johansson. An Explicit Algebraic Reynolds Stress Model for Incompressible and Compressible Turbulent Flows. *J. Fluid Mechanics*, 403:89–132, 2000.

[395] D. K. Walters and D. Cokljat. A three-equation eddy-viscosity model for Reynolds-averaged Navier-Stokes simulations of transitional flows. *Journal of Fluids Engineering*, 130, 2008.

[396] L. Wang, Z. Liu, S. Chen, and C. Zheng. Comparison of different global combustion mechanisms under hot and diluted oxidation conditions. *Combustion Science and Technology*, 184(2):259–276, 2012.

[397] J. Warnatz, U. Maas, and R. Dibble. *Combustion: physical and chemical fundamentals, modelling and simulation, experiments, pullutant formation*. Springer, 3^{th} edition, 2006.

[398] R. Weber. Scaling characteristics of aerodynamics, heat transfer, and pollutant emissions in industrial flames. *Symposium (International) on Combustion*, 26(2):3343 – 3354, 1996.

[399] R. Weber. Energy efficient and environmentally friendly technologies for furnaces and boilers. technical concerns and expectations overseas. In *Forum on High Performance Industrial Furnaces and Boilers, Science Museum, Tokyo, Japan*, 1999.

[400] R. Weber. Combustion of natural gas, oil and coal with air preheated to temperatures in excess of 1000 ^{o}c. In *Proceedings of the 13th IFRF Members Conference*, Leeuwenhorst Congres Center, Noordwijkerhout, Netherlands, 5 2001. IFRF.

[401] R. Weber. Extracting mathematically exact kinetic parameters from experimental data on combustion and pyrolysis of solid fuels. *Journal of the Energy Institute*, 81:226–233, 2008.

[402] R. Weber, F. Boysan, and J. Swithenbank. Simulation of dispersion of heavy particles in confined turbulent flows. *AIChE Journal*, 30(3):S. 490–492, 1984.

[403] R. Weber, F. Boysan, J. Swithenbank, and P. A. Roberts. Computations of Near Field Aerodynamics of Swirling Expanding Flows. *The 21st Symposium (International) on Combustion. The Combustion Institute*, pages 1435–1443, 1986.

[404] R. Weber, T. Kupka, and K. Zając. Jet flames of a Refuse Derived Fuel. *Combustion and Flame*, 156(4):922–927, 2009.

[405] R. Weber and M. Mancini. On predicting char burnout in pulverized coal combustion. *Z. Phys. Chem*, 229(5):619–641, 2015.

[406] R. Weber, M. Mancini, N. Schaffel-Mancini, and T. Kupka. On predicting the ash behaviour using Computational Fluid Dynamics. *Fuel Processing Technology*, 105:113 – 128, 2013.

[407] R. Weber, S. Orsino, N. Lallemant, and A. Verlaan. Combustion of natural gas with high temperature air and large quantities of flue gas. *Proceedings of the Combustion Institute*, 28:1315–1321, 2000.

[408] R. Weber, A. A. F. Peters, P.P. Breithaoupt, and B. M. Visser. Mathematical modeling of swirling flames of pulverized coal: What can combustion engineers expect from modeling? *Journal of Fluid Engineering*, 117:289–297, 1995.

[409] R. Weber, N. Schaffel-Mancini, M. Mancini, and T. Kupka. Fly ash deposition modelling: Requirements for accurate predictions of particle impaction on tubes using RANS-based computational fluid dynamics. *Fuel*, 108:586 – 596, 2013.

[410] R. Weber, John P. Smart, and Willem vd Kamp. On the (MILD) combustion of gaseous, liquid, and solid fuels in high temperature preheated air. *Proceedings of the Combustion Institute*, 30(2):2623–2629, 2005.

[411] R. Weber, A. L. Verlaan, S. Orsino, and N. Lallemant. On Emerging Furnace Design Methodology that Provides Substantial Energy Savings and Drastic Reductions in CO2, CO and NOx Emissions. *J. of the Inst. Energy*, 72:S. 77–83, 1999.

[412] R. Weber, B. M. Visser, and F. Boysan. Assessement of turbulence modeling for engineering prediction of swirling vortices in near burner zone. *Int. J. Heat Fluid Flow*, 11:225–235, 1990.

[413] J. O. L. Wendt. Fundamental coal combustion mechanisms and pollutant formation in furnaces. *Prog. Energy Combust. Sci.*, 6:201–222, 1980.

[414] J. Werther, M. Saenger, E.-U. Hartge, T. Ogada, and Z. Siagi. Combustion of agricultural residues. *Progress in Energy and Combustion Science*, 26(1):1–27, 2000.

[415] Ch. K. Westbrook. Chemical kinetics of hydrocarbon ignition in practical combustion systems. *Proceedings of the Combustion Institute*, 28(2):1563 – 1577, 2000.

[416] Ch. K. Westbrook and F. L. Dryer. Simplified reaction mechanisms for the oxidation of hydrocarbon fuels in flames. *Combustion Science and Technology*, 27(1-2):31–43, 1981.

[417] Ch. K. Westbrook and F. L. Dryer. Chemical kinetic modeling of hydrocarbon combustion. *Progress in Energy and Combustion Science*, 10(1):1 – 57, 1984.

[418] C.K. Westbrook, Y. Mizobuchi, T.J. Poinsot, P.J. Smith, and J. Warnatz. Computational combustion. *Proc. Comb. Inst.*, 30(1):125 – 157, 2005.

[419] A. Wheeler. Reaction rates and selectivity in catalyst pores. In *Advances in Catalysis*, volume 3, pages 249–327. Academic Press, Inc, New York, 1951.

[420] B. Widom. Mean-first-passage times and the collision theory of bimolecular reactions. *J. Chem. Phys.*, 31:1387–1394, 1959.

[421] D.C. Wilcox. Re-assessment of the scale-determining equation for advanced turbulence models. *AIAA Journal*, 26(11):1299–1310, 1988.

[422] D.C. Wilcox. *Turbulence modeling for CFD*. DCW Industries, La Cañada, California, 1993.

[423] R. K. Wilk. *Low-Emission Combustion*. Wydawniktwo Politechniki Slaskiej, Gliwice, 2002.

[424] A. Williams, M. Pourkashanian, and J.M. Jones. Combustion of pulverised coal and biomass. *Progress in Energy and Combustion Science*, 27(6):587–610, 2001.

[425] F.A. Williams. *Combustion Theory*. Benjamin/Cummings Publishing Company, Inc., Menlo Park, CA, 1985.

[426] B. M. Wong, D. M. Matheu, and W. H. Green. Temperature and molecular size dependence of the high-pressure limit. *J. Phys. Chem. A*, 107:6206–6211, 2003.

[427] Mary J. Wornat, R. H. Hurt, Nancy Y.C. Yang, and T. J. Headley. Structural and compositional transformations of biomass chars during combustion. *Combustion and Flame*, 100(1-2):131–143, 1995.

[428] H. Wu, G. W. Bryant, K.E. Benfell, and T. F. Wall. An experimental study on the effect of system pressure on char structure of an australian bituminous coal. *Energy Fuels*, 14:282, 2000.

[429] J.-S. Wu, Y.-J. Liu, and H.-J. Sheen. Effects of ambient turbulence and fuel properties on the evaporation rate of single droplets. *International Journal of Heat and Mass Transfer*, 44(24):4593 – 4603, 2001.

[430] W.-C. Xu and A. Tomita. Effect of coal type on the flash pyrolysis of various coals. *Fuel*, 66(5):627 – 631, 1987.

[431] V. Yakhot and S. A. Orszag. Renormalization group analysis of turbulence: I. basic theory. *Journal of Scientific Computing*, 1(1):1–51, 1986.

[432] K. Yamagata, K. Nishikawa, S. Hasegawa, T. Fuji, and S. Yoshida. Forced convective heat transfer to supercritical water flowing in tubes. *Int. J. Heat Mass Transfer*, 15:2575–2593, 1972.

[433] S. Yaman. Pyrolysis of biomass to produce fuels and chemical feedstocks. *Energy Conversion and Management*, 45(5):651–671, 2004.

[434] R.A. Yetter, F.L. Dryer, and H. Rabitz. A comprehensive reaction mechanism for carbon monoxide hydrogen oxygen kinetics. *Combust. Sci. Tech.*, 79:97–128, 1991.

[435] M. J. Yu, S. W. Baek, and S. J. Kang. Modeling of Pulverized Coal Combustion with Non-Gray Gas Radiation Effects. *Combustion Science and Technology*, 166(1):151–174, 2001.

[436] D. Zabrodiec, J. Hees, A. Massmeyer, F. vom Lehn, M. Habermehl, O. Hatzfeld, and R. Kneer. Experimental investigation of pulverized coal flames in CO2/O2- and N2/O2-atmospheres: Comparison of solid particle radiative characteristics. *Fuel*, 201:136 – 147, 2017. 1st International Workshop on Oxy-Fuel Combustion.

[437] J. Zelkowski. *Kohlecharakterisierung und Kohleverbrennung*. VGB PowerTech Service GmbH, 2004.

[438] D. Zeng, M. Clark, T. Gunderson, W. C. Hecker, and T. H. Fletcher. Swelling properties and intrinsic reactivities of coal chars produced at elevated pressures and high heating rates. *Proceedings of the Combustion Institute*, 30(2):2213 – 2221, 2005.

[439] D. Zeng and T. H. Fletcher. Effects of Pressure on Coal Pyrolysis and Char Morphology. *Energy & Fuels*, 19(5):1828–1838, 2005.

[440] K. Zhao, P. Glarborg, and A. D. Jensen. NO reduction over biomass and coal char during simultaneous combustion. *Energy & Fuels*, 27(12):7817–7826, 2013.

[441] A. Zolin, A. D. Jensen, P. A. Jensen, and K. Dam-Johansen. Experimental study of char thermal deactivation. *Fuel*, 81(8):1065 – 1075, 2002.